Discovery of Novel Natural Products that Inhibit Eukaryotic Translation Initiation Factor 4E (eIF4E) Protein-Protein Interactions

by

Yihao Zhuang

A dissertation submitted in partial fulfillment
of the requirements for the degree of
Doctor of Philosophy
(Medicinal Chemistry)
in the University of Michigan
2023

Doctoral Committee:

Associate Professor Amanda L. Garner, Co-Chair
Associate Research Professor Ashootosh Tripathi, Co-Chair
Assistant Professor Roland Kersten
Professor David H. Sherman

Yihao Zhuang

peterzyh@umich.edu

ORCID iD: 0000-0002-4731-0730

Dedication

I would like to dedicate my work to my family. None of this would have been possible without their unwavering support and love.

Acknowledgments

I would like to thank Professor Amanda L. Garner and Professor Ashootosh Tripathi for their unwavering support and guidance throughout my Ph.D. career at the University of Michigan. I would like to thank my committee members, Professor David H. Sherman and Professor Roland Kersten for their advice and guidance. Also, I am deeply thankful for my fellow undergraduate students, graduate students, postdocs, and staff scientists with whom I had the honor of working within the Garner Group, Natural Product Discovery Core, and Sherman Group. Last but not least, I would like to thank my beloved cat, Jessie, for her unconditional companionship during the past three and a half years.

Table of Contents

List of Figures

List of Tables

List of Appendices

Abstract

In critically fatal diseases like cancer, the regulation of gene expression at the level of cap-dependent translation (CDT) initiation is crucial for tumor initiation and progression. The protein-protein interactions (PPIs) between eukaryotic translation initiation factor 4E (eIF4E), eIF4E- binding protein (4EBP1), and eukaryotic translation initiation factor 4G (eIF4G) regulate the initiation of CDT. As a result, they are therapeutic targets of interest. While small molecule inhibitors of eIF4E PPIs have been reported, these compounds exhibit modest potency and cellular target engagement remains to be demonstrated. Thus, we were driven to identify new scaffolds for inhibiting eIF4E PPIs.

Natural products have been invaluable sources of drug-like and lead-like molecules for developing front-line therapeutics against cancer, microbial infection, and parasites. We utilized our catalytic enzyme-linked click chemistry assay (cat-ELCCA) technology to perform a high-throughput screen (HTS) against full-length eIF4E PPIs using a marine natural product extract library (>34000 extracts). From this effort, we isolated monophenazine- and diphenazine-based natural products as inhibitors of eIF4E PPIs from an active strain *Streptomyces papuanewguineus*, leading to the discovery of a novel diphenazine, izumiphenazine E, which showed promising binding to eIF4E in cellular assays, representing a novel scaffold targeting eIF4E PPIs.

Discovery and structural elucidation of natural products structure available in infinitesimally small quantities is a recognized challenge. This challenge is epitomized by the diphenazine class of molecules which contain three bridged stereocenters, several conformations,

ring fusions, and multiple spatially-isolated phenols. Since empirical NMR and spatial analyses using ROESY/NOESY were unsuccessful in tackling these challenges, we developed a computational pipeline to determine the stereochemistry and phenol positions of diphenazines. In this pipeline, we incorporated electronic circular dichroism (ECD) and NMR calculations coupled with DP4+ probability measure, enabling the structural revision of phenazinolin D, izumiphenazine A, and baraphenazine G, and the structural characterization of two new diphenazines, baraphenazine H and izumiphenazine E. Importantly, through these efforts, we demonstrated the feasibility of NMR/DP4+ analysis for the determination of phenol positions in phenazine-based molecules, further expanding the limits of computational methods in the structural elucidation of complex natural products.

Chapter 1 Natural Products as Protein-Protein Interaction Modulators

Protein-protein interactions (PPI) are interactions between two identical or unique proteins at their domain interfaces that mediate the function of a protein complex.[1] The human interactome is predicted to contain 650,000 PPIs that regulate critical physiological and pathological processes, including signal transduction, cell growth, proliferation, and apoptosis among others.[2, 3] Because of the significance of PPIs, they have been potential drug targets for a broad range of therapeutic areas, including cancer,[4, 5] neglected tropical diseases,[6] central nervous system (CNS) disorders,[7] cardiovascular diseases,[8] and inflammation and oxidative stress.[9] Nevertheless, PPIs were commonly regarded as 'undruggable' twenty years ago. High-resolution crystal structures of protein complexes in the 1980s and 1990s revealed that PPI interfaces are usually flat, hydrophobic, and solvent-exposed with large (1,000-2,000 $Å^2$) buried surface areas (BSAs), which are in stark contrast to traditional targets such as enzyme active sites (~300-500 $Å^2$).[10-12] Furthermore, these surfaces lack endogenous small molecule ligands and contain very few grooves or pockets for potential exogenic small molecules to bind, which poses a challenge for designing small molecules as PPI modulators.[13]

Despite these challenges, promising signs emerged after 1995. With the advancement of genetics, kinetics, energetics, X-Ray crystallography, and computational tools, we now have a much deeper understanding of PPI structures and energetics, facilitating the discovery of potent PPI modulators. Mutagenesis studies on PPI interfaces revealed that the binding energy of a PPI is often not evenly distributed across the entire BSA of a PPI interface; instead, small 'hot spots'

confer most of the binding energy.[14] These hot spots tended to cluster at the center of the interface and cover about 250-900 Å^2 BSA,[15, 16] which is comparable to the BSA of a typical enzyme active site and the size of a small molecule.

Since the discovery of hot spots, significant effort has been put into the discovery of PPI-targeting molecules. For example, high-throughput screening (HTS) campaigns of small molecule libraries successfully identified nutlins,[17] benzodiazepinediones,[18] and chromenotriazolo-pyrimidines[19] as inhibitors of the mouse double minute 2 (MDM2)/p53 interaction in cancer. Since PPI interfaces often contain discontinuous hot spots, fragment-based drug discovery (FBDD) has also been proven to be a powerful method for identifying hot spot-binding low-complexity fragments which can be linked together to generate potent PPI modulators. FBDD approaches can be coupled with surface plasmon resonance (SPR), nuclear magnetic resonance (NMR), X-ray crystallography, and mass spectrometry (MS) for the discovery, validation, and optimization of linked hit fragments.[20] The iconic example of the success of FBDD in the discovery of PPI modulators is the development of the FDA-approved drug, Venetoclax (ABT-199), as an inhibitor of the B-cell lymphoma 2 (Bcl-2)/ Bcl-2-associated X protein (BAX) interaction for the treatment of chronic lymphocytic leukemia.[21, 22] Virtual screening campaigns have also yielded some success in discovering molecules that target the ubiquitin-conjugating enzyme Ubc13/Uev1,[23] MDM2/p53,[24] and T cell factor (TCF)/β-catenin interactions.[25]

Aside from synthetic small molecules, peptide-based PPI modulators have also been discovered through both HTS and rational structure-based design. Tirofiban, a clinically approved antagonist of integrin IIbIIIa, was designed to mimic the tripeptide Arg-Gly-Asp, the epitope of fibrinogen that binds to IIbIIIa.[26] Other primary structure peptide mimics that target

leukocyte function-associated antigen-1 (LFA-1),[27, 28] inhibitor of apoptosis proteins (IAPs),[29, 30] bromodomains,[31, 32] and HIV integrase PPIs[33] have also been advanced into clinical trials. Peptidomimetics that resemble secondary structure epitopes, including non-peptidic mimics and hydrocarbon-stapled peptide mimics, have also been reported as modulators of, for instance, MDM2-p53[34, 35] and Bcl-2/BAX[36, 37] interactions.

Besides synthetic molecules and peptidomimetics, another important source of PPI modulators is natural products. Often defined as compounds derived from natural sources, natural products have served as invaluable sources of drug-like and lead-like molecules that possess anticancer, antiviral, antibacterial, antimalarial, and parasiticidal activities. Importantly, a recent survey of all 259 FDA-approved small molecule anticancer drugs approved between 1946-2019 showed that 65% were either natural products or natural product mimics, indicating the overwhelming success of natural products in human pharmacopeia.[38] In fact, most of the earliest discovered PPI modulators were natural products, including taxanes and rapamycin.[11, 39] Interestingly, while synthetic molecules and rationally designed peptidomimetics often show inhibitory activities toward PPIs, natural products confer their activities mainly by stabilizing specific PPIs, either the interactions between two naturally bound proteins or proteins that do not normally bind to each other.[40] In the remainder of this chapter, I will review natural product-based PPI modulators, including their discoveries and mechanisms of action. These natural products will be classified according to their natural sources of isolation (bacteria, plants, fungi, etc.).

1.1 Natural Product-Based PPI Modulators Isolated from Plants

1.1.1 Taxanes

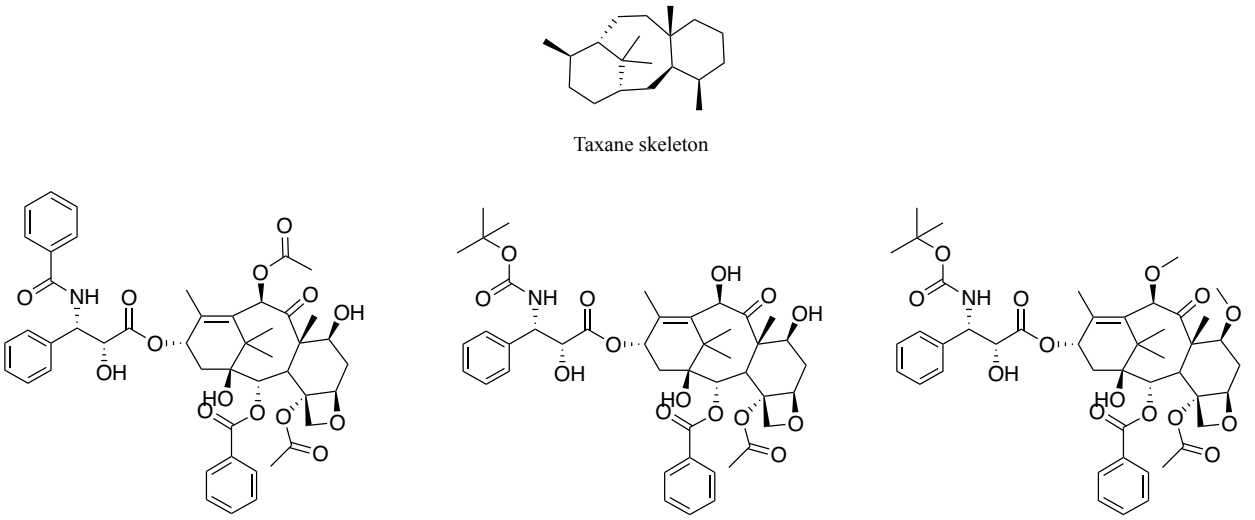

Figure 1. Structures of the taxane skeleton, paclitaxel, docetaxel, and cabazitaxel.

Taxanes are a group of diterpenoids isolated from Yews (*Taxus*) with a characteristic (1*S*,3*R*,4*R*,8*S*,11*S*,12*R*)-4,8,12,15,15-pentamethyltricyclo[9.3.1.03,8]pentadecane skeleton (**Figure 1**).[41] They represent one of the most well-known natural product-based anti-neoplastic agents in the past few decades. So far, there are three classes of taxanes available on the market, including Taxol, also known as PTX or paclitaxel, and two synthetic analogs of Taxol, DTX (docetaxel) and CTX (cabazitaxel, **Figure 1**).[41] In 1971, Taxol was isolated from an extract from the bark of *Taxus brevifolia* that showed antitumor activities.[42] It was approved by the FDA for the treatment of breast, pancreatic, ovarian, non-small-cell lung cancers, and Kaposi's sarcoma.[43] Despite its broad antitumor activities, the direct extraction from *T. brevifolia* could not economically support large-scale production, with each fully grown tree only yielding 0.5 g of Taxol.[44] As a result, a significant amount of effort has been put into developing economical chemical and bio-catalyzed synthetic and semi-synthetic strategies for the mass production of Taxol to meet the market's needs.[45-49] Hyper-production of Taxol (up to 1.6g/L) has also been

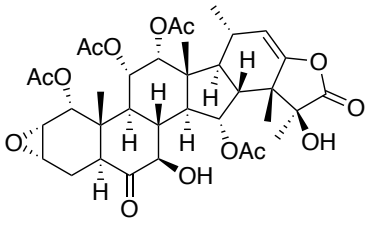

Taccalonolide A

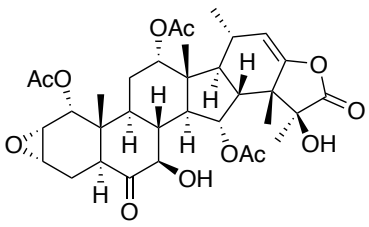

Taccalonolide E

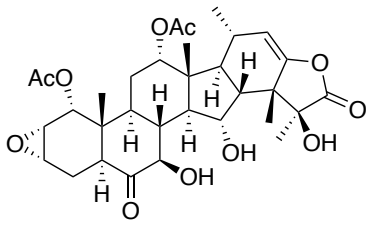

Taccalonolide N

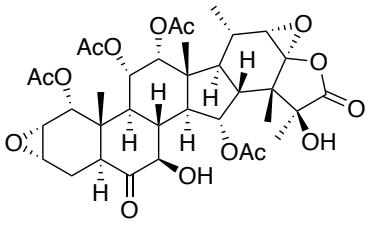

Taccalonolide AF

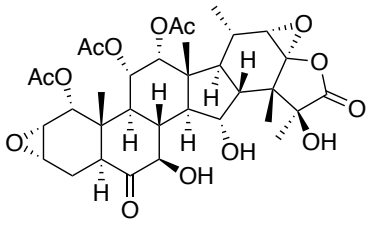

Taccalonolide AJ

Figure 2. Structures of representative taccalonolides.

conducted using fermentation of *Aspergillus fumigatus*, an endophytic fungus isolated from *Taxus sp.* of the Northern Himalayan region.[50]

The mechanistic target of Taxol was first described in studies by Schiff and co-workers in 1979.[51, 52] They found that Taxol promotes the aggregation of microtubules, resulting in the formation of stable, dysfunctional microtubules that lead to cell arrest in the G2/M phase.[51, 52] Microtubules, formed by the polymerization of heterodimers of α-tubulin and β-tubulin, are crucial in cell division for the formation of the mitotic spindle.[53] High-resolution co-crystal structures of microtubules and Taxol revealed that it binds to a hydrophobic allosteric pocket of β-tubulin with high affinity, suppressing microtubule dynamics and strengthening the lateral contacts of neighboring β-tubulin in the microtubule filament.[54-56] Taxol represents one of the first antimitotic agents isolated from nature.

1.1.2 Taccalonolides

Taccalonolides are highly acetylated pentacyclic steroids that were first isolated in 1963 when Scheuer and co-workers were investigating the 'bitter principle' from the starchy tubers of

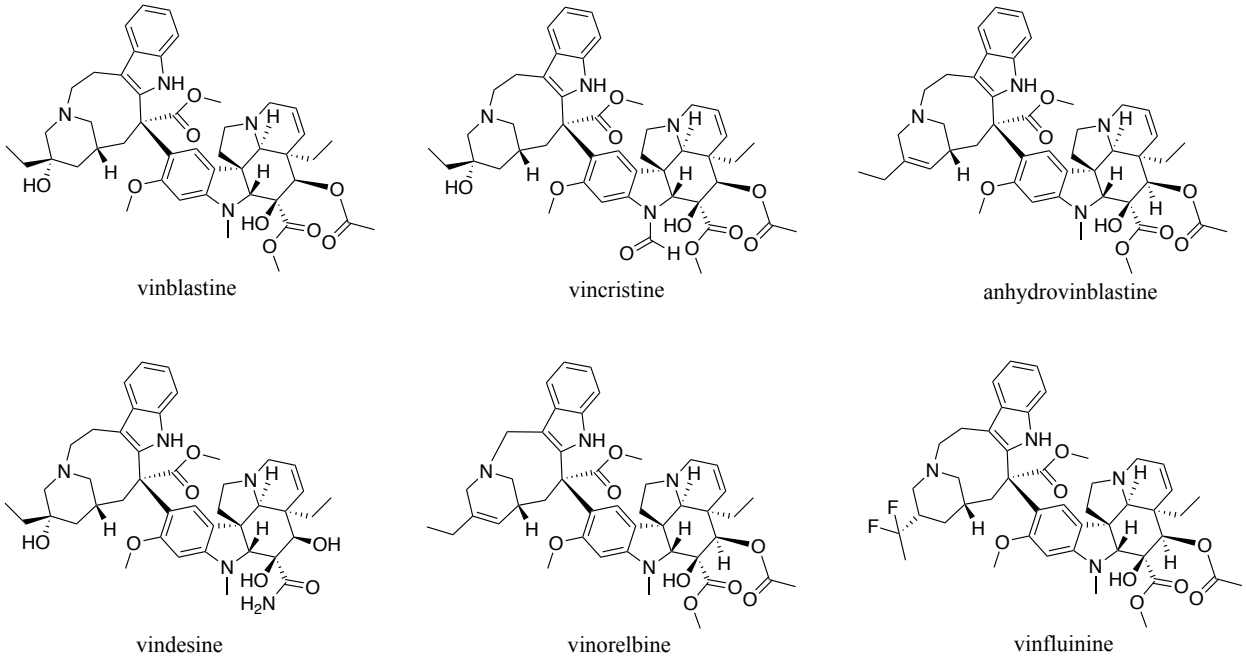

Figure 3. Structures of first-generation and selected semisynthetic derivatives of vinca alkaloids.

Tacca leontopetaloides.[57] So far, more than 40 natural taccalonolides have been isolated.[58] Taccalonolides A, E, and N were the first few derivatives of this class that were found to possess antiproliferative activities against drug-sensitive and multidrug-resistant cell lines via the stabilization of microtubule polymers (**Figure 2**).[59] Interestingly, taccalonolides AF and AJ (**Figure 2**), the two epoxidized derivatives of taccalonolides A, were shown to exhibit potent activity against Taxol-resistant tumors and a high degree of cellular persistence after drug washout, suggestive of a distinct mechanism of action from Taxol.[60, 61] Further investigations of the cocrystal structure of the AJ-tubulin complex revealed covalent binding between the C22-C23 epoxide in taccalonolide AJ and Asp226 of β-tubulin through an SN2 reaction mechanism, resulting in its enhanced binding and *in vivo* activity compared to taxanes.[62]

1.1.3 Vinca Alkaloids

Vinca alkaloids are another class of antimitotic and microtubule-targeting natural products first isolated from an antileukemic extract of the periwinkle plant, *Catharanthus*

roseus.[63] These compounds comprise two fragments, an upper catharanthine ring system connected to a lower vindoline ring system by a single bond (**Figure 3**). The first generation of vinca alkaloids includes vincaleukoblastine (later shortened to vinblastine),[64] and leurocristine (later shortened into vinblastine).[65] Vincristine is used in combination chemotherapy for the treatment of lymphoblastic leukemias and lymphomas whereas vinblastine is used in combination chemotherapy for the treatment of bladder and breast cancers.[66] Semisynthetic derivatives of first-generation vinca alkaloids including anhydrovinblastine,[67] vindesine,[68] vinorelbine,[69] and vinflunine (Javlor®)[70] have also been developed into clinical treatments against leukemia, NSCLC, bladder cancer, and breast cancer.

Mechanistic studies revealed that vinca alkaloids binds to β-tubulin near the GTP-binding site, altering the dimeric conformation, and inhibiting tubulin-dependent GTP hydrolysis and GTP-GDP exchange.[71] In stark contrast to taxanes and taccalonolides that act through microtubule stabilization, vinca alkaloids inhibit microtubule polymerization, arresting cell division at prometaphase.

1.1.4 Emodins

Emodin, named 1,3,8-trihydroxy-6-methyl anthraquinone, is an anthraquinone derivative

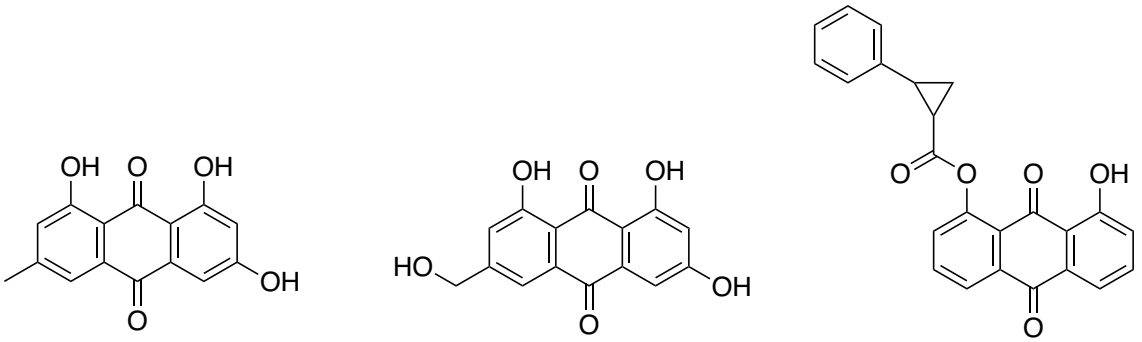

Figure 4. Structures of representative emodins.

isolated from various Chinese herbs, including *Rheum emodi*, *Polygonum cuspidatum*, *Polygonum multiflorum*, and *Aloe vera* (**Figure 4**).[72] Its close analog, aloe-emodin, named 1,8-dihydroxy-3-hydroxymethyl anthraquinone, was also reported to be isolated from similar sources.[73] This class of metabolites possesses a wide range of bioactivities, including laxative, antibacterial, and autoinflammatory effects.[72, 73]

Studies have revealed that the inflammatory activities of the emodin class of molecules rely on their interferences with nuclear factor kappa B (NF-κB) signaling pathways which play a crucial role in inflammation, immune responses, and cell survival and proliferation. Specifically, iNUB (**Figure 4**), an emodin analog, binds to NF-κB essential modulator, a scaffolding subunit of the IκB kinase complex that is required for NF-κB activation, and disrupts its interaction with methionine-1-linked linear ubiquitin chains, thereby inhibiting NF-κB signaling.[74]

Recently, the antiviral activity of emodin against coronaviruses such as SARS-CoV-2 was also described and it was formulated as one of the primary active components in antiviral Traditional Chinese Medicine (TCM), Lianhuaqingwen.[75, 76] Its antiviral activity resulted from its inhibition of the PPI between SARS-CoV spike protein (S) and angiotensin-converting enzyme 2 (ACE2) which is crucial for viral attachment to host cells for SARS-CoV infection.[77]

1.1.5 Forskolins

Forskolin, also known as colforsin, is a labdane diterpene isolated from *Coleus forskohlii* in 1977 as a blood pressure-lowering and cardioactive natural product (**Figure 5**).[78] Later, forskolin was found to confer its activity by increasing the level of the secondary messenger molecule cyclic adenosine monophosphate (cAMP) through the activation of adenylyl cyclase, a transmembrane enzyme that catalyzes the conversion of ATP to 3',5'-cyclic AMP and pyrophosphate.[79] It was found that forskolin activates adenylyl cyclase by stabilizing the binding

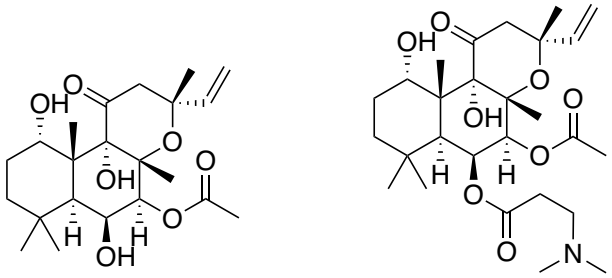

forskolin NKH477

Figure 5. Structures of forskolin and NKH477.

between the two cytoplasmic domains of this enzyme, the C1 and C2 subunits.[80] Later, crystallographic studies suggested that forskolin binds to a hydrophobic pocket at the rim of the dimer interface, stabilizing the interaction between the C1 and C2 subunits.[81, 82]

Despite its exciting activities, forskolin has poor water solubility, resulting in poor oral bioavailability. A few attempts at chemical derivatizations of forskolin focusing on improving its water solubility have been reported.[83-87] The most well-known example is NKH477, also known as colforsin dapropate hydrochloride (**Figure 5**). It is a potent, water-soluble forskolin derivative with a promising bronchodilator effect in humans and an inotropic effect in rats with chronic heart failure after myocardial infarction.[88-90]

1.1.6 Phytohormones: Auxins and Jasmonates

Phytohormones are signaling molecules produced within plants that control all plant growth and development aspects. Auxins, first isolated from oat coleoptile tip, were the first

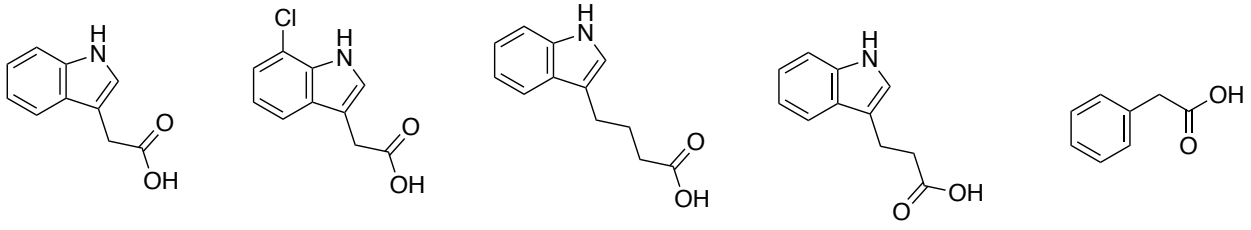

IAA 4Cl-IAA IBA IPA PAA

Figure 6. Structures of the five endogenous auxins.

significant plant hormones discovered. Five endogenous auxins include indole-3-acetic acid (IAA, **Figure 6**), the most important one of the family, 4-chloroindole-3-acetic acid (4Cl-IAA), phenylacetic acid (PAA), indole-3-butyric acid (IBA), and indole-3-propionic acid (IPA).[91] Auxin was found to target the transporter inhibitor response 1 (TIR1), an auxin-signaling F-box protein (ABF) that promotes ubiquitin-dependent proteolysis.[92] In the presence of auxin, TIR1 promotes the proteolytic degradation of the transcriptional repressor family Aux/IAA. Subsequently, it dissociates and activates auxin-responsive factors (ARFs), a transcription factor family that binds to Aux/IAA.[93] Later, crystallography studies revealed that auxin binds to TIR1, generates a new interface that allows the auxin/TIR1 complex binding with Aux/IAA, and thereby releases ARFs for auxin signaling.[94]

Jasmonates (JAs) are lipid-based plant hormones that are critical for the wound defense of plants.[95] Methyl jasmonate, the first of this class, was isolated from jasmine oil extracted from *Jasminum grandiflorum* (**Figure 7**).[96] The bioactive jasmonate, (3*R*,7*S*)-jasmonoyl-*L*-isoleucine (JA-Ile), showed a similar signaling mechanism as auxins.[97] It binds to the F-box protein, coronatine insensitive 1 (COI1), induces the binding between the JA-Ile/COI1 complex and the transcriptional repressor, jasmonate zinc-finger inflorescence meristem domain (JAZ), and releases the jasmonate-inducing transcriptional factor MYC2.[97]

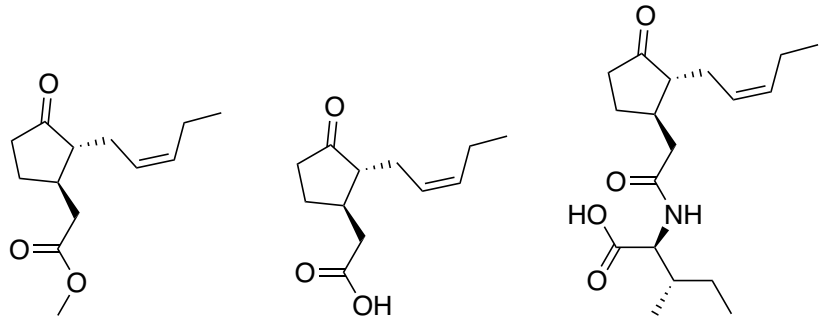

methyl JA JA JA-Ile

Figure 7. Structures of the three endogenous jasmonates.

1.2 Natural Product-Based PPI Modulators Isolated from Fungi

1.2.1 Chlorofusin

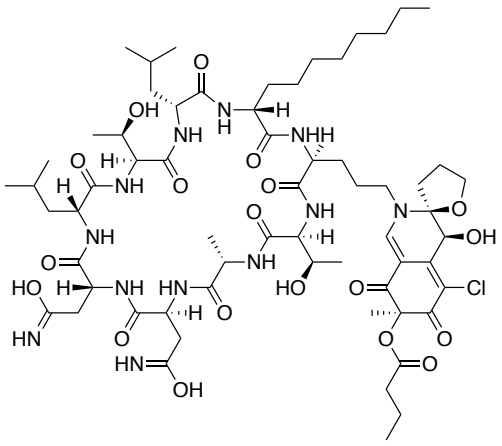

chlorofusin

Figure 8. Structure of chlorofusin.

p53, the 'guardian of the genome', is a potent tumor suppressor critical in regulating the cell cycle, stress signals, senescence, and apoptosis.[98] The *p53* gene is one of the most frequently mutated genes in cancer and it is mutated in nearly 50% of all cancers.[99] p53 is regulated by MDM2, an E3 ubiquitin ligase that functions as a crucial negative regulator of p53 through an autoregulatory feedback loop.[100] In this loop, MDM2 binds to p53 for ubiquitin-dependent degradation; p53 binds to the p2 promoter of the MDM2 gene and activates the expression of this protein; the increased level of MDM2 induces the negative feedback on p53, decreasing the level and activity of p53. Thus, when overexpressed in cancer cells, MDM2 promotes tumorigenesis by binding and inhibiting the tumor suppressor p53.[101]

A lot of effort has been put into targeting the p53-MDM2 PPI. Using structure-based design strategy and HTS methods, β-hairpin peptidomimetics,[102] chalcone derivatives (the base form chalcone was originally isolated from plants),[103] nutlins,[17] spiro-oxindoles,[104]

benzodiazepines,[18] and chromenotriazolo-pyrimidines[19] have been identified as p53-MDM2 PPI inhibitors. Besides peptide-based and small-molecule inhibitors, the fungal natural product chlorofusin (**Figure 8**), was also discovered as an inhibitor of p53/MDM2 PPI from a screen of over 53,000 microbial extracts.[105] It is an orange lipopeptide first isolated in 2001 from the fungal strain *Microdochium caespitosum* fermentation broth.[105] It consists of a fully functionalized, azaphilone-derived chromophore linked through ornithine to a cyclic peptide moiety composed of nine amino acids. Despite all the structural elucidation effort through NMR and chemical syntheses, the absolute stereochemistry of the two Asp residues could not be determined and was established to have opposite configurations (L and D).[106-108] It exhibits inhibitory activity against the p53/MDM2 PPI in ELISA with an IC_{50} of 4.6 μM[105] and direct binding to the N-terminus of MDM2 with a K_D of 4.7 μM in surface plasmon resonance (SPR) experiments.[109] Despite its promising activity, the molecular detail of this binding has yet to be reported.

1.2.2 Fusicoccanes: Fusicoccin A and Cotylenin A

Fusicoccin A (FCA, **Figure 9**), a wilting phytotoxin first isolated from the fungal parasite *Fusicoccum amygdali*, is a diterpenoid glycoside that possesses a 5-8-5 fusicoccane ring structure.[110] It was shown to bind to a complex between 14-3-3 proteins, a family of regulatory proteins, and the plasma membrane H^+-ATPase (PMA), stabilizing the PPI and activating the proton pump permanently.[111] 14-3-3 proteins bind to several hundreds of signaling proteins in eukaryotic cells, such as kinases, phosphatases, and transmembrane receptors, and directly inhibit or activate the activities of these target proteins.[112] Thorough examination of the co-crystal structure of FCA and 14-3-3/PMA complex revealed that FCA fills a hydrophobic gap at the interface of the two proteins, with the sugar moiety exposed to the solvent.[113] It was also

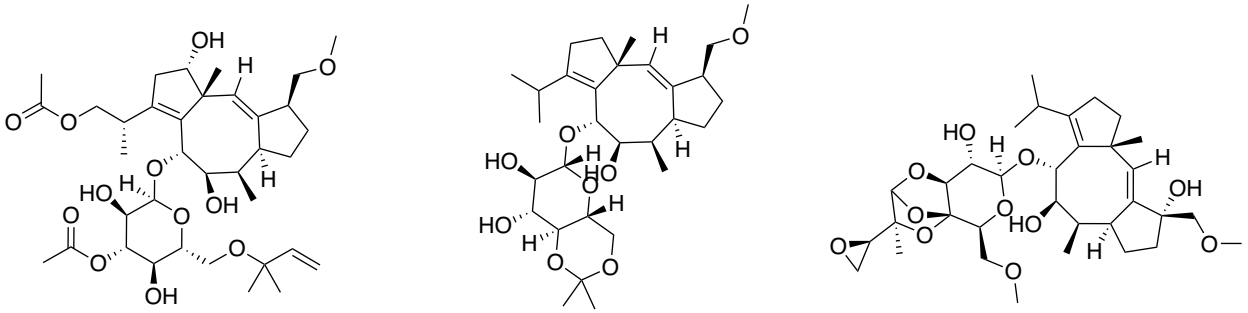

fusicoccin A FC-THF cotylenin A

Figure 9. Structures of representative fusicoccanes.

shown that the binding of FCA to the protein complex enhances the affinity of the two proteins by about 90-fold.[113] FCA can also stabilize the PPI between 14-3-3 with the F domain of estrogen receptor α (ERα) and inhibit the transcriptional activity of this nuclear receptor.[114] A semi-synthetic derivative of FCA, FC-THF (**Figure 9**), was shown to stabilize the PPI between 14-3-3 and a potassium channel, TWIK-related acid-sensitive K channel 3 (TASK3), enhancing the transport of TASK3 to the cell membrane and resulting in an increased level and activity of this ion channel.[115, 116]

Cotylenin A (CNA, **Figure 9**) is a derivative of FCA that was first isolated from the fungal strain *Cladosporium sp.* 501-7W and showed cytokinin-like activity in plants.[117] CNA has been shown to induce differentiation in murine and human myeloid leukemia cells and inhibit the proliferation of breast cancer cells.[118, 119] At the molecular level, it binds and stabilizes the protein complex of 14-3-3 and protein kinase C-Raf, thereby inhibiting the activity of C-Raf.[120] Interestingly, while CNA alone is not active in *RAS* mutant cancer models, the combined treatment with anti-EGFR (epidermal growth factor receptor) antibody and CNA synergistically repress tumor growth *in vitro* and *in vivo*, presenting a novel strategy for treating *RAS* mutant cancer.[120]

1.2.3 Chetomin

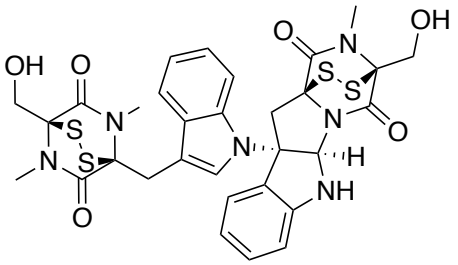

Chetomin

Figure 10. The structure of chetomin.

Chetomin is a dimeric epidithiodiketopiperazine first isolated from the fungus *Chaetomium cochliodes* (**Figure 10**).[121] Due to its complex structural features, no successful total synthesis of this natural product has yet been reported. Chetomin was discovered to inhibit the PPI between the hetero-dimeric transcription factor hypoxia-inducible factor 1 (HIF-1) and 300-kDa coactivator, p300, from an HTS campaign of over 600,000 synthetic and natural compounds.[122] Hypoxia, or decreased oxygen in the cellular environment, is an almost universal hallmark of solid tumors and adaptation of tumor cells to hypoxia is crucial for tumor survival and growth.[123] This adaptation is mainly achieved by activating the HIF-1 pathway, which also requires the binding of HIF-1α subunit to cAMP-response element binding protein (CBP)/p300 complex.[124] Overexpression of HIF-1 was associated with resistance to certain therapies and increased risk of metastasis.[125] Chetomin was found to bind to the CH1 domain of p300/CBP complex, inhibit the binding of HIF-1 to the protein complex, and thus deactivate the HIF-1-mediated signaling pathways.[122] Despite its promising submicromolar inhibitory activities against hypoxia-induced HIF-1 activation and downstream targets in both *in vitro* and *in vivo* assays, it suffers from high toxicity, which dampens the interest in further developing this scaffold.[122] So far, no co-crystal structure of the chetomin/p300 complex has been reported.

1.2.4 Brefeldin A

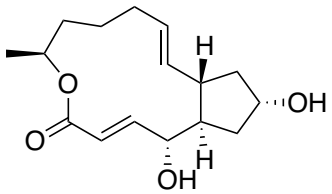

brefeldin A

Figure 11. The structure of brefeldin A.

Brefeldin A is an unsaturated macrolactone originally isolated from the fungal strain *Penicillium decumbens* in 1958 (**Figure 11**).[126] It is also produced by *Penicillium brefeldianum and Penicillium cyaneum*.[127, 128] The complete structural elucidation of brefeldin A was not accomplished until 1971 by Weber and co-workers.[129] Later, it was found to inhibit protein transport between the endoplasmic reticulum (ER) and the Golgi apparatus.[130] This transportation of proteins is regulated by the small guanine nucleotide-binding protein ADP ribosylation factor 1 (ARF1), which is involved in forming of transport vesicles.[131] Further biochemical and crystallography studies found that brefeldin A inhibits Golgi function by binding to guanine nucleotide exchange factors (ARF-GEFs) and stabilizing the PPI between this protein and ARF1.[132, 133] This stabilization results in the impairment of the GDP/GTP exchange activity of ARF-GEFs, thereby inhibiting Golgi function. Despite the modest IC_{50} of 15 μM of brefeldin A and only 10-fold increase in binding affinity of ARF-1 and ARF-GEF, a visible fusion of ER and Golgi already occurs minutes after the dosing of this molecule in cells, likely due to the underlying uncompetitive inhibition mode.[132] Because of this activity, brefeldin A has been widely used as a biology tool to study membrane trafficking and protein transportation in cells.[134]

1.2.5 Cyclosporin A

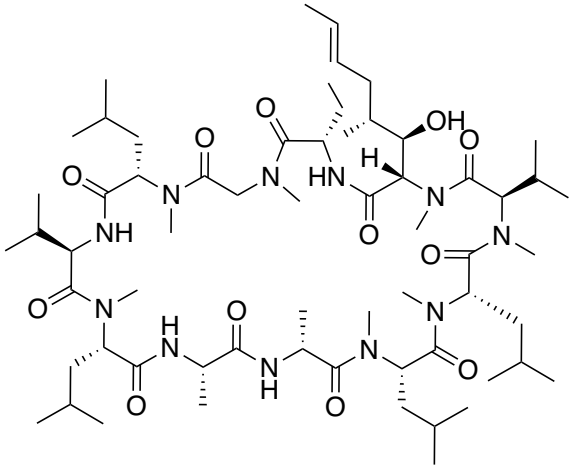

cyclosporin A

Figure 12. The structure of cyclosporin A.

Cyclosporin A (**Figure 12**) is a cyclic undecapeptide first isolated from ascomycete *Tolypocladium inflatum* in 1970 with immunosuppressive properties.[135] Its chemical structure was determined in 1976, containing several N-methylated peptide bonds and noncanonical amino acids aminobutyric acid, (4R)-4-[€-2-butenyl]-4,*N*-dimethyl-*L*-threonine (MeBmt) and *D*-alanine.[135] The FDA approved it to prevent transplant rejection in 1983.[136] As the active component of Neoral (Novartis), it is also used for treating patients with severe active rheumatoid arthritis. It has also been formulated into Apo-cyclosporin (Novartis) for treating steroid-dependent and steroid-resistant nephrotic syndrome. In addition, a cyclosporine ophthalmic emulsion (Verkazia) was approved by FDA in 2020 for the treatment of vernal keratoconjunctivitis in adults and children.

As an immunosuppressant, cyclosporin A was found to act on the immune system by inhibiting T-lymphocyte activation and lymphokine production.[137, 138] Later, the molecular target of cyclosporin A was found to be the peptidyl-prolyl isomerase, cyclophilin A (CypA).[139] As a 'molecular glue', cyclosporin A binds to CypA and this cyclosporin A/CypA complex can bind to and inhibit calcineurin (CaN), a calcium- and calmodulin-dependent serine/threonine

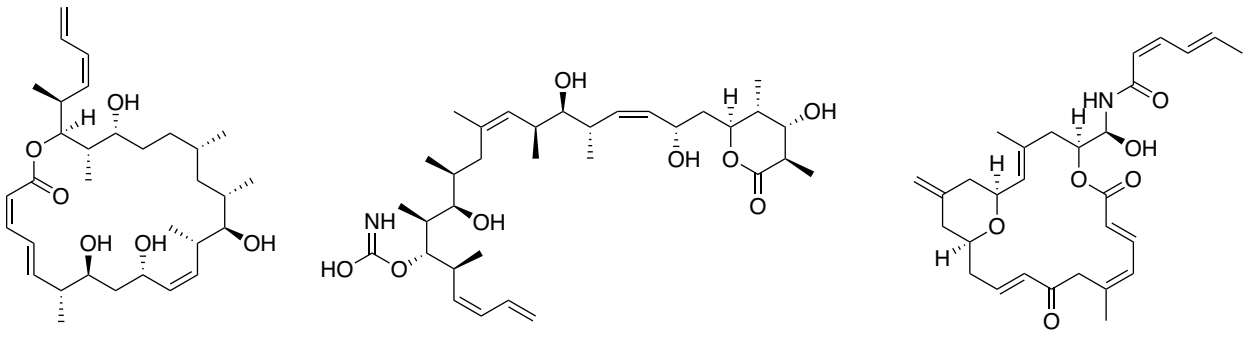

(-)-dictyostatin (+)-discodermolide (-)-zampanolide

Figure 13. Structures of microtubule-stabilizing macrolides isolated from marine sponges.

phosphatase.[140-142] As a critical enzyme in Ca^{2+}-dependent signal transduction pathways, CaN dephosphorylates and activates the transcription factor nuclear factor of activated T cells (NF-AT), which upregulates the transcription of cytokine signaling protein interleukin 2 (IL-2) and thereby activates T-cell responses.[143] As cyclosporin A/CypA complex binds to CaN, it inhibits the dephosphorylation of NF-AT by CaN and reduces T-cell responses in the adaptive immune system.[144]

1.3 Natural Product-Based PPI Modulators Isolated from Marine Sponges

1.3.1 Microtubule-stabilizing macrolides: (-)-dictyostatin, (-)-zampanolide, and (+)-discodermolide

Marine invertebrates have been fruitful sources of macrolactone-based microtubule targeting natural products. (-)-Dictyostatin is a 22-membered macrolactone first isolated from a marine sponge species *Spongia sp.* in 1986, collected from the Republic of Maldives, showing antiproliferative activities in cancer cells (**Figure 13**).[145] It has been shown to exhibit similar microtubule-stabilizing activity as the taxanes and bind to β-tubulin at the Taxol-binding site, but with higher binding affinity.[146, 147] Interestingly, it retained the antiproliferative activity against

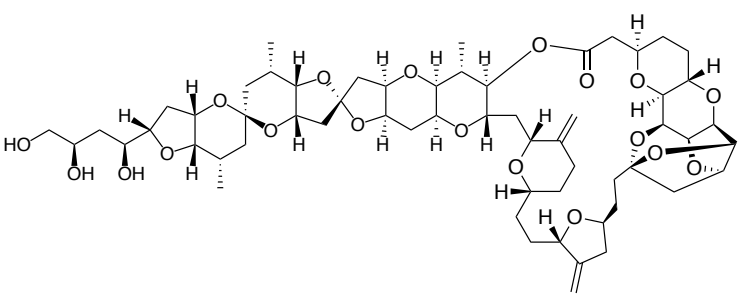

halichondrin B

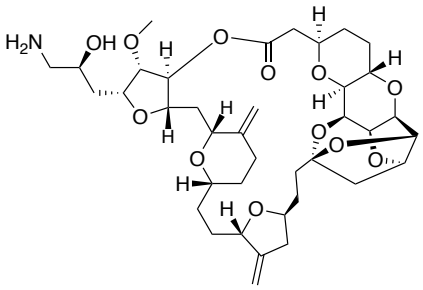

eribulin

Figure 14. The structure of halichondrin B.

human ovarian carcinoma cells resistant to Taxol due to β-tubulin mutations.[146] (-)-Zampanolide, another macrolactone, was first isolated from the marine sponge *Fasciospongia rimosa* in 1996 with anticancer activities (**Figure 13**).[148] Mechanistic studies suggested that it is another microtubule-stabilizing agent that can compete with Taxol for covalent binding to β-tubulin.[149, 150] (+)-Discodermolide, a polyhydroxylated lactone that shares great structural similarity to dictyostatin, was first isolated from a Caribbean marine sponge *Discodermia dissoluta* in 1990 as an immunosuppressive agent (**Figure 13**).[151] It was also found to stabilize microtubule polymers and compete with Taxol for its binding site on β-tubulin.[152] Interestingly, significant synergistic activity was found between Taxol and discodermolide in ovarian carcinoma xenograft-bearing mice, suggestive of potential combination therapy for ovarian carcinoma.[153]

1.3.2 Microtubule-destabilizing macrolides: halichondrin B and eribulin

Halichondrin B (**Figure 14**), an antitumor polyether macrolide, was first isolated from the marine sponge *Halichondria okadai* in 1986.[154] It is a microtubule-destabilizing natural product and it was shown to be a noncompetitive inhibitor of the binding of vinblastine to microtubules in the '60-cell line screen' project led by National Cancer Institute (NCI).[155] With significant mechanistic studies and total synthesis effort toward this scaffold, eribulin (**Figure 14**), the synthetic intermediate derivative of halichondrin B, was identified as a potential clinical

candidate for the treatment of cancer in 2004.[156] Eribulin was later shown to bind to a restricted range of high-affinity sites at the plus ends of microtubules, suppressing the dynamic instability at the plus end and inhibiting microtubule polymerization.[157] It was approved in 2010 by the FDA to treat patients with metastatic breast cancer who have received at least two prior chemotherapy regimens, including anthracycline- and taxane-based drugs, for late-stage cancers and also in 2016 to treat patients with unresectable or metastatic liposarcoma who have received anthracycline-containing regimens.[158]

1.4 Natural Product-Based PPI Modulators Isolated from Bacteria

1.4.1 Epothilones

Epothilone A and B belong to the epothilone class of macrolactone with a methylthiazole group (**Figure 15**). They were first isolated from the bacterial strain *Sorangium cellulosum* with antifungal and cytotoxic activities.[159] Their structures were first determined in 1996 using NMR and X-ray crystallography.[160] They exhibited a similar microtubule-stabilizing effect as Taxol and bind to tubulin on the same Taxol binding site.[161, 162] Compared to Taxol, epothilones have better solubility and less intracellular toxicity.[163] They also possess potent antiproliferative activity against Taxol-sensitive and P-glycoprotein (Pgp)-expressing multidrug-resistant cells.[162]

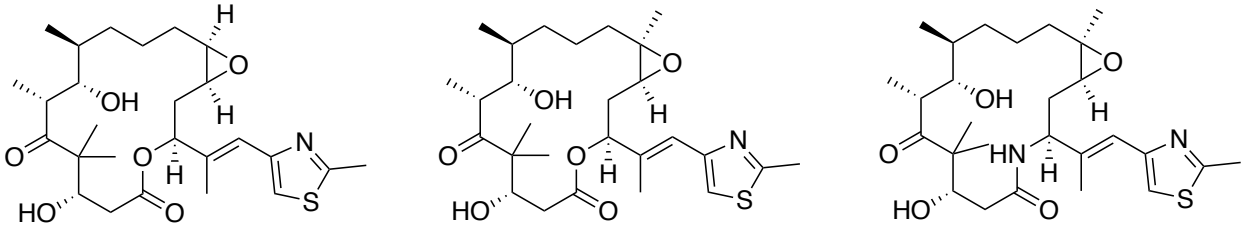

Figure 15. Structures of representative epothilone derivatives.

Because of their superior activities, a lot of effort has been devoted to this scaffold's chemical syntheses and derivatizations, enabling SAR investigations for structural optimization.[164, 165] Ixabepilone (**Figure 15**) was a semisynthetic lactam derivative of epothilone B developed by Bristol-Myers Squibb (BMS) with improved metabolic stability and pharmacokinetics compared to the parent compound.[166, 167] It was approved by the FDA in 2007 for the treatment of metastatic or locally advanced breast cancer in patients whose tumors are resistant to anthracyclines, taxanes, and capecitabine. Besides ixabepilone, other epothilone derivatives are currently being evaluated in Phase I, II, or III clinical trials, including Patupilone, BMS-247550, BMS-310705, Sagopilone, epothilone D, and KOS-1584.[168]

1.4.2 Tacrolimus (FK506)

Tacrolimus (**Figure 16**), also named FK506, is a 23-membered macrolactone first isolated from *Streptomyces tsukubaensis* in 1987.[169] The FDA approved it as an oral immunosuppressant for the prevention of liver, lung, kidney, and heart transplant rejection under the brand name Prograf®.[170] The molecular target of FK506 is the peptidyl-prolyl isomerase FK506 binding protein 12 (FKBP12).[171] Similar to cyclosporin A, FK506 binds to FKBP12 and

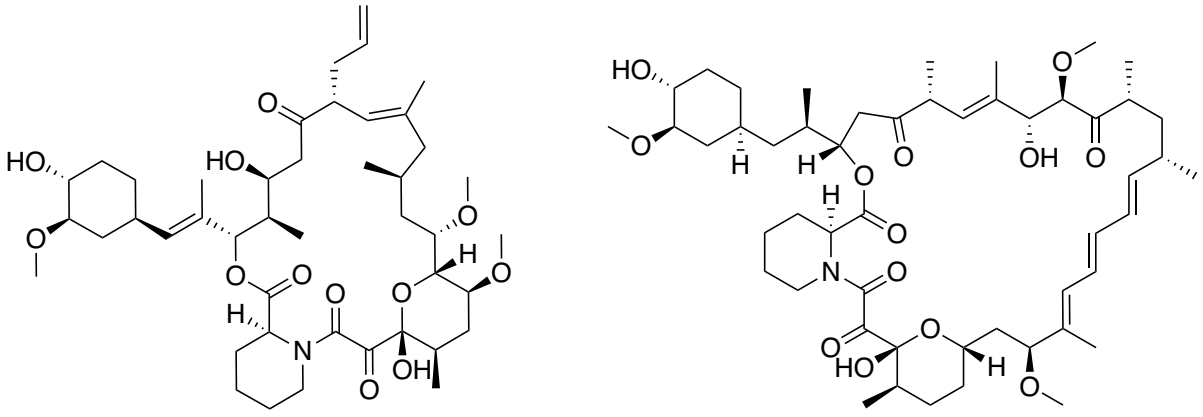

tacrolimus (FK506) rapamycin

Figure 16. Structures of tacrolimus (FK506) and rapamycin.

induces the binding of FK506/FKBP12 complex to calcineurin, which inhibits both IL-2 transcription and T-lymphocyte signaling.[172]

1.4.3 Rapamycin

Rapamycin (**Figure 16**) is an antifungal macrolactone first isolated in 1975 from *Streptomyces hygroscopicus* found on Rapa Nui island.[173] It was approved by the FDA in 1999 under the brand name Rapamune® for preventing renal transplant rejection. Similar to FK506, rapamycin binds to FKBP12 but instead of binding to calcineurin, the rapamycin/FKBP12 complex binds to and inhibits the mammalian target of rapamycin (mTOR).[174, 175] As the core component of two protein complexes mTOR complex 1 (mTORC1) and mTOR complex 2 (mTORC2), mTOR plays critical roles in the regulation of diverse cellular processes such as protein synthesis, cell growth, cell proliferation, and autophagy.[176] The role of mTOR in regulating protein translation initiation pathways will be further discussed in Chapter 2. Through the inhibition of mTOR, rapamycin inhibits IL-2 signal transduction and the activation of T cells in a similar manner to cyclosporin A and FK506.[177]

1.4.4 Manumycins: manumycin A and asukamycin

Manumycin A and asukamycin (**Figure 17**) belong to the manumycin class of polyketides with two unsaturated polyene chains linked by a six-membered ring. Manumycin A was first isolated in 1963 from *Streptomyces parvulus* and it was found to exhibit inhibitory activity against Ras farnesyltransferase in a microbial screening project in 1993.[178-180] Asukamycin was another manumycin first isolated in 1976 from *Streptomyces nodosus* subsp. *asukaensis* with a terminal cyclohexane moiety in the upper chain.[181, 182] Along with over 20 other manumycins isolated, this class of natural products exhibits potent activities against

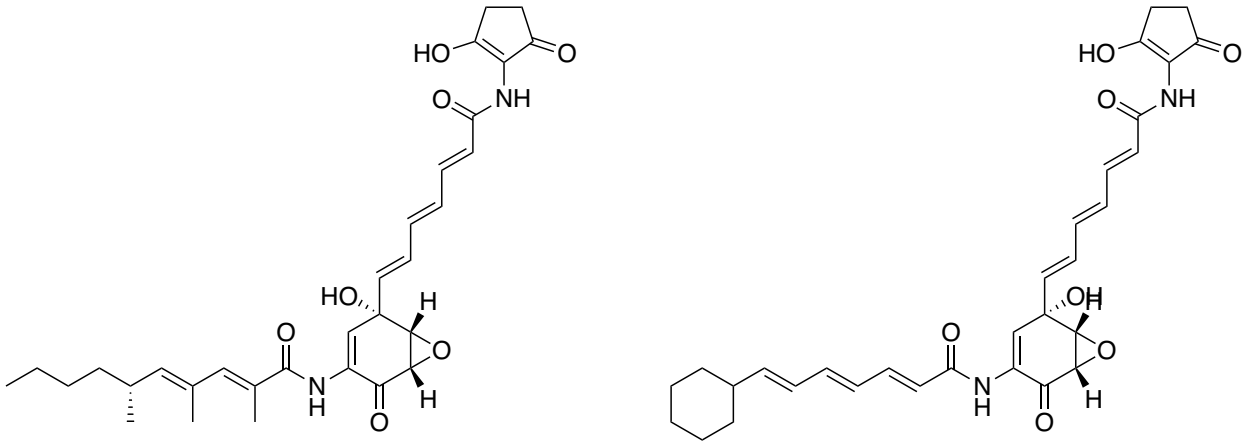

manumycin A asukamycin

Figure 17. Structures of manumycin A and asukamycin.

farnesyltransferase, interleukin-1β-converting enzymes, IκB kinase β, and acetylcholinesterase and are considered promising clinical candidates for treating cancers, inflammation, and Alzheimer disease.[183-186]

Recently, Isobe et al. postulated that multiple electrophilic moieties within the manumycin class of molecules could potentially react covalently with nucleophilic residues in proteins such as cysteines and form bifunctional or molecular glue-type interactions.[187] Using Activity-Based Protein Profiling (ABPP)-based chemoproteomic platforms, they demonstrated that one of the primary targets of asukamycin and manumycin A is Cys374 of E3 ubiquitin ligase UBR7. Asukamycin binds to UBR7 in breast cancer cells and the resulting complex engages in molecular glue interactions with the tumor suppressor p53, leading to the transcriptional activation of p53 and cell death. Both molecules can activate p53 activity more so than the anthracycline anticancer drug doxorubicin.

1.5 Conclusion

Natural products have been used for thousands of years for almost every aspect of our lives such as medicine, agriculture, and cosmetics. They can be derived from various natural sources including plants, bacterial and fungi fermentations, and even marine vertebrates. As reviewed in this chapter, natural products have been one of the most critical sources of modulators of 'undruggable' PPIs with disease relevance. Many of these natural product-based PPI modulators have been developed into FDA-approved drugs for treating lethal diseases. These successes have motivated us to search for potential natural product-based PPI inhibitors of the RNA-binding protein eIF4E in this work.

1.6 References

(1) Milroy, L. G.; Grossmann, T. N.; Hennig, S.; Brunsveld, L.; Ottmann, C. Modulators of Protein-Protein Interactions. *Chem Rev* **2014**, *114* (9), 4695-4748.

(2) Venkatesan, K.; Rual, J. F.; Vazquez, A.; Stelzl, U.; Lemmens, I.; Hirozane-Kishikawa, T.; Hao, T.; Zenkner, M.; Xin, X. F.; Goh, K. I.; et al. An empirical framework for binary interactome mapping. *Nat Methods* **2009**, *6* (1), 83-90.

(3) Stumpf, M. P. H.; Thorne, T.; de Silva, E.; Stewart, R.; An, H. J.; Lappe, M.; Wiuf, C. Estimating the size of the human interactome. *P Natl Acad Sci USA* **2008**, *105* (19), 6959-6964.

(4) Nero, T. L.; Morton, C. J.; Holien, J. K.; Wielens, J.; Parker, M. W. Oncogenic protein interfaces: small molecules, big challenges. *Nat Rev Cancer* **2014**, *14* (4), 248-262.

(5) Li, Z. G.; Ivanov, A. A.; Su, R. N.; Gonzalez-Pecchi, V.; Qi, Q.; Liu, S. L.; Webber, L. P.; McMillan, E.; Rusnak, L.; Pham, C.; et al. The OncoPPi network of cancer-focused protein-protein interactions to inform biological insights and therapeutic strategies (vol 8, 14356, 2017). *Nat Commun* **2017**, *8*.

(6) Dawidowski, M.; Emmanouilidis, L.; Kalel, V. C.; Tripsianes, K.; Schorpp, K.; Hadian, K.; Kaiser, M.; Maser, P.; Kolonko, M.; Tanghe, S.; et al. Inhibitors of PEX14 disrupt protein import into glycosomes and kill Trypanosoma parasites. *Science* **2017**, *355* (6332), 1416-+.

(7) Hayes, M. P.; Soto-Velasquez, M.; Fowler, C. A.; Watts, V. J.; Roman, D. L. Identification of FDA-Approved Small Molecules Capable of Disrupting the Calmodulin-Adenylyl Cyclase 8 Interaction through Direct Binding to Calmodulin. *Acs Chem Neurosci* **2018**, *9* (2), 346-357.

(8) Anand, P.; Brown, J. D.; Lin, C. Y.; Qi, J.; Zhang, R. L.; Artero, P. C.; Alaiti, M. A.; Bullard, J.; Alazem, K.; Margulies, K. B.; et al. BET Bromodomains Mediate Transcriptional Pause Release in Heart Failure. *Cell* **2013**, *154* (3), 569-582.

(9) Lu, M. C.; Tan, S. J.; Ji, J. A.; Chen, Z. Y.; Yuan, Z. W.; You, Q. D.; Jiang, Z. Y. Polar Recognition Group Study of Keap1-Nrf2 Protein-Protein Interaction Inhibitors. *Acs Med Chem Lett* **2016**, *7* (9), 835-840.

(10) Arkin, M. R.; Tang, Y. Y.; Wells, J. A. Small-Molecule Inhibitors of Protein-Protein Interactions: Progressing toward the Reality. *Chem Biol* **2014**, *21* (9), 1102-1114.

(11) Ran, X.; Gestwicki, J. E. Inhibitors of protein-protein interactions (PPIs): an analysis of scaffold choices and buried surface area. *Curr Opin Chem Biol* **2018**, *44*, 75-86.

(12) Fuller, J. C.; Burgoyne, N. J.; Jackson, R. M. Predicting druggable binding sites at the protein-protein interface. *Abstr Pap Am Chem S* **2009**, *238*.

(13) Buchwald, P. Small-Molecule Protein-Protein Interaction Inhibitors: Therapeutic Potential in Light of Molecular Size, Chemical Space, and Ligand Binding Efficiency Considerations. *Iubmb Life* **2010**, *62* (10), 724-731.

(14) Moreira, I. S.; Fernandes, P. A.; Ramos, M. J. Hot spots-A review of the protein-protein interface determinant amino-acid residues. *Proteins* **2007**, *68* (4), 803-812.

(15) Basse, M. J.; Betzi, S.; Bourgeas, R.; Bouzidi, S.; Chetrit, B.; Hamon, V.; Morelli, X.; Roche, P. 2P2Idb: a structural database dedicated to orthosteric modulation of protein-protein interactions. *Nucleic Acids Res* **2013**, *41* (D1), D824-D827.

(16) Smith, M. C.; Gestwicki, J. E. Features of protein-protein interactions that translate into potent inhibitors: topology, surface area and affinity. *Expert Rev Mol Med* **2012**, *14*.

(17) Vassilev, L. T.; Vu, B. T.; Graves, B.; Carvajal, D.; Podlaski, F.; Filipovic, Z.; Kong, N.; Kammlott, U.; Lukacs, C.; Klein, C.; et al. In vivo activation of the p53 pathway by small-molecule antagonists of MDM2. *Science* **2004**, *303* (5659), 844-848.

(18) Grasberger, B. L.; Lu, T. B.; Schubert, C.; Parks, D. J.; Carver, T. E.; Koblish, H. K.; Cummings, M. D.; LaFrance, L. V.; Milkiewicz, K. L.; Calvo, R. R.; et al. Discovery and cocrystal structure of benzodiazepinedione HDM2 antagonists that activate p53 in cells. *J Med Chem* **2005**, *48* (4), 909-912.

(19) Allen, J. G.; Bourbeau, M. P.; Wohlhieter, G. E.; Bartberger, M. D.; Michelsen, K.; Hungate, R.; Gadwood, R. C.; Gaston, R. D.; Evans, B.; Mann, L. W.; et al. Discovery and Optimization of Chromenotriazolopyrimidines as Potent Inhibitors of the Mouse Double Minute 2-Tumor Protein 53 Protein-Protein Interaction. *J Med Chem* **2009**, *52* (22), 7044-7053.

(20) Magee, T. V. Progress in discovery of small-molecule modulators of protein-protein interactions via fragment screening. *Bioorg Med Chem Lett* **2015**, *25* (12), 2461-2468.

(21) Oltersdorf, T.; Elmore, S. W.; Shoemaker, A. R.; Armstrong, R. C.; Augeri, D. J.; Belli, B. A.; Bruncko, M.; Deckwerth, T. L.; Dinges, J.; Hajduk, P. J.; et al. An inhibitor of Bcl-2 family proteins induces regression of solid tumours. *Nature* **2005**, *435* (7042), 677-681.

(22) Venetoclax (Venclexta) for Chronic Lymphocytic Leukemia. *Med Lett Drugs Ther* **2016**, *58* (1500), 101-102.

(23) Scheper, J.; Guerra-Rebollo, M.; Sanclimens, G.; Moure, A.; Masip, I.; Gonzalez-Ruiz, D.; Rubio, N.; Crosas, B.; Meca-Cortes, O.; Loukili, N.; et al. Protein-Protein Interaction Antagonists as Novel Inhibitors of Non-Canonical Polyubiquitylation. *Plos One* **2010**, *5* (6).

(24) Lawrence, H. R.; Li, Z. Y.; Yip, M. L. R.; Sung, S. S.; Lawrence, N. J.; McLaughlin, M. L.; McManus, G. J.; Zaworotko, M. J.; Sebti, S. M.; Chen, J. D.; et al. Identification of a disruptor of the MDM2-p53 protein-protein interaction facilitated by high-throughput in silico docking. *Bioorg Med Chem Lett* **2009**, *19* (14), 3756-3759.

(25) Tian, W.; Han, X. F.; Yan, M. C.; Xu, Y.; Duggineni, S.; Lin, N.; Luo, G. F.; Li, Y. M.; Han, X. B.; Huang, Z. W.; et al. Structure-Based Discovery of a Novel Inhibitor Targeting the beta-Catenin/Tcf4 Interaction. *Biochemistry-Us* **2012**, *51* (2), 724-731.

(26) Hartman, G. D.; Egbertson, M. S.; Halczenko, W.; Laswell, W. L.; Duggan, M. E.; Smith, R. L.; Naylor, A. M.; Manno, P. D.; Lynch, R. J.; Zhang, G. X.; et al. Nonpeptide Fibrinogen Receptor Antagonists .1. Discovery and Design of Exosite Inhibitors. *J Med Chem* **1992**, *35* (24), 4640-4642.

(27) Gadek, T. R.; Burdick, D. J.; McDowell, R. S.; Stanley, M. S.; Marsters, J. C.; Paris, K. J.; Oare, D. A.; Reynolds, M. E.; Ladner, C.; Zioncheck, K. A.; et al. Generation of an LFA-1 antagonist by the transfer of the ICAM-1 immunoregulatory epitope to a small molecule. *Science* **2002**, *295* (5557), 1086-1089.

(28) Zhong, M.; Gadek, T. R.; Bui, M.; Shen, W.; Burnier, J.; Barr, K. J.; Hanan, E. J.; Oslob, J. D.; Yu, C. H.; Zhu, J.; et al. Discovery and Development of Potent LFA-1/ICAM-1 Antagonist SAR 1118 as an Ophthalmic Solution for Treating Dry Eye. *Acs Med Chem Lett* **2012**, *3* (3), 203-206.

(29) Dubrez, L.; Berthelet, J.; Glorian, V. IAP proteins as targets for drug development in oncology. *Oncotargets Ther* **2013**, *6*, 1285-1304.

(30) Flygare, J. A.; Beresini, M.; Budha, N.; Chan, H.; Chan, I. T.; Cheeti, S.; Cohen, F.; Deshayes, K.; Doerner, K.; Eckhardt, S. G.; et al. Discovery of a Potent Small-Molecule Antagonist of Inhibitor of Apoptosis (IAP) Proteins and Clinical Candidate for the Treatment of Cancer (GDC-0152). *J Med Chem* **2012**, *55* (9), 4101-4113.

(31) Mirguet, O.; Gosmini, R.; Toum, J.; Clement, C. A.; Barnathan, M.; Brusq, J. M.; Mordaunt, J. E.; Grimes, R. M.; Crowe, M.; Pineau, O.; et al. Discovery of Epigenetic Regulator

I-BET762: Lead Optimization to Afford a Clinical Candidate Inhibitor of the BET Bromodomains. *J Med Chem* **2013**, *56* (19), 7501-7515.

(32) Gehling, V. S.; Hewitt, M. C.; Vaswani, R. G.; Leblanc, Y.; Cote, A.; Nasveschuk, C. G.; Taylor, A. M.; Harmange, J. C.; Audia, J. E.; Pardo, E.; et al. Discovery, Design, and Optimization of Isoxazole Azepine BET Inhibitors. *Acs Med Chem Lett* **2013**, *4* (9), 835-840.

(33) Fader, L. D.; Malenfant, E.; Parisien, M.; Carson, R.; Bilodeau, F.; Landry, S.; Pesant, M.; Brochu, C.; Morin, S.; Chabot, C.; et al. Discovery of BI 224436, a Noncatalytic Site Integrase Inhibitor (NCINI) of HIV-1. *Acs Med Chem Lett* **2014**, *5* (4), 422-427.

(34) Ray-Coquard, I.; Blay, J. Y.; Italiano, A.; Le Cesne, A.; Penel, N.; Zhi, J. G.; Heil, F.; Rueger, R.; Graves, B.; Ding, M. C.; et al. Effect of the MDM2 antagonist RG7112 on the P53 pathway in patients with MDM2-amplified, well-differentiated or dedifferentiated liposarcoma: an exploratory proof-of-mechanism study. *Lancet Oncol* **2012**, *13* (11), 1133-1140.

(35) Robinson, J. A. beta-Hairpin Peptidomimetics: Design, Structures and Biological Activities. *Accounts Chem Res* **2008**, *41* (10), 1278-1288.

(36) Tse, C.; Shoemaker, A. R.; Adickes, J.; Anderson, M. G.; Chen, J.; Jin, S.; Johnson, E. F.; Marsh, K. C.; Mitten, M. J.; Nimmer, P.; et al. ABT-263: A potent and orally bioavailable Bcl-2 family inhibitor. *Cancer Res* **2008**, *68* (9), 3421-3428.

(37) Muppidi, A.; Doi, K.; Edwardraja, S.; Drake, E. J.; Gulick, A. M.; Wang, H. G.; Lin, Q. Rational Design of Proteolytically Stable, Cell-Permeable Peptide-Based Selective Mcl-1 Inhibitors. *J Am Chem Soc* **2012**, *134* (36), 14734-14737.

(38) Newman, D. J.; Cragg, G. M. Natural Products as Sources of New Drugs over the Nearly Four Decades from 01/1981 to 09/2019. *J Nat Prod* **2020**, *83* (3), 770-803.

(39) Thiel, P.; Kaiser, M.; Ottmann, C. Small-Molecule Stabilization of Protein-Protein Interactions: An Underestimated Concept in Drug Discovery? *Angew Chem Int Edit* **2012**, *51* (9), 2012-2018.

(40) Giordanetto, F.; Schafer, A.; Ottmann, C. Stabilization of protein-protein interactions by small molecules. *Drug Discov Today* **2014**, *19* (11), 1812-1821.

(41) Mosca, L.; Ilari, A.; Fazi, F.; Assaraf, Y. G.; Colotti, G. Taxanes in cancer treatment: Activity, chemoresistance and its overcoming. *Drug Resist Update* **2021**, *54*.

(42) Wani, M. C.; Taylor, H. L.; Wall, M. E.; Coggon, P.; Mcphail, A. T. Plant Antitumor Agents .6. Isolation and Structure of Taxol, a Novel Antileukemic and Antitumor Agent from Taxus-Brevifolia. *J Am Chem Soc* **1971**, *93* (9), 2325-&.

(43) https://www.accessdata.fda.gov/drugsatfda_docs/label/2015/020262s051lbl.pdf (accessed Mar 13th 2023).

(44) Li, Y.; Zhang, G. J.; Pfeifer, B. A. Current and Emerging Options for Taxol Production. *Adv Biochem Eng Biot* **2015**, *148*, 405-425.

(45) Gennari, C.; Carcano, M.; Donghi, M.; Mongelli, N.; Vanotti, E.; Vulpetti, A. Taxol semisynthesis: A highly enantio- and diastereoselective synthesis of the side chain and a new method for ester formation at C-13 using thioesters. *J Org Chem* **1997**, *62* (14), 4746-4755.

(46) Holton, R. A.; Somoza, C.; Kim, H. B.; Liang, F.; Biediger, R. J.; Boatman, P. D.; Shindo, M.; Smith, C. C.; Kim, S. C.; Nadizadeh, H.; et al. First Total Synthesis of Taxol .1. Functionalization of the B-Ring. *J Am Chem Soc* **1994**, *116* (4), 1597-1598.

(47) Holton, R. A.; Kim, H. B.; Somoza, C.; Liang, F.; Biediger, R. J.; Boatman, P. D.; Shindo, M.; Smith, C. C.; Kim, S. C.; Nadizadeh, H.; et al. First Total Synthesis of Taxol .2. Completion of the C-Ring and D-Ring. *J Am Chem Soc* **1994**, *116* (4), 1599-1600.

(48) Kanda, Y.; Nakamura, H.; Umemiya, S.; Puthukanoori, R. K.; Appala, V. R. M.; Gaddamanugu, G. K.; Paraselli, B. R.; Baran, P. S. Two-Phase Synthesis of Taxol. *J Am Chem Soc* **2020**, *142* (23), 10526-10533.

(49) Kanda, Y.; Ishihara, Y.; Wilde, N. C.; Baran, P. S. Two-Phase Total Synthesis of Taxanes: Tactics and Strategies. *J Org Chem* **2020**, *85* (16), 10293-10320.

(50) Kumar, P.; Singh, B.; Thakur, V.; Thakur, A.; Thakur, N.; Pandey, D.; Chand, D. Hyper-production of taxol from Aspergillus fumigatus, an endophytic fungus isolated from Taxus sp. of the Northern Himalayan region. *Biotechnol Rep (Amst)* **2019**, *24*, e00395.

(51) Schiff, P. B.; Fant, J.; Horwitz, S. B. Promotion of Microtubule Assembly Invitro by Taxol. *Nature* **1979**, *277* (5698), 665-667.

(52) Schiff, P. B.; Horwitz, S. B. Taxol stabilizes microtubules in mouse fibroblast cells. *Proc Natl Acad Sci U S A* **1980**, *77* (3), 1561-1565.

(53) Desai, A.; Mitchison, T. J. Microtubule polymerization dynamics. *Annu Rev Cell Dev Bi* **1997**, *13*, 83-117.

(54) Nogales, E.; Wolf, S. G.; Khan, I. A.; Luduena, R. F.; Downing, K. H. Structure of Tubulin at 6.5 Angstrom and Location of the Taxol-Binding Site. *Nature* **1995**, *375* (6530), 424-427.

(55) Nogales, E.; Whittaker, M.; Milligan, R. A.; Downing, K. H. High-resolution model of the microtubule. *Cell* **1999**, *96* (1), 79-88.

(56) Lowe, J.; Li, H.; Downing, K. H.; Nogales, E. Refined structure of alpha beta-tubulin at 3.5 A resolution. *J Mol Biol* **2001**, *313* (5), 1045-1057.

(57) Scheuer, P. J.; Madamba, L. A.; Swanholm, C. E.; Hudgins, W. R. Constituents of Tacca Leontopetaloides. *Lloyd* **1963**, *26* (3), 133-&.

(58) Chen, X. Y.; Winstead, A.; Yu, H. T.; Peng, J. N. Taccalonolides: A Novel Class of Microtubule-Stabilizing Anticancer Agents. *Cancers* **2021**, *13* (4).

(59) Tinley, T. L.; Randall-Hlubek, D. A.; Leal, R. M.; Jackson, E. M.; Cessac, J. W.; Quada, J. C.; Hemscheidt, T. K.; Mooberry, S. L. Taccalonolides E and A: Plant-derived steroids with microtubule-stabilizing activity. *Cancer Res* **2003**, *63* (12), 3211-3220.

(60) Risinger, A. L.; Mooberry, S. L. Cellular studies reveal mechanistic differences between taccalonolide A and paclitaxel. *Cell Cycle* **2011**, *10* (13), 2162-2171.

(61) Risinger, A. L.; Li, J.; Bennett, M. J.; Rohena, C. C.; Peng, J.; Schriemer, D. C.; Mooberry, S. L. Taccalonolide Binding to Tubulin Imparts Microtubule Stability and Potent In Vivo Activity. *Cancer Res* **2013**, *73* (22), 6780-6792.

(62) Wang, Y.; Yu, Y.; Li, G. B.; Li, S. A.; Wu, C.; Gigant, B.; Qin, W.; Chen, H.; Wu, Y.; Chen, Q.; et al. Mechanism of microtubule stabilization by taccalonolide AJ. *Nat Commun* **2017**, *8*, 15787.

(63) Cutts, J. H.; Beer, C. T.; Noble, R. L. Biological Properties of Vincaleukoblastine, an Alkaloid in Vinca-Rosea Linn, with Reference to Its Antitumor Action. *Cancer Res* **1960**, *20* (7), 1023-1031.

(64) Noble, R. L.; Beer, C. T.; Cutts, J. H. Role of chance observations in chemotherapy: Vinca rosea. *Ann N Y Acad Sci* **1958**, *76* (3), 882-894.

(65) Svoboda, G. H.; Gorman, M.; Barnes, A. J., Jr.; Oliver, A. T. Alkaloids of Vinca rosea Linn. (Catharanthus roseus G. Don.) XII. Preparation and characterization of trace alkaloids. *J Pharm Sci* **1962**, *51*, 518-523.

(66) Kingston, D. G. Tubulin-interactive natural products as anticancer agents. *J Nat Prod* **2009**, *72* (3), 507-515.

(67) Ramnath, N.; Schwartz, G. N.; Smith, P.; Bong, D.; Kanter, P.; Berdzik, J.; Creaven, P. J. Phase I and pharmacokinetic study of anhydrovinblastine every 3 weeks in patients with refractory solid tumors. *Cancer Chemother Pharmacol* **2003**, *51* (3), 227-230.

(68) Joel, S. The comparative clinical pharmacology of vincristine and vindesine: does vindesine offer any advantage in clinical use? *Cancer Treat Rev* **1996**, *21* (6), 513-525.

(69) Gralla, R. J.; Gatzemeier, U.; Gebbia, V.; Huber, R.; O'Brien, M.; Puozzo, C. Oral vinorelbine in the treatment of non-small cell lung cancer: rationale and implications for patient management. *Drugs* **2007**, *67* (10), 1403-1410.

(70) Kruczynski, A.; Barret, J. M.; Etievant, C.; Colpaert, F.; Fahy, J.; Hill, B. T. Antimitotic and tubulin-interacting properties of vinflunine, a novel fluorinated Vinca alkaloid. *Biochem Pharmacol* **1998**, *55* (5), 635-648.

(71) Rai, S. S.; Wolff, J. Localization of the vinblastine-binding site on beta-tubulin. *J Biol Chem* **1996**, *271* (25), 14707-14711.

(72) Dong, X. X.; Fu, J.; Yin, X. B.; Cao, S. L.; Li, X. C.; Lin, L. F.; Huyiligeqi; Ni, J. Emodin: A Review of its Pharmacology, Toxicity and Pharmacokinetics. *Phytother Res* **2016**, *30* (8), 1207-1218.

(73) Dong, X. X.; Zeng, Y. W.; Liu, Y.; You, L. T.; Yin, X. B.; Fu, J.; Ni, J. Aloe-emodin: A review of its pharmacology, toxicity, and pharmacokinetics. *Phytother Res* **2020**, *34* (2), 270-281.

(74) Vincendeau, M.; Hadian, K.; Messias, A. C.; Brenke, J. K.; Halander, J.; Griesbach, R.; Greczmiel, U.; Bertossi, A.; Stehle, R.; Nagel, D.; et al. Inhibition of Canonical NF-kappa B Signaling by a Small Molecule Targeting NEMO-Ubiquitin Interaction. *Sci Rep-Uk* **2016**, *6*.

(75) Zhou, Y. D.; Hou, Y.; Shen, J. Y.; Huang, Y.; Martin, W.; Cheng, F. X. Network-based drug repurposing for novel coronavirus 2019-nCoV/SARS-CoV-2. *Cell Discov* **2020**, *6* (1).

(76) Li, R. F.; Hou, Y. L.; Huang, J. C.; Pan, W. Q.; Ma, Q. H.; Shi, Y. X.; Li, C. F.; Zhao, J.; Jia, Z. H.; Jiang, H. M.; et al. Lianhuaqingwen exerts anti-viral and anti-inflammatory activity against novel coronavirus (SARS-CoV-2) (vol 156, 104761, 2020). *Pharmacol Res* **2021**, *174*.

(77) Ho, T. Y.; Wu, S. L.; Chen, J. C.; Li, C. C.; Hsiang, C. Y. Emodin blocks the SARS coronavirus spike protein and angiotensin-converting enzyme 2 interaction. *Antivir Res* **2007**, *74* (2), 92-101.

(78) Bhat, S. V.; Bajwa, B. S.; Dornauer, H.; Souza, N. J. D.; Fehlhaber, H. W. Structures and Stereochemistry of New Labdane Diterpenoids from Coleus Forskohlii Briq. *Tetrahedron Lett* **1977**, (19), 1669-1672.

(79) Seamon, K. B.; Padgett, W.; Daly, J. W. Forskolin - Unique Diterpene Activator of Adenylate-Cyclase in Membranes and in Intact-Cells. *P Natl Acad Sci-Biol* **1981**, *78* (6), 3363-3367.

(80) Sunahara, R. K.; Dessauer, C. W.; Whisnant, R. E.; Kleuss, C.; Gilman, A. G. Interaction of G(s alpha) with the cytosolic domains of mammalian adenylyl cyclase. *J Biol Chem* **1997**, *272* (35), 22265-22271.

(81) Tesmer, J. J. G.; Sunahara, R. K.; Gilman, A. G.; Sprang, S. R. Crystal structure of the catalytic domains of adenylyl cyclase in a complex with G(s alpha).GTP gamma S. *Science* **1997**, *278* (5345), 1907-1916.

(82) Zhang, G. Y.; Liu, Y.; Ruoho, A. E.; Hurley, J. H. Structure of the adenylyl cyclase catalytic core (vol 386, pg 247, 1997). *Nature* **1997**, *388* (6638), 204-204.

(83) Bhat, S. V.; Dohadwalla, A. N.; Bajwa, B. S.; Dadkar, N. K.; Dornauer, H.; Desouza, N. J. The Antihypertensive and Positive Inotropic Diterpene Forskolin - Effects of Structural Modifications on Its Activity. *J Med Chem* **1983**, *26* (4), 486-492.

(84) Laurenza, A.; Khandelwal, Y.; Desouza, N. J.; Rupp, R. H.; Metzger, H.; Seamon, K. B. Stimulation of Adenylate-Cyclase by Water-Soluble Analogs of Forskolin. *Mol Pharmacol* **1987**, *32* (1), 133-139.

(85) Tatee, T.; Narita, A.; Narita, K.; Izumi, G.; Takahira, T.; Sakurai, M.; Fujita, A.; Hosono, M.; Yamashita, K.; Enomoto, K.; et al. Forskolin derivatives .1. Synthesis, and cardiovascular and adenylate cyclase-stimulating activities of water-soluble forskolins. *Chem Pharm Bull* **1996**, *44* (12), 2274-2279.

(86) Toya, Y.; Schwencke, C.; Ishikawa, Y. Forskolin derivatives with increased selectivity for cardiac adenylyl cyclase. *J Mol Cell Cardiol* **1998**, *30* (1), 97-108.

(87) Pinto, C.; Papa, D.; Hubner, M.; Mou, T. C.; Lushington, G. H.; Seifert, R. Activation and inhibition of adenylyl cyclase isoforms by forskolin analogs. *J Pharmacol Exp Ther* **2008**, *325* (1), 27-36.

(88) Sanbe, A.; Takeo, S. Effects of NKH477, a water-soluble forskolin derivative, on cardiac function in rats with chronic heart failure after myocardial infarction. *J Pharmacol Exp Ther* **1995**, *274* (1), 120-126.

(89) Morinobu, S.; Fujimaki, K.; Okuyama, N.; Takahashi, M.; Duman, R. S. Stimulation of adenylyl cyclase and induction of brain-derived neurotrophic factor and TrkB mRNA by NKH477, a novel and potent forskolin derivative. *J Neurochem* **1999**, *72* (5), 2198-2205.

(90) Wajima, Z.; Yoshikawa, T.; Ogura, A.; Imanaga, K.; Shiga, T.; Inoue, T.; Ogawa, R. Intravenous colforsin daropate, a water-soluble forskolin derivative, prevents thiamylal-fentanyl-induced bronchoconstriction in humans. *Crit Care Med* **2002**, *30* (4), 820-826.

(91) Simon, S.; Petrasek, J. Why plants need more than one type of auxin. *Plant Sci* **2011**, *180* (3), 454-460.

(92) Leyser, H. M.; Lincoln, C. A.; Timpte, C.; Lammer, D.; Turner, J.; Estelle, M. Arabidopsis auxin-resistance gene AXR1 encodes a protein related to ubiquitin-activating enzyme E1. *Nature* **1993**, *364* (6433), 161-164.

(93) Zenser, N.; Ellsmore, A.; Leasure, C.; Callis, J. Auxin modulates the degradation rate of Aux/IAA proteins. *Proc Natl Acad Sci U S A* **2001**, *98* (20), 11795-11800.

(94) Tan, X.; Calderon-Villalobos, L. I.; Sharon, M.; Zheng, C.; Robinson, C. V.; Estelle, M.; Zheng, N. Mechanism of auxin perception by the TIR1 ubiquitin ligase. *Nature* **2007**, *446* (7136), 640-645.

(95) Browse, J. Jasmonate passes muster: a receptor and targets for the defense hormone. *Annu Rev Plant Biol* **2009**, *60*, 183-205.

(96) Demole, E.; Lederer, E.; Mercier, D. Isolement Et Determination De La Structure Du Jasmonate De Methyle, Constituant Odorant Caracteristique De Lessence De Jasmin. *Helv Chim Acta* **1962**, *45* (2), 675-&.

(97) Sheard, L. B.; Tan, X.; Mao, H.; Withers, J.; Ben-Nissan, G.; Hinds, T. R.; Kobayashi, Y.; Hsu, F. F.; Sharon, M.; Browse, J.; et al. Jasmonate perception by inositol-phosphate-potentiated COI1-JAZ co-receptor. *Nature* **2010**, *468* (7322), 400-405.

(98) Brown, C. J.; Lain, S.; Verma, C. S.; Fersht, A. R.; Lane, D. P. Awakening guardian angels: drugging the p53 pathway. *Nat Rev Cancer* **2009**, *9* (12), 862-873.

(99) Shangary, S.; Wang, S. M. Small-Molecule Inhibitors of the MDM2-p53 Protein-Protein Interaction to Reactivate p53 Function: A Novel Approach for Cancer Therapy. *Annu Rev Pharmacol* **2009**, *49*, 223-241.

(100) Picksley, S. M.; Lane, D. P. The p53-mdm2 autoregulatory feedback loop: a paradigm for the regulation of growth control by p53? *Bioessays* **1993**, *15* (10), 689-690.

(101) Brown, D. R.; Thomas, C. A.; Deb, S. P. The human oncoprotein MDM2 arrests the cell cycle: elimination of its cell-cycle-inhibitory function induces tumorigenesis. *EMBO J* **1998**, *17* (9), 2513-2525.

(102) Fasan, R.; Dias, R. L.; Moehle, K.; Zerbe, O.; Vrijbloed, J. W.; Obrecht, D.; Robinson, J. A. Using a beta-hairpin to mimic an alpha-helix: cyclic peptidomimetic inhibitors of the p53-HDM2 protein-protein interaction. *Angew Chem Int Ed Engl* **2004**, *43* (16), 2109-2112.

(103) Stoll, R.; Renner, C.; Hansen, S.; Palme, S.; Klein, C.; Belling, A.; Zeslawski, W.; Kamionka, M.; Rehm, T.; Muhlhahn, P.; et al. Chalcone derivatives antagonize interactions between the human oncoprotein MDM2 and p53. *Biochemistry-Us* **2001**, *40* (2), 336-344.

(104) Ding, K.; Lu, Y.; Nikolovska-Coleska, Z.; Qiu, S.; Ding, Y.; Gao, W.; Stuckey, J.; Krajewski, K.; Roller, P. P.; Tomita, Y.; et al. Structure-based design of potent non-peptide MDM2 inhibitors. *J Am Chem Soc* **2005**, *127* (29), 10130-10131.

(105) Duncan, S. J.; Gruschow, S.; Williams, D. H.; McNicholas, C.; Purewal, R.; Hajek, M.; Gerlitz, M.; Martin, S.; Wrigley, S. K.; Moore, M. Isolation and structure elucidation of Chlorofusin, a novel p53-MDM2 antagonist from a Fusarium sp. *J Am Chem Soc* **2001**, *123* (4), 554-560.

(106) Desai, P.; Pfeiffer, S. S.; Boger, D. L. Synthesis of the chlorofusin cyclic peptide: assignment of the asparagine stereochemistry. *Org Lett* **2003**, *5* (26), 5047-5050.

(107) Lee, S. Y.; Clark, R. C.; Boger, D. L. Total synthesis, stereochemical reassignment, and absolute configuration of chlorofusin. *J Am Chem Soc* **2007**, *129* (32), 9860-+.

(108) Clark, R. C.; Lee, S. Y.; Searcey, M.; Boger, D. L. The isolation, total synthesis and structure elucidation of chlorofusin, a natural product inhibitor of the p53-MDM2 protein-protein interaction. *Nat Prod Rep* **2009**, *26* (4), 465-477.

(109) Duncan, S. J.; Cooper, M. A.; Williams, D. H. Binding of an inhibitor of the p53/MDM2 interaction to MDM2. *Chem Commun (Camb)* **2003**, (3), 316-317.

(110) Ballio, A.; Mauri, M.; Chain, E. B.; Deleo, P.; Tonolo, A.; Erlanger, B. F. Fusicoccin - New Wilting Toxin Produced by Fusicoccum Amygdali Del. *Nature* **1964**, *203* (494), 297-&.

(111) Oecking, C.; Eckerskorn, C.; Weiler, E. W. The fusicoccin receptor of plants is a member of the 14-3-3 superfamily of eukaryotic regulatory proteins. *FEBS Lett* **1994**, *352* (2), 163-166.

(112) Yang, X. W.; Lee, W. H.; Sobott, F.; Papagrigoriou, E.; Robinson, C. V.; Grossmann, J. G.; Sundstrom, M.; Doyle, D. A.; Elkins, J. M. Structural basis for protein-protein interactions in the 14-3-3 protein family. *P Natl Acad Sci USA* **2006**, *103* (46), 17237-17242.

(113) Wurtele, M.; Jelich-Ottmann, C.; Wittinghofer, A.; Oecking, C. Structural view of a fungal toxin acting on a 14-3-3 regulatory complex. *Embo Journal* **2003**, *22* (5), 987-994.

(114) De Vries-van Leeuwen, I. J.; da Costa Pereira, D.; Flach, K. D.; Piersma, S. R.; Haase, C.; Bier, D.; Yalcin, Z.; Michalides, R.; Feenstra, K. A.; Jimenez, C. R.; et al. Interaction of 14-3-3 proteins with the estrogen receptor alpha F domain provides a drug target interface. *Proc Natl Acad Sci U S A* **2013**, *110* (22), 8894-8899.

(115) Rajan, S.; Preisig-Muller, R.; Wischmeyer, E.; Nehring, R.; Hanley, P. J.; Renigunta, V.; Musset, B.; Schlichthorl, G.; Derst, C.; Karschin, A.; et al. Interaction with 14-3-3 proteins promotes functional expression of the potassium channels TASK-1 and TASK-3. *J Physiol* **2002**, *545* (1), 13-26.

(116) Anders, C.; Higuchi, Y.; Koschinsky, K.; Bartel, M.; Schumacher, B.; Thiel, P.; Nitta, H.; Preisig-Muller, R.; Schlichthorl, G.; Renigunta, V.; et al. A semisynthetic fusicoccane stabilizes a protein-protein interaction and enhances the expression of K+ channels at the cell surface. *Chem Biol* **2013**, *20* (4), 583-593.

(117) Sassa, T.; Tojyo, T.; Munakata, K. Isolation of a new plant growth substance with cytokinin-like activity. *Nature* **1970**, *227* (5256), 379.

(118) Asahi, K.; Honma, Y.; Hazeki, K.; Sassa, T.; Kubohara, Y.; Sakurai, A.; Takahashi, N. Cotylenin A, a plant-growth regulator, induces the differentiation in murine and human myeloid leukemia cells. *Biochem Biophys Res Commun* **1997**, *238* (3), 758-763.

(119) Kasukabe, T.; Okabe-Kado, J.; Kato, N.; Sassa, T.; Honma, Y. Effects of combined treatment with rapamycin and cotylenin A, a novel differentiation-inducing agent, on human breast carcinoma MCF-7 cells and xenografts. *Breast Cancer Res* **2005**, *7* (6), R1097-1110.

(120) Molzan, M.; Kasper, S.; Roglin, L.; Skwarczynska, M.; Sassa, T.; Inoue, T.; Breitenbuecher, F.; Ohkanda, J.; Kato, N.; Schuler, M.; et al. Stabilization of Physical RAF/14-3-3 Interaction by Cotylenin A as Treatment Strategy for RAS Mutant Cancers. *Acs Chem Biol* **2013**, *8* (9), 1869-1875.

(121) Waksman, S. A.; Bugie, E. Chaetomin, a New Antibiotic Substance Produced by Chaetomium cochliodes: I. Formation and Properties. *J Bacteriol* **1944**, *48* (5), 527-530.

(122) Kung, A. L.; Zabludoff, S. D.; France, D. S.; Freedman, S. J.; Tanner, E. A.; Vieira, A.; Cornell-Kennon, S.; Lee, J.; Wang, B.; Wang, J.; et al. Small molecule blockade of transcriptional coactivation of the hypoxia-inducible factor pathway. *Cancer Cell* **2004**, *6* (1), 33-43.

(123) Zhong, H.; De Marzo, A. M.; Laughner, E.; Lim, M.; Hilton, D. A.; Zagzag, D.; Buechler, P.; Isaacs, W. B.; Semenza, G. L.; Simons, J. W. Overexpression of hypoxia-inducible factor 1alpha in common human cancers and their metastases. *Cancer Res* **1999**, *59* (22), 5830-5835.

(124) Smith, T. G.; Robbins, P. A.; Ratcliffe, P. J. The human side of hypoxia-inducible factor. *Br J Haematol* **2008**, *141* (3), 325-334.

(125) Hockel, M.; Vaupel, P. Biological consequences of tumor hypoxia. *Semin Oncol* **2001**, *28* (2 Suppl 8), 36-41.

(126) Singleton, V. L.; Bohonos, N.; Ullstrup, A. J. Decumbin, a new compound from a species of Penicillium. *Nature* **1958**, *181* (4615), 1072-1073.

(127) Harri, E.; Tamm, C.; Sigg, H. P.; Stahelin, H.; Loeffler, W. Uber Die Isolierung Neuer Stoffwechselprodukte Aus Penicillium Brefeldianum Dodge. *Helv Chim Acta* **1963**, *46* (4), 1235-&.

(128) Betina, V.; Nemec, P.; Dobias, J.; Barath, Z. Cyanein, a new antibiotic from Penicillium cyaneum. *Folia Microbiol (Praha)* **1962**, *7*, 353-357.

(129) Weber, H. P.; Hauser, D.; Sigg, H. P. Structure of brefeldin A. *Helv Chim Acta* **1971**, *54* (8), 2763-2766.

(130) Perkel, V. S.; Miura, Y.; Magner, J. A. Brefeldin A inhibits oligosaccharide processing of glycoproteins in mouse hypothyroid pituitary tissue at several subcellular sites. *Proc Soc Exp Biol Med* **1989**, *190* (3), 286-293.

(131) Pasqualato, S.; Renault, L.; Cherfils, J. Arf, Arl, Arp and Sar proteins: a family of GTP-binding proteins with a structural device for 'front-back' communication. *EMBO Rep* **2002**, *3* (11), 1035-1041.

(132) Peyroche, A.; Antonny, B.; Robineau, S.; Acker, J.; Cherfils, J.; Jackson, C. L. Brefeldin A acts to stabilize an abortive ARF-GDP-Sec7 domain protein complex: involvement of specific residues of the Sec7 domain. *Mol Cell* **1999**, *3* (3), 275-285.

(133) Renault, L.; Guibert, B.; Cherfils, J. Structural snapshots of the mechanism and inhibition of a guanine nucleotide exchange factor. *Nature* **2003**, *426* (6966), 525-530.

(134) Anders, N.; Jurgens, G. Large ARF guanine nucleotide exchange factors in membrane trafficking. *Cell Mol Life Sci* **2008**, *65* (21), 3433-3445.

(135) Borel, J. F.; Feurer, C.; Gubler, H. U.; Stahelin, H. Biological Effects of Cyclosporin-a - New Antilymphocytic Agent. *Agents Actions* **1976**, *6* (4), 468-475.

(136) Stahelin, H. F. The history of cyclosporin A (Sandimmune) revisited: another point of view. *Experientia* **1996**, *52* (1), 5-13.

(137) Kalman, V. K.; Klimpel, G. R. Cyclosporin A inhibits the production of gamma interferon (IFN gamma), but does not inhibit production of virus-induced IFN alpha/beta. *Cell Immunol* **1983**, *78* (1), 122-129.

(138) Thomson, A. W.; Moon, D. K.; Nelson, D. S. Suppression of delayed-type hypersensitivity reactions and lymphokine production by cyclosporin A in the mouse. *Clin Exp Immunol* **1983**, *52* (3), 599-606.

(139) Handschumacher, R. E.; Harding, M. W.; Rice, J.; Drugge, R. J.; Speicher, D. W. Cyclophilin: a specific cytosolic binding protein for cyclosporin A. *Science* **1984**, *226* (4674), 544-547.

(140) Liu, J.; Farmer, J. D., Jr.; Lane, W. S.; Friedman, J.; Weissman, I.; Schreiber, S. L. Calcineurin is a common target of cyclophilin-cyclosporin A and FKBP-FK506 complexes. *Cell* **1991**, *66* (4), 807-815.

(141) O'Keefe, S. J.; Tamura, J.; Kincaid, R. L.; Tocci, M. J.; O'Neill, E. A. FK-506- and CsA-sensitive activation of the interleukin-2 promoter by calcineurin. *Nature* **1992**, *357* (6380), 692-694.

(142) Clipstone, N. A.; Crabtree, G. R. Identification of calcineurin as a key signalling enzyme in T-lymphocyte activation. *Nature* **1992**, *357* (6380), 695-697.

(143) Rusnak, F.; Mertz, P. Calcineurin: form and function. *Physiol Rev* **2000**, *80* (4), 1483-1521.

(144) Youn, T. J.; Piao, H.; Kwon, J. S.; Choi, S. Y.; Kim, H. S.; Park, D. G.; Kim, D. W.; Kim, Y. G.; Cho, M. C. Effects of the calcineurin dependent signaling pathway inhibition by cyclosporin A on early and late cardiac remodeling following myocardial infarction. *Eur J Heart Fail* **2002**, *4* (6), 713-718.

(145) Pettit, G. R.; Cichacz, Z. A.; Gao, F.; Boyd, M. R.; Schmidt, J. M. Isolation and Structure of the Cancer Cell-Growth Inhibitor Dictyostatin-1. *J Chem Soc Chem Comm* **1994**, (9), 1111-1112.

(146) Madiraju, C.; Edler, M. C.; Hamel, E.; Raccor, B. S.; Balachandran, R.; Zhu, G.; Giuliano, K. A.; Vogt, A.; Shin, Y.; Fournier, J. H.; et al. Tubulin assembly, taxoid site binding, and cellular effects of the microtubule-stabilizing agent dictyostatin. *Biochemistry-Us* **2005**, *44* (45), 15053-15063.

(147) Trigili, C.; Barasoain, I.; Sanchez-Murcia, P. A.; Bargsten, K.; Redondo-Horcajo, M.; Nogales, A.; Gardner, N. M.; Meyer, A.; Naylor, G. J.; Gomez-Rubio, E.; et al. Structural Determinants of the Dictyostatin Chemotype for Tubulin Binding Affinity and Antitumor Activity Against Taxane- and Epothilone-Resistant Cancer Cells. *ACS Omega* **2016**, *1* (6), 1192-1204.

(148) Tanaka, J.; Higa, T. Zampanolide, a new cytotoxic macrolide from a marine sponge. *Tetrahedron Lett* **1996**, *37* (31), 5535-5538.

(149) Field, J. J.; Singh, A. J.; Kanakkanthara, A.; Halafihi, T.; Northcote, P. T.; Miller, J. H. Microtubule-Stabilizing Activity of Zampanolide, a Potent Macrolide Isolated from the Tongan Marine Sponge Cacospongia mycofijiensis. *J Med Chem* **2009**, *52* (22), 7328-7332.

(150) Field, J. J.; Pera, B.; Calvo, E.; Canales, A.; Zurwerra, D.; Trigili, C.; Rodriguez-Salarichs, J.; Matesanz, R.; Kanakkanthara, A.; Wakefield, S. J.; et al. Zampanolide, a potent new microtubule-stabilizing agent, covalently reacts with the taxane luminal site in tubulin alpha,beta-heterodimers and microtubules. *Chem Biol* **2012**, *19* (6), 686-698.

(151) Gunasekera, S. P.; Gunasekera, M.; Longley, R. E.; Schulte, G. K. Discodermolide - a New Bioactive Polyhydroxylated Lactone from the Marine Sponge Discodermia-Dissoluta. *J Org Chem* **1990**, *55* (16), 4912-4915.

(152) Honore, S.; Kamath, K.; Braguer, D.; Horwitz, S. B.; Wilson, L.; Briand, C.; Jordan, M. A. Synergistic suppression of microtubule dynamics by discodermolide and paclitaxel in non-small cell lung carcinoma cells. *Cancer Res* **2004**, *64* (14), 4957-4964.

(153) Huang, G. S.; Lopez-Barcons, L.; Freeze, B. S.; Smith, A. B., 3rd; Goldberg, G. L.; Horwitz, S. B.; McDaid, H. M. Potentiation of taxol efficacy and by discodermolide in ovarian carcinoma xenograft-bearing mice. *Clin Cancer Res* **2006**, *12* (1), 298-304.

(154) Hirata, Y.; Uemura, D. Halichondrins - Antitumor Polyether Macrolides from a Marine Sponge. *Pure Appl Chem* **1986**, *58* (5), 701-710.

(155) Bai, R. L.; Paull, K. D.; Herald, C. L.; Malspeis, L.; Pettit, G. R.; Hamel, E. Halichondrin B and homohalichondrin B, marine natural products binding in the vinca domain of tubulin. Discovery of tubulin-based mechanism of action by analysis of differential cytotoxicity data. *J Biol Chem* **1991**, *266* (24), 15882-15889.

(156) Zheng, W.; Seletsky, B. M.; Palme, M. H.; Lydon, P. J.; Singer, L. A.; Chase, C. E.; Lemelin, C. A.; Shen, Y.; Davis, H.; Tremblay, L.; et al. Macrocyclic ketone analogues of halichondrin B. *Bioorg Med Chem Lett* **2004**, *14* (22), 5551-5554.

(157) Smith, J. A.; Wilson, L.; Azarenko, O.; Zhu, X.; Lewis, B. M.; Littlefield, B. A.; Jordan, M. A. Eribulin binds at microtubule ends to a single site on tubulin to suppress dynamic instability. *Biochemistry-Us* **2010**, *49* (6), 1331-1337.

(158) https://www.fda.gov/drugs/resources-information-approved-drugs/eribulin (accessed Mar 17th 2023).

(159) Höfle, G. B., N.; Gerth, K.; Reichenbach, H. Epothilones, Process for Preparing the Same and Their Use as Medicaments and as Plant Protecting Agents. Patent DE4138042, May 27, 1993.

(160) Hofle, G. H.; Bedorf, N.; Steinmetz, H.; Schomburg, D.; Gerth, K.; Reichenbach, H. Epothilone A and B - Novel 16-membered macrolides with cytotoxic activity: Isolation, crystal structure, and conformation in solution. *Angewandte Chemie-International Edition in English* **1996**, *35* (13-14), 1567-1569.

(161) Bollag, D. M.; McQueney, P. A.; Zhu, J.; Hensens, O.; Koupal, L.; Liesch, J.; Goetz, M.; Lazarides, E.; Woods, C. M. Epothilones, a new class of microtubule-stabilizing agents with a taxol-like mechanism of action. *Cancer Res* **1995**, *55* (11), 2325-2333.

(162) Kowalski, R. J.; Giannakakou, P.; Hamel, E. Activities of the microtubule-stabilizing agents epothilones A and B with purified tubulin and in cells resistant to paclitaxel (Taxol(R)). *J Biol Chem* **1997**, *272* (4), 2534-2541.

(163) Muhlradt, P. F.; Sasse, F. Epothilone B stabilizes microtubuli of macrophages like taxol without showing taxol-like endotoxin activity. *Cancer Res* **1997**, *57* (16), 3344-3346.

(164) Balog, A.; Meng, D. F.; Kamenecka, T.; Bertinato, P.; Su, D. S.; Sorensen, E. J.; Danishefsky, S. Total synthesis of (-)-epothilone A. *Angewandte Chemie-International Edition in English* **1996**, *35* (23-24), 2801-2803.

(165) Nicolaou, K. C.; He, Y.; Vourloumis, D.; Vallberg, H.; Roschangar, F.; Sarabia, F.; Ninkovic, S.; Yang, Z.; Trujillo, J. I. The olefin metathesis approach to epothilone A and its analogues. *J Am Chem Soc* **1997**, *119* (34), 7960-7973.

(166) Lee, F. Y. F.; Borzilleri, R.; Fairchild, C. R.; Kim, S. H.; Long, B. H.; Reventos-Suarez, C.; Vite, G. D.; Rose, W. C.; Kramer, R. A. BMS-247550: A novel epothilone analog with a mode of action similar to paclitaxel but possessing superior antitumor efficacy. *Clinical Cancer Research* **2001**, *7* (5), 1429-1437.

(167) Lee, F. Y. F.; Borzilleri, R.; Fairchild, C. R.; Kamath, A.; Smykla, R.; Kramer, R.; Vite, G. Preclinical discovery of ixabepilone, a highly active antineoplastic agent. *Cancer Chemoth Pharm* **2008**, *63* (1), 157-166.

(168) Zagouri, F.; Sergentanis, T. N.; Chrysikos, D.; Dimopoulos, M. A.; Bamias, A. Epothilones in epithelial ovarian, fallopian tube, or primary peritoneal cancer: a systematic review. *Oncotargets Ther* **2015**, *8*, 2187-2198.

(169) Kino, T.; Hatanaka, H.; Miyata, S.; Inamura, N.; Nishiyama, M.; Yajima, T.; Goto, T.; Okuhara, M.; Kohsaka, M.; Aoki, H.; et al. FK-506, a novel immunosuppressant isolated from a Streptomyces. II. Immunosuppressive effect of FK-506 in vitro. *J Antibiot (Tokyo)* **1987**, *40* (9), 1256-1265.

(170) https://www.fda.gov/drugs/news-events-human-drugs/fda-approves-new-use-transplant-drug-based-real-world-evidence (accessed Mar 19th 2023).

(171) Siekierka, J. J.; Hung, S. H.; Poe, M.; Lin, C. S.; Sigal, N. H. A cytosolic binding protein for the immunosuppressant FK506 has peptidyl-prolyl isomerase activity but is distinct from cyclophilin. *Nature* **1989**, *341* (6244), 755-757.

(172) Griffith, J. P.; Kim, J. L.; Kim, E. E.; Sintchak, M. D.; Thomson, J. A.; Fitzgibbon, M. J.; Fleming, M. A.; Caron, P. R.; Hsiao, K.; Navia, M. A. X-ray structure of calcineurin inhibited by the immunophilin-immunosuppressant FKBP12-FK506 complex. *Cell* **1995**, *82* (3), 507-522.

(173) Sehgal, S. N.; Baker, H.; Vezina, C. Rapamycin (AY-22,989), a new antifungal antibiotic. II. Fermentation, isolation and characterization. *J Antibiot (Tokyo)* **1975**, *28* (10), 727-732.

(174) Brown, E. J.; Albers, M. W.; Shin, T. B.; Ichikawa, K.; Keith, C. T.; Lane, W. S.; Schreiber, S. L. A mammalian protein targeted by G1-arresting rapamycin-receptor complex. *Nature* **1994**, *369* (6483), 756-758.

(175) Choi, J.; Chen, J.; Schreiber, S. L.; Clardy, J. Structure of the FKBP12-rapamycin complex interacting with the binding domain of human FRAP. *Science* **1996**, *273* (5272), 239-242.

(176) Hay, N.; Sonenberg, N. Upstream and downstream of mTOR. *Genes Dev* **2004**, *18* (16), 1926-1945.

(177) Gonzalez, J.; Harris, T.; Childs, G.; Prystowsky, M. B. Rapamycin blocks IL-2-driven T cell cycle progression while preserving T cell survival. *Blood Cells Mol Dis* **2001**, *27* (3), 572-585.

(178) Buzzetti, F.; Zahner, H.; Hutter, R.; Gaumann, E.; Neipp, L.; Prelog, V.; Kellerschierlein, W. Stoffwechselprodukte Von Mikroorganismen .41. Manumycin. *Pharm Acta Helv* **1963**, *38* (12), 871-&.

(179) Hara, M.; Akasaka, K.; Akinaga, S.; Okabe, M.; Nakano, H.; Gomez, R.; Wood, D.; Uh, M.; Tamanoi, F. Identification of Ras Farnesyltransferase Inhibitors by Microbial Screening. *P Natl Acad Sci USA* **1993**, *90* (6), 2281-2285.

(180) Tamanoi, F.; Esson, K.; Gomez, R.; Wood, D.; Uh, M.; Hara, M.; Akasaka, K.; Okabe, M.; Nakano, H. Identification of Ras Farnesyltransferase Inhibitors. *Faseb J* **1993**, *7* (7), A1049-A1049.

(181) Omura, S.; Kitao, C.; Tanaka, H.; Oiwa, R.; Takahashi, Y.; Nakagawa, A.; Shimada, M.; Iwai, Y. New Antibiotic, Asukamycin, Produced by Streptomyces. *J Antibiot* **1976**, *29* (9), 876-881.

(182) Kakinuma, K.; Ikekawa, N.; Nakagawa, A.; Omura, S. Structure of Asukamycin, a Possible Shunt Metabolite from 3-Dehydroquinic Acid in the Shikimate Pathway. *J Am Chem Soc* **1979**, *101* (12), 3402-3404.

(183) Sattler, I.; Thiericke, R.; Zeeck, A. The manumycin-group metabolites. *Nat Prod Rep* **1998**, *15* (3), 221-240.

(184) Shipley, P. R.; Donnelly, C. C.; Le, C. H.; Bernauer, A. D.; Klegeris, A. Antitumor activity of asukamycin, a secondary metabolite from the actinomycete bacterium Streptomyces nodosus subspecies asukaensis. *Int J Mol Med* **2009**, *24* (5), 711-715.

(185) Bernier, M.; Kwon, Y. K.; Pandey, S. K.; Zhu, T. N.; Zhao, R. J.; Maciuk, A.; He, H. J.; DeCabo, R.; Kole, S. Binding of manumycin A inhibits I kappa B kinase beta activity. *J Biol Chem* **2006**, *281* (5), 2551-2561.

(186) Zheng, Z. H.; Dong, Y. S.; Zhang, H.; Lu, X. H.; Ren, X.; Zhao, G.; He, J. G.; Si, S. Y. Isolation and characterization of N98-1272 A, B and C, selective acetylcholinesterase inhibitors from metabolites of an actinomycete strain. *J Enzyme Inhib Med Chem* **2007**, *22* (1), 43-49.

(187) Isobe, Y.; Okumura, M.; McGregor, L. M.; Brittain, S. M.; Jones, M. D.; Liang, X.; White, R.; Forrester, W.; McKenna, J. M.; Tallarico, J. A.; et al. Manumycin polyketides act as molecular glues between UBR7 and P53. *Nat Chem Biol* **2020**, *16* (11), 1189-1198.

Chapter 2 Bioactivity-Guided Discovery of Diphenazines as Inhibitors of eIF4E PPIs[†]

In critically fatal diseases like cancer, the regulation of gene expression at the level of translation initiation is paramount for proper control of cellular growth, proliferation, differentiation, and apoptosis. Dysregulation of mRNA translation is a hallmark of tumorigenesis and tumor progression across various cancer types.[1] Cap-dependent mRNA translation initiation (CDT) is regulated by the availability of eukaryotic translation initiation factor 4E (eIF4E, **Figure 18**).[2] eIF4E is an RNA-binding protein that plays two important roles in the initiation of cap-dependent translation: (1) it binds to the m^{7}GpppX-cap at the 5′ terminus of coding mRNAs to promote the assembly of the eIF4F translation initiation complex, and (2) it promotes the nuclear export of selected cap-dependent translation transcripts.[3-5] Based on the significance of these functions in maintaining cellular homeostasis, eIF4E is the rate-limiting translation factor and its overexpression has been shown to induce tumorigenesis across various cancer types.

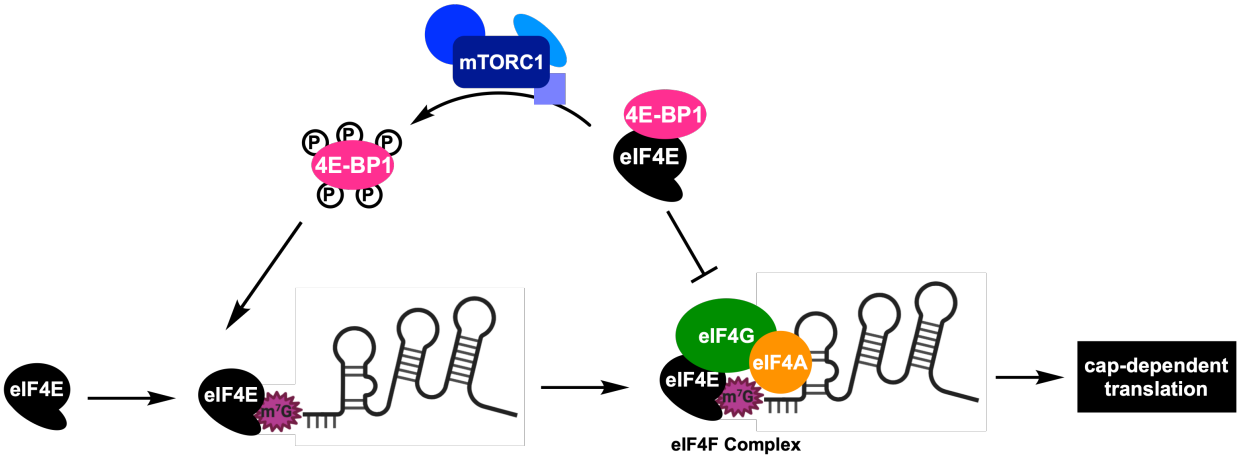

Figure 18.The mechanism of eIF4E-mediated cap-dependent translation initiation.

[†] This study has been submitted to Journal of Natural Products.

Because of the important nature of eIF4E, it is highly regulated, in part through protein-protein interactions (PPIs) with its negative regulator 4E binding protein 1 (4E-BP1), and eukaryotic translation initiation factor 4G (eIF4G), a scaffolding protein that aids the formation of the eIF4F translation initiation complex that drives cap-dependent translation.[6, 7] 4E-BP1 is regulated by mTORC1-mediated phosphorylation: hypophosphorylated 4E-BP1 binds strongly to eIF4E whereas hyperphosphorylation of 4E-BP1 at multiple sites (T37, T46, S65, T70) releases eIF4E, allowing the formation of the eIF4F complex and the initiation of cap-dependent mRNA translation.[8]

Significant effort has been put into developing inhibitors of eIF4E and its PPIs. The development of m^7G-cap-based antagonists has been extensively explored.[9, 10] Unfortunately, poor permeability has hindered the application of most of these compounds in cellular assays, including recent derivatives reported by Amgen and proteolysis targeting chimeras (PROTACs) developed by our group.[11, 12] In addition to m^7G-cap competitive ligands, small molecule inhibitors of eIF4E PPIs have also been reported, notably 4EGI-1 and 4E1RCat.[13, 14] However, cellular target engagement for these molecules remains to be demonstrated,[13] raising concern regarding their usage as chemical probes for targeting eIF4E. Based on the shortcomings of 4EGI-1 and 4E1RCat as eIF4E PPI inhibitors, our group worked toward the rational design and development of peptide inhibitors based on eIF4E's canonical protein-binding partners.[15-17] eIF4E forms PPIs with 4E-BP1 and eIF4G (Figure 1), whereby, each competes for the same binding site on eIF4E, establishing a competitive binding model for the initiation of cap-dependent translation.[18, 19] Although these peptides were very active in biochemical assays (IC_{50} values of ~3.1−6.7 nM), they showed significantly weaker activities in cells (low μM IC_{50}). This large discrepancy was likely due to limited cellular permeability of these highly charged

peptides. Thus, there remains a need for fully profiled small molecules targeting eIF4E and its PPIs so that rigorous validation can be performed in disease models for future clinical development. Based on the past successes of natural products in targeting PPIs as discussed in Chapter 1, we were eager to search within mother Nature for potential eIF4E PPI inhibitors.

2.1 High-Throughput Screening (HTS)

2.1.1 Development of PPI Cat-ELCCA

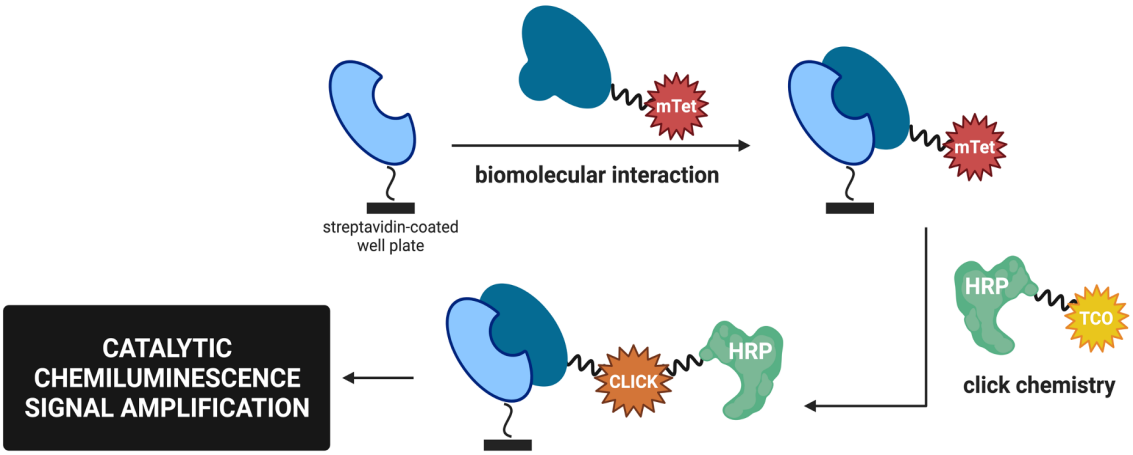

Figure 19. An illustration of PPI cat-ELCCA. mTet: methyl-tetrazine; TCO: *trans*-cyclooctene; HRP: horseradish peroxidase.

We recently developed catalytic enzyme-linked click chemistry assay (cat-ELCCA) technology for enabling the screening of full-length PPIs, including the interaction of eIF4E with 4E-BP1 and eIF4G (**Figure 19**).[20, 21] In this assay, a biotinylated protein is immobilized in the wells of a streptavidin-coated microtiter plate. The wells are then incubated with a methyl-tetrazine (mTet)-labeled protein-binding partner to form the PPI. Detection occurs via an initial inverse electron demand Diels-Alder (IEDDA) click reaction with trans-cyclooctene (TCO)-labeled horseradish peroxidase (HRP), followed by the addition of an HRP substrate. Unlike

traditional fluorescent-based assays such as FRET and fluorescence polarization, cat-ELCCA relies on chemiluminescence measurement of the reaction between HRP and HRP substrate. As a result, it is not subject to compound interference by colored or fluorescent compounds that typically litter natural product extract (NPE) libraries, thereby minimizing false positives encountered in screening.

Using this approach, we developed a miniaturized cat-ELCCA in 384-well format amenable to automated liquid handling for high-throughput screening (HTS).[22] HTS-compatible PPI cat-ELCCA was subsequently employed to perform a proof-of-concept HTS against commercial fragment libraries (~3,000 compounds).[22] Based on the success of NPs in targeting

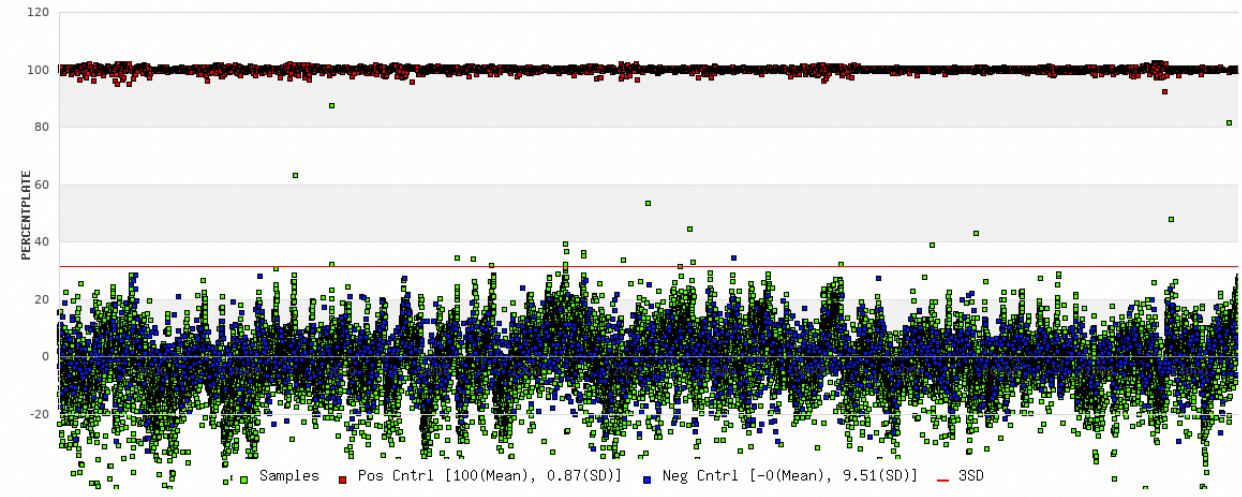

Compound	K_d (μM)	IC_{50} (μM)	n_H
W000116041_P20	5.2 ± 0.2	177.8	-0.9
W000112230_B11	4.5 ± 0.6	162	-0.4
W000112312_E10	12 ± 3	263	-1.0
W000112300_J06	N/A	102	-1.7
W000112312_N14	N/A	35	-0.5
W000112264_O12	N/A	60	-0.74
W000112226_D10	5.1 ± 0.6	123	-0.8
W000112304_I16	13 ± 2	110	-1.1
W000116059_D13	5.1 ± 0.9	100	-0.9

Figure 20.HTS campaign overview of the BIC library. N=20793, Z'=0.7; red dots: positive controls; blue dots: negative controls; green dots: samples tested in the screen; red line represents the 3 × standard deviation value; hit compound, K_d , IC_{50}, and Hill Slope listed in the table.

"undruggable" proteins like eIF4E and its PPIs,[23] coupled with the demonstrated applicability of cat-ELCCA for screening small-molecules as well as complex NPE libraries,[24] we were eager to deploy this assay technology to complete a larger HTS campaign to identify small-molecule and NP-based inhibitors of eIF4E PPIs.

2.1.2 PPI Cat-ELCCA-Based HTS

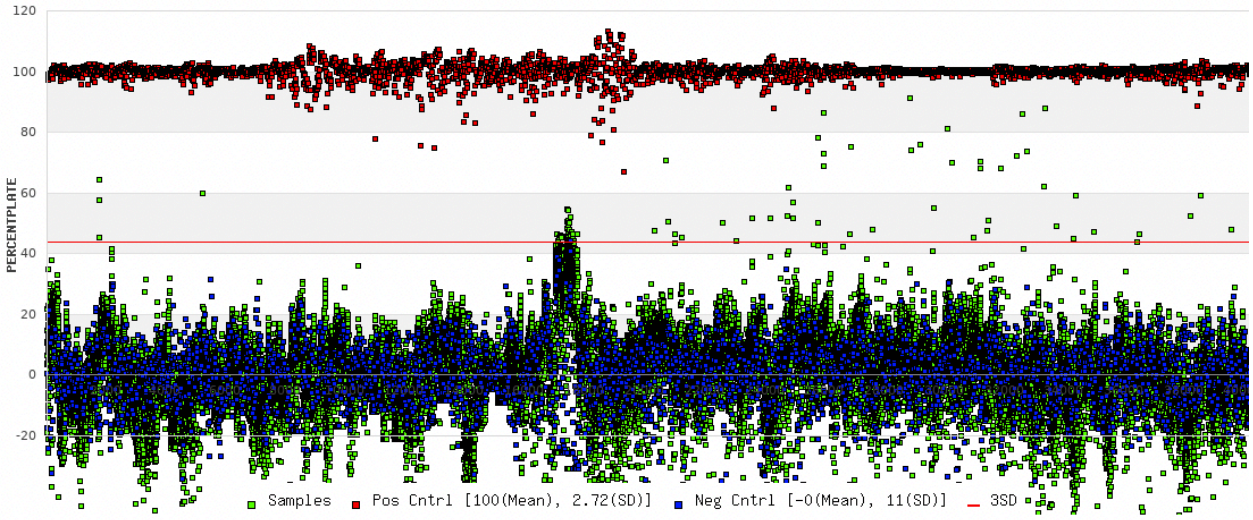

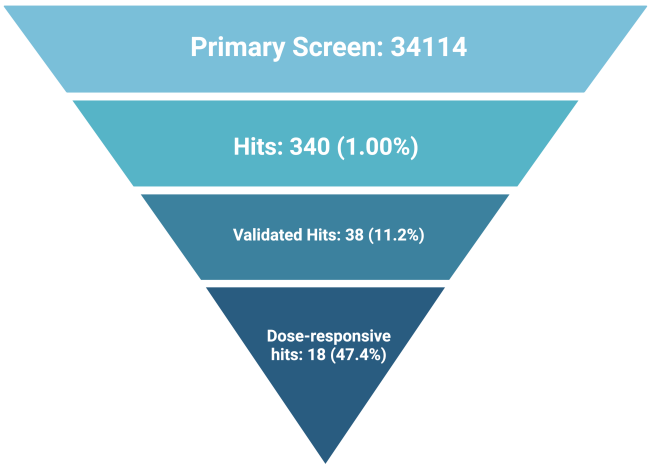

CCG ID	Strain ID	EC_{50} (mg/mL)
31194	06-282-1I	0.04
171929	39017-N1I	0.07
171960	86930-1I	0.09
140817	82379-N3I	0.11
171740	87745-N2I	0.12
27002	32420-N3I	0.14
142833	87797-1N	0.14
31146	49424-A2I	0.16
185588	N383-A3I	0.17
33025	34365-A1N	0.19
174310	GXXG380I	0.20
185042	R02-N5R	0.20
31195	06-282-1I	0.23
27623	34360-3I	0.30
33785	58236I	0.39
174443	YNYX265C	0.41
173549	90357-4R	0.79

Figure 21. HTS campaign overview of the NPE library. N=34114, Z'=0.62; red dots: positive controls; blue dots: negative controls; green dots: samples tested in the screen; red line represents 3 × standard deviation value; CCG ID, Strain ID, and IC_{50} listed.

For HTS, we utilized a collection of drug-like small molecules, the Eli Lilly Biological Interrogation Cassette (BIC; 20,793 compounds), as well as the NPE library housed at the Center of Chemical Genomics of the University of Michigan (34,114 NPEs). The Natural Product

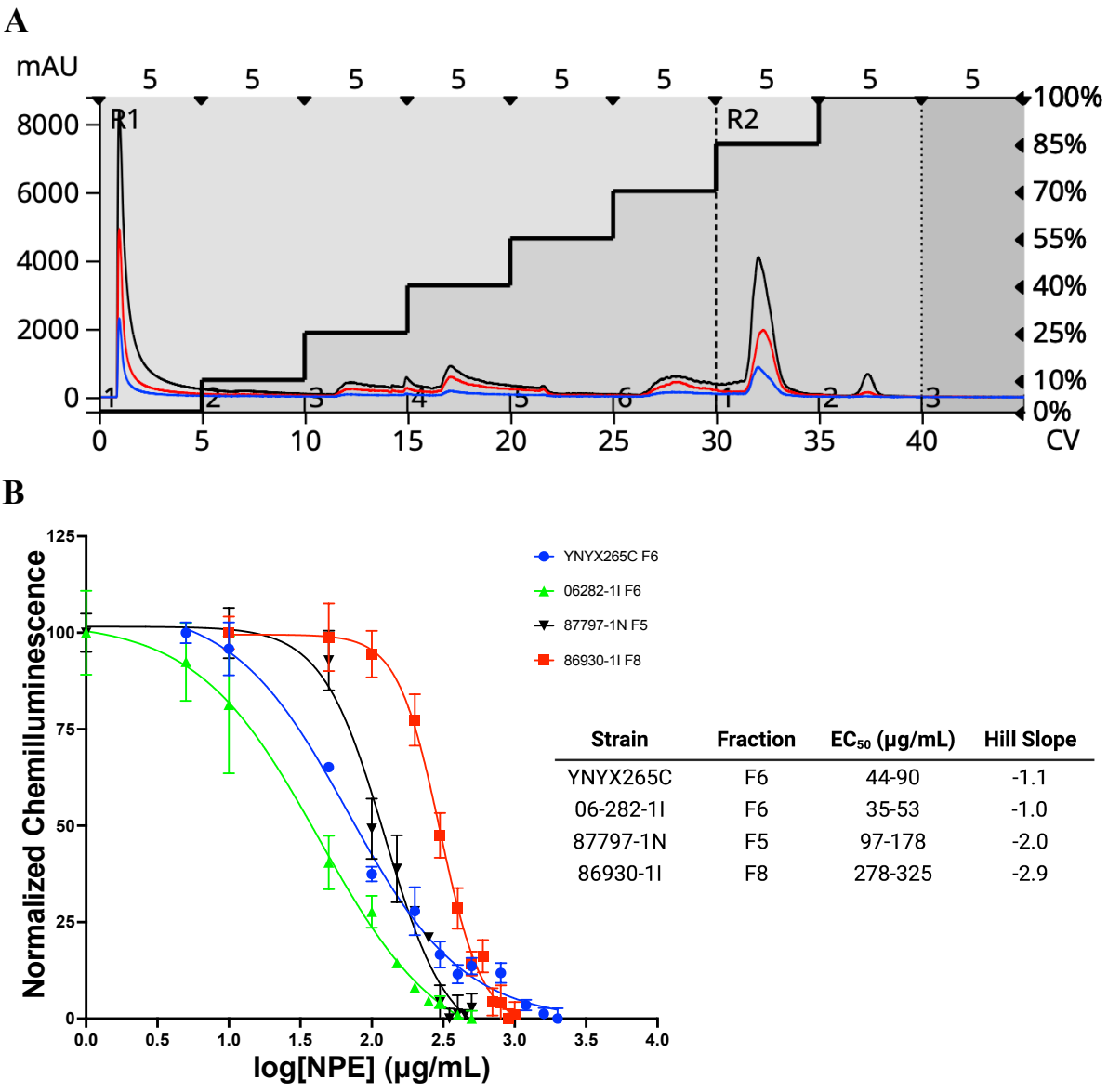

Strain	Fraction	EC_{50} (µg/mL)	Hill Slope
YNYX265C	F6	44-90	-1.1
06-282-1I	F6	35-53	-1.0
87797-1N	F5	97-178	-2.0
86930-1I	F8	278-325	-2.9

Figure 22. (A) Representative Biotage® fractionation chromatogram during the hit reconfirmation stage. R1: rack one; R2: rack two; bold dark line: concentration gradient; dark curve: signal at all wavelength (198 – 810 nm); red curve: signal at 235 nm; blue curve: signal at 285 nm; left Y-axis: mAU; right Y axis: percentage of methanol in water (except for the last fraction, the percentage of acetonitrile in water); X-axis: number of column volumes (CV). (B) Dose-dependent NPEs tested in eIF4E–4E-BP1 cat-ELCCA with a table of EC_{50} values presented as 95% confidence intervals with Hill slope values.

Extract (NPE) library housed at the University of Michigan Center for Chemical Genomics contains ~50,000 (and growing) pre-fractionated natural product extracts derived from a unique collection of diverse marine and terrestrial actinomycetes, fungi, and cyanobacteria collected from various locations throughout the world, including but not limited to, Antarctica, Brazil, China, Costa Rica, Israel, Panama, Papua New Guinea, Peru, and United States. The methods for

A

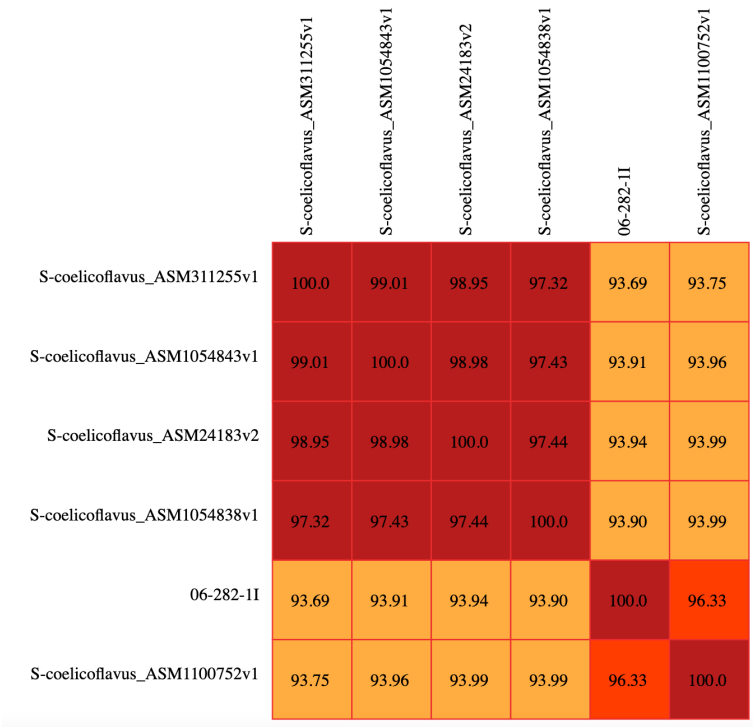

B

Query strain	Subject strain	dDDH (d0, in %)	C.I. (d0, in %)	dDDH (d4, in %)	C.I. (d4, in %)	dDDH (d6, in %)	C.I. (d6, in %)	G+C content difference (in %)
'S-coelicoflavus ASM311255v1'	'S-coelicoflavus ASM1054843v1'	89.1	[85.8 - 91.8]	89.8	[87.4 - 91.7]	91.9	[89.4 - 93.8]	0.08
'S-coelicoflavus ASM24183v2'	'S-coelicoflavus ASM311255v1'	81.4	[77.5 - 84.7]	88.8	[86.4 - 90.9]	85.6	[82.4 - 88.2]	0.39
'S-coelicoflavus ASM24183v2'	'S-coelicoflavus ASM1054843v1'	81.7	[77.9 - 85.1]	88.4	[85.9 - 90.5]	85.8	[82.7 - 88.4]	0.31
'S-coelicoflavus ASM1054838v1'	'S-coelicoflavus ASM1054843v1'	74.1	[70.1 - 77.7]	73.1	[70.1 - 75.9]	76.6	[73.1 - 79.7]	0.14
'S-coelicoflavus ASM24183v2'	'S-coelicoflavus ASM1054838v1'	68.5	[64.6 - 72.1]	72.9	[69.9 - 75.7]	71.5	[68.1 - 74.8]	0.17
'S-coelicoflavus ASM311255v1'	'S-coelicoflavus ASM1054838v1'	71.9	[68.0 - 75.6]	72.5	[69.4 - 75.3]	74.5	[71.1 - 77.7]	0.22
'06-282-1I'	'S-coelicoflavus ASM1100752v1'	74.2	[70.3 - 77.9]	64	[61.1 - 66.8]	74.8	[71.3 - 77.9]	0.08
'S-coelicoflavus ASM1054838v1'	'S-coelicoflavus ASM1100752v1'	62.6	[58.8 - 66.2]	49.8	[47.1 - 52.4]	61.1	[57.8 - 64.2]	0.16
'S-coelicoflavus ASM24183v2'	'S-coelicoflavus ASM1100752v1'	63.8	[60.0 - 67.4]	49.8	[47.2 - 52.4]	62.1	[58.8 - 65.3]	0.33
'06-282-1I'	'S-coelicoflavus ASM1054843v1'	64.9	[61.1 - 68.6]	49.6	[46.9 - 52.2]	63	[59.7 - 66.2]	0.09
'S-coelicoflavus ASM1054843v1'	'S-coelicoflavus ASM1100752v1'	63.8	[60.0 - 67.4]	49.5	[46.9 - 52.1]	62	[58.7 - 65.2]	0.02
'06-282-1I'	'S-coelicoflavus ASM24183v2'	62.9	[59.2 - 66.5]	49.4	[46.8 - 52.0]	61.2	[58.0 - 64.4]	0.41
'06-282-1I'	'S-coelicoflavus ASM1054838v1'	61.2	[57.5 - 64.8]	49.2	[46.6 - 51.8]	59.7	[56.5 - 62.9]	0.23
'S-coelicoflavus ASM311255v1'	'S-coelicoflavus ASM1100752v1'	64	[60.2 - 67.6]	48.6	[46.0 - 51.2]	61.9	[58.6 - 65.1]	0.06
'06-282-1I'	'S-coelicoflavus ASM311255v1'	63.7	[59.9 - 67.3]	48.3	[45.7 - 50.9]	61.6	[58.3 - 64.8]	0.02

Figure 23. (A) Heatmap showing ANI values between *S. coelicoflavus* strains and *S. papuanewguineus*. The numbers are shown as %. Values of ≥95% indicate same species. (B) Pairwise comparisons of genomes under examination using in silico DDH experiments.

preparation, purification, and maintenance of these extracts were described in previous literature.[25, 26] BIC and NPE samples were screened at final concentrations of 25 μM and 75 μg/mL, respectively, using the eIF4E–4E-BP1 PPI cat-ELCCA. While 9 confirmed hits were identified from the BIC Library following primary biochemical testing and secondary biophysical assays, the compounds failed to meet the potency thresholds and were not selected for further analyses (**Figure 20**). Excitingly, out of 340 initial hits from the NPE library, 38 NPEs were validated after retesting. After that 18 NPEs from 18 strains out of the 38 validated hits showed promising dose-responsive inhibition in PPI cat-ELCCA (**Figure 21**).

2.1.3 Hit regrowth and re-confirmation

To reconfirm the activity and reproducibility of validated hits, all 18 strains were subsequently re-grown using standard protocol on 1-L scale. The crude extracts were subjected to Biotage fractionation based on polarity (**Figure 22A**). All crude extracts and Biotage fractions

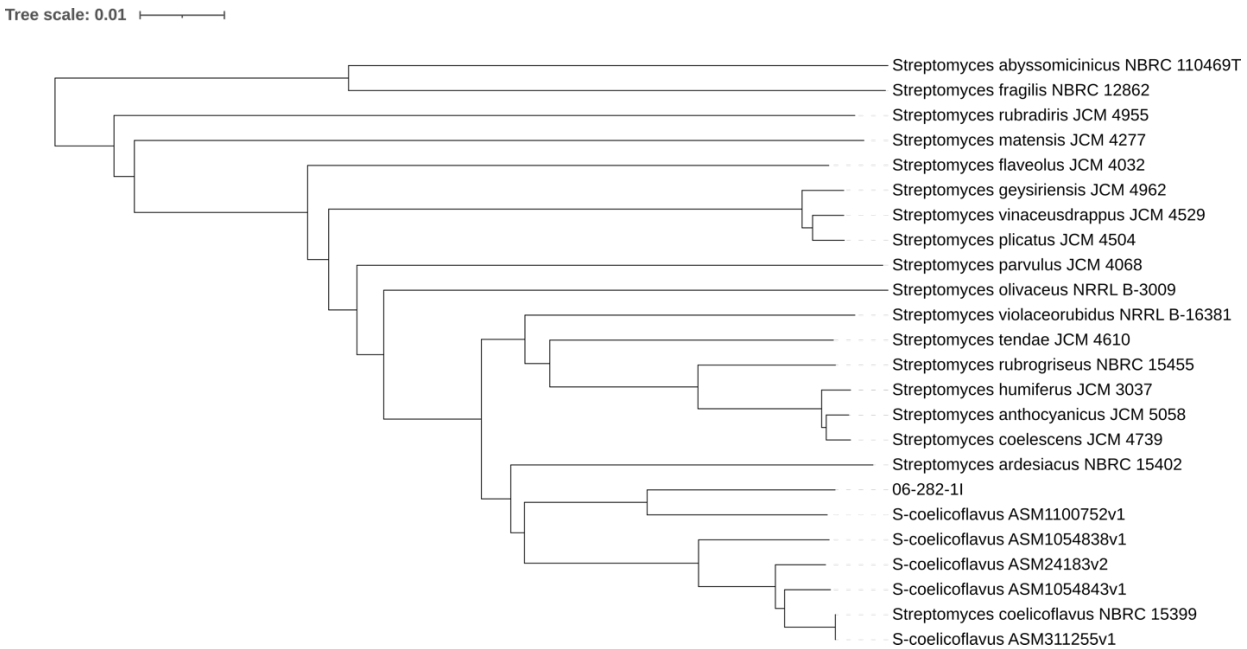

Figure 24. Phylogenetic tree (whole-genome sequence-based). The strain 06-282-1I is most similar to *Streptomyces coelicoflavus* ASM1100752v1.

were first tested for bioactivity in cat-ELCCA at fixed concentrations. Active fractions were then tested in a dose-dependent manner and four strains contained fractions with dose-dependent inhibitory activity <500 µg/mL (**Figure 22B**). The most active fraction came from strain 06-282-1I (EC_{50} ~43 µg/mL), which was selected for further deconvolution.

2.2 A Multi-Prong Approach for the Deconvolution of 06-282-1I

2.2.1 Genomic characterization of 06-282-1I

06-282-1I was isolated from marine sediment collected in Papua New Guinea. Its genome was extracted and sequenced at the MiGS-Seq Center on the Illumina NextSeq 2000 platform. Whole-genome similarity metrics including Average Nucleotide Identity (ANI) and DNA-DNA Hybridization (DDH) were obtained to estimate genetic relatedness and define the

Region	Type	From	To	Most similar known cluster		Similarity
Region 5.1	T2PKS	91,689	134,242	spore pigment	Polyketide	66%
Region 10.1	terpene	37,313	59,181			
Region 11.1	terpene	11,987	34,188	geosmin	Terpene	100%
Region 13.1	lanthipeptide-class-i	1,364	23,954			
Region 14.1	terpene	69,338	89,367	isorenieratene	Terpene	100%
Region 18.1	RRE-containing	50,524	71,765	naphthomycin A	Polyketide	9%
Region 19.1	terpene	21,904	48,636	hopene	Terpene	100%
Region 21.1	NRPS	23	79,450	coelibactin	NRP	100%
Region 27.1	NRPS	43,122	67,101	coelichelin	NRP	36%
Region 38.1	terpene	16,550	37,563	albaflavenone	Terpene	100%
Region 41.1	siderophore	22,331	34,229			
Region 55.1	siderophore	9,967	21,745	desferrioxamin B / desferrioxamine E	Other	83%
Region 65.1	T3PKS	5,345	40,585	herboxidiene	Polyketide	8%
Region 70.1	butyrolactone	31,167	38,169	prejadomycin / rabelomycin / gaudimycin C / gaudimycin D / UWM6 / gaudimycin A	Polyketide:Type II + Saccharide:Hybrid/tailoring	6%
Region 71.1	melanin	15,891	26,466	istamycin	Saccharide	4%
Region 72.1	RiPP-like	11,318	22,784			
Region 78.1	NRPS-like , T1PKS	3,852	35,902	undecylprodigiosin	NRP + Polyketide	50%
Region 83.1	ectoine	1,626	12,024	ectoine	Other	100%
Region 87.1	T3PKS	6,601	32,835	germicidin	Other	100%
Region 88.1	terpene	18,730	32,723	carotenoid	Terpene	36%
Region 95.1	RiPP-like	14,154	24,369	informatipeptin	RiPP:Lanthipeptide	42%
Region 107.1	NRPS	1	26,430	coelichelin	NRP	72%
Region 112.1	lanthipeptide-class-iii	1	12,857	SapB	RiPP:Lanthipeptide	50%
Region 116.1	NRPS-like	1	24,307	paulomycin	Other	13%
Region 126.1	RiPP-like	14,771	22,167			
Region 135.1	indole	2,655	19,947	5-isoprenylindole-3-carboxylate β-D-glycosyl ester	Other	23%
Region 143.1	T2PKS	1	17,125	auricin	Polyketide:Type II + Saccharide:Hybrid/tailoring	48%
Region 146.1	siderophore	1	10,370			
Region 181.1	phenazine	1	10,508	marinophenazine A / phenaziterpene A	Other:Phenazine	30%
Region 183.1	T1PKS , NRPS	1	10,470	α-lipomycin	NRP:Lipopeptide + Polyketide:Modular type I + Saccharide:Hybrid/tailoring	45%

Figure 25. AntiSMASH analysis of the genome of *S. papuanewguineus*.

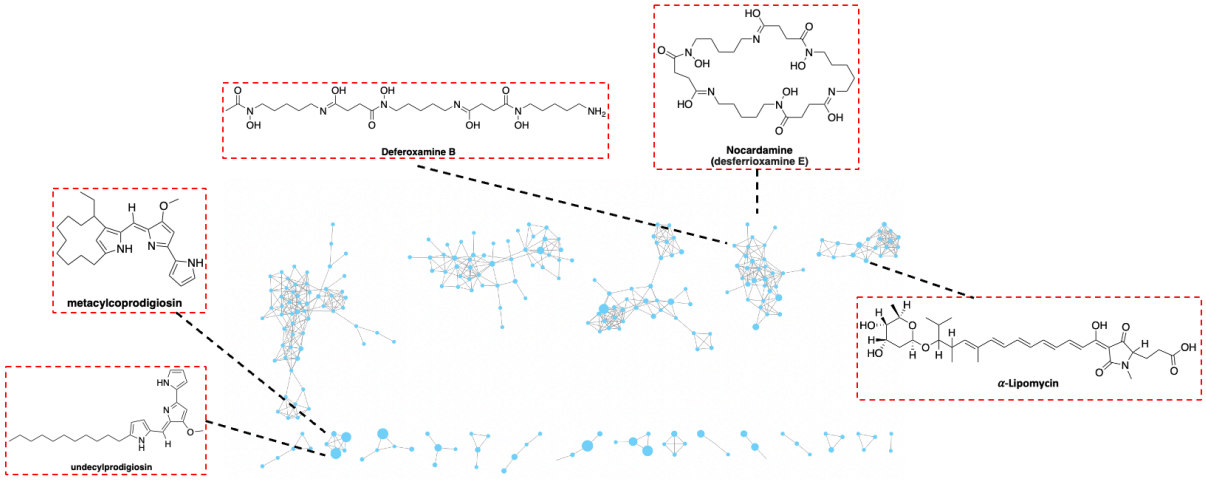

Figure 26. GNPS molecular networking of *S. papuanewguineus* in the positive mode; networks in the three red boxes: clusters containing deferoxamine-related molecules (top), prodigiosin-related molecules (bottom left), phenazine related molecules (bottom mid), and *α*-lipomycin (bottom right); structures of molecules are shown in dashed red box.

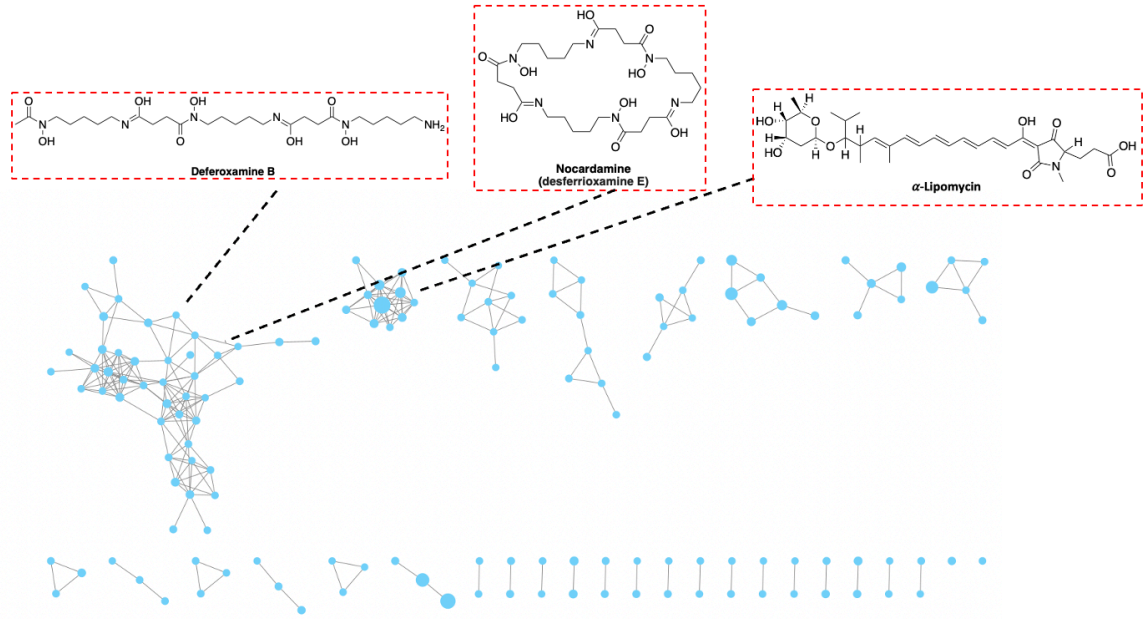

Figure 27. GNPS molecular networking of *S. papuanewguineus* in the negative mode annotated with hits.

phylogeny of this strain.[27-29] The strain 06-282-1I showed a 96.33% ANI value to *Streptomyces coelicoflavus* (Accession number: ASM1100752v1) indicating that they belong to the same species (ANI≥95% for the same species) (**Figure 23A**). When comparing 06-282-1I and *S. coelicoflavus*_ ASM1100752v1 (query sequences) to the other 4 publicly available *S.*

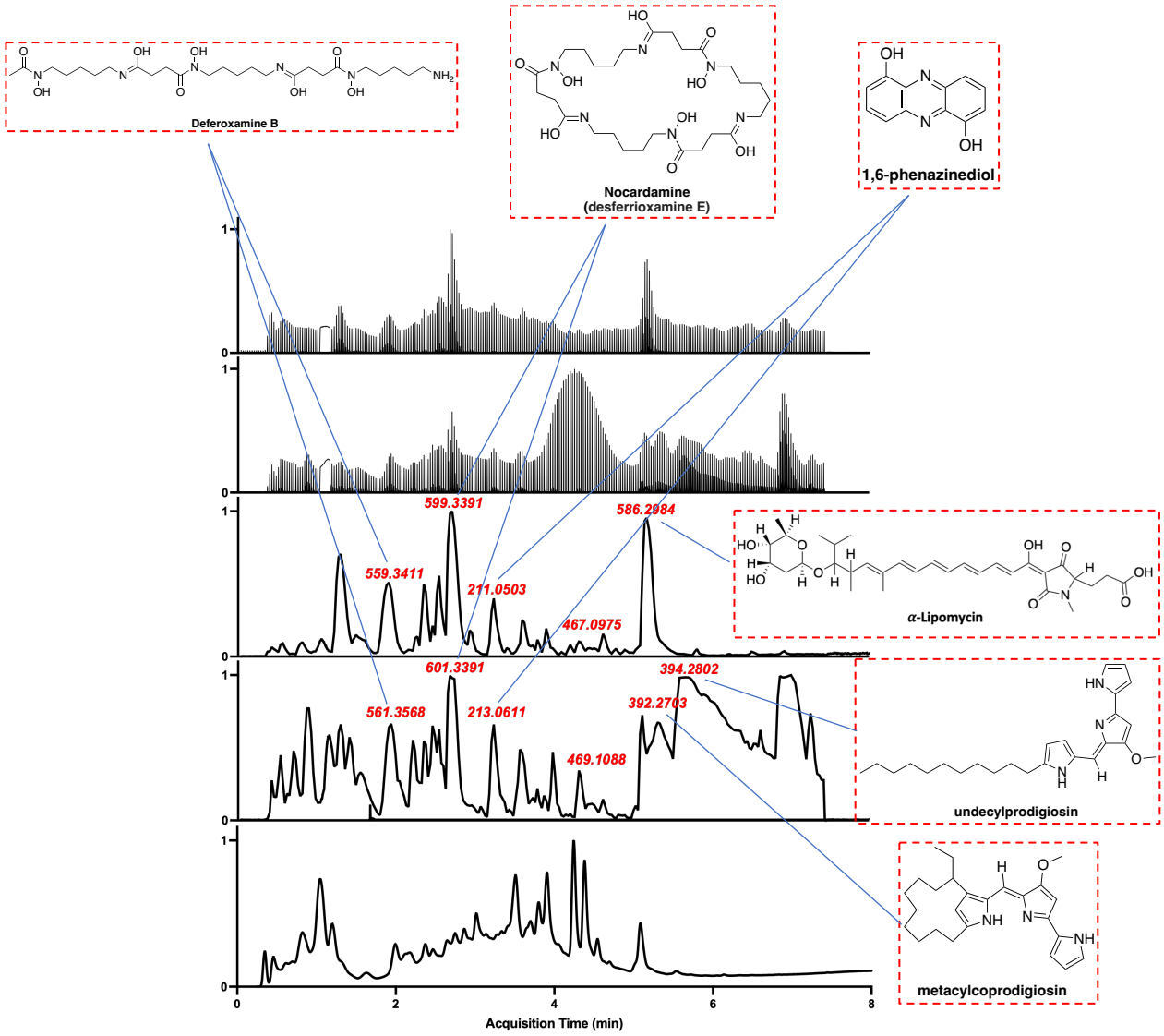

Figure 28. Chemical Profile of *S. papuanewguineus*. From the top to the bottom: LC-MS/MS trace in negative mode; LC-MS/MS trace in positive mode; extracted Base Peak Chromatogram(BPC) of LC-MS/MS chromatogram in negative mode; extracted Base Peak Chromatogram(BPC) of LC-MS/MS chromatogram in positive mode; UV trace of LC-MS/MS chromatogram; selected peaks including deferoxamine B/E, compound 1-7, *α*-lipomycin, and prodigiosins were labeled with exact masses; Y axis: normalized ion count (except for UV, it's normalized absorbance); X-axis: acquisition time (min).

coelicoflavus genomes (ASM311255v1, ASM1054843v1, ASM24183v2, ASM1054838v1), ANI values below the ≥95% ANI literature threshold for same species were obtained. Furthermore, *in silico* DDH experiments showed a dDDH (d6) value of 74.8% for the two query genomes (06-282-1I and ASM1100752v1) further validating their genetic relatedness (≥70% for the same species, **Figure 23B**). Additional DDH experiments revealed that the query sequences

(ASM311255v1, ASM1054843v1, ASM24183v2, ASM1054838v1) showed dDDH (d6) values between 61.1 to 61.9% to the subject sequences (06-282-1I and ASM1100752v1), meanwhile, the subject sequences had values between 71.5 to 91.9% when compared to one another (Figure S). These results suggested that (1) *S. coelicoflavus_* ASM1100752v1 was mislabeled possibly due to assignments based on 16S rRNA identity only and (2) 06-282-1I and *S. coelicoflavus_* ASM1100752v1 belong to a new species closely related to *S. coelicoflavus* as shown in the phylogenetic tree (**Figure 24**). Thus, strain 06-282-1I was named *Streptomyces papuanewguineus 06-282-1I* in recognition of the location from which it was originally collected and isolated. Subsequent genome mining of this strain using antiSMASH[30] revealed the presence of putative biosynthetic gene clusters (BGCs) for the phenazine class of molecules, as well as undecylprodigiosin, α-lipomycin, and deferoxamine B/E (**Figure 25**).

2.2.2 Chemical profiling of S. papuanewguineus

Global Natural Product Social (GNPS) molecular networking is a powerful *in silico* tool for LC-MS/MS-based metabolomic analyses of crude natural product extracts.[31] The processed LC-MS/MS data of the crude extract of *S. papuanewguineus* was subject to GNPS workflow using LC-MS/MS data of the medium, ISP2, and methanol blank as filters. Both positive mode (**Figure 26**) and negative mode (**Figure 27**) data were analyzed. The LC/MS traces of crude extract in positive and negative modes were also compared and labeled with GNPS hits(**Figure 28**).

From these analyses, we observed the clusters containing undecylprodigiosin, α-lipomycin, and deferoxamine B/E, matching the predictions by antiSMASH. Prodigiosins are a family of red-colored pigments isolated from *Streptomyces*.[32] Even though potential antitumor activities of prodigiosins have been reported, they have a wide range of reported bioactivities,[32]

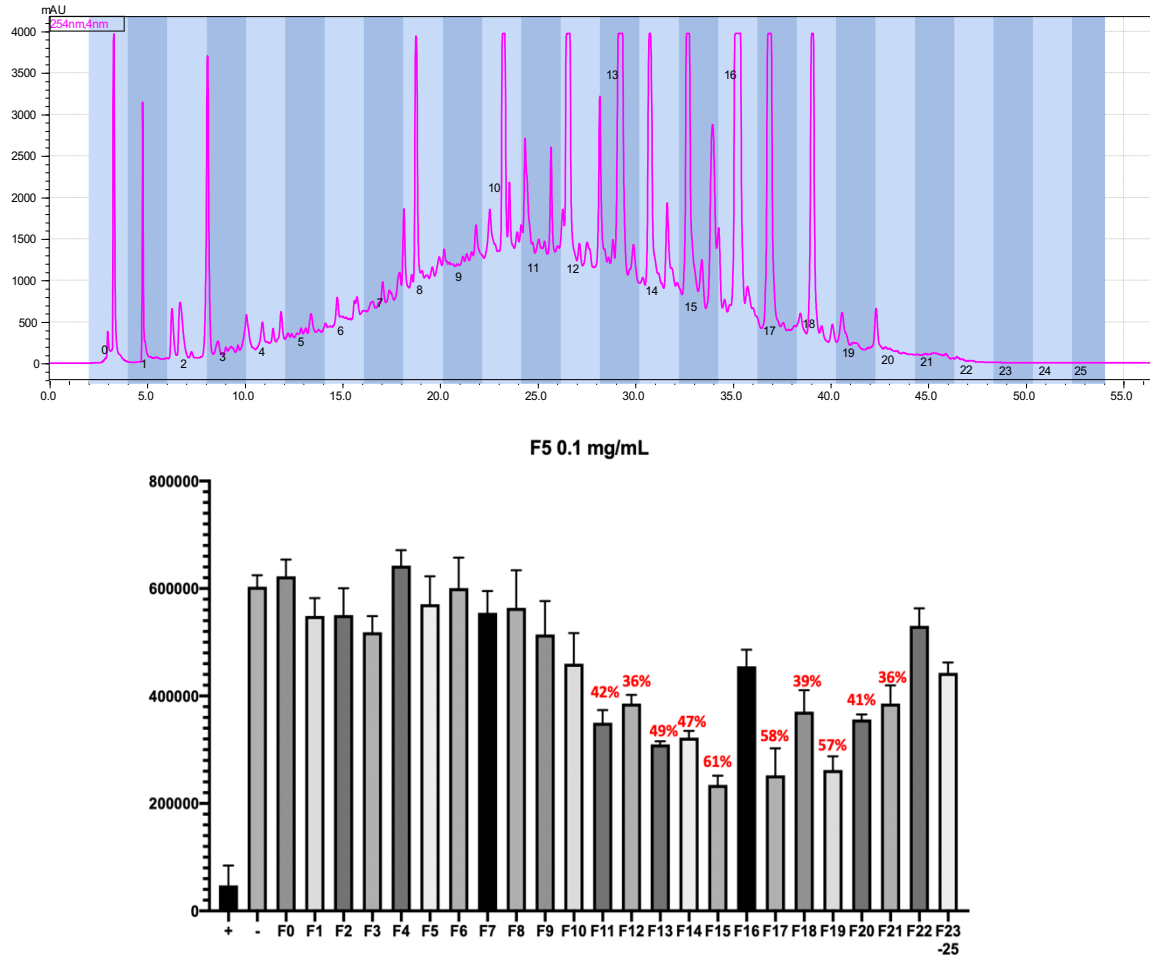

Figure 29. Representative HPLC trace of active biotage fraction and the bioactivity of HPLC fractions; column: C18; gradient: 2-42 min: 10-60% B (acetonitrile with 0.01% TFA) in A (water with 0.01% TFA), and then 10 min of 95% B in A; pink curve: UV absorbance at 254 nm; Left Y axis: mAU; X axis: acquisition time (min); for the bioactivity plot, Left Y axis: chemiluminescence; X axis: fraction number; some active fractions were labeled with percentage of inhibition.

which dampened enthusiasm for developing this scaffold for targeting eIF4E PPIs. Commercial undecyl-prodigiosin showed 50% inhibition of eIF4E PPI at ~0.1 mg/mL (approximately 200 μM) and when compared to the active fraction of *S. papuanewguineus*, it was approximately one-fold less active. Desferrioxamine E, also known as nocardamine, is a ferrioxamine siderophore commonly found in *Streptomyces* strains that exhibits antibacterial, antitumor, and biofilm inhibitory activities.[33, 34] However, nocardamine-containing Biotage and HPLC fractions were not active in eIF4E PPI cat-ELCCA. α-lipomycin is an orange-red colored acyclic polyene antibiotic that shows potent gram-positive antibacterial activity with no activity against the

growth of fungi, yeasts, and gram-negative bacteria.[35] α-lipomycin-containing Biotage and HPLC fractions were not active in eIF4E PPI cat-ELCCA. This evidence suggested that there were other active natural products in the crude extract of *S. papuanewguineus*, which further motivated us to deconvolute this strain.

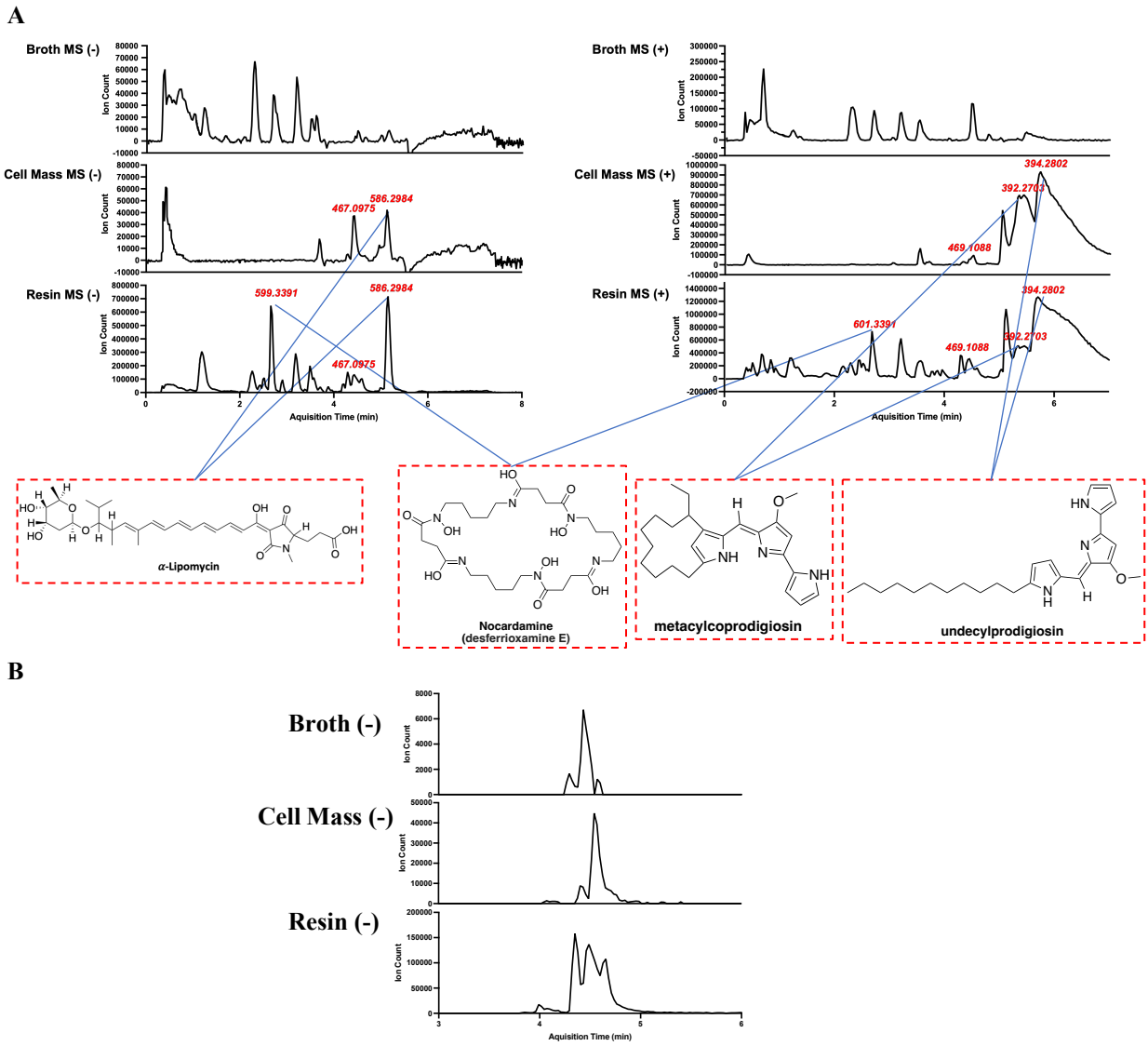

Figure 30. Chemical profile comparison between broth, cell mass extract, and resin extract of *S. papuanewguineus*. (A) Extracted Base Peak Chromatogram(BPC) of the LC-MS/MS chromatograms of broth, cell mass extract, and resin extract of *S. papuanewguineus* in both positive and negative modes. (B) Extracted Ion Chromatograms of the phenazine peaks (m/z 467.0975) in the LC-MS/MS chromatograms of broth, cell mass extract, and resin extract of *S. papuanewguineus* in negative mode (EIC of the positive mode chromatogram was the same as that in negative mode when searching m/z 469.1088).

2.2.3 Bioactivity-guided isolation and purification of phenazine class of molecules

To obtain enough biomass for the next steps of deconvolution, a 40-L scale-up growth of *S. papuanewguineus* was conducted using standard protocol in ISP2+salt medium and approximately 200 grams of dried biomass was yielded (5 g per liter). To confirm the activity, about 1-L of biomass (5 g) was subjected to the same stepwise-gradient Biotage fractionation and F5 and F6 were found to be the most active fractions. To identify the mass(es) of the active component(s) in these fractions, they were then fractionated using reverse-phase high-

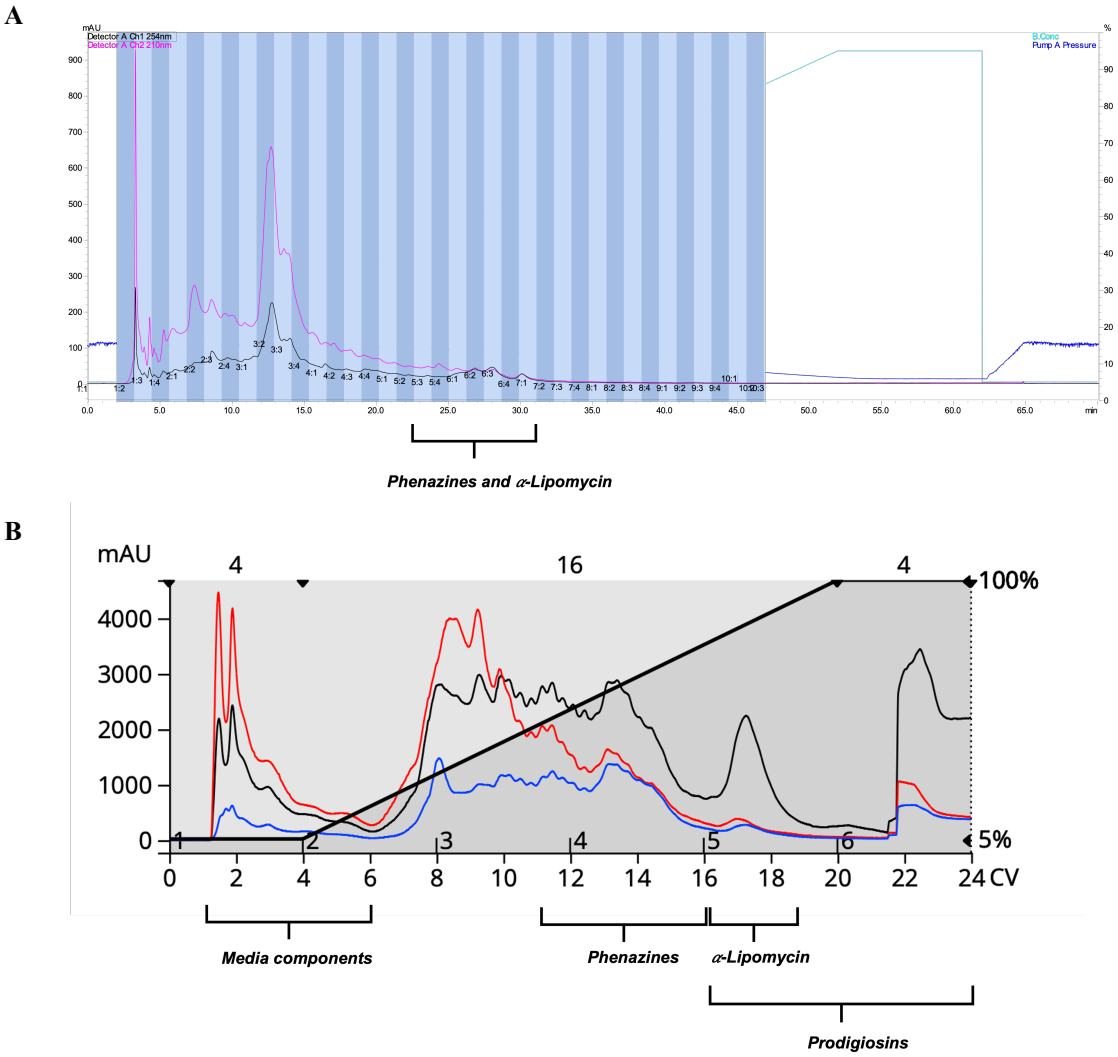

Figure 31. Representative prep HPLC and biotage chromatograms of *S. papuanewguineus* crude extract. (A) Representative prep HPLC chromatogram; (B) Representative biotage chromatogram.

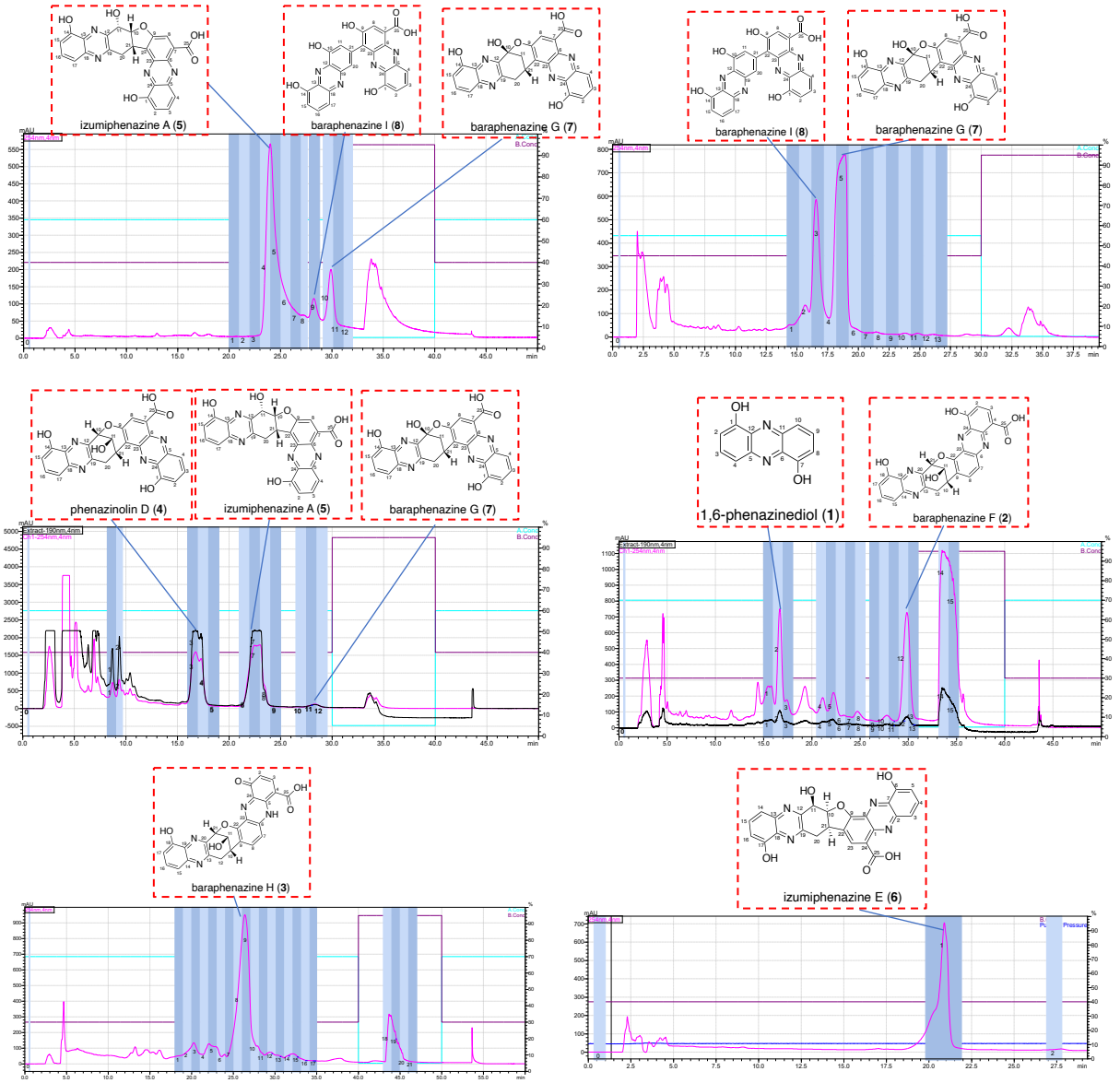

Figure 32. Semi-prep HPLC chromatograms of the purifications of phenazines. Detailed concentration gradients were discussed in the Materials and Methods section; Light blue line: concentration of B (acetonitrile in 0.01% TFA); purple line: concentration of A (water in 0.01% TFA); dark blue line: pump A pressure; pink curve: UV absorbance at 254 nm; black curve: UV absorbance at 190 nm; Left Y axis: mAU; Right Y-axis: concentration of B; X axis: acquisition time (min).

performance liquid chromatography (RF-HPLC) and tested in cat-ELCCA (**Figure 29**). We noticed that the mass $[M+H]^+$ 469.11443 was found across multiple active HPLC fractions. Thus, we decided to focus on the targeted isolation of this mass during the processing of the remaining biomass (195 g).

First, we compared the content of the mass $[M+H]^+$ 469.11443 (or the equivalence in negative mode) in broth, cell mass, and resin extract using LC-MS (**Figure 30**). Based on the quantitative analyses by extracted ion chromatograms (EICs), we found that expectedly, most of this mass appeared in the resin extract. Then, we developed a preparative HPLC purification method the of the resin extract (**Figure 31A**). One challenge was the contamination of pink color in fractions, which was found to be prodigiosins by LC-MS. These colored molecules retained on the column very well and spanned across ~80% of all HPLC fractions; they were also hard to be entirely washed off, potentially damaging the column and contaminating other samples. To eliminate these unwanted pigments, we moved to reverse-phase flash chromatography on Biotage Selekt (**Figure 31B**). We successfully developed a Biotage method to separate water-soluble media components, masses of interest, and pink pigments using pre-packed C-18 columns, which were much cheaper than the Phenomenex C-18 column used in prep-HPLC and were disposable after several uses. This method enabled the initial fast and effective processing of crude extract from ~200 g to ~20 g of less complex extract containing masses of interest.

The next round of purification was conducted on both prep-HPLC and semi-prep HPLC. Several factors were taken into account during the method development: (1) column: among the available columns, the phenylhexyl column worked the best, likely due to the presence of multiple aromatic rings in the structures; (2) solvent system: acetonitrile (ACN)/water worked slightly better than methanol (MeOH)/water; (3) acid-modifier: we found that adding an acid-modifier, either 0.1% formic acid (FA) or 0.01% trifluoroacetic acid (TFA), significantly improved the elution patterns and resolutions of peaks of interest; and (4) gradients: isocratic gradient using 30%, 35%, 40%, and 45% ACN/water were chosen for the final rounds of

purification of molecules of interest (**Figure 32**). After several rounds of purification, we successfully identified and isolated eight phenazine molecules from the active fractions.

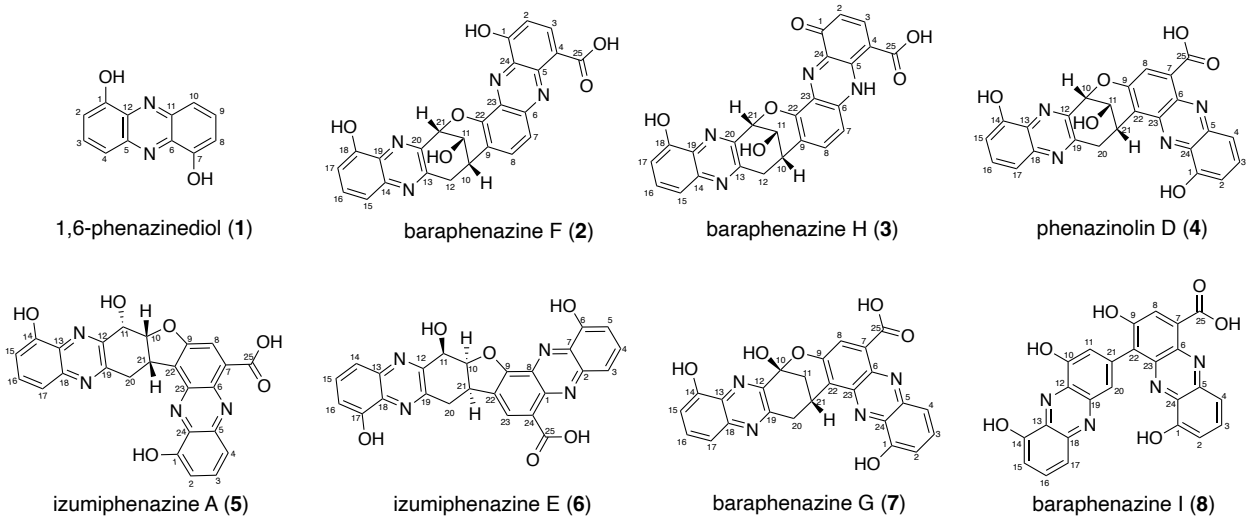

Figure 33. Structures of isolated phenazines from *S. papuanewguineus*.

Phenazines are chorismate-derived dibenzo-annulated pyrazine-based secondary metabolites produced by soil microbes reported with antibiotic, antifungal, insecticidal, and antitumor activities.[36, 37] While over 150 phenazine-based NPs have been reported, only a tiny portion is composed of two phenazine monomers, including diphenazithionin,[38] phenazostatins A–D,[39-41] izumiphenazines A–D,[42, 43] esmeraldines A and B,[44] phenazinolins A–E,[45] diastaphenazine,[46] and baraphenazines A–G.[47] In this study, we isolated 1,6-phenazinediol, baraphenazine F, phenazinolin D, izumiphenazine A, baraphenazine G, baraphenazine I, which was the spontaneous conversion product of baraphenazine G, and two new diphenazines, izumiphenazine E and baraphenazine H (**Figure 33**). The detailed structure elucidation of these molecules will be further discussed in Chapter 3.

2.3 Biochemical and Cellular Activities of Isolated Phenazines

2.3.1 Biochemical activities in PPI cat-ELCCA

With phenazine **1**-**7** in hand, we first tested their inhibitory activity in PPI cat-ELCCA for the eIF4E–4E-BP1 PPI (**Figure 34**). Izumiphenazine E (**6**) was the most potent molecule with a

Compound	EC_{50} (μM)	Hill Slope
1: 1,6-phenazinediol	not active	N/A
2: baraphenazine F	310	-1.3
3: baraphenazine H	68	-0.9
4: phenazinolin D	256	-2.2
5: izumiphenazine A	237	-1.2
6: izumiphenazine E	7.8	-1.1
7: baraphenazine G	not active	N/A

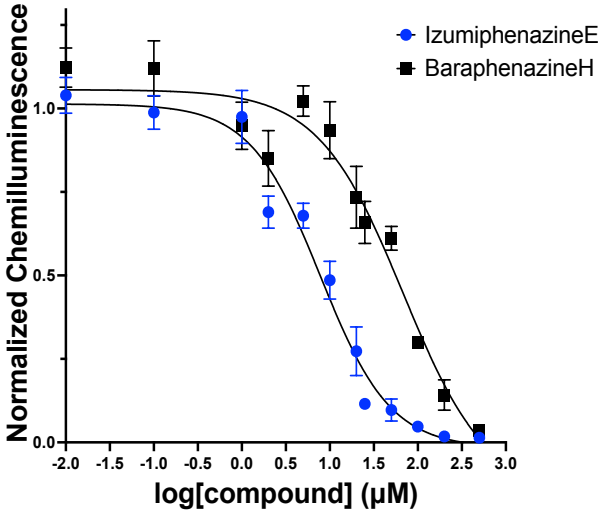

Figure 34. Biochemical activities of isolated phenazines and dose-response curves of izumiphenazine E and baraphenazine H.

measured EC_{50} of 7.8 μM, followed by baraphenazine H (**3**) with an EC_{50} of 68 μM. Since we postulated that the beta-unsaturated ketone might serve as a Michael acceptor in baraphenazine H as its mechanism of inhibition, another phenazine-1-one containing phenazine, pyocyanin was purchased and tested, which turned out to be inactive. Both **6** and **3** showed a Hill slope value of around -1, suggesting a noncooperative inhibition mechanism. As structurally diverse phenazines were isolated, we were able to glean preliminary structure-activity relationships (SAR) around this scaffold. Since neither 1,6-phenazinediol nor pyocyanin showed any activity, a fused-phenazine geometry is probably required for inhibition. While a defining feature of many of the isolated NPs was the presence of a phenazinediol unit with phenol groups at different positions, **6**

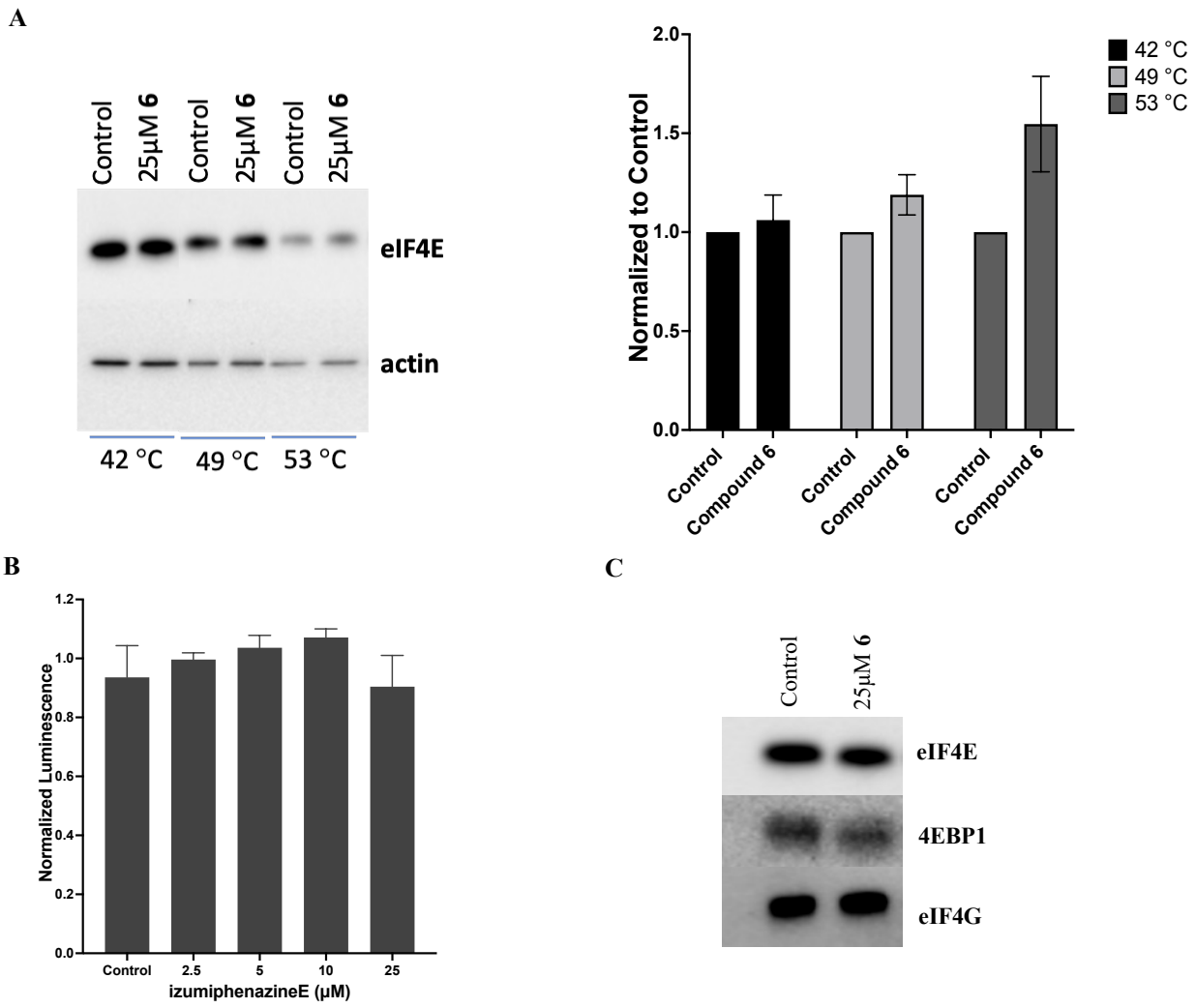

Figure 35. Biological activities of **6**. (A) Representative western blot of CETSA assay in HEK 293 cells with 0 (control) and 25 μM of compound **5** at 42, 49 and 53 °C, probing for eIF4E and actin (control), and the quantification of band intensities in the western blots of three replicates by ImageJ; (B) Cell Titer-Glo® in Mia-PaCa-2 cells with compound **6** at 0, 2.5, 5, 10, 25 μM, 48-hour incubation; (C) Cap pull down assay in HEK 293 cells with 25 μM of **6**, 1 hour incubation.

is the only compound that contains a 1,6-phenazinediol unit. This suggests that the phenol positions of the 1,6-phenazinediol unit in **6** may be important for its enhanced inhibitory activity. Furthermore, compared to the 10*R*,11*S*,21*S* configuration in **5**, **6** possesses an enantiomeric configuration of 10*S*,11*R*,21*R*, suggesting that this configuration may also be responsible for the ~30-fold increase in activity of **6** compared to **5**.

2.3.2 Cellular activities of izumiphenazine E (6)

Since **6** was the most active compound, we further characterized its activity in cellular assays. We first determined whether it could bind to eIF4E in the complex cellular milieu using the cellular thermal shift assay (CETSA)[48] in HEK293 cell lysate. Encouragingly, an increase in the stability of eIF4E was observed following treatment with 25 μM, suggesting that it can bind and stabilize eIF4E (**Figure 35A**). Of note, this concentration was chosen based on solubility limitations. We next profiled the antiproliferative activity of **6** in MiaPaca-2 cells whose growth is known to be affected by modulation of eIF4E and cap-dependent translation,[49] using the CellTiter-Glo® cell viability assay. Unfortunately, the compound exhibited no anti-proliferative activity in this assay (**Figure 35B**), and upon further profiling in additional cell-based assays, including the m^7GDP cap affinity assay,[16] it was further found to be inactive (**Figure 35C**). As the biochemical activity of this compound is much weaker than our previously disclosed peptide-based inhibitors, it is possible that **6** is not potent enough to disrupt cellular eIF4E PPIs, which exhibit nanomolar binding affinity. It is also possible that **6** suffers from poor cellular permeability due to the presence of its carboxylic acid. Indeed, previous investigations of baraphenazines found that only when the carboxylic acid was a primary amide as in baraphenazine E, was anti-proliferative activity observed in A549 and PC3 cells, likely due to improved cellular uptake.[47] In the future, we will perform additional medicinal chemistry optimization on **6** to improve its cellular uptake and activities and further develop this scaffold for targeting 'undruggable' eIF4E and its PPIs.

2.4 Biosynthesis of Phenazine Class of Molecules

Toward the goal of obtaining chemically modified diphenazine analogs, we became curious about their biosynthesis. The biosynthesis of mono-phenazines has been intensively

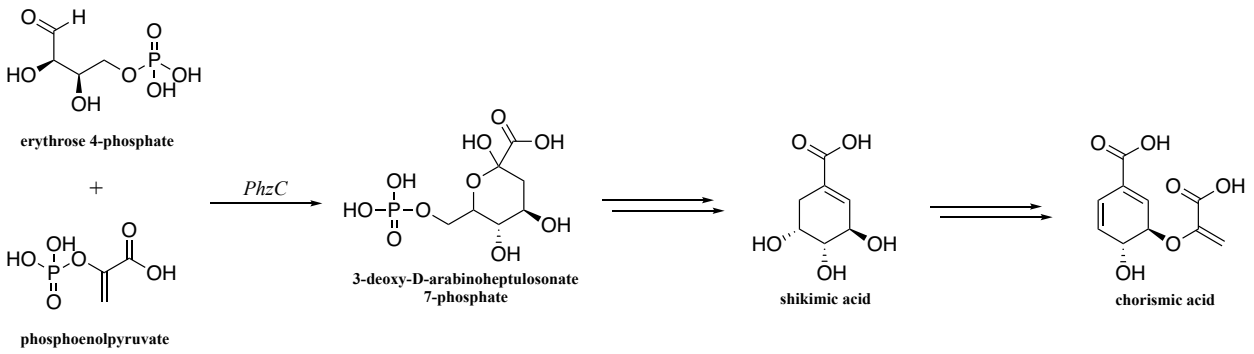

Figure 36. The biosynthesis of chorismic acid, the common precursor of phenazines.

studied since the mid 20th century.[36] All natural phenazines share several conserved enzymes in their BGCs including *PhzA/B*, *PhzC*, *PhzD*, *PhzE*, *PhzF*, and *PhzG*, which serve to synthesize the common phenazine monomers including phenazine, phenazine-1-carboxylic acid (PDC), and phenazine-1,6-dicarboxylic acid (PDA).

2.4.1 Biosynthesis of phenazine, PDC, and PDA

Chorismic acid, an intermediate in the shikimate pathway, is a critical precursor for many primary and secondary metabolites in plants and microorganisms such as phenazine, aromatic amino acids, vitamin K, and alkaloids.[50] In the first step of the biosynthesis of chorismic acid by the shikimate pathway, *phzC*, encoding the 3-deoxy-*D*-arabinoheptulosonate 7-phosphate (DHAP) synthase, catalyzes the formation of DAHP from the starting materials erythrose 4-phosphate (E4P) and phosphoenolpyruvate (PEP, Figure36).[51] After that, through a series of enzymes in the shikimate pathway including 3-dehydroquinate (DHQ) synthase, DHQ dehydratase, shikimate dehydrogenase, shikimate kinase, 5-enolpyruvylshikimate 3-phosphate (EPSP), and chorismate synthase, DHAP is converted into shikimic acid, and then chorismic acid as the final product.[51] Next, chorismic acid is converted to 2-amino-4-desoxyisochorismate (ADIC) by *phzE*, an Mg^{2+}-dependent ADIC synthase.[52] The vinyl ether group of ADIC is then cleaved by an isochorismatase *phzD* to form the side product pyruvate and the major product

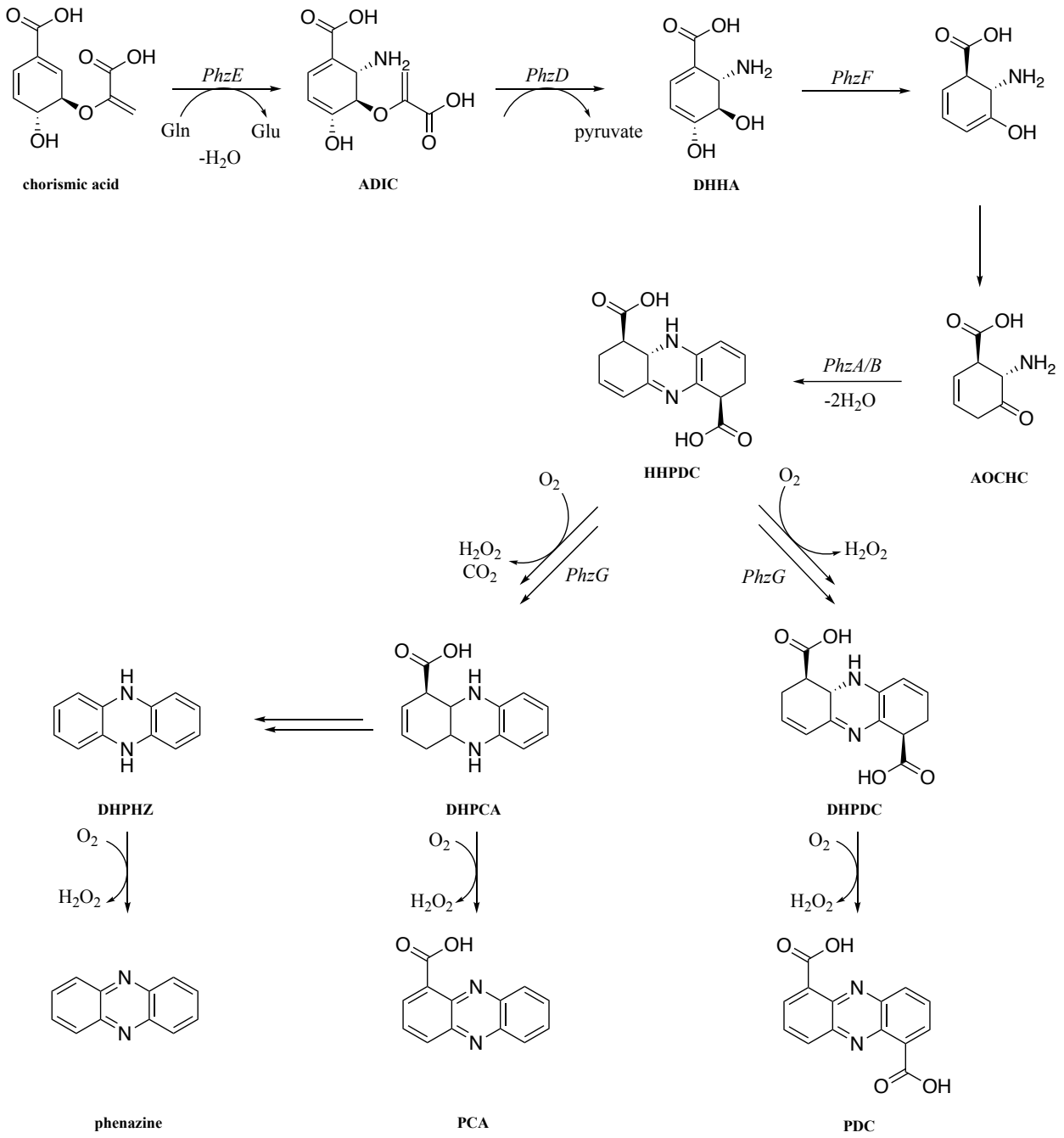

Figure 37. The biosynthesis of phenazine, PCA, and PDC from chorismic acid using phenazine core enzymes *phzA/B*, *phzD*, *phzE*, *phzF*, and *phzG*. ADIC: 2-amino-4-desoxyisochorismate; DHHA: *trans*-2,3-dihydro-3-hydroxyanthranillic acid; AOCHC: 6-amino-5-oxocyclohex-2-ene-1-carboxylic acid; HHPDC: hexahydrophenazine-1,6-dicarboxylic acid; DHPHZ: dihydrophenazine; DHPDC: 5,10-dihydro-PDC; DHPCA: 5,10-dihydro-PCA.

trans-2,3-dihydro-3-hydroxyanthranillic acid (DHHA).[53] The subsequent enol tautomerization of DHHA catalyzed by *phzF* yielded 6-amino-5-oxocyclohex-2-ene-1-carboxylic acid (AOCHC).[54] After that, the double condensations of AOCHC, aided by the Δ^5-3-ketosteroid isomerase/nuclear

transport factor family *phzB*, give the key dimerized intermediate hexahydrophenazine-1,6-dicarboxylic acid (HHPDC).[55] *Pseudomonas* species contain *phzA*, a copy of *phzB* that shares a 70% sequence identity and as a result, *phzB* is also referred to as *phzA/B*.[56] Then, catalyzed by flavin-dependent dihydrophenazinedicarboxylate synthase *phzG*, HHPDC undergoes oxidative decarboxylation to form either dihydrophenazine (DHPHZ), 5,10-dihydro-PDC (DHPDC), or 5,10-dihydro-PCA (DHPCA), which are further oxidized into the final products phenazine, PDC, or PCA, respectively.[57]

2.4.2 Biosynthesis of diphenazine

Dimeric natural products have been extensively isolated from bacteria, fungi, and plants and they exhibited a wide range of biological activities.[58] A lot of these dimeric compounds have been developed into potential therapeutic agents, for instance, vinblastine (anticancer agent), gossypol (immunosuppressant), hypericin (kinase inhibitor), etc. From a biosynthesis standpoint, dimerization reactions of natural products are catalyzed by a variety of enzymes, including cytochrome P450s that catalyze coupling reactions via a free radical mechanism,[59] laccases that catalyze the dimerization of phenolic compounds,[60] [4+2] cyclases that catalyze the coupling reactions between two polyene units,[61] etc. The biosynthetic pathway of phenazine monomers including phenazine, phenazine-1-carboxylic acid (PCA), phenazine-1,6-dicarboxylic acid (PDA), and 1,6-phenazinediol have been well studied whereas how these phenazine monomers dimerize into di-phenazines remain poorly understood. To date, only one enzyme, *dap5*, has been discovered to catalyze the dimerization of phenazine-type metabolites.[62] *dap5*, a NTF2-like superfamily protein harboring a snoaL-like polyketide cyclase domain, has been shown to be responsible for the dimerization of two PCA units into diastaphenazine by knockout studies.[62] However, the catalytic mechanism of this enzyme has not been fully elucidated, which

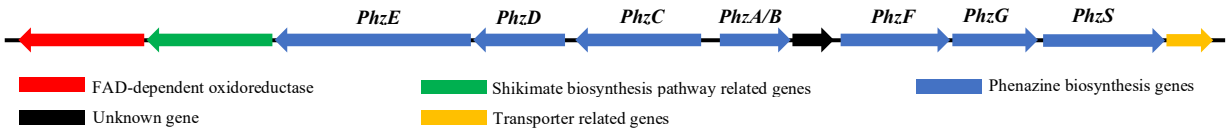

Locus tag	sequence	Homolog	Accession number	coverage (%)	identity (%)
ctg181_1	2-1216	3-hydroxyhenzoate 6-monooxygenase	RZB16712.1	97.8	48.0
ctg181_2	1213-2460	3-phosposhikimate 1-carboxyvinyltransferase	AKC91623.1	50.8	67.0
ctg181_3	1457-4346	PhzE	QJS40198.1	100	99.36
ctg181_4	4343-5002	PhzD	AFW04565.1	95	74.0
ctg181_5	5044-6216	PhzC	AFW04567.1	97.2	65.0
ctg181_6	6470-6958	PhzA/B	WP_061444507.1	100	100
ctg181_7	6958-7287	EsmH1/hypothetical protein	AFB35619.1	100	100
ctg181_8	7342-8178	PhzF	WP_061444505.1	91.7	55.0
ctg181_9	8194-8853	PhzG	QJS40192.1	91	99.5
ctg181_10	8867-10123	PhzS	QJS40191.1	96	99.75
ctg181_11	10120-10479	Nuclear transport factor 2 family protein	WP_061444502.1	100	100

Figure 38. Annotation of the phenazine BGC in *S. papuanewguineus*.

further motivated us to analyze the phenazine BGC in *S. papuanewguineus*.

Annotation of phenazine BGC in contig181 of the genome of *S. papuanewguineus* revealed the presence of (1) *PhzA/B*, *PhzC*, *PhzD*, *PhzE*, *PhzF*, and *PhzG* that were responsible for the production of phenazine, PCA, and PDA from chorismate (**Figure 38**); (2) *PhzS* (accession number: QJS40191.1), a flavin-containing monooxygenase that is responsible for the generation of 1,6-phenazinediol from PDA;[63] (3) 3-phosphoshikimate 1-carboxyvinyltransferase (also known as EPSP, accession number: AKC91623.1), an enzyme in the shikimate pathway that catalyzes the coupling of shikimate 3-phosphate and phosphoenol pyruvate into 5-enolpyruvylshikimate-3-phosphate, which is a key intermediate of the biosynthesis of chorismate;[51] (4) a FAD-dependent monooxygenase/3-hydroxybenzoate 6-hydroxylase (accession number: RZB16712.1) that catalyzes the conversion of 3-hydroxybenzoate to gentisate in the biosynthesis of diazaquinomycins;[64, 65] and (5) an unknown gene that shares 53% sequence identity with *EsmH1* gene (accession number: AFB35619.1) in the biosynthetic gene cluster of esmeraldins whose function has not been characterized.[66] However, genes that could potentially catalyze the dimerization of phenazines were not identified in contig181 and its neighboring contigs, contig180 and contig182, which impeded us from further elucidating the

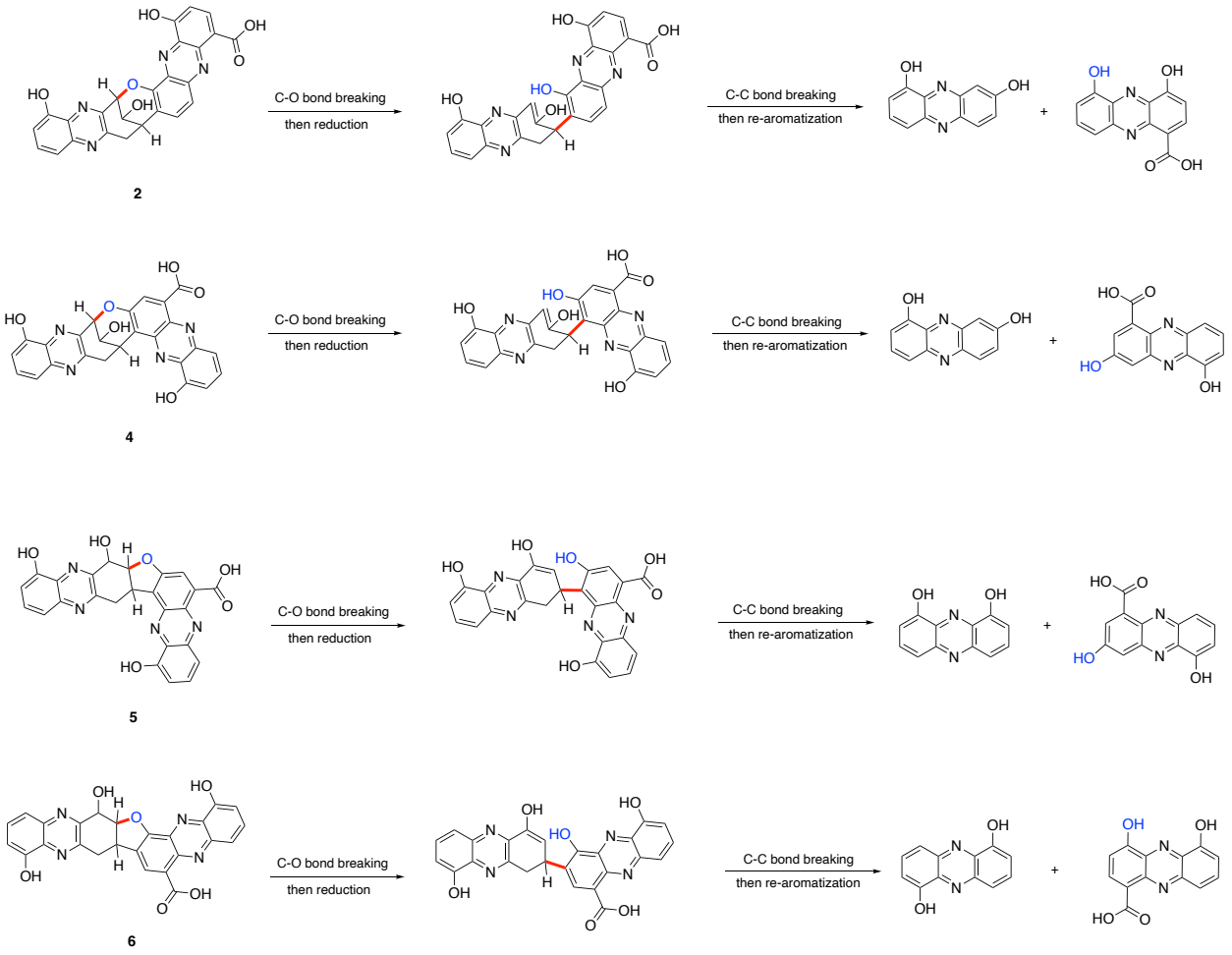

Figure 39. Retro-synthetic analyses of isolated diphenazines.

biosynthetic pathway of the isolated diphenazines.

Retro-synthetic analyses of these molecules suggested that they were likely constructed *via* a two-step mechanism in no particular order: (1) aryl coupling of a phenazinediol unit and a dihydroxy phenazine-carboxylic acid to form a new C-C bond, and (2) phenol-aryl coupling to form either a tetrahydrofuran or a tetrahydropyran ring through a new C-O bond (**Figure 39**). Cytochrome P450s, a superfamily of oxidative hemoproteins commonly found in nature, are known to be able to catalyze these bi-phenol C-C and C-O coupling reactions. For instance, *JulI*, a P450 enzyme in the biosynthesis pathway of julichromes, catalyzed the dimerization of

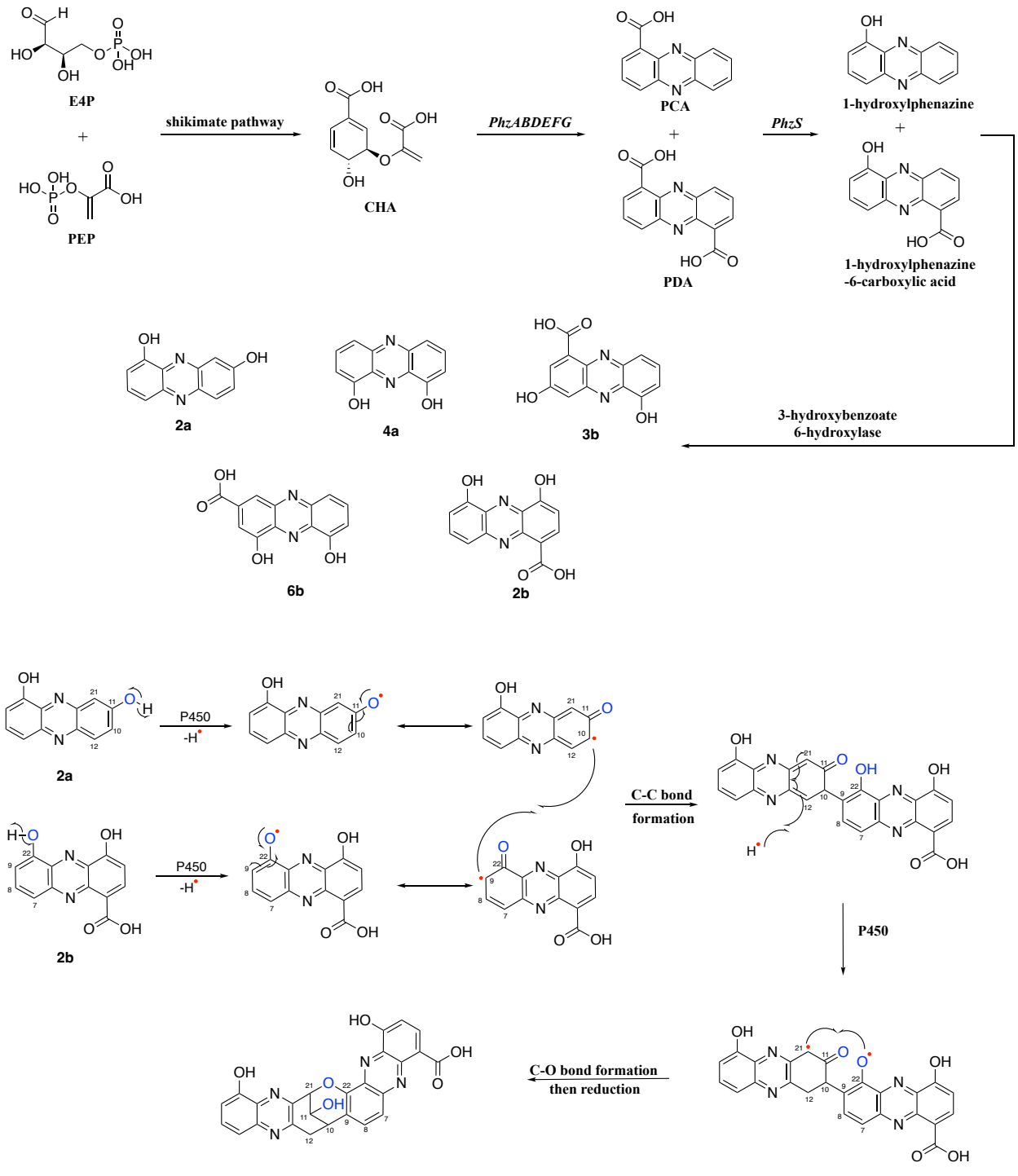

Figure 40. Proposed biosynthesis pathway of isolated diphenazines catalyzed by a hypothetical P450 enzyme.

julichrome Q_6 to form julichrome $Q_{6\text{-}6}$ *via C-C* coupling.[67, 68] *BmP7*, a P450 found in *P. luteoviolacea 2ta16*, catalyzed the dimerization of polybromophenol-based metabolites via *C-O* coupling.[69] These bi-phenol C-C and C-O coupling reactions go through a common radical

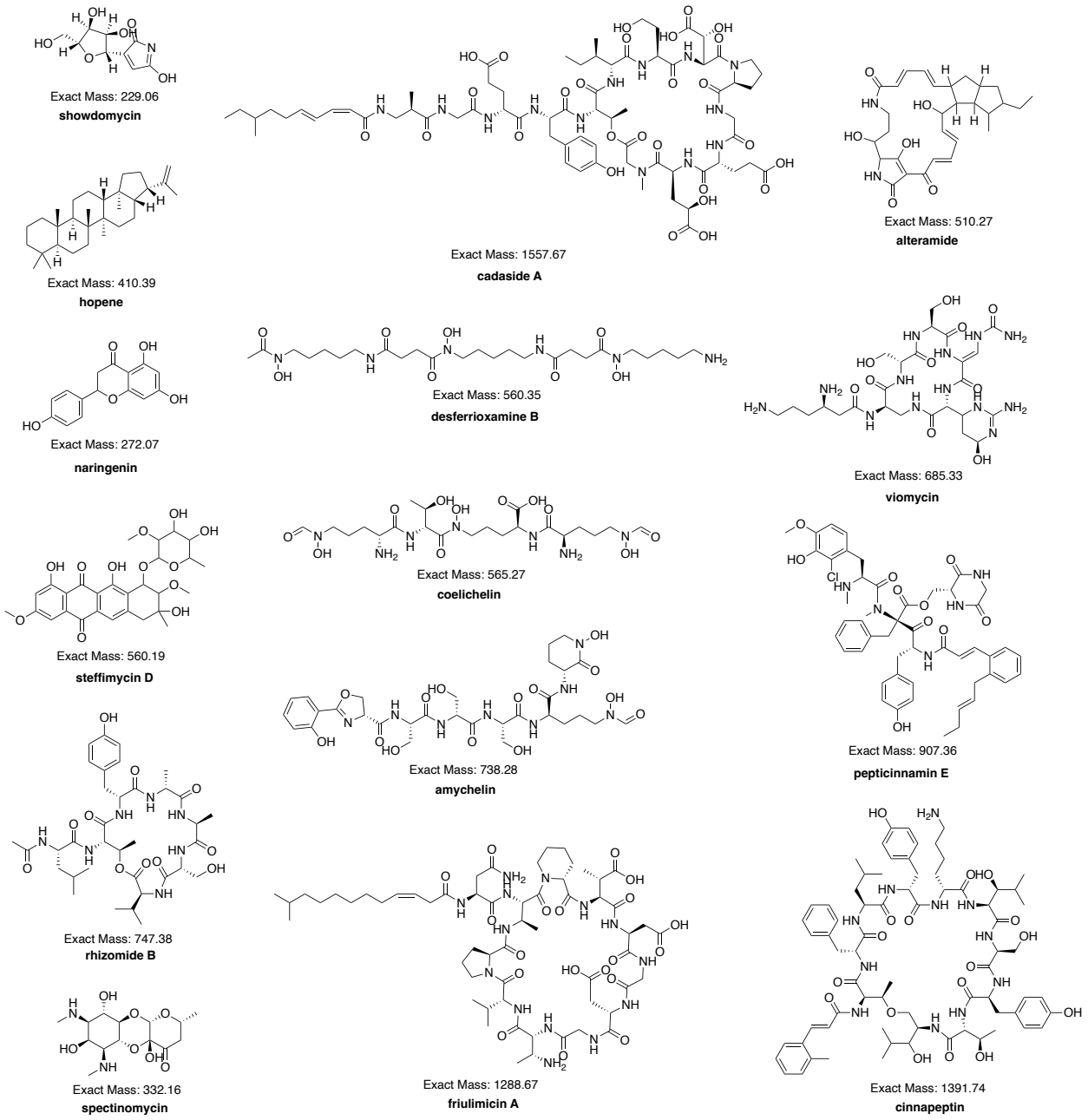

Figure 41. Structures of selected antiSMASH hits from YNYX265C.

mechanism: P450 enzymes generate oxygen-centered radicals on the phenolic hydroxyl group or carbon-center radicals on the carbon located in the *ortho* or *para* position of the phenolic hydroxyl group through the delocalized benzene ring system.[70, 71]

Based on these established mechanisms of P450-catalyzed bi-phenol coupling, a hypothetical mechanism of dimerization for the isolated diphenazines was proposed (**Figure 40**).

First, these starting phenazine units with variations in the positions of hydroxyl and carboxyl groups are generated from **1**, PDA, and PCA, most likely catalyzed by the identified 3-hydroxybenzoate 6-hydroxylase. Then, taking compound **2** as an example, the P450 enzyme generates carbon radicals at C-10 of the phenazinediol and C-9 of the dihydroxylphenazine-carboxylic acid. After that, the diradical combination results in the C-C bond formation between C-9 and C-10, and the tautomerization of C-22 carbonyl regenerates the 22-OH of the carboxyl phenazinediol. The carbon radical at C-21 generated by a free hydrogen radical through a delocalized ring system, combined with the oxygen radical at O-22 generated by the P450, closes the six-membered ring through the new C-O bond between C-21 and O-22. The subsequent reduction of the C-11 carbonyl by free hydrogen radical results in the final product, compound **2**. Contrary to **2** and **4**, the dimerization mechanisms of **5** and **6** require the generation of carbon radical at the *meta* position of the phenolic hydroxyl group, which is uncommon for P450-catalyzed bi-aryl coupling. All of these speculations need to be further investigated to fully elucidate the mechanism of the dimerization reactions that generate **2**–**7**.

2.5 Deconvolution of Other Strains

2.5.1 Other HTS hit strains:YNYX265C, 87797-1N, and 86930-1I

YNYX265C was another hit strain in the HTS campaign. This strain was deconvoluted using the same strategy as 06-282-1I: genome sequencing, chemical profiling, and bioactivity-guided purification. antiSMASH analysis of its genomic DNA revealed diverse classes of metabolites, including multiple non-ribosomal peptide synthetases (NRPSs), a few terpenoids, several polyketide synthases (PKSs), and one polycyclic tetramate macrolactone (PTM), which

is a PKS/NRPS hybrid (**Figure 41**). GNPS molecular networking analyses provided no interesting hits other than deferoxamine and fatty acids.

The crude extract of this strain was saturated with pink pigments of unknown origin that retained on the column and contaminated almost all HPLC fractions, which posed a challenge in the purification processes. The initial prep-HPLC followed by testing in PPI cat-ELCCA yielded F29 as the active fraction (**Figure 42**). Subsequent semi-prep HPLC and testing gave us F29-F7 as the active fractions. However, the molecule(s) were very low in quantity (800µg out of 40L of growth), which was not enough for a full characterization by NMR, and it only exhibited very modest activity (IC_{50} ~0.1 mg/mL). Thus, we decided not to follow up on this strain further. The strain 87797-1N was the third most active strain. Detailed deconvolution of this strain will be

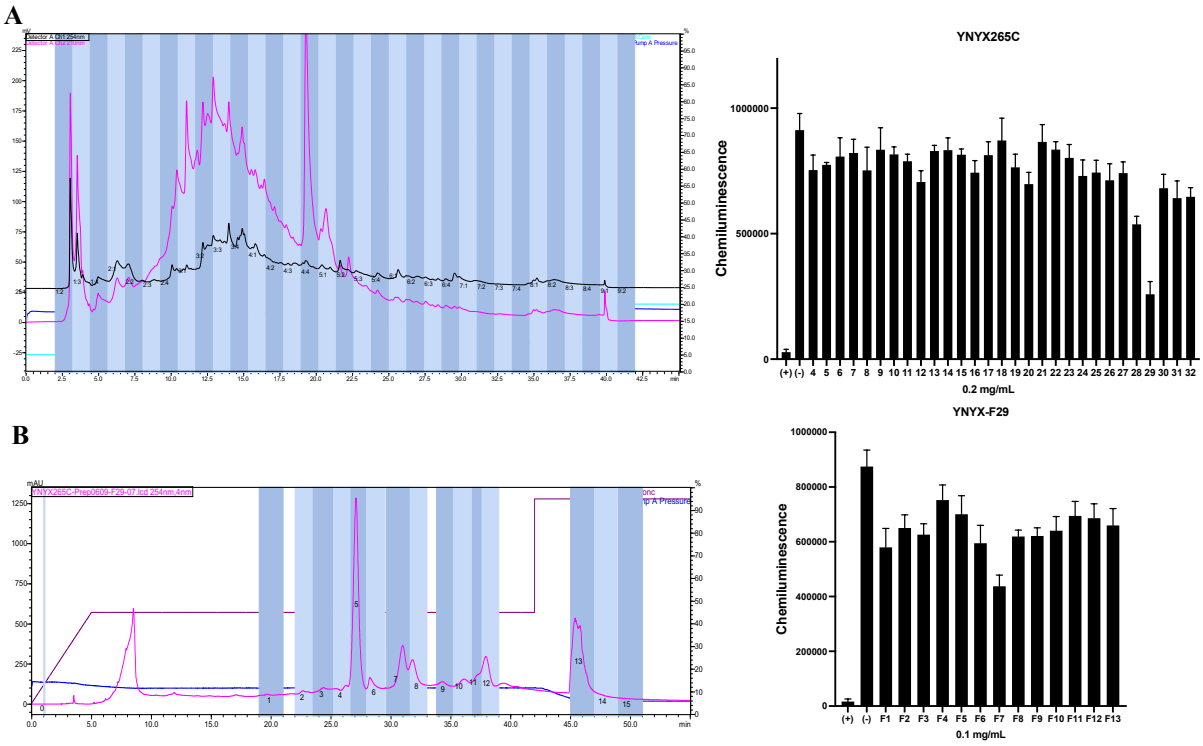

Figure 42. (A) Prep-HPLC chromatogram of crude extract of YNYX265C and the activities of fractions; 5% to 95% acetonitrile/H_2O (B/A) gradient; (B) Semiprep-HPLC chromatogram of F29 and the activities of fractions; 45% isocratic B/A gradient; C18 column, purple line: concentration of B (acetonitrile) in A (water); dark blue line: pump A pressure; pink curve: UV absorbance at 254 nm; black curve: UV absorbance at 190 nm; Left Y axis: mAU; Right Y-axis: concentration of B; X axis: acquisition time (min).

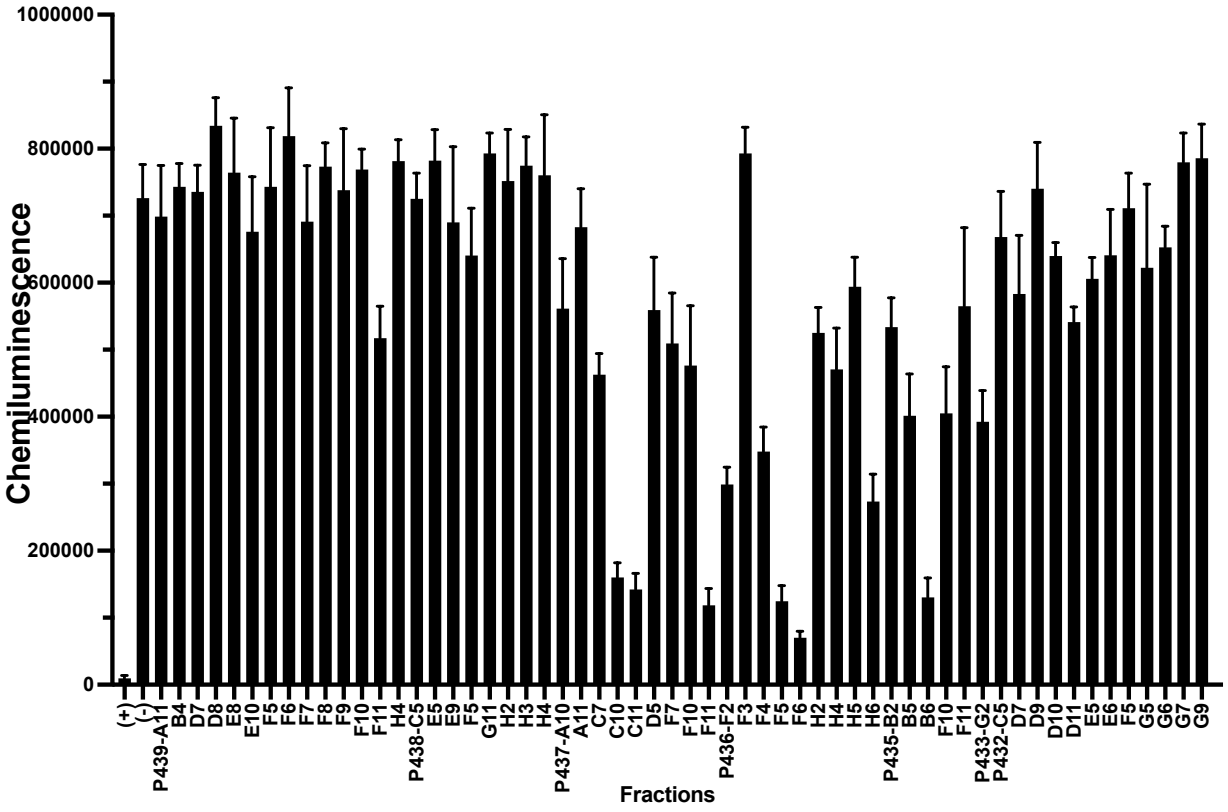

Figure 43. Activities of selected crude extracts and fractions.

further elaborated in Chapter 4. 86930-1I was inactive after the first round of preparative HPLC, so it was not followed up further.

2.5.2 Additional natural product extract plates

8 plates, namely P432-P439, were tested in PPI cat-ELCCA in two rounds: (1) all crude extracts and fractions were tested at a fixed concentration (0.15 mg/mL); (2) active fractions were retested at the same fixed concentration (0.15 mg/mL, **Figure 43**). BR55-I (P439-F11), A-M5-I (P436-F2, F4, F5, F6), 41383-MH10I (P436-H2, H4, H5, H6), P256-3I (P435-F10, F11), EMU227-I (P437-C10, C11), and EMU247-I (P437-A10, A11) were selected for the subsequent regrowth and deconvolution. All strains were regrown in a 4-L scale and the crude extracts were fractionated by prep-HPLC using 5-95% acetonitrile/H_2O without any acid modifiers and then tested. All fractions were tested at 0.1 mg/mL concentration and only a few fractions from A-

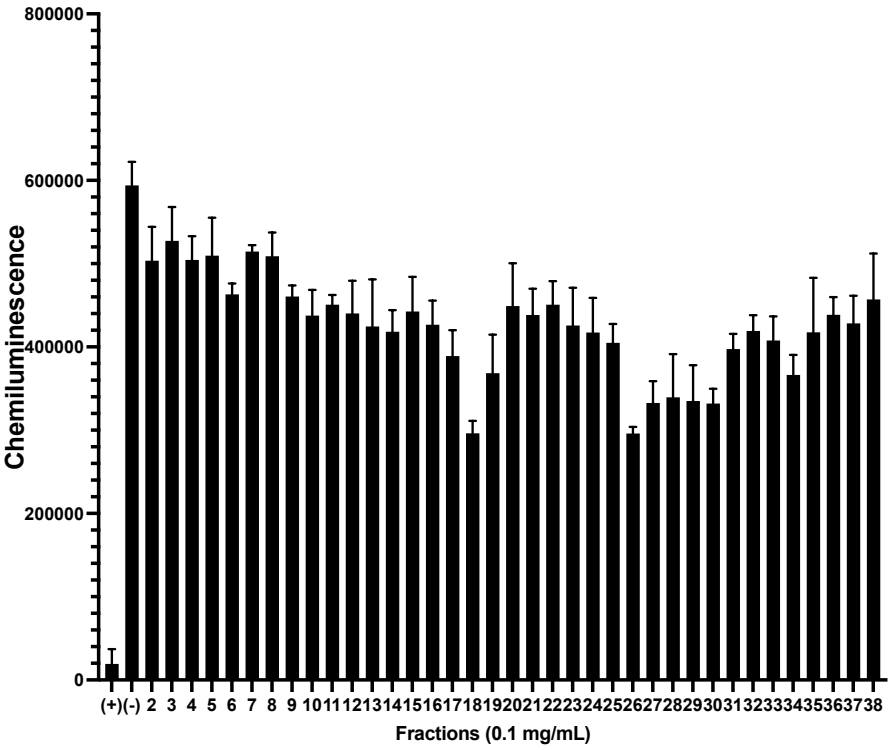

Figure 44. Activities of prep-HPLC fractions of A-M5-I.

M5-I were active (**Figure 44**). By comparing the LC-MS and LC-MS/MS profiling with the active diphenazines isolated from 06-282-1I, we found that their masses and retention times match with each other, suggesting that the active components in A-M5-I were also diphenazines. This was further confirmed by proton NMR.

2.6 Conclusion

In this study, we adopted catalytic enzyme-linked click chemistry assay (cat-ELCCA) technology for enabling the screening of full-length PPIs, including the interaction of eIF4E with 4E-BP1 and eIF4G. Based on the success of NPs in targeting "undruggable" proteins like eIF4E and its PPIs, coupled with the demonstrated applicability of cat-ELCCA for screening small-molecules as well as complex NPE libraries, we deployed the assay to complete an HTS campaign to NP-based inhibitors of eIF4E PPIs. From these efforts, we isolated monophenazine-

and diphenazine-based NPs as inhibitors of eIF4E PPIs from an active strain, *S. papuanewguineus*, leading to the discovery of a novel diphenazine, izumiphenazine E (**6**), which shows promising binding to eIF4E in cellular assays, representing a novel scaffold targeting eIF4E PPIs.

2.7 Methods and Materials

2.7.1 General LC-MS/MS methods and materials

LC-HRMS/MS analyses of Biotage fractions, HPLC fractions, and purified compounds were performed using an Agilent 1290 Infinity II UPLC coupled to an Agilent 6545 ESI-Q-TOF-MS system operating in both positive and negative modes. Chromatography was performed using a Phenomenex Kinetex® 1.7 μm Phenyl-Hexyl 100 Å (2.1 × 50 mm) column. The injection volume was 2 μL per sample. The samples were eluted utilizing a gradient starting with a 1 min isocratic wash step consisting of 90% A (95% water/5% acetonitrile with 0.1% formic acid) and 10% B (100% acetonitrile with 0.1% formic acid), then 6 min linear gradient step starting from 10% B to 100% B and ended with 2 min of 100% B wash with a flow rate of 0.4 mL/min. The divert valve was set to MS for 0 – 7.4 min and set to waste from 7.4 - 9 min. The conditions of the dual AJS ESI were set with gas temperature at 320 °C, sheath gas temperature at 350 °C, sheath gas flow rate at 11 L/min, and source capillary voltage at 3500 V. The mass range of MS was set to 100 – 2000 m/z and acquisition rate was set to 10 spectra per second. The mass range of MS/MS was set to 50 – 2000 m/z; acquisition rate was set to 6 spectra per second, and isolation width was set to ~1.3 m/z. The collision energy was set based on the formula: Collision Energy = (5 × m/z)/100 + 10. Maximum precursor per cycle was set to 9 and the MS/MS mass

error tolerance was ± 20 ppm. The reference masses for positive mode are purine $C_5H_4N_4$ $[M+H]^+$ ion (m/z 121.050873) and hexakis(1H,1H,3H-terafluoropropoxy)-phosphazine $C_{18}H_{18}F_{24}N_3O_6P_3$ $[M+H]^+$ ion (m/z 922.009798). The reference masses for negative mode are trifluoroacetic acid $C_2HF_3O_2$ $[M-H]^-$ (m/z 112.985587) and hexakis(1H,1H,3H-terafluoropropoxy)-phosphazine $C_{18}H_{18}F_{24}N_3O_6P_3$ $[M+TFA-H]^-$ (m/z 1033.988109). All solvents used for Biotage fractionation were ACS grade and those used for HPLC purification and LC-HRMS/MS analyses were HPLC grade or better unless otherwise stated.

2.7.2 General assay and biology methods and materials

For screening, plate washing was performed using a Biotek 405 ELX plate washer. Liquid handling was performed using a Multidrop Combi Reagent Dispenser (Thermo Scientific). All samples were dispensed using a Sciclone (Caliper) liquid handler with V&P pintool. For PPI cat-ELCCA, Horseradish peroxidase (HRP), streptavidin-coated 384-well plates (white, high binding capacity; cat#15505), and SuperSignal West Pico Chemiluminescent substrate kit were purchased from Pierce. Preparation of biotin-eIF4E, biotin-eIF4G, mTet-4E-BP1, mTet-eIF4E, and TCO-HRP was carried out as previously described.[16] Pyocyanin,1,6-phenazinediol, phenazine, and undecylprodigiosin were all purchased from commercial sources. NPE library HTS, hit reconfirmation, and testing of biotage fractions, HPLC fractions, and purified compounds were conducted using PPI Cat-ELCCA as previously described.[16] Chemiluminescence data was collected on a BioTek Cytation3 or PHERAstat plate reader using LUM plus module (BMG Labtech). For cellular assays, gels were imaged on a ProteinSimple Fluorchem M Gel Imager or a Biorad ChemiDoc imaging system. BL21DE3 *E.Coli* were used for protein expression. Mia-Paca-2 and HEK293T cells were cultured in DMEM (Corning) supplemented with 2 mM *L*-glutamine, 1% Penicillin/streptomycin (Gibco), and 10% FBS

(Atlanta Biologicals). Cells Were incubated at 37 °C in a humidified atmosphere containing 5% CO_2.

2.7.3 General data analysis method

All LC-MS/MS chromatograms, Extracted Base Peak Chromatograms (BPCs), extracted UV (254 nm) traces, cat-ELCCA data, and quantification of CESTA data were plotted using GraphPad Prism 9 (version 9.4.1) for MacOS (GraphPad Software, www. Graphpad.com).

2.7.4 Natural product extract library

The Natural Product Extract (NPE) library housed at the University of Michigan Center for Chemical Genomics contains ~50,000 (and growing) pre-fractionated natural product extracts derived from a unique collection of diverse marine and terrestrial actinomycetes, fungi, and cyanobacteria collected from various locations throughout the world, including but not limited to, Antarctica, Brazil, China, Costa Rica, Israel, Panama, Papua New Guinea, Peru, and United States. The methods for preparation, purification, and maintenance of these extracts were described in previous literature.[25, 26]

2.7.5 HTS PPI cat-ELCCA Protocol (384-well format)

Buffer A: 50 mM Phosphate Buffer (pH 7.4), 200 mM NaCl, 0.01% Tween-20, 2 mM DTT

Buffer B: 50 mM Phosphate Buffer (pH 7.4), 200 mM NaCl, 0.05% Tween-20

Buffer C: 50 mM Phosphate Buffer (pH 7.4)

Pre-wash the plate with Buffer A

1. Immobilization of biotin-eIF4E (10 µL of 50 nM in Buffer A)
    a. **Prime the tubing well with buffer**
    b. POS Ctrl (usually columns 23-24): add Buffer A (10 µL)

c. NEG Ctrl (usually columns 1-2): add biotin-eIF4E (10 µL)

d. Compound wells (usually columns 3-22): add biotin-eIF4E (10 µL)

e. Cover the wells with plate-sealing tape.

f. Spin down on centrifuge (1000×RPM, 1 min, 4 °C)

g. Overnight incubation (4 °C)

h. **Thoroughly wash and clean the dispensing cassette with Buffer C, and then with water**

2. Removing well contents

    a. Prime ELX405 with Buffer B and wash

    b. Lay absorbent towel, smack the plates post wash (should see residual liquid leaving stains on the towel)

    c. Finish washing the rest of the plates in the exact same way prior to the next step

3. PPI incubation of mTet 4E-BP1 (10 µL of 4 nM in Buffer A)

    a. **Prime the tubing well with buffer**

    b. Add mTet-4E-BP1 (10 µL of 4 nM in Buffer A) to all the wells

    c. Dispense the compounds

    d. Cover the wells with plate-sealing tape

    e. Spin down on centrifuge (1000×RPM, 1 min, 4 °C)

    f. Incubate at 4 °C for 30 min

4. Removing well contents

    a. Prime ELX405 with Buffer B and wash

    b. Lay absorbent towel, smack the plates post wash (should see residual liquid leaving stains on the towel)

c. Finish washing the rest of the plates in the exact same way prior to the next step

5. Click chemistry with TCO-HRP (10 µL of 1 µM in Buffer A)
    a. **Prime the tubing well with buffer**
    b. Add TCO-HRP (10 µL of 1 µM in Buffer A) to all the wells
    c. Cover the wells with plate-sealing tape
    d. Spin down on centrifuge (1000×RPM, 1 min, 4 °C)
    e. Incubate at room temperature for 30 min
6. Removing well contents
    a. Prime ELX405 with Buffer B and wash
    b. Lay absorbent towel, smack the plates post wash (should see residual liquid leaving stains on the towel)
    c. Finish washing the rest of the plates in the exact same way prior to the next step
7. Final wash with Buffer C
    a. Prime ELX405 with Buffer C and wash
    b. Lay absorbent towel, smack the plates post wash (should see residual liquid leaving stains on the towel)
    c. Finish washing the rest of the plates in the exact same way prior to the next step
8. Chemiluminescence detection
    a. **Prime the tubing well with buffer**
    b. Add chemiluminescent substrate (25 µL of 1:1 mixture of black & white components of the chemiluminescence substrates) to all the wells
    c. Stack the plates from bottom up
9. Readout

a. Load up the stacker with the plates, and start the data collection
    i. The protocol takes the focal adjustment from the first plate and keeps that constant throughout the rest of the plates
    ii. The protocol marks the gain from A2, and sets it to 60% for each plate

2.7.6 Fermentation for hit reconfirmation

All strains were streaked onto **R2YE agar**: 5g yeast extract, 103 g sucrose, 10 g dextrose, 0.1 g casamino acid, 0.25 g K_2SO_4, 10.12 g $MgCl_2 \bullet 6H_2O$, 5.73 g TES buffer, 2 mL trace element solution (10 mg $(NH_4)_6Mo_7O_{24} \bullet 4H_2O$, 10 mg $Na_2B_4O_7 \bullet 10H_2O$, 10 mg $MnCl_2 \bullet 4H_2O$, 10 mg $CuCl_2 \bullet 2H_2O$, 200 mg $FeCl_3 \bullet 6H_2O$, 40 mg $ZnCl_2$, 1 L ddH_2O, filter sterilize), 10 mL of 0.5% KH_2PO_4, 4 mL of 5M $CaCl_2 \bullet 2H_2O$, 15 mL of 20% *L*-Proline, 7 mL 1N NaOH, 25 μg/mL nalidixic acid, 10 μg/mL benomyl, 15 g agar, 1 L ddH_2O. Plates were grown for 5-7 days at 28 °C. For each strain, 3 mL seed cultures in 14-mL dual-position cap tubes were inoculated with a loop-full of vegetative cells from R2YE plates and grown for 5 days at 28 °C, 200 r.p.m. 3-mL seed cultures were inoculated into 100-mL seed cultures in 250-mL baffled flask and they were grown for 7 days at 28 °C, 200 r.p.m. 50-mL of seed cultures were inoculated into 1 L fermentation media in 2.8 L baffled Fernbach flasks and grown for 7 days at 28 °C, 200 r.p.m. For 06-282-1I, 39017-N1I, 86930-1I, 82379-N3I, 87745-N2I, 32420-N3I, N383-A3I, GXXG380I, 34360-3I and 58236I, **ISP2** media (4 g yeast extract, 10 g malt extract, 4 g dextrose, 30 g NaCl, 1 L ddH_2O) were used in both seed cultures and fermentation. For 34365-A1N and 87797-1N, ISP2 was used for seed cultures and **Nutrient Poor** media (0.25 g yeast extract, 0.64 g malt extract, 0.25 g dextrose, 30 g NaCl, 1 L ddH_2O) was used for fermentation.

For R02-N5R, YNYX265C, and 90357-4R, **A3M** media (3 g yeast extract, 10 g soluble starch, 4 g dextrose, 2 g pharma-media, 20 mL glycerol, 1 L ddH_2O) were used in both seed cultures and fermentations. In addition, 10 mL of *Corneybacterium* cultured in **V22** media (2 g yeast extract, 10 g soluble starch, 5 g dextrose, 3 g NZ Case, 0.5 g $MgSO_4 \bullet 7H_2O$, 3 g $CaCO_3$, 1 g K_2HPO_4, 1 L ddH_2O) was added to the fermentation medium of YNYX265C on day 2 of fermentation. 10 mL of *Rhodococcus* cultured in V22 media was added to each of the fermentation media of R02-N5R and 90357-4R on day 2 of fermentation.

At day 7 of the fermentation, 25 g of Amberlite XAD16 resin contained within a polypropylene mesh bag was added to each fermentation culture, and shaken overnight at 28 °C, 200 r.p.m, except for R02-N5R, YNYX265C, and 90357-4R, resin bags were added at day 3 of fermentations. At day 8, all resin bags were removed and washed extensively with dIH_2O to remove any water-soluble media components and residual cell mass adsorbed on the resin bags. Each washed resin bag was extracted with 250 mL methanol and 250 mL ethyl acetate (EtOAc). The combined organic fractions were dried *in vacuo*, and then re-dissolved in minimal methanol. The solutions were centrifuged, and the supernatants were loaded onto C18 resin and dried extensively *in vacuo* prior to Biotage C18 fractionation.

2.7.7 Fractionation of crude extracts of HTS hits for reconfirmation

Flash chromatography was performed using an automated chromatography system (Isolera Selekt, Biotage®) utilizing a pre-packed Phenomenex® reverse phase C18 column (12g, column volume = 17 mL). Dried C18 loaded with crude extracts was packed into a separate column that was attached to the Phenomenex® C18 column for fractionation. Materials were eluted with a flow rate of 20 mL/min collecting 5CV (85 mL) fractions. Materials were eluted utilizing a stepwise methanol/water gradient: 5CV of 100% water (F1);10% methanol in water

(F2); 25% methanol in water (F3); 40% methanol in water (F4); 55% methanol in water (F5); 70% methanol in water (F6); 85% methanol in water (F7); 100% methanol (F8); final wash with 100% acetonitrile (F9) into a total 9 fractions. All fractions were dried into pre-weighed scintillation vials using a V10-touch evaporator (Biotage®) coupled with a Gilson GX-271 Liquid Handler. All crude extracts and fractions were dissolved into 1 mg/mL in methanol and MS/MS data in both positive and negative modes were acquired using the method described in general methods and materials section above.

2.7.8 GNPS molecular networking

The acquired MS/MS data for all crude extracts and Biotage® fractions were converted from Agilent MassHunter data files (.d) to mzXML file format using MSConvert software, which is part of the ProteoWizard package.[72] The mzXML files were then transferred to the global Natural Products Social Molecular Networking server (GNPS) (gnps.ucsd.edu). A molecular network was created using the GNPS data analysis workflow.[31] The precursor ion mass tolerance was set to 0.05 Da and a MS/MS fragment ion mass tolerance to 0.05 Da. A network was then created where edges were filtered to have a cosine score above 0.7, a minimum of 6 matched fragment ions and a minimum cluster size of 2 nodes. Furthermore, edges between two nodes were kept in the network of and only if each of the nodes appeared in each other's respective top 10 most similar nodes. Finally, the maximum connected component size in a cluster was set to 100. The spectra in the input network were then searched against GNPS' spectral libraries. All matches were required to have a score above 0.7 and at least 6 matched peaks. The resulting network was imported into Cytoscape (version 3.9.1) for visualization,[73] where nodes corresponding to media components and solvent were subtracted. The remaining

nodes represent parent (+) or (-) m/z metabolites detected in analyzed extracts, with node size indicating metabolite abundance.

2.7.9 Scale-up growth, extraction, and fractionation of S. papuanewguineus

S. papuanewguineus was streaked onto R2YE agar plates. Plates were grown for 5-7 days at 28 °C. 3 mL ISP2 + salt medium in 14-mL dual-position cap tubes were inoculated with a loop-full of vegetative cells from R2YE plates and grown for 5 days at 28 °C, 200 r.p.m (20×). 3-mL seed cultures were inoculated into 100 mL ISP + salt in a 250-mL baffled flask and they were grown for 7 days at 28 °C, 200 r.p.m (20×). 50-mL seed cultures were inoculated into 1 L fermentation media in 2.8-L baffled Fernbach flasks and grown for 7 days at 28 °C, 200 r.p.m (40×). On day 7 of the fermentation, 25 g of Amberlite XAD16 resin contained within a polypropylene mesh bag was added to each fermentation culture and shaken overnight at 28 °C, 200 r.p.m. At day 8, all resin bags were removed and washed extensively with dIH_2O to remove any water-soluble media components and residual cell mass adsorbed on the resin bags. Washed resin bags were combined and extracted with 250 mL methanol and 250 mL ethyl acetate (EtOAc) per bag. The combined organic fractions were dried *in vacuo*, and then re-dissolved in minimal methanol. The solutions were centrifuged, and the supernatants were divided into two portions that were processed using two different methods. One portion of the material (~20 L) was loaded onto C18 resin and dried extensively *in vacuo* prior to Biotage® C18 fractionation and the other portion (~20 L) was directly subject to preparative RF-HPLC fractionation.

Preparative RF-HPLC fractionation was performed using Shimadzu LC-20AP system equipped with a reverse-phase Phenomenex Kinetex® 5 μm C18 100 Å (250 × 21.2 mm) column, and an autosampler. The injection volume was set to either 1 mL or 2 mL. The materials

(brought up in methanol at ~100 to 200 mg/mL) were eluted with a flow rate of 20 mL/min and a linear gradient starting with a 2 min isocratic wash step consisting of 95% water and 5% acetonitrile, then 40 min linear gradient step starting from 5% acetonitrile in water to 95% acetonitrile in water, then 10 min wash with 95% acetonitrile in water, ended with a 10 min equilibration with 5% acetonitrile in water. Flash chromatography was performed using an automated chromatography system (Isolera Selekt, Biotage®) utilizing a pre-packed Phenomenex® reverse phase C18 column (12g, column volume = 17 mL). The materials were either eluted with a flow rate of 15 mL/min collecting 4CV (68 mL) fractions. Materials were eluted utilizing a linear gradient of acetonitrile/water: 4CV of 5% acetonitrile in water with 0.01% trifluoroacetic acid(F1);16CV of linear gradient of 5% acetonitrile in water to 100% acetonitrile with 0.01% trifluoroacetic acid (F2-F5); final wash with 100% acetonitrile with 0.01% trifluoroacetic acid (F6) into a total 6 fractions. All Biotage® and prep-HPLC fractions were dried into pre-weighed scintillation vials using a V10-touch evaporator (Biotage®) coupled with a Gilson GX-271 Liquid Handler. All crude extracts and fractions were dissolved into 1 mg/mL in methanol and MS/MS data in both positive and negative modes were acquired using the method described in the general methods and materials section above.

2.7.10 Purification of Compounds 1-8

Biotage® fraction F3 containing compounds **1**, **2**, and **3** were subject to two rounds of semi-preparative HPLC purification using Shimadzu LC-20AT system equipped with a reverse-phase Phenomenex Luna® 5 μm Phenyl-Hexyl 100 Å (250 × 10 mm) column and an autosampler. The injection volume was set to 200 μL. The materials (brought up in methanol at ~10 to 20 mg/mL) were eluted with a flow rate of 4 mL/min and an isocratic gradient of 35%

acetonitrile in water with 0.01% trifluoroacetic acid (TFA) for 35 min, then 7 min isocratic wash with 95% acetonitrile in water with 0.01% TFA, ended with a 7 min equilibration with 5% acetonitrile in water with 0.01% TFA. HPLC fractions that contains compound **1**, **2**, and **3** were subject to a second round of semi-preparative HPLC purification using the same system and column. The injection volume was set to 200 μL. The materials (brought up in methanol at ~5 to 10 mg/mL) were eluted with a flow rate of 4 mL/min and an isocratic gradient of 30% acetonitrile in water with 0.01% TFA for 30 min, then 7 min isocratic wash with 95% TFA in water with 0.01% TFA, ended with a 7 min equilibration with 5% acetonitrile in water with 0.01% TFA, yielding 0.3 mg/L of **1**, 0.05 mg/L of **2**, and 0.04 mg/L of **3**.

Biotage® fraction F4 containing compounds **4**-**7** were first subject to one round of preparative HPLC purification using Shimadzu LC-20AP system equipped with a reverse-phase Phenomenex Kinetex® 5 μm Phenyl-Hexyl 100 Å (250 × 21.2 mm) column. The injection volume was set to 2 mL. The materials (brought up in methanol at ~100 mg/mL) were eluted with a flow rate of 20 mL/min and an isocratic gradient of 40% acetonitrile in water with 0.01% TFA for 20 min, then 10 min isocratic wash with 95% acetonitrile in water with 0.01% TFA, ended with a 10 min equilibration with 40% acetonitrile in water with 0.01% TFA. Fractions containing compounds 4-6 were then subject to one round of semi-preparative HPLC purification using Shimadzu LC-20AT system equipped with a reverse-phase Phenomenex Luna® 5 μm Phenyl-Hexyl 100 Å (250 × 10 mm) column. The injection volume was set to 200 μL. The materials (brought up in methanol at ~10 mg/mL) were eluted with a flow rate of 4 mL/min and an isocratic gradient of 40% acetonitrile in water with 0.01% TFA for 30 min, then 7 min isocratic wash with 95% TFA in water with 0.01% TFA, ended with a 7 min equilibration with

40% acetonitrile in water with 0.01% TFA, yielding 0.4 mg/L of **4**, 1 mg/L of compound **5**, 0.05 mg/L of **6**, and 0.2 mg/L of **7**.

The fractions obtained from initial preparative RF-HPLC fractionation that contain compound **1**-**7** were then subject to two to three round of semi-preparative HPLC purification using Shimadzu LC-20AT system equipped with a reverse-phase Phenomenex Luna® 5 μm Phenyl-Hexyl 100 Å (250 × 10 mm) column. Fractions that contain compounds **1**, **2**, and **3** (brought up in methanol at ~5 mg/mL) were eluted with a flow rate of 4 mL/min and an isocratic gradient of 30% acetonitrile in water with 0.01% TFA for 30 min, then 10 min isocratic wash with 95% acetonitrile in water with 0.01% TFA, ended with a 10 min equilibration with 5% acetonitrile in water with 0.01% TFA with similar yields. Fractions that contain compounds **4**-**7** were eluted with a flow rate of 4 mL/min and an isocratic gradient of 40% acetonitrile in water with 0.01% TFA for 30 min, then 10 min isocratic wash with 95% acetonitrile in water with 0.01% TFA, ended with a 10 min equilibration with 5% acetonitrile in water with 0.01% TFA with similar yields.

2.7.11 Genome extraction, sequencing, assembly, and annotation

The genomic DNA for 06-282-1I was extracted using the Lucigen MasterPure Complete DNA and RNA Purification Kit following the manufacturer's protocol with minor modifications including an additional lysis step using EDTA (50mM) and lysozyme (10 mg/mL). The genomic DNA was sequenced at the MiGS-Seq Center in Pittsburg. The sample library was prepared using the Illumina DNA Prep kit and IDT 10bp UDI indices and sequenced to 1GB depth on an Illumina NextSeq 2000 platform, generating paired end reads (2x151bp) with a quality score of Q30 or higher. Demultiplexing, quality control and adapter trimming was performed with bcl-convert (v3.9.3).[74] A total of 7,538,537 read pairs were obtained. The 06-282-1I strain was

assembled using Unicycler v0.4.8 with the following parameters: -t 8 –min_fasta _length 300 –keep 2 –no_pilon, and polished using Pilon 1.23 with 2 rounds of iteration as part of the comprehensive genome analysis service at PATRIC.[75] QUAST v5.0.2 was used for quality assessment and Bandage 0.8.1 for assembly visualization. The resulting assembled genome has an estimated length of 7,871,553 bp long and an average GC content of 72.19% (**Figure S6**). The genome was annotated using RAST tool kit (RASTtk)[76] to reveal a total of 7,466 protein coding sequences (CDS), 53 transfer RNA (tRNA) genes, and 2 ribosomal RNA (rRNA) genes. The annotation included 1,908 hypothetical proteins and 5,558 proteins with functional assignment that included 1,314 proteins with Enzyme Commission (EC) numbers,[77] 1,139 with Gene Ontology (GO) assignments,[78] and 1,023 proteins that were mapped to KEGG pathways.[79]

Whole-genome similarity metrics including Average Nucleotide Identity (ANI) and DNA-DNA Hybridization (DDH) were obtained to estimate genetic relatedness and define phylogeny. ANI values were calculated using the gANI method in the FBAC.fmicrobe.cn platform.[29] For the phylogenomic inference, all pairwise comparisons among the set of genomes were conducted using GBDP and accurate intergenomic distances inferred under the algorithm 'trimming' and distance formula d5.[28] 100 distance replicates were calculated each. Digital DDH values and confidence intervals were calculated using the recommended settings of the GGDC 3.0.[28, 29] A whole-genome sequence-based phylogenetic tree was built using the TYGS analysis method. The tree was inferred with FastME 2.1.6.1 from GBDP distances calculated from genome sequences.[80] The branch lengths were scaled in terms of GBDP distance formula d5. The numbers above branches were GBDP pseudo-bootstrap support values >60 % from 100 replications, with an average branch support of 92.8 %. The tree was rooted at the midpoint. The genome sequence of *S. papuanewguineus* was then analyzed by antiSMASH in relax mode to

identify plausible BGC of compound **1**-**7**. All genes in the putative phenazine BGC were annotated by protein BLAST.[81]

2.7.12 Cell viability assay

The Cell Titer-Glo® assay kit was purchased from Promega and was performed according to the manufacturer's instructions. Briefly, 2,000 cells of Mia Paca -2 cell line were plated in a white, 96-well tissue culture-treated plate. Cells were treated with the compounds at different concentrations in triplicate and incubated for 48 hours. After 48 hours, the cell culture media was replaced with 100 µl of OptiMEM and then lysed with 100 µl of Cell Titer-Glo® reagent. Total luminescence was read within 1 h using a BioTek Cytation 3 reader. Data was normalized and processed in GraphPad Prism 9.

2.7.13 Cellular thermo shift assay (CETSA)

Cultured HEK 293 cells were trypsinized and washed with PBS. The cells were then diluted in PBS supplemented with protease inhibitors. The cell suspensions were freeze-thawed three times using liquid nitrogen. The soluble fraction (lysate) was separated from the cell debris by centrifugation at 15000 rpm for 25 minutes at 4°C.The cell lysates were then divided and treated with either the control (DMSO) or the compounds. After one-hour incubation at room temperature, lysates were divided into 100µL aliquots and heated at 42°C ,49°C and 53°C for 3 minutes followed by cooling at 20°C for 3 minutes. The heated lysates were centrifuged 15000 rpm for 25 minutes at 4°C to separate the soluble fractions from precipitates. The supernatants were transferred to new tubes and analyzed by sodium dodecyl sulfate-polyacrylamide gel electrophoresis (SDS-PAGE). Samples were run on a 4–12% Bis-Tris gel and transferred to PVDF membrane in Towbin's Buffer. The membrane was blocked in 5% milk for 1 h at 25 °C,

and then incubated with a primary antibody (overnight at 4 °C) and secondary antibody (1 h at 25 °C). eIF4E antibody was purchased from cell signaling technology (# 9742) and Actin-HRP antibody was purchased from Santa Cruz Biotechnology (#sc-47778). Proteins were visualized in a Biorad ChemiDoc imaging system. Figures were formatted in Adobe Illustrator.

2.7.14 M^7GDP cap affinity assay

The cap pull-down assay was carried out as previously described.[16] For whole cell cap pull-down, cells were grown in 6-cm dishes and treated with the compound for 6 h. Cells were then lysed in cap pull-down buffer (50 mM HEPES-KOH (pH 7.5), 150 mM KCl, 1 mM EDTA, 2 mM DTT and 0.1% Tween 20) containing protease inhibitors and freeze-thawed three times. The cell lysate was centrifuged at 15,000 rpm for 25 min. The supernatant was subsequently incubated for 2 hours at 4 °C with m^7GDP agarose resin. Beads were washed 3× with the cap pull-down buffer, 1× with TBS, and 1× with water. Proteins were eluted by boiling in 2× LDS sample buffer for 10 min at 70 °C, resolved on a 4–12% Bis-Tris gel and proteins were probed by western blot as described above. For cell lysate cap pull-down, cells grown in a 6-cm tissue culture plate were harvested in cap pull-down buffer and freeze-thawed three times. The cell lysate was centrifuged at 15000 rpm for 25 minutes to remove cell debris. The supernatant was incubated with the compound for 1 hour at room temperature and pull-down and western blot was carried out as described for whole cell cap pull-down assay.

2.8 References

(1) Ruggero, D. Translational Control in Cancer Etiology. *Csh Perspect Biol* **2013**, *5* (2).

(2) Smith, R. C. L.; Kanellos, G.; Vlahov, N.; Alexandrou, C.; Willis, A. E.; Knight, J. R. P.; Sansom, O. J. Translation initiation in cancer at a glance. *J Cell Sci* **2021**, *134* (1).

(3) Mamane, Y.; Petroulakis, E.; Rong, L. W.; Yoshida, K.; Ler, L. W.; Sonenberg, N. eIF4E - from translation to transformation. *Oncogene* **2004**, *23* (18), 3172-3179.

(4) Pelletier, J.; Graff, J.; Ruggero, D.; Sonenberg, N. Targeting the eIF4F Translation Initiation Complex: A Critical Nexus for Cancer Development. *Cancer Res* **2015**, *75* (2), 250-263.

(5) Osborne, M. J.; Borden, K. L. The eukaryotic translation initiation factor eIF4E in the nucleus: taking the road less traveled. *Immunol Rev* **2015**, *263* (1), 210-223.

(6) Brunn, G. J.; Hudson, C. C.; Sekulic, A.; Williams, J. M.; Hosoi, H.; Houghton, P. J.; Lawrence, J. C.; Abraham, R. T. Phosphorylation of the translational repressor PHAS-I by the mammalian target of rapamycin. *Science* **1997**, *277* (5322), 99-101.

(7) Richter, J. D.; Sonenberg, N. Regulation of cap-dependent translation by eIF4E inhibitory proteins. *Nature* **2005**, *433* (7025), 477-480.

(8) Gingras, A. C.; Gygi, S. P.; Raught, B.; Polakiewicz, R. D.; Abraham, R. T.; Hoekstra, M. F.; Aebersold, R.; Sonenberg, N. Regulation of 4E-BP1 phosphorylation: a novel two-step mechanism. *Gene Dev* **1999**, *13* (11), 1422-1437.

(9) Ziemniak, M.; Strenkowska, M.; Kowalska, J.; Jemielity, J. Potential therapeutic applications of RNA cap analogs. *Future Med Chem* **2013**, *5* (10), 1141-1172.

(10) Chen, X. Q.; Kopecky, D. J.; Mihalic, J.; Jeffries, S.; Min, X. S.; Heath, J.; Deignan, J.; Lai, S. J.; Fu, Z. C.; Guimaraes, C.; et al. Structure-Guided Design, Synthesis, and Evaluation of Guanine-Derived Inhibitors of the eIF4E mRNA-Cap Interaction. *J Med Chem* **2012**, *55* (8), 3837-3851.

(11) Kaur, T.; Menon, A.; Garner, A. L. Synthesis of 7-benzylguanosine cap-analogue conjugates for eIF4E targeted degradation. *Eur J Med Chem* **2019**, *166*, 339-350.

(12) Fischer, P. D.; Papadopoulos, E.; Dempersmier, J. M.; Wang, Z. F.; Nowak, R. P.; Donovan, K. A.; Kalabathula, J.; Gorgulla, C.; Junghanns, P. P. M.; Kabha, E.; et al. A biphenyl inhibitor of eIF4E targeting an internal binding site enables the design of cell-permeable PROTAC-degraders. *Eur J Med Chem* **2021**, *219*.

(13) Moerke, N. J.; Aktas, H.; Chen, H.; Cantel, S.; Reibarkh, M. Y.; Fahmy, A.; Gross, J. D.; Degterev, A.; Yuan, J. Y.; Chorev, M.; et al. Small-molecule inhibition of the interaction between the translation initiation factors eIF4E and eIF4G. *Cell* **2007**, *128* (2), 257-267.

(14) Cencic, R.; Hall, D. R.; Robert, F.; Du, Y. H.; Min, J.; Li, L.; Qui, M.; Lewis, I.; Kurtkaya, S.; Dingledine, R.; et al. Reversing chemoresistance by small molecule inhibition of the translation initiation complex eIF4F (vol 108, pg 1046, 2010). *P Natl Acad Sci USA* **2011**, *108* (16), 6689-6689.

(15) Song, J. M.; Gallagher, E. E.; Menon, A.; Mishra, L. D.; Garner, A. L. The role of olefin geometry in the activity of hydrocarbon stapled peptides targeting eukaryotic translation initiation factor 4E (eIF4E). *Org Biomol Chem* **2019**, *17* (26), 6414-6419.

(16) Gallagher, E. E.; Song, J. M.; Menon, A.; Mishra, L. D.; Chmiel, A. F.; Garner, A. L. Consideration of Binding Kinetics in the Design of Stapled Peptide Mimics of the Disordered Proteins Eukaryotic Translation Initiation Factor 4E-Binding Protein 1 and Eukaryotic Translation Initiation Factor 4G. *J Med Chem* **2019**, *62* (10), 4967-4978.

(17) Gallagher, E. E.; Menon, A.; Chmiel, A. F.; Deprey, K.; Kritzer, J. A.; Garner, A. L. A cell-penetrant lactam-stapled peptide for targeting eIF4E protein-protein interactions. *Eur J Med Chem* **2020**, *205*.

(18) Marcotrigiano, J.; Gingras, A. C.; Sonenberg, N.; Burley, S. K. Cap-dependent translation initiation in eukaryotes is regulated by a molecular mimic of eIF4G. *Mol Cell* **1999**, *3* (6), 707-716.

(19) Marcotrigiano, J.; Lomakin, I. B.; Sonenberg, N.; Pestova, T. V.; Hellen, C. U. T.; Burley, S. K. A conserved HEAT domain within eIF4G directs assembly of the translation initiation machinery. *Mol Cell* **2001**, *7* (1), 193-203.

(20) Garner, A. L. cat-ELCCA: catalyzing drug discovery through click chemistry. *Chem Commun* **2018**, *54* (50), 6531-6539.

(21) Song, J. M.; Menon, A.; Mitchell, D. C.; Johnson, O. T.; Garner, A. L. High-Throughput Chemical Probing of Full-Length Protein-Protein Interactions. *Acs Comb Sci* **2017**, *19* (12), 763-769.

(22) Lorenz, D. A.; Song, J. M.; Garner, A. L. High-Throughput Platform Assay Technology for the Discovery of pre-microRNA-Selective Small Molecule Probes. *Bioconjugate Chem* **2015**, *26* (1), 19-23.

(23) Newman, D. J.; Cragg, G. M. Natural Products as Sources of New Drugs over the Nearly Four Decades from 01/1981 to 09/2019. *J Nat Prod* **2020**, *83* (3), 770-803.

(24) Robertson, A. W.; Sandoval, J.; Mohamed, O. G.; Zhuang, Y.; Gallagher, E. E.; Schmidt, J.; Caratelli, L.; Menon, A.; Schultz, P. J.; Torrez, R. M.; et al. Discovery of Surfactins as Inhibitors of MicroRNA Processing Using Cat-ELCCA. *Acs Med Chem Lett* **2021**, *12* (6), 878-886.

(25) Magarvey, N. A.; Keller, J. M.; Bernan, V.; Dworkin, M.; Sherman, D. H. Isolation and characterization of novel marine-derived actinomycete taxa rich in bioactive metabolites. *Appl Environ Microb* **2004**, *70* (12), 7520-7529.

(26) Park, S. R.; Tripathi, A.; Wu, J. F.; Schultz, P. J.; Yim, I.; McQuade, T. J.; Yu, F. A.; Arevang, C. J.; Mensah, A. Y.; Tamayo-Castillo, G.; et al. Discovery of cahuitamycins as biofilm inhibitors derived from a convergent biosynthetic pathway. *Nat Commun* **2016**, *7*.

(27) Liang, Q.; Liu, C.; Xu, R.; Song, M.; Zhou, Z.; Li, H.; Dai, W.; Yang, M.; Yu, Y.; Chen, H. fIDBAC: A Platform for Fast Bacterial Genome Identification and Typing. *Front Microbiol* **2021**, *12*, 723577.

(28) Meier-Kolthoff, J. P.; Auch, A. F.; Klenk, H. P.; Goker, M. Genome sequence-based species delimitation with confidence intervals and improved distance functions. *BMC Bioinformatics* **2013**, *14*, 60.

(29) Meier-Kolthoff, J. P.; Carbasse, J. S.; Peinado-Olarte, R. L.; Goker, M. TYGS and LPSN: a database tandem for fast and reliable genome-based classification and nomenclature of prokaryotes. *Nucleic Acids Res* **2022**, *50* (D1), D801-D807.

(30) Blin, K.; Shaw, S.; Kloosterman, A. M.; Charlop-Powers, Z.; van Wezel, G. P.; Medema, M. H.; Weber, T. antiSMASH 6.0: improving cluster detection and comparison capabilities. *Nucleic Acids Res* **2021**, *49* (W1), W29-W35.

(31) Wang, M. X.; Carver, J. J.; Phelan, V. V.; Sanchez, L. M.; Garg, N.; Peng, Y.; Nguyen, D. D.; Watrous, J.; Kapono, C. A.; Luzzatto-Knaan, T.; et al. Sharing and community curation of mass spectrometry data with Global Natural Products Social Molecular Networking. *Nat Biotechnol* **2016**, *34* (8), 828-837.

(32) Li, D.; Liu, J.; Wang, X.; Kong, D.; Du, W.; Li, H. B.; Hse, C. Y.; Shupe, T.; Zhou, D. P.; Zhao, K. Biological Potential and Mechanism of Prodigiosin from Serratia marcescens Subsp lawsoniana in Human Choriocarcinoma and Prostate Cancer Cell Lines. *Int J Mol Sci* **2018**, *19* (11).

(33) Fujisawa, K.; Takami, T.; Matsumoto, T.; Yamamoto, N.; Yamasaki, T.; Sakaida, I. An iron chelation-based combinatorial anticancer therapy comprising deferoxamine and a lactate excretion inhibitor inhibits the proliferation of cancer cells. *Cancer Metab* **2022**, *10* (1).

(34) Ishida, S.; Arai, M.; Niikawa, H.; Kobayashi, M. Inhibitory Effect of Cyclic Trihydroxamate Siderophore, Desferrioxamine E, on the Biofilm Formation of Mycobacterium Species. *Biol Pharm Bull* **2011**, *34* (6), 917-920.

(35) Kunze, B.; Schabach.K; Zeeck, A.; Zahner, H. Metabolic Products of Microorganisms .3. Lipomycins .1. Isolation, Characterization and First Investigations of Structure and Mechanism of Action. *Arch Mikrobiol* **1972**, *86* (2), 147-+.

(36) Guttenberger, N.; Blankenfeldt, W.; Breinbauer, R. Recent developments in the isolation, biological function, biosynthesis, and synthesis of phenazine natural products. *Bioorgan Med Chem* **2017**, *25* (22), 6149-6166.

(37) Yan, J. J.; Liu, W. W.; Cai, J. T.; Wang, Y. M.; Li, D. H.; Hua, H. M.; Cao, H. Advances in Phenazines over the Past Decade: Review of Their Pharmacological Activities, Mechanisms of Action, Biosynthetic Pathways and Synthetic Strategies. *Mar Drugs* **2021**, *19* (11).

(38) Hosoya, Y.; Adachi, H.; Nakamura, H.; Nishimura, Y.; Naganawa, H.; Okami, Y.; Takeuchi, T. The structure of diphenazithionin, a novel antioxidant from Streptomyces griseus ISP 5236. *Tetrahedron Lett* **1996**, *37* (51), 9227-9228.

(39) Kim, W. G.; Ryoo, I. J.; Yun, B. S.; ShinYa, K.; Seto, H.; Yoo, I. D. New diphenazines with neuronal cell protecting activity, phenazostatins A and B, produced by Streptomyces sp. *J Antibiot* **1997**, *50* (9), 715-721.

(40) Kim, W. G.; Ryoo, I. J.; Yun, B. S.; Shin-ya, K.; Seto, H.; Yoo, I. D. Phenazostatin C, a new diphenazine with neuronal cell protecting activity from Streptomyces sp. *J Antibiot* **1999**, *52* (8), 758-761.

(41) Maskey, R. P.; Kock, I.; Helmke, E.; Laatsch, H. Isolation and structure determination of phenazostatin D, a new phenazine from a marine actinomycete isolate Pseudonocardia sp B6273. *Z Naturforsch B* **2003**, *58* (7), 692-694.

(42) Abdelfattah, M. S.; Kazufumi, T.; Ishibashi, M. Izumiphenazines A-C: Isolation and Structure Elucidation of Phenazine Derivatives from Streptomyces sp. IFM 11204. *J Nat Prod* **2010**, *73* (12), 1999-2002.

(43) Abdelfattah, M. S.; Toume, K.; Ishibashi, M. Izumiphenazine D, a New Phenazoquinoline N-Oxide from Streptomyces sp IFM 11204. *Chem Pharm Bull* **2011**, *59* (4), 508-510.

(44) Kellerschierlein, W.; Geiger, A.; Zahner, H.; Brandl, M. The Esmeraldine-a and Esmeraldine-B Green Pigments from Streptomyces-Antibioticus, Strain-Tu-2706. *Helv Chim Acta* **1988**, *71* (8), 2058-2070.

(45) Ding, Z. G.; Li, M. G.; Ren, J.; Zhao, J. Y.; Huang, R.; Wang, Q. Z.; Cui, X. L.; Zhu, H. J.; Wen, M. L. Phenazinolins A-E: novel diphenazines from a tin mine tailings-derived Streptomyces species. *Org Biomol Chem* **2011**, *9* (8), 2771-2776.

(46) Li, Y. Q.; Han, L.; Rong, H.; Li, L. Y.; Zhao, L. X.; Wu, L. X.; Xu, L. H.; Jiang, Y.; Huang, X. S. Diastaphenazine, a new dimeric phenazine from an endophytic Streptomyces diastaticus subsp ardesiacus. *J Antibiot* **2015**, *68* (3), 210-212.

(47) Wang, X. C.; Abbas, M.; Zhang, Y. N.; Elshahawi, S. I.; Ponomareva, L. V.; Cui, Z.; Van Lanen, S. G.; Sajid, I.; Voss, S. R.; Shaaban, K. A.; et al. Baraphenazines A-G, Divergent Fused Phenazine-Based Metabolites from a Himalayan Streptomyces. *J Nat Prod* **2019**, *82* (6), 1686-1693.

(48) Molina, D. M.; Jafari, R.; Ignatushchenko, M.; Seki, T.; Larsson, E. A.; Dan, C.; Sreekumar, L.; Cao, Y. H.; Nordlund, P. Monitoring Drug Target Engagement in Cells and Tissues Using the Cellular Thermal Shift Assay. *Science* **2013**, *341* (6141), 84-87.

(49) Martineau, Y.; Azar, R.; Muller, D.; Lasfargues, C.; El Khawand, S.; Anesia, R.; Pelletier, J.; Bousquet, C.; Pyronnet, S. Pancreatic tumours escape from translational control through 4E-BP1 loss. *Oncogene* **2014**, *33* (11), 1367-1374.

(50) Mentel, M.; Ahuja, E. G.; Mavrodi, D. V.; Breinbauer, R.; Thomashow, L. S.; Blankenfeldt, W. Of Two Make One: The Biosynthesis of Phenazines. *Chembiochem* **2009**, *10* (14), 2295-2304.

(51) Herrmann, K. M.; Weaver, L. M. The shikimate pathway. *Annu Rev Plant Phys* **1999**, *50*, 473-503.

(52) Li, Q. A.; Mavrodi, D. V.; Thomashow, L. S.; Roessle, M.; Blankenfeldt, W. Ligand Binding Induces an Ammonia Channel in 2-Amino-2-desoxyisochorismate (ADIC) Synthase PhzE. *J Biol Chem* **2011**, *286* (20), 18213-18221.

(53) Parsons, J. F.; Calabrese, K.; Eisenstein, E.; Ladner, J. E. Structure and mechanism of Pseudomonas aeruginosa PhzD, an isochorismatase from the phenazine biosynthetic pathway. *Biochemistry-Us* **2003**, *42* (19), 5684-5693.

(54) Parsons, J. F.; Song, F. H.; Parsons, L.; Calabrese, K.; Eisenstein, E.; Ladner, J. E. Structure and function of the phenazine biosynthesis protein PhzF from Pseudomonas fluorescens 2-79. *Biochemistry-Us* **2004**, *43* (39), 12427-12435.

(55) Ahuja, E. G.; Janning, P.; Mentel, M.; Graebsch, A.; Breinbauer, R.; Hiller, W.; Costisella, B.; Thomashow, L. S.; Mavrodi, D. V.; Blankenfeldt, W. PhzA/B Catalyzes the Formation of the Tricycle in Phenazine Biosynthesis. *J Am Chem Soc* **2008**, *130* (50), 17053-17061.

(56) McDonald, M.; Mavrodi, D. V.; Thomashow, L. S.; Floss, H. G. Phenazine biosynthesis in Pseudomonas fluorescens: Branchpoint from the primary shikimate biosynthetic pathway and role of phenazine-1,6-dicarboxylic acid. *J Am Chem Soc* **2001**, *123* (38), 9459-9460.

(57) Parsons, J. F.; Calabrese, K.; Eisenstein, E.; Ladner, J. E. Structure of the phenazine biosynthesis enzyme PhzG. *Acta Crystallogr D* **2004**, *60*, 2110-2113.

(58) Liu, J. W.; Liu, A. A.; Hu, Y. C. Enzymatic dimerization in the biosynthetic pathway of microbial natural products. *Nat Prod Rep* **2021**, *38* (8), 1469-1505.

(59) Podust, L. M.; Sherman, D. H. Diversity of P450 enzymes in the biosynthesis of natural products. *Nat Prod Rep* **2012**, *29* (10), 1251-1266.

(60) Kudanga, T.; Nyanhongo, G. S.; Guebitz, G. M.; Burton, S. Potential applications of laccase-mediated coupling and grafting reactions: A review. *Enzyme Microb Tech* **2011**, *48* (3), 195-208.

(61) Jeon, B. S.; Wang, S. A.; Ruszczycky, M. W.; Liu, H. W. Natural [4 + 2]-Cyclases. *Chem Rev* **2017**, *117* (8), 5367-5388.

(62) Dong, J. L.; He, B. B.; Wang, R. N.; Zuo, X. L.; Zhan, R.; Hu, L. F.; Li, Y. Q.; He, J. Characterization of the diastaphenazine/izumiphenazine C biosynthetic gene cluster from plant endophyte Streptomyces diastaticus W2. *Microb Biotechnol* **2022**, *15* (4), 1168-1177.

(63) Greenhagen, B. T.; Shi, K.; Robinson, H.; Gamage, S.; Bera, A. K.; Ladner, J. E.; Parsons, J. F. Crystal structure of the pyocyanin biosynthetic protein PhzS. *Biochemistry-Us* **2008**, *47* (19), 5281-5289.

(64) Schreuder, H. A.; Vanderlaan, J. M.; Swarte, M. B. A.; Kalk, K. H.; Hol, W. G. J.; Drenth, J. Crystal-Structure of the Reduced Form of P-Hydroxybenzoate Hydroxylase Refined at 2.3-a Resolution. *Proteins-Structure Function and Genetics* **1992**, *14* (2), 178-190.

(65) Braesel, J.; Lee, J. H.; Arnould, B.; Murphy, B. T.; Eustaquio, A. S. Diazaquinomycin Biosynthetic Gene Clusters from Marine and Freshwater Actinomycetes. *J Nat Prod* **2019**, *82* (4), 937-946.

(66) Rui, Z.; Ye, M.; Wang, S. G.; Fujikawa, K.; Akerele, B.; Aung, M.; Floss, H. G.; Zhang, W. J.; Yu, T. W. Insights into a Divergent Phenazine Biosynthetic Pathway Governed by a Plasmid-Born Esmeraldin Gene Cluster. *Chem Biol* **2012**, *19* (9), 1116-1125.

(67) Ji, X. Q.; Dong, Y. L.; Ling, C. Y.; Zhou, Z. B.; Li, Q. L.; Ju, J. H. Elucidation of the Tailoring Steps in Julichrome Biosynthesis by Marine Gastropod Mollusk-Associated Streptomyces sampsonii SCSIO 054. *Organic Letters* **2020**, *22* (17), 6927-6931.

(68) Prag, A.; Gruning, B. A.; Hackh, M.; Ludeke, S.; Wilde, M.; Luzhetskyy, A.; Richter, M.; Luzhetska, M.; Gunther, S.; Muller, M. Regio- and Stereoselective Intermolecular Oxidative Phenol Coupling in Streptomyces. *J Am Chem Soc* **2014**, *136* (17), 6195-6198.

(69) Agarwal, V.; El Gamal, A. A.; Yamanaka, K.; Poth, D.; Kersten, R. D.; Schorn, M.; Allen, E. E.; Moore, B. S. Biosynthesis of polybrominated aromatic organic compounds by marine bacteria. *Nature Chemical Biology* **2014**, *10* (8), 640-U182.

(70) Aldemir, H.; Richarz, R.; Gulder, T. A. M. The Biocatalytic Repertoire of Natural Biaryl Formation. *Angew Chem Int Edit* **2014**, *53* (32), 8286-8293.

(71) Tang, M. C.; Zou, Y.; Watanabe, K.; Walsh, C. T.; Tang, Y. Oxidative Cyclization in Natural Product Biosynthesis. *Chem Rev* **2017**, *117* (8), 5226-5333.

(72) Chambers, M. C.; Maclean, B.; Burke, R.; Amodei, D.; Ruderman, D. L.; Neumann, S.; Gatto, L.; Fischer, B.; Pratt, B.; Egertson, J.; et al. A cross-platform toolkit for mass spectrometry and proteomics. *Nat Biotechnol* **2012**, *30* (10), 918-920.

(73) Shannon, P.; Markiel, A.; Ozier, O.; Baliga, N. S.; Wang, J. T.; Ramage, D.; Amin, N.; Schwikowski, B.; Ideker, T. Cytoscape: A software environment for integrated models of biomolecular interaction networks. *Genome Res* **2003**, *13* (11), 2498-2504.

(74) *Bcl-convert: A proprietary Illumina software for the conversion of bcl files to basecalls*. https://support-docs.illumina.com/SW/BCL_Convert/Content/SW/FrontPages/BCL_Convert.htm (accessed 2022 Jun).

(75) Wattam, A. R.; Davis, J. J.; Assaf, R.; Boisvert, S.; Brettin, T.; Bun, C.; Conrad, N.; Dietrich, E. M.; Disz, T.; Gabbard, J. L.; et al. Improvements to PATRIC, the all-bacterial

Bioinformatics Database and Analysis Resource Center. *Nucleic Acids Res* **2017**, *45* (D1), D535-D542.

(76) Brettin, T.; Davis, J. J.; Disz, T.; Edwards, R. A.; Gerdes, S.; Olsen, G. J.; Olson, R.; Overbeek, R.; Parrello, B.; Pusch, G. D.; et al. RASTtk: a modular and extensible implementation of the RAST algorithm for building custom annotation pipelines and annotating batches of genomes. *Sci Rep* **2015**, *5*, 8365.

(77) Schomburg, I.; Chang, A.; Ebeling, C.; Gremse, M.; Heldt, C.; Huhn, G.; Schomburg, D. BRENDA, the enzyme database: updates and major new developments. *Nucleic Acids Res* **2004**, *32* (Database issue), D431-433.

(78) Ashburner, M.; Ball, C. A.; Blake, J. A.; Botstein, D.; Butler, H.; Cherry, J. M.; Davis, A. P.; Dolinski, K.; Dwight, S. S.; Eppig, J. T.; et al. Gene ontology: tool for the unification of biology. The Gene Ontology Consortium. *Nat Genet* **2000**, *25* (1), 25-29.

(79) Kanehisa, M.; Sato, Y.; Kawashima, M.; Furumichi, M.; Tanabe, M. KEGG as a reference resource for gene and protein annotation. *Nucleic Acids Res* **2016**, *44* (D1), D457-462.

(80) Lefort, V.; Desper, R.; Gascuel, O. FastME 2.0: A Comprehensive, Accurate, and Fast Distance-Based Phylogeny Inference Program. *Mol Biol Evol* **2015**, *32* (10), 2798-2800.

(81) *NCBI Protein Bosic Lacal Alignment Search tool (Protein BLAST)*. https://blast.ncbi.nlm.nih.gov/Blast.cgi?PROGRAM=blastp&PAGE_TYPE=BlastSearch&LINK_LOC=blasthome. (accessed.

Chapter 3 An ECD and NMR/DP4+ Computational Pipeline for Structural Revision and Elucidation of Diphenazine-Based Natural Products

The complete structural characterization of natural products, especially those produced in sub-microgram levels, is recognized as a significant bottleneck in the field of natural product discovery and is highlighted on multiple occasions by structure revisions reported in the chemical literature.[1] Also, traditional natural product characterization approaches often lead to misreporting absolute configurations of identified new natural products.[1] This challenge is epitomized by the diphenazine class of molecules which contain three bridged stereocenters, several conformations, and ring fusions. The bond length of bridged stereocenters is usually too close, leading to experimental NMR parameters that are a weighted average of an ensemble of conformations using empirical NMR and spatial analyses using ROESY/NOESY. In addition, the determination of phenol positions in diphenazines is often challenging or even neglected because of the lack of NMR correlations between the phenols and the rest of the molecules. Even though ^{1}H-^{15}N HMBC experiments can predict the phenol positions, it requires a large amount of compound which can be unobtainable for low-yielding molecules.

Computational analyses of spectroscopic data, such as Optical Rotation Dispersion (ORD), Electronic Circular Dichroism (ECD), and NMR, have been widely used for the structural characterization of complex natural products.[2, 3] In particular, the calculation of ^{1}H and ^{13}C NMR data using Density Functional Theory (DFT) has been recently proven to be a reliable tool for the structural revision of natural products.[4, 5] The development of DP4 and DP4+

probability measure by Goodman and Sarotti further enabled the statistical comparison between calculated and experimental NMR data.[6, 7] In this study, we developed a computational pipeline using ECD and Gauge-Independent Atomic Orbital (GIAO) NMR shift calculations coupled with DP4+ probability measure to determine the relative and absolute configurations, as well as phenol positions of diphenazine-based natural products. Using this pipeline, we propose the structural revision of molecules isolated from our efforts, phenazinolin D (**4**),[8] izumiphenazine A (**5**),[9] and baraphenazine G (**7**).[10] We also report the isolation and structural elucidation of two new diphenazines, izumiphenazine E (**6**) and baraphenazine H (**3**), guided by the same computational platform. Importantly, we proved the feasibility of NMR/DP4+ analysis for determining not only relative/absolute configurations but also phenol positions in diphenazines, further expanding the limits of this tool for the complete structural elucidation of complex natural products.

3.1 ECD and NMR Computations in Structure Elucidation of Natural Products

3.1.1 Density functional theory (DFT) functionals, basis sets, and solvent effects

First-principles calculations aim to describe a molecule's physical properties at the scale of atoms and subatomic particles using the theories of quantum mechanics.[11] The quantum mechanical description of a molecule is based on the nonrelativistic electronic Schrödinger equation in the Born-Oppenheimer approximation.[2] However, the Schrödinger equation is too complicated to be exactly solved for more than a few electrons. One commonly used alternative is the Hartree-Fock method, named after Douglas Hartree and Vladimir Fock who developed this method in the late 1920s. This method assumes that the many-electron wave function of a system can be approximated as an independent linear combination of one-electron wave functions,

which are also known as molecular orbitals. It considers the electrostatic repulsion between electrons and exchange interaction, resulting from the requirement that wave functions are antisymmetric with respect to exchanging two electrons. However, one of the drawbacks of the HF method is that it assumes that electrons move independently of each other, neglecting the electron correlation.

Another widely used alternative is density functional theory, or DFT, first proposed by Pierre Hohenberg and Walter Kohn in the 1960s and later developed by Walter Kohn and Lu Jeu Sham into Kohn-Sham DFT. In Kohn-Sham DFT, all the properties of the ground state of a molecule are determined by its total electron density rather than the wave functions.[2] This method involves an initial calculation of the energy of non-interacting electrons, neglecting both exchange energy (calculated by the HF method) and correlation energy (also neglected in the HF method). The energy can be corrected by additional exchange-correlation functionals which estimate the exchange and correlation energies by summing separate exchange and correlation functionals. In general, the name of a DFT functional is the combination of the names of the exchange and correlation functionals. For instance, the BLYP functional is composed of the exchange functional developed by Becke (B)[12] and the correlation functional developed by Lee, Yang, and Parr (LYP).[13]

There are several main categories of DFT functionals, including (1) local density approximation (LDA), which assumes that the exchange and correlation energy density of a point can be estimated using a function of the electron density only at that point; (2) generalized gradient approximation (GGA, such as BLYP) that assumes that the energy density at a point also depends on the gradient of the electron density at that point; (3) meta-GGA functionals (such as M06-L) that include additional terms beyond the GGA that depend on the kinetic energy

density and its derivatives; (4) hybrid functionals (such as B3LYP or BPE0) which combine the LDA or GGA with a fraction of HF exchange energy; (5) range-separated hybrid functionals (such as CAM-B3LYP) that take into account the different behavior of the electron density at different distances by using different functionals for the exchange-correlation energy at long-range and short-range distances; and (6) functionals with empirical dispersion (such as B3LYP-D3) that improves the accuracy by taking into account London dispersion forces.[2] Out of all available DFT functionals, B3LYP is the most used functional in DFT calculations.[14] First proposed in 1994, it is a hybrid functional that includes GGA exchange and correlation functions and a moderate amount (20%) of HF exchange energy, with three empirical parameters.[15] It is typically the first-attempt functional general-purpose calculations with relatively low computational costs and high accuracy. Despite its popularity, B3LYP has some major problems, including the inaccurate calculation of the energies of conformers and the overestimation of energy of many UV/ECD transitions.[16] In these cases, alternative functionals including M06-2X, PBE0, B3LYP-D3, CAM-B3LYP, and ωB97X-D should be considered.

Basis sets are a set of mathematical functions used to describe the molecular orbitals of a molecule. The most common choices for the basis functions are hydrogen-like s, p, and d atomic orbital centered at each nucleus. These basis functions are represented by Gaussian exponentially decaying functions and a sum of multiple Gaussian functions is often needed to describe the exponential radial decay accurately. The most popular basis sets are the 6-31G and its variants that belong to the Pople basis sets.[17] In these 6-31G sets, each core orbital is described by one basis function which is the sum of six different Gaussian functions (the ‘6’ in the name of this basis set). In addition, each valence orbital is described by two independent basis functions: one comprised of 3 Gaussian functions (the ‘3’ in the name of this basis set) and one comprised of 1

Gaussian function (the '1' in the name of this basis set). As a result, 6-31G is considered a double-zeta (double-ζ) basis set. Similarly, 6-311G is considered a triple-ζ basis set whose valence orbitals are described by 3 independent basis functions, one composed of 3 Gaussian functions, and the other two composed of 1 Gaussian function each.

This minimal set of functions can be further enriched into, for example, 6-311++G(d,p) using additional polarization basis functions and diffuse basis functions. Polarization basis functionals (p-functions for hydrogen atoms denoted as * or (p) and both p-functionals and d-functionals for H and non-H atoms denoted as ** or (d,p)) provide the mathematical flexibility needed to describe changes in the electronic charge when a chemical bond is forming. Diffuse basis functionals are slowly decaying Gaussian functions that do not significantly change the electron density in the proximity of the nucleus, but still maintain a considerable value when far away from the nucleus, which provides a more realistic description of the electron density far from the nuclei. Pople basis sets denote diffuse functions for non-H atoms as + and for all atoms as ++. Diffuse functions are known to be crucial when anions are involved,[18] when charge-transfer UV transitions are present,[16] and when performing optical rotation (OR) calculations.[19, 20] Other basis sets, including Dunning's basis set[21] and Ahlrichs basis set,[22] have also been proposed and used in calculations. Generally, a triple-ζ basis set such as 6-311++G(d,p) is adequate for DFT calculations of medium-sized natural products.

When a quantum mechanical calculation of the physical properties of an isolated molecule is conducted, it is described as an *in vacuo* calculation, or calculation of a molecule in the gas phase. It neglects all the potential interactions between the molecule and the solvent, which often affect on the geometry and energy profiles of the molecule. The solvent effect can be calculated using two major categories of models, explicit solvation models, and implicit

solvation models.[18] In explicit solvation models, hundreds of individual solvent molecules surrounding the solutes are included to accurately reproduce the various spheres of solvation. As the more popular solvent model, the implicit solvation model treats the solvent as a continuum medium, stimulating the solvent's the average effect on the solute. The most commonly used implicit solvation model is the polarizable continuum model (PCM). In this model, the continuum solvent is treated as a dielectric that becomes polarized in response to the polarity of the solute, which, in turn, affects the polarity of the solute. PCM considers the solvent's polarization caused by the solute as well as the electrostatic interactions between the solvent and the solute, which are crucial in the calculations of properties of molecules in different solvent systems.

3.1.2 ECD

With the development of computing power, the reliability and convenience of quantum mechanical prediction of chiroptical properties have significantly increased. As a result, there have been overwhelming successes in using computational methods for structural elucidation and revision, especially in determining the absolute configurations of complex natural products.[2, 23] There are several chiroptical techniques currently used for stereochemistry determinations, including specific optical rotation (SOR), optical rotation dispersion (ORD), electronic circular dichroism ECD, and vibrational circular dichroism (VCD). SOR is based on circular birefringence (CB), which measures the difference in refractive indices of left- and right-circularly polarized light at a fixed wavelength (typically yellow sodium D line at 589 nm). ORD measures the change in optical rotation as a function of wavelength in the near-infrared (NIR) and UV-Vis range. ORD and ECD provide similar information and are mathematically linked, but ECD is much more sensitive and is more commonly used nowadays.

ECD (electronic circular dichroism) is a highly sensitive chiroptical technique used for stereochemical studies of natural products. It relies on the Cotton effect, which is the difference between the absorption coefficients of left- and right-circularly polarized electromagnetic radiations in the UV-Vis range, or differential UV absorption. A positive Cotton effect means that CD increases as the wavelength decreases, while a negative Cotton effect means that CD decreases as the wavelength decreases. One limitation of ECD is that it requires at least one chromophore in close proximity to the chiral center(s). To address this, many chemical derivatization methods introduce chromophores in UV-inactive molecules. VCD (vibrational circular dichroism) is another technique that measures the difference between the absorption coefficients of left- and right-circularly polarized infrared radiation (IR) during vibrational excitation. Unlike ECD, it doesn't require the presence of a chromophore, and the IR spectrum provides richer information. However, it suffers from low sensitivity, requiring milligrams of material and hours of acquisition time, and there are no simple methods to correlate the VCD spectrum with the molecule's stereochemical properties without quantum mechanical calculations. Nevertheless, ECD is widely used because of its high sensitivity (a few micrograms of material is sufficient) and the availability of ECD spectropolarimeters. In contrast, VCD has lower sensitivity and is more complex to analyze but provides more detailed information about molecular properties.

ECD relies on the transitions between ground states and excited states in a molecule, which are computed using time-dependent DFT (TDDFT). TDDFT describes how the electron density of a molecule behaves in the presence of an electromagnetic field. A UV/ECD calculation output is a set of electronic transitions, each characterized by its energy difference (intensity) and wavelength. In UV spectroscopy, the intensity is proportional to the dipole

strength, while in ECD, it's proportional to the rotational strength (positive or negative Cotton effect). The procedures and outputs for ECD calculations will be discussed in detail in Chapter 3.2.

3.1.3 GIAO NMR and DP4+

Nuclear magnetic resonance (NMR) is the most important technique in the field of natural product chemistry for stereochemical studies. NMR parameters such as chemical shifts (mainly protons and carbons), two- and three-bond proton-proton coupling constants ($^3J_{H,H}$) and nuclear Overhauser effects (NOEs) provide useful information for conformational and configurational assignments. Besides the empirical NMR experiments, the quantum mechanical calculation of ^{1}H and ^{13}C NMR using DFT methods has been proven to be a reliable tool for the structural revision of natural products.[4, 5] Out of the methods developed for calculating DFT-NMR, including the gauge-including atomic orbitals method (GIAO), the individual gauge for localized orbitals method (IGLO), and the continuous set of gauge transformation method (CSGT), GIAO is the most commonly used for its relatively low computational cost and high accuracy.[24-26]

After the NMR parameters of one or more candidate structures have been calculated, it is necessary to use some methods such as ANN-PRA, CP3, and DP4, to evaluate the fit between the theoretical and experimental data, either to select among possible candidate structures or to accept or reject a single proposed structure.[27] ANN-PRA, or Artificial Neural Network Pattern Recognition Analysis method, evaluates the correctness of a single proposed structure.[28] CP3 method assigns the absolute configurations by comparing two diastereomers' experimental and calculated data.[29] DP4 is used to select between candidate structures using the experimental data of only one stereoisomer,[6] which matches better with our needs in this research project.

The DP4 method in R-based applet was originally developed by Goodman in 2009 to improve CP3 for determining the correct structure among multiple plausible isomers.[6] However, it can sometimes be challenging to use DP4 to distinguish between closely related isomeric compounds when only one set of experimental values is available, leading to incorrect configurational assignments. An improved version of DP4, called DP4+, was then developed by Sarotti with a great accuracy improvement, mainly by including unscaled data and using higher levels of theory.[7] It is also more user-friendly: all analyses can be performed in a publicly available EXCEL sheet and no coding experience is required. There are a few other versions of DP4 developed by the same group, including *J*-DP4,[30, 31] which include proton-proton coupling constants as an additional parameter in the DP4 analyses, and customizable DP4+,[31] where different statistical parameters in the DP4+ analyses could be tuned for different levels of theory used. An automated NMR data analyses tool, DP4-AI, was also developed by Goodman to enable automatic processing and assignment of raw ^{1}H and ^{13}C NMR data and structure elucidation of the molecules of interest.[32] We chose DP4+ for this study because it is both highly accurate and easy to use. and will be further elaborated in Chapter 3.2.

3.2 The Complete Protocol for ECD and NMR Calculations

An overview of the entire calculation process is described in **Figure 45**. In this sub-chapter, we will elaborate on these processes from the initial conformational search of the starting 3D model of the molecule of interest all the way to the final quantum mechanical calculations of ECD and NMR chemical shifts.

3.2.1 Conformational search using CONFLEX

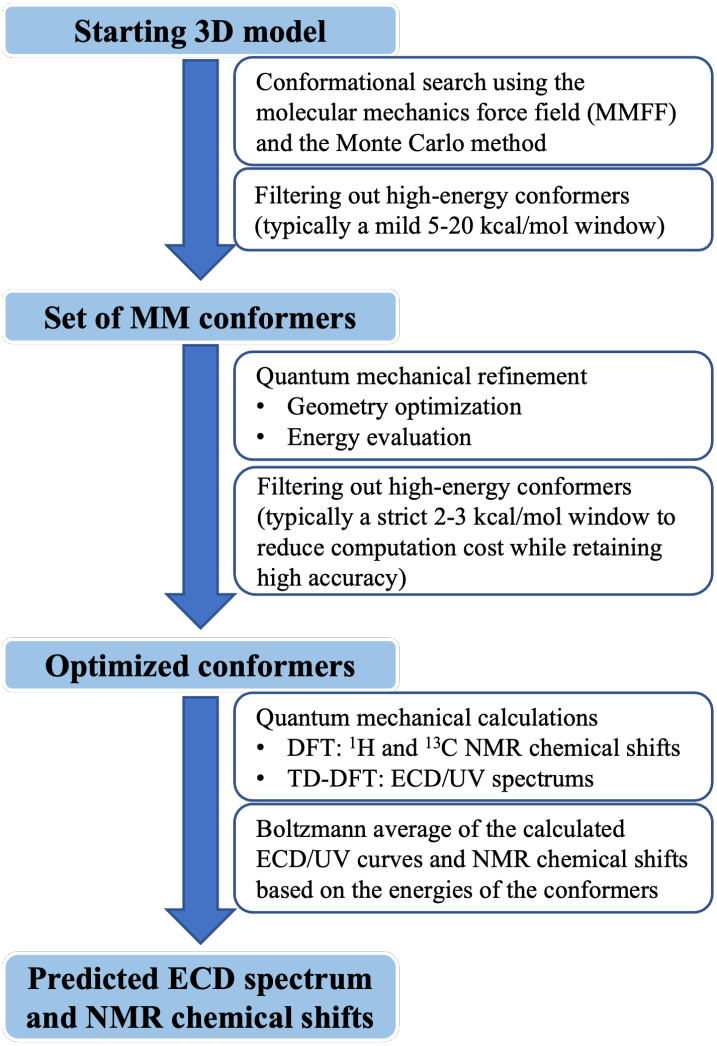

Figure 45. An overview of the proposed computational pipeline.

All physical and chemical properties of a molecule are dependent on its conformation. A medium-sized natural product may possess thousands of conformers; depending on their associated energies, only a fraction are significantly populated. Modern algorithms for conformational search require fast energy minimization and conformer search of a flexible molecule, often being done using molecular mechanics force fields rather than quantum mechanical calculations. Force field is a mathematical model used to describe a molecule's geometry in terms of its potential energy profile (bond length, bond angle, dihedral angle, electrostatic, London dispersion, etc.). The most commonly used force field is Merck molecular

force field (MMFF94) first proposed by Merck Research Group in 1996.[33] MMFF94s ('s' for 'static') was later developed as a variant of MMFF94 which reflects time-averaged geometries better than MMFF94.[34]

There are mainly three conformational search methods: systematic search, Monte Carlo methods, and Molecular Dynamics (MD).[2] A systematic search attempts to analyze all the possible geometries of a molecule by adjusting each torsion angle of the molecules and considering all the possible combinations between these values. Afterward, each geometry is subjected to minimization to the closest local minimum. While this method guarantees that no conformer is overlooked, it is only feasible for small, acyclic molecules with a limited flexible part. MD simulates a molecule's conformational changes using classical Newton's laws of motion in a force field. During this simulation, the geometry of the molecule is recorded at set intervals and used as the starting point for minimization. The Monte Carlo method uses random conformational changes to explore the potential energy surface of a molecule in order to identify its low-energy conformers. In this method, the Cartesian coordinates of a molecule are changed to random values, and then generated geometries are evaluated based on the energy difference between the current and previous conformations. This process is repeated until the lowest-energy conformations are identified. Since it is the most used method, many tools have been developed to incorporate the Monte Carlo method into conformational search, including GMMX module of GaussView 6, MacroModel, Spartan, and CONFLEX. As CONFLEX is the only software we are aware of that supports Monte Carlo conformational search using MMFFs, it was chosen for the conformational search of our molecules.

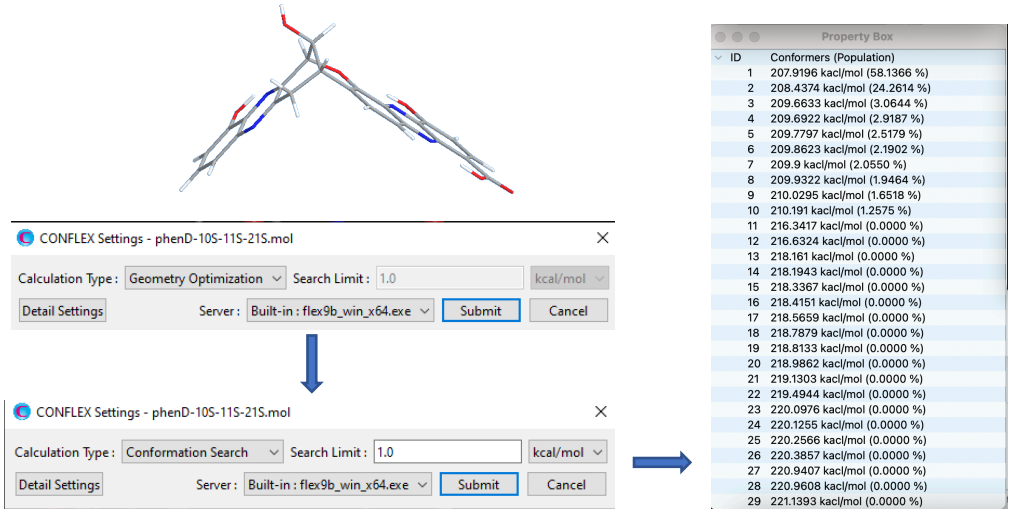

Figure 46. Geometry optimization, conformation search, and the output list of conformers with their energy and population profiles using CONFLEX.

In CONFLEX 9 (Rev. B, Tokyo, Japan), the starting 3D structure of the molecule of interest will first undergo 'Geometry Optimization' using MMFFs in the gas phase (**Figure 46**). The optimized structure will then undergo 'Conformation Search' using the same MMFFs in the gas phase. Depending on how flexible the molecule is, the search limit can be adjusted, typically ranging from 1-3 kcal/mol. The higher the search limit set, the longer it will take to finish the search. This step will yield a list of conformers of the molecule labeled with their energies and populations calculated according to the Boltzmann equation. The Boltzmann equation states that the ratio of two conformers' populations depends only on their energy difference. For instance, when there is a 2.5 kcal/mol energy difference between two conformers, it means that they have a population ratio of 99:1, with the higher energy conformer only accounting for 1% of the total population. Since the energy of conformers is only evaluated using an imperfect force field at this stage, the threshold used to filter out high-energy conformers should be set high, typically 5-20 kcal/mol. An extremely low threshold may filter out some important conformers while an extremely high threshold will create massive computation demand in the subsequent optimization step.

The Cartesian coordinates of each picked conformer are saved into one separate .mol file. Then each .mol file is converted into a .gjf file (Gaussian input file) using Chem3D. Each .gjf file contains not only the Cartesian coordinates for each atom but also the molecule's net charge and spin multiplicity (**Figure 47**). This information will be incorporated into the script for the next round of the calculation.

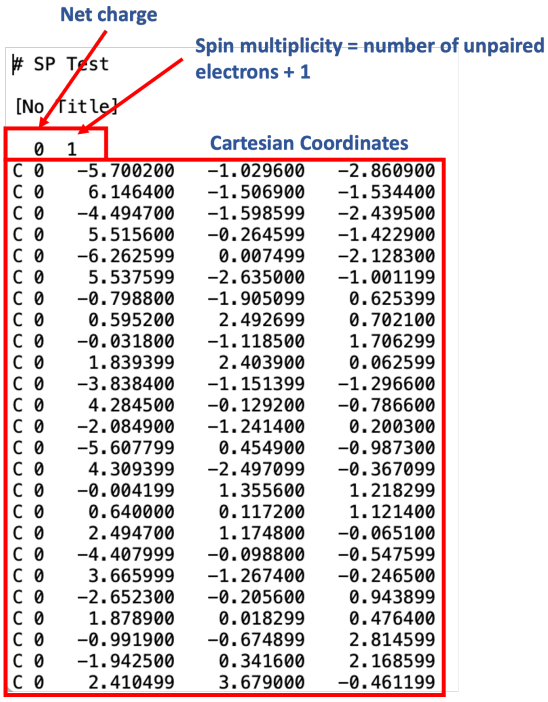

Figure 47. An example of the .gjf file of a conformer.

3.2.2 Geometry optimization

After the low-energy conformers are picked, they are then subjected to quantum mechanical optimization using Gaussian 16. This process is computationally demanding because energy minimization is an iterative numerical procedure that requires a DFT calculation for each step. Typically, a total of 20-100 steps are required to reach a local minimum. As a result, a relatively low-level basis set (B3LYP/6-31G(d)) was selected for this step. Also, solvent effects need to be considered from this step all way to the final DFT/TDDFT calculations.

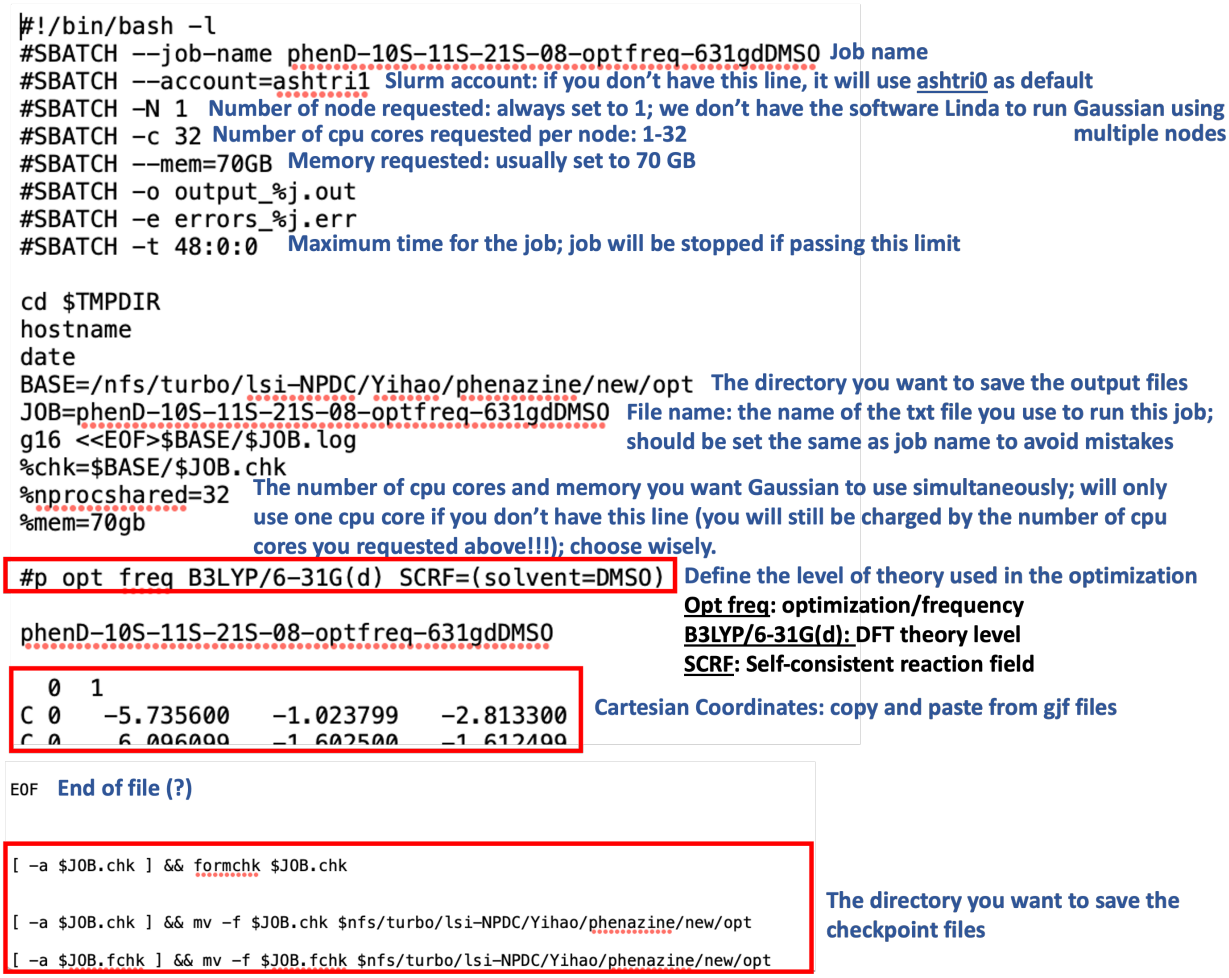

Figure 48. A sample of the script for Gaussian 16 optimization with explanations.

A sample of the Gaussian 16 optimization script is shown in **Figure 48**. It contains information about the number of nodes, cores, and memory requested and used, the directory of the script, the checkpoint files, and the output file, the level of theory and solvent effect model used in the calculation, and the Cartesian coordinates copied from the .gjf files of selected conformers. One important note is that the speedup of the calculation is not perfectly proportional to the number of CPU cores used. As a result, tests run are often needed to find the 'sweet spot' with a balance between CPU hour consumed and the actual run time. For instance, this optimization step of our diphenazine class of molecule took about 9 minutes using one node, 32 cores, and 70 GB of memory, or 16 minutes using one node, 16 cores, and 70 GB of memory.

```
 SCF Done:  E(RB3LYP) =  -1632.67636055     A.U. after   14 cycles
 SCF Done:  E(RB3LYP) =  -1632.69573616     A.U. after   12 cycles
 SCF Done:  E(RB3LYP) =  -1632.69687196     A.U. after   12 cycles
 SCF Done:  E(RB3LYP) =  -1632.69888672     A.U. after   11 cycles
 SCF Done:  E(RB3LYP) =  -1632.70006074     A.U. after   11 cycles
 SCF Done:  E(RB3LYP) =  -1632.70035319     A.U. after   10 cycles
 SCF Done:  E(RB3LYP) =  -1632.70033861     A.U. after   10 cycles
 SCF Done:  E(RB3LYP) =  -1632.70037263     A.U. after   10 cycles
 SCF Done:  E(RB3LYP) =  -1632.70041341     A.U. after    9 cycles
 SCF Done:  E(RB3LYP) =  -1632.70041827     A.U. after    9 cycles
 SCF Done:  E(RB3LYP) =  -1632.70042529     A.U. after    8 cycles
 SCF Done:  E(RB3LYP) =  -1632.70042616     A.U. after    8 cycles
 SCF Done:  E(RB3LYP) =  -1632.70042636     A.U. after    7 cycles
 SCF Done:  E(RB3LYP) =  -1632.70042640     A.U. after    6 cycles
 SCF Done:  E(RB3LYP) =  -1632.70042640     A.U. after    1 cycles
```

phenD 10S-11S-21S conformer	energy (A.U.)	energy (kcal/mol)	relative energy
phenD 10S-11S-21S-01	-1632.67698524	-1024520.31866946	0.00000000
phenD 10S-11S-21S-02	-1632.67598685	-1024519.69217025	0.62649921
phenD 10S-11S-21S-03	-1632.66432183	-1024512.37225938	7.94641008
phenD 10S-11S-21S-04	-1632.66443345	-1024512.44230199	7.87636747
phenD 10S-11S-21S-05	-1632.66323027	-1024511.68729511	8.63137435
phenD 10S-11S-21S-06	-1632.66332792	-1024511.74857142	8.57009804
phenD 10S-11S-21S-07	-1632.66340848	-1024511.79912358	8.51954588
phenD 10S-11S-21S-08	-1632.66320750	-1024511.67300672	8.64566274
phenD 10S-11S-21S-09	-1632.66216680	-1024511.01995758	9.29871188
phenD 10S-11S-21S-10	-1632.66210974	-1024510.98415189	9.33451757

Figure 50. An example of energy search in the log file of Gaussian optimization and energy comparison between all conformers using EXCEL.

```
#!/bin/bash -l
#SBATCH --job-name izuA-4OH-RRS-05-optfreq-631gdMeOH-ECD-50nstates
#SBATCH --account=ashtri1
#SBATCH -N 1
#SBATCH -c 32          Use 8 and above
#SBATCH --mem=70GB
#SBATCH -o output_%j.out
#SBATCH -e errors_%j.err
#SBATCH -t 48:0:0      Set the time limit to 48 hours

cd $TMPDIR
hostname
date
BASE=/nfs/turbo/lsi-NPDC/Yihao/phenazine/new/ECD
JOB=izuA-4OH-RRS-05-optfreq-631gdMeOH-ECD-50nstates
g16 <<EOF>$BASE/$JOB.log
%chk=$BASE/$JOB.chk
%nprocshared=32     Use 8 and above
%mem=70gb

#p td=(nstates=50) apfd/6-311+g(2d,p) SCRF=(IEFPCM,Solvent=Methanol)

izuA-4OH-RRS-05-optfreq-631gdMeOH-ECD-50nstates

0 1
 C                  1.24046000   -1.75065200    0.76534000
 O                  0.21267500   -2.75355800    0.47846300
 C                 -0.96525200   -2.10517100    0.31727700
 C                 -2.18023700   -2.78481500    0.06792400
 C                 -3.34651200   -2.06502000   -0.07286700
 C                 -4.59635400   -2.86652700   -0.33288000
 O                 -5.74459000   -2.19001300   -0.44956100
 O                 -4.57738400   -4.07995000   -0.43226100
 C                 -3.31372600   -0.62321800    0.03722700
 N                 -4.43505700    0.10388900   -0.09406500
```

Figure 49. An example of the ECD calculation script.

The output file records all the iterative steps and their results in the optimization process.

The most important part of this log file is the potential energy of the optimized geometry, which

can be found by searching 'SCF done'. SCF stands for the Self-Consistent Field, the method used to calculate a molecule's electronic structure, or potential energy. The lowest energy from the list, or the energy associated with the largest cycle number, must be recorded for later comparison. The energy is in the Hartree-Fock unit, or atomic unit (A.U.), and it can be converted to kcal/mol by 1 A.U. = 627.5095 kcal/mol. After the energies for all conformers are recorded and ranked in EXCEL, the relative energy of each conform with respect to the lowest-energy conformer can be calculated. At this stage, a strict filter is often applied. Only those conformers that are within 2-3 kcal/mol (1% population) compared to the lowest energy conformer will be selected for the final ECD or NMR calculations. The log files of these selected conformers need to be converted into .gjf files using GaussView 6. These .gjf files contain Cartesian coordinates of the optimized conformers that are used for the final calculation of ECD/UV and NMR chemical shifts.

3.2.3 ECD/UV calculation and data interpretation

The ECD (TDDFT) calculation is carried out in Gaussian 16 as well and a higher level of theory and a larger basis set is usually required for high accuracy. APFD (Austin-Frisch-Peterson

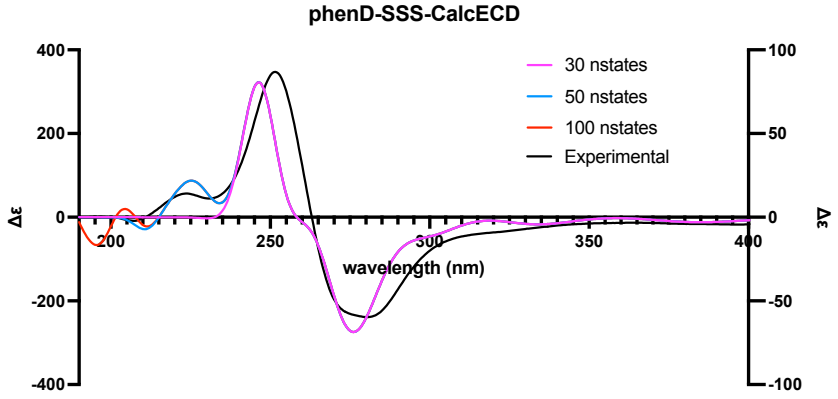

Figure 51. The comparisons between the experimental ECD curve and the calculated ECD curves using 30, 50, and 100 excited states of the 10*S*,11*S*,21*S* stereoisomer of phenazinolin D.

Dispersion)[35] was selected over B3LYP for this study because B3LYP has some problems with the inaccurate calculation of the energies of conformers and the overestimation of energy of

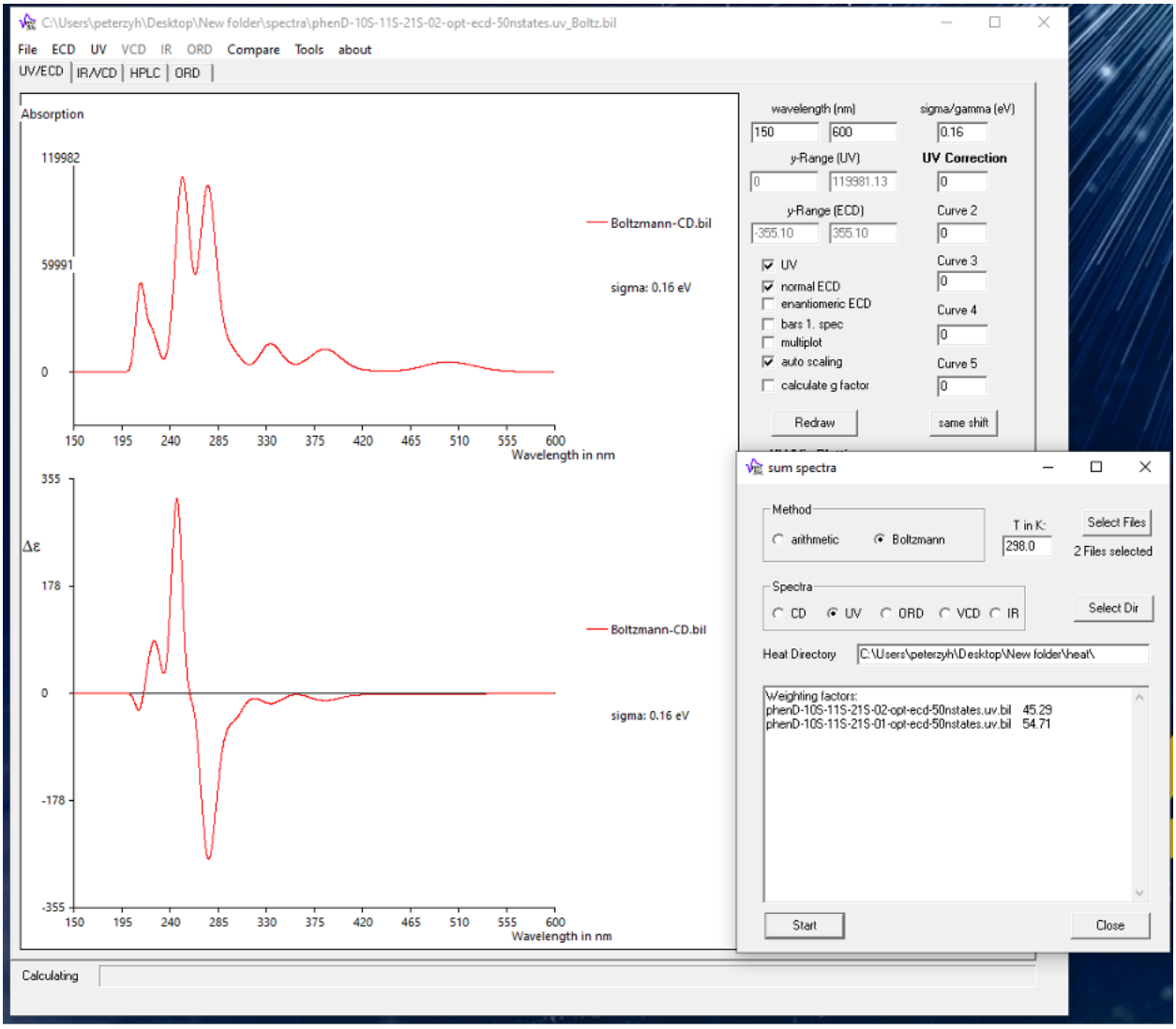

Figure 52.ECD averaging using SpecDisc.

many UV/ECD transitions[16] and it ignores dispersion forces. APFD/6-311G(2d,p) was the final basis set in the ECD calculations conducted in this study.

A representative script for this step is shown in **Figure 50**. Solvent effect using the PCM model is necessary and the solvent needs to be consistent from experimental to optimization and to this final calculation. Since ECD relies on the transition between ground and excited states, it is also important to define how many excited states to calculate for each time point (or

wavelength). 30 excited states is usually a fair starting point and increasing the number of excited states would provide more details only in the low wavelength range (190 nm to 240 nm) but not the higher wavelength (>240 nm, **Figure 51**). For the diphenazine class of molecules in this study, this calculation (using 32 CPU cores) took around 1 hour 10 min for 30 excited states, 1 hour 43 min for 50 excited states, and 3 hours 4 min for 100 excited states. Therefore, it is crucial to perform testing runs to determine how many excited states are sufficient to yield ECD curves that best match the experimental ones.

```
#!/bin/bash -l
#SBATCH --job-name phenD-10S-11S-21S-01-opt-631gdDMSO-DFT-6311G+dp-DMSO
#SBATCH --account=ashtri1
#SBATCH -N 1
#SBATCH -c 32    Less than 4 hours when using 1 core
#SBATCH --mem=70GB
#SBATCH -o output_%j.out
#SBATCH -e errors_%j.err
#SBATCH -t 48:0:0

cd $TMPDIR
hostname
date
BASE=/nfs/turbo/lsi-NPDC/Yihao/phenazine/new/DFT
JOB=phenD-10S-11S-21S-01-opt-631gdDMSO-DFT-6311G+dp-DMSO
g16 <<EOF>$BASE/$JOB.log
%chk=$BASE/$JOB.chk
%nprocshared=32
%mem=70gb

#p nmr=giao B3LYP/6-311+G(d,p) SCRF=(IEFPCM,Solvent=DMSO) method

phenD-10S-11S-21S-01-opt-631gdDMSO-DFT-6311G+dp-DMSO

0 1
 C                 -5.68532700   -0.93036900   -2.87239600
 C                  6.18077700   -1.41904200   -1.50500500
 C                 -4.49737200   -1.54209200   -2.52206000
 C                  5.59655300   -0.17634000   -1.41544100
 C                 -6.26117300    0.10245600   -2.09375600
 C                  5.56524300   -2.59112600   -0.98449700
 C                 -0.81799400   -1.95918700    0.60688700
 C                  0.62686000    2.49138700    0.70909500
 C                 -0.05362300   -1.16259500    1.68936800
 C                  1.84810300    2.45976300    0.08773300
 C                 -3.82926800   -1.12584400   -1.34530700
 C                  4.33214100   -0.05660100   -0.78053300
 C                 -2.08512800   -1.27158900    0.14932800
 C                 -5.62833400    0.52681600   -0.94200400
 C                  4.34044800   -2.50755400   -0.36414200
 C                  0.00981500    1.31245800    1.21722300
 C                  0.61282100    0.07363700    1.12046600
 C                  2.51908000    1.19195600   -0.05190600
 C                 -4.39728400   -0.08458600   -0.55410300
```

Figure 53. An example of the script for NMR calculation.

After the calculated ECD/UV curves for each conformer are obtained, Boltzmann-weighted summation using SpecDisc is calculated.[36] In the software, the ECD/UV spectrums and the energy associated with each conformer and average the ECD/UV curves using the population calculated by the Boltzmann equation was extracted(**Figure 52**). The averaged spectrums can then be exported into .csv files for comparison with the experimental ones.

There are a few parameters that can be modified for ECD spectrums. One of them is the half-width of the Gaussian curve, or σ, expressed in eV. The half-width is not predicted by quantum mechanical calculation, and it is an adjustable parameter that can be optimized to better fit with the experimental curve. In many ECD calculations, while the sign and relative intensities of state transitions are correctly predicted, the calculated transition energies are not accurate, resulting in a red- or blue-shift of wavelength. As a result, the calculated ECD curve can be shifted along the wavelength (or X-axis) from -30 nm to +30 nm to better match with the experimental curve. Finally, the overall intensity of the calculated curve (or scaling factor) can be adjusted. More often, when there is a significant difference between the intensity of calculated and experimental ECD curves, instead of changing the scaling factor, they could be plotted using separate Y-axes with different scales like what we did in this study.

3.2.4 GIAO NMR calculation and data interpretation

NMR chemical shift calculation is also done using Gaussian 16 and GaussView 6. The most commonly used DFT functional is B3LYP and another family of hybrid functionals based on the Perdew-Wang exchange correlations such as mPW1PW91.[37] In this study, we chose B3LYP/6-311+G(d,p) as our functional and basis set with PCM as the solvent model (DMSO) and GIAO as our method. An example of the script for this calculation is shown in **Figure 53**. This process is much less computationally demanding than ECD calculations, usually less than 10 min when using 32 cores for diphenazine class of molecules.

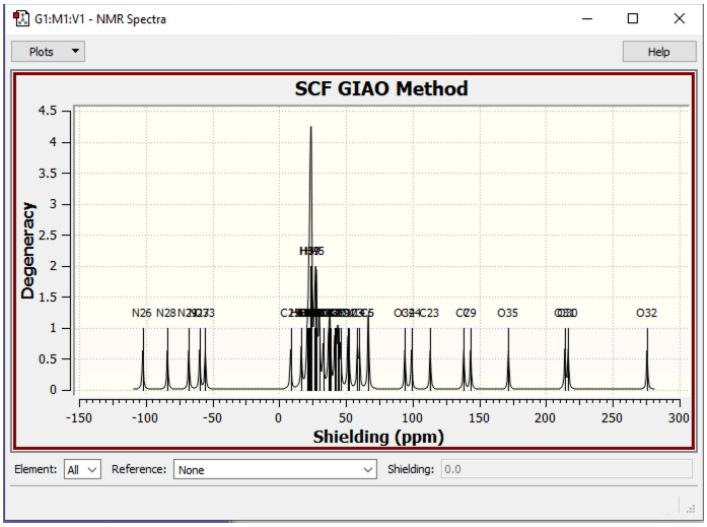


```
#  SCF GIAO Magnetic shielding
# X-Axis:  Shielding (ppm)
# Y-Axis:  Degeneracy
# NMR Degeneracy Tolerance:  0.05
#
#                      X                    Y
25-C        8.4709000000         1.0000000000
13-C       20.9462000000         1.0000000000
14-C       21.7883000000         1.0000000000
15-C       22.0629000000         1.0000000000
16-C       22.3155000000         1.0000000000
21-C       30.4945000000         1.0000000000
11-C       32.9104000000         1.0000000000
22-C       37.5506000000         1.0000000000
18-C       37.9326000000         1.0000000000
12-C       38.6483000000         1.0000000000
 2-C       41.7976000000         1.0000000000
 1-C       43.6138000000         1.0000000000
20-C       43.8606000000         1.0000000000
 8-C       44.3068000000         1.0000000000
19-C       45.6664000000         1.0000000000
17-C       50.7420000000         1.0000000000
10-C       52.2483000000         1.0000000000
 3-C       59.1468000000         1.0000000000
 4-C       60.2136000000         1.0000000000
 6-C       66.9078000000         1.0000000000
 5-C       67.5111000000         1.0000000000
24-C      101.3846000000         1.0000000000
23-C      112.6194000000         1.0000000000
 7-C      143.0089000000         1.0000000000
 9-C      144.0537000000         1.0000000000
```

Figure 54. Calculated NMR shielding tensors in GaussView 6.

The output log file can then be opened in GaussView 6 for data visualization and the magnetic shielding tensors of all atoms of the molecule can be exported into .txt files (**Figure 54**). One important note is that the numbering of the atoms by GaussView 6 is based on the rank (from low to high) of the shielding tensors and will need to be reorganized to match your numbering of the atoms in the molecule for future DP4+ analyses. Shielding tensors of the reference compound, tetramethylsilane (TMS), using the same exact procedure for the DFT calculation of the molecule (B3LYP/6-31G(d) with PCM in DMSO for optimization and B3LYP/6-311G(d,p) with PCM in DMSO for the DFT calculation) also need to be calculated. The theoretical chemical shift (δ_i) can be calculated using:

$$\delta_i = \sigma_{ref} - \sigma_i + \delta_{ref},$$

where σ_{ref} and σ_i are the calculated shielding tensors of the nuclei of interest (proton and carbon) of the reference compound and the molecule and δ_{ref} is the experimental chemical shifts of the reference compound (set to zero for both proton and carbon for TMS). The calculated shielding tensors can also be corrected using:

$$\delta_i = (\text{intercept} - \delta_{exp})/\text{slope},$$

where the intercept and slope are empirical values obtained from the linear regression of the calculated shielding tensors of the molecule against its experimental chemical shifts.

The calculated chemical shifts of all selected conformers are then averaged using Boltzmann population, which can be calculated in EXCEL using the energy recorded from the

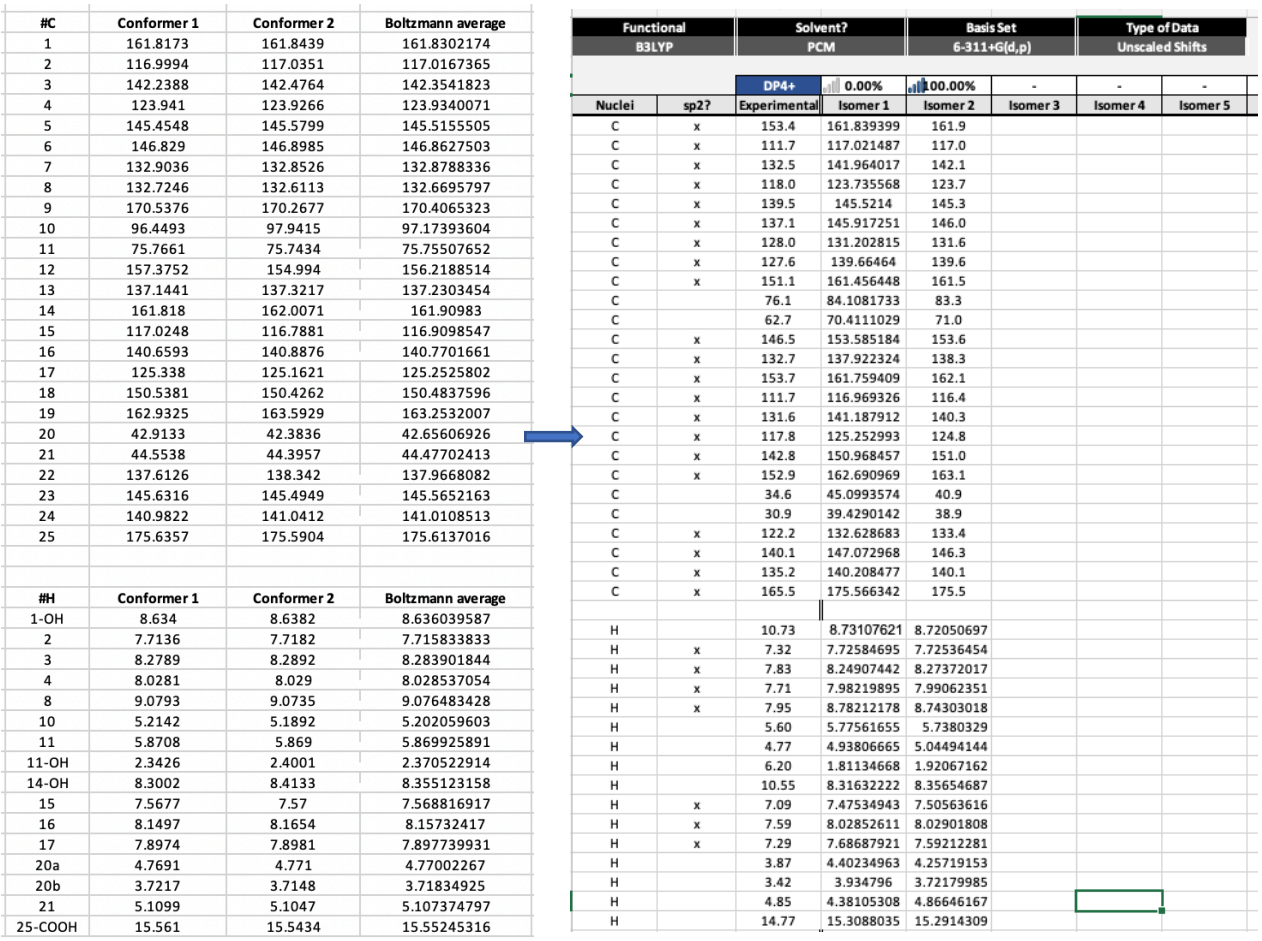

#C	Conformer 1	Conformer 2	Boltzmann average
1	161.8173	161.8439	161.8302174
2	116.9994	117.0351	117.0167365
3	142.2388	142.4764	142.3541823
4	123.941	123.9266	123.9340071
5	145.4548	145.5799	145.5155505
6	146.829	146.8985	146.8627503
7	132.9036	132.8526	132.8788336
8	132.7246	132.6113	132.6695797
9	170.5376	170.2677	170.4065323
10	96.4493	97.9415	97.17393604
11	75.7661	75.7434	75.75507652
12	157.3752	154.994	156.2188514
13	137.1441	137.3217	137.2303454
14	161.818	162.0071	161.90983
15	117.0248	116.7881	116.9098547
16	140.6593	140.8876	140.7701661
17	125.338	125.1621	125.2525802
18	150.5381	150.4262	150.4837596
19	162.9325	163.5929	163.2532007
20	42.9133	42.3836	42.65606926
21	44.5538	44.3957	44.47702413
22	137.6126	138.342	137.9668082
23	145.6316	145.4949	145.5652163
24	140.9822	141.0412	141.0108513
25	175.6357	175.5904	175.6137016

#H	Conformer 1	Conformer 2	Boltzmann average
1-OH	8.634	8.6382	8.636039587
2	7.7136	7.7182	7.715833833
3	8.2789	8.2892	8.283901844
4	8.0281	8.029	8.028537054
8	9.0793	9.0735	9.076483428
10	5.2142	5.1892	5.202059603
11	5.8708	5.869	5.869925891
11-OH	2.3426	2.4001	2.370522914
14-OH	8.3002	8.4133	8.355123158
15	7.5677	7.57	7.568816917
16	8.1497	8.1654	8.15732417
17	7.8974	7.8981	7.897739931
20a	4.7691	4.771	4.77002267
20b	3.7217	3.7148	3.71834925
21	5.1099	5.1047	5.107374797
25-COOH	15.561	15.5434	15.55245316

Functional	Solvent?	Basis Set	Type of Data
B3LYP	PCM	6-311+G(d,p)	Unscaled Shifts

		DP4+	0.00%	100.00%	-	-	-
Nuclei	sp2?	Experimental	Isomer 1	Isomer 2	Isomer 3	Isomer 4	Isomer 5
C	x	153.4	161.839399	161.9			
C	x	111.7	117.021487	117.0			
C	x	132.5	141.964017	142.1			
C	x	118.0	123.735568	123.7			
C	x	139.5	145.5214	145.3			
C	x	137.1	145.917251	146.0			
C	x	128.0	131.202815	131.6			
C	x	127.6	139.66464	139.6			
C	x	151.1	161.456448	161.5			
C		76.1	84.1081733	83.3			
C		62.7	70.4111029	71.0			
C	x	146.5	153.585184	153.6			
C	x	132.7	137.922324	138.3			
C	x	153.7	161.759409	162.1			
C	x	111.7	116.969326	116.4			
C	x	131.6	141.187912	140.3			
C	x	117.8	125.252993	124.8			
C	x	142.8	150.968457	151.0			
C	x	152.9	162.690969	163.1			
C		34.6	45.0993574	40.9			
C		30.9	39.4290142	38.9			
C	x	122.2	132.628683	133.4			
C	x	140.1	147.072968	146.3			
C	x	135.2	140.208477	140.1			
C	x	165.5	175.566342	175.5			
H		10.73	8.73107621	8.72050697			
H	x	7.32	7.72584695	7.72536454			
H	x	7.83	8.24907442	8.27372017			
H	x	7.71	7.98219895	7.99062351			
H	x	7.95	8.78212178	8.74303018			
H		5.60	5.77561655	5.7380329			
H		4.77	4.93806665	5.04494144			
H		6.20	1.81134668	1.92067162			
H		10.55	8.31632222	8.35654687			
H	x	7.09	7.47534943	7.50563616			
H	x	7.59	8.02852611	8.02901808			
H	x	7.29	7.68687921	7.59212281			
H		3.87	4.40234963	4.25719153			
H		3.42	3.934796	3.72179985			
H		4.85	4.38105308	4.86646167			
H		14.77	15.3088035	15.2914309			

Figure 55. Boltzmann average of calculated NMR chemical shifts and DP4+ analyses of two possible isomers.

DFT log files (**Figure 55**). The same procedures are repeated for another possible isomer and the calculated NMR chemical shifts of all isomers are compared in the DP4+ EXCEL sheet. In this sheet, the functional (B3LYP or mPW1PW91), solvent model (PCM or gas phase), basis set (6-31G(d), 6-31G(d,p), 6-31+G(d,p), 6-311G(d), or 6-311G(d,p)) and the type of data (unscaled

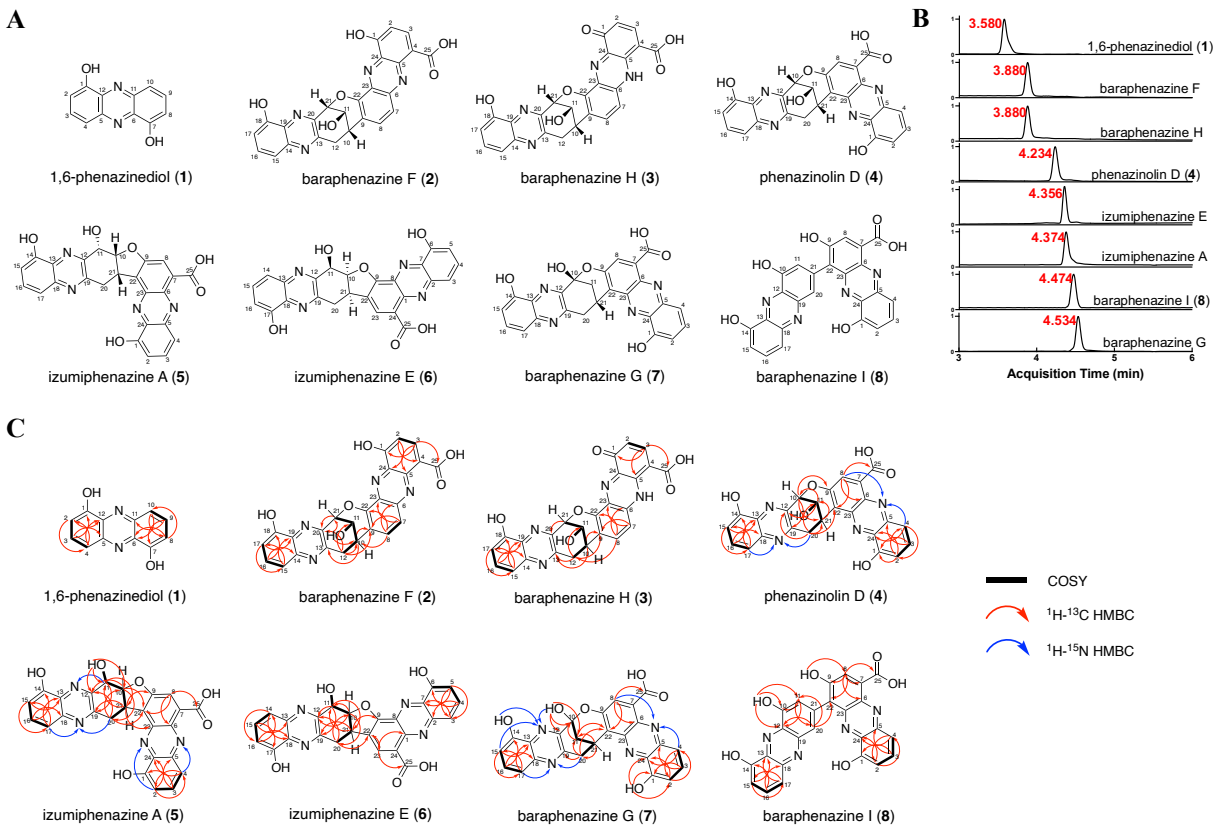

Figure 56. Structure elucidation of 1,6-phenazinediol (**1**), baraphenazine F (**2**), baraphenazine H (**3**), phenazinolin D (**4**), izumiphenazine A (**5**), izumiphenazine E (**6**), baraphenazine G (**7**), and baraphenazine I (**8**). (A) Structures of isolated molecules. (B) LC-MS UV traces of **1**–**8** labelled with respective retention times. (C) Key COSY, ^{1}H-^{13}C HMBC and ^{1}H-^{15}N HMBC correlations for **1**–**8**.

shifts, scaled shifts, or shielding tensors) will be selected according to the calculation methods. Based on the probability calculated on the sheet, the isomer that best fits with the experimental data can be determined.

3.3 Structural Revision and Elucidation of Diphenazines

Using the pipeline described in Chapter 3.2, we propose the structural revision of phenazinolin D (**4**),[8] izumiphenazine A (**5**),[9] and baraphenazine G (**7**),[10] and the structural elucidation of two new diphenazines, izumiphenazine E (**6**) and baraphenazine H (**3**, **Figure 56**).

3.3.1 Baraphenazine F (2)

Compound **2** was isolated as a dark yellow solid with a molecular formula of $C_{25}H_{16}N_4O_6$, which was derived from an HRESIMS ion peak of $C_{25}H_{17}N_4O_6$ $[M+H]^+$ (m/z: found 469.11443, calcd 469.11481). Proton and COSY NMR spectra exhibited three aromatic proton spin systems: H-15(δ_H 7.36), H-16(δ_H 7.60), and H-17(δ_H 7.07); H-7(δ_H 7.89) and H-8(δ_H 8.06); and H-2(δ_H 7.28) and H-3(δ_H 8.59, Table S2). Proton and HSQC spectra suggested the presence of two phenolic alcohols, 1-OH(δ_H 12.03) and 18-OH(δ_H 10.61); one non-phenolic alcohol, 11-OH(δ_H 6.20); one carboxylic acid, 25-COOH(δ_H 14.91); 3 methines, H-10(δ_H 3.82), H-11(δ_H 4.79), and H-21(δ_H 5.74); and 1 methylene, H-12$_{ax}$(δ_H 3.80) and H-12$_{eq}$(δ_H 3.39). The observed COSY correlations between H-11(δ_H 4.79)/H-10(δ_H 3.82), 11-OH(δ_H 6.20), and H-21(δ_H 5.74), and H-10(δ_H 3.82)/H-12$_{ax}$(δ_H 3.80), H-12$_{eq}$(δ_H 3.39) indicated the presence of a rigid oxabicylco[3.3.1]nonadienol moiety for connecting the 7,9-disubstituted tetrahydro-phenazine-1,8-diol unit and 8,9-disubstituted 1-hydroxyl-phenazine-4-carboxylic acid unit (**Figure 56**). The positions for H-10(δ_H 3.82) and H-21(δ_H 5.74) were assigned based on the HMBC correlation between H-21(δ_H 5.74)/C-20(δ_C 146.7) and H-10(δ_H 3.82)/C-9(δ_C 123.0) and

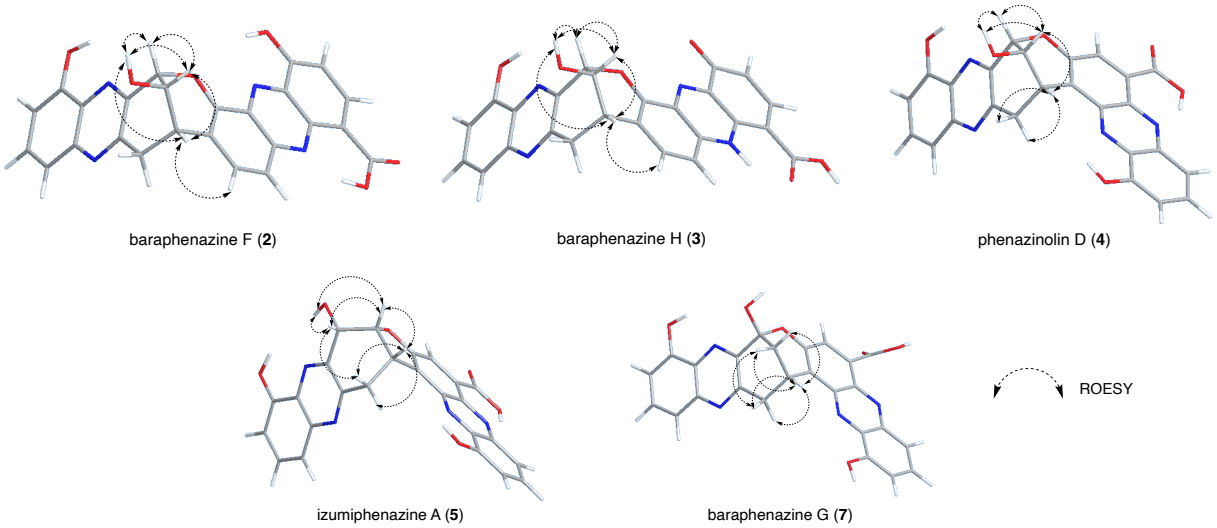

Figure 57. Key ROESY correlations in **2**–**5**, and **7**; all shown 3-D structures were the most stable conformer of each molecule optimized at B3LYP/6-311+G(d,p) level with solvent effects of dimethyl sulfoxide (DMSO) included using a polarizable continuum model (PCM).

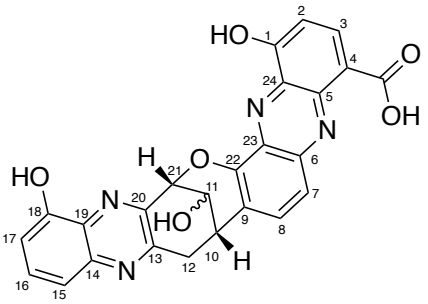

2a: 11*S*
2b: 11*R*

baraphenazine F (**2**)

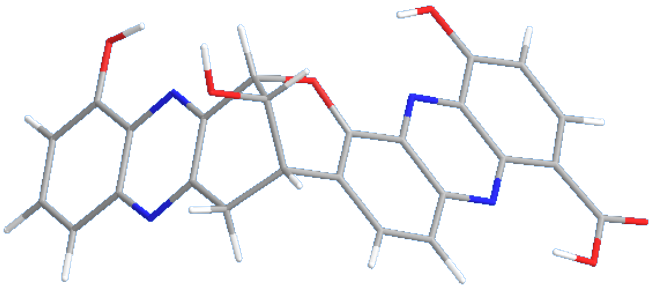

2a

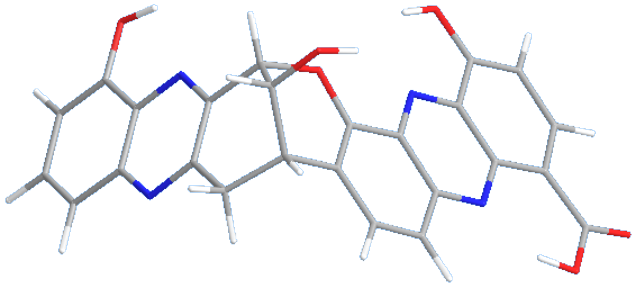

2

baraphenazine F	Proton Distances (Å)	
	2b	**2a**
H-21/H-11	2.5	2.5
H-21/OH-11	2.9	2.6
H-21/H-10	4.3	4.3
H-21/H-12$_{ax}$	4.4	4.4
H-21/H-12$_{eq}$	4.9	4.9
H-11/OH-11	2.8	2.3
H-11/H-10	2.6	2.5
H-11/H-12$_{ax}$	2.5	3.8
H-11/H-12$_{eq}$	3.7	4.3
OH-11/H-10	3.0	3.5
OH-11/H-12$_{ax}$	4.6	3.5
OH-11/H-12$_{eq}$	4.9	4.8
H-10/H-12$_{ax}$	2.4	2.4
H-10/H-12$_{eq}$	2.6	2.6

Dihedral Angles (degrees)		
	2b	**2a**
H-21–C-21–C-11–H-11	61.3	62.4
H-11–C-11–O-11–OH-11	171.0	50.9
H-11–C-11–C-10–H-10	70.1	54.9
H-10–C-10–C-12–H-12$_{ax}$	48.1	47.6
H-10–C-10–C-12–H-12$_{eq}$	68.8	69.5

Figure 58. The comparisons of the atomic distances and dihedral angels of **2a** and **2b**; all shown 3-D structures were the most stable conformer of each isomer optimized at B3LYP/6-311+G(d,p) level with solvent effects of DMSO included using PCM model.

the ROESY correlation between H-10(δ_H 3.82)/H-8(δ_H 8.06, **Figure 57**). Because of the strict geometry of the bicyclic rings, H-10(δ_H 3.82) and H-21(δ_H 5.74) must point in the same facial direction, leaving only four possible configurations for the three chiral centers: **2a** (10*S*,11*S*,21*S*), **2b** (10*S*,11*R*,21*S*), and their enantiomers. Although strong ROESY correlations were observed between H-10(δ_H 3.82)/H-11(δ_H 4.79) and H-21(δ_H 5.74)/H-11(δ_H 4.79), the calculated atomic

distances between H-10/H-11 and H-21/H-11 were identical for both **2a** and **2b**, suggesting that these ROESY correlations were not sufficient in determining the relative configuration at C-11. Instead, the 10*S*,11*S*,21*S* configuration was determined based on the small vicinal coupling constant observed between H-11(δ_H 4.79) and OH-11 (δ_H 6.20, J = 3.7Hz), which matched better with the observed dihedral angle of H-11–C-11–O-11–OH-11 in **2a** (50.9°) compared to **2b** (171.0°, **Figure 58**).[38] The obtained NMR data of **2** matched that of the known compound, baraphenazine F;[10] however, the absolute configuration of baraphenazine F remained unknown.

Determination of phenol positions has been challenging for diphenazine molecules, mainly due to the lack of NMR correlations between the phenols and the rest of the molecule. In addition, the sample amount requirement for ^{1}H-^{15}N HMBC to determine phenol positions for

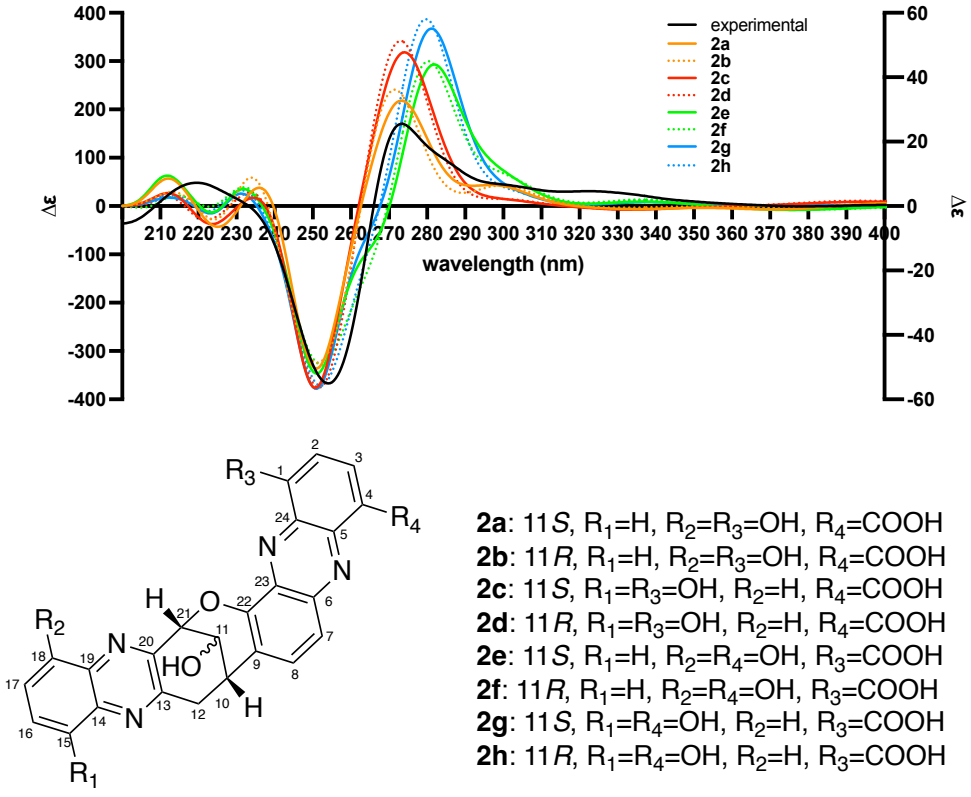

Figure 59. Calculated ECD curves of **2a**–**2h** at apfd/6-311+G(2d,p) level with solvent effects PCM=methanol for a total of 50 excited states; calculated ECD curves were scaled using left Y-axis; experimental ECD curves were scaled using right Y-axis; σ=0.16eV.

low-yielding natural products like compound **2** (<0.05 mg/L) renders it ineffective. Therefore, to establish a platform for configurational analysis of the isolated molecules in our study, we performed ECD calculations and NMR/DP4+ analyses[2, 6, 7] to determine the absolute configurations and phenol positions of **2**.

First, we randomly selected configurations **2a** and **2b** as the starting point and calculated the theoretical ECD of 8 possible isomers (**Figure**). We found that the experimental ECD curve matched better with **2a**, **2b**, **2c**, and **2d** compared to the other four isomers with phenol position at 4OH (**Figure 4B**). **2a** and **2b** were slightly favored over **2c** and **2d** because they shared an extra minor peak at ~300nm with the experimental curve. Nevertheless, we could not differentiate **2a** and **2b** solely based on ECD likely because the chromophores in **2** are too far from C-11. To tackle this problem, we then performed ^{1}H and ^{13}C NMR shift calculations of **2a**–**2d** and compared them with the experimental chemical shifts using DP4+ to determine the most probable isomer.[6, 7] During our calculations, we observed that while most carbon-bound hydrogens showed < 0.5 ppm differences between the calculated and the experimental chemical shifts, exchangeable protons, especially OHs, showed much larger differences (1-OH: ~3 ppm; 11-OH: ~4.5 ppm; 18-OH: ~2 ppm). In addition, we barely observed any improvement in the differences in the chemical shifts of these exchangeable protons when we switched from B3LYP to mPW1PW91 as the DFT functional during the calculations.[37] This challenge was successfully overcome by the DP4+ analyses where both unscaled and scaled (corrected) chemical shifts were taken into account for accuracy. Our analyses showed that the isolated molecule **2** most likely exists as the **2a** conformation with an overall DP4+ probability score of 95.95%, compared to 0.09% for **2b**, 3.94% for **2c**, and 0.03% for **2d (Figure 60)**. It is important to note that for isomers **2a**, we observed a DP4+ probability of 59.50% for ^{1}H NMR data and 36.32% for ^{13}C

NMR data compared to isomer **2c** with a probability of 1.41% for ^{1}H NMR data and 63.08% for ^{13}C NMR data. While the carbon NMR data favored **2c** as the structure isomer, the combined DP4+ probability supported **2a** as the final structure isomer of **2**, confirming the reported structure of baraphenazine F.[10]

3.3.2 Baraphenazine H (3)

Compound **3** was isolated as a dark red solid with a molecular formula of $C_{25}H_{16}N_4O_6$, which was derived from an HRESIMS ion peak of $C_{25}H_{17}N_4O_6$ $[M+H]^+$ (*m/z*: found 469.11485, calcd 469.11481). Analyses of NMR spectra of **3** suggested that it shared the same 7,9-disubstituted tetrahydro-phenazinediol and 8,9-disubstituted hydroxyl-phenazine-carboxylic acid units and the oxabicylco[3.3.1]nonadienol moiety as **2**. It also shared the same 10*S*,11*S*,21*S* relative configuration as **2**, which was supported by the small vicinal coupling constant observed between H-11(δ_H 4.74) and OH-11 (δ_H 6.06, J = 3.1Hz) that matched better to the observed dihedral angle of H-11–C-11–O-11–OH-11 in (10*S*,11*S*,21*S*)-**3** (50.7°) rather than

baraphenazine F (**2**)		baraphenazine H (**3**)		phenazinolin D (**4**)	
isomer	DP4+ (%)	isomer	DP4+ (%)	isomer	DP4+ (%)
2a	95.95	**3a**	100.00	**4a**	100.00
2b	0.09	**3b**	0.00	**4b**	0.00
2c	3.94	**3c**	0.00		
2d	0.03	**3d**	0.00		

izumiphenazine A (**5**)		izumiphenazine E (**6**)			
isomer	DP4+ (%)	isomer	DP4+ (%)	isomer	DP4+ (%)
5d	100.00	**6e**	91.83	**6e**	2.30
5h	0.00	**6g**	8.17	**6i**	1.41
				6j	65.64
				6k	30.66

Figure 60. DP4+ probabilities of possible isomers of **2**–**6**. All NMR calculations were conducted at B3LYP/6-311+G(d,p) level of theory with solvent effects of DMSO included using PCM model.

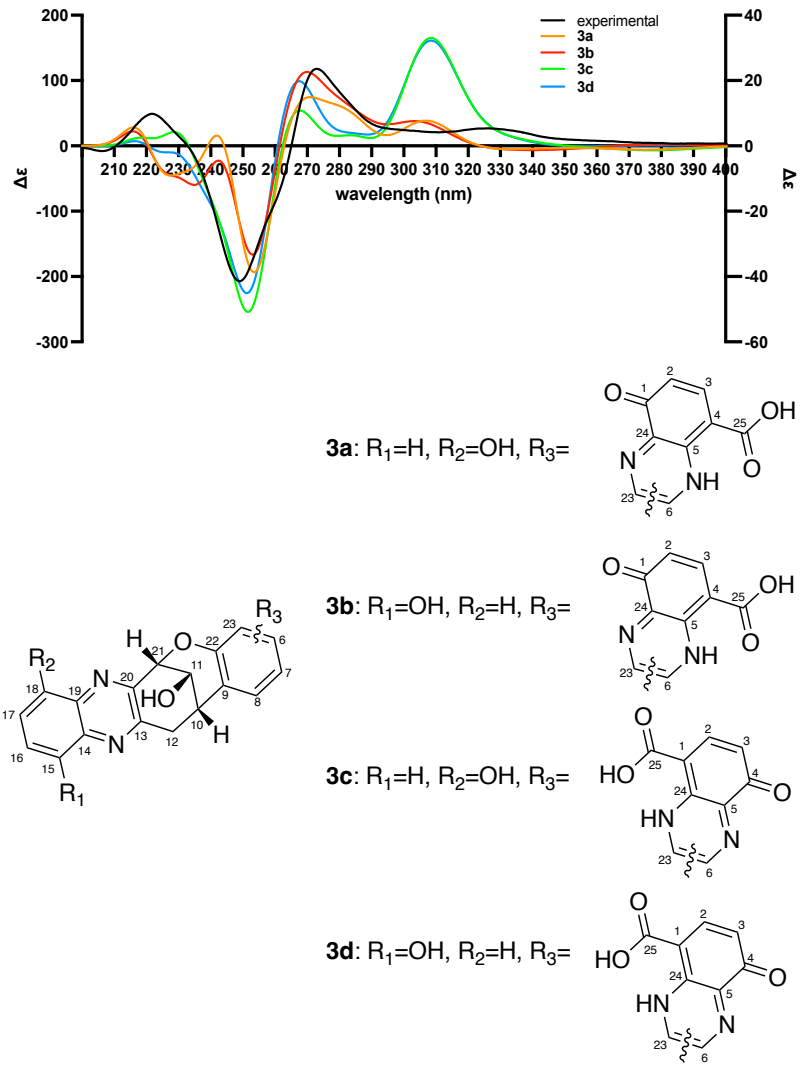

Figure 61. Calculated ECD curves of **3a**–**3d** at apfd/6-311+G(2d,p) level with solvent effects PCM=methanol for a total of 50 excited states; calculated ECD curves were scaled using left Y-axis; experimental ECD curves were scaled using right Y-axis; σ=0.16eV.

(10*S*,11*R*,21*S*)-**3** (171.8°). However, the proton peak for 1-OH (δ_H 12.03) of **2** was missing in **3**. In addition, a deshielded chemical shift of 6.15 ppm was observed for H-2, which is often observed in resorcinol-like structures that contain two electron-donating groups at *ortho* and *para* positions relative to the proton. Furthermore, an HMBC correlation between H-3(δ_H 8.15) and a carbon with δ_C of 177.5 ppm was observed, indicating the presence of a carbonyl at C-1 and supporting the presence of a 6-hydroxy-4-oxo-4,10-dihydrophenazine-1-carboxylic acid moiety. However, the 5-NH proton was not observed in the ^{1}H NMR spectrum, and therefore,

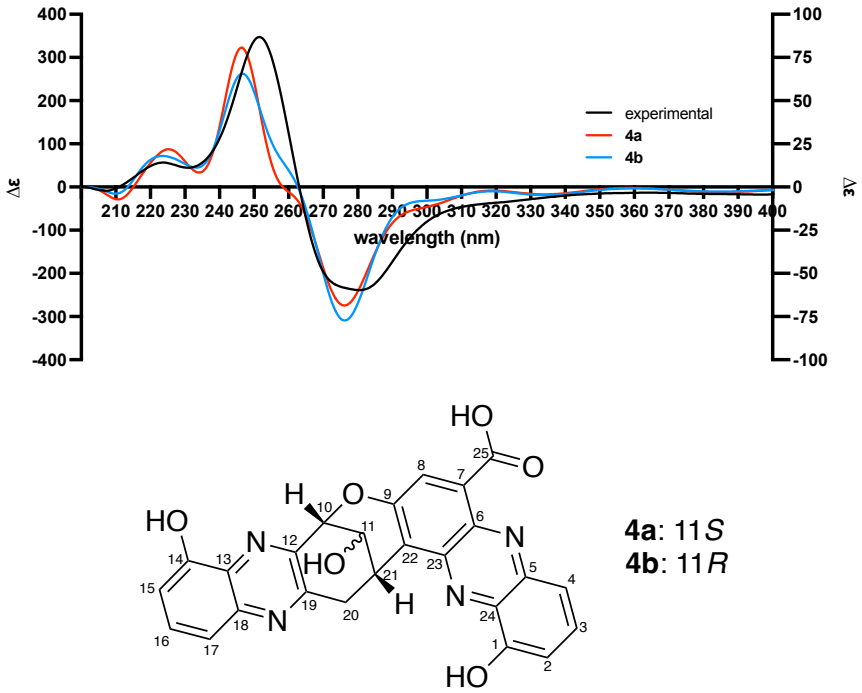

Figure 62. Calculated ECD curves of **4a** and **4b** at apfd/6-311+G(2d,p) level with solvent effects PCM=methanol for a total of 50 excited states; calculated ECD curves were scaled using left Y-axis; experimental ECD curves were scaled using right Y-axis; σ=0.16eV.

the position of this proton could not be determined solely by NMR. To tackle this challenge and determine absolute configurations and the positions of the carboxylic acid and phenols in compound **3**, we utilized our established ECD calculation methodology on all four possible isomers, **3a**–**3d**, as described for **2** (**Figure 61**). However, we could not determine which ECD curve fits better with the experimental ECD curve unambiguously. Therefore, we performed NMR calculations for the four possible isomers. Our analyses showed that **3a** had an overall DP4+ probability score of 100.00% (98.02% for ^{1}H NMR data and 10.64% for ^{13}C NMR data) compared to 0.00% (0.00% for ^{1}H NMR data and 89.36% for ^{13}C NMR data) for **3b**, suggestive of **3a** as the final structure isomer of **3**, which was named baraphenazine H based on its structural similarities to baraphenazine F (**2**, **Figure 60**).

3.3.3 Phenazinolin D (4)

Compound **4** was isolated as a yellow-orange solid with a molecular formula of $C_{25}H_{16}N_4O_6$, which was derived from an HRESIMS ion peak of $C_{25}H_{17}N_4O_6$ $[M+H]^+$ (*m/z*: found

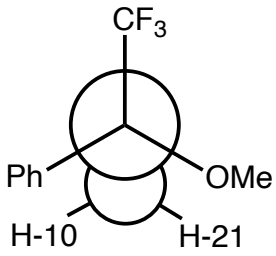

4a-*S*-MTPA ester

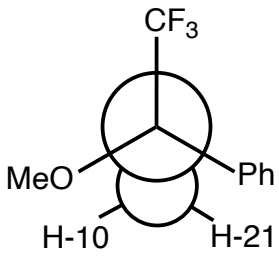

4a-*R*-MTPA ester

Proton	δ **4a**-*S*-MTPA ester (ppm)	δ **4a**-*R*-MTPA ester (ppm)	$\Delta\delta$ (δ_S-δ_R) (ppm)
H-10	5.71	5.62	**+0.09**
H-21	4.46	4.60	**-0.14**

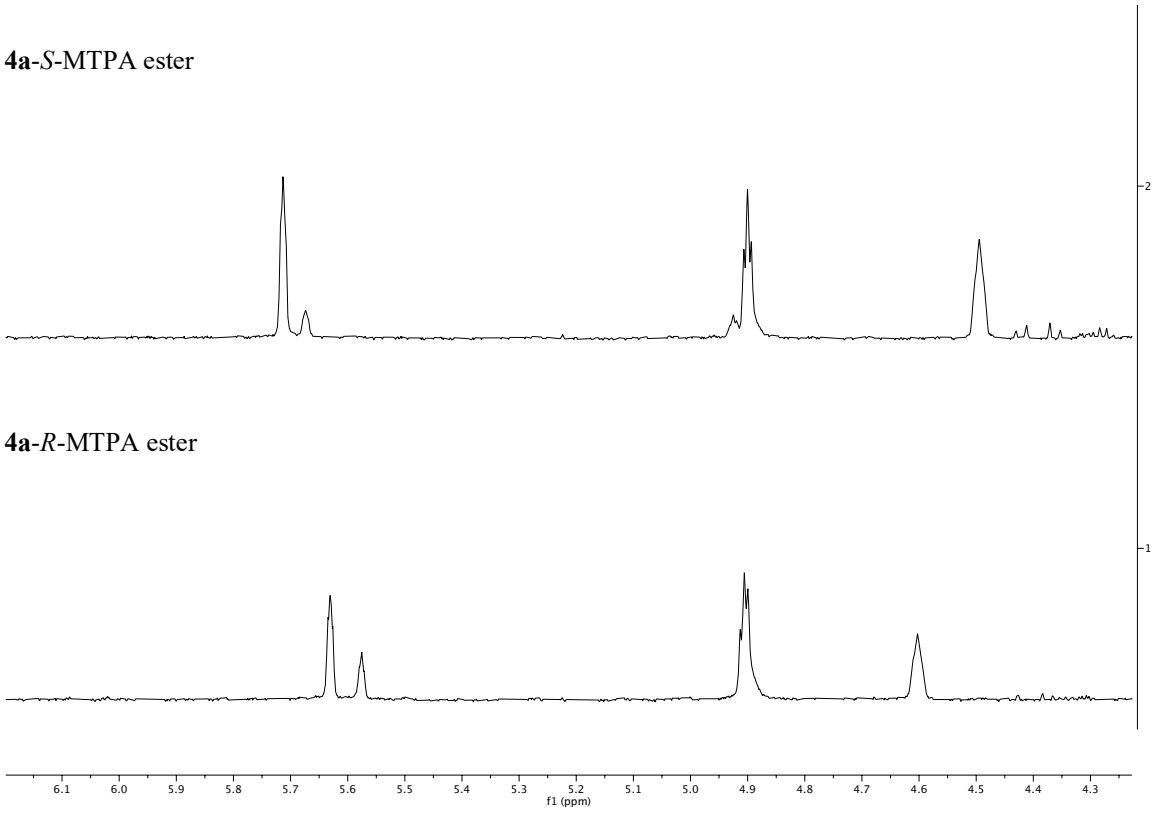

Figure 63. Mosher's analysis to determine the absolute configuration of C-11 of 4. Fischer projection representations of **4a**-S-MTPA ester and **4a**-R-MTPA ester around C-11; differences in chemical shifts of H-10 and H-21 in **4a**-S-MTPA ester and **4a**-R-MTPA ester in $CDCl_3$.

469.11552, calcd 469.11481). Proton, COSY, and HSQC spectra revealed the presence of different aromatic proton spin systems compared to **2** and **3**: H-15, H-16, and H-17; H-8; and H-2, H-3, and H-4. The observed COSY correlations between H-11(δ_H 4.77)/H-10(δ_H 5.60), 11-OH(δ_H 6.20) and H-21(δ_H 4.85) suggested the same oxabicylco[3.3.1]nonadienol moiety as **2** and **3**. The positions of H-10 and H-21 and the linkage between C-21(δ_C 30.9) and C-22 (δ_C 122.2) were established by the observed HMBC correlations between H-10(δ_H 5.60)/C-9 (δ_C 151.1), and H-21(δ_H 4.85)/C-9, C-22(δ_C 151.1, 122.2), suggesting the presence of 7,9-disubstituted tetrahydro-phenazine-diol and 8,9-disubstituted hydroxyl-phenazine-carboxylic acid units. The positions of the two phenols were assigned based on ^{1}H-^{15}N HMBC correlations between H-17/N-18(δ_H 7.29/δ_N 324.5), H-20$_{ax}$,H-20$_{eq}$/N-18(δ_H 3.87,3.42/δ_N 324.5), H-4/N-5(δ_H 7.71/δ_N 298.6), H-8/N-5(δ_H 7.71/δ_N 298.6), H-10/N-12(δ_H 5.60/δ_N 325.9), and H-15/N-12(δ_H 7.09/δ_N 325.9). All of these NMR data matched the known molecule phenazinolin D.[8] However, contrary to the reported relative configuration 10S,11R,21S (**4b**), our analysis suggested the relative configuration to be 10*S*,11*S*,21*S* (**4a**). Firstly, ROESY between H-11(δ_H 4.77) and H-12$_{ax}$(δ_H 3.87) was not observed, which contradicted the observed 2.5 Å distance between H-11/H-12$_{ax}$ in conformer **4b**. Secondly, a weak ROESY was observed between 11-OH(δ_H 6.20) and H-12$_{ax}$(δ_H 3.87), which matched better with the observed 3.5 Å distance between 11-OH/H-12$_{ax}$ in conformer **4a** compared to 4.6 Å in **4b** (**Figure 57**). Thirdly, and most importantly, we calculated an overall DP4+ probability score of 100.00% for **4a** (100% for ^{1}H NMR data and 95.51% for ^{13}C NMR data, **Figure 60**). These observations and the match between the experimental ECD curve with the calculated ECD curve of **4a** (**Figure 62**), unequivocally confirmed the revised structure. Therefore, we propose that the absolute configuration of phenazinolin D (**4**) should be corrected to 10*S*,11*S*,21*S* from that previously reported (10*S*,11*R*,21*S*).[8] In order to validate our

in silico analysis and determination of the absolute configuration of C-11, we prepared the S and R-MTPA esters of the hydroxyl group at C-11 of **4** (**Figures 63**).[39] The $\Delta\delta_{S-R}$ values of H-10 and H-21 unambiguously confirmed that C-11 possesses the *S* configuration, further validating our proposed ECD/NMR pipeline.

3.3.4 Izumiphenazine A (5)

Compound **5** was isolated as an orange-red solid. It has a molecular formula of $C_{25}H_{16}N_4O_6$, which was derived from an HRESIMS ion peak of $C_{25}H_{17}N_4O_6$ $[M+H]^+$ (*m/z*: found 469.11489, calcd 469.11481). Initially, we could not obtain a clean NMR spectrum of **5** even from pure HPLC fractions, and the ^{1}H NMR spectrum always showed a mixture of **5** and another structurally related phenazine, which was later found to be **7** (**Figure 64**). This impurity, which shared the same isotopic mass, was generated after **5** was dried, indicating that **5** was vulnerable to heat. Detailed 1D and 2D NMR spectra revealed the presence of three groups of aromatic protons at H-15, H-16, and H-17; H-8; and H-2, H-3, and H-4; two phenols, 1-OH and 14-OH; one hydroxyl group, 11-OH; one carboxylic acid, 25-COOH; 3 methines, H-10, H-11, and H-21; and one methylene, H-20_{ax} and H-20_{eq}. Further COSY and HMBC correlations indicated the presence of a unique tetrahydrobenzofuran-7-ol moiety connecting a 7,8-disubstituted tetrahydro-phenazinediol unit and an 8,9-disubstituted hydroxyl-phenazine-carboxylic acid unit. While all of these NMR data matched the known molecule izumiphenazine A,[9] there were still a few concerns regarding the structure of **5**.

Due to the relatively flexible planar bicyclic moiety, H-10(δ_H 5.59) and H-21(δ_H 4.84) could face either the same or opposite directions, resulting in eight possible configurations: **5a** (10*S*,11*R*,21*S*), **5b** (10*S*,11*S*,21*S*), **5c** (10*R*,11*R*,21*S*), **5d** (10*R*,11*S*,21*S*), and their respective enantiomers. Since we observed strong ROESY correlations between H-10/H-21(δ_H 5.59/δ_H

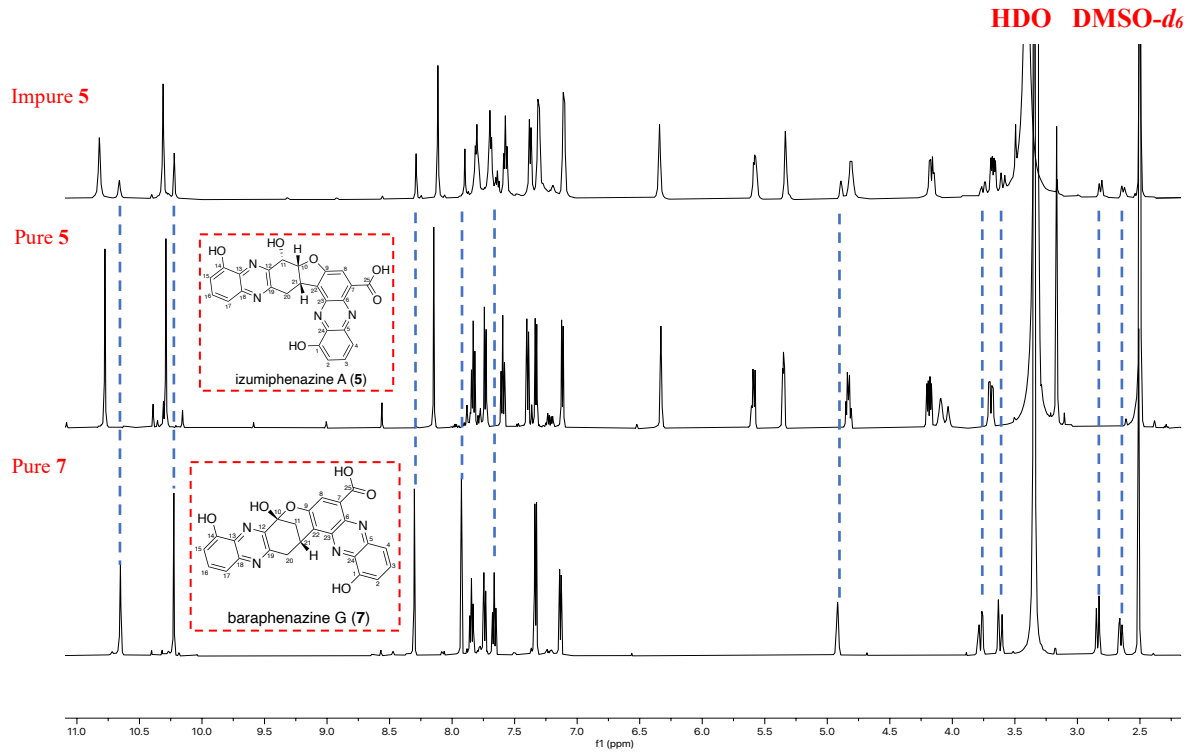

Figure 64. ^{1}H NMR spectrums (600 MHz) comparison between partially converted **5**, pure **5**, and pure **7** in DMSO-d_6; dashed lines match the proton peaks of **7** in the impure **5** sample.

4.84) and H-11/H-20$_{eq}$(δ_H 5.35/δ_H 3.69), **5c** and **5d** were favored due to the observed smaller atomic distances. The observed vicinal coupling constant between H-10(δ_H 5.59)/H-11(δ_H 5.35 *J*=5.6Hz) matched better with the dihedral angle of H-10–C-10–C-11–H-11 or **5d** (59.9°) compared to **5c** (161.6°), undeniably contradicting the reported 10*R*,11*R*,21*S* configuration for izumiphenazine A.[9] The position of the phenol in the 7,8-disubstituted tetrahydro-phenazinediol unit was assigned to C-14 based on the observed ^{1}H-^{15}N HMBC correlations between H-17/N-18(δ_H 7.40/δ_N 321.9) and H-20$_{ax}$, H-20$_{eq}$/N-18(δ_H 4.19,3.69/δ_N 321.9). Due to insufficient NMR data to determine the position of the phenol in the hydroxyl-phenazine-carboxylic acid unit, we first calculated the theoretical ECD curves of all possible isomers **5a**–**5h** (**Figure 65**) to determine the absolute configuration and the positional analysis of this phenol. Since the experimental ECD curve matched better to **5d** and **5h**, we subjected these two configurations to

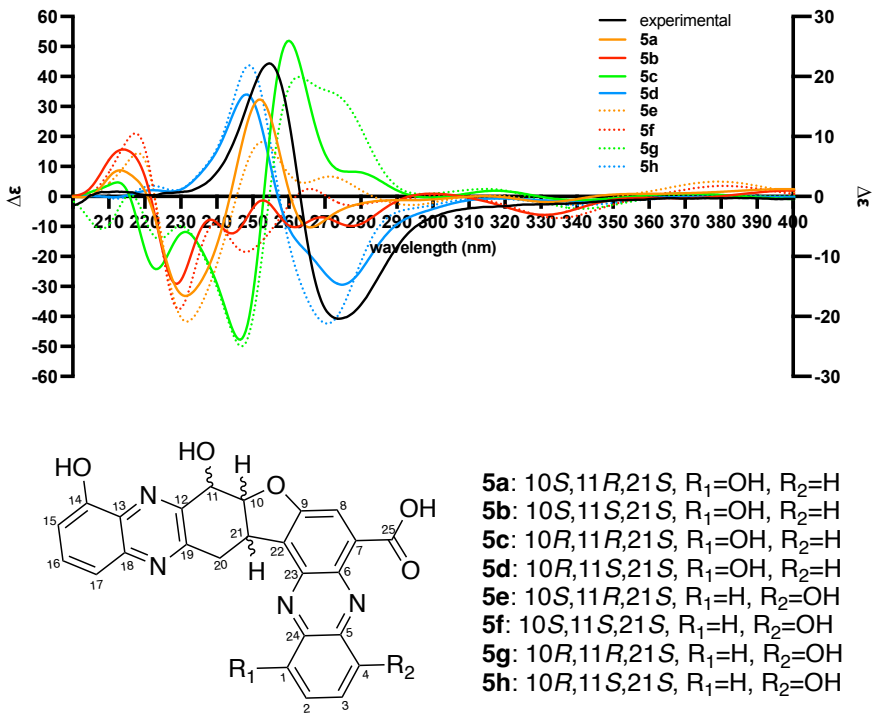

Figure 65. Calculated ECD curves of **5a**-**5h** at apfd/6-311+G(2d,p) level with solvent effects PCM=methanol for a total of 50 excited states; calculated ECD curves were scaled using left Y-axis; experimental ECD curves were scaled using right Y-axis; σ=0.16eV.

NMR/DP4+ analyses. Our analyses showed an overall DP4+ probability of 100.00% for **5d** (100.00% for ^{1}H NMR data and 100.00% for ^{13}C NMR data), suggesting the phenol at position C-1 (**Figure 60**). Therefore, we propose that the absolute configuration of izumiphenazine A (**5**) should be corrected to 10*R*,11*S*,21*S* from the previously reported 10*R*,11*R*,21*S*.[9]

3.3.5 Izumiphenazine E (6)

Compound **6** was isolated as an orange-red solid with a molecular formula of $C_{25}H_{16}N_4O_6$, which was derived from an HRESIMS ion peak of $C_{25}H_{17}N_4O_6$ $[M+H]^+$ (*m/z*: found 469.11461, calcd 469.11481). Similarities between the NMR spectra of **5** and **6** suggested the same skeleton and tetrahydrobenzofuran-7-ol moiety for connecting the two phenazine units. The major differences were a singlet aromatic proton in **6** (δ_H 7.05 ppm) compared to the more deshielded H-8 (δ_H 8.15) in **5**, and C-22 in **6** (δ_C 116.6 ppm) compared to 124.9 ppm in **5**. These

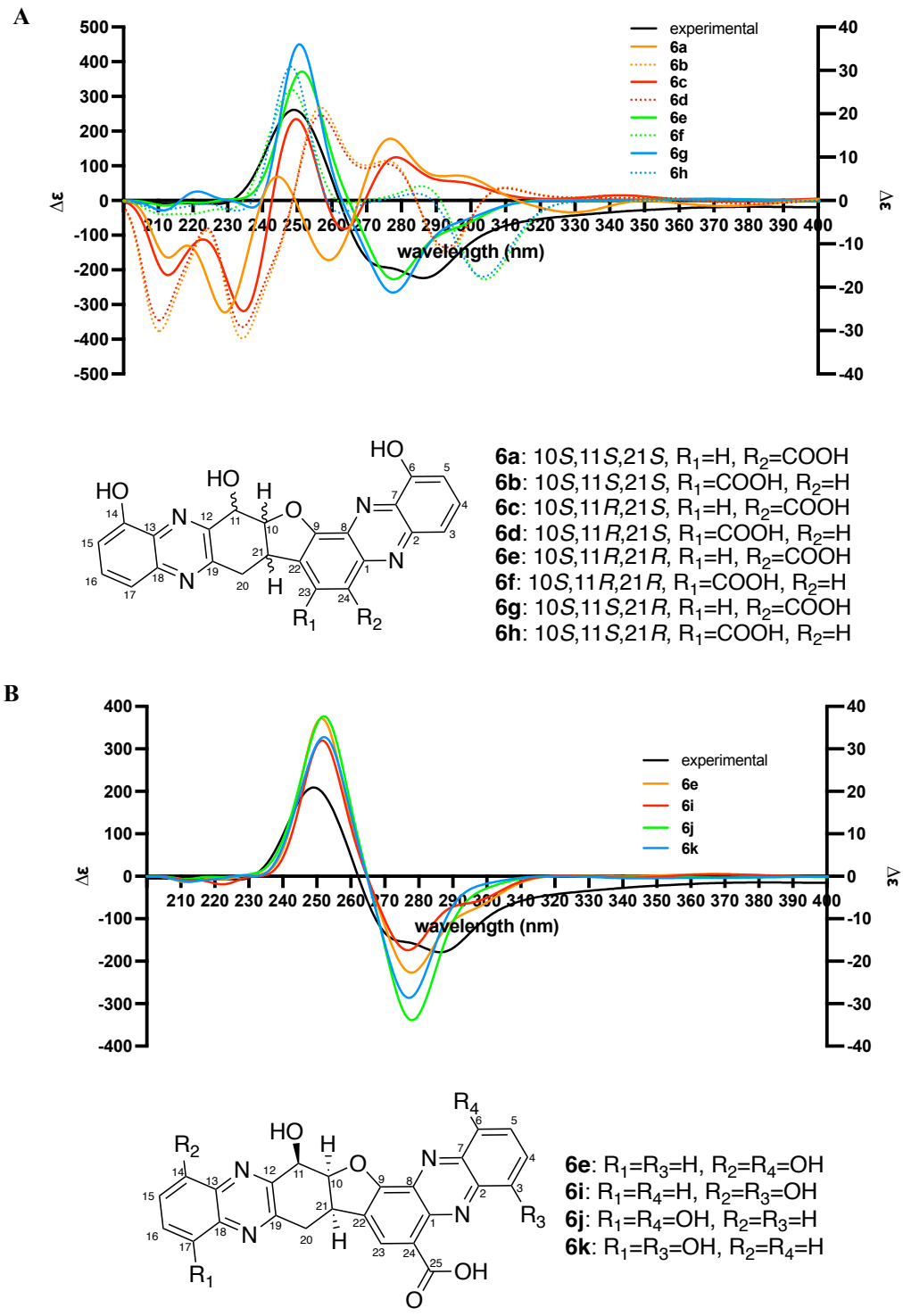

Figure 66. Calculated ECD curves of (A) **6a-6h** and (B) **6e** and **6i-6h** at apfd/6-311+G(2d,p) level with solvent effects PCM=methanol for a total of 50 excited states; calculated ECD curves were scaled using left Y-axis; experimental ECD curves were scaled using right Y-axis; σ=0.16eV.

data, combined with the observed HMBC correlations between the singlet aromatic proton (δ_H

7.05) and C-22(δ_C 116.6), suggested that **6** contained a flipped hydroxyl-phenazine-carboxylic acid unit compared to **5**. However, there was insufficient information to determine whether this proton was at C-23 or C-24.

To investigate δ_H 7.05 proton's position and the absolute configuration of **6**, we first calculated the ECD curves of eight possible isomers **6a**–**6h** (**Figure 66A**). To reduce the computational cost, we chose to tentatively assign the two phenols to C-14 and C-6 based on the established phenol positions in compounds **2**–**5.** Our analyses showed that the experimental ECD matched better with **6e** and **6g**, both with 10*S*,11*R*,21*R* configurations. NMR calculations indicated that **6e** was favored with an overall DP4+ probability of 91.83% (97.36% for ^{1}H NMR data and 23.39% for ^{13}C NMR data) compared to 8.17% for **6g** (2.64% for ^{1}H NMR data and 76.61% for ^{13}C NMR data, **Figure 60**), establishing that the proton was at C-23. Next, to

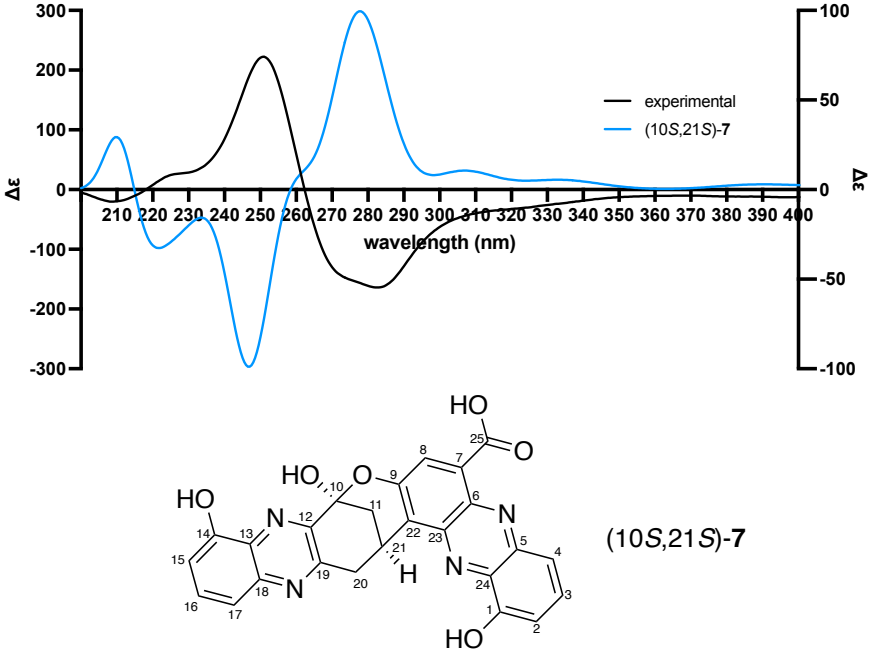

Figure 67. Calculated ECD curves of (10*S*,21*S*)-**7** at apfd/6-311+G(2d,p) level with solvent effects PCM=methanol for a total of 50 excited states; calculated ECD curves were scaled using left Y-axis; experimental ECD curves were scaled using right Y-axis; σ=0.16eV.

determine the phenol positions, we attempted ECD calculations for isomers **6e** and **6i**–**6k**, which we observed to be indistinguishable (**Figure 66B**). The following NMR/DP4+ calculations of these four isomers established that **6** as the **6j** conformer with an overall DP4+ probability score of 65.64% (66.72% for ^{1}H NMR data and 0.01% for ^{13}C NMR data) compared to 30.66% (0.00% for ^{1}H NMR data and 93.18% for ^{13}C NMR data) for **6k**, suggesting phenols at positions C-6 and C-17, respectively. In addition, analysis of the biosynthetic pathway of these diphenazines revealed that they should all share the same 1-hydroxyl phenazine-6-carboxylic acid unit (**Figure 39** and **40**), which agreed with the predicted phenol position at C-6 (**6j**) instead of C-3 (**6k**) as suggested by DP4+ analysis.

3.3.6 Baraphenazine G (7)

Compound **7** was isolated as an orange-red solid with a molecular formula of

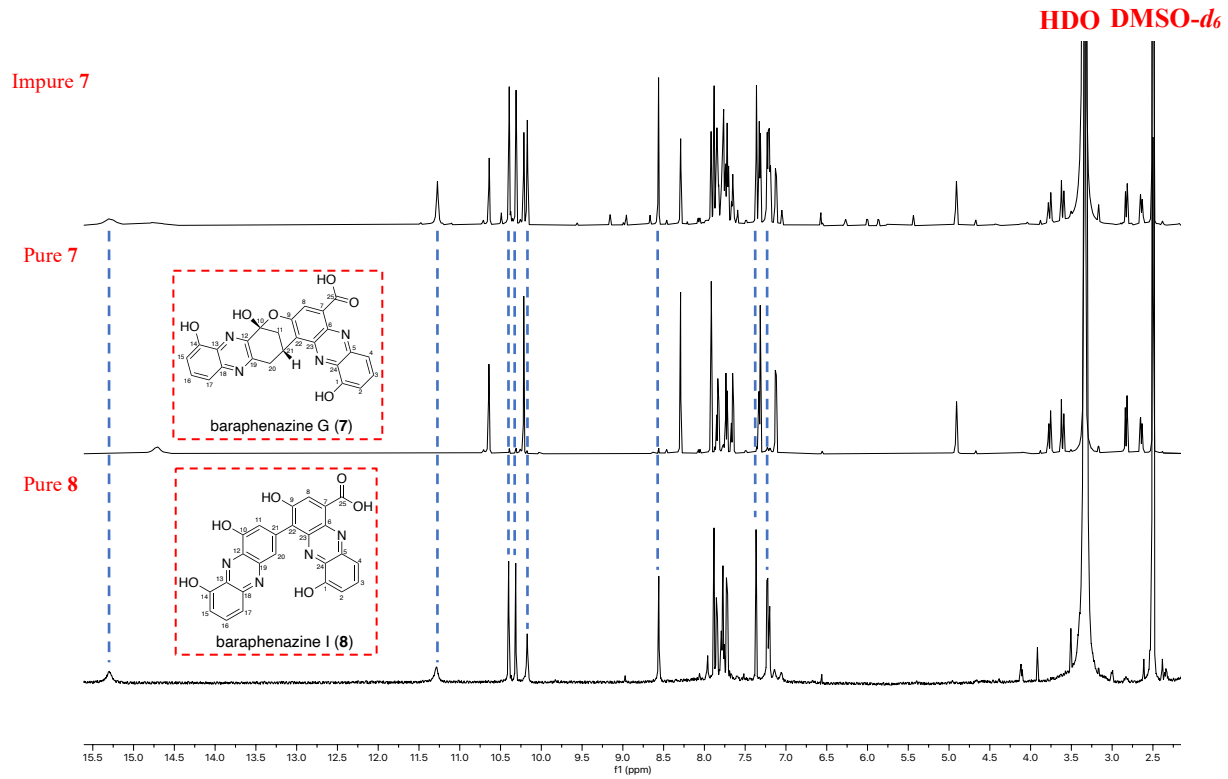

Figure 68. ^{1}H NMR spectrums (600MHz) comparison between, from top to the bottom, partially converted **7** after stored in DMSO, pure **7**, and **8** in DMSO-*d*$_6$; dashed lines match the protons peaks of **8** in partially converted **7**.

$C_{25}H_{16}N_4O_6$, which was derived from a HRESIMS ion peak of $C_{25}H_{17}N_4O_6$ $[M+H]^+$ (*m/z*: found 469.11545, calcd 469.11481). While it shares the same 7,8-disubstituted tetrahydrophenazine-1,9-diol unit and 8,9-disubstituted 1-hydroxylphenazine-6-carboxylic acid unit as **5**, it possesses two methylenes at C-11(δ_H 2.64, 2.83) and C-20(δ_H 3.61, 3.77) and a hemi-ketal carbon C-10(δ_C 97.3). The NMR data matched perfectly with the known molecule, baraphenazine G.[10] Again, we observed ^1H-^{15}N HMBC correlations between 14-OH/N-12(δ_H 10.23/δ_N 302.8), 10-OH/N-12(δ_H 8.30/δ_N 302.8), H-8/N-5(δ_H 7.92/δ_N 298.1) and H-4/N-5(δ_H 7.73/δ_N 298.1), suggesting that the positions of the two phenols, 1-OH(δ_H 10.67) and 14-OH(δ_H 10.23), were different from the reported structure of baraphenazine G.[10] From these analyses, we propose that the phenol position in baraphenazine G (**7**) should be corrected to C-4 from C-1. Furthermore, the calculated ECD curve of (10*S*,21*S*)-**7** showed exactly the opposite of the experimental curve, confirming the reported absolute configuration of 10*R*,21*R* (**Figure 67**).[10]

By comparing the proton NMR spectrums of **7** and degraded **5**, we found that proton peaks of **7** and the degradation product of **5** matched perfectly, indicating that **5** readily rearranged into **7** under heat (**Figure 64**). This suggested that **7** might not be naturally produced by the bacteria but rather a degradation product of **5**. Compound **7** was stable throughout the purification and drying stages, but it readily degraded even when stored in a cold and dark environment after dissolved in DMSO-d_6 and going through a few NMR experiments (**Figure 68**). The degradation product was isolated as a brown solid and had a molecular formula of $C_{25}H_{16}N_4O_6$, which was derived from HRESIMS of $C_{25}H_{15}N_4O_6$ $[M+H]^+$ (*m/z*: found 467.0979, calcd 467.0992). Initially, we proposed that the degradation mechanism involved the decomposition of the hemiketal moiety in **7** and the subsequent ring-opening yielded a new cyclohexanone and a phenol, which was exactly izumiphenazine B (**Figure 69**). However, after

examining NMR spectra, we found that the predominant proton peaks of this degradation product were all in the aromatic regions and the anticipated retainment of two methylenes in izumiphenazine B were not observed. In fact, the proton peaks for the middle bicyclic structure in **7** completely disappeared. Proton, Carbon, COSY, and HSQC spectra revealed the presence of one carboxylic acid (25-COOH), four phenolic hydroxyl groups (1-OH, 14-OH, 9-OH, 10-OH), and two groups of triplet/doublet/doublet (H-15 to H-17, H-2 to H-5) combinations, indicating the retainment of two phenolic moieties in the two phenazine units. The connection part of the two phenazine units was assigned based on the HMBC correlations between H-20/C-11, 10-OH/C-11, H-11/C-22, H-8/C-25, and H-8/C-22, giving us the final structure of **8**. Comparing the structures of **7** and **8**, we found that the two methylenes were reduced and the aromaticity was regenerated in the phenazinediol unit, suggesting that izumiphenazineB might be an intermediate in the degradation mechanism. No degradation was observed for compounds **1**-**6** when stored in DMSO. Both of these degradation transformations are novel in the field of phenazines and their mechanisms need to be further investigated.

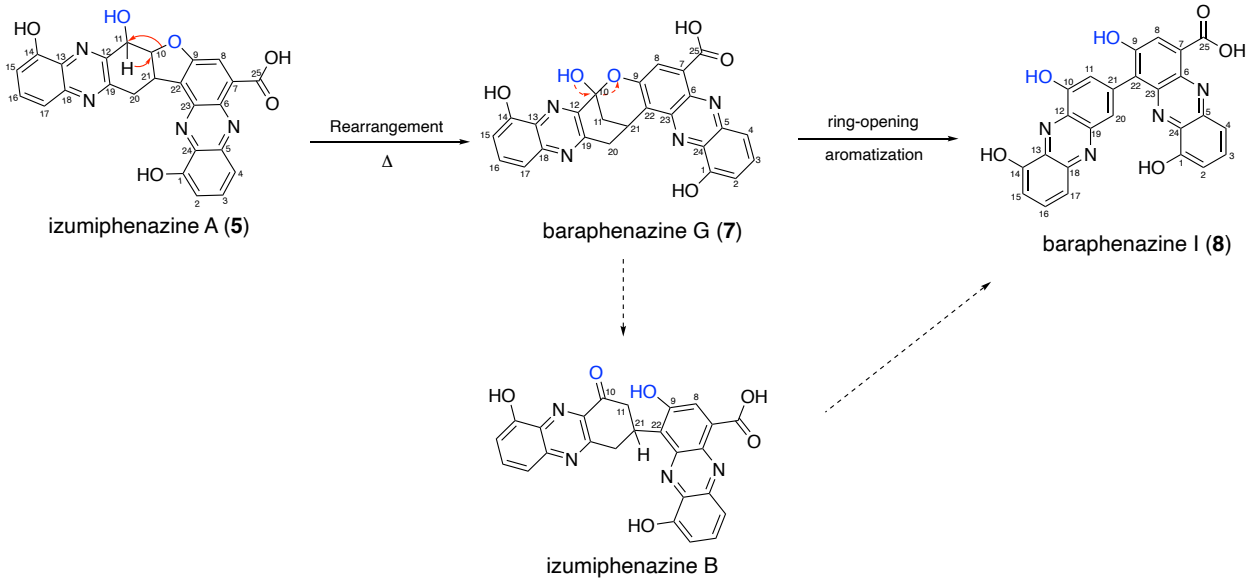

Figure 69. Proposed degradation mechanism of **5** and **7**.

3.4 Conclusion

In conclusion, through our structure determination efforts, we have developed a powerful pipeline for structural elucidation of diphenazines using ECD and GIAO NMR calculations coupled with DP4+ probability measure. Compared to traditional NMR-based structural analyses, this method is advantageous because: (1) it can determine the absolute configuration of chiral centers on the bridge of isolated diphenazines unlike ROESY/NOESY-based spatial analyses, and (2) it can determine the phenol positions of low-yielding diphenazines that typically give low-quality ^{1}H-^{15}N HMBC spectra. Subsequent use of this methodology led to several structural revisions, including resolving the absolute configuration of C-11 of phenazinolin D (**4**) and izumiphenazine A (**5**) from *R* to *S*. We also corrected the position of the phenol from C-4 to C-1 in baraphenazine G using ^{1}H-^{15}N HMBC experiments. Moreover, we isolated two new diphenazines, baraphenazine H (**3**), a stable keto-enol tautomer of baraphenazine F (**2**), and izumiphenazine E (**6**) that bear a unique 1,6-phenazinediol moiety. The structural diversity of **2**–**7** suggests *S. papuanewguineus* as a new source for further characterization of the biosynthetic mechanisms of late-stage dimerization of phenazine monomers.

3.5 Materials and Methods

3.5.1 General NMR and LC-HRMS/MS Materials and Methods

Nuclear Magnetic Resonance (NMR) spectra were collected using a Bruker 600 NMR spectrometer (^{1}H: 600 MHz, ^{13}C: 150 MHz) equipped with a Magnex 600/54 active shielded

premium magnet, a Bruker liquid N_2 cooled Prodigy cryo-probe and a Bruker NEO600 console, or a Bruker 800 NMR (^{1}H: 800 MHz, ^{13}C: 200 MHz) equipped with an Ascend magnet with active shield, a 5mm Triple resonance inverse detection TCI cryoprobe and a Bruker NEO console. All NMR data analyses were performed using MestReNova NMR software. All chemical shifts were referenced to residual solvent peaks [^{1}H (DMSO-*d*$_6$): 2.50 ppm; ^{13}C (DMSO-*d*$_6$): 39.51 ppm].

LC-HRMS/MS analyses of Biotage fractions, HPLC fractions, and purified compounds were performed using an Agilent 1290 Infinity II UPLC coupled to an Agilent 6545 ESI-Q-TOF-MS system operating in both positive and negative modes. Chromatography was performed using a Phenomenex Kinetex® 1.7 μm Phenyl-Hexyl 100 Å (2.1 × 50 mm) column. The injection volume was 2 μL per sample. The samples were eluted utilizing a gradient starting with a 1 min isocratic wash step consisting of 90% A (95% water/5% acetonitrile with 0.1% formic acid) and 10% B (100% acetonitrile with 0.1% formic acid), then 6 min linear gradient step starting from 10% B to 100% B and ended with 2 min of 100% B wash with a flow rate of 0.4 mL/min. The divert valve was set to MS for 0 – 7.4 min and set to waste from 7.4 - 9 min. The conditions of the dual AJS ESI were set with gas temperature at 320 °C, sheath gas temperature at 350 °C, sheath gas flow rate at 11 L/min, and source capillary voltage at 3500 V. The mass range of MS was set to 100 – 2000 m/z and acquisition rate was set to 10 spectra per second. The mass range of MS/MS was set to 50 – 2000 m/z; acquisition rate was set to 6 spectra per second, and isolation width was set to ~1.3 m/z. The collision energy was set based on the formula: Collision Energy = (5 × m/z)/100 + 10. Maximum precursor per cycle was set to 9 and the MS/MS mass error tolerance was ± 20 ppm. The reference masses for positive mode are purine $C_5H_4N_4$ $[M+H]^+$ ion (m/z 121.050873) and hexakis(1H,1H,3H-terafluoropropoxy)-phosphazine

$C_{18}H_{18}F_{24}N_3O_6P_3$ $[M+H]^+$ ion (m/z 922.009798). The reference masses for negative mode are trifluoroacetic acid $C_2HF_3O_2$ $[M-H]^-$ (m/z 112.985587) and hexakis(1H,1H,3H-terafluoropropoxy)-phosphazine $C_{18}H_{18}F_{24}N_3O_6P_3$ $[M+TFA-H]^-$ (m/z 1033.988109). All solvents used for Biotage fractionation were ACS grade and those used for HPLC purification and LC-HRMS/MS analyses were HPLC grade or better unless otherwise stated. All LC-MS/MS chromatograms, Extracted Base Peak Chromatograms (BPCs), and extracted UV (254 nm) traces in this work were subtracted from the chromatograms of methanol (MeOH) blank and were plotted using GraphPad Prism version 9.4.1 for Mac OS X (GraphPad Software, www. Graphpad.com).

3.5.2 ECD and DFT calculations

Experiment ECD spectra of isolated compounds were obtained by a J-815 spectropolarimeter (JASCO Co. Tokyo, Japan) using the following parameters: photometric mode: circular dichroism (CD), high voltage (HT), and absorbance (Abs); wavelength range: 190 nm to 600 nm; data pitch: 0.5 nm; sensitivity: standard; digital integration time (DIT): 4 seconds; bandwidth: 1 nm; start mode: immediately; start mode: immediately; scanning mode: continuous; scanning speed: 100 nm/minute; baseline correction: HPLC grade methanol; accumulations: 3.

For ECD calculations, Monte Carlo conformational searches were carried out by CONFLEX 9 (Rev. B, Tokyo, Japan) using Merck Molecular Force Field static (MMFFs) force field in the gas phase. All conformers within 5 kcal/mol of the lowest energy conformer were subjected to further optimization by Gaussian 16 (Rev. C01, Wallingford, CT, USA) using density functional theory (DFT) at B3LYP/6-31G(d) level with solvent effects of methanol included using a polarizable continuum model (PCM).[40] Optimized conformers within 3

kcal/mol of the lowest energy conformer were then selected for time-dependent DFT (TDDFT) calculations by Gaussian 16 (Rev. C01, Wallingford, CT, USA) at APFD/6-311+G(2d,p) level with PCM in methanol for a total of 50 excited states. Calculated ECD and UV spectra of the conformers were averaged by SpecDis (Version 1.71, Berlin, Germany)[36] according to their Boltzmann distributions and their relative Gibb's free energy to generate the theoretical ECD and UV spectra of each configuration. The sigma value was set to σ=0.16 eV. All theoretical and experimental ECD and UV curves were plotted using GraphPad Prism version 9.4.1 for Mac OS X (GraphPad Software, www. Graphpad.com).

For ^{13}C and ^{1}H NMR calculations, Monte Carlo conformational searches were carried out by CONFLEX 9 (Rev. B, Tokyo, Japan) using Merck Molecular Force Field static (MMFFs) force field in the gas phase. All conformers within 5 kcal/mol of the lowest energy conformer were subjected to further optimization by Gaussian 16 (Rev. C01, Wallingford, CT, USA) using DFT at B3LYP/6-31G(d) level with PCM in dimethyl sulfoxide (DMSO). Optimized conformers within 3 kcal/mol of the lowest energy conformer were then selected for Gauge-independent atomic orbital (GIAO) calculations of ^{13}C and ^{1}H NMR chemical shifts by Gaussian 16 (Rev. C01, Wallingford, CT, USA) at B3LYP/6-311+G(d,p) level with PCM in DMSO. The ^{13}C and ^{1}H chemical shifts of TMS were calculated by the same protocol and were used as the reference. The referenced NMR data of selected conformers of each configuration were averaged according to their Boltzmann distributions and their relative Gibb's free energy. The experimental and theoretical NMR data were analyzed by the improved probability DP4+ method to determine the absolute configurations and phenol positions of all isolated molecules.[7] When comparing the NMR chemical shifts of the same molecule with different phenol positions, the carbon

numbering of the corresponding benzene ring was changed accordingly to allow the comparison between the same carbon and proton.

3.5.3 Mosher's Analysis

To stir a solution of phenazinolin D (**4**, 1 mg, 2.14 μmol) and dry pyridine-d_5 (5 μL, 128 μmol, 60 equiv.) in dry deuterochloroform (1 mL) at room temperature for 2 hours, *R*-(−)-MTPA-Cl (16 uL, 85.6 μmol, 40 equiv.) was added. The reaction progress was monitored by LC-MS. The ^{1}H NMR spectrum of the **4**-*R*-MTPA ester product was obtained using the crude reaction solution. In an entirely analogous fashion, the **4**-*S*-MTPA ester was prepared using *S*-(+)-MTPA-Cl.

3.6 References

(1) Nicolaou, K.; Snyder, S. A. Chasing molecules that were never there: misassigned natural products and the role of chemical synthesis in modern structure elucidation. *Angewandte Chemie International Edition* **2005**, *44* (7), 1012-1044.

(2) Grauso, L.; Teta, R.; Esposito, G.; Menna, M.; Mangoni, A. Computational prediction of chiroptical properties in structure elucidation of natural products. *Nat Prod Rep* **2019**, *36* (7), 1005-1030.

(3) Nugroho, A. E.; Morita, H. Computationally-assisted discovery and structure elucidation of natural products. *J Nat Med-Tokyo* **2019**, *73* (4), 687-695.

(4) Shan, H.; Wilson, W. K.; Kamaric, E. NOESY and DFT-GIAO Calculations Reveal Pervasive Errors in C20 Configurations of Taraxastane-3,20-diols: Proposals to Improve NMR Structure Determinations. *Org Lett* **2020**, *22* (5), 1714-1719.

(5) Holt, T. A.; Reddy, D. S.; Huple, D. B.; West, L. M.; Rodriguez, A. D.; Crimmins, M. T.; Kutateladze, A. G. The Discreet Structural Diversity of Briarellins: DU8+Guided Multiple Structure Revisions Yielded Two Unknown Structural Types. *J Org Chem* **2020**, *85* (9), 6201-6205.

(6) Smith, S. G.; Goodman, J. M. Assigning Stereochemistry to Single Diastereoisomers by GIAO NMR Calculation: The DP4 Probability. *Journal of the American Chemical Society* **2010**, *132* (37), 12946-12959.

(7) Grimblat, N.; Zanardi, M. M.; Sarotti, A. M. Beyond DP4: an Improved Probability for the Stereochemical Assignment of Isomeric Compounds using Quantum Chemical Calculations of NMR Shifts. *J Org Chem* **2015**, *80* (24), 12526-12534.

(8) Ding, Z. G.; Li, M. G.; Ren, J.; Zhao, J. Y.; Huang, R.; Wang, Q. Z.; Cui, X. L.; Zhu, H. J.; Wen, M. L. Phenazinolins A-E: novel diphenazines from a tin mine tailings-derived Streptomyces species. *Org Biomol Chem* **2011**, *9* (8), 2771-2776.

(9) Abdelfattah, M. S.; Kazufumi, T.; Ishibashi, M. Izumiphenazines A-C: isolation and structure elucidation of phenazine derivatives from Streptomyces sp. IFM 11204. *J Nat Prod* **2010**, *73* (12), 1999-2002.

(10) Wang, X.; Abbas, M.; Zhang, Y.; Elshahawi, S. I.; Ponomareva, L. V.; Cui, Z.; Van Lanen, S. G.; Sajid, I.; Voss, S. R.; Shaaban, K. A.; et al. Baraphenazines A-G, Divergent Fused Phenazine-Based Metabolites from a Himalayan Streptomyces. *J Nat Prod* **2019**, *82* (6), 1686-1693.

(11) Bonhomme, C.; Gervais, C.; Babonneau, F.; Coelho, C.; Pourpoint, F.; Azais, T.; Ashbrook, S. E.; Griffin, J. M.; Yates, J. R.; Mauri, F.; et al. First-Principles Calculation of NMR Parameters Using the Gauge Including Projector Augmented Wave Method: A Chemist's Point of View. *Chem Rev* **2012**, *112* (11), 5733-5779.

(12) Becke, A. D. Density-Functional Exchange-Energy Approximation with Correct Asymptotic-Behavior. *Phys Rev A* **1988**, *38* (6), 3098-3100.

(13) Lee, C. T.; Yang, W. T.; Parr, R. G. Development of the Colle-Salvetti Correlation-Energy Formula into a Functional of the Electron-Density. *Phys Rev B* **1988**, *37* (2), 785-789.

(14) Burke, K. Perspective on density functional theory. *J Chem Phys* **2012**, *136* (15), 150901.

(15) Stephens, P. J.; Devlin, F. J.; Chabalowski, C. F.; Frisch, M. J. Ab-Initio Calculation of Vibrational Absorption and Circular-Dichroism Spectra Using Density-Functional Force-Fields. *J Phys Chem-Us* **1994**, *98* (45), 11623-11627.

(16) Adamo, C.; Jacquemin, D. The calculations of excited-state properties with Time-Dependent Density Functional Theory. *Chem Soc Rev* **2013**, *42* (3), 845-856.

(17) Rassolov, V. A.; Ratner, M. A.; Pople, J. A.; Redfern, P. C.; Curtiss, L. A. 6-31G*basis set for third-row atoms. *J Comput Chem* **2001**, *22* (9), 976-984.

(18) Cramer, C. J. *Essentials of Computational Chemistry: Theories and Models*; Wiley, 2013.

(19) Grimme, S. Calculation of frequency dependent optical rotation using density functional response theory. *Chem Phys Lett* **2001**, *339* (5-6), 380-388.

(20) Stephens, P. J.; Devlin, F. J.; Cheeseman, J. R.; Frisch, M. J.; Rosini, C. Determination of absolute configuration using optical rotation calculated using density functional theory. *Org Lett* **2002**, *4* (26), 4595-4598.

(21) Dunning, T. H. Gaussian-Basis Sets for Use in Correlated Molecular Calculations .1. The Atoms Boron through Neon and Hydrogen. *Journal of Chemical Physics* **1989**, *90* (2), 1007-1023.

(22) Weigend, F.; Ahlrichs, R. Balanced basis sets of split valence, triple zeta valence and quadruple zeta valence quality for H to Rn: Design and assessment of accuracy. *Phys Chem Chem Phys* **2005**, *7* (18), 3297-3305.

(23) Mandi, A.; Kurtan, T. Applications of OR/ECD/VCD to the structure elucidation of natural products Dedicated to Professor Dr Sandor Antus on the occasion of his 75th anniversary. *Nat Prod Rep* **2019**, *36* (6), 889-918.

(24) Menna, M.; Imperatore, C.; Mangoni, A.; Della Sala, G.; Taglialatela-Scafati, O. Challenges in the configuration assignment of natural products. A case-selective perspective This paper is dedicated to the memory of Prof. Ernesto Fattorusso (1937-2012). *Nat Prod Rep* **2019**, *36* (3), 476-489.

(25) Semenov, V. A.; Krivdin, L. B. Computational NMR of natural products. *Russ Chem Rev+* **2022**, *91* (5).

(26) Nugroho, A. E.; Morita, H. Computationally-assisted discovery and structure elucidation of natural products (vol 73, pg 687, 2019). *J Nat Med-Tokyo* **2019**, *73* (4), 696-696.

(27) Tantillo, D. J. Walking in the woods with quantum chemistry - applications of quantum chemical calculations in natural products research. *Nat Prod Rep* **2013**, *30* (8), 1079-1086.

(28) Zanardi, M. M.; Sarotti, A. M. GIAO C-H COSY Simulations Merged with Artificial Neural Networks Pattern Recognition Analysis. Pushing the Structural Validation a Step Forward. *J Org Chem* **2015**, *80* (19), 9371-9378.

(29) Smith, S. G.; Goodman, J. M. Assigning the Stereochemistry of Pairs of Diastereoisomers Using GIAO NMR Shift Calculation. *J Org Chem* **2009**, *74* (12), 4597-4607.

(30) Grimblat, N.; Gavin, J. A.; Daranas, A. H.; Sarotti, A. M. Combining the Power of J Coupling and DP4 Analysis on Stereochemical Assignments: The J-DP4 Methods. *Org Lett* **2019**, *21* (11), 4003-4007.

(31) Zanardi, M. M.; Sarotti, A. M. Sensitivity Analysis of DP4+with the Probability Distribution Terms: Development of a Universal and Customizable Method. *J Org Chem* **2021**, *86* (12), 8544-8548.

(32) Howarth, A.; Ermanis, K.; Goodman, J. M. DP4-AI automated NMR data analysis: straight from spectrometer to structure. *Chem Sci* **2020**, *11* (17), 4351-4359.

(33) Halgren, T. A. Merck molecular force field .1. Basis, form, scope, parameterization, and performance of MMFF94. *J Comput Chem* **1996**, *17* (5-6), 490-519.

(34) Halgren, T. A. MMFF VI. MMFF94s option for energy minimization studies. *J Comput Chem* **1999**, *20* (7), 720-729.

(35) Austin, A.; Petersson, G. A.; Frisch, M. J.; Dobek, F. J.; Scalmani, G.; Throssell, K. A Density Functional with Spherical Atom Dispersion Terms. *J Chem Theory Comput* **2012**, *8* (12), 4989-5007.

(36) Bruhn, T.; Schaumloffel, A.; Hemberger, Y.; Bringmann, G. SpecDis: Quantifying the Comparison of Calculated and Experimental Electronic Circular Dichroism Spectra. *Chirality* **2013**, *25* (4), 243-249.

(37) Adamo, C.; Barone, V. Exchange functionals with improved long-range behavior and adiabatic connection methods without adjustable parameters: The mPW and mPW1PW models. *Journal of Chemical Physics* **1998**, *108* (2), 664-675.

(38) King, G. F.; Mobli, M. Derivation of Peptide and Protein Structure using NMR Spectroscopy. *Comprehensive Natural Products Ii: Chemistry and Biology, Vol 9: Modern Methods in Natural Products Chemistry* **2010**, 279-325.

(39) Hoye, T. R.; Jeffrey, C. S.; Shao, F. Mosher ester analysis for the determination of absolute configuration of stereogenic (chiral) carbinol carbons. *Nat Protoc* **2007**, *2* (10), 2451-2458.

(40) *Gaussian 16 Rev. C.01*; Wallingford, CT, 2016. (accessed.

Chapter 4 Other Natural Products Isolated from Various Marine and Terrestrial Sources

4.1 PTM: PKS/NRPS Type of Natural Products

Besides *S. Papuanewguineus*, another active strain out of the HTS against eIF4E PPI was 87797-1N, which was isolated from a soil sample collected from Costa Rica. In this chapter, we will discuss in detail the discovery and structural characterization of polycyclic tetramate macrolactams (PTMs) from this strain, including one novel molecule, capsimycin H.

4.1.1 An introduction to ikarugamycin type of 5/6/5 PTM

PTMs are a growing class of natural products that share a common tetramate-containing macrolactam fused to a diverse subset of carbocyclic rings, such as 5/5 in alteramide[1] and cylindramide,[2] 5/5/6/ in heat-stable antifungal factor (HSAF),[3] frontalamides,[4] and discodermide,[5] and 5/6/5 in ikarugamycin (**9**)[6] and clifednamides (**Figure 70**).[7] The structural diversity of PTMs is further enriched by tailoring modifications such as epoxidation, hydroxylation, and N-methylation. More than 30 PTM-class of molecules have been isolated so far from a variety of sources, including both terrestrial and marine bacteria and marine sponges.[8]

The first ever PTM, ikarugamycin (**9**), was isolated in 1972 from a soil *Streptomyces* strain.[6] Five years later in 1977, the 5/6/5 tricyclic ring-containing macrolactam structure and absolute configurations of ikarugamycin (**9**) were elucidated utilizing a combination of spectroscopic and chemical degradation methods.[9] In 2003, ikarugamycin (**9**) was re-isolated together with epoxyikarugamycin (**10**) and ripromycin from a soil *Streptomyces* sp. Tü 6239 by

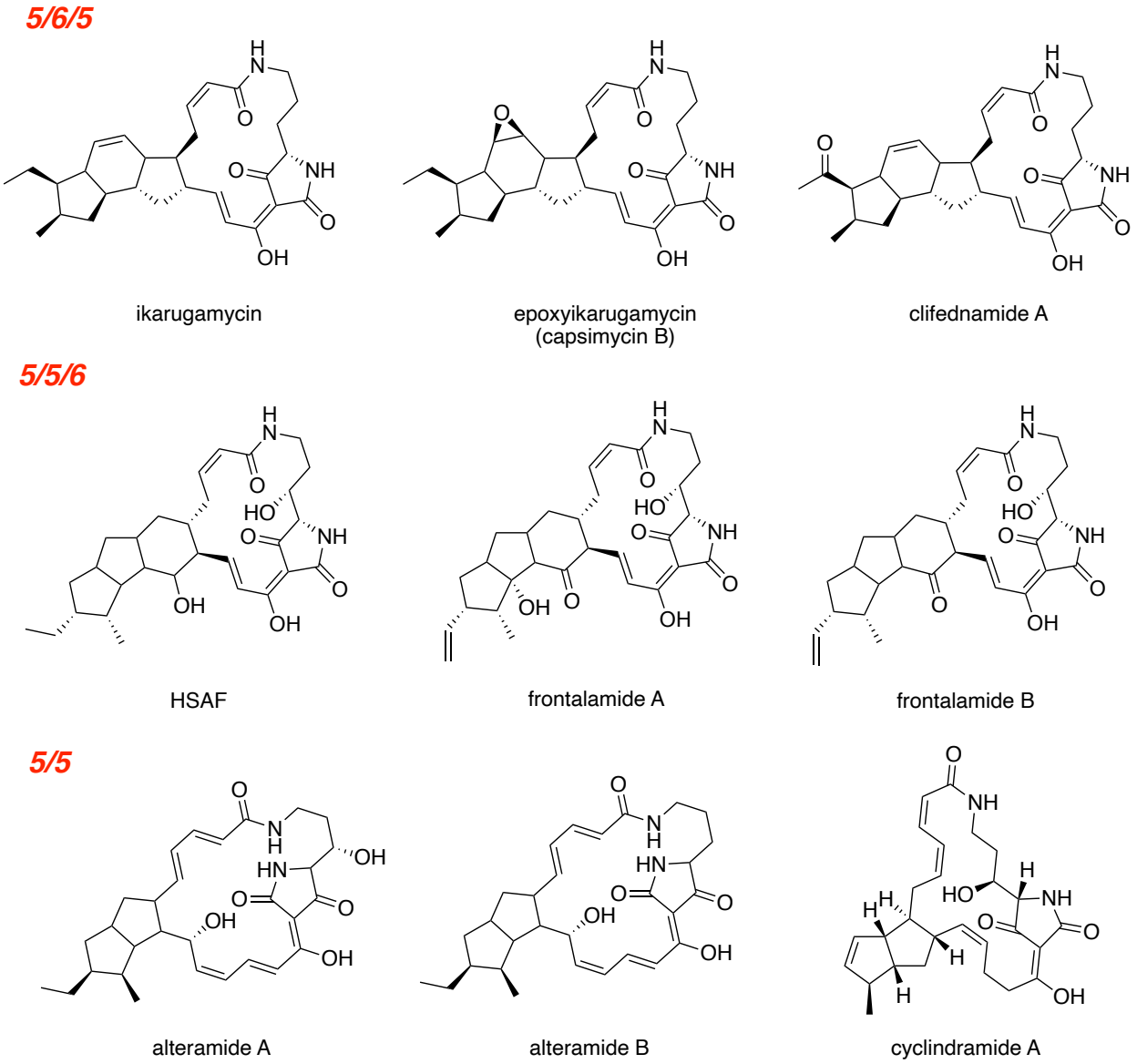

Figure 70. Representative PTMs with 5/6/5, 5/5/6, and 5/5 ring systems.

the Fiedler group.[10] Later, capsimycin (**12**) that contains a methoxy group at C-29 of epoxyikarugamycin (**10**) was isolated from *Streptomyces* NO. C49-87,[11] and its analogs, capsimycin C-G were also reported recently.[12] Utilizing a PCR screening method targeting conserved PTM biosynthetic genes in *Streptomyces* sp. JV178, the Clardy group reported the isolation of clifednamides A and B that contain an unusual ketone at C-29 position.[7]

These 5/6/5 PTMs exhibited a variety of bioactivities, including antimicrobial, antitumor, antiulcer, and antiprotozoal activities.[8] In particular, as the most studied PTM molecule,

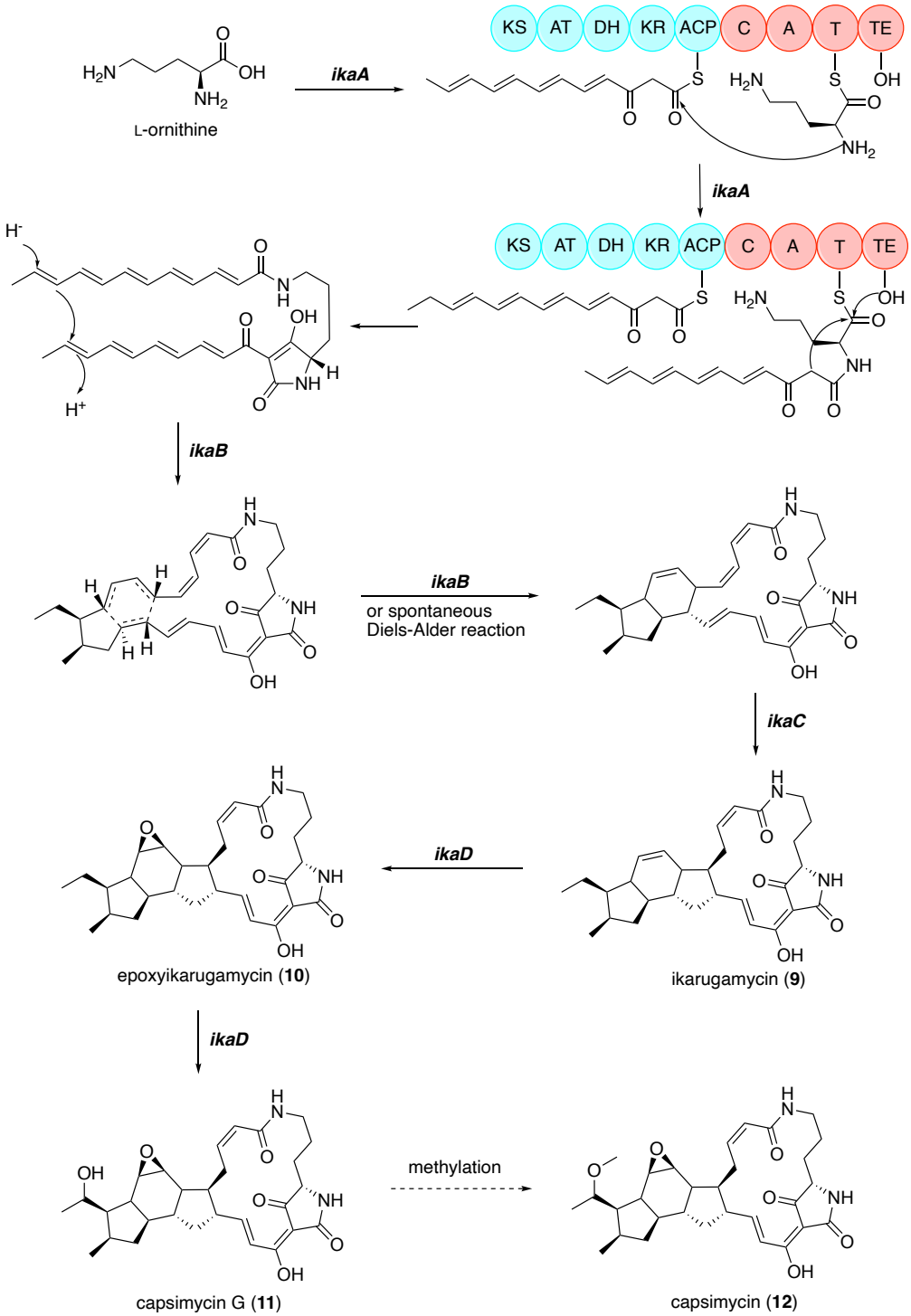

Figure 71. Biosynthetic pathway of ikarugamycin (**9**), epoxyikarugamycin (**10**), capsimycin G (**11**), and capsimycin (**12**).

ikarugamycin (**9**) was reported to exert significant cytotoxicity against different cancer cell lines, such as MCF-7 breast cancer, HMO2 gastric adenocarcinoma, Hep G2 hepatocellular carcinoma,

and Huh 7 hepatoma cells.[10] It was also demonstrated to induce apoptosis in HL-60 cells through genotoxicity and caspase activation to cause DNA damage.[13] It also inhibited clathrin-dependent endocytosis[14] and oxidized low-density lipoprotein-induced uptake.[15] It was also shown to block Nef-induced cell surface CD4 down-regulation on type I HIV-infected T cells.[16] These diverse and potent bioactivities make ikarugamycin (**9**) a promising lead for drug development.

The biosynthetic pathway of **9** has been well characterized through heterologous reconstitution, knockout studies, and feeding experiments.[17, 18] These studies revealed that the core biosynthetic genes of **9** consist of *ikaA* (a hybrid PKS/NRPS), *ikaB* (a flavin-dependent phytoene desaturase family enzyme), and *ikaC* (an alcohol dehydrogenase, **Figure 71**). *IkaA* acts iteratively to synthesize two slightly different polyene chains that are then condensed respectively with the α- and δ-amino groups of L-ornithine loaded on the peptidyl carrier protein (PCP or T) domain of the NRPS module of *ikaA*. Then the two polyene chains undergo an intramolecular Dieckmann-type cyclization to form the tetramate ring, and the product is then released from the NRPS module by the thioesterase (TE) domain. After that, *ikaB* catalyzes the formation of the first five-membered ring in the 5/6/5 ring system and the intermediate will undergo a Diels-Alder reaction to form the cyclohexene ring by either a spontaneous or *ikaB*-catalyzed [4+2] cycloaddition. Finally, *ikaC* catalyzes the formation of the last five-membered ring to give the structure of ikarugamycin (**9**). A tailoring enzyme of **9**, *ikaD*, was recently characterized as a putative cytochrome P450 enzyme through knockout and complementation experiments.[12] It was shown to be able to catalyze the epoxidation of **9** to form epoxyikarugamycin (**10**) and also the hydroxylation of **10** to form capsimycin G (**11**). This hydroxy group in **11** was further O-methoxylated to form capsimycin (**12**), which was achieved by the non-enzymatic *in vitro* incubation of methanol and **11**.

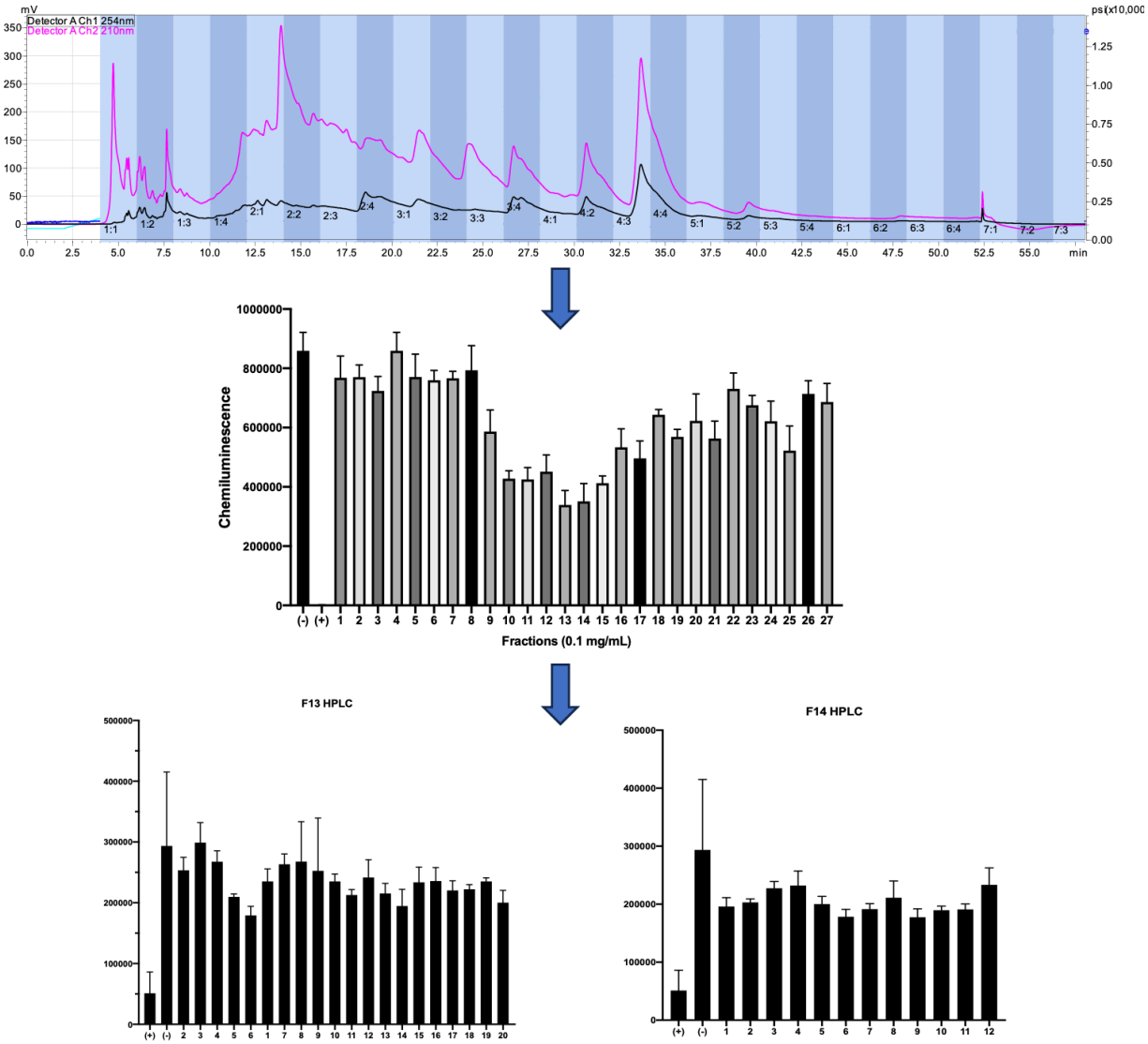

Figure 72. Representative prep-HPLC chromatogram (5%-95% acetonitrile/H_2O with 0.1% formic acid); PPI Cat-ELCCA results of prep-HPLC fractions and semi-prep HPLC fractions of prep-HPLC fractions F13 and F14 (0.1 mg/mL for all fractions).

4.1.2 Isolation and structure characterization of ikarugamycin analogs from 87797-1N

During the initial hit re-confirmation, we found that the most active fraction showed an EC_{50} of around 0.1-0.2 mg/mL against eIF4E–4E-BP1 PPI in cat-ELCCA (**Figure 22**). However, during our purification processes, we observed a complete loss of activity from preparative HPLC to semi-preparative HPLC (**Figure 72**). By comparing the chemical profiles of the crude extract (**Figure 73**) and prep-HPLC fractions, we found that the masses $[M-H]^-$ 509.2642,

539.2727, and 523.2793 in the crude extract changed to 527.2774, 557.2885, and 541.2944, and

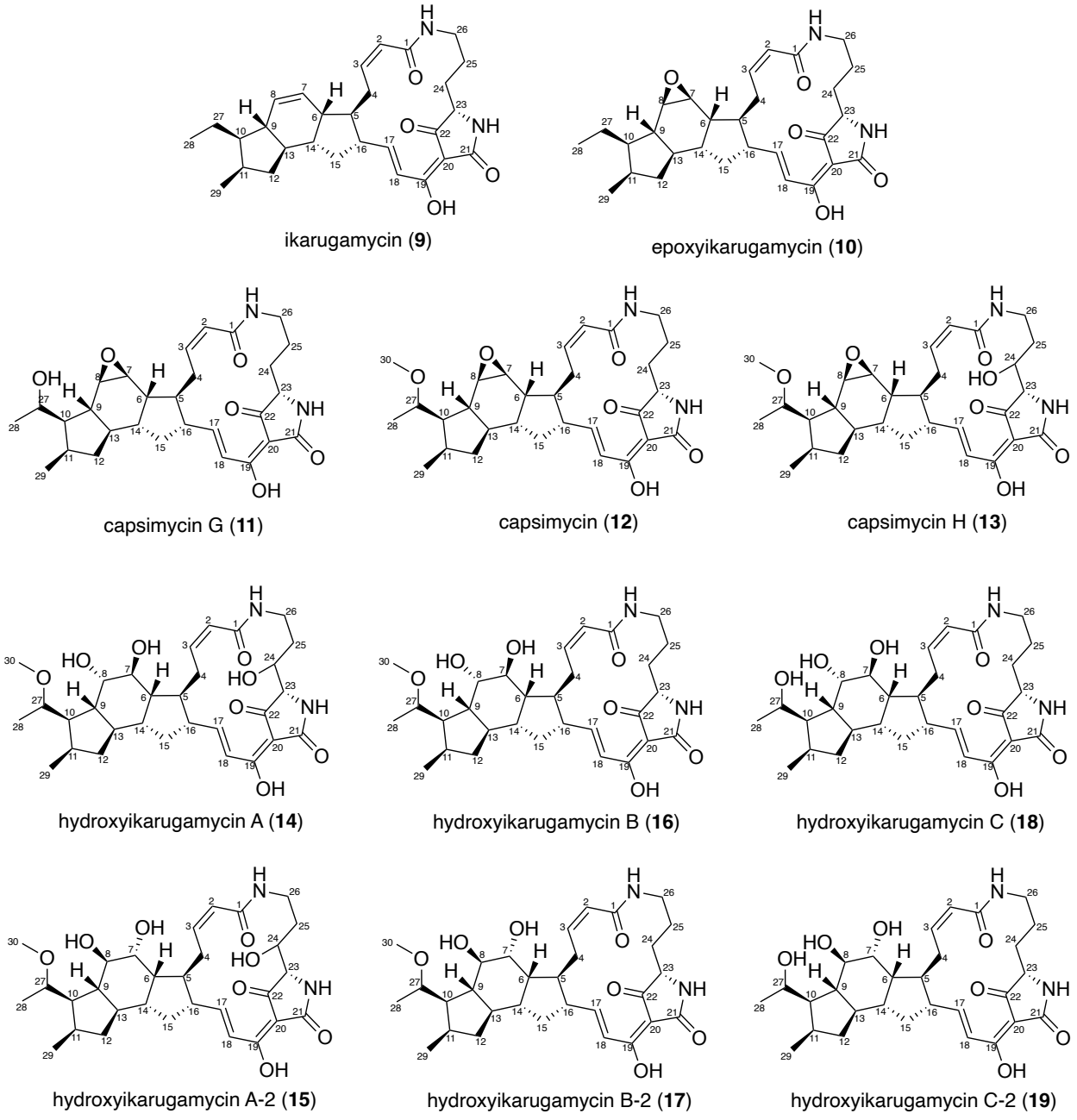

Figure 73. Structures of isolated ikarugamycin analogs from 87797-1N.

the masses 493.2706 and 477.2743 disappeared. Using antiSMASH analysis, we identified the biosynthetic gene cluster for the ikarugamycin class of natural products. By comparing the

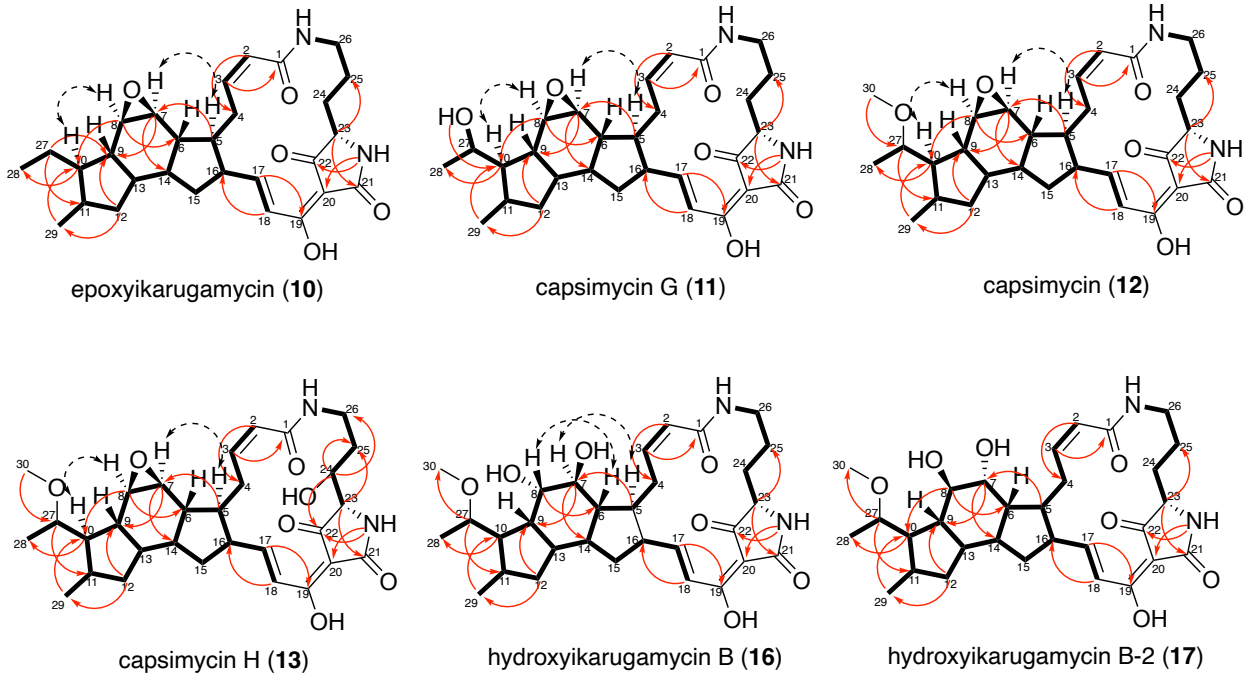

Figure 74. Key COSY, HMBC, and ROESY/NOESY correlations in **10**–**13**, **16**, and **17**.

masses of known ikarugamycin analogs to ours, we found the masses $[M-H]^-$ 477.2743, 493.270, 509.2642, 523.2793, 557.2885, 541.2944, and 527.2774 matched the known molecule ikarugamycin (**9**) and epoxyikarugamycin (**10**),[6, 10] capsimycin G (**11**), capsimycin (**12**),[12] hydroxyikarugamycin A (**14**), hydroxyikarugamycin B (**16**), and hydroxyikarugamycin C (**18**),[19] respectively. Targeted purification of masses 557.2885, 541.2944, and 527.2774 yielded not only known compounds **14**, **16**, and **18** but also their close analogs hydroxyikarugamycin A-2 (**15**), hydroxyikarugamycin B-2 (**17**), and hydroxyikarugamycin C-2 (**19**, **Figure 73**).

With the highest yield among these compounds, compound **16** was first purified and characterized. It was isolated as a yellow powder with a molecular formula of $C_{30}H_{42}N_2O_7$, which was derived from an HRESIMS ion peak of $C_{30}H_{41}N_2O_7$ $[M-H]^-$ (m/z: found 541.2944, calcd 541.2914). Its ^1H, ^{13}C, and 2D NMR data matched those of the known compound, hydroxyikarugamycin B (**Table 1**).[19] The observed NOE correlations between H-8 (δ_H 3.68)/H-6 (δ_H 1.88) and H-7 (δ_H 3.73)/H-5 (δ_H 1.95) suggested that H-8 and H-6 were on the same side and

Table 1. ^{1}H and ^{13}C NMR data for hydroxyikarugamycin B (**16**) and B-2 (**17**) in DMSO-d_6.

	hydroxyikarugamycin B (16)		hydroxyikarugamycin B-2 (17)	
Position	δ_C (type)	δ_H, multiplets (*J* in Hz)	δ_C (type)	δ_H, multiplets (*J* in Hz)
1	165.6 (C)		166.2 (C)	
2	123.9 (CH)	5.75, d (11.4)	124.3 (CH)	5.76, d (11.4)
3	140.2 (CH)	5.94, ddd (11.5, 10.0, 4.0)	141.3 (CH)	5.98, dd (10.8, 3.8)
4a	26.0 (CH_2)	2.35, dt (16.8, 3.5)	27.0 (CH_2)	2.32, m
4b	26.0 (CH_2)	3.39, tq (10.2, 4.9, 3.9)	27.0 (CH_2)	3.39, m
5	44.7 (CH)	1.95, m	43.9 (CH)	2.05, ddt (15.1, 10.5, 4.1)
6	41.5 (CH)	1.88, m	43.1 (CH)	2.18, m
7	70.8 (CH)	3.73, dd (3.6, 1.9)	74.9 (CH)	3.58, m
7-OH				
8	71.5 (CH)	3.68, t (3.0)	75.8 (CH)	3.51, m
8-OH				
9	40.2 (CH)	1.56, ddd (12.1, 8.8, 4.5)	50.2 (CH)	1.23, m
10	44.5 (CH)	1.96, m	52.0 (CH)	1.75, m
11	33.3 (CH)	2.09, ddd (15.8, 9.0, 7.0)	33.9 (CH)	2.20, m
12a	39.7 (CH_2)	0.59, tq (18.3, 10.3, 9.4)	39.9 (CH_2)	0.60, m
12b	39.7 (CH_2)	1.97, m	39.9 (CH_2)	1.96, dt (12.0, 7.2)
13	43.9 (CH)	1.56, ddd (12.1, 8.8, 4.5)	43.0 (CH)	1.71, m
14	47.1 (CH)	1.87, m	45.2 (CH)	1.74, m
15a	34.8 (CH_2)	1.19, ddd (13.1, 9.5, 3.2)	37.8 (CH_2)	1.14, m
15b	34.8 (CH_2)	1.98, m	37.8 (CH_2)	1.85, tq (13.8, 6.9)
16	49.4 (CH)	2.22, p (9.8)	49.8 (CH)	2.29, m
17	151.1 (CH)	6.65, dd (15.4, 10.2)		6.59, s
18	121.7 (CH)	6.94, d (15.5)		7.03, d (15.4)
19	171.2 (C)			
20	100.7 (C)			
21	175.0 (C)			
21-NH		8.68, s		
22	195.8 (C)		195.8 (C)	
23	61.0 (CH)	3.84, dd (5.8, 2.2)	61.2 (CH)	3.77, m
24a	27.0 (CH_2)	1.72, m	27.5 (CH_2)	1.71, m
24b	27.0 (CH_2)	1.84, m	27.5 (CH_2)	1.84, m
25a	20.6 (CH_2)	1.05, m	21.3 (CH_2)	1.05, m
25b	20.6 (CH_2)	1.39, m	21.3 (CH_2)	1.36, m
26a	38.2 (CH_2)	1.49, m	38.7 (CH_2)	2.47, m
26b	38.2 (CH_2)	3.23, m	38.7 (CH_2)	3.25, m
26-NH		7.85, t (5.7)		7.82, t (5.7)
27	76.9 (CH)	3.26, m	77.3 (CH)	3.44, m
28	16.9 (CH_3)	1.12, d (6.2)	17.5 (CH_3)	1.23, d (6.1)
29	18.1 (CH_3)	0.96, d (7.1)	18.8 (CH_3)	0.91, d (7.1)
30	54.8 (CH_3)	3.18, s	55.6 (CH_3)	3.23, s

H-7 and H-5 were on the same side (**Figure 74**), matched the previously reported 7*S*,8*S* configuration.

Compound **17** was isolated in pairs with **16** as a yellow powder with a molecular formula of $C_{30}H_{42}N_2O_7$, which was derived from an HRESIMS ion peak of $C_{30}H_{41}N_2O_7$ $[M-H]^-$ (m/z: found 541.2864, calcd 541.2914). Its ^{1}H, ^{13}C, and 2D NMR data were very similar to those of the **16**, suggesting a structure very similar to **16** (**Table 1**). By a close comparison of their NMR data, we found that most of the differences were located in the C-6 to C-10 region with ~5-10 ppm differences in ^{13}C chemical shifts and ~0.2-0.5 ppm in ^{1}H chemical shifts. Thus, we postulated that the configurations of C-7 and C-8 were switched to 7*R*,8*R* from 7*S*,8*S* in **16**. Unfortunately, the ^{1}H peaks of H-7 and H-8 were buried under the water noise peak, and we

were unable to observe any NOE of these two protons to determine their absolute configurations. In the future, DFT calculations could be applied to validate this hypothesis.

Compounds **14** and **15** were isolated in pairs as brown solids with the same molecular formula of $C_{30}H_{42}N_2O_8$, which was derived from an HRESIMS ion peak of $C_{30}H_{41}N_2O_8$ $[M-H]^-$ (m/z: found 557.2885 for **14** and 557.2864 for **15**, calcd 557.2863). We observed that the ^1H peaks of the methylene at C-24 in **16** were missing and a new peak at ~3.9 ppm was gained, suggesting a potential hydroxylation at C-24 (**Figure 75**). These data matched the known compound hydroxyikarugamycin A.[19] Since we observed almost identical ^1H NMR spectrums between **14** and **15**, we postulated that their only structural difference was the configurations of C-7 and C-8, similar to what we observed for the hydroxyikarugamycin B pairs. For the determination of the configuration of C-24, more material is needed to obtain good 2D NMR

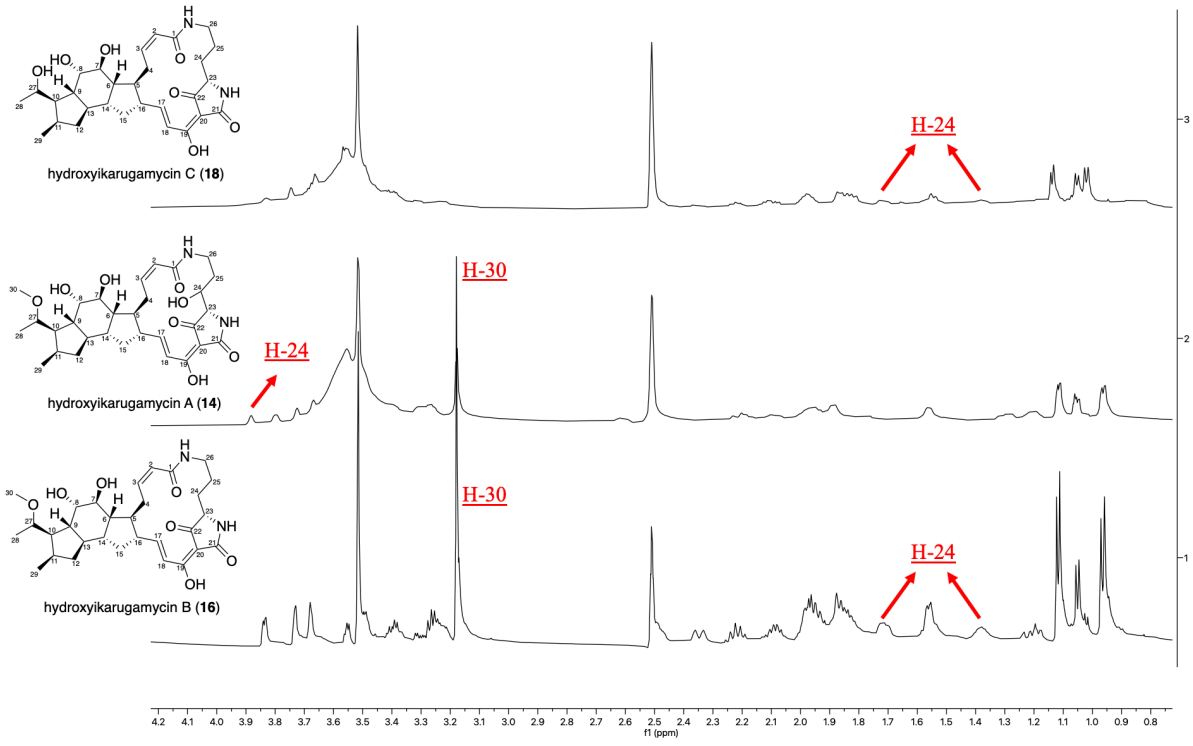

Figure 75. ^1H NMR data comparison of **14**, **16**, and **18** between 0.8 to 4.2 ppm in DMSO-d_6.

spectrums, especially ROESY/NOESY.

Compounds **18** and **19** were isolated in pairs as brown solids with the same molecular formula of $C_{29}H_{40}N_2O_7$, which was derived from an HRESIMS ion peak of $C_{29}H_{39}N_2O_7$ $[M-H]^-$ (m/z: found 527.2774 for **18** and 527.2695 for **19**, calcd 557.2757). We observed that while the ^1H NMR spectrums of **16** and **18** were almost identical, the methoxy group on C-30 was missing (**Figure 75**). Based on this and the observed difference of 14 in their molecular weights, we postulated that compound **18** was the known compound, hydroxyikarugamycin C.[19] Since we observed almost identical ^1H NMR spectrums between **18** and **19**, we hypothesized that their only structural difference was the configurations of C-7 and C-8, similar to what we observed for the hydroxyikarugamycin A and B pairs.

Then, we put our efforts into developing methods for the isolation of other masses, including $[M-H]^-$ 509.2642, 539.2727, 523.2793, and the disappeared 493.2706 and 477.2743. Previous studies have shown the vulnerability of the epoxide groups in capsimycins and epoxyikarugamycin in the presence of trifluoroacetic acid (TFA), suggesting that non-acidic solvents were necessary to isolate these compounds.[12] An initial prep-HPLC fractionation followed by several rounds semi-Prep HPLC purification using acetonitrile/H_2O without acid successfully yielded **9**–**13** (**Figure 73**).

As the most basic structure of all ikarugamycin analogs, ikarugamycin (**9**, **Figure 73**) was first isolated as a light-yellow solid with a molecular formula of $C_{29}H_{38}N_2O_4$, which was derived from an HRESIMS ion peak of $C_{29}H_{37}N_2O_4$ $[M-H]^-$ (m/z: found 477.2703, calcd 477.2753). Its structure was confirmed by the observed BGC in the antiSMASH analyses and by comparing the LC-MS retention time with that of the commercial ikarugamycin. Its epoxidized analog, epoxyikarugamycin (**10**, **Figure 73**), was then isolated as a light-yellow solid with a

Table 2. ^{1}H NMR data for **10**–**13** in DMSO-d_6.

	epoxyikarugamycin (10)	capsimycin G (11)	capsimycin (12)	capsimycin H (13)
Position	δ_H, multiplets (*J* in Hz)	δ_H, multiplets (*J* in Hz)	δ_H, multiplets (*J* in Hz)	δ_H, multiplets (*J* in Hz)
1				
2	5.85, d (11.5)	5.85, d (12.0)	5.88, d (11.7)	5.82, dd (11.4, 2.8)
3	5.99, td (11.1, 2.8)	5.98, t (11.1)	5.97, t (11.5, 2.0)	6.00, td (11.3, 2.6)
4a	2.21, m	2.19, dd (19.1, 12.4)	2.19, m	2.15, m
4b	3.48, m	3.47, m	3.49, m	3.63, ddd (16.2, 11.0, 4.0)
5	1.50, ddd (15.8, 12.2, 3.7)	1.48, ddd (14.9, 11.6, 4.3)	1.49, tt (12.2, 3.8)	1.55, td (12.4, 5.9)
6	2.33, dd (12.8, 9.5)	1.63, m	1.63, m	1.63, m
7	2.92, d (4.0)	2.88, dd (4.1, 1.2)	2.88, d (4.0)	2.88, d (4.0)
8	3.12, dd (3.9, 2.1)	3.17, t (3.3)	3.18, t (3.3)	3.18, t (2.9)
9	0.84, m	0.87, t (12.1)	0.89, t (12.1)	0.88, td (11.9, 2.3)
10	1.67, m	1.76, m	1.88, m	1.88, dq (16.2, 7.7, 6.3)
11	2.20, m	2.26, m	2.25, m	2.25, m
12a	0.60, tq (11.9, 7.6)	0.59, q (11.6)	0.60, td (11.9, 8.6)	0.60, td (11.9, 8.6)
12b	2.00, m	1.98, m	1.97, m	1.97, m
13	1.06, m	1.09, dd (11.7, 6.8)	1.09, dd (11.7, 6.4)	1.10, m
14	1.63, m	2.29, m	2.29, m	2.31, dd (12.7, 9.7)
15a	1.03, m	1.02, m	1.03, m	1.07, m
15b	1.98, m	1.97, m	1.98, m	1.97, m
16	2.23, m	2.22, m	2.22, m	2.22, m
17	6.06, dd (15.2, 9.8)	6.06, dd (15.5, 9.8)	6.07, dd (15.2, 9.7)	6.10, br s
18	7.51, d (15.3)	7.51, d (15.2)	7.52, d (15.3)	7.25, d (11.2)
19				
20				
21				
21-NH	6.47, d (6.1)	6.47, s	6.57, s	
22				
23	3.32, m	3.31, m	3.32, m	3.56, m
24a	1.67, m	1.65, m	1.67, m	3.78, d (6.7)
24b	1.74, dd (11.7, 8.2)	1.74, m	1.75, td (13.3, 1.9)	–
25a	1.18, m	1.18, m	1.18, m	1.14, m
25b	1.27, m	1.26, m	1.26, d (7.4)	1.41, q (13.6)
26a	2.41, m	2.40, m	2.39, m	2.60, tq (13.3, 8.3, 6.6)
26b	3.31, m	3.30, m	3.31, m	3.32, m
26-NH	7.72, t (5.9)	7.72, t (6.0)	7.80, t (5.5)	7.98, t (5.5)
27a	1.45, m	3.71, m	3.32, m	3.32, m
27b	1.45, m	–	–	–
28	0.98, t (7.3)	1.22, d (6.2)	1.21, d (6.1)	1.20, d (6.1)
29	0.86, d (7.1)	1.01, d (7.2)	0.94, d (7.1)	0.94, d (7.1)
30	–	–	3.21, s	3.20, s

molecular formula of $C_{29}H_{38}N_2O_5$, which was derived from an HRESIMS ion peak of $C_{29}H_{37}N_2O_5$ $[M-H]^-$ (m/z: found 493.2667, calcd 493.3702). Its ^{1}H, ^{13}C, and 2D NMR data matched the previous molecule, epoxyikarugamycin (also named ikarugamycin epoxide or capsimycin B).[10, 12] Its epoxide group was confirmed by the observed chemical shifts of H-7 (δ_H 2.92) and H-8 (δ_H 3.12, **Table 2**) and their respective carbons, C-7 (δ_C 53.2) and C-8 (δ_C 57.0, **Table 3**). C-27 was proven to be unfunctionalized by the observed methylene at this carbon (δ_H 1.45) and the triplet methyl group at C-28 (δ_H 13.5). The absolute configurations of C-7 and C-8 were determined to be 7*S*,8*R* based on the observed NOE between H-7 (δ_H 2.92)/H-5 (δ_H 1.50) and H-8 (δ_H 3.12)/H-10 (δ_H 1.67).

Table 3. ^{13}C NMR data for **10**–**13** in DMSO-d_6.

	epoxyikarugamycin (10)	capsimycin G (11)	capsimycin (12)	capsimycin H (13)
Position	**δ_C (type)**	**δ_C (type)**	**δ_C (type)**	**δ_C (type)**
1	165.9 (C)	165.3 (C)	165.5 (C)	165.9 (C)
2	125.6 (CH)	125.1 (CH)	125.2 (CH)	124.8 (CH)
3	138.0 (CH)	137.4 (CH)	137.4 (CH)	138.0 (CH)
4a	25.6 (CH_2)	25.2 (CH_2)	25.1 (CH_2)	24.9 (CH_2)
4b	25.6 (CH_2)	25.2 (CH_2)	25.1 (CH_2)	24.9 (CH_2)
5	45.7 (CH)	45.6 (CH)	45.6 (CH)	45.6 (CH)
6	40.6 (CH)	40.6 (CH)	40.5 (CH)	40.5 (CH)
7	53.2 (CH)	53.1 (CH)	53.1 (CH)	53.1 (CH)
8	57.0 (CH)	57.4 (CH)	57.3 (CH)	57.3 (CH)
9	50.1 (CH)	46.8 (CH)	46.9 (CH)	46.9 (CH)
10	46.2 (CH)	51.4 (CH)	49.4 (CH)	49.5 (CH)
11	33.1 (CH)	33.2 (CH)	33.3 (CH)	33.3 (CH)
12a	38.7 (CH_2)	38.8 (CH_2)	38.9 (CH_2)	38.9 (CH_2)
12b	38.7 (CH_2)	38.8 (CH_2)	38.9 (CH_2)	38.9 (CH_2)
13	47.6 (CH)	47.2 (CH)	47.0 (CH)	46.9 (CH)
14	40.7 (CH)	39.8 (CH)	39.6 (CH)	39.4 (CH)
15a	37.3 (CH_2)	37.1 (CH_2)	37.1 (CH_2)	36.8 (CH_2)
15b	37.3 (CH_2)	37.1 (CH_2)	37.1 (CH_2)	36.8 (CH_2)
16	47.3 (CH)	46.7 (CH)	46.8 (CH)	47.2 (CH)
17	140.3 (CH)	139.6 (CH)	139.8 (CH)	
18	132.7 (CH)	132.3 (CH)	132.2 (CH)	
19	181.6 (C)	181.2 (C)	181.3 (C)	176.6 (C)
20	102.5 (C)	102.0 (C)	102.0 (C)	100.9 (C)
21	177.2 (C)	176.7 (C)	176.8 (C)	177.6 (C)
21-NH				
22	195.9 (C)	195.4 (C)	195.5 (C)	193.6 (C)
23	58.9 (CH)	58.4 (CH)	58.5 (CH)	66.8 (CH)
24a	27.7 (CH_2)	27.2 (CH_2)	27.2 (CH_2)	70.8 (CH_2)
24b	27.7 (CH_2)	27.2 (CH_2)	27.2 (CH_2)	
25a	21.8 (CH_2)	21.2 (CH_2)	21.2 (CH_2)	31.3 (CH_2)
25b	21.8 (CH_2)	21.2 (CH_2)	21.2 (CH_2)	31.3 (CH_2)
26a	38.4 (CH_2)	37.9 (CH_2)	37.9 (CH_2)	36.1 (CH_2)
26b	38.4 (CH_2)	37.9 (CH_2)	37.9 (CH_2)	36.1 (CH_2)
26-NH				
27	22.8 (CH_2)	66.5 (CH)	76.8 (CH)	76.8 (CH)
28	13.5 (CH_3)	23.4 (CH_3)	17.2 (CH_3)	17.2 (CH_3)
29	17.8 (CH_3)	18.1 (CH_3)	17.7 (CH_3)	17.7 (CH_3)
30			54.6 (CH_3)	54.8 (CH_3)

Compound **11** was then isolated as a light-yellow solid with a molecular formula of $C_{29}H_{38}N_2O_6$, which was derived from an HRESIMS ion peak of $C_{29}H_{37}N_2O_6$ $[M-H]^-$ (m/z: found 509.2605, calcd 509.2652). Its ^1H, ^{13}C, and 2D NMR data matched the previously reported molecule, capsimycin G.[12] Its epoxide group was confirmed by the observed chemical shifts of

H-7 (δ_H 2.88) and H-8 (δ_H 3.17, **Table 2**) and their respective carbons, C-7 (δ_C 53.1) and C-8 (δ_C 57.4, **Table 3**). The absolute configurations of C-7 and C-8 were determined to be the same 7*S*,8*R* as those in **9** based on the observed NOE between H-7 (δ_H 2.88)/H-5 (δ_H 1.48) and H-8 (δ_H 3.17)/H-10 (δ_H 1.76). The hydroxy group at C-27 was confirmed by the observed COSY correlation between 27-OH (δ_H 4.34) and H-27 (δ_H 3.71) and the HMBC correlation between 27-OH (δ_H 4.34) and C-10 (δ_C 51.4).

Compound **12** was isolated as a light-yellow solid with a molecular formula of $C_{30}H_{40}N_2O_6$, which was derived from an HRESIMS ion peak of $C_{30}H_{39}N_2O_6$ $[M-H]^-$ (m/z: found 523.2757, calcd 523.2808). Its ^1H, ^{13}C, and 2D NMR data matched the previously reported molecule, capsimycin.[12] Its epoxide group was confirmed by the observed chemical shifts of H-7 (δ_H 2.88) and H-8 (δ_H 3.18, **Table 2**) and their respective carbons, C-7 (δ_C 53.1) and C-8 (δ_C 57.3, **Table 3**). The absolute configurations of C-7 and C-8 were determined to be the same 7*S*,8*R* as those in other capsimycins based on the observed NOE between H-7 (δ_H 2.88)/H-5 (δ_H 1.49) and H-8 (δ_H 3.18)/H-10 (δ_H 1.88, **Figure 74**). The methoxy group at C-27 was confirmed by the observed singlet methyl group at C-30 (δ_H 3.21, δ_C 54.6), and the HMBC correlation between this methoxy to C-27 (δ_C 76.8, **Figure 74**).

Compound **13** was isolated as a light-yellow solid with a molecular formula of $C_{30}H_{40}N_2O_7$, which was derived from an HRESIMS ion peak of $C_{30}H_{39}N_2O_7$ $[M-H]^-$ (m/z: found 539.2773, calcd 539.2757). By comparing its NMR spectrums to those of **12**, we found that they were almost identical, except that the methylene at C-24 (δ_H 1.67, 1.75) in **12** was missing (**Table 2**). Instead, a new proton with δ_H 3.78 was observed, and it's correlating with C-22 (δ_C 193.6), C-25 (δ_C 31.3), and C-26 (δ_C 36.1, **Figure 74**). These observations, combined with its molecular weight and the observed HSQC correlation of this proton to a carbon δ_C 70.8,

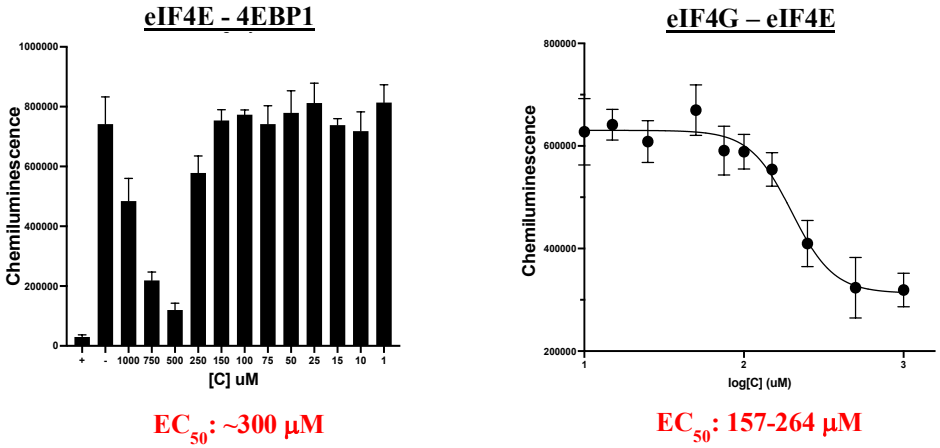

Figure 76. eIF4E–4E-BP1 and eIF4G–eIF4E PPI Cat-ELCCA activities of ikarugamycin (**9**).

suggested that C-24 was hydroxylated. Based on its structural similarity to capsimycin, it was named capsimycin H. This hydroxylation at C-24 has also been found in other PTMs, including HSAF, frontalamide A, alteramide A, cylindramide, etc, and most importantly, this hydroxy group was shown to bear a conserved *S* configuration.[20] By comparing the dihedral angle of H-24–C-24–H-25a-C-25 in 24*S*-**13** (135.2°) and 24*R*-**13** (110.3°), we found that the coupling constant of 6.7 Hz between H-24 (δ_H 3.78) and H-25a (δ_H 1.14) matched better with 24*S*-**13**. In the future, the configuration of this secondary alcohol could be further validated using DFT calculations or Mosher's analysis.

4.1.3 Bioactivity of ikarugamycin analogs 9–19

Out of these ikarugamycin analogs, ikarugamycin was the only active molecule in eIF4E PPI cat-ELCCA. It showed an EC_{50} of ~300 µM against eIF4E–4E-BP1 PPI and ~200 µM in eIF4G–eIF4E PPI (**Figure 76**). We noticed that it suffered from poor solubility in the assay buffer at >500 µM, which significantly lowered its potency at high concentrations. To further characterize its cellular activity, we tested this molecule in a series of cell-based assays. First, it showed an LD_{50} ~1 µM against Mia Paca-2 cells in the Cell Titer-Glo assay (**Figure 77A**).

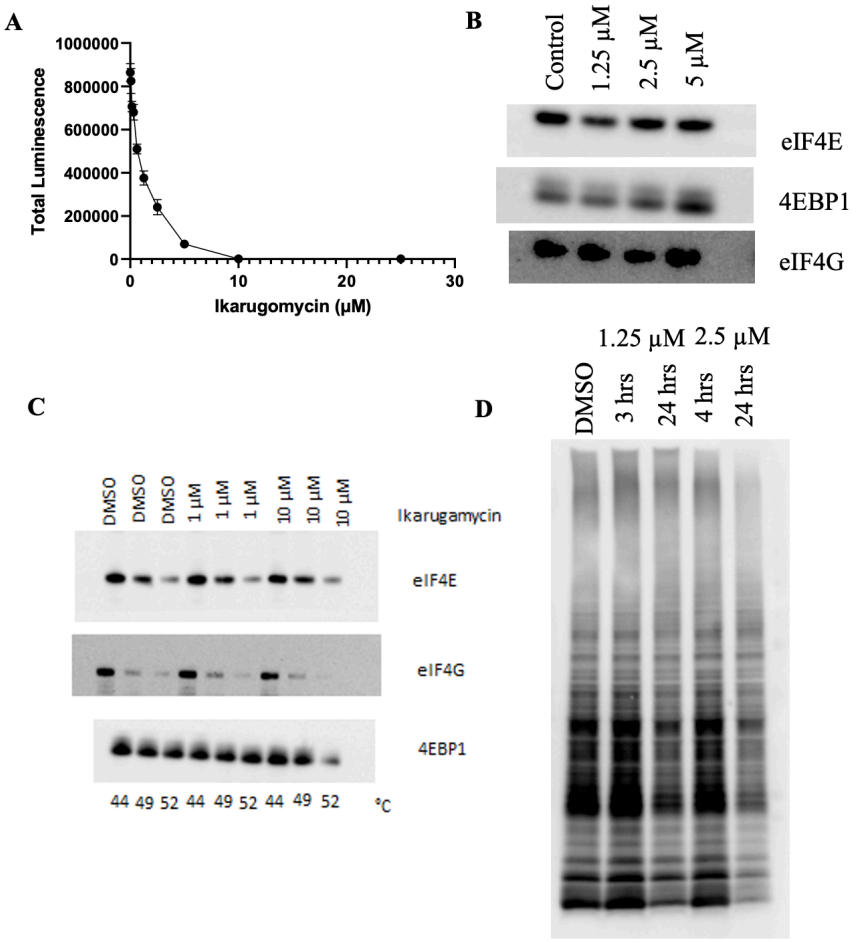

Figure 77. Cellular activities of ikarugamycin (**9**). (A) Cell Titor-Glo assay in Mia Paca-2 cells; (B) m^7GDP cap pull-down assay in Mia Paca-2 cells at 1.25, 2.5, and 5 μM of **9**; (C) CETSA assay in HEK293 cells at 1 and 10 μM of **9**; (D) SunSET assay in Mia Paca-2 cells at 1.25 and 2.5 μM of **9**.

However, this compound exhibited no noticeable inhibition against eIF4E PPIs in the m^7GDP cap pull-down assay at 5 μM or any significant binding to eIF4E in the CETSA assay at 10 μM (**Figures 77B** and 77**C**). The large discrepancy between its cytotoxicity and its inhibitory activity against eIF4E PPIs suggested that it has significant off-target effects. Interestingly, we found that it readily downregulated the overall protein translation in the SunSET assay (**Figure 77D**), which might correlate with its reported apoptotic activity.[13] Based on these results, we decided to not further develop this scaffold into an eIF4E PPI inhibitor.

4.1.4 Biosynthesis of capsimycin H

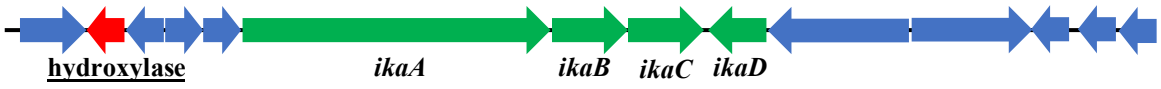

Figure 78. Annotated ikarugamycin BGC in Contig 18 of the genome of 87797-1N.

With the isolation of a new PTM, capsimycin H, we became curious about its biosynthesis, especially the mechanism of the hydroxylation at C-24. As discussed in Chapter 4.1.1, its precursor, capsimycin, was generated through a two-step mechanism that involves an epoxidation, and then hydroxylation of ikarugamycin catalyzed by the P450 enzyme, *ikaD*.[12] We found that for other PTMs bearing a hydroxy at C-24, this hydroxylation is often catalyzed by a hydroxylase upstream of core ikarugamycin BGC, such as the sterol desaturase (*SD*) gene for HSAF, *ftdA* gene for frontalamides, and *cftE* gene for clifednamides.[20] antiSMASH analysis of the genome of 87797-1N successfully identified the BGC of ikarugamycin in contig 18. Annotation of genes in Contig 18 revealed the presence of ikarugamycin core genes *ikaA–ikaD* that are responsible for the biosynthesis of capsimycin G (**Figure 78**). However, no gene that shares any sequence similarity with the previously reported *SD*, *ftdA*, or *cftE* genes was identified in Contig 17–19. Annotation of the upstream of the ikarugamycin BGC revealed a hydroxylase gene that could potentially catalyze the observed hydroxylation at C-24 (**Figure 78**).

We then cloned and expressed this hydroxylase as well as *ikaD*, the P450 enzyme that might be able to further hydroxylate capsimycin into capsimycin H. We observed the complete conversion of ikarugamycin (**9**) to capsimycin G (**11**) in 10 minutes using 2 μM *ikaD*, and we were able to trap the intermediate, epoxyikarugamycin (**10**), using 0.5 μM *ikaD* with the same reaction duration (**Figure 79**), confirming the two-step mechanism of the biosynthesis of **11**. However, we did not observe the further conversion of **11** to capsimycin (**12**) or capsimycin H (**13**) even when we extended the reaction time to 2 hours (data not shown). Neither did we

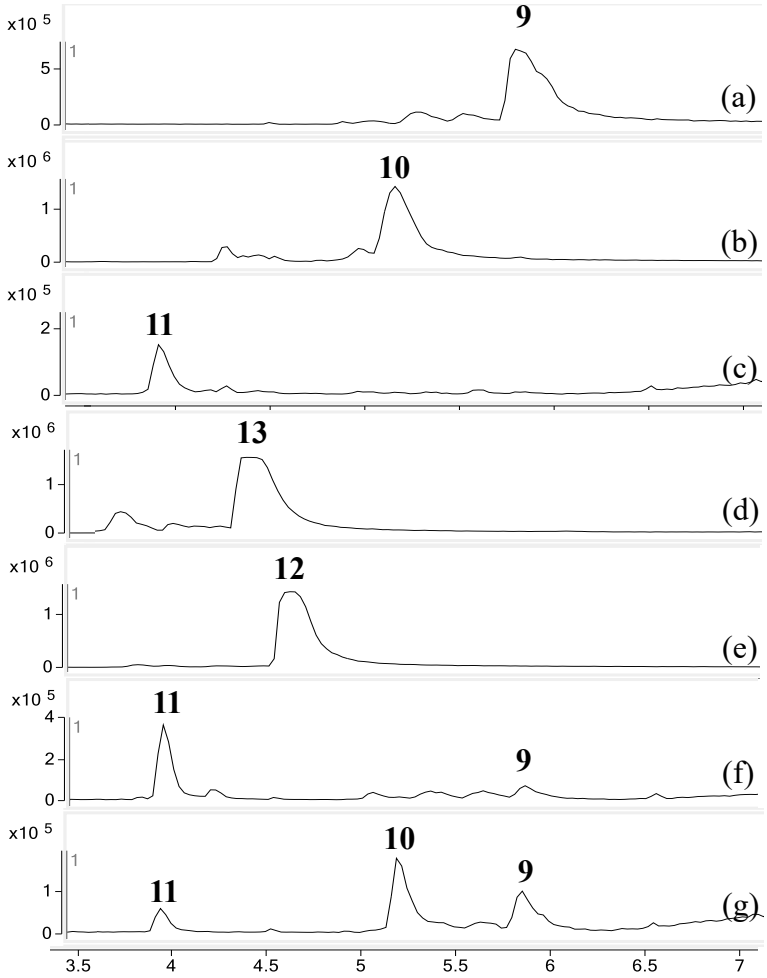

Figure 79. LC-MS analyses of the conversion of ikarugamycin (**9**) to capsimycin G (**11**) catalyzed by *ikaD*. X axis: acquisition time; Y axis: ion counts; (a) standard curve of ikarugamycin (**9**); (b) standard curve of epoxyikarugamycin (**10**); (c) standard curve of capsimycin G (**11**); (d) standard curve of capsimycin H (**13**); (e) standard curve of capsimycin (**12**); (f) conversion of ikarugamycin (**9**) to capsimycin G (**11**) using 2 μM *ikaD* for 10 minutes at room temperature; (g) trapping of the intermediate, epoxyikarugamycin (**10**), using 0.5 μM *ikaD* for 10 minutes at room temperature.

observe the conversion from capsimycin (**12**) to capsimycin H (**13**) using the hydroxylase upstream of the ikarugamycin BGC under similar reaction conditions. Further gene knockout studies are necessary to fully elucidate the mechanism of C-24 hydroxylation in capsimycin H (**13**).

4.2 Actiphenols and cycloheximides isolated from 44321-A2I

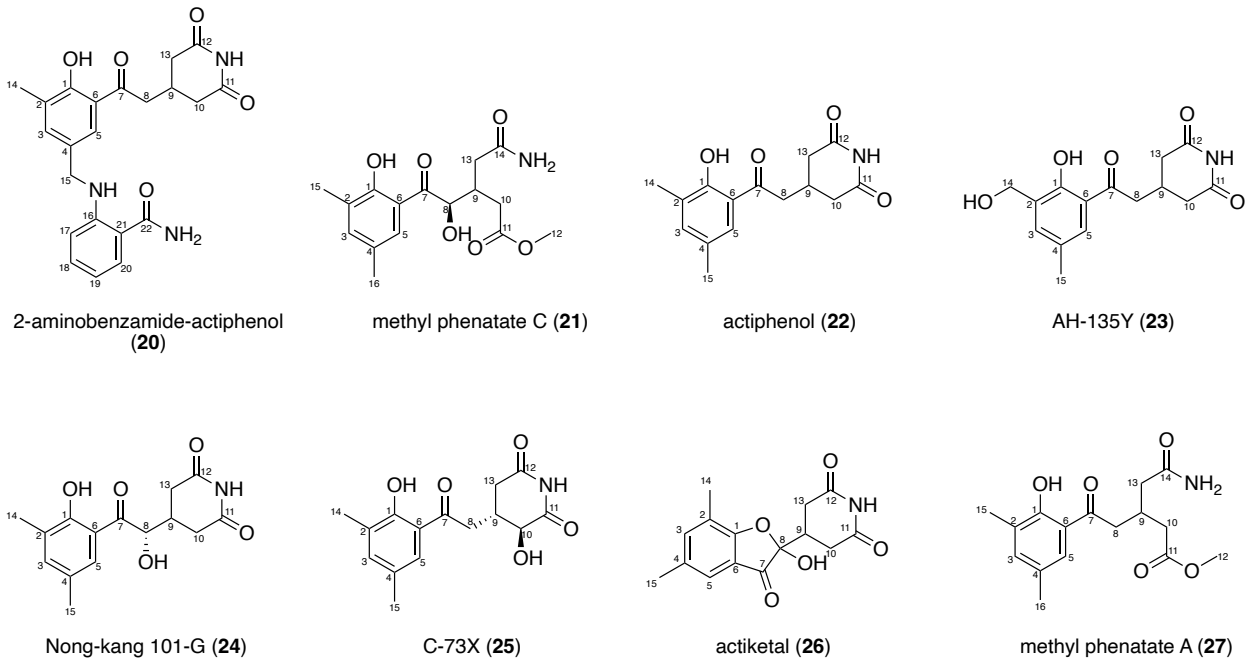

Figure 80. Structures of actiphenol analogs **20**–**27** isolated from strain 44321-A2I.

Through our collaboration with Sun Pharma Advanced Research Company (SPARC), we conducted an HTS campaign using the marine natural product extract library to identify natural products that exhibit selective antiproliferative activity against HCT15 cells, a $KRAS^{G13D}$ mutant colon cancer cell line. One of the most active strains was 44321-A2I, from which we isolated and characterized a series of actiphenols and cycloheximides. Cycloheximide (**28**) is one of the most well-known members of the glutarimide-containing polyketide family of natural products. It is most well-known for its inhibitory activity of eukaryotic translation by blocking the translocation step in the polypeptide elongation process.[21] Actiphenol (**22**, **Figure 80**) shares the same carbon skeleton as but has a phenol in place of a cyclohexanone moiety.[22] It was shown to exhibit potent antiviral and antifungal activities.[23, 24] In this section, we will elaborate on the structure elucidation of cycloheximides and actiphenols isolated from 44321-A2I.

4.2.1 Structure elucidation of actiphenol analogs 20–27

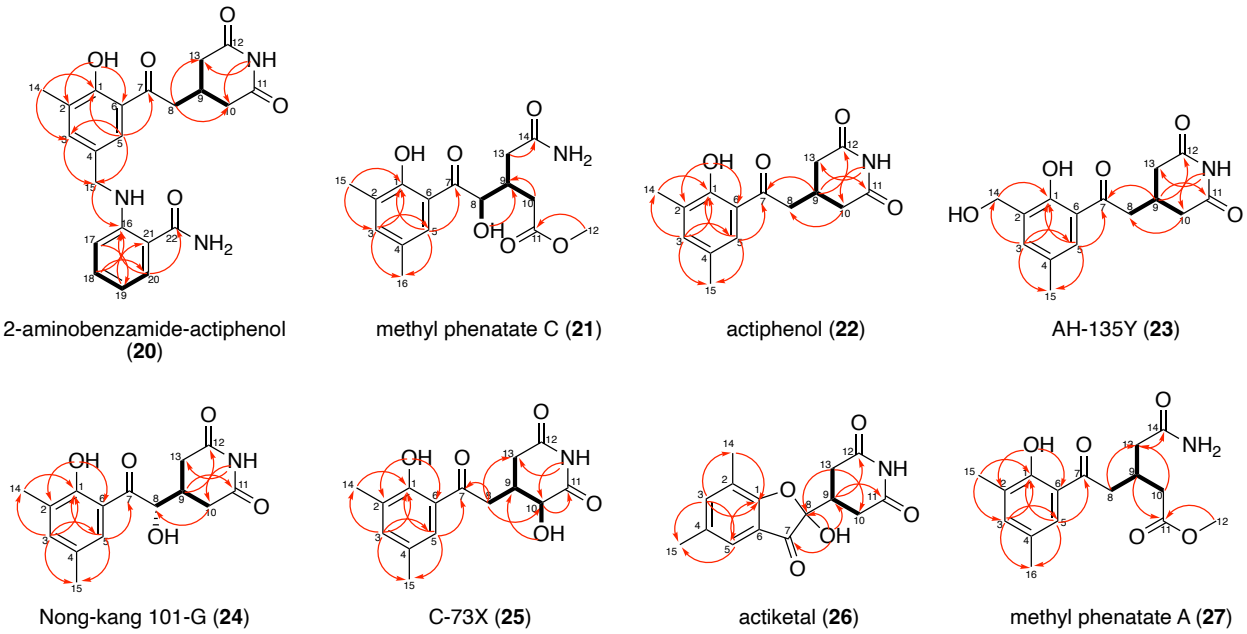

Figure 81. Key COSY and HMBC correlations in **20**–**27**.

The base form actiphenol (**22**) was isolated as a yellow solid with a molecular formula of $C_{15}H_{17}NO_4$, which was derived from an HRESIMS ion peak of $C_{15}H_{16}NO_4$ $[M-H]^-$ (m/z: found 274.1073, calcd 274.1079). The 2,4-dimethyl-phenol structure was confirmed by the observed HMBC correlations of H-3 (δ_H 7.27) to C-1 (δ_C 157.7), C-5 (δ_C 127.9), C-14 (δ_C 15.1), and C-15 (δ_C 20.0, **Figure 81**). The glutarimide moiety was elucidated by the observed amide proton 11-NH (δ_H 10.76, **Table 5**), amide carbons C-11 and C-12 (δ_C 172.9, **Table 4**), and two methylenes at C-10 and C-13. The connection between the glutarimide and the phenol was established by the COSY correlation between H-9 (δ_H 2.64) and methylene H-8 (δ_H 3.17) and the HMBC correlation between H-10a/H-10b (δ_H 3.64, 2.59)/C-8 (δ_C 42.3) and H-9 (δ_H 2.64)/C-7 (δ_C 205.3). The final structure matched with the known molecule, actiphenol.[22]

Compound **23** was isolated as a yellow solid with a molecular formula of $C_{15}H_{17}NO_5$, which was derived from an HRESIMS ion peak of $C_{15}H_{16}NO_5$ $[M-H]^-$ (m/z: found 290.1033, calcd 290.1028). By comparing its NMR spectrums to those of **22**, we found that they were almost identical, except that the methyl at C-2 of the phenol was missing. Instead, a new

Table 4. ^{13}C NMR data of **20** and **22**–**27** in DMSO-d_6.

	20	**22**	**23**	**24**	**25**	**26**
Position	**δ_C (type)**	**δ_C (type)**	**δ_C (type)**	**δ_C (type)**	**δ_C (type)**	**δ_C (type)**
1	159.3 (C)	157.7 (C)	156.8 (C)	158.6 (C)	158.2 (C)	167.7 (C)
2	127.0 (C)	127.2 (C)	156.8 (C)	127.8 (C)	127.6 (C)	123.2 (C)
3	136.9 (CH)	138.4 (CH)	131.2 (CH)	139.1 (CH)	138.7 (CH)	141.2 (CH)
4	130.0 (C)	126.1 (C)	127.8 (C)	126.7 (C)	126.5 (C)	132.2 (C)
5	127.6 (CH)	127.9 (CH)	128.9 (CH)	128.4 (CH)	128.3 (CH)	121.2 (CH)
6	118.7 (C)	118.3 (C)	118.7 (C)	117.4 (C)	118.9 (C)	120.9 (C)
7	205.6 (C)	205.3 (C)	205.9 (C)	206.3 (C)	206.2 (C)	199.4 (C)
8	42.9 (CH_2)	42.3 (CH_2)	42.8 (CH_2)	73.5 (CH)	40.4 (CH_2)	105.2 (C)
9	26.6 (CH)	26.0 (CH)	26.5 (CH)	33.9 (CH)	34.1 (CH)	35.5 (CH)
10	37.5 (CH_2)	37.0 (CH_2)	37.5 (CH_2)	35.0 (CH_2)	70.8 (CH)	31.9 (CH_2)
11	173.4 (C)	172.9 (C)	173.4 (C)	173.4 (C)	175.2 (C)	172.6 (C)
12	173.4 (C)	172.9 (C)	173.4 (C)	173.4 (C)	172.3 (C)	172.9 (C)
13	37.5 (CH_2)	37.0 (CH_2)	37.5 (CH_2)	32.4 (CH_2)	36.6 (CH_2)	31.0 (CH_2)
14	15.8 (CH_3)	15.1 (CH_3)	57.7 (CH_2)	15.7 (CH_3)	15.6 (CH_3)	14.2 (CH_3)
15	45.9 (CH_2)	20.0 (CH_3)	20.7 (CH_3)	20.6 (CH_3)	20.5 (CH_3)	20.5 (CH_3)
16	149.9 (C)					
17	112.1 (CH)					
18	132.8 (CH)					
19	114.9 (CH)					
20	129.5 (CH)					
21	114.9 (C)					
22	171.9 (C)					

methylene H-14 (δ_H 4.51, **Table 5**) at C-2 was observed and it showed HMBC correlation to C-1 (δ_C 156.8) and C-3 (δ_C 127.9, **Figure 81**), suggesting the hydroxylation at C-14. These NMR data matched with the known compound, AH-135Y.[25]

Compound **24** was isolated as a yellow solid with a molecular formula of $C_{15}H_{17}NO_5$, which was derived from an HRESIMS ion peak of $C_{15}H_{16}NO_5$ $[M-H]^-$ (m/z: found 290.1033, calcd 290.1028). By comparing its NMR spectrums to those of **22**, we found that the methylene at C-8 was missing. Instead, a new proton H-8 (δ_H 5.03, **Table 5**) at C-8 and a new broad peak of δ_H 5.78 were observed, suggesting the hydroxylation at C-8. These data matched the known

Table 5.[1]H NMD data of **20** and **22**–**26** in DMSO-d_6.

	δ_H, multiplets (*J* in Hz)					
Position	**20**	**22**	**23**	**24**	**25**	**26**
1-OH	12.33, s	12.23, s	12.19, s	12.03, s	12.27, s	
3	7.45, s	7.27, s	7.48, s	7.31, s	7.29, s	7.43, s
5	7.82, s	7.59, s	7.64, s	7.69, s	7.59, s	7.25, s
8a	3.18, d (6.4)	3.17, d (6.4)	3.19, d (6.4)	5.03, d (4.4)	3.04, dd (17.1, 8.0)	
8b	3.18, d (6.4)	3.17, d (6.4)	3.19, d (6.4)		3.48, dd (17.1, 3.6)	8.04, s
8-OH				5.78, br s		8.04, s
9	2.62, m	2.64, dt (10.7, 5.3)	2.64, dt (10.7, 5.3)	2.58, m	2.57, m	2.59, m
10a	2.39, dd (16.5, 10.7)	2.38, dd (16.5, 10.7)	2.38, dd (16.5, 10.7)	2.55, m	4.06, dd (10.5, 4.2)	2.29, m
10b	2.58, dd (16.5, 10.7)	2.59, dd (16.2, 4.0)	2.59, dd (16.2, 4.0)	2.58, m		2.45, dd (17.0, 5.1)
10-OH					5.80, d (5.5)	
11-NH	10.76, s	10.76, s	10.76, s	10.69, s	10.84, s	10.73, s
12						
13a	2.39, d (16.5, 10.7)	2.38, dd (16.5, 10.7)	2.38, dd (16.5, 10.7)	2.28, dd (17.0, 10.3)	2.54, m	2.67, m
13b	2.58, d (16.5, 10.7)	2.59, dd (16.2, 4.0)	2.59, dd (16.2, 4.0)	2.44, dd (17.0, 10.3)	2.62, dd (15.6, 3.6)	2.67, m
14	2.17, s	2.14, s	4.51, s	2.16, s	2.16, s	2.20, s
15a	4.30, s	2.24, s	2.29, s	2.25, s	2.26, s	2.29, s
15b	4.30, s					
15-NH	8.47, br s					
16						
17	6.69, d (8.4)					
18	7.23, t (7.9)					
19	6.54, t (7.5)					
20	7.61, d (7.8)					
21						
22						
22-NHa	7.17, br s					
22-NHb	7.86, br s					

compound, Nong-kang 101-G.[26] To determine the absolute stereochemistry of H-8, we performed ECD calculations of 8*S*-**24** and 8*R*-**24** (**Figure 82**). We found that the ECD curve of 8*S*-**24** fit the experimental ECD curve better, suggesting an *S* configuration at C-8.

Compound **25** was isolated as a yellow solid with a molecular formula of $C_{15}H_{17}NO_5$, which was derived from an HRESIMS ion peak of $C_{15}H_{16}NO_5$ $[M-H]^-$ (m/z: found 290.1040, calcd 290.1028). Since it has the same molecular weight as **23** and **24**, we suspected that it was another hydroxylated actiphenol analog. The hydroxylation was confirmed at C-10 based on the observed HMBC correlations between 11-NH (δ_H 10.84)/C-10 (δ_C 70.8) and H-10 (δ_H 4.06)/C-11 (δ_C 175.2, **Figure 81**). These data matched with the known molecule, C-73X.[27] Next, we attempted to determine the configuration of C-9 and C-10 based on ROESY analyses. As we observed a weak ROESY correlation between H-5 (δ_H 7.59) and H-9 (δ_H 2.57), we examined the atomic distance between H-5 and H-9 in all four possible stereoisomers, 9*S*,10*S*-**25**, 9*S*,10*R*-**25**,

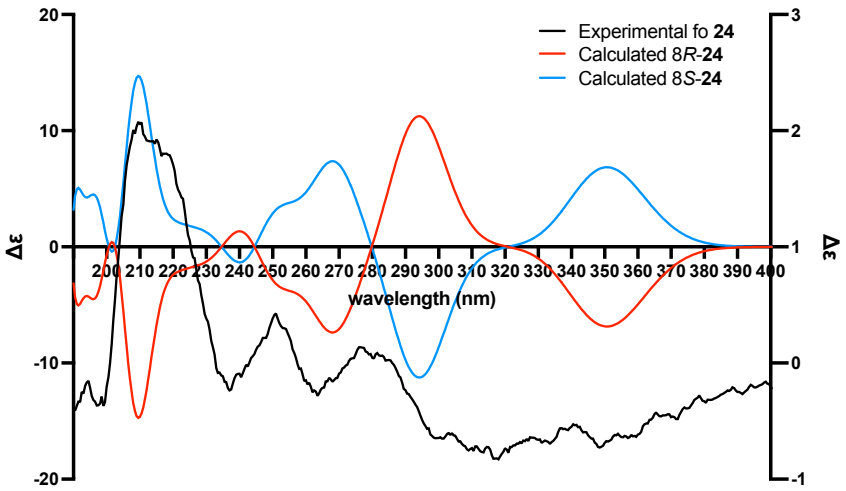

Figure 82. Calculated ECD curves of 8*R*-**24** and 8*S*-**24** at apfd/6-311+G(2d,p) level with solvent effects PCM=methanol for a total of 30 excited states; calculated ECD curves were scaled using the left Y-axis; experimental ECD curves were scaled using the right Y-axis; σ=0.16eV.

9*R*,10*S*-**25**, and 9*R*,10*R*-**25**. We found that this ROESY matched better with the atomic distances in 9*R*,10*S*-**25** and 9*R*,10*R*-**25** (~5.0 Å) than those observed in 9*S*,10*S*-**25** and 9*S*,10*R*-**25** (>6.0 Å), suggesting a *R* configuration at C-9. For the configuration of C-10, we compared the atomic distances between H-9 and H-13a/13b (δ_H 2.54, 2.62) in 9*S*,10*S*-**25** and 9*S*,10*R*-**25**. We found that the atomic distances in 9*S*,10*S*-**25** (2.6 Å and 3.8 Å) matched better with the strong ROESY between H-9 and H-13a/13b than those in 9*S*,10*R*-**25** (3.8 Å and 4.3 Å), suggesting a *S* configuration at C-10. Together, the final configuration of 9*S*,10*S* was elucidated for C-73X (**25**) and in the future, this configuration needs further validation using the established ECD/NMR/DP4+ computational pipeline or Mosher's analysis.

Compound **26** was isolated as a yellow solid with a molecular formula of $C_{15}H_{15}NO_5$, which was derived from an HRESIMS ion peak of $C_{15}H_{14}NO_5$ $[M-H]^-$ (m/z: found 288.0847, calcd 288.0872). After comparing its NMR data with Nong-kang 101-G (**24**), we found that it possessed an unusual carbon with a chemical shift of 105.2 ppm (**Table 4**), suggestive of the presence of a hemiketal. We also observed that a hydroxy with a chemical shift of 8.04 ppm was

Table 6. ^{1}H and ^{13}C NMR data of **21** and **27** in DMSO-d_6.

	methyl phenatate C (**21**)		methyl phenatate A (**27**)	
Position	**δ_C (type)**	**δ_H, multiplets (*J* in Hz)**	**δ_C (type)**	**δ_H, multiplets (*J* in Hz)**
1	158.1 (C)		158.2 (C)	
1-OH		12.21, s		12.35, s
2	126.5 (C)		126.4 (C)	
3	138.9 (CH)	7.31, s	138.7 (CH)	7.29, s
4	127.4 (C)		126.7 (C)	
5	128.2 (CH)	7.99, s	128.4 (CH)	7.65, s
6	118.9 (C)		118.8 (C)	
7	207.7 (C)		206.9 (C)	
8a	72.7 (CH)	5.14, dd (6.0, 2.7)	42.3 (CH_2)	3.07, dd (16.5, 7.1)
8b			42.3 (CH_2)	3.16, dd (16.5, 6.1)
8-OH		5.38, d (5.9)		
9	36.1 (CH)	2.80, m	28.9 (CH)	2.77, h (2.77)
10a	32.4 (CH_2)	2.20, m	32.4 (CH_2)	2.36, dd (16.8, 6.5)
10b	32.4 (CH_2)	2.31, dd (16.4, 6.0)	32.4 (CH_2)	2.46, dd (16.8, 6.5)
11	172.8 (C)		172.8 (C)	
12	51.7 (CH_3)	3.46, s	51.7 (CH_3)	3.57, s
13a	37.0 (CH_2)	2.19, m	39.1 (CH_2)	2.19, d (7.0)
13b	37.0 (CH_2)	2.45, dd (15.7, 9.7)	39.1 (CH_2)	2.19, d (7.0)
14	173.6 (C)		173.2 (C)	
14-NHa		6.99, s		6.84, s
14-NHb		7.47, s		7.34, s
15	15.6 (CH_3)	2.17, s	15.6 (CH_3)	2.15, s
16	20.5 (CH_3)	2.26, s	20.5 (CH_3)	2.26, s

correlating with the ketone at C-7 (δ_C 199.4), this hemiketal carbon, and C-9 (δ_C 35.5) in the glutarimide, confirming the hemiketal at C-8. These data matched the known compound, actiketal.[28] In the future, the configuration at C-7 can be determined using ECD calculations.

Compound **20** was isolated as a yellow solid with a molecular formula of $C_{22}H_{23}N_3O_5$, which was derived from an HRESIMS ion peak of $C_{22}H_{22}N_3O_5$ $[M-H]^-$ (m/z: found 408.1455, calcd 408.1559). After comparing its NMR data with actiphenol (**20**), we found that it possesses all the structural features of actiphenol except that the methyl group on C-4 is missing. Instead, we observed a new methylene (δ_H 4.30) at C-15 (δ_C 45.9) that is correlating with C-3 (δ_C 136.9), C-5 (δ_C 127.6), and an aromatic carbon C-16 with a chemical shift of (δ_C 149.9) that is not in the actiphenol spin systems (**Figure 81**, **Tables 4** and **5**). Further examination of its NMR data

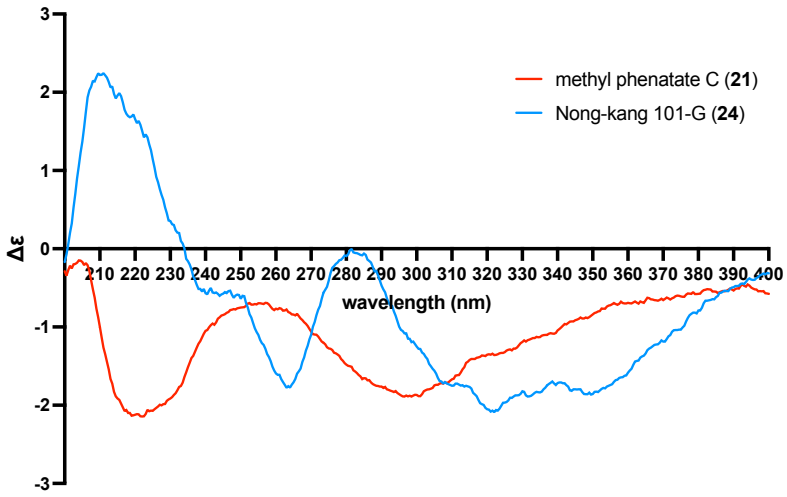

Figure 83. Experimental ECD curves of **21** and **24**.

revealed the presence an additional aminobenzamide moiety attached to the actiphenol through an N-C bond. The HMBC correlations between the triplet H-18 (δ_H 7.23)/C-16 (δ_C 149.9) and the doublet H-20 (δ_H 7.61)/C-16 (δ_C 149.9) and C-22 (δ_C 171.9) confirmed the relative position of the secondary amine (δ_H 7.23) and the primary amide on this aromatic ring. Based on its structure, we named this molecule 2-aminobenzamide-actiphenol (**20**).

Compound **27** was isolated as a yellow solid with a molecular formula of $C_{16}H_{21}NO_5$, which was derived from an HRESIMS ion peak of $C_{16}H_{20}NO_5$ $[M-H]^-$ (m/z: found 306.1344, calcd 306.1341). Examination of its NMR data revealed the presence of the same phenol and glutarimide methylenes as in actiphenol. However, we observed a new methoxy (δ_H 3.57) as well as two new amide protons (δ_H 6.84, 7.34), suggestive of an opening of the glutarimide ring (**Table 6**). This was likely a non-enzymatic conversion of actiphenol (**22**) by methanol and acid. These data matched the known compound, methyl phenatic acid A.[24]

Compound **21** was isolated as a yellow solid with a molecular formula of $C_{16}H_{21}NO_6$, which was derived from an HRESIMS ion peak of $C_{16}H_{20}NO_6$ $[M-H]^-$ (m/z: found 323.1291, calcd 323.1292). Similar to compound **27**, we observed an opening of the glutarimide ring of

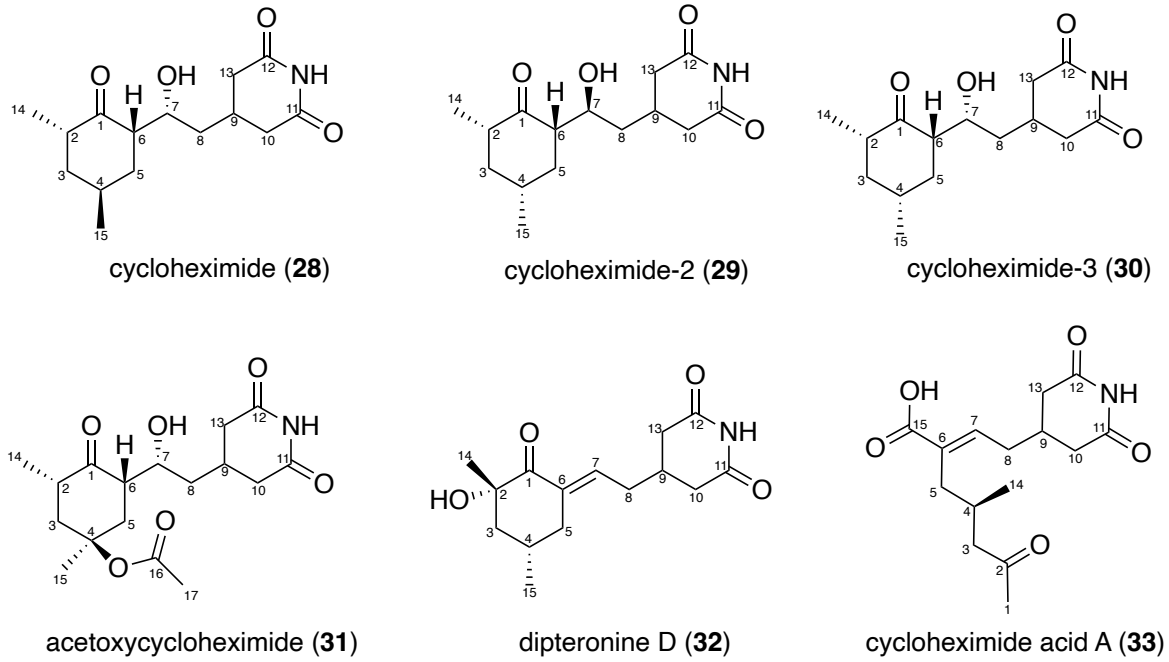

Figure 84. Structures of cycloheximide analogs **28**–**33** isolated from 44321-A2I.

Nong-kang 101-G (**24**), which yielded a new methoxy (δ_H 3.46) as well as two new amide protons (δ_H 6.99, 7.47, **Table 6**). Because of its structural similarity to **27**, we named this molecule methyl phenatate C. To determine the absolute configuration of C-8, we compared the experimental ECD curves of **24** and **21** and we observed that they were completed the opposite of each other, suggesting an 8*R* configuration (**Figure 83**). This needs further confirmation through ECD calculations.

4.2.2 Structure elucidation of cycloheximide analogs 28–33

Compound **28** (**Figure 84**) was isolated as a yellow solid with a molecular formula of $C_{15}H_{23}NO_4$, which was derived from an HRESIMS ion peak of $C_{15}H_{22}NO_4$ $[M-H]^-$ (m/z: found 280.1509, calcd 280.1549). The glutarimide moiety was confirmed by the observed amide proton 11-NH (δ_H 10.58, **Table 8**) amide carbons C-11 and C-12 (δ_C 173.8 and 173.9, **Table 7**), and two methylenes at C-10 and C-13. The 2,4-dimethyl-cyclohexanone structure was confirmed by

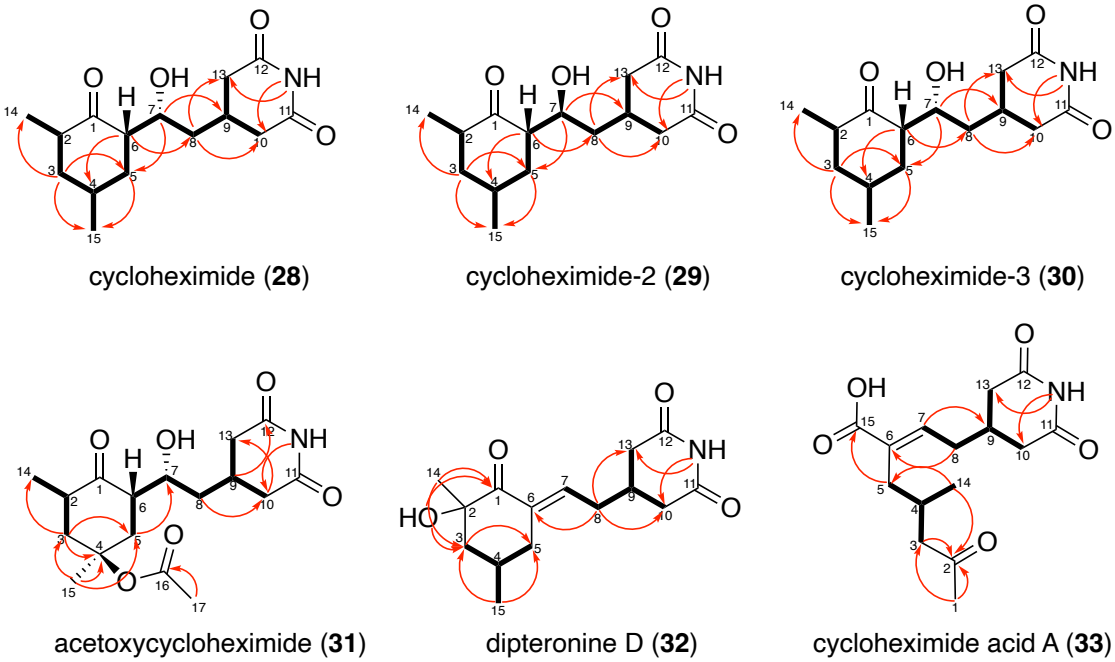

Figure 85. Key COSY and HMBC correlations in **28**–**33**.

the observed HMBC correlations of H-3a/H-3b (δ_H 1.42, 1.73) to C-5 (δ_C 35.5), C-14 (δ_C 15.0), and C-15 (δ_C 18.7, **Figure 85**). The connection between the glutarimide and the cyclohexane was established by the COSY correlation between H-6 (δ_H 2.39) and methylene H-7 (δ_H 3.76) and the HMBC correlation between H-6 (δ_H 2.39) and both C-4 (δ_C 26.6) and C-8 (δ_C 40.5). The position of the hydroxy was elucidated at C-7 based on the observed HMBC correlation between H-7 (δ_H 3.76) and C-5 (δ_C 35.5). Using the method developed by Breit and Schmidt,[29] the relative stereochemistry of the two methyl groups on the cyclohexanone was determined to be *anti* based on the small chemical shift difference between H-3a/H-3b (~0.31 ppm). This was also supported by the observed ROESY between H-2 (δ_H 2.55) and H-15 (δ_H 1.12, **Figure 86**). The relative stereochemistry of H-6 and H-7 was determined to be *syn* to H-15 based on the observed strong ROESY between H-6/H-15 and H-6/H-7 (**Figure 86**). These data matched the known molecule, cycloheximide.[30] While we believe its absolute configurations are the same as cycloheximide, this needs further validation, potentially by ECD calculations.

Table 7. ^{13}C NMR data of **28**–**33** in DMSO-d6.

	δ_C (type)					
Position	**28**	**29**	**30**	**31**	**32**	**33**
1	213.4 (C)	214.7 (C)	213.9 (C)	212.2 (C)	200.6 (C)	30.6 (CH_3)
2	44.1 (CH)	42.3 (CH)	40.3 (CH)	39.8 (CH)	72.4 (C)	208.7 (C)
3	45.0 (CH_2)	44.8 (CH_2)	42.8 (CH_2)	45.0 (CH_2)	46.7 (CH_2)	50.3 (CH_2)
4	31.4 (CH)	26.6 (CH)	26.9 (CH)	80.2 (C)	25.1 (CH)	29.3 (CH)
5	36.7 (CH_2)	36.7 (CH_2)	35.5 (CH_2)	37.7 (CH_2)	35.6 (CH_2)	33.4 (CH_2)
6	55.4 (CH)	58.5 (CH)	51.0 (CH)	50.8 (CH)	138.0 (C)	133.3 (C)
7	65.9 (CH)	66.0 (CH)	65.4 (CH)	65.6 (CH)	134.7 (CH)	139.9 (CH)
8	38.0 (CH_2)	40.5 (CH_2)	40.6 (CH_2)	37.8 (CH_2)	32.5 (CH_2)	33.4 (CH_2)
9	27.5 (CH)	27.0 (CH)	27.4 (CH)	27.5 (CH)	30.0 (CH)	30.1 (CH)
10	38.9 (CH_2)	38.7 (CH_2)	38.4 (CH_2)	38.8 (CH_2)	37.6 (CH_2)	37.6 (CH_2)
11	173.8 (C)	173.8 (C)	173.8 (C)	173.8 (C)	173.5 (C)	173.5 (C)
12	174.0 (C)	173.9 (C)	173.9 (C)	173.9 (C)	173.5 (C)	173.5 (C)
13	37.2 (CH_2)	37.0 (CH_2)	37.2 (CH_2)	37.2 (CH_2)	37.4 (CH_2)	37.6 (CH_2)
14	14.8 (CH_3)	15.2 (CH_3)	15.0 (CH_3)	14.3 (CH_3)	25.4 (CH_3)	19.9 (CH_3)
15	21.7 (CH_3)	21.0 (CH_3)	18.7 (CH_3)	25.1 (CH_3)	22.2 (CH_3)	169.0 (C)
16				170.4 (C)		
17				22.5 (CH_3)		

Compound (**29**, **Figure 84**) was isolated as a yellow solid with a molecular formula of $C_{15}H_{23}NO_4$, which was derived from an HRESIMS ion peak of $C_{15}H_{22}NO_4$ $[M-H]^-$ (m/z: found 280.1592, calcd 280.1549). While its planar structure was determined to be identical to **27** based on the similarities between their NMR data, some chemical shifts in the cyclohexanone moiety significantly differed (**Tables 7** and **8**), suggesting some changes in the stereochemistry. We found that the chemical shift difference between H-3a/H-3b was ~0.96 ppm, suggesting a *syn* configuration between the methyl groups. Similarly, the relative configuration between H-6/H-15 was determined to be *anti* based on the large chemical shift difference of ~1.02 ppm between H-5a/H-5b, in stark contrast to ~0.33 ppm observed in cycloheximide (**27**). The relative stereochemistry of H-6 and H-7 was determined to be *anti* based on the observed weak ROESY between H-6/H-7 (**Figure 86**). This was further confirmed by the observed coupling constant of

Table 8. ^{1}H NMR data of **28**–**33** in DMSO-d_6.

	δ_H, multiplets (*J* in Hz)					
Position	**28**	**29**	**30**	**31**	**32**	**33**
1						2.06, s
2	2.51, m	2.46, m	2.55, m	2.63, tq (12.9, 6.5)		
2-OH					5.24, br s	
3a	1.01, m	1.00, m	1.42, td (12.9, 4.7)	1.52, m	1.45, t (13.0)	2.26, m
3b	1.96, m	1.96, ddt (12.7, 6.0, 3.5)	1.73, ddt (13.0, 5.7, 2.8)	2.52, m	1.85, t (13.0)	2.33, m
4	2.00, m	2.21, m	2.01, m		2.11, m	2.07, m
5a	1.07, q (14.1)	1.22, m	1.56, td (13.1, 4.1)	1.59, m	1.81, dt (15.5, 3.6)	2.13, m
5b	2.02, m	2.24, m	1.89, ddt (13.2, 5.7, 2.9)	2.54, m	2.71, dt (15.5, 3.6)	2.16, m
6	2.57, m	2.09, ddd (9.3, 5.3, 1.9)	2.39, dd (12.1, 5.7)	2.72, dt (14.0, 4.9)		
7	3.87, dt (8.7, 4.0)	3.90, d (9.9)	3.76, dd (6.3, 5.9)	3.92, dt (9.8, 3.4)	6.25, dt (7.7, 2.6)	6.68, t (7.0)
7-OH	4.45, br s	5.00, br s	4.33, br s	4.51, br s		
8a	1.29, m	0.95, m	1.24, m	1.28, m	2.14, m	2.24, m
8b	1.29, m	1.26, ddd (13.1, 10.1, 2.8)	1.24, m	1.28, m	2.18, m	2.24, m
9	2.25, m	2.25, m	2.18, m	2.23, m	2.24, m	2.24, m
10a	2.28, m	2.27, m	2.21, m	2.29, m	2.28, m	2.31, m
10b	2.52, m	2.47, m	2.42, m	2.52, m	2.50, m	2.49, m
11						
11-NH	10.65, br s	10.65, br s	10.58, br s	10.65, br s	10.72, br s	10.72, br s
12						
13a	2.26, m	2.20, m	2.19, m	2.26, m	2.30, m	2.31, m
13b	2.58, m	2.60, m	2.51, m	2.58, m	2.30, m	2.49, m
14	0.86, d (6.5)	0.85, d (6.4)	0.79, d (6.4)	0.86, d (6.6)	1.17, s	0.78, d (6.4)
15	0.94, d (6.2)	0.90, d (6.3)	1.12, d (7.2)	1.50, s	0.94, d (6.6)	
15-COOH						12.28, br s
16						
17				2.05, s		

9.9 Hz between H-6/H-7 (**Table 8**), which matched better with the dihedral angle H-6–C-6–C-7–H-6 in 7*S*-**29** (168.6°) than that in 7*R*-**29** (65.2°). The absolute configurations need further confirmation by ECD calculations.

Compound **30** was isolated as a yellow solid with a molecular formula of $C_{15}H_{23}NO_4$, which was derived from an HRESIMS ion peak of $C_{15}H_{22}NO_4$ $[M-H]^-$ (m/z: found 280.1509, calcd 280.1549). Similar to the previous analyses, the relative configurations between H-14 (δ_H 0.86), H-15 (δ_H 0.94), and H-6 (δ_H 2.57) were found to be *syn*,*anti* based on the large chemical shift differences between H-3a/H-3b (~0.95 ppm) and H-5a/H-5b (~0.95 ppm). The relative stereochemistry of H-6 and H-7 (δ_H 3.87) was determined to be *syn* based on the observed strong ROESY between H-6 and H-7 (**Figure 86**). The absolute configurations need further confirmation by ECD calculations.

Compound **31** was isolated as a yellow solid with a molecular formula of $C_{17}H_{25}NO_6$, which was derived from an HRESIMS ion peak of $C_{17}H_{24}NO_6$ $[M-H]^-$ (m/z: found 338.1629, calcd 338.1604). Examination of its NMR data led to the identification of the HMBC correlation between an extra singlet methyl group with δ_H of 2.05 ppm to a carbon with δ_C of 170.4 (**Figure 85**, Tables **7** and **8**), suggesting the presence of an acetyl group. The position of this acetylation at C-4 was determined by the observed HMBC correlations between H-3b (δ_H 2.52) /C-4 (δ_C 80.2) and H-15 (δ_H 1.50)/C-4 (δ_C 80.2). Next, the relative stereochemistry of H-6 (δ_H 2.72) and H-7 (δ_H 3.92) was determined to be *syn* based on the observed strong ROESY between H-6 and H-7 (**Figure 86**). We also observed a weak ROESY between H-6 and H-17 (δ_H 2.05), which matched better with the observed distance of these two protons in the 4*R*-**31** isomer (3.3 Å) than in the 4*S*-**31** isomer (6.8 Å), suggesting a *syn* relation between H-16 and the acetyl at C-4. Since we observed a large chemical shift difference for both methylenes H-3a/H-3b (~1.0 ppm) and H-5a/H-5b (~0.95 ppm), the relative stereochemistry of H-2 (δ_H 2.63) and the acetyl at C-4 should also be *syn*. These data matched with the known compound, acetoxycycloheximide,[31] which is the acetylation product of cycloheximide. The absolute configurations need further confirmation by ECD calculations.

Compound **32** was isolated as a yellow solid with a molecular formula of $C_{15}H_{21}NO_4$, which was derived from an HRESIMS ion peak of $C_{15}H_{20}NO_4$ $[M-H]^-$ (m/z: found 278.1379, calcd 278.1392). While the glutarimide moiety remained intact, the 7-OH group was missing in the structure. We also observed the presence of two alkene carbons (δ_C 134.7, 138.0) and one alkene proton (δ_H 6.25, Tables **7** and **8**), suggestive of a dehydration at C-6/C-7. The position of the new hydroxy at C-2 was determined by the observed HMBC correlations between 7-OH (δ_H 5.24) and C-1 (δ_C 200.6)/C-3 (δ_C 46.7). Because of its structural similarities to the dipteronine

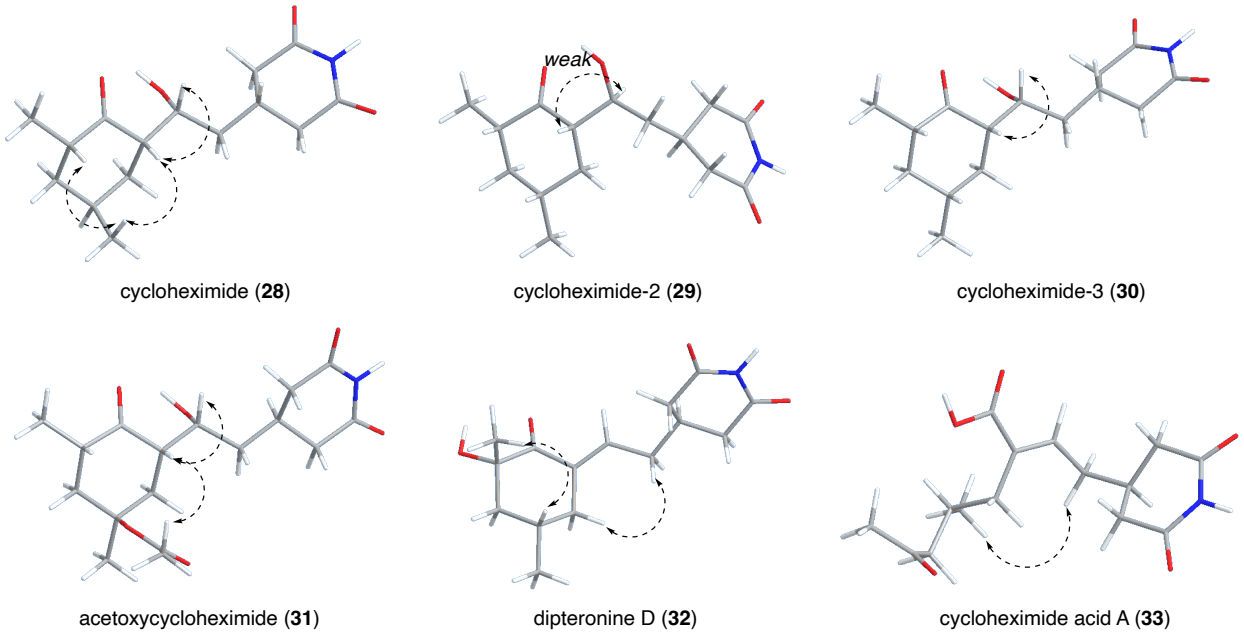

Figure 86. Key ROESY/NOESY correlations in **28**–**33** in DMSO-d_6; all shown conformers were energy minimized using MMFF94 molecular force field in Chem3D.

class of molecules, it was named dipteronine D.[32] The (*E*)-configuration of the C-6/C-7 alkene was determined based on the observed ROESY between H-5b (δ_H 2.71) and 8a/8b (δ_H 2.14, 2.18, **Figure 86**). The relative stereochemistry of H-14 (δ_H 1.17) and H-4 (δ_H 2.11) was determined to be *syn* based on the observed ROESY between them (**Figure 86**). The absolute configurations need further confirmation by ECD calculations.

Compound **33** was isolated as a yellow solid with a molecular formula of $C_{15}H_{21}NO_5$, which was derived from an HRESIMS ion peak of $C_{15}H_{20}NO_5$ $[M-H]^-$ (m/z: found 294.1316, calcd 294.1341). Even though it was eluted as a single peak on the HPLC as well as LC-MS, its NMR data showed a mixture of two structurally related molecules. Nevertheless, we were able to pick out the peaks for the major component based on their relative intensities and elucidated its structure. Similar to compound **32**, this molecule possesses an alkene at C6/C7 based on the observed two alkene carbons (δ_C 133.3, 139.9) and one alkene proton H-7 (δ_H 6.68, Tables **7** and **8**). The presence of a broad proton peak with δ_H 12.28 and the HMBC correlations between H-7 (δ_H 6.68) and a carbon peak with δ_C 169.0 suggested a carboxylic acid at C-6. The presence of a

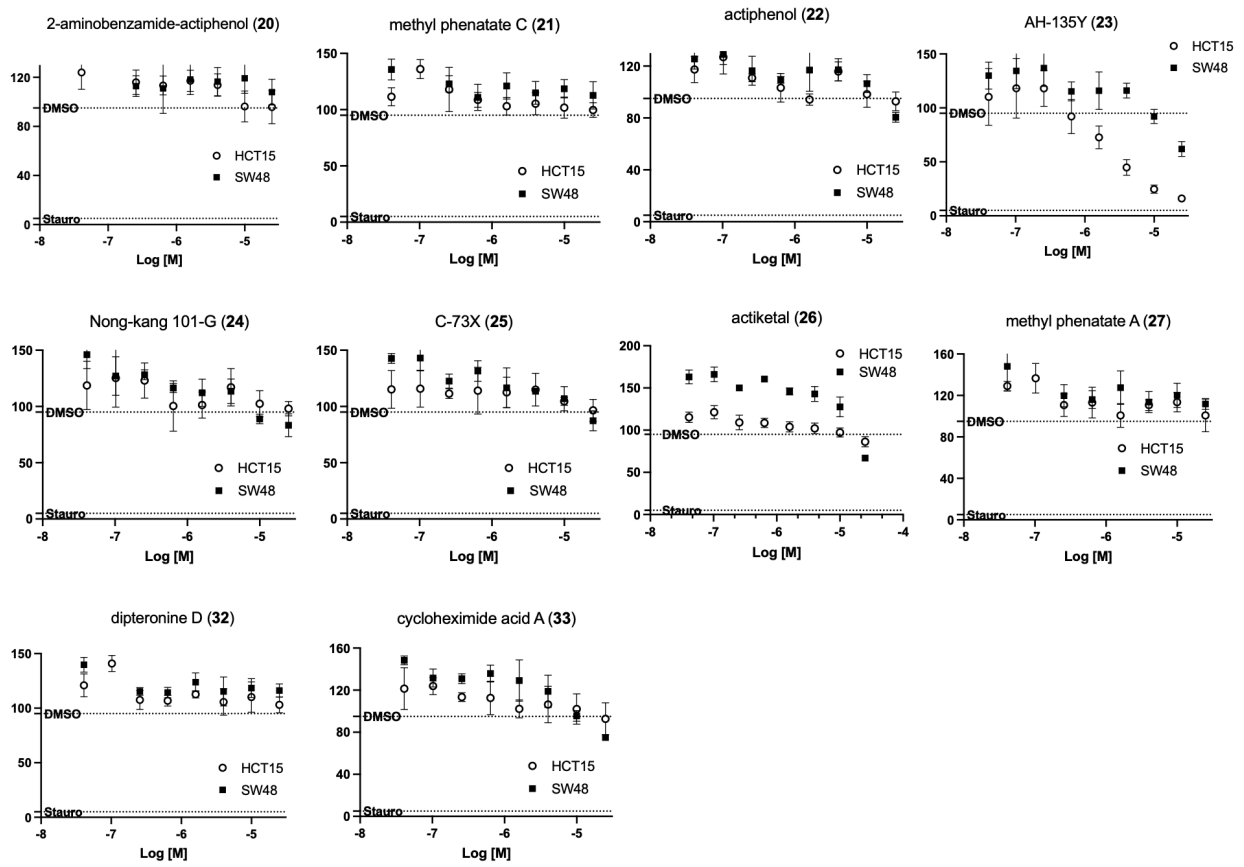

Figure 87. Antiproliferative activities of **20**–**27**, **32**, and **33**.

single methyl group H-1 (δ_H 2.06) correlating with the ketone with δ_C 208.7 and a doublet methyl group H-14 (δ_H 0.78) correlating with two methylenes established the ring-opened cyclohexanone moiety. The (*E*)-configuration of the C-6/C-7 alkene was determined based on the observed ROESY between H-8 (δ_H 2.24) and H-14 (δ_H 0.78, **Figure 86**). Also, by comparing the atomic distance between H-8/H-14 in 4*R*-**33** and 4*S*-**33**, we found that this strong ROESY matched better with the 2.6 Å in 4*R*-**33** than 3.2 Å in 4*S*-**33**, suggesting an *R* configuration at C-4. These NMR data matched the known molecule, cycloheximide acid A.[33] The absolute configuration of the C-4 needs further confirmation by ECD calculations or chemical derivatizations.

4.2.3 Bioactivity of 20–33

With molecules **20**–**33** in hand, we tested their antiproliferative activities against the HCT15 cell line, $KRAS^{G13D}$ mutant, and the SW48 cell line, which contains wild-type KRAS. AH-135Y (**23**) was the only compound that showed antiproliferative activity against both cell lines and most importantly, it showed selectivity against HCT15 over SW48 (**Figure 87**). The base form actiphenol was inactive, suggesting the importance of hydroxylation for its activity. The position of the hydroxylation at C-14 was also crucial to its activity as the C-8 hydroxylation in Nong-kang 101-G and C-10 hydroxylation C-73X completely depleted their activities. Future studies are needed to further investigate the mechanism of action. In addition, because of the reported protein translation inhibition activity of cycloheximide, we will also test these molecules in the SunSET assay to probe their impact on overall protein synthesis in various cancer cell lines.

4.3 Borrelidins: Type-I PKS Class of Natural Products

Another active strain from our collaboration project with SPARC was a terrestrial bacterial strain, EMU190C. Through our bioactivity-guided deconvolution efforts, we were able to identify borrelidin type of natural products that showed selective antiproliferative activity against HCT15 cells. Borrelidin is a nitrile-containing 18-membered macrolide that was first isolated from *Streptomyces rochei* in 1949.[34] Its structure was first elucidated in 1967 and then confirmed by NMR and X-ray crystallography.[35-37] Since its initial discovery as an antibiotic,[34] a variety of biological activities have been reported for borrelidin, including antifungal,[38] anti-angiogenic,[39] antiviral,[40] and antimalarial activities.[41] However, its exhibits significant toxicity toward nonmalignant cell types through the inhibition of threonyl tRNA synthetase (ThRS),

eventually preventing normal protein synthesis, preventing its advancement as a clinical candidate.[42-44]

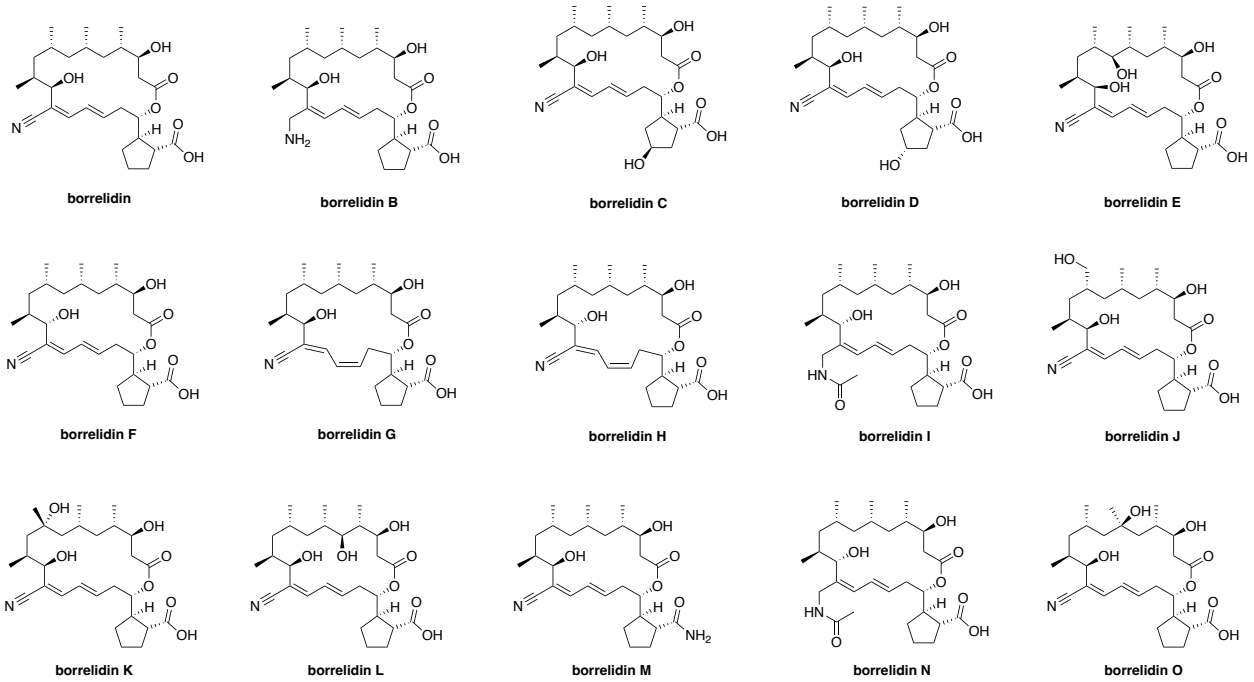

Figure 88. Structures of previously reported borrelidins A–O.

The biosynthesis of borrelidin has been described by Salas et.al. in 2004.[45] A key component of the BGC of borrelidin is *borA*, the PKS module gene that consists of *borA1*, the loading module, and *BorA2–BorA6*, five genes with eight PKS modules for the biosynthesis of the polyketide chain. The last gene *BorA6* contains a thioesterase gene at the end to catalyze the closing of the macrolactone ring. The BGC of borrelidin also contains *borI* and *borJ*, the P450 and the aminotransferase that are responsible for the synthesis of the nitrile group, and *borB–H* and *borK–N* that are responsible for the stereospecific synthesis of the starting unit, *trans*-cyclopentane-(1*R*,2*R*)-dicarboxylic acid (*trans*-1,2-CPDA). The stereochemistry of the chiral centers and alkenes of the macrolactone ring is achieved by the stereospecific keto-reductases (KRs), dehydratases (DHs), and enoyl-reductases (ERs) in the BGC.

Besides the base form borrelidin, there are a total of fifteen analogs reported for this class of molecule, namely borrelidin B–O (**Figure 88**).[46-50] Borrelidin B contains an aminomethyl group in place of the nitrile functionality in borrelidin. It retained the antiproliferative activities against N87, MDA-MB0361-DYT2, and HT29 cancer cell lines through a mitotic stalling mechanism.[46] Borrelidins C–E were reported to be hydroxylated borrelidin derivatives. While Borrelidin C and D exhibited weaker antiproliferative activities against A549, HCT116, SNU638, SK-HEP1, MDA-MB231, and K562 cancer cell lines than borrelidin, borrelidin E showed no toxicity against these cell lines.[47] Borrelidins F–H were reported as stereoisomers of borrelidin with variations in the absolute configurations of the C-11 hydroxy and the C-14/C-15 alkene.[48] Borrelidin I contains a homoacetamide (NAc-capped methylene) instead of the nitrile group. As the most active derivative among borrelidin F–H, borrelidin H showed IC_{50} values ranging from 0.12 to 2.05 μM against A549, CNE2, HeLa, HepG2, and MCF-7 cancer cell lines. Moreover, it exhibited significant anti-cancer selectivity over nonmalignant cell lines. In addition, in a wound-healing assay, borrelidin H effectively inhibited cell migration of both HeLa and A549 tumor cells even at the concentrations of half of IC_{50}. Six additional borrelidin derivatives, borrelidin J–O, were also recently reported with antimicrobial activities.[49, 50] The biosynthetic origin of these reported modifications of borrelidin remains elusive.

In this section, we report the structural characterization of known molecules, borrelidin (**34**), borrelidins C–F (**35**–**38**), borrelidins J (**39**) and K (**40**) as well as four new borrelidin analogs, which we named borrelidins P–S (**39**–**44**, **Figure 89**).

4.3.1 Structure elucidation of 34–44

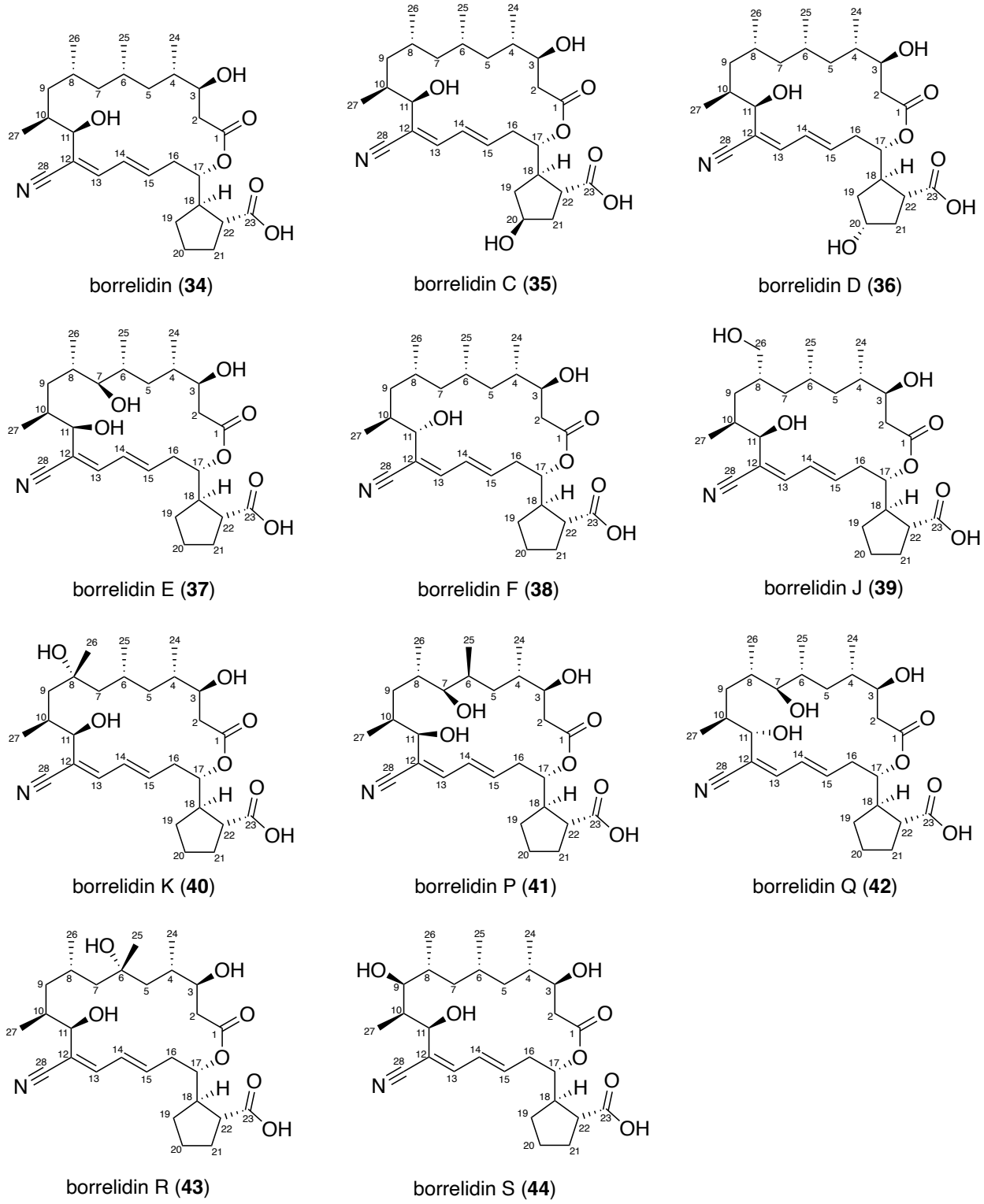

Figure 89. Structures of borrelidin derivatives **34**–**44** isolated from EMU190C.

Compound **34** (**Figure 89**) was isolated as a white powder with a molecular formula of $C_{28}H_{43}NO_6$, which was derived from an HRESIMS ion peak of $C_{28}H_{42}NO_6$ $[M\text{-}H]^-$ (m/z: found

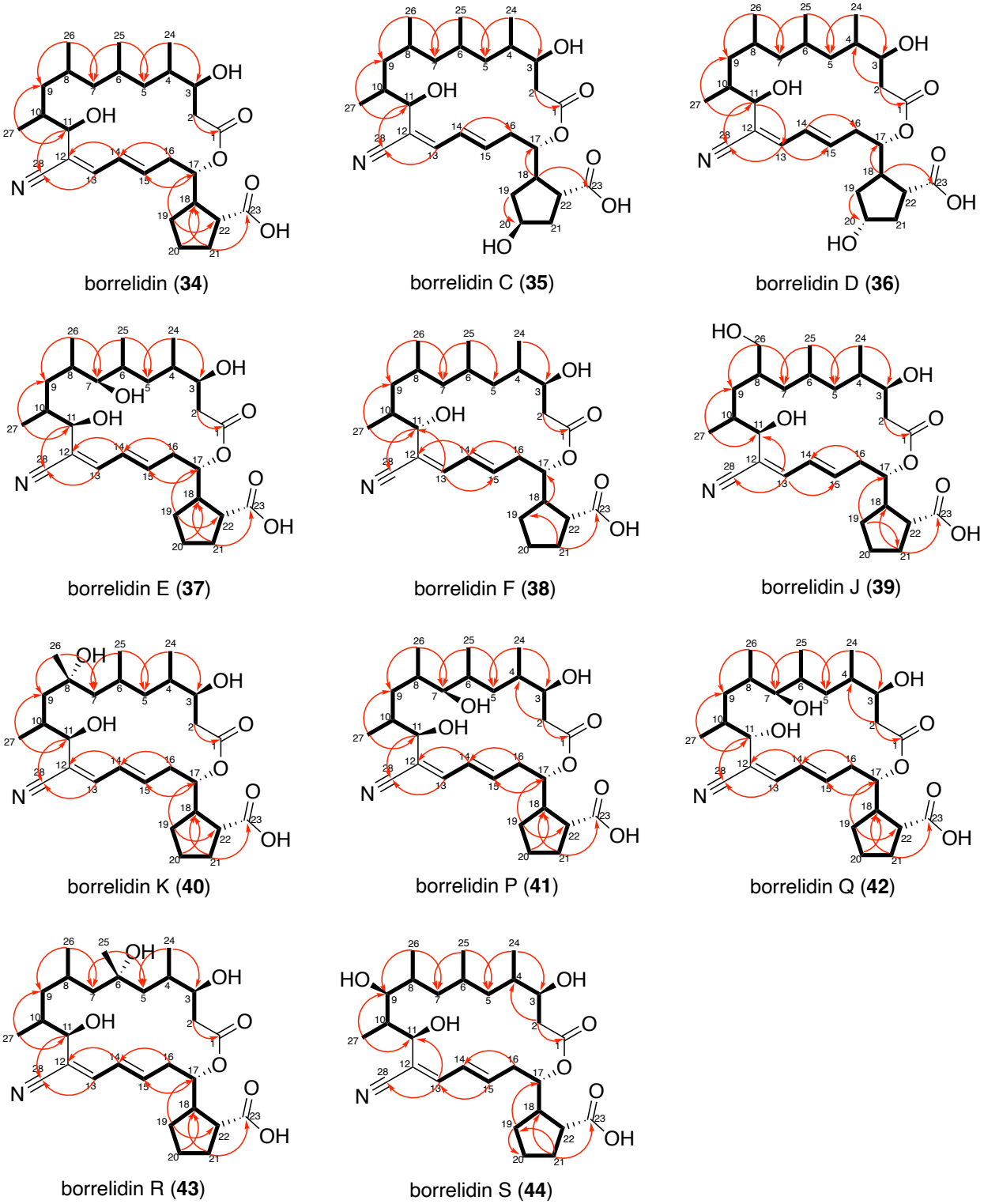

Figure 90. Key COSY and HMBC correlations in **34**–**44**.

488.2990, calcd 488.3012). When we searched this molecular formula in the publicly available marine natural product database, MarinLit, we found a few matches to several borrelidin analogs.

Table 9. ^{13}C NMR data of **34**–**44** in DMSO-d_6.

	δ_C (type)										
Position	**34**	**35**	**36**	**37**	**38**	**39**	**40**	**41**	**42**	**43**	**44**
1	171.5 (C)	171.5 (C)	171.4 (C)	171.8 (C)	171.9 (C)	171.4 (C)	171.4 (C)	171.6 (C)	172.6 (C)	171.4 (C)	171.2 (C)
2	37.4 (CH_2)	37.7 (CH_2)	37.4 (CH_2)	36.6 (CH_2)	39.6 (CH_2)	37.7 (CH_2)	39.4 (CH_2)	37.9 (CH_2)	37.8 (CH_2)	38.9 (CH_2)	39.7 (CH_2)
3	70.8 (CH)	70.6 (CH)	70.8 (CH)	71.3 (CH)	70.1 (CH)	70.7 (CH)	70.7 (CH)	70.2 (CH)	70.0 (CH)	71.2 (CH)	69.5 (CH)
4	35.8 (CH)	35.8 (CH)	35.8 (CH)	35.3 (CH)	35.8 (CH)	35.7 (CH)	36.4 (CH)	35.4 (CH)	34.9 (CH)	33.1 (CH)	34.5 (CH)
5	43.4 (CH_2)	48.2 (CH_2)	48.1 (CH_2)	37.7 (CH_2)	43.4 (CH_2)	43.7 (CH_2)	43.8 (CH_2)	40.4 (CH_2)	30.8 (CH_2)	46.7 (CH_2)	42.8 (CH_2)
6	27.3 (CH)	27.4 (CH)	27.4 (CH)	33.0 (CH)	27.7 (CH)	27.3 (CH)	27.8 (CH)	31.2 (CH)	32.2 (CH)	71.2 (C)	33.0 (CH)
7	48.2 (CH_2)	43.4 (CH_2)	43.5 (CH_2)	79.5 (CH)	48.3 (CH_2)	42.4 (CH_2)	53.0 (CH_2)	80.4 (CH)	79.2 (CH)	50.5 (CH_2)	42.5 (CH_2)
8	26.5 (CH)	26.5 (CH)	26.6 (CH)	30.9 (CH)	26.4 (CH)	34.6 (CH)	72.2 (C)	33.2 (CH)	31.2 (CH)	25.2 (C)	28.1 (CH)
9	37.7 (CH_2)	37.7 (CH_2)	37.7 (CH_2)	29.8 (CH_2)	37.4 (CH_2)	33.4 (CH_2)	42.8 (CH_2)	35.5 (CH_2)	37.0 (CH_2)	41.8 (CH_2)	74.0 (CH)
10	35.0 (CH)	35.0 (CH)	35.0 (CH)	34.6 (CH)	35.4 (CH)	35.0 (CH)	34.8 (CH)	34.9 (CH)	34.9 (CH)	35.6 (CH)	42.1 (CH)
11	71.1 (CH)	71.1 (CH)	71.1 (CH)	71.6 (CH)	77.6 (CH)	71.0 (CH)	70.7 (CH)	71.1 (CH)	78.1 (CH)	68.8 (CH)	69.8 (CH)
12	117.0 (C)	116.9 (C)	116.9 (C)	117.0 (C)	115.3 (C)	117.0 (C)	117.5 (C)	116.8 (C)	115.8 (C)	117.5 (C)	118.3 (C)
13	143.7 (CH)	143.7 (CH)	143.7 (CH)	143.7 (CH)	144.5 (CH)	143.6 (CH)	143.6 (CH)	143.9 (CH)	144.4 (CH)	143.3 (CH)	141.7 (CH)
14	127.9 (CH)	127.8 (CH)	127.8 (CH)	127.7 (CH)	128.4 (CH)	127.9 (CH)	128.1 (CH)	127.8 (CH)	128.7 (CH)	128.0 (CH)	127.6 (CH)
15	139.3 (CH)	139.2 (CH)	139.3 (CH)	139.2 (CH)	141.2 (CH)	139.3 (CH)	139.1 (CH)	139.5 (CH)	134.0 (CH)	139.5 (CH)	138.5 (CH)
16	36.0 (CH_2)	36.0 (CH_2)	35.9 (CH_2)	36.2 (CH_2)	37.5 (CH_2)	36.1 (CH_2)	35.4 (CH_2)	35.9 (CH_2)	37.5 (CH_2)	36.1 (CH_2)	35.9 (CH_2)
17	75.4 (CH)	75.5 (CH)	76.0 (CH)	75.2 (CH)	75.4 (CH)	75.5 (CH)	75.6 (CH)	75.5 (CH)	75.2 (CH)	75.5 (CH)	75.4 (CH)
18	46.0 (CH)	47.2 (CH)	44.0 (CH)	46.1 (CH)	48.2 (CH)	46.0 (CH)	45.8 (CH)	46.1 (CH)	47.3 (CH)	46.1 (CH)	46.1 (CH)
19a	29.3 (CH_2)	40.5 (CH_2)	38.3 (CH_2)	29.4 (CH_2)	29.6 (CH_2)	29.3 (CH_2)	29.3 (CH_2)	29.3 (CH_2)	29.3 (CH_2)	29.2 (CH_2)	29.4 (CH_2)
20	25.3 (CH_2)	70.9 (CH)	71.4 (CH)	25.3 (CH_2)	25.8 (CH_2)	25.3 (CH_2)	25.3 (CH_2)	25.2 (CH_2)	25.2 (CH_2)	25.4 (CH_2)	25.3 (CH_2)
21a	31.3 (CH_2)	38.6 (CH_2)	40.7 (CH_2)	31.2 (CH_2)	31.6 (CH_2)	31.3 (CH_2)	31.3 (CH_2)	31.2 (CH_2)	31.3 (CH_2)	31.4 (CH_2)	31.4 (CH_2)
22	48.5 (CH)	43.3 (CH)	46.7 (CH)	48.6 (CH)	49.0 (CH)	48.6 (CH)	48.3 (CH)	48.6 (CH)	48.6 (CH)	48.2 (CH)	48.3 (CH)
23	177.8 (C)	177.2 (C)	177.6 (C)	177.7 (C)		177.7 (C)	177.7 (C)	177.7 (C)	177.7 (C)	177.6 (C)	177.7 (C)
24	18.7 (CH_3)	18.6 (CH_3)	18.7 (CH_3)	19.2 (CH_3)	18.3 (CH_3)	18.5 (CH_3)	17.3 (CH_3)	18.3 (CH_3)	17.7 (CH_3)	17.9 (CH_3)	16.5 (CH_3)
25	18.8 (CH_3)	18.9 (CH_3)	18.9 (CH_3)	16.6 (CH_3)	19.1 (CH_3)	19.0 (CH_3)	22.5 (CH_3)	11.2 (CH_3)	17.2 (CH_3)	29.3 (CH_3)	16.4 (CH_3)
26	20.9 (CH_3)	20.9 (CH_3)	21.0 (CH_3)	17.5 (CH_3)	20.7 (CH_3)	65.0 (CH_2)	29.3 (CH_3)	16.4 (CH_3)	16.3 (CH_3)	22.9 (CH_3)	19.5 (CH_3)
27	15.5 (CH_3)	15.5 (CH_3)	15.5 (CH_3)	15.5 (CH_3)	16.2 (CH_3)	15.9 (CH_3)	18.1 (CH_3)	15.4 (CH_3)	16.0 (CH_3)	15.4 (CH_3)	13.7 (CH_3)
28	119.7 (C)	119.6 (C)	119.6 (C)	119.7 (C)	117.3 (C)	119.7 (C)	120.1 (C)	119.7 (C)	117.2 (C)	120.3 (C)	120.6 (C)

Deep analyses of its NMR data revealed the presence of two hydroxy groups, four doublet methyl groups, two carboxyl groups, three alkene protons, and a nitrile, matching the key structural features of the base form borrelidin (**Tables 9** and **10**). Later, we found that its NMR data matched perfectly with the commercial borrelidin, confirming its planar structure and absolute configurations.

Compound **35** was isolated as a white powder with a molecular formula of $C_{28}H_{43}NO_7$, which was derived from an HRESIMS ion peak of $C_{28}H_{42}NO_7$ $[M-H]^-$ (m/z: found 504.2983, calcd 504.2961). It NMR data was almost identical to those of **34**, except that the methylene at C-20 was missing (**Tables 9** and **10**). Instead, we observed a new hydroxy (δ_H 4.68) and a new proton (δ_C 4.15), suggesting a hydroxylation at C-20. In the original study that reported these C-20 hydroxylated borrelidins, they used ROESY and Mosher's analysis to determine the absolute configuration of the C-20 hydroxy.[47] Using the same ROESY strategy, we observed the ROESY correlation between H-20 and H-18 (**Figure 91**), suggesting an *S* configuration at C-20. These data matched the known compound, borrelidin C.

Table 10. ^{1}H NMR data of **34**–**39** in DMSO-d_6.

	δ_H, multiplets (*J* in Hz)					
Position	**34**	**35**	**36**	**37**	**38**	**39**
2a	2.08, dd (15.5, 9.7)	2.09, m	2.09, dd (15.6, 9.6)	2.20, dd (15.5, 3.7)	2.11, dd (15.1, 8.5)	2.10, ddd (15.5, 9.5, 2.7)
2b	2.26, dd (15.6, 3.5)	2.26, dd (15.6, 3.5)	2.25, dd (15.6, 3.6)	2.32, m	2.32, dd (15.0, 3.8)	2.27, m
3	3.76, dq (10.3, 3.5)	3.76, dq (10.3, 3.5)	3.75, dt (9.7, 3.3)	3.78, dt (9.6, 2.9)	3.63, dt (8.5, 4.2)	3.77, dq (9.7, 3.4)
3-OH	4.47, d (4.2)	4.47, br s	4.68, br s	4.36, br s		4.50, br s
4	1.74, m	1.74, m	1.73, m	1.80, m	1.64, dq (12.3, 6.9)	1.74, m
5a	0.88, ddd (14.1, 10.7, 3.1)	0.88, ddd (13.9, 10.6, 3.1)	0.96, m	0.63, t (10.9)	0.79, m	0.91, m
5b	1.12, ddd (14.0, 7.0, 4.4)	1.12, dt (14.0, 7.7)	1.01, ddd (13.9, 11.1, 3.1)	1.81, m	1.22, m	1.17, ddd (13.5, 10.9, 2.3)
6	1.83, m	1.83, m	1.82, m	1.86, m	1.59, q (7.2, 6.3)	1.80, m
7a	0.96, m	0.96, m	0.88, ddd (13.6, 10.4, 3.0)	2.82, dd (9.9, 1.9)	0.98, m	0.88, m
7b	1.00, m	1.01, td (12.5, 11.2, 3.1)	1.13, m		1.04, m	1.28, m
7-OH				4.27, br s		
8	1.56, m	1.56, m	1.56, ddd (13.1, 9.8, 6.3)	1.69, m	1.53, dq (12.7, 5.9)	1.54, dtt (11.0, 7.3, 3.4)
9a	0.61, ddd (13.8, 11.0, 3.2)	0.61, ddd (13.8, 11.1, 3.3)	0.62, ddd (13.7, 11.1, 3.3)	0.81, m	0.73, m	0.87, m
9b	1.12, ddd (14.0, 7.0, 4.4)	1.12, dt (14.4, 7.7)	1.12, m	1.07, ddd (14.7, 11.7, 3.1)	0.97, m	0.95, m
10	1.63, m	1.63, m	1.64, m	1.53, ddqd (12.6, 9.7, 6.3, 3.0)	1.67, m	1.66, m
11	4.07, dd (9.7, 3.8)	4.07, d (9.6)	4.07, d (9.6)	4.03, d (9.8)	3.74, d (8.0)	4.06, d (9.0)
11-OH	5.48, d (4.1)	5.48, s	5.47, s	5.46, br s	5.48, br s	5.46, br s
13	6.97, d (11.2)	6.96, d (11.2)	6.98, d (11.3)	6.95, d (11.2)	6.82, d (11.1)	6.95, d (11.3)
14	6.47, dd (14.7, 11.3)	6.47, dd (14.7, 11.3)	6.48, ddd (13.2, 11.4, 1.6)	6.43, dd (13.2, 11.3)	6.34, dd (15.0, 11.1)	6.45, dd (14.7, 11.0)
15	6.32, ddd (14.8, 10.5, 4.3)	6.30, ddd (14.8, 10.6, 4.3)	6.28, ddd (4.8, 10.4, 4.5)	6.31, ddd (14.7, 10.5, 4.2)	6.06, ddd (14.9, 9.8, 5.0)	6.32, ddd (14.9, 10.9, 4.7)
16a	2.38, ddd (14.9, 10.4, 4.2)	2.38, ddd (14.9, 10.6, 4.3)	2.39, ddd (15.0, 10.4, 4.2)	2.36, m	2.37, m	2.38, ddd (14.9, 10.4, 4.1)
16b	2.50, m	2.51, m	2.48, m	2.51, m	2.57, d (14.7)	2.51, m
17	4.89, dt (10.7, 3.6)	4.98, dt (10.5, 3.7)	4.87, dt (10.5, 3.7)	4.92, dt (10.5, 3.6)	4.94, t (8.4)	4.89, dt (10.6, 3.6)
18	2.51, m	2.52, m	2.32, q (8.5)	2.51, m	2.39, dd (10.6, 3.4)	2.51, m
19a	1.37, dq (12.2, 8.5)	1.35, ddd (12.5, 7.5, 4.2)	1.66, m	1.37, dq (12.4, 8.6)	1.30, m	1.37, dq (12.1, 8.5)
19b	1.88, m	1.88, m	2.16, ddd (13.0, 9.0, 5.7)	1.88, m	1.74, dq (13.1, 6.8)	1.88, m
20a	1.66, m	4.20, p (4.7)	4.15, p (5.6)	1.66, m	1.59, m	1.67, m
20b	1.66, m			1.66, m	1.59, m	1.67, m
20-OH		4.47, br s	4.44, br s			
21a	1.69, m	1.78, m	1.57, m	1.70, m	1.67, m	1.69, m
21b	1.90, m	1.82, m	1.74, m	1.89, m	1.73, m	1.89, m
22	2.31, q (7.9)	2.79, m	2.55, m	2.32, m	2.24, q (7.8)	2.30, q (8.4)
23-COOH	12.03, s	12.05, s	12.05, s	12.04, s		12.04, s
24	0.76, d (6.3)	0.76, d (6.3)	0.76, d (6.3)	0.79, d, (6.2)	0.79, d (6.6)	0.77, d (6.3)
25	0.78, d (6.3)	0.78, d (6.3)	0.78, d (6.3)	0.72, d (6.3)	0.76, d, (6.6)	0.79, d (6.3)
26-Me	0.78, d, (6.3)	0.79, d, (6.3)	0.79, d, (6.3)	0.83, d (6.7)	0.78, d (6.6)	
26a						3.02, dd, (10.3, 7.4)
26b						3.39, dd (10.2, 3.9)
27	0.94, d (6.3)	0.94, d (6.3)	0.94, d (6.3)	0.92, d (6.4)	0.92, d (6.6)	0.97, d (6.5)

Compound **36** was isolated as a white powder with a molecular formula of $C_{28}H_{43}NO_7$, which was derived from an HRESIMS ion peak of $C_{28}H_{42}NO_7$ $[M-H]^-$ (m/z: found 504.2983, calcd 504.2961). Comparing its NMR data to those of **35**, we found that it also possesses a hydroxylation at C-20. However, the chemical shifts of its neighboring protons (H-18, H-19a/H-19b, H-21a/H-21b, and H-22) changed dramatically (**Table 10**), suggesting a different configuration on the hydroxy group. Since we observed the ROESY between H-20 (δ_H 4.20) and H-22 (δ_H 2.55, **Figure 91**), the absolute configuration of the hydroxy was determined to be *S*, matching the known molecule borrelidin D.

Compound **37** was isolated as a white powder with a molecular formula of $C_{28}H_{43}NO_7$, which was derived from an HRESIMS ion peak of $C_{28}H_{42}NO_7$ $[M-H]^-$ (m/z: found 504.2983, calcd 504.2961). When comparing its NMR data to those of **34**, we found that the methylene at C-7 was missing. Instead, we observed that two methyl groups H-25 (δ_H 0.72) and H-26 (δ_H 0.83) were correlating to the same carbon C-7 with a chemical shift of 79.5 ppm, suggesting a

Table 11. ^{1}H NMR data of **40**–**44** in DMSO-d_6.

	δ_H, multiplets (*J* in Hz)				
Position	**40**	**41**	**42**	**43**	**44**
2a	2.15, dd (14.3, 8.4)	2.11, dd (15.5, 9.2)	2.25, m	2.32, m	2.29, m
2b	2.30, dd (13.7, 4.7)	2.27, dd (15.6, 3.9)	2.25, m	2.32, m	2.29, m
3	3.66, dt (8.5, 4.4)	3.76, dt (9.2, 3.3)	3.74, t (6.5)	3.73, td (6.4, 3.9)	3.72, t (7.2)
3-OH	4.46, br s	4.37, s	4.10, s	4.74, br s	4.48, s
4	1.54, tt (7.4, 4.3)	1.70, m	1.78, m	1.87, m	1.60, m
5a	0.76, m	1.14, m	0.64, m	1.07, m	0.72, m
5b	1.28, m	1.18, m	1.13, dq (11.8, 7.7)	1.58, dd (14.1, 6.1)	1.36, m
6	1.65, m	1.98, p (7.0)	1.73, m		1.68, m
6-OH				4.14, br s	
7a	1.20, td (13.5, 6.8)	2.75, dd (8.0, 3.0)	2.91, dd (8.0, 3.0)	1.33, m	0.79, dd (8.0, 3.0)
7b	1.24, m			1.45, dd (14.6, 5.1)	1.37, s
7-OH			4.27, s		
8		1.45, dddd (12.2, 9.7, 6.3, 3.	1.67, m	1.87, m	1.58, m
8-OH	3.92, br s				
9a	1.10, m	0.62, td (13.5, 2.3)	0.67, m	1.11, m	3.16, m
9b	1.28, m	0.95, m	1.78, m	1.15, t (7.1)	
9-OH					4.22, br s
10	1.78, td (7.3, 2.2)	1.62, m	1.57, m	1.66, dt (13.7, 7.4)	1.69, m
11	4.15, d (8.4)	4.05, d (9.8)	3.67, d (8.6)	4.28, d (6.5)	4.40, d (6.8)
11-OH	5.38, br s	5.48, br s	5.47, br s	5.39, br s	5.43, br s
13	6.92, d (11.2)	6.97, d (11.1)	6.75, d (11.0)	6.89, d (11.3)	6.80, d (11.2)
14	6.48, dd (14.8, 11.3)	6.47, dd (14.4, 11.4)	6.37, dd (14.9, 11.1)	6.50, dd (14.8, 11.4)	6.48, dd (15.3, 11.4)
15	6.28, ddd (14.8, 9.1, 5.5)	6.32, ddd (14.8, 10.3, 4.4)	6.00, ddd (14.8, 10.1, 4.5)	6.26, dt (14.9, 7.4)	6.25, ddd (14.7, 9.3, 5.1)
16a	2.47, m	2.39, ddd (14.9, 10.4, 4.1)	2.36, m	2.43, dd (7.6, 4.0)	2.40, ddd (14.9, 11.2, 4.8)
16b	2.47, m	2.51, m	2.60, dd (16.1, 3.8)	2.43, dd (7.6, 4.0)	2.49, m
17	4.82, dt (10.2, 3.8)	4.91, tt (10.6, 3.8)	5.01, tt (7.8, 3.1)	4.88, dq (9.9, 6.0, 5.0)	4.88, dt (10.1, 3.9)
18	2.52, m	2.51, m	2.39, m	2.48, m	2.52, m
19a	1.36, dt (12.4, 8.5)	1.37, dq (12.4, 8.5)	1.37, dq (11.8, 7.7)	1.36, dt (12.3, 8.4)	1.36, m
19b	1.85, m	1.87, m	1.80, m	1.88, m	1.85, m
20	1.65, m	1.67, m	1.62, m	1.65, m	1.65, m
21a	1.70, m	1.69, m	1.68, m	1.68, m	1.69, m
21b	1.89, m	1.90, m	1.87, dq (13.5, 6.8)	1.89, m	1.90, m
22	2.33, q (7.8)	2.31, q (8.0)	2.39, m	2.33, m	2.34, m
23-COOH	12.06, s	12.04, s	12.04, s	12.02, s	12.04, s
24	0.79, d (6.3)	0.77, d, (6.9)	0.76, d, (5.6)	0.84, d (6.3)	0.77, d, (5.4)
25	0.90, d (6.3)	0.70, d (6.5)	0.73, d (6.5)	1.10, s	0.80, d (6.4)
26-Me	1.06, s	0.84, d (6.3)	0.84, d (6.8)	0.86, d, (6.3)	0.81, d (6.4)
27	1.09, d (6.3)	0.94, d (6.5)	0.90, d (6.4)	0.92, d (6.3)	0.97, d (6.9)

hydroxylation at C-7. The absolute configuration of the C-7 was characterized as *S* based on the observed strong ROESY correlations between H-25 (δ_H 0.72)/H-7 (δ_H 2.82) and H-26 (δ_H 0.83)/H-7 (δ_H 2.82, **Figure 91**). These data matched the known compound, borrelidin E.[47] The 7*S* configuration was further confirmed based on the observed $^{3}J_{H7H8}$ of 9.9 Hz compared to the reported value of 9.0 Hz.

Compound **38** was isolated, by Prof. Ashootosh Tripathi from strain 58119I, as a white powder with a molecular formula of $C_{28}H_{43}NO_6$, which was derived from an HRESIMS ion peak of $C_{28}H_{42}NO_6$ $[M-H]^-$ (m/z: found 488.2990, calcd 488.3012). When comparing its NMR data to those of **34**, we found that major differences were located in the C-10 to C-15 region, suggesting

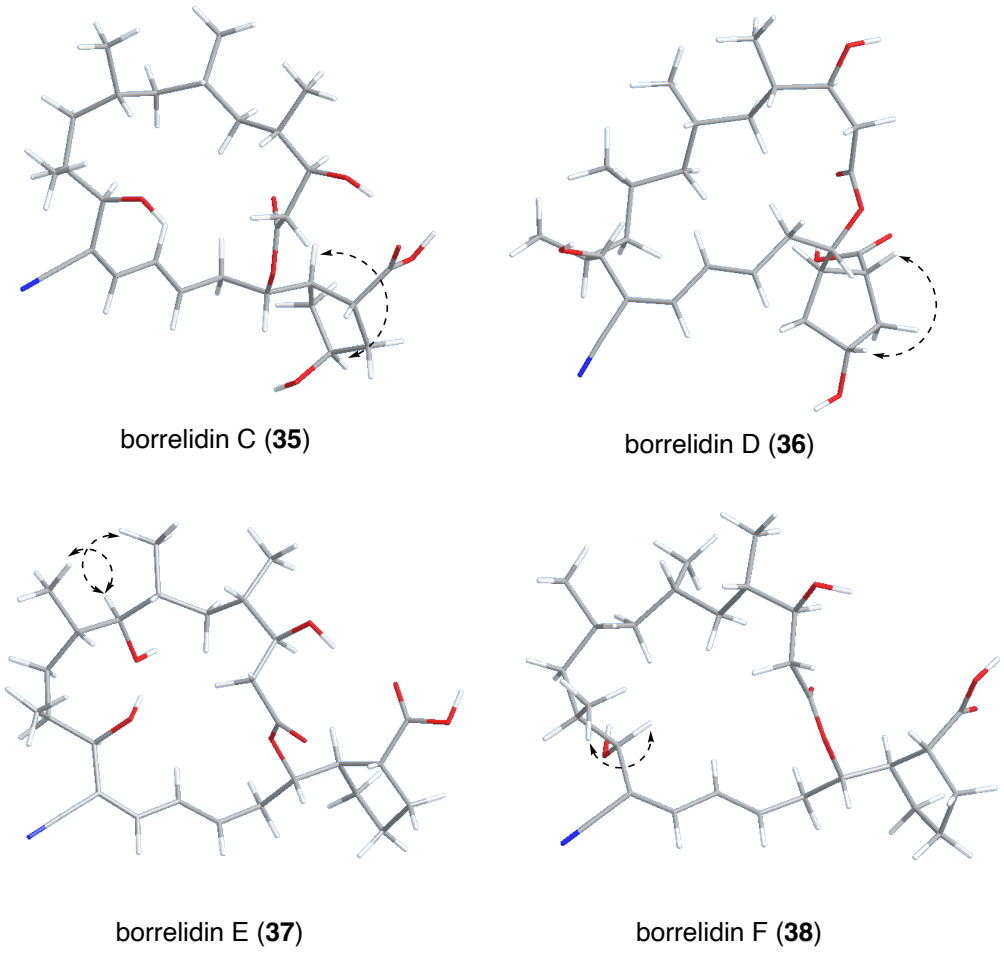

Figure 91. Key ROESY correlations observed in **35**–**38**; all shown conformers were energy minimized using MMFF molecular force field in Chem3D.

a potential stereochemistry change in this area. Specifically, we observed a dramatic change in chemical shifts at C-11 in **38** (δ_H 3.74/δ_C 77.6) compared to **34** (δ_H 4.07/δ_C 71.1, **Tables 9** and **10**), indicating a change in absolute configuration at this position. These data matched with the reported chemical shifts for borrelidin F, which possesses an *S* configuration at C-11.[48] This configuration was further validated by the strong ROESY between the methyl group H-27 (δ_H 0.92) and H-11 (δ_H 3.74) in **38** compared to only a weak ROESY between the same protons in **34**.

Compound **39** was isolated as a white powder with a molecular formula of $C_{28}H_{43}NO_7$, which was derived from an HRESIMS ion peak of $C_{28}H_{42}NO_7$ $[M-H]^-$ (m/z: found 504.2906,

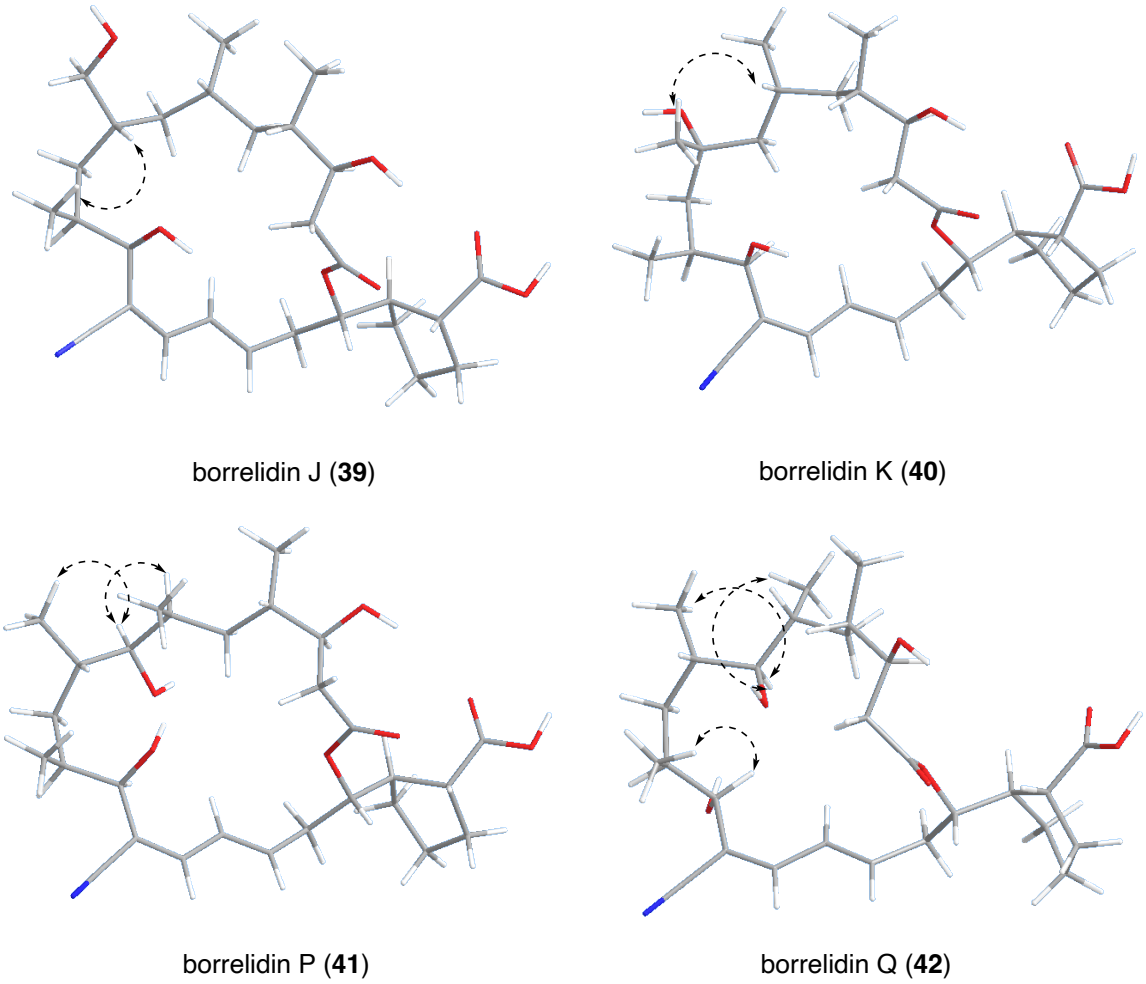

Figure 92. Key ROESY correlations observed in **39**–**42**; all shown conformers were energy minimized using MMFF molecular force field in Chem3D.

calcd 504.2961). When comparing its NMR data to those of **34**, we found that one of the four methyl groups was missing. Instead, we observed a new methylene (δ_H 3.02, 3.39) that was correlating with C-7 (δ_C 42.4) and C-9 (δ_C 33.4, **Figure 90**), suggesting a hydroxylation at C-26. The absolute configuration of C-8 remained unchanged based on the observed ROESY between H-8 (δ_H 1.54) and H-27 (δ_H 0.97, **Figure 92**). These data matched the known compound, borrelidin J.[49]

Compound **40** was isolated as a white powder with a molecular formula of $C_{28}H_{43}NO_7$, which was derived from an HRESIMS ion peak of $C_{28}H_{42}NO_7$ $[M-H]^-$ (m/z: found 504.2983,

calcd 504.2961). After comparing its NMR data to those of **34**, we found that one of the methyl groups with δ_H 1.06 ppm changed from a doublet to a singlet, and this methyl group was correlating with a carbon with δ_C 72.2 ppm and two methylenes at C-7 (δ_H 1.20, 1.24/δ_C 53.0) and C-9 (δ_H 1.10, 1.28/δ_C 42.8, **Figure 90**), suggestive of a hydroxylation at C-8. These data matched the known compound, borrelidin K.[49] The unsolved absolute configuration of C-8 was determined as *R* based on the observed ROESY between H-6 (δ_H 1.65) and H-26 (δ_H 1.06, **Figure 92**).

Compound **41** was isolated as a white powder with a molecular formula of $C_{28}H_{43}NO_7$, which was derived from an HRESIMS ion peak of $C_{28}H_{42}NO_7$ $[M-H]^-$ (m/z: found 504.2983, calcd 504.2961). Same as what we observed in **37**, we found that two methyl groups H-25 (δ_H 0.70) and H-26 (δ_H 0.84) were correlating to the same carbon C-7 with a chemical shift of 80.4 ppm (**Figure 90**), suggesting a hydroxylation at C-7. While we observed a strong ROESY between H-7 (δ_H 2.82) and H-26 (δ_H 0.83), the ROESY between H-7 (δ_H 2.82) to H-25 (δ_H 0.72) was missing (**Figure 92**). In addition, the chemical shift of the C-24 changed dramatically from 16.6 ppm in **37** to 11.2 ppm in **41** (**Table 9**), a low chemical shift that was never observed in the reported borrelidin analogs. Furthermore, the chemical shift difference between two methylene protons at C-5 changed from 1.18 ppm in **37** to 0.04 ppm in **41**, suggesting an *anti* configuration between C-4 and C-6 methyl groups based on the established method.[29] All of these data supported an *S* configuration at C-6, the opposite of the conserved *R* configuration at C-6 in previously reported borrelidin derivatives. This compound was named borrelidin P.

Compound **42** was isolated as a white powder with a molecular formula of $C_{28}H_{43}NO_7$, which was derived from an HRESIMS ion peak of $C_{28}H_{42}NO_7$ $[M-H]^-$ (m/z: found 504.2906, calcd 504.2961). Same as what we observed in **37** and **39**, we found that two methyl groups H-25

(δ_H 0.73) and H-26 (δ_H 0.84) were correlating to the same carbon C-7 with a chemical shift of 79.2 ppm (**Figure 90**), suggesting a hydroxylation at C-7. The strong ROESY correlations between H-25 (δ_H 0.73)/H-7 (δ_H 2.91) and H-26 (δ_H 0.84)/H-7 (δ_H 2.91, **Figure 92**) suggest an *S* configuration at C-7. We also observed δ_H 3.67/δ_C 78.1 chemical shifts at C-11, similar to those in **38** (δ_H 3.74/δ_C 77.6, **Tables 9** and **11**), confirming an *S* configuration at this position. This was further validated by the strong ROESY between the methyl group H-27 (δ_H 0.90) and H-11 (δ_H 3.67, **Figure 92**). This compound was named borrelidin Q.

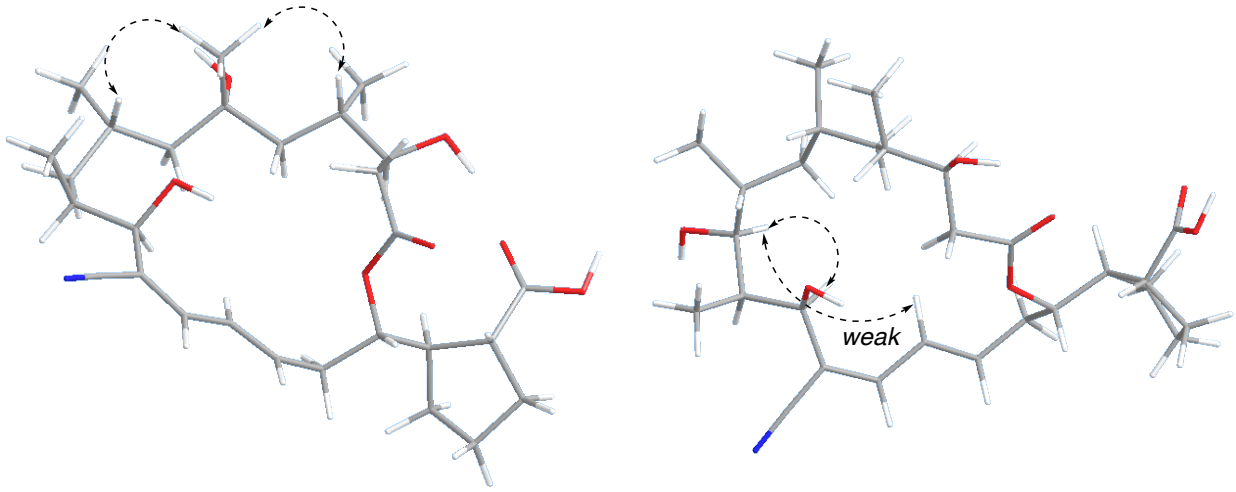

Figure 93. Key ROESY correlations observed in **43**–**44**; all shown conformers were energy minimized using MMFF molecular force field in Chem3D.

Compound **43** was isolated as a white powder with a molecular formula of $C_{28}H_{43}NO_7$, which was derived from an HRESIMS ion peak of $C_{28}H_{42}NO_7$ $[M-H]^-$ (m/z: found 504.2906, calcd 504.2961). Similar to **40**, we found that one of the methyl groups with δ_H 1.10 ppm changed from a doublet to a singlet, and this methyl group was correlating with a carbon with δ_C 71.2 ppm and two methylenes at C-5 (δ_H 1.07, 1.58/δ_C 46.7) and C-7 (δ_H 1.33, 1.45/δ_C 50.5, **Figure 90**), suggestive of a hydroxylation at C-6. The absolute configuration of C-6 was determined as *S* based on the observed ROESY between H-4 (δ_H 1.87)/H-25 (δ_H 1.10) and H-8

(δ_H 1.87)/H-25 (δ_H 1.10, **Figure 91**). This compound was a diastereomer of the known compound, borrelidin O,[50] and was named borrelidin R.

Compound **44** was isolated as a white powder with a molecular formula of $C_{28}H_{43}NO_7$, which was derived from an HRESIMS ion peak of $C_{28}H_{42}NO_7$ $[M-H]^-$ (m/z: found 504.2983, calcd 504.2961). When comparing its NMR data to those of **34**, we found that the methylene at C-9 was missing. Instead, we observed that two methyl groups H-26 (δ_H 0.81) and H-27 (δ_H 0.97) were correlating to the same carbon C-9 with a chemical shift of 74.0 ppm, suggesting a hydroxylation at C-9 (**Figure 90**). We then observed a strong ROESY correlation between H-9 (δ_H 3.16)/H-11 (δ_H 4.40), which matched better with the atomic distance between these two protons in 9*S*-**44** (2.4 Å) than that in 9*R*-**44** (3.6 Å) and very weak ROESY observed between (δ_H 2.82, **Figure 91**). The weak ROESY between H-9 and H-14 also matched better with the atomic distance between these two protons in 9*S*-**44** (4.3 Å) than that in 9*R*-**44** (5.8 Å). This evidence suggested that the C-9 position likely possessed an *S* configuration. Because of the low yield and low-quality NMR data, this needs further confirmation using DFT/DP4+ calculations. This molecule is named borrelidin S.

4.3.2 Biological activities of borrelidin 34–44

With 11 borrelidin derivatives on hand, we tested their antiproliferative activities against the HCT15 cell line, $KRAS^{G13D}$ mutant, and the SW48 cell line, which contains wild-type KRAS. Out of all borrelidin derivatives isolated from EMU190C, the original borrelidin (**34**) was the most active molecule with highly selective antiproliferative activity against HCT15 cells. Importantly, we observed a significant ~100-fold decrease in activity in **38** when compared with the base form borrelidin (**34**), suggesting that the *R* configuration of C-11 hydroxy is crucial for its antiproliferative activity. We also found that an additional hydroxylation, regardless of its

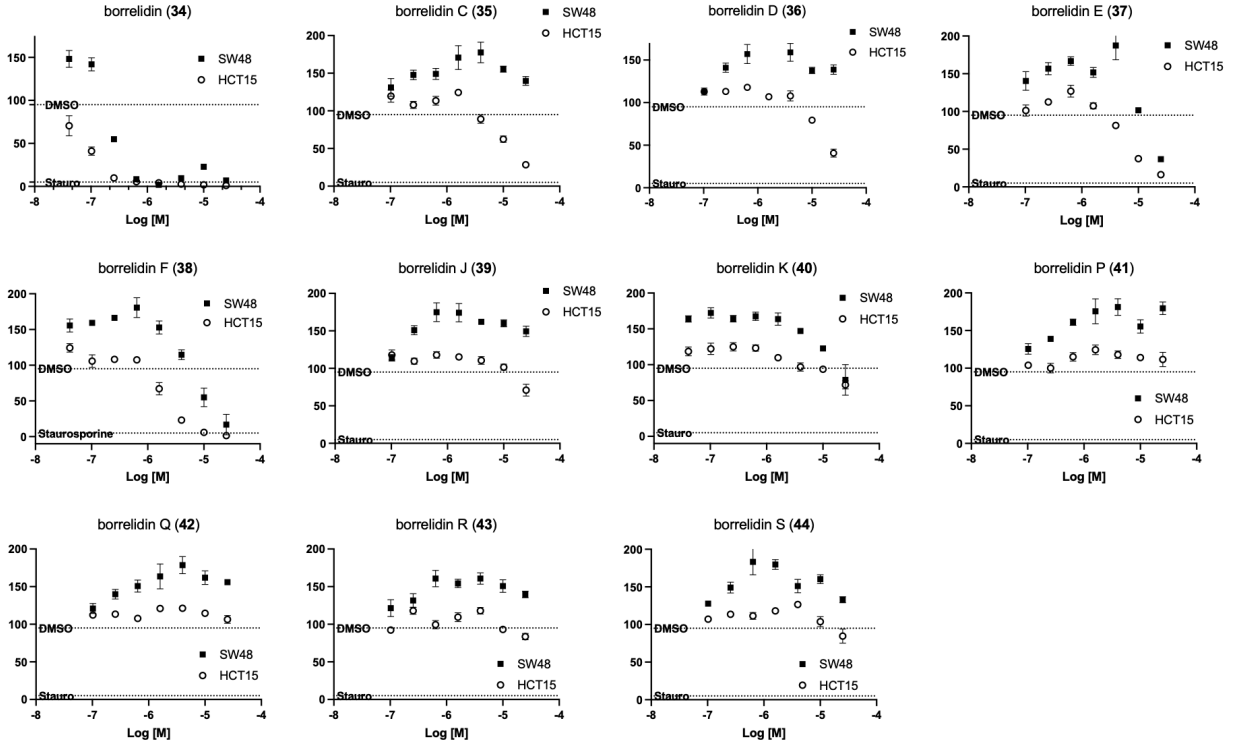

Figure 94. Antiproliferative activities of **34**–**44**.

stereochemistry or position, completely depleted its activity. The molecular mode of action needs further investigations.

4.4 Tunicamycins, the Fatty Acyl Nucleoside Antibiotics

Tunicamycins are fatty acyl nucleoside antibiotics first isolated in 1971 from the soil actinomycete *Streptomyces lysosuperificus*.[51] Their structures consist of an unusual eleven carbon aminodialdose core (tunicamine) decorated with uracil, N-acetylglucosamine (GlcNAc), and a range of amide-linked unsaturated fatty acids (**Figure 95**).[52] Several other natural products that share the same carbohydrate core have also been reported, including streptovirudins,[53] corynetoxins,[54] MM19290,[55] mycospocidin,[56] and antibiotic 24010.[57]

Tunicamycins are well known for their inhibition against bacterial cell wall biosynthesis. More specifically, they inhibit the formation of peptidoglycan precursor lipid I by targeting

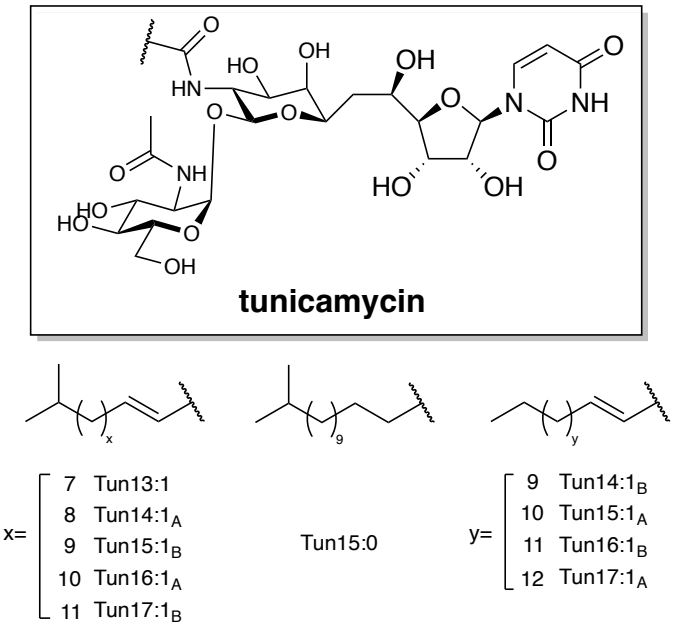

Figure 95. Structures of known tunicamycin analogs.

enzyme MraY.[51, 52, 58] They also inhibit eukaryotic N-linked glycoprotein synthesis at the first committed step,[59] resulting in significant cytotoxicity in mammalian cells. Although, this cytotoxicity precludes these antibiotics from clinical uses, it renders them a crucial tool in glycobiology.[60]

In this sub chapter, we reported the isolation and structure elucidation of four known tunicamycins **45**–**48** from strain 69078-5R (**Figure 96**), another active strain from the SPARC project.

4.4.1 Identification and structural elucidation of 45–48

Using the bioactivity-guided fractionation strategy, we identified prep HPLC fraction HF9 as the active fraction. GNPS analysis of the LC-MS/MS data of this fraction revealed the presence of a cluster featuring tunicamycin analogs (**Figure 96A**). antiSMASH analysis also suggested the presence of tunicamycin BGC (data not shown). Further purification efforts yield tunicamycin **45**–**48** as the active components of this fraction (**Figure 96B**).

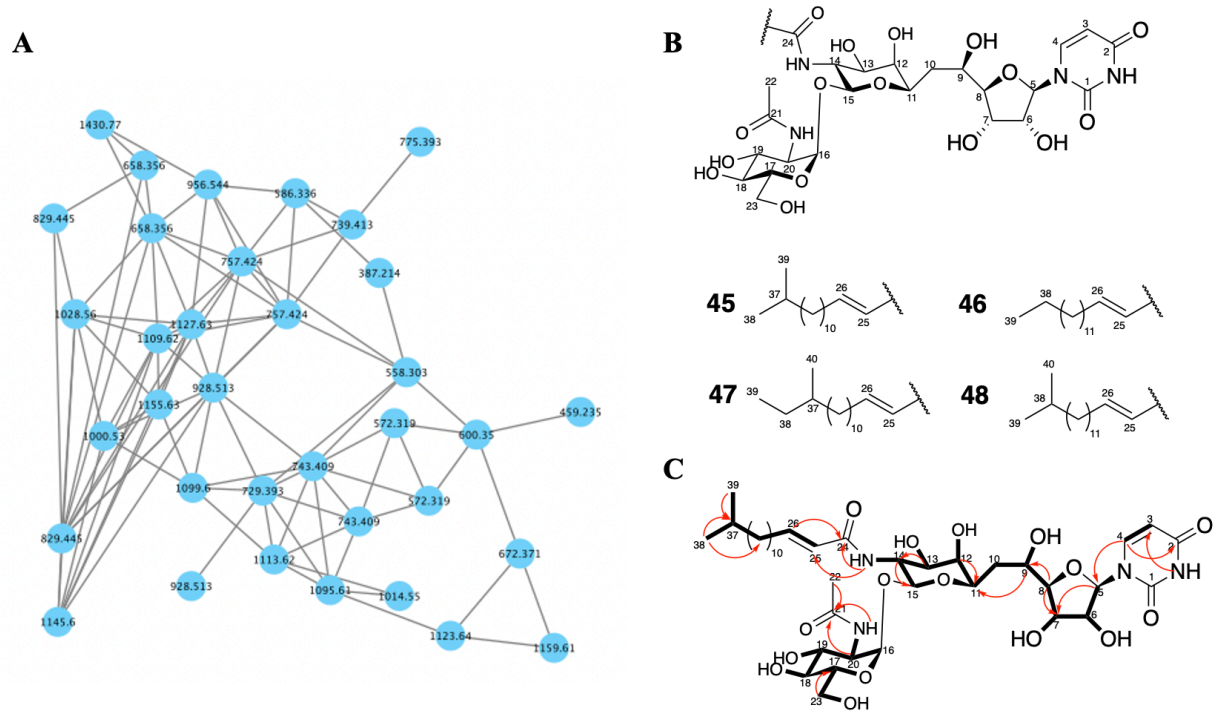

Figure 96. (A) Cluster of tunicamycins in GNPS analysis of HF7 in negative mode; (B) structures of isolated tunicamycins **45**–**48** from 69078-5R; (C) key COSY and HMBC correlations in **45**.

Compound **45** was isolated as a white powder with a molecular formula of $C_{39}H_{64}N_4O_{16}$, which was derived from an HRESIMS ion peak of $C_{39}H_{63}N_4O_{16}$ $[M-H]^-$ (m/z: found 843.4211, calcd 843.4239). Compound **46** was isolated as a white powder with the same molecular formula of $C_{39}H_{64}N_4O_{16}$ as **45**, which was derived from an HRESIMS ion peak of $C_{39}H_{63}N_4O_{16}$ $[M-H]^-$ (m/z: found 843.4211, calcd 843.4239). Compound **47** was isolated as a white powder with a molecular formula of $C_{40}H_{66}N_4O_{16}$, which was derived from an HRESIMS ion peak of $C_{40}H_{65}N_4O_{16}$ $[M-H]^-$ (m/z: found 857.4412, calcd 857.4396). Compound **48** was isolated as a white powder with the same molecular formula of $C_{39}H_{64}N_4O_{16}$ as **47**, which was derived from an HRESIMS ion peak of $C_{39}H_{63}N_4O_{16}$ $[M-H]^-$ (m/z: found 857.4311, calcd 857.4396). Analysis of the NMR data of **45** confirmed all the structural features of tunicamycin (**Figure 96C**, **Table 12**). By comparing the NMR data and masses of **45**–**48**, we found that their ^{1}H NMR data were

Table 12. ^{1}H and ^{13}C NMR data of **45** in DMSO-d_6.

Position	δ_C (type)	δ_H, multiplets (*J* in Hz)	Position	δ_C (type)	δ_H, multiplets (*J* in Hz)
1	163.5 (C)		16	99.3 (CH)	4.74, d (3.4)
1-NH		11.32, s	17	71.1 (CH)	3.59, m
2	151.4 (CH)		18	67.3 (CH)	3.72, m
3	102.6 (CH)	5.70, dd (8.1, 2.2)	18-OH		5.06, d (6.3)
4	140.8 (CH)	7.79, dd, (8.4)	19	71.4 (CH)	3.60, m
5	86.8 (CH)	5.83, d (6.9)	19-OH		
6	73.9 (CH)	3.99, dd (12.3, 6.4)	20	53.5 (CH)	3.63, m
6-OH		5.34, d (6.3)	20-NH		6.65, d (8.9)
7	69.7 (CH)	4.03, td (4.8, 2.1)	21	169.6 (C)	
7-OH		5.08, d (4.5)	22	23.4 (CH_3)	1.77, s
8	89.0 (CH)	3.63, m	23	70.4 (CH_2)	3.52, m
9	71.6 (CH)	3.42, m	23-OH		4.61, t (5.8)
9-OH		4.69, m	24	166.5 (C)	
10a	61.0 (CH_2)	3.53, m	25	125.3 (CH)	5.88, d (15.3)
10b	61.0 (CH_2)	3.58, m	26	143.1 (CH)	6.60, dt (15.4, 6.9)
11	73.6 (CH)	3.70, m	27	31.7 (CH_2)	2.12, dt
12	70.4 (CH)	3.22, ddd	28	28.3 (CH_2)	1.38, t (7.3)
12-OH		5.04, d (5.2)	29-35	29.4 (CH_2)	1.25, m
13	70.8 (CH)	3.44, m	36	38.9 (CH_2)	1.14, q (6.9)
13-OH		4.68, m	37	27.9 (CH)	1.50, qq (13.1, 6.5)
14	53.4 (CH)	3.74, m	38	23.0 (CH_3)	0.85, d (6.6)
14-NH		7.78, d (6.2)	39	23.0 (CH_3)	0.85, d (6.6)
15	101.4 (CH)	4.42, d (8.3)			

almost identical, and their masses differed by a unit of 14, suggesting a difference in the length and branching of lipid chain. Using the established method for determining the branching of lipid chain,[61, 62] we compared their ^{13}C NMR spectrums of **45**–**48** (**Figure 97**). In both **45** and **48**, we identified a terminally branched (*iso*-) carbon with a single chemical shift (corresponding to both methyl group carbons) at ~23.0 ppm. For **46**, we identified a linear type (*n*-) carbon with a single shift at ~14.4 ppm. For **47**, we identified an *anteiso*- type branching with two carbons at ~11.7 ppm and ~19.6 ppm. These observations suggested that **45**–**48** were known compounds tunicamycin VII, tunicamycin VIII, corynetoxin H17a,[63] and tunicamycin X, respectively.

4.4.2 Biological activities of tunicamycins analogs 45–48

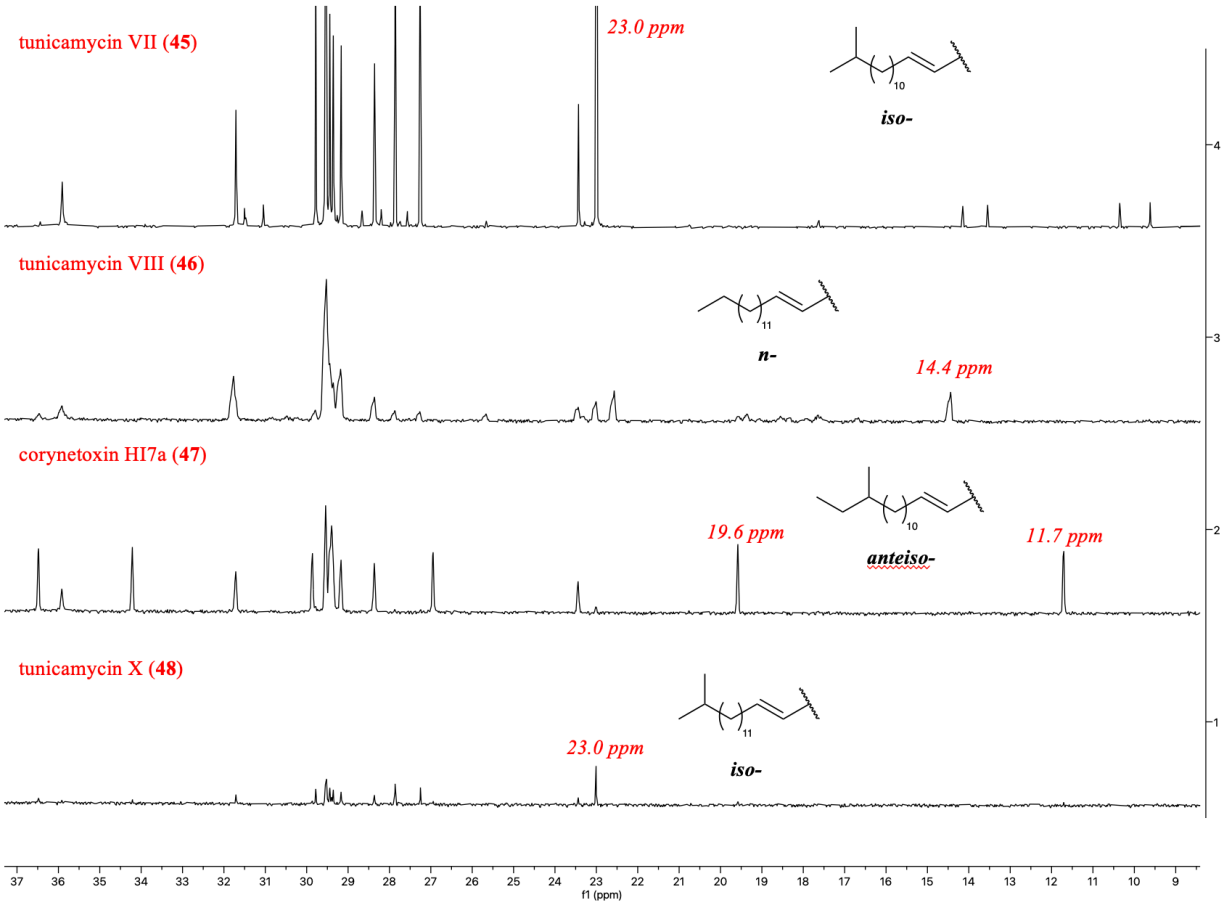

Figure 97. Comparison of the ^{13}C data (DMSO-d_6) of **45**–**48** to determine the branching of their lipid chains.

With 4 tunicamycin derivatives on hand, we tested their antiproliferative activities against the HCT15 cell line, $KRAS^{G13D}$ mutant, and the SW48 cell line, which contains wild-type KRAS. All four molecules showed selective antiproliferative activities against HCT15 over SW48 with similar potencies (**Figure 98**), which was consistent with the reported activities of this class of molecules. Further studies are needed to assess their cytotoxicity against nonmalignant mammalian cells for consideration into clinical development.

4.5 Conclusion

Besides phenazines, we also isolated and characterized ikarugamycin, actiphenol and cycloheximide, borrelidin, and tunicamycin classes of molecules with exciting structural features

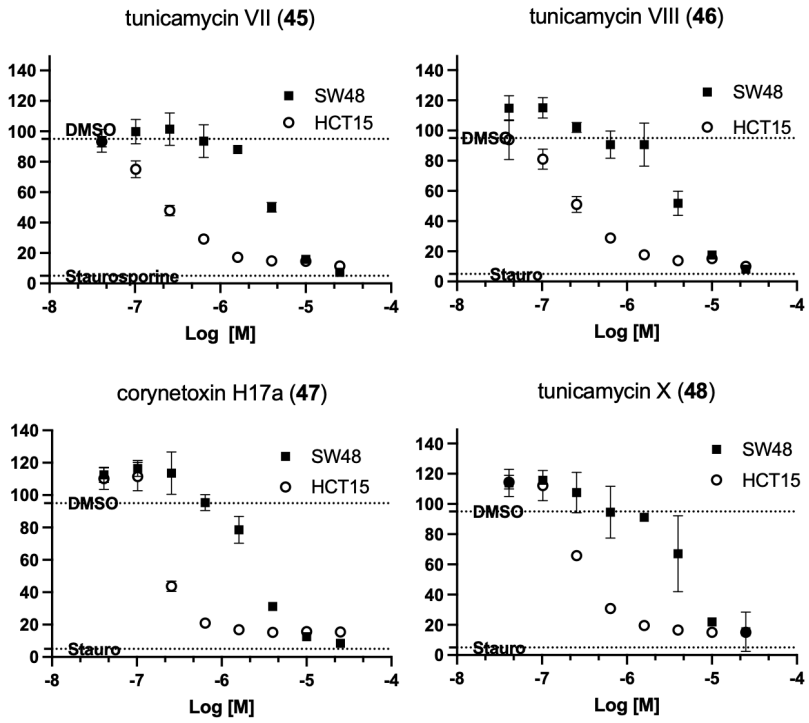

Figure 98.Antiproliferative activities of **45**–**48**.

and biological activities. For ikarugamycin analogs, we identified a new molecule capsimycin H, which is the C-24 hydroxylated product of known compound, capsimycin (**13**). While the ikarugamycin BGC was identified in the genome of 87797-1N, we did not identify any potential P450 or hydroxylase that could potentially catalyze this hydroxylation. Further investigations will focus on knock-out experiments of genes upstream and downstream of the ikarugamycin BGC to elucidate the mechanism of this hydroxylation. For actiphenol and cycloheximide classes of molecules, we reported the structures of three new molecules, namely 2-aminobenzamide-actiphenol (**20**), methyl phenatate C (**21**), and dipteronine D (**32**), as well as 11 known molecules isolated from strain 44321-A2I. In addition, we reported the discovery and structure elucidation of 4 new hydroxylated borrelidins, namely borrelidin P–S (**41**–**44**), and 7 known borrelidins, all isolated from local Michigan strain EMU190C. Last but not least, we identified four known tunicamycin analogs **45**–**48** from strain the Costa Rican strain 69078-5R.

AH-135Y (**23**), borrelidin (**34**), and four tunicamycins **45**–**48** showed selective antiproliferative activity against the $KRAS^{G13D}$ HCT15 cells over the wild-type KRAS SW48. Further studies are necessary to investigate their molecular modes of action for future clinical development.

4.6 Materials and Methods

4.6.1 General NMR and LC-MS/MS methods

Nuclear Magnetic Resonance (NMR) spectra were collected using a Bruker 600 NMR spectrometer (^{1}H: 600 MHz, ^{13}C: 150 MHz) equipped with a Magnex 600/54 active shielded premium magnet, a Bruker liquid N_2 cooled Prodigy cryo-probe and a Bruker NEO600 console, or a Bruker 800 NMR (^{1}H: 800 MHz, ^{13}C: 200 MHz) equipped with an Ascend magnet with active shield, a 5mm Triple resonance inverse detection TCI cryoprobe and a Bruker NEO console. All NMR data analyses were performed using MestReNova NMR software. All chemical shifts were referenced to residual solvent peaks [^{1}H (DMSO-d_6): 2.50 ppm; ^{13}C (DMSO-d_6): 39.51 ppm].

LC-HRMS/MS analyses of Biotage fractions, HPLC fractions, and purified compounds were performed using an Agilent 1290 Infinity II UPLC coupled to an Agilent 6545 ESI-Q-TOF-MS system operating in both positive and negative modes. Chromatography was performed using a Phenomenex Kinetex® 1.7 μm Phenyl-Hexyl 100 Å (2.1 × 50 mm) column. The injection volume was 2 μL per sample. The samples were eluted utilizing a gradient starting with a 1 min isocratic wash step consisting of 90% A (95% water/5% acetonitrile with 0.1% formic acid) and 10% B (100% acetonitrile with 0.1% formic acid), then 6 min linear gradient step starting from 10% B to 100% B and ended with 2 min of 100% B wash with a flow rate of 0.4 mL/min. The

divert valve was set to MS for 0 – 7.4 min and set to waste from 7.4 - 9 min. The conditions of the dual AJS ESI were set with gas temperature at 320 °C, sheath gas temperature at 350 °C, sheath gas flow rate at 11 L/min, and source capillary voltage at 3500 V. The mass range of MS was set to 100 – 2000 m/z and acquisition rate was set to 10 spectra per second. The mass range of MS/MS was set to 50 – 2000 m/z; acquisition rate was set to 6 spectra per second, and isolation width was set to ~1.3 m/z. The collision energy was set based on the formula: Collision Energy = (5 × m/z)/100 + 10. Maximum precursor per cycle was set to 9 and the MS/MS mass error tolerance was ± 20 ppm. The reference masses for positive mode are purine $C_5H_4N_4$ $[M+H]^+$ ion (m/z 121.050873) and hexakis(1H,1H,3H-terafluoropropoxy)-phosphazine $C_{18}H_{18}F_{24}N_3O_6P_3$ $[M+H]^+$ ion (m/z 922.009798). The reference masses for negative mode are trifluoroacetic acid $C_2HF_3O_2$ $[M-H]^-$ (m/z 112.985587) and hexakis(1H,1H,3H-terafluoropropoxy)-phosphazine $C_{18}H_{18}F_{24}N_3O_6P_3$ $[M+TFA-H]^-$ (m/z 1033.988109). All solvents used for Biotage fractionation were ACS grade and those used for HPLC purification and LC-HRMS/MS analyses were HPLC grade or better unless otherwise stated. All LC-MS/MS chromatograms, Extracted Base Peak Chromatograms (BPCs), and extracted UV (254 nm) traces in this work were subtracted from the chromatograms of methanol (MeOH) blank and were plotted using GraphPad Prism version 9.4.1 for Mac OS X (GraphPad Software, www. Graphpad.com).

4.6.2 Scale-up fermentation of 87797-1N, 44321-N2I, EMU190C, and 69078-5R

All strains were scaled up to 40 liters. All strains were streaked onto R2YE agar plates and were grown for 5-7 days at 28 °C. For each strain, 3 mL seed cultures in 14-mL dual-position cap tubes were inoculated with a loop-full of vegetative cells from R2YE plates and grown for 5 days at 28 °C, 200 r.p.m. 3-mL seed cultures were inoculated into 100-mL seed

cultures in 250-mL baffled flask and they were grown for 7 days at 28 °C, 200 r.p.m. 50-mL of seed cultures were inoculated into 1 L fermentation media in 2.8 L baffled Fernbach flasks and grown for 7 days at 28 °C, 200 r.p.m. For 87797-1N and 44321-N2I, ISP2 broth was used in both seed cultures and fermentation. For 69078-5R and EMU190C, A3M medium was used in both seed cultures and fermentations. In addition, 10 mL of *Corneybacterium* cultured in V22 media was added to the fermentation medium of EMU190C on day 2 of fermentation. 10 mL of *Rhodococcus* cultured in V22 media was added to each of the fermentation media of 69078-5R on day 2 of fermentation.

On day 7 of the fermentation, 25 g of Amberlite XAD16 resin contained within a polypropylene mesh bag was added to each fermentation culture, and shaken overnight at 28 °C, 200 r.p.m. On day 8, all resin bags were removed and washed extensively with dIH_2O to remove any water-soluble media components and residual cell mass adsorbed on the resin bags. Each washed resin bag was extracted with 250 mL methanol and 250 mL ethyl acetate (EtOAc). The combined organic fractions were dried *in vacuo*.

4.6.3 Purification of PTMs 9-19

For compounds **9**–**13**, preparative RF-HPLC fractionation of the crude extract of 87797-1N was performed using a Shimadzu LC-20AP system equipped with a reverse-phase Phenomenex Kinetex® 5 μm C18 100 Å (250 × 21.2 mm) column, and an autosampler. The injection volume was set to either 1 mL or 2 mL. The materials (brought up in methanol at ~100 to 200 mg/mL) were eluted with a flow rate of 20 mL/min and a linear gradient starting with a 2 min isocratic wash step using 10% acetonitrile/H_2O, then 40 min linear gradient step from 10% acetonitrile/H_2O to 70% acetonitrile/H_2O, and then 10 min wash with 95% acetonitrile/H_2O followed by 10 min equilibration with 10% acetonitrile/H_2O.

These compounds were then purified using semi-preparative HPLC purification using a Shimadzu LC-20AT system equipped with a reverse-phase Phenomenex Luna® 5 μm Phenyl-Hexyl 100 Å (250 × 10 mm) column and an autosampler. **9** (~0.3 mg/L) was purified from prep HPLC fraction F20–F26 using 20 min of an isocratic 30% acetonitrile/H_2O gradient, and then 10 min of 70% acetonitrile/H_2O. **10** (~0.5 mg/L) was purified from prep HPLC fraction F15–F16 using 6 min of an isocratic 50% acetonitrile/H_2O gradient, and then 8 min of 95% acetonitrile/H_2O wash. **11** (~1 mg/L) was purified from prep HPLC fraction F9–F10 using 25 min of an isocratic 10% acetonitrile/H_2O gradient and then 10 min of 95% acetonitrile/H_2O wash. **12** (~2 mg/L) was purified from prep HPLC fraction F12–F14 using 10 min of a 5% to 20% acetonitrile/H_2O gradient and then 20 min of an isocratic 20% acetonitrile/H_2O gradient followed by a 10 min 95% acetonitrile/H_2O wash. **13** (~0.3 mg/L) was purified from prep HPLC fraction F11 using 20 min of an isocratic 20% acetonitrile/H_2O gradient followed by a 10 min 95% acetonitrile/H_2O wash.

For compounds **14**–**19**, preparative RF-HPLC fractionation was performed using the same Shimadzu LC-20AP system equipped with a reverse-phase Phenomenex Kinetex® 5 μm C18 100 Å (250 × 21.2 mm) column, and an autosampler. The materials (brought up in methanol at ~100 to 200 mg/mL) were eluted with a flow rate of 20 mL/min and a linear gradient starting with a 2 min isocratic wash step using 20% acetonitrile/H_2O (with 0.1% formic acid), then 30 min linear gradient step from 20% acetonitrile/H_2O (with 0.1% formic acid) to 95% acetonitrile/H_2O (with 0.1% formic acid), and then 10 min wash with 95% acetonitrile/H_2O (with 0.1% formic acid) followed by a 10 min equilibration with 20% acetonitrile/H_2O (with 0.1% formic acid).

These compounds were then purified using semi-preparative HPLC purification using the same Shimadzu LC-20AT system equipped with a reverse-phase Phenomenex Luna® 5 μm Phenyl-Hexyl 100 Å (250 × 10 mm) column and an autosampler. **14** (~0.1 mg/L) and **15** (~0.05 mg/L) were purified from prep HPLC fraction F13–F15 using 10 min of a 0% to 40% acetonitrile/H_2O gradient, and then 20 min of an isocratic 40% acetonitrile/H_2O gradient followed by a 10 min 95% acetonitrile/H_2O wash. **16** (~0.4 mg/L) and **17** (~0.2 mg/L) were purified from prep HPLC fraction F16–F18 using 10 min of a 0% to 45% acetonitrile/H_2O gradient, and then 20 min of an isocratic 45% acetonitrile/H_2O gradient followed by a 10 min 95% acetonitrile/H_2O wash. **18** (~0.1 mg/L) and **19** (~0.05 mg/L) were purified from prep HPLC fraction F16–F18 using 10 min of a 0% to 45% acetonitrile/H_2O gradient, and then 20 min of an isocratic 45% acetonitrile/H_2O gradient followed by a 10 min 95% acetonitrile/H_2O wash.

4.6.4 Expression and purification of ikaD

The pET-28a(+) vector containing *ikaD* was purchased from Twist Bioscience. The plasmid was transformed into BL21(DE3) cells on LB agar plate containing kanamycin (50 μg/L) overnight at 37 °C. A single colony was then inoculated into 10 mL of LB broth containing 1 mM kanamycin and incubated overnight at 37 °C. The overnight culture into 1 L of TB broth containing kanamycin (50 μg/L) and shaken at 37°C (160 r.p.m.). When the OD_{600} reached 0.6–1.0, IPTG (isopropyl β-D-thiogalactoside, 1 mM) and δ-aminolevulinic acid (0.4 mM) were added to induce protein expression and to promote the production of the heme cofactor in *E. coli*, respectively. The cultures were grown at 16 °C for 18–20 hours before the cells were harvested by centrifugation and stored at -80 °C. The following purification steps were performed on ice or at 4 °C. The cells were thawed and resuspended in 50 mL of lysis

buffer [50 mM Tris-HCl, pH 7.4 at rt, 50 mM NaCl, 10% (v/v) glycerol, 1mM PMSF (phenylmethylsulphonyl fluoride), 15 mg/L lysozyme, 2mg/L DNase] per 1 L of the original overexpression culture. The cell suspension was then sonicated using a model 705 Sonic Dismembrator (Thermo Fisher Scientific) and centrifuged at 50000g for 20 min to remove cellular debris. The resulting clarified lysate was loaded onto a prepacked column containing 7 mL of Ni-NTA resin (Qiagen). The loaded material was washed with 4 column volumes (CV) of wash buffer 1 [50 mM Tris-HCl, pH 7.4, 300 mM NaCl, 20 mM imidazole, 10% (v/v) glycerol], 4 CV of wash buffer 2 [50 mM Tris-HCl, pH 7.4, 300 mM NaCl, 50 mM imidazole, 10% (v/v) glycerol], and then eluted with 2 CV of elution buffer [50 mM Tris-HCl, pH 7.4, 300 mM NaCl, 300 mM imidazole, 10% (v/v) glycerol]. Elution fractions containing pure material were accessed by gel electrophoresis and by monitoring absorbance A_{420}/A_{280}. Pooled fractions were concentrated using 10 KD molecular weight cut-off (MWCO) centrifugal filters. Concentrated protein was loaded onto a desalting column and eluted using 4 mL of storage buffer [50 mM Tris, pH 7.4, 10% (v/v) glycerol]. Aliquots of purified protein were flash-frozen in liquid N_2 and stored at -80 °C. The concentration of functional P450 was assessed by obtaining CO difference spectra according to the established protocol.[64]

4.6.5 Expression and purification of hydroxylase

The pET-28a(+) vector containing *ikaD* was purchased from Twist Bioscience. The plasmid was transformed into BL21 Rosetta 2 cells on LB agar plate containing kanamycin (50 μg/L) overnight at 37 °C. A single colony was then inoculated into 10 mL of LB broth containing 1 mM kanamycin and incubated overnight at 37 °C. The overnight culture into 1 L of TB broth containing kanamycin (50 μg/L) and shaken at 37°C (250 rpm). When the OD_{600} reached 0.6–1.0, IPTG (1 mM) was added to induce protein expression. The cultures were grown

overnight at 20 °C for before the cells were harvested by centrifugation and stored at -80 °C. The following purification steps were performed on ice or at 4 °C. The cells were thawed and resuspended in 50 mL of lysis buffer [25 mM Tris-HCl, pH 7.4 at rt, 150 mM NaCl, 1mM DTT (dithiothreitol), 2mg/L Aprotinin] per 1 L of the original overexpression culture. The cell suspension was then sonicated using a model 705 Sonic Dismembrator (Thermo Fisher Scientific) and centrifuged at 40000g for 30 min to remove cellular debris. The resulting clarified lysate was loaded onto a prepacked column containing 3.5 mL of Ni-NTA resin (Qiagen). The loaded material was washed with 4 CV of wash buffer [25 mM Tris-HCl, pH 7.4, 150 mM NaCl, 1mM DTT, 20 mM imidazole], and then eluted with 6 CV of elution buffer [25 mM Tris-HCl, pH 7.4, 150 mM NaCl, 1mM DTT, 300 mM imidazole]. Elution fractions containing pure material were accessed by gel electrophoresis. Pooled elution fractions were concentrated using 10 KD molecular weight cut-off (MWCO) centrifugal filters. The concentration of the protein was assessed using NanoDrop. Aliquots of purified protein were flash-frozen in liquid N_2 and stored at -80 °C.

4.6.6 In vitro conversion of ikarugamycin by ikaD and hydroxylase

A standard conversion of ikarugamycin to capsimycin G was achieved by combining 2 μM ikaD, 200 μM ikarugamycin, 40 μM spinach ferredoxin, 6 μM spinach ferredoxin-$NADP^+$ reductase, 5 mM G6P (glucose-6-phosphate), 1 U/mL G6PDH (G6P dehydrogenase), and 1 mM $NADP^+$ in the reaction buffer (50 mM Tris-HCl, pH 7.5), and incubating the reaction mixture (100 μL in total) for 10 min at rt. The trapping of the intermediate, epoxyikarugamycin (**10**), was achieved using 0.5 μM ikaD, 200 μM ikarugamycin, 10 μM spinach ferredoxin, 1.5 μM spinach ferredoxin-$NADP^+$ reductase, 5 mM G6P (glucose-6-phosphate), 1 U/mL G6PDH (G6P dehydrogenase), and 1 mM $NADP^+$ in the reaction buffer (50 mM Tris-HCl, pH 7.5), and

incubating the reaction mixture (100 μL in total) for 10 min at rt. Similar reaction conditions were applied for the hydroxylase.

4.6.7 ECD and DFT calculations

Experiment ECD spectra of isolated compounds were obtained by a J-815 spectropolarimeter (JASCO Co. Tokyo, Japan) using the following parameters: photometric mode: circular dichroism (CD), high voltage (HT), and absorbance (Abs); wavelength range: 190 nm to 600 nm; data pitch: 0.5 nm; sensitivity: standard; digital integration time (DIT): 4 seconds; bandwidth: 1 nm; start mode: immediately; start mode: immediately; scanning mode: continuous; scanning speed: 100 nm/minute; baseline correction: HPLC grade methanol; accumulations: 3.

For ECD calculations, Monte Carlo conformational searches were carried out by CONFLEX 9 (Rev. B, Tokyo, Japan) using Merck Molecular Force Field static (MMFFs) force field in the gas phase. All conformers within 5 kcal/mol of the lowest energy conformer were subjected to further optimization by Gaussian 16 (Rev. C01, Wallingford, CT, USA) using density functional theory (DFT) at B3LYP/6-31G(d) level with solvent effects of methanol included using a polarizable continuum model (PCM).[65] Optimized conformers within 3 kcal/mol of the lowest energy conformer were then selected for time-dependent DFT (TDDFT) calculations by Gaussian 16 (Rev. C01, Wallingford, CT, USA) at APFD/6-311+G(2d,p) level with PCM in methanol for a total of 50 excited states. Calculated ECD and UV spectra of the conformers were averaged by SpecDis (Version 1.71, Berlin, Germany)[66] according to their Boltzmann distributions and their relative Gibb's free energy to generate the theoretical ECD and UV spectra of each configuration. The sigma value was set to σ=0.16 eV. All theoretical and

experimental ECD and UV curves were plotted using GraphPad Prism version 9.4.1 for Mac OS X (GraphPad Software, www. Graphpad.com).

4.6.8 Purification of cycloheximides and actiphenols 20–33

Preparative RF-HPLC fractionation was performed using the same Shimadzu LC-20AP system equipped with a reverse-phase Phenomenex Kinetex® 5 μm C18 100 Å (250 × 21.2 mm) column. The materials of strain 44321-A2I (brought up in methanol at ~100 to 200 mg/mL) were eluted with a flow rate of 20 mL/min and a linear gradient starting with a 2 min isocratic wash step using 10% acetonitrile/H_2O (with 0.01% TFA), then 30 min linear gradient step from 10% acetonitrile/H_2O (with 0.01% TFA) to 100% acetonitrile/H_2O (with 0.01% TFA), and then 5 min wash with 100% acetonitrile/H_2O (with 0.01% TFA) followed by an 8 min equilibration with 10% acetonitrile/ H_2O (with 0.01% TFA).

The following compounds were then further purified using the same prep HPLC system and semi-preparative HPLC purification using the Shimadzu LC-20AT system equipped with a reverse-phase Phenomenex Luna® 5 μm C-18 100 Å (250 × 10 mm) column. For **23**, prep HPLC fraction HF12 was first fractionated using 40 min of an isocratic 17% acetonitrile/H_2O (with 0.01% TFA) gradient using prep HPLC. **23** (~1 mg/L) was then purified from HF12_F28–30 using 40 min of an isocratic 13% acetonitrile/H_2O (with 0.01% TFA) gradient. For **28**–**31**, prep HPLC fraction HF13–15 was first fractionated using 40 min of an isocratic 17% acetonitrile/H_2O (with 0.01% TFA) gradient using prep HPLC. **29** (~0.3 mg/L) was then purified from HF13–15_F18–20 using 40 min of an isocratic 25% acetonitrile/H_2O (with 0.01% TFA) gradient using semi-prep HPLC. **28** (~0.3 mg/L) and **31** (~1 mg/L) were purified from HF13–15_F22–30 using 20 min of an isocratic 25% acetonitrile/H_2O (with 0.01% TFA) gradient using semi-prep

HPLC. **30** (~2 mg/L) was collected by combining HF13–15_F18–20. **22** (~2 mg/L) was purified from HF19 using 25 min of an isocratic 40% acetonitrile/H_2O (with 0.01% TFA) gradient using semi-prep HPLC.

Prep HPLC HF16–18 was fractionated using 40 min of an isocratic 33% acetonitrile/H_2O (with 0.01% TFA) gradient. The following compounds were purified using the same semi-prep system with a reverse-phase Phenomenex Luna® 5 μm Phenylhexyl 100 Å (250 × 10 mm) column. **32** (~0.025 mg/L) and **33** (~0.075 mg/L) were purified from HF16–18_F2–7 using 25 min of an isocratic 20% acetonitrile/H_2O (with 0.01% TFA) gradient. **24** (~0.05 mg/L) and **26** (~0.025 mg/L) were purified from HF16–18_F11–13 using 30 min of an isocratic 30% acetonitrile/H_2O (with 0.01% TFA) gradient. **21** (~0.025 mg/L) and **25** (~0.075 mg/L) were purified from HF16–18_F14–15 using 30 min of an isocratic 30% acetonitrile/H_2O (with 0.01% TFA) gradient. **27** (~0.04 mg/L) was purified from HF16–18_F24–28 using 25 min of an isocratic 35% acetonitrile/H_2O (with 0.01% TFA) gradient. **20** (~0.05 mg/L) was purified from HF16–18_F24–28 using 30 min of an isocratic 35% acetonitrile/H_2O (with 0.01% TFA) gradient.

4.6.9 Purification of borrelidins 34–44

Preparative RF-HPLC fractionation was performed using the same Shimadzu LC-20AP system equipped with a reverse-phase Phenomenex Kinetex® 5 μm C18 100 Å (250 × 21.2 mm) column. The materials of strain EMU190C (brought up in methanol at ~ 300 to 400 mg/mL) were eluted with a flow rate of 20 mL/min and a linear gradient starting with a 2 min isocratic wash step using 10% acetonitrile/H_2O (with 0.01% TFA), then 30 min linear gradient step from 10% acetonitrile/H_2O (with 0.01% TFA) to 100% acetonitrile/H_2O (with 0.01% TFA), and then

5 min wash with 100% acetonitrile/H_2O (with 0.01% TFA) followed by an 8 min equilibration with 10% acetonitrile/ H_2O (with 0.01% TFA).

The following compounds were then further purified using the same prep HPLC system and semi-preparative HPLC purification using the Shimadzu LC-20AT system equipped with a reverse-phase Phenomenex Luna® 5 μm Phenylhexyl 100 Å (250 × 10 mm) column. Prep HPLC fractions HF15−16 were subjected to 35 min of an isocratic 30% acetonitrile/H_2O (with 0.01% TFA) gradient, yielding (in order of elution) **41** (~0.05 mg/L), **39** (~0.025 mg/L), and **40** (~0.1 mg/L). Prep HPLC fractions HF17−18 was subjected to 40 min of an isocratic 35% acetonitrile/H_2O (with 0.01% TFA) gradient, yielding (in order of elution) **43** (~0.2 mg/L), **36** (~0.04 mg/L), **35** (~0.15 mg/L), **37** (~0.3 mg/L), and **42** (~0.06 mg/L). Prep HPLC fractions HF19−20 was subjected to 45 min of an isocratic 35% acetonitrile/H_2O (with 0.01% TFA) gradient, yielding **44** (~0.08 mg/L). HF21−22 was subjected to 35 min of an isocratic 45% acetonitrile/H_2O (with 0.01% TFA) gradient, yielding **34** (0.6 mg/L). Compound **38** was isolated by Prof. Ashootosh Tripathi from strain 58119I.

4.6.10 Purification of tunicamycins 45−48

Preparative RF-HPLC fractionation was performed using the same Shimadzu LC-20AP system equipped with a reverse-phase Phenomenex Kinetex® 5 μm C18 100 Å (250 × 21.2 mm) column. The materials of strain 69078-5R (brought up in methanol at ~ 300 to 400 mg/mL) were eluted with a flow rate of 20 mL/min and a linear gradient starting with a 2 min isocratic wash step using 10% acetonitrile/H_2O (with 0.01% TFA), then 30 min linear gradient step from 10% acetonitrile/H_2O (with 0.01% TFA) to 100% acetonitrile/H_2O (with 0.01% TFA), and then 5 min

wash with 100% acetonitrile/H_2O (with 0.01% TFA) followed by an 8 min equilibration with 10% acetonitrile/ H_2O (with 0.01% TFA).

The following compounds were then further purified using the same prep HPLC system and semi-preparative HPLC purification using the Shimadzu LC-20AT system equipped with a reverse-phase Phenomenex Luna® 5 μm Phenylhexyl 100 Å (250 × 10 mm) column. Prep HPLC fractions HF17−18 were subjected to 35 min of an isocratic 40% acetonitrile/H_2O (with 0.01% TFA) gradient, yielding (in order of elution) **45** (~1 mg/L), **46** (~0.5 mg/L), **47** (~0.4 mg/L), and **48** (~0.08 mg/L).

4.7 References

(1) Shigemori, H.; Bae, M. A.; Yazawa, K.; Sasaki, T.; Kobayashi, J. Alteramide-a, a New Tetracyclic Alkaloid from a Bacterium-Alteromonas Sp Associated with the Marine Sponge Halichondria-Okadai. *J Org Chem* **1992**, *57* (15), 4317-4320.

(2) Kanazawa, S.; Fusetani, N.; Matsunaga, S. Cylindramide - Cytotoxic Tetramic Acid Lactam from the Marine Sponge Halichondria-Cylindrata Tanita and Hoshino. *Tetrahedron Lett* **1993**, *34* (6), 1065-1068.

(3) Yu, F. G.; Zaleta-Rivera, K.; Zhu, X. C.; Huffman, J.; Millet, J. C.; Harris, S. D.; Yuen, G.; Li, X. C.; Du, L. C. Structure and biosynthesis of heat-stable antifungal factor (HSAF), a broad-spectrum antimycotic with a novel mode of action. *Antimicrob Agents Ch* **2007**, *51* (1), 64-72.

(4) Blodgett, J. A. V.; Oh, D. C.; Cao, S. G.; Currie, C. R.; Kolter, R.; Clardy, J. Common biosynthetic origins for polycyclic tetramate macrolactams from phylogenetically diverse bacteria. *P Natl Acad Sci USA* **2010**, *107* (26), 11692-11697.

(5) Gunasekera, S. P.; Gunasekera, M.; Mccarthy, P. Discodermide - a New Bioactive Macrocyclic Lactam from the Marine Sponge Discodermia-Dissoluta. *J Org Chem* **1991**, *56* (16), 4830-4833.

(6) Jomon, K.; Ajisaka, M.; Sakai, H.; Kuroda, Y. New Antibiotic, Ikarugamycin. *J Antibiot* **1972**, *25* (5), 271-&.

(7) Cao, S. G.; Blodgett, J. A. V.; Clardy, J. Targeted Discovery of Polycyclic Tetramate Macrolactams from an Environmental Streptomyces Strain. *Org Lett* **2010**, *12* (20), 4652-4654.

(8) Zhang, G. T.; Zhang, W. J.; Saha, S.; Zhang, C. S. Recent Advances in Discovery, Biosynthesis and Genome Mining of Medicinally Relevant Polycyclic Tetramate Macrolactams. *Curr Top Med Chem* **2016**, *16* (15), 1727-1739.

(9) Ito, S.; Hirata, Y. Structure of Ikarugamycin, an Acyltetramic Acid Antibiotic Possessing a Unique Asymmetric-Hydrindacene Skeleton. *B Chem Soc Jpn* **1977**, *50* (7), 1813-1820.

(10) Bertasso, M.; Holzenkampfer, M.; Zeeck, A.; Stackebrandt, E.; Beil, W.; Fiedler, H. P. Ripromycin and other polycyclic macrolactams from Streptomyces sp Tu 6239: Taxonomy, fermentation, isolation and biological properties. *J Antibiot* **2003**, *56* (4), 364-371.

(11) Aizawa, S.; Akutsu, H.; Satomi, T.; Nagatsu, T.; Taguchi, R.; Seino, A. Capsimycin, a New Antibiotic .1. Production, Isolation and Properties. *J Antibiot* **1979**, *32* (3), 193-196.

(12) Yu, H. L.; Jiang, S. H.; Bu, X. L.; Wang, J. H.; Weng, J. Y.; Yang, X. M.; He, K. Y.; Zhang, Z. G.; Ao, P.; Xu, J.; et al. Structural diversity of anti-pancreatic cancer capsimycins identified in mangrove-derived Streptomyces xiamenensis 318 and post-modification via a novel cytochrome P450 monooxygenase. *Sci Rep-Uk* **2017**, *7*.

(13) Popescu, R.; Heiss, E. H.; Ferk, F.; Peschel, A.; Knasmueller, S.; Dirsch, V. M.; Krupitza, G.; Kopp, B. Ikarugamycin induces DNA damage, intracellular calcium increase, p38 MAP kinase activation and apoptosis in HL-60 human promyelocytic leukemia cells. *Mutat Res-Fund Mol M* **2011**, *709-10*, 60-66.

(14) Moscatelli, A.; Ciampolini, F.; Rodighiero, S.; Onelli, E.; Cresti, M.; Santo, N.; Idilli, A. Distinct endocytic pathways identified in tobacco pollen tubes using charged nanogold. *J Cell Sci* **2007**, *120* (21), 3804-3819.

(15) Hasumi, K.; Shinohara, C.; Naganuma, S.; Endo, A. Inhibition of the Uptake of Oxidized Low-Density-Lipoprotein in Macrophage-J774 by the Antibiotic Ikarugamycin. *Eur J Biochem* **1992**, *205* (2), 841-846.

(16) Luo, T. C.; Fredericksen, B. L.; Hasumi, K.; Endo, A.; Garcia, J. V. Human immunodeficiency virus type 1 Nef-induced CD4 cell surface downregulation is inhibited by ikarugamycin. *J Virol* **2001**, *75* (5), 2488-2492.

(17) Zhang, G. T.; Zhang, W. J.; Zhang, Q. B.; Shi, T.; Ma, L.; Zhu, Y. G.; Li, S. M.; Zhang, H. B.; Zhao, Y. L.; Shi, R.; et al. Mechanistic Insights into Polycycle Formation by Reductive Cyclization in Ikarugamycin Biosynthesis. *Angew Chem Int Edit* **2014**, *53* (19), 4840-4844.

(18) Antosch, J.; Schaefers, F.; Gulder, T. A. M. Heterologous Reconstitution of Ikarugamycin Biosynthesis in E. coli. *Angew Chem Int Edit* **2014**, *53* (11), 3011-3014.

(19) Zhang, W. J.; Zhang, G. T.; Zhang, L. P.; Liu, W.; Jiang, X. D.; Jin, H. B.; Liu, Z. W.; Zhang, H. B.; Zhou, A. H.; Zhang, C. S. New polycyclic tetramate macrolactams from marine-derived Streptomyces sp SCSIO 40060. *Tetrahedron* **2018**, *74* (47), 6839-6845.

(20) Li, Y. Y.; Huffman, J.; Li, Y.; Du, L. C.; Shen, Y. M. 3-Hydroxylation of the polycyclic tetramate macrolactam in the biosynthesis of antifungal HSAF from Lysobacter enzymogenes C3. *Medchemcomm* **2012**, *3* (8), 982-986.

(21) Schneider-Poetsch, T.; Ju, J. H.; Eyler, D. E.; Dang, Y. J.; Bhat, S.; Merrick, W. C.; Green, R.; Shen, B.; Liu, J. O. Inhibition of eukaryotic translation elongation by cycloheximide and lactimidomycin. *Nat Chem Biol* **2010**, *6* (3), 209-217.

(22) Highet, R. J.; Prelog, V. Stoffwechselprodukte Von Actinomyceten .18. Actiphenol. *Helv Chim Acta* **1959**, *42* (5), 1523-1526.

(23) Ji, X. Y.; Zhong, Z. J.; Xue, S. T.; Meng, S. A.; He, W. Y.; Gao, R. M.; Li, Y. H.; Li, Z. R. Synthesis and Antiviral Activities of Synthetic Glutarimide Derivatives. *Chem Pharm Bull* **2010**, *58* (11), 1436-1441.

(24) Fukuda, T.; Matsumoto, A.; Takahashi, Y.; Tomoda, H.; Omura, S. Phenatic acids A and B, new potentiators of antifungal miconazole activity produced by Streptomyces sp K03-0132. *J Antibiot* **2005**, *58* (4), 252-259.

(25) Uyeda, M.; Aoki, M.; Nakajima, K.; Shiromoto, C.; Tatsuguchi, N.; Yokomizo, K.; Kido, Y.; Kino, Y. A New Antiherpetic Agent, Ah-135y, Produced by Streptomyces-Albovinaceus Strain No Ah-135. *J Antibiot* **1992**, *45* (8), 1370-1372.

(26) Hua, J. X., Y. The isolation and structure of antibiotics Nong-kang 101-F and G. *Acta chimica sinica* **1980**, *38* (3), 275-282.

(27) Aszalos, A.; Hoberech.H; Cohen, A. I. Structure of Antibiotic C-73x. *J Med Chem* **1967**, *10* (2), 281-&.

(28) Sonoda, T.; Osada, H.; Uzawa, J.; Isono, K. Actiketal, a New Member of the Glutarimide Antibiotics. *J Antibiot* **1991**, *44* (2), 160-163.

(29) Schmidt, Y.; Breit, B. Direct Assignment of the Relative Configuration in 1,3,n-Methyl-Branched Carbon Chains by H-1 NMR Spectroscopy. *Org Lett* **2010**, *12* (10), 2218-2221.

(30) Leach, B. E.; Ford, J. H.; Whiffen, A. J. Actidione, an Antibiotic from Streptomyces Griseus. *J Am Chem Soc* **1947**, *69* (2), 474-474.

(31) Johnson, F.; Duquette, L. G.; Hennis, H. E. Glutarimide Antibiotics .13. Comment on Stereochemistry of Streptovitacin-a and E-73. *J Org Chem* **1968**, *33* (2), 904-&.

(32) Shi, Y. N.; Zhou, Y. P.; Long, C. L.; Li, M. L.; Wang, Y. H.; Li, X. Y.; Guo, R.; Wang, H. S. Cycloheximide Derivatives from the Fruits of Dipteronia dyeriana. *Helv Chim Acta* **2009**, *92* (8), 1545-1549.

(33) Xu, X. L.; Yin, L. Y.; Wang, S. Y.; Liu, H. H.; Gao, J. H.; Zhao, S. J. Cycloheximide Acid A, a New Cycloheximide Derivative from Marine Derived Streptomyces sp from East China Sea. *Rec Nat Prod* **2013**, *7* (4), 292-295.

(34) Berger, J.; Jampolsky, L. M.; Goldberg, M. W. Borrelidin, a New Antibiotic with Anti-Borrelia Activity and Penicillin Enhancement Properties. *Arch Biochem* **1949**, *22* (3), 476-478.

(35) Keller-Schierlein, W. [Metabolic products of microorganisms. Concerning the constitution of borrelidin]. *Helv Chim Acta* **1967**, *50* (3), 731-753.

(36) Kuo, M. S.; Yurek, D. A.; Kloosterman, D. A. Assignment of H-1 and C-13 Nmr Signals and the Alkene Geometry at C-7 in Borrelidin. *J Antibiot* **1989**, *42* (6), 1006-1007.

(37) Anderson, B. F.; Herlt, A. J.; Rickards, R. W.; Robertson, G. B. Macrolide Antibiotic-Studies .18. Crystal and Molecular-Structures of 2 Isomorphous Solvates of the Macrolide Antibiotic Borrelidin - Absolute-Configuration Determination by Incorporation of a Chiral Solvent in the Crystal-Lattice. *Aust J Chem* **1989**, *42* (5), 717-730.

(38) Gao, Y. M.; Wang, X. J.; Zhang, J.; Li, M.; Liu, C. X.; An, J.; Jiang, L.; Xiang, W. S. Borrelidin, a Potent Antifungal Agent: Insight into the Antifungal Mechanism against Phytophthora sojae. *J Agr Food Chem* **2012**, *60* (39), 9874-9881.

(39) Kawamura, T.; Liu, D.; Towle, J.; Kageyama, R.; Tsukahara, N.; Wakabayashi, T.; Littlefield, B. A. Anti-angiogenesis effects of borrelidin are mediated through distinct pathways: Threonyl-tRNA synthetase and caspases are independently involved in suppression of proliferation and induction of apoptosis in endothelial cells. *J Antibiot* **2003**, *56* (8), 709-715.

(40) Dickinson, L.; Griffiths, A. J.; Mason, C. G.; Mills, R. F. N. Anti-Viral Activity of 2 Antibiotics Isolated from a Species of Streptomyces. *Nature* **1965**, *206* (4981), 265-+.

(41) Azcarate, I. G.; Marin-Garcia, P.; Camacho, N.; Perez-Benavente, S.; Puyet, A.; Diez, A.; de Pouplana, L. R.; Bautista, J. M. Insights into the preclinical treatment of blood-stage malaria by the antibiotic borrelidin. *Brit J Pharmacol* **2013**, *169* (3), 645-658.

(42) Gafiuc, D.; Weiss, M.; Mylonas, I.; Bruning, A. Borrelidin has limited anti-cancer effects in bcl-2 overexpressing breast cancer and leukemia cells and reveals toxicity in non-malignant breast epithelial cells. *J Appl Toxicol* **2014**, *34* (10), 1109-1113.

(43) Paetz, W.; Nass, G. Biochemical and Immunological Characterization of Threonyl-Transfer-Rna Synthetase of 2 Borrelidin-Resistant Mutants of Escherichia-Coli K-12. *Eur J Biochem* **1973**, *35* (2), 331-337.

(44) Gantt, J. S.; Bennett, C. A.; Arfin, S. M. Increased Levels of Threonyl-Transfer Rna-Synthetase in a Borrelidin-Resistant Chinese-Hamster Ovary Cell-Line. *P Natl Acad Sci-Biol* **1981**, *78* (9), 5367-5370.

(45) Olano, C.; Wilkinson, B.; Sanchez, C.; Moss, S. J.; Sheridan, R.; Math, V.; Weston, A. J.; Brana, A. F.; Martin, C. J.; Oliynyk, M.; et al. Biosynthesis of the angiogenesis inhibitor borrelidin by Streptomyces parvulus Tu4055: Cluster analysis and assignment of functions. *Chem Biol* **2004**, *11* (1), 87-97.

(46) Schulze, C. J.; Bray, W. M.; Loganzo, F.; Lam, M. H.; Szal, T.; Villalobos, A.; Koehn, F. E.; Linington, R. G. Borrelidin B: Isolation, Biological Activity, and Implications for Nitrile Biosynthesis. *J Nat Prod* **2014**, *77* (11), 2570-2574.

(47) Kim, J.; Shin, D.; Kim, S. H.; Park, W.; Shin, Y.; Kim, W. K.; Lee, S. K.; Oh, K. B.; Shin, J.; Oh, D. C. Borrelidins C-E: New Antibacterial Macrolides from a Saltern-Derived Halophilic Nocardiopsis sp. *Mar Drugs* **2017**, *15* (6).

(48) Sun, J. B.; Shao, J. L.; Sun, C. L.; Song, Y. X.; Li, Q. L.; Lu, L. C.; Hu, Y. F.; Gui, C.; Zhang, H.; Ju, J. H. Borrelidins F-I, cytotoxic and cell migration inhibiting agents from mangrove-derived Streptomyces rochei SCSIO ZJ89. *Bioorgan Med Chem* **2018**, *26* (8), 1488-1494.

(49) Zhang, L.; Shi, J.; Liu, C. L.; Xiang, L.; Ma, S. Y.; Li, W.; Jiao, R. H.; Tan, R. X.; Ge, H. M. New borrelidin derivatives from an endophytic Streptomyces sp. *Tetrahedron Lett* **2018**, *59* (51), 4517-4520.

(50) Zhou, Z.; Wu, Q.; Xie, Q.; Ling, C.; Zhang, H.; Sun, C.; Ju, J. New Borrelidins from Onchidium sp. Associated Streptomyces olivaceus SCSIO LO13. *Chem Biodivers* **2020**, *17* (1), e1900560.

(51) Takatsuki, A.; Arima, K.; Tamura, G. Tunicamycin, a New Antibiotic .1. Isolation and Characterization of Tunicamycin. *J Antibiot* **1971**, *24* (4), 215-+.

(52) Takatsuki, A.; Kawamura, K.; Okina, M.; Kodama, Y.; Ito, T.; Tamura, G. Structural Elucidation of Tunicamycin .2. Structure of Tunicamycin. *Agr Biol Chem Tokyo* **1977**, *41* (11), 2307-2309.

(53) Tonew, E.; Tonew, M.; Eckardt, K.; Thrum, H.; Gumpert, B. Streptovirudins - New Antibiotics with Antiviral Activity - Antiviral Spectrum and Inhibition of Newcastle-Disease Virus in Cell-Cultures. *Acta Virol* **1975**, *19* (4), 311-317.

(54) Vogel, P.; Petterson, D. S.; Berry, P. H.; Frahn, J. L.; Anderton, N.; Cockrum, P. A.; Edgar, J. A.; Jago, M. V.; Lanigan, G. W.; Payne, A. L.; et al. Isolation of a Group of Glycolipid Toxins from Seedheads of Annual Ryegrass (Lolium-Rigidum Gaud) Infected by Corynebacterium-Rathayi. *Aust J Exp Biol Med* **1981**, *59* (Aug), 455-467.

(55) Kenig, M.; Reading, C. Holomycin and an Antibiotic (Mm-19290) Related to Tunicamycin, Metabolites of Streptomyces-Clavuligerus. *J Antibiot* **1979**, *32* (6), 549-554.

(56) Nakamura, S.; Arai, M.; Karasawa, K.; Yonehara, H. On an Antibiotic, Mycospocidin. *J Antibiot* **1957**, *10* (6), 248-253.

(57) Mizuno, M.; Shimojima, Y.; Sugawara, T.; Takeda, I. Antibiotic 24010. *J Antibiot* **1971**, *24* (12), 896-+.

(58) Brandish, P. E.; Kimura, K.; Inukai, M.; Southgate, R.; Lonsdale, J. T.; Bugg, T. D. H. Modes of action of tunicamycin, liposidomycin B, and mureidomycin A: Inhibition of phospho-

N-acetylmuramyl-pentapeptide translocase from Escherichia coli. *Antimicrob Agents Ch* **1996**, *40* (7), 1640-1644.

(59) Heifetz, A.; Keenan, R. W.; Elbein, A. D. Mechanism of Action of Tunicamycin on the Udp-Glcnac-Dolichyl-Phosphate Glcnac-1-Phosphate Transferase. *Biochemistry-Us* **1979**, *18* (11), 2186-2192.

(60) Elbein, A. D. The Tunicamycins - Useful Tools for Studies on Glycoproteins. *Trends Biochem Sci* **1981**, *6* (8), 219-221.

(61) Kanatomo, S.; Nagai, S.; Ohki, K.; Yasuda, Y. Study on Surfactin, a Cyclic Depsipeptide .1. Isolation and Structure of 8 Surfactin Analogs Produced by Bacillus-Natto Kmd-2311. *Yakugaku Zasshi* **1995**, *115* (9), 756-764.

(62) Robertson, A. W.; Sandoval, J.; Mohamed, O. G.; Zhuang, Y. H.; Gallagher, E. E.; Schmidt, J.; Caratelli, L.; Menon, A.; Schultz, P. J.; Torrez, R. M.; et al. Discovery of Surfactins as Inhibitors of MicroRNA Processing Using Cat-ELCCA. *Acs Med Chem Lett* **2021**, *12* (6), 878-886.

(63) Edgar, J. A.; Frahn, J. L.; Cockrum, P. A.; Anderton, N.; Jago, M. V.; Culvenor, C. C. J.; Jones, A. J.; Murray, K.; Shaw, K. J. Corynetoxins, Causative Agents of Annual Ryegrass Toxicity - Their Identification as Tunicamycin Group Antibiotics. *J Chem Soc Chem Comm* **1982**, (4), 222-224.

(64) Omura, T.; Sato, R. Carbon Monoxide-Binding Pigment of Liver Microsomes .I. Evidence for Its Hemoprotein Nature. *J Biol Chem* **1964**, *239* (7), 2370-+.

(65) *Gaussian 16 Rev. C.01*; Wallingford, CT, 2016. (accessed.

(66) Bruhn, T.; Schaumloffel, A.; Hemberger, Y.; Bringmann, G. SpecDis: Quantifying the Comparison of Calculated and Experimental Electronic Circular Dichroism Spectra. *Chirality* **2013**, *25* (4), 243-249.

Appendices

Appendix A: Compound Data

(Please see Appendix B for all the NMR data)

1,6-phenazinediol (**1**): yellow solid; HRESIMS of $C_{12}H_9N_2O_2$ $[M+H]^+$ (*m/z*: found 213.06817, calcd 213.06640), Δppm=8.30; HRESIMS of $C_{12}H_7N_2O_2$ $[M-H]^-$ (*m/z*: found 211.05063, calcd 211.05075), Δppm=-0.57.

baraphenazine F (**2**): dark yellow solid; UV (MeOH) λ_{max} (log ε) 214 (3.55), 259 (3.65), 278.5 (3.67), 370 (2.78) nm; ECD (c 2.14×10^{-4} M, MeOH) λ_{max} ($\Delta\varepsilon$) 219.5 (+7.25), 230 (+2.27), 254 (-55.06), 273.5 (+25.53), 298.5 (+6.88), 322 (+4.63) nm; HRESIMS of $C_{25}H_{17}N_4O_6$ $[M+H]^+$ (*m/z*: found 469.11443, calcd 469.11481), Δppm=-0.81; HRESIMS of $C_{25}H_{15}N_4O_6$ $[M-H]^-$ (*m/z*: found 467.10357, calcd 467.09916), Δppm=9.44.

baraphenazine H (**3**): dark red solid; UV (MeOH) λ_{max} (log ε) 217.5 (3.53), 258 (3.73), 274 (3.64), 303 (3.35) nm; ECD (c 2.14×10^{-4} M, MeOH) λ_{max} ($\Delta\varepsilon$) 206.5 (-1.58), 222 (+9.83), 230 (+2.99), 249 (-41.45), 273 (+23.61), 326 (+5.35) nm; HRESIMS of $C_{25}H_{17}N_4O_6$ $[M+H]^+$ (*m/z*: found 469.11485, calcd 469.11481), Δppm=0.09; HRESIMS of $C_{25}H_{15}N_4O_6$ $[M-H]^-$ (*m/z*: found 467.10345, calcd 467.09916), Δppm=9.18.

phenazinolin D (**4**): yellow-orange solid; UV (MeOH) λ_{max} (log ε) 217.5 (3.50), 261 (3.69), 272 (3.65), 320 (2.90), 396.5 (2.90) nm; ECD (*c* 2.14×10^{-4} M, MeOH) λ_{max} ($\Delta\varepsilon$) 207.5 (-2.12), 223.5 (+14.15), 251.5 (+86.85), 273 (-55.91), 280.5 (-59.70) nm; HRESIMS of $C_{25}H_{17}N_4O_6$ $[M+H]^+$ (*m/z*: found 469.11552, calcd 469.11481), Δppm=1.51; HRESIMS of $C_{25}H_{15}N_4O_6$ $[M-H]^-$ (*m/z*: found 467.09928, calcd 467.09916), Δppm=0.26.

izumiphenazine A (**5**): orange-red solid; UV (MeOH) λ_{max} (log ε) 216.5 (3.21), 261.5 (3.42), 275.5 (3.41), 328 (2.52), 393 (2.52) nm; ECD (*c* 2.14×10^{-4} M, MeOH) λ_{max} ($\Delta\varepsilon$) 212.5 (+0.83), 254.5 (+22.19), 274 (-20.39) nm; HRESIMS of $C_{25}H_{17}N_4O_6$ $[M+H]^+$ (*m/z*: found 469.11489, calcd 469.11481), Δppm=0.17; HRESIMS of $C_{25}H_{15}N_4O_6$ $[M-H]^-$ (*m/z*: found 467.10001, calcd 467.09916), Δppm=1.82.

izumiphenazine E (**6**): brown solid; UV (MeOH) λ_{max} (log ε) 218 (3.56), 258 (3.65), 272 (3.62), 328 (2.87) nm; ECD (*c* 2.14×10^{-4} M, MeOH) λ_{max} ($\Delta\varepsilon$) 210 (-0.57), 249 (+20.90), 273 (-15.01), 286 (-17.89) nm; HRESIMS of $C_{25}H_{17}N_4O_6$ $[M+H]^+$ (*m/z*: found 469.11461, calcd 469.11481), Δppm=-0.43; HRESIMS of $C_{25}H_{15}N_4O_6$ $[M-H]^-$ (*m/z*: found 467.09489, calcd 467.09916), Δppm=-9.14.

baraphenazine G (**7**): orange-red solid; UV (MeOH) λ_{max} (log ε) 218 (3.55), 261.5 (3.68), 276 (3.64) nm; ECD (*c* 2.14×10^{-4} M, MeOH) λ_{max} ($\Delta\varepsilon$) 208 (-6.71), 224 (+7.44), 251 (+74.14), 272 (-47.31), 283 (-54.66) nm; HRESIMS of $C_{25}H_{17}N_4O_6$ $[M+H]^+$ (*m/z*: found 469.11545, calcd

469.11481), Δppm=1.36; HRESIMS of $C_{25}H_{15}N_4O_6$ $[M-H]^-$ (*m/z*: found 467.10202, calcd 467.09916), Δppm=6.12.

baraphenazine I (**8**): red solid; HRESIMS of $C_{25}H_{15}N_4O_6$ $[M+H]^+$ (*m/z*: found 467.09791, calcd 467.09916) Δppm=-2.68; HRESIMS of $C_{25}H_{13}N_4O_6$ $[M-H]^-$ (*m/z*: found 465.08699, calcd 465.08351), Δppm=7.48.

ikarugamycin (**9**): light-yellow solid; UV: λ_{max} 238, 320 nm; HRESIMS of $C_{29}H_{39}N_2O_4$ $[M+H]^+$ (*m/z*: found 479.2903, calcd 479.2910), Δppm=-1.46; HRESIMS of $C_{29}H_{37}N_2O_4$ $[M-H]^-$ (*m/z*: found 477.2703, calcd 477.2753), Δppm=-10.48.

epoxyikarugamycin (**10**): light-yellow solid; UV: λ_{max} 239, 312 nm; HRESIMS of $C_{29}H_{39}N_2O_5$ $[M+H]^+$ (*m/z*: found 495.2799, calcd 495.2859), Δppm=-12.11; HRESIMS of $C_{29}H_{37}N_2O_5$ $[M-H]^-$ (*m/z*: found 493.2667, calcd 493.2702), Δppm=-7.09.

capsimycin G (**11**): yellow-brown solid; UV: λ_{max} 209, 325 nm; HRESIMS of $C_{29}H_{39}N_2O_6$ $[M+H]^+$ (*m/z*: found 511.2806, calcd 511.2808), Δppm=-0.39; HRESIMS of $C_{29}H_{37}N_2O_6$ $[M-H]^-$ (*m/z*: found 509.2605, calcd 509.2652), Δppm=-9.23.

capsimycin (**12**): yellow-brown solid; UV: λ_{max} 236, 318 nm; HRESIMS of $C_{30}H_{41}N_2O_6$ $[M+H]^+$ (*m/z*: found 525.2969, calcd 525.2965), Δppm=0.76; HRESIMS of $C_{30}H_{39}N_2O_6$ $[M-H]^-$ (*m/z*: found 523.2757, calcd 523.2808), Δppm=-9.46.

capsimycin H (**13**): yellow-brown solid; UV: λ_{max} 240, 315 nm; HRESIMS of $C_{30}H_{41}N_2O_7$ $[M+H]^+$ (*m/z*: found 541.2867, calcd 541.2914), Δppm=-8.68; HRESIMS of $C_{30}H_{39}N_2O_7$ $[M-H]^-$ (*m/z*: found 539.2773, calcd 539.2757), Δppm=2.97.

hydroxyikarugamycin A (**14**): brown solid; UV: λ_{max} 230, 326 nm; HRESIMS of $C_{30}H_{43}N_2O_8$ $[M+H]^+$ (*m/z*: found 559.2969, calcd 559.3019), Δppm=-8.94; HRESIMS of $C_{30}H_{41}N_2O_8$ $[M-H]^-$ (*m/z*: found 557.2885, calcd 557.2863), Δppm=3.95.

hydroxyikarugamycin A-2 (**15**): brown solid; UV: λ_{max} 228, 329 nm; HRESIMS of $C_{30}H_{41}N_2O_8$ $[M-H]^-$ (*m/z*: found 557.2864, calcd 557.2863), Δppm=0.18.

hydroxyikarugamycin B (**16**): brown solid; UV: λ_{max} 229, 328 nm; HRESIMS of $C_{30}H_{43}N_2O_7$ $[M+H]^+$ (*m/z*: found 543.3003, calcd 543.3070), Δppm=-12.33; HRESIMS of $C_{30}H_{41}N_2O_7$ $[M-H]^-$ (*m/z*: found 541.2944, calcd 541.2914), Δppm=-5.54.

hydroxyikarugamycin B-2 (**17**): brown solid; UV: λ_{max} 222, 325 nm; HRESIMS of $C_{30}H_{43}N_2O_7$ $[M+H]^+$ (*m/z*: found 543.3003, calcd 543.3070), Δppm=-14.17; HRESIMS of $C_{30}H_{41}N_2O_7$ $[M-H]^-$ (*m/z*: found 541.2864, calcd 541.2914), Δppm=-14.78.

hydroxyikarugamycin C (**18**): brown solid; UV: λ_{max} 221, 327 nm; HRESIMS of $C_{30}H_{41}N_2O_7$ $[M+H]^+$ (*m/z*: found 529.2839, calcd 529.2914), Δppm=-14.17; HRESIMS of $C_{30}H_{39}N_2O_7$ $[M-H]^-$ (*m/z*: found 527.2774, calcd 527.2757), Δppm=3.22.

hydroxyikarugamycin C-2 (**19**): brown solid; UV: λ_{max} 221, 326 nm; HRESIMS of $C_{30}H_{41}N_2O_7$ $[M+H]^+$ (*m/z*: found 529.2839, calcd 529.2914), Δppm=-14.17; HRESIMS of $C_{30}H_{39}N_2O_7$ $[M-H]^-$ (*m/z*: found 527.2695, calcd 527.2757), Δppm=-11.76.

2-aminobenzamide-actiphenol (**20**): yellow solid; UV: λ_{max} 213, 258, 344 nm; HRESIMS of $C_{22}H_{24}N_3O_5$ $[M+H]^+$ (*m/z*: found 410.1684, calcd 410.1716), Δppm=-7.80; HRESIMS of $C_{22}H_{23}N_3O_5$ $[M-H]^-$ (*m/z*: found 408.1569, calcd 408.1559), Δppm=2.45.

methyl phenatate C (**21**): yellow solid; UV: λ_{max} 215, 267, 354 nm; HRESIMS of $C_{16}H_{21}NO_6Na$ $[M+Na]^+$ (*m/z*: found 346.1226, calcd 346.1267), Δppm=-11.85; HRESIMS of $C_{16}H_{20}NO_6$ $[M-H]^-$ (*m/z*: found 322.1304, calcd 322.1291), Δppm=4.04.

actiphenol (**22**): yellow solid; UV: λ_{max} 223, 259, 347 nm; HRESIMS of $C_{15}H_{18}NO_4$ $[M+H]^+$ (*m/z*: found 276.1216, calcd 276.1236), Δppm=-7.24; HRESIMS of $C_{15}H_{16}NO_4$ $[M-H]^-$ (*m/z*: found 274.1073, calcd 274.1079), Δppm=-2.19.

AH-135Y (**23**): yellow solid; UV: λ_{max} 203, 260, 344 nm; HRESIMS of $C_{15}H_{16}NO_5$ $[M-H]^-$ (*m/z*: found 290.1033, calcd 290.1028), Δppm=1.72.

Nong-kang 101-G (**24**): yellow solid; UV: λ_{max} 219, 264, 336 nm; HRESIMS of $C_{15}H_{18}NO_5$ $[M+H]^+$ (*m/z*: found 292.1187, calcd 292.1185), Δppm=0.68; HRESIMS of $C_{15}H_{16}NO_5$ $[M-H]^-$ (*m/z*: found 290.1033, calcd 290.1028), Δppm=1.72.

C-73X (**25**): yellow solid; UV: λ_{max} 220, 268, 355 nm; HRESIMS of $C_{15}H_{18}NO_5$ $[M+H]^+$ (*m/z*: found 292.1153, calcd 292.1185), Δppm=-10.95; HRESIMS of $C_{15}H_{16}NO_5$ $[M-H]^-$ (*m/z*: found 290.1054, calcd 290.1028), Δppm=8.96.

actiketal (**26**): yellow solid; UV: λ_{max} 219, 268, 355 nm; HRESIMS of $C_{15}H_{16}NO_5$ $[M+H]^+$ (*m/z*: found 290.1009, calcd 290.1028), Δppm=-6.55; HRESIMS of $C_{15}H_{14}NO_5$ $[M-H]^-$ (*m/z*: found 288.0882, calcd 288.0872), Δppm=3.47.

methyl phenatate A (**27**): yellow solid; UV: λ_{max} 214, 261, 346 nm; HRESIMS of $C_{15}H_{22}NO_5$ $[M+H]^+$ (*m/z*: found 308.1491, calcd 308.1498), Δppm=-2.27; HRESIMS of $C_{16}H_{20}NO_5$ $[M-H]^-$ (*m/z*: found 306.1344, calcd 282.1705), Δppm=0.98.

cycloheximide (**28**): yellow solid; UV: λ_{max} 202 nm; HRESIMS of $C_{15}H_{24}NO_4$ $[M+H]^+$ (*m/z*: found 282.1713, calcd 282.1705), Δppm=2.84; HRESIMS of $C_{15}H_{22}NO_4$ $[M-H]^-$ (*m/z*: found 280.1557, calcd 280.1549), Δppm=2.86.

cycloheximide-2 (**29**): yellow solid; UV: λ_{max} 200, 295 nm; HRESIMS of $C_{15}H_{24}NO_4$ $[M+H]^+$ (*m/z*: found 282.1703, calcd 282.1705), Δppm=-0.71; HRESIMS of $C_{15}H_{22}NO_4$ $[M-H]^-$ (*m/z*: found 280.1558, calcd 280.1549), Δppm=3.21.

cycloheximide-3 (**30**): yellow solid; UV: λ_{max} 202 nm; HRESIMS of $C_{15}H_{24}NO_4$ $[M+H]^+$ (*m/z*: found 282.1721, calcd 282.1705), Δppm=5.67; HRESIMS of $C_{15}H_{22}NO_4$ $[M-H]^-$ (*m/z*: found 280.1567, calcd 280.1549), Δppm=6.43.

acetoxycycloheximide (**31**): yellow solid; UV: λ_{max} 201 nm; HRESIMS of $C_{17}H_{25}NO_6Na$ $[M+Na]^+$ (*m/z*: found 362.1587, calcd 362.1580), Δppm=1.93; HRESIMS of $C_{17}H_{24}NO_6$ $[M-H]^-$ (*m/z*: found 338.1645, calcd 338.1604), Δppm=12.12.

dipteronine D (**32**): yellow solid; UV: λ_{max} 203, 248 nm; HRESIMS of $C_{15}H_{21}NO_4Na$ $[M+Na]^+$ (*m/z*: found 302.1358, calcd 302.1368), Δppm=-3.31; HRESIMS of $C_{15}H_{20}NO_4$ $[M-H]^-$ (*m/z*: found 278.1397, calcd 278.1392), Δppm=1.80.

cycloheximide acid A (**33**): yellow solid; UV: λ_{max} 203, 220 nm; HRESIMS of $C_{15}H_{21}NO_5Na$ $[M+Na]^+$ (*m/z*: found 318.1314, calcd 318.1317), Δppm=-0.94; HRESIMS of $C_{15}H_{20}NO_5$ $[M-H]^-$ (*m/z*: found 294.1351, calcd 294.1341), Δppm=3.40.

borrelidin (**34**): white powder; UV: λ_{max} 258 nm; HRESIMS of $C_{28}H_{43}NO_6Na$ $[M+Na]^+$ (*m/z*: found 512.2988, calcd 512.2988), Δppm=0.00; HRESIMS of $C_{28}H_{42}NO_6$ $[M-H]^-$ (*m/z*: found 488.2990, calcd 488.3012), Δppm=-4.51.

borrelidin C (**35**): white powder; UV: λ_{max} 258 nm; HRESIMS of $C_{28}H_{43}NO_7Na$ $[M+Na]^+$ (*m/z*: found 528.2942, calcd 528.2937), Δppm=0.95; HRESIMS of $C_{28}H_{42}NO_7$ $[M-H]^-$ (*m/z*: found 504.2983, calcd 504.2961), Δppm=4.36.

borrelidin D (**36**): white powder; UV: λ_{max} 258 nm; HRESIMS of $C_{28}H_{43}NO_7Na$ $[M+Na]^+$ (*m/z*: found 528.2948, calcd 528.2937), Δppm=2.08; HRESIMS of $C_{28}H_{42}NO_7$ $[M-H]^-$ (*m/z*: found 504.2983, calcd 504.2961), Δppm=4.36.

borrelidin E (**37**): white powder; UV: λ_{max} 258 nm; HRESIMS of $C_{28}H_{43}NO_7Na$ $[M+Na]^+$ (*m/z*: found 528.2934, calcd 528.2937), Δppm=-0.57; HRESIMS of $C_{28}H_{42}NO_7$ $[M-H]^-$ (*m/z*: found 504.2983, calcd 504.2961), Δppm=4.36.

borrelidin F (**38**): white powder; UV: λ_{max} 258 nm; HRESIMS of $C_{28}H_{43}NO_6Na$ $[M+Na]^+$ (*m/z*: found 512.2980, calcd 512.2988), Δppm=-1.56; HRESIMS of $C_{28}H_{42}NO_6$ $[M-H]^-$ (*m/z*: found 488.2990, calcd 488.3012), Δppm=-4.51.

borrelidin J (**39**): white powder; UV: λ_{max} 258 nm; HRESIMS of $C_{28}H_{43}NO_7Na$ $[M+Na]^+$ (*m/z*: found 528.2946, calcd 528.2937), Δppm=1.70; HRESIMS of $C_{28}H_{42}NO_7$ $[M-H]^-$ (*m/z*: found 504.2980, calcd 504.2961), Δppm=3.77.

borrelidin K (**40**): white powder; UV: λ_{max} 258 nm; HRESIMS of $C_{28}H_{43}NO_7Na$ $[M+Na]^+$ (*m/z*: found 528.2935, calcd 528.2937), Δppm=-0.38; HRESIMS of $C_{28}H_{42}NO_7$ $[M-H]^-$ (*m/z*: found 504.2983, calcd 504.2961), Δppm=4.36.

borrelidin P (**41**): white powder; UV: λ_{max} 258 nm; HRESIMS of $C_{28}H_{43}NO_7Na$ $[M+Na]^+$ (*m/z*: found 528.2943, calcd 528.2937), Δppm=1.14; HRESIMS of $C_{28}H_{42}NO_7$ $[M-H]^-$ (*m/z*: found 504.2983, calcd 504.2961), Δppm=4.36.

borrelidin Q (**42**): white powder; UV: λ_{max} 258 nm; HRESIMS of $C_{28}H_{43}NO_7Na$ $[M+Na]^+$ (*m/z*: found 528.2938, calcd 528.2937), Δppm=0.19; HRESIMS of $C_{28}H_{42}NO_7$ $[M-H]^-$ (*m/z*: found 504.2906, calcd 504.2961), Δppm=-10.91.

borrelidin R (**43**): white powder; UV: λ_{max} 258 nm; HRESIMS of $C_{28}H_{43}NO_7Na$ $[M+Na]^+$ (*m/z*: found 528.2919, calcd 528.2937), Δppm=-3.14; HRESIMS of $C_{28}H_{42}NO_7$ $[M-H]^-$ (*m/z*: found 504.2975, calcd 504.2961), Δppm=2.78.

borrelidin S (**44**): white powder; UV: λ_{max} 218 nm; HRESIMS of $C_{28}H_{43}NO_7Na$ $[M+Na]^+$ (*m/z*: found 528.2937, calcd 528.2937), Δppm=0.00; HRESIMS of $C_{28}H_{42}NO_7$ $[M-H]^-$ (*m/z*: found 504.2993, calcd 504.2961), Δppm=6.35.

tunicamycin VII (**45**): white powder; UV: λ_{max} 209, 258 nm; HRESIMS of $C_{39}H_{65}N_4O_{16}$ $[M+H]^+$ (*m/z*: found 845.4342, calcd 845.4396), Δppm=-6.39; HRESIMS of $C_{39}H_{63}N_4O_{16}$ $[M-H]^-$ (*m/z*: found 843.4211, calcd 843.4239), Δppm=-3.32.

tunicamycin VIII (**46**): white powder; UV: λ_{max} 209, 258 nm; HRESIMS of $C_{39}H_{65}N_4O_{16}$ $[M+H]^+$ (*m/z*: found 845.4342, calcd 845.4396), Δppm=-6.39; HRESIMS of $C_{39}H_{63}N_4O_{16}$ $[M-H]^-$ (*m/z*: found 843.4211, calcd 843.4239), Δppm=-3.32.

corynetoxin H17a (**47**): white powder; UV: λ_{max} 209, 260 nm; HRESIMS of $C_{40}H_{67}N_4O_{16}$ $[M+H]^+$ (*m/z*: found 859.4559, calcd 859.4552), Δppm=0.81; HRESIMS of $C_{40}H_{65}N_4O_{16}$ $[M-H]^-$ (*m/z*: found 857.4412, calcd 857.4396), Δppm=1.87.

tunicamycin X (**48**): white powder; UV: λ_{max} 209, 260 nm; HRESIMS of $C_{40}H_{67}N_4O_{16}$ $[M+H]^+$ (*m/z*: found 859.4564, calcd 859.4552), Δppm=1.40; HRESIMS of $C_{40}H_{65}N_4O_{16}$ $[M-H]^-$ (*m/z*: found 857.4422, calcd 857.4396), Δppm=3.03.

Appendix B: NMR data of 1–48

(All NMR data were captured in DMSO-d_6)

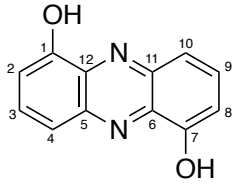

1,6-phenazinediol (**1**)

Position	δ_C (type)	δ_H, multiplets (*J* in Hz)	COSY	HMBC
1	153.3 (C)			
1-OH		10.36, s		
2	109.2 (CH)	7.2, dd (7.5, 1.0)	3, 4	3, 4, 12
3	132.7 (CH)	7.84, dd (8.8, 7.5)	2, 4	1, 5
4	118.7 (CH)	7.69, dd (8.8, 1.1)	2, 3	2, 12
5	143.8 (C)			
6	132.6 (C)			
7	153.3 (C)			
7-OH		10.36, s		
8	109.2 (CH)	7.2, dd (7.5, 1.0)	9, 10	6, 9, 10
9	132.7 (CH)	7.84, dd (8.8, 7.5)	8, 10	7, 11
10	118.7 (CH)	7.69, dd (8.8, 1.1)	8, 9	6, 8
11	143.8 (C)			
12	132.6 (C)			

^{1}H spectrum of 1, 6-phenazinediol (**1**)

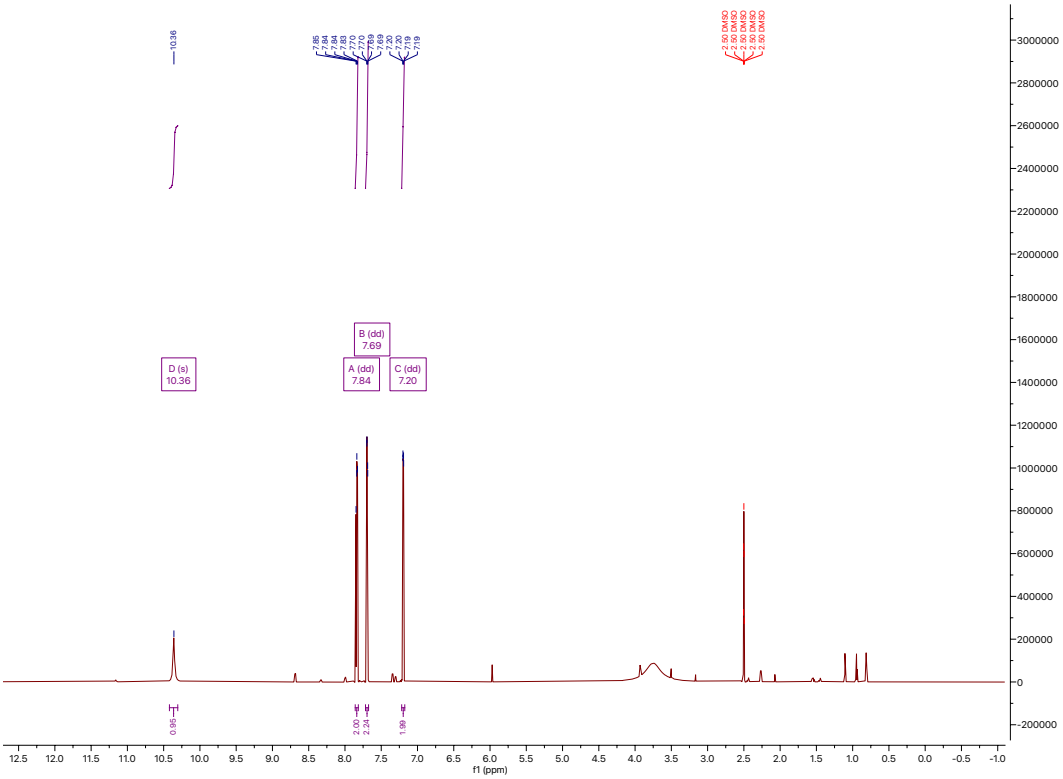

^{13}C spectrum of 1, 6-phenazinediol (**1**)

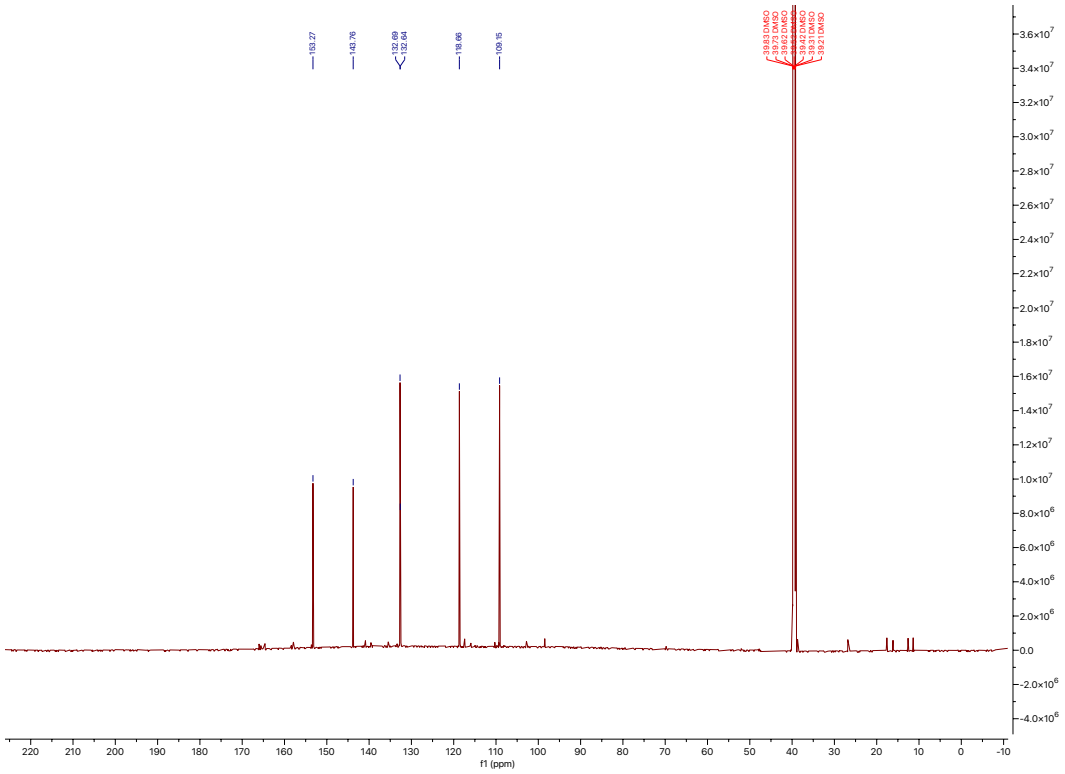

COSY spectrum of 1, 6-phenazinediol (**1**)

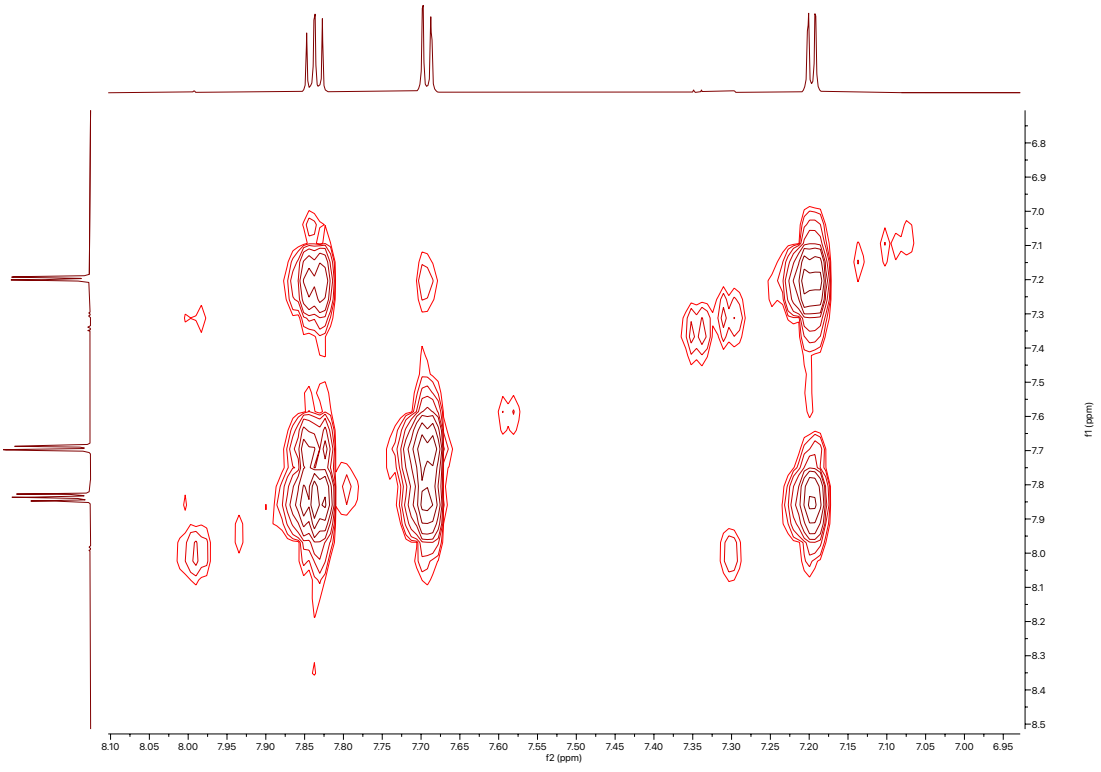

HSQC spectrum of 1, 6-phenazinediol (**1**)

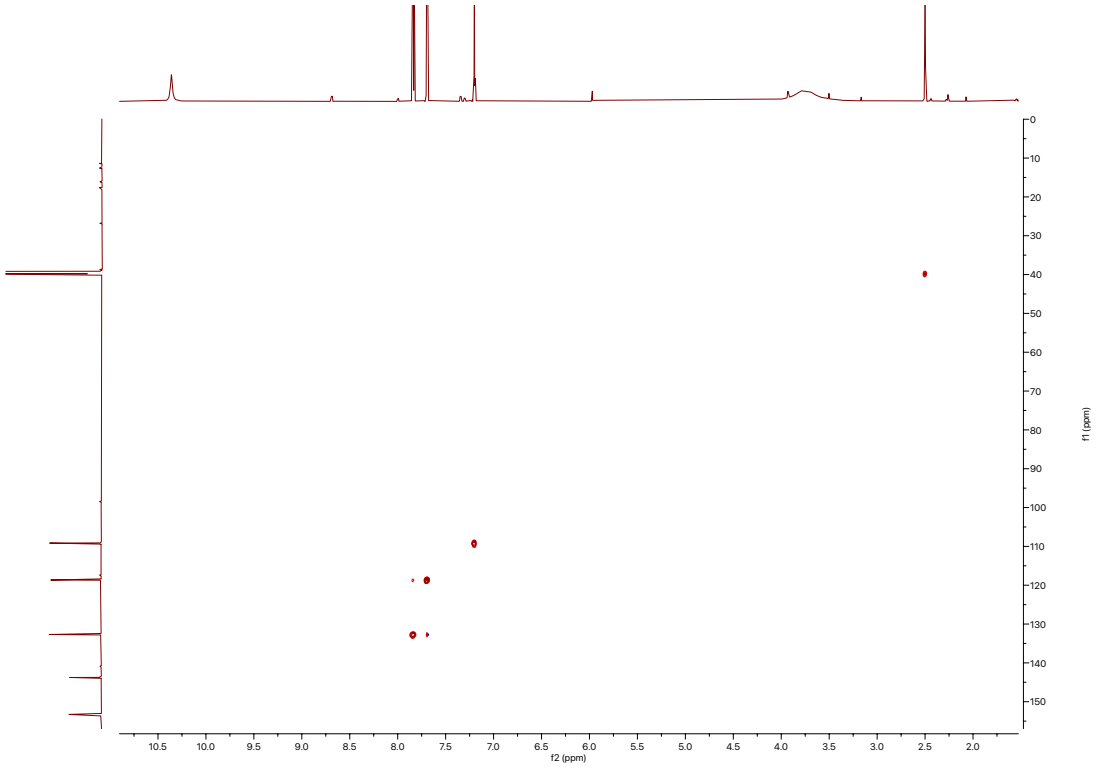

HMBC spectrum of 1, 6-phenazinediol (**1**)

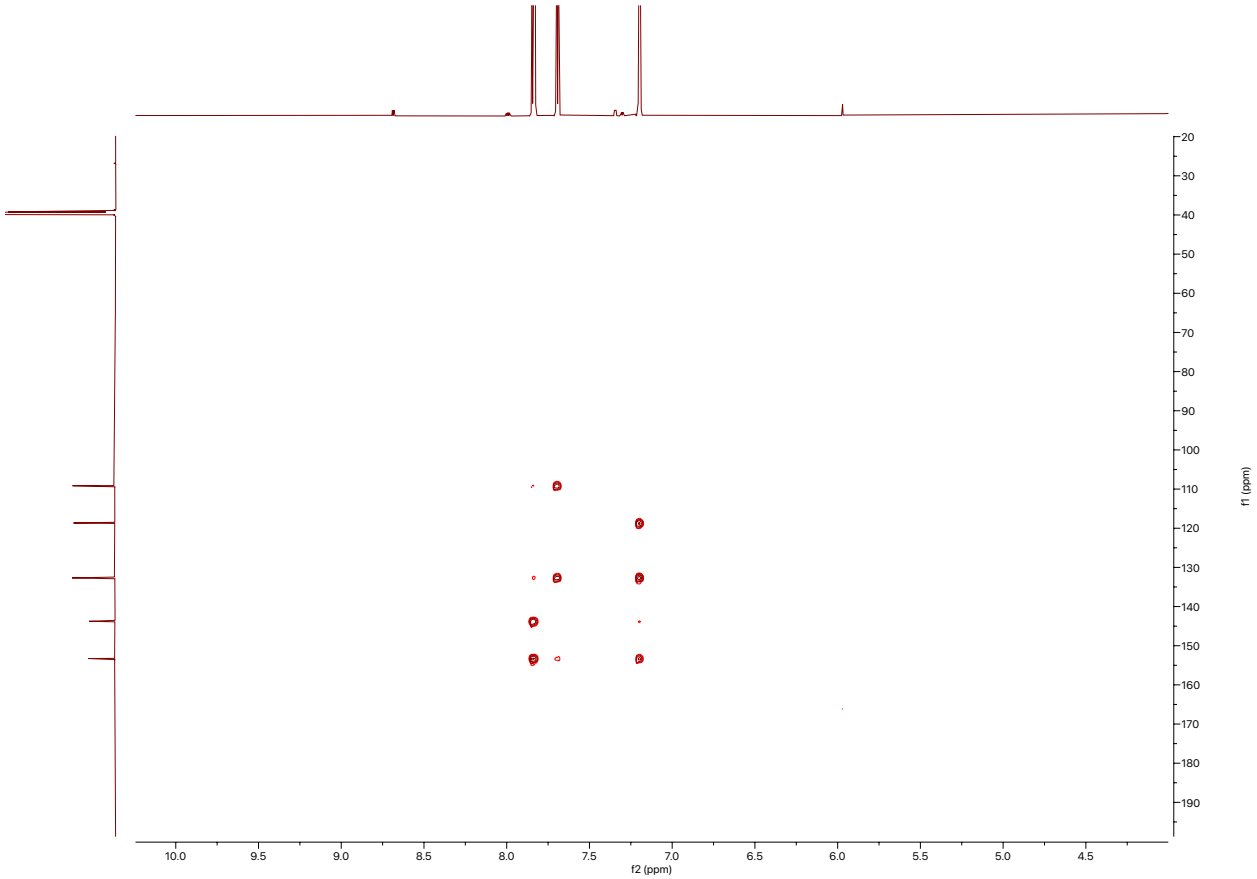

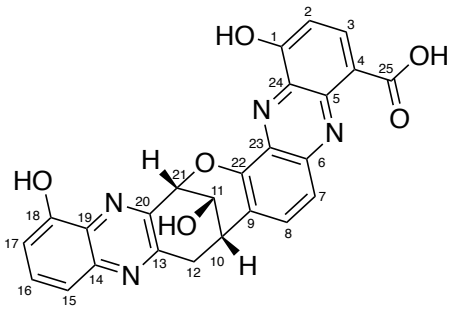

baraphenazine F (**2**)

Position	δ_C (type)	δ_H, multiplets (*J* in Hz)	COSY	HMBC	NOE
1	159.9 (C)				
1-OH		12.03, br s			
2	110.5 (CH)	7.28, d (8.2)	3		
3	139.1 (CH)	8.59, d (8.2)	2	1, 5, 25	
4	114.5 (CH)				
5	140.7 (C)				
6	139.8 (C)				
7	119.8 (CH)	7.89, d (9.0)	8	9, 23	
8	135.8 (CH)	8.06, d (9.1)	7	6, 10, 22	10
9	123 (C)				
10	35.9 (CH)	3.82 - 3.85, m	11, 12a, 12b	9, 13	8, 11, 11-OH
11	63.0 (CH)	4.79, q (3.7)	10, 11-OH, 21		10, 11-OH, 21
11-OH		6.20, d (3.2)	11	10, 21	10, 11, 21
12a	35.5 (CH_2)	3.80, dd (17.6, 5.3)	12b	10	
12b	35.5 (CH_2)	3.39, dd (17.6, 5.3)	10, 12a	9, 10, 11, 13, 20	
13	152.2 (C)				
14	142.8 (C)				
15	117.8 (CH)	7.36, d (8.4)	16	17, 19	
16	131.6 (CH)	7.60, t (8.0)	15, 17	14, 18	
17	111.8 (CH)	7.07, d (7.6)	16	15, 19	
18	153.7 (C)				
18-OH		10.61, s		17, 18, 19	
19	132.6 (C)				
20	146.7 (C)				
21	75.6 (CH)	5.74, dd (3.7, 2.1)	10, 11	20	11, 11-OH
22	146.7 (C)				
23	134.2 (C)				
24	134.2 (C)				
25	165.7 (C)				
25-COOH		14.91, s			

^{1}H spectrum of baraphenazine F (**2**)

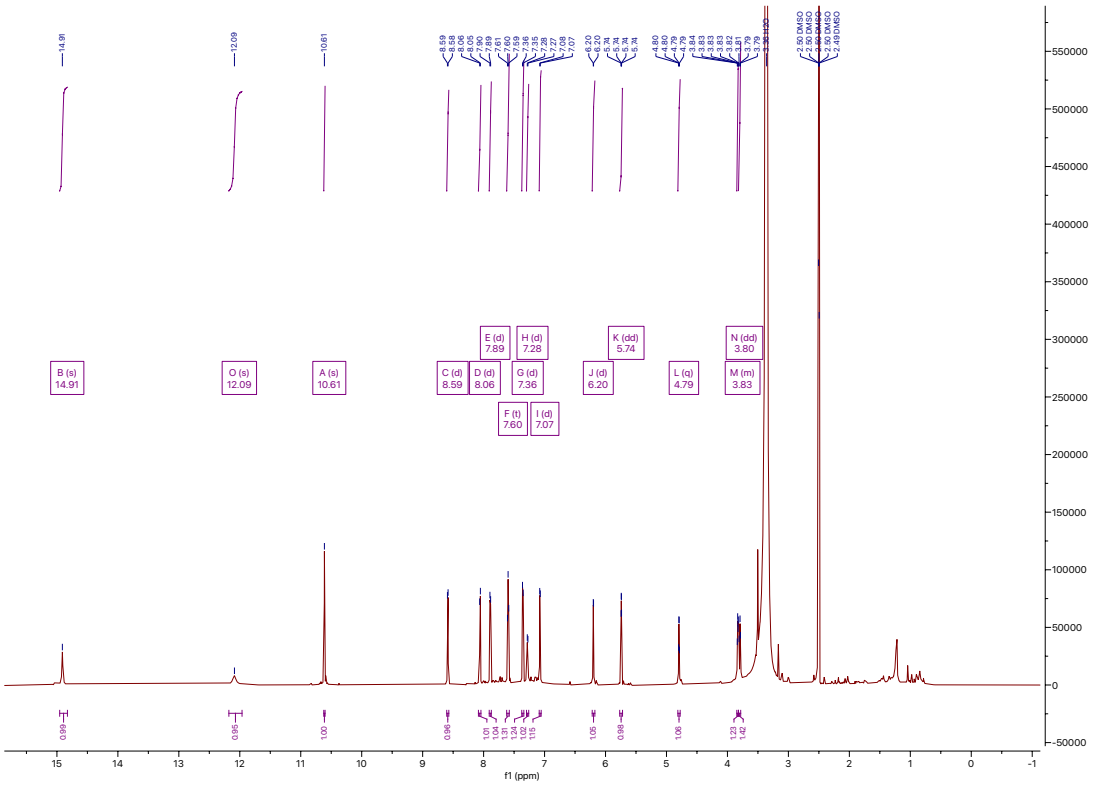

^{13}C spectrum of baraphenazine F (**2**)

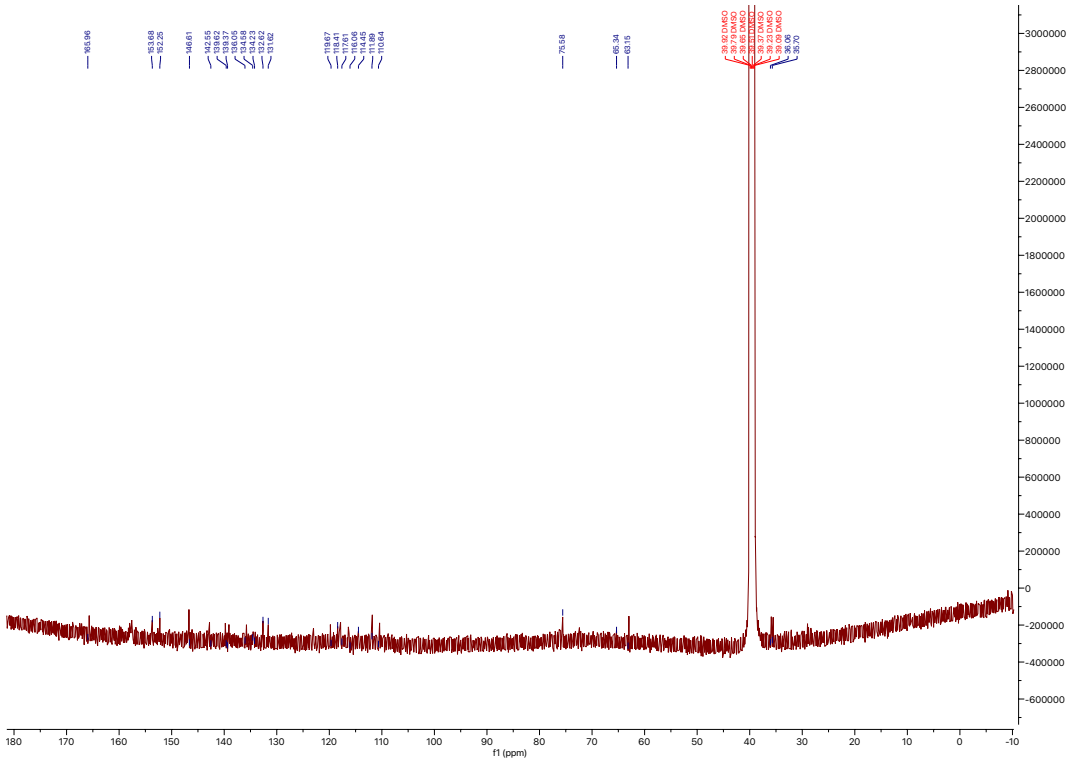

COSY spectrum of baraphenazine F (**2**)

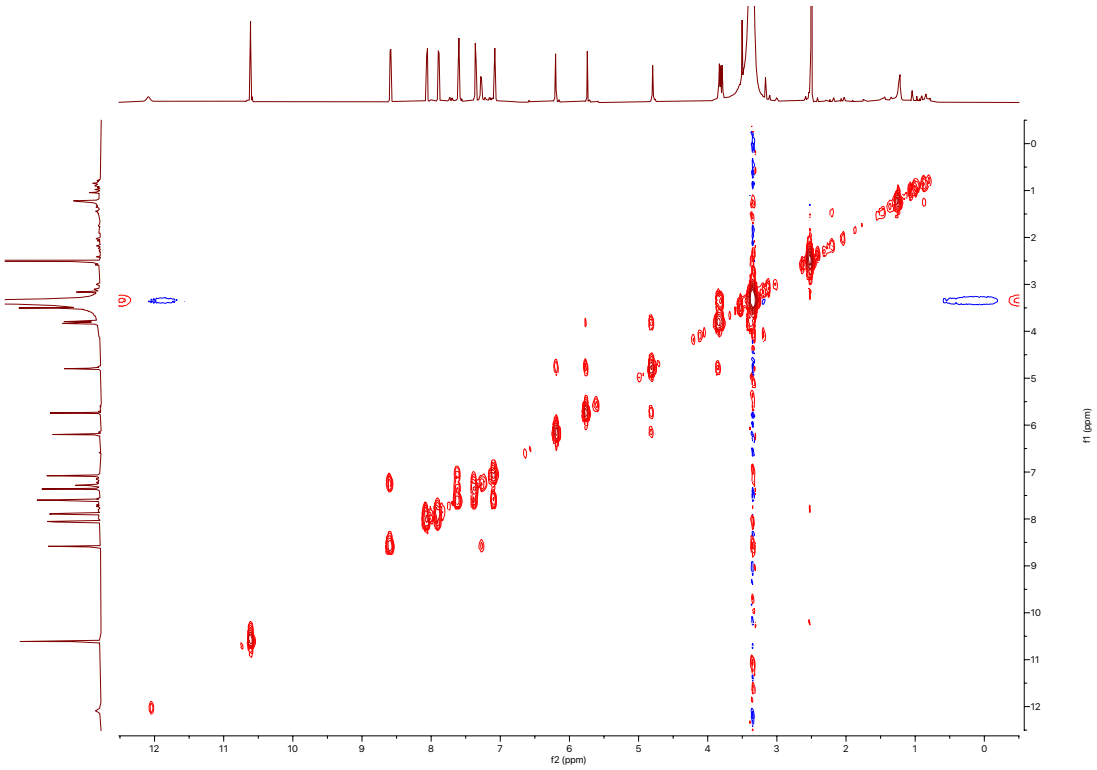

HSQC spectrum of baraphenazine F (**2**)

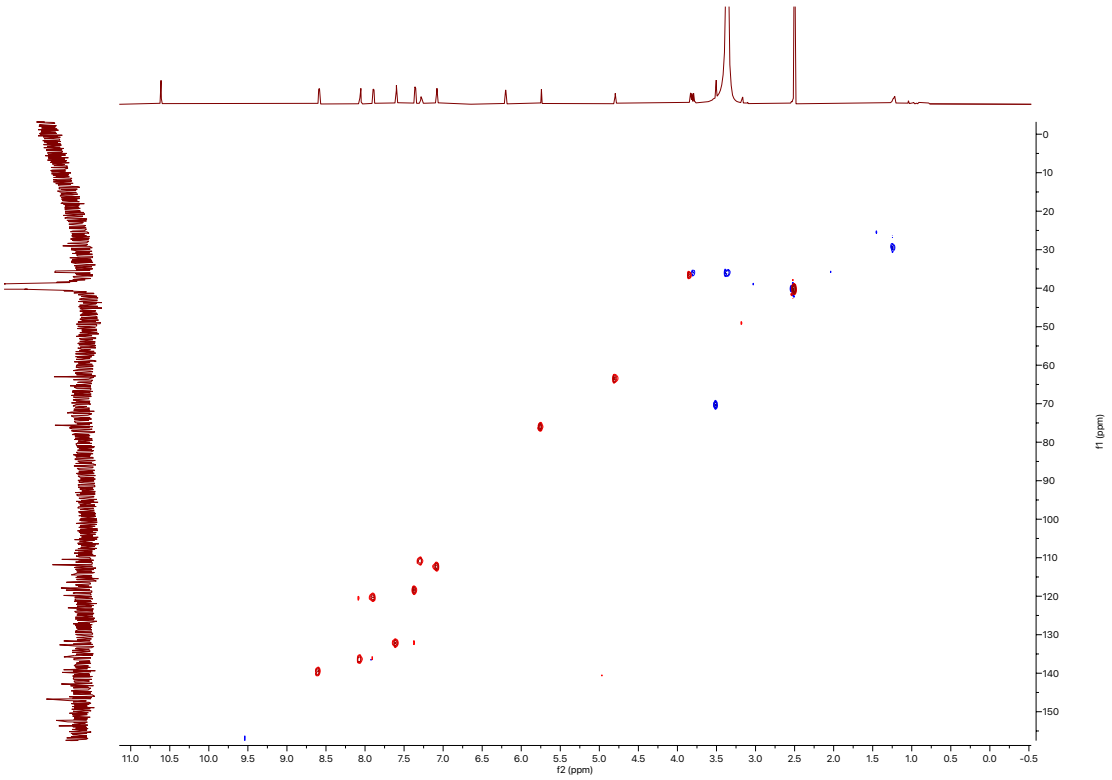

^{1}H-^{13}C HMBC spectrum of baraphenazine F (**2**)

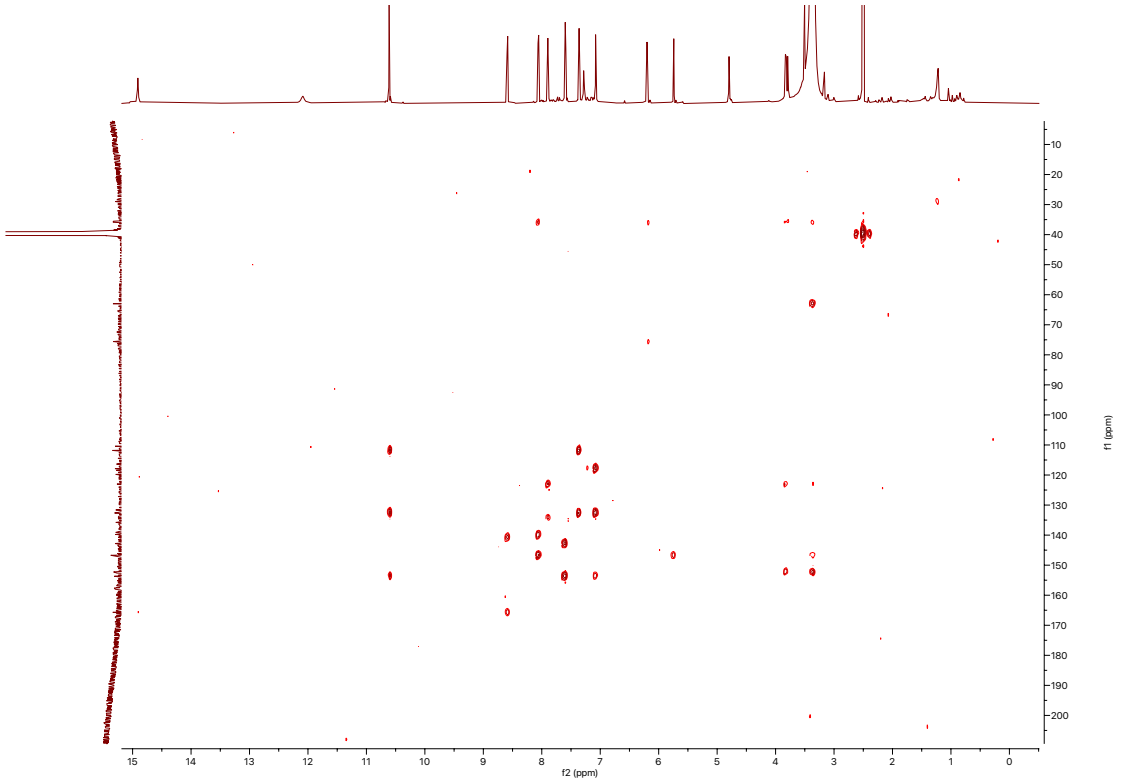

TOCSY spectrum of baraphenazine F (**2**)

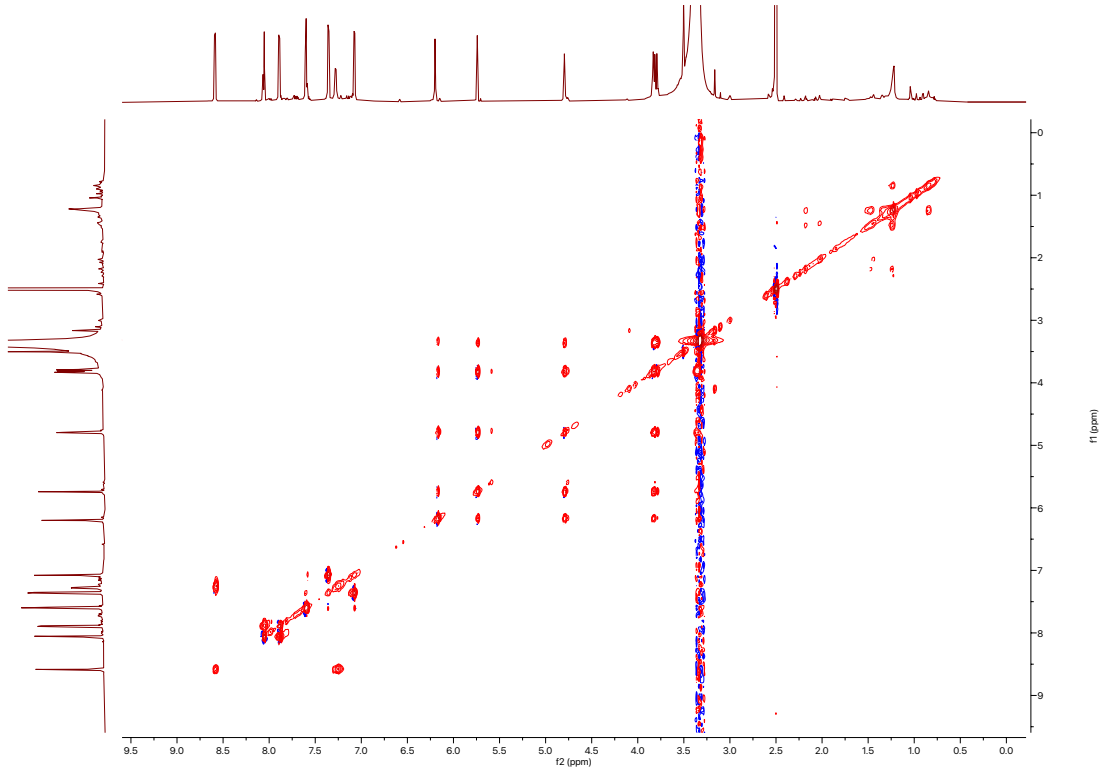

ROESY spectrum of baraphenazine F (**2**)

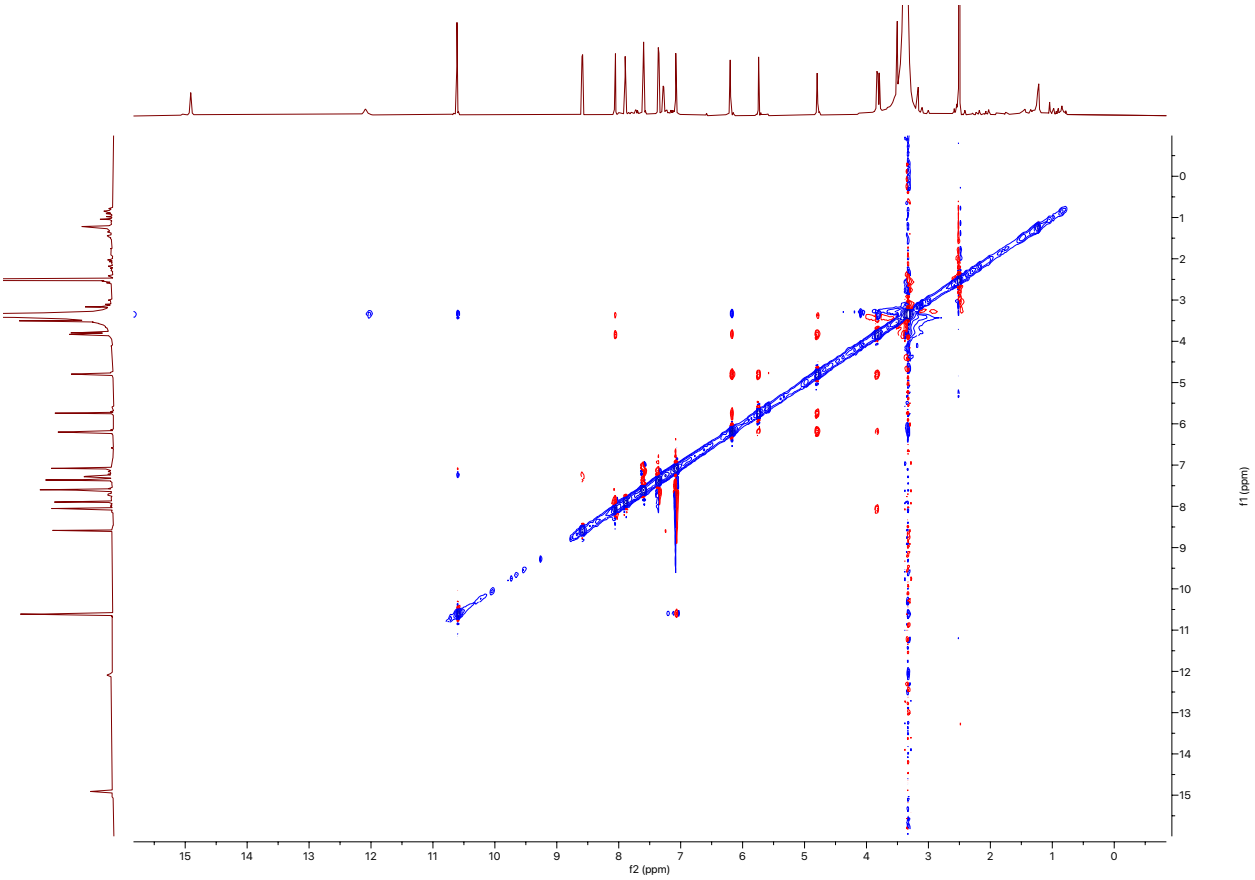
15 14 13 12 11 10 9 8 7 6 5 4 3 2 1 0
f2 (ppm)
0 1 2 3 4 5 6 7 8 9 10 11 12 13 14 15
f1 (ppm)

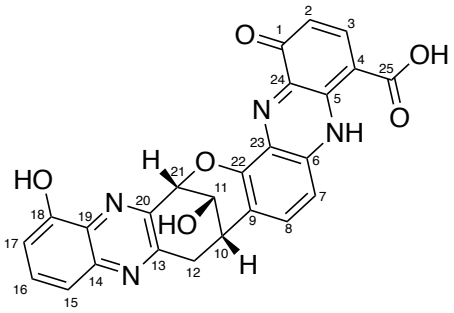

baraphenazine H (**3**)

Position	δ_C (type)	δ_H, multiplets (*J* in Hz)	COSY	HMBC	NOE
1	177.5 (C)				
2	112.7 (CH)	6.15, d (9.3)	3		
3	141.7 (CH)	8.15, d (9.3)	2	1, 5, 25	
4					
5	145.8 (C)				
6	139.7 (C)				
7	118.6 (CH)	7.48, d (8.9)	8	9, 23	
8	134.2 (CH)	7.76, d (8.9)	7	6, 12, 22	10
9	119.6 (C)				
10	36.1 (CH)	3.72, dq (4.9, 2.7, 2.3)	11, 12a, 21	9, 13	8, 11
11	63.8 (CH)	4.74, q (3.4)	10, 11-OH, 21		10, 11-OH, 21
11-OH		6.06, d (3.1)	11		10, 11, 21
12a	36.3 (CH_2)	3.76, dd (17.5, 5.2)	12b	9, 13	
12b	36.3 (CH_2)	3.30	12a	11, 13	
13	153.0 (C)				
14	143.3 (C)				
15	118.3 (CH)	7.36, dd (8.4, 1.3)	16	17, 19	
16	132.1 (CH)	7.61, t (8.0)	15, 17	14, 18	
17	112.5 (CH)	7.05, d (7.7)	16	15, 18, 19	
18	154.2 (C)				
18-OH		10.62, s			
19	133.1 (C)				
20	147.5 (C)				
21	75.7 (CH)	5.66, dd (3.6, 2.0)	10, 11		11, 11-OH
22	147.9 (C)				
23	130.5 (C)				
24					
25	168.1 (C)				
25-COOH		14.95, s		25	

^{1}H spectrum of baraphenazine H (**3**)

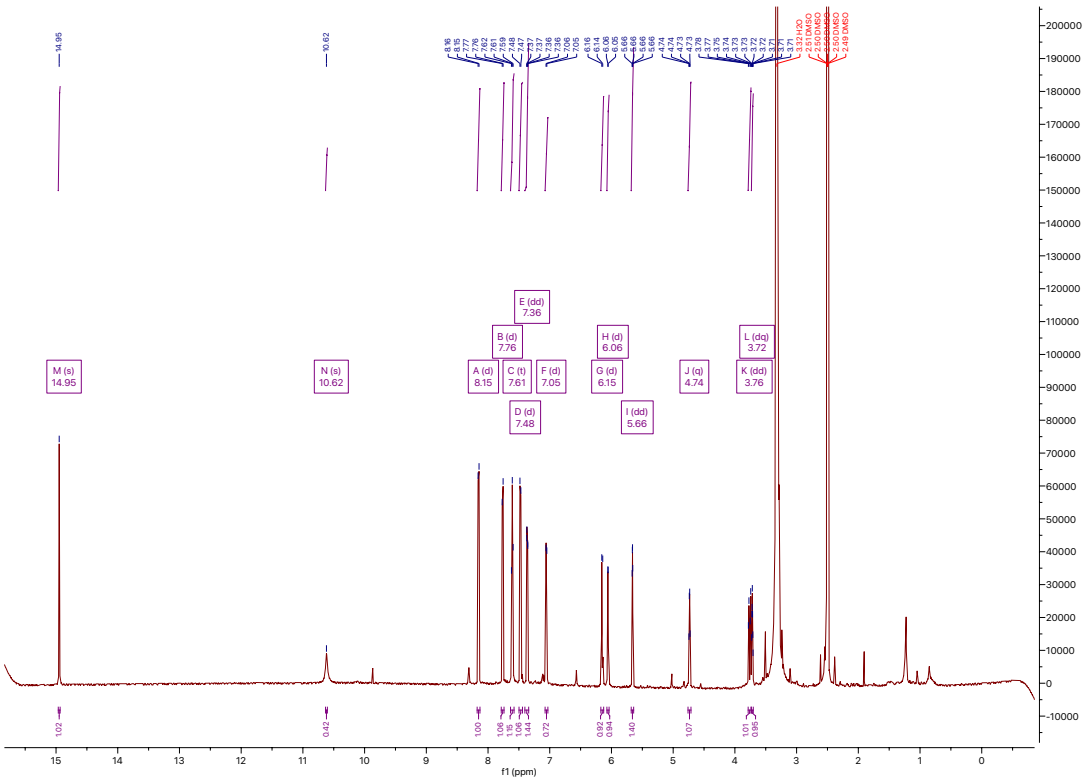

^{13}C spectrum of baraphenazine H (**3**)

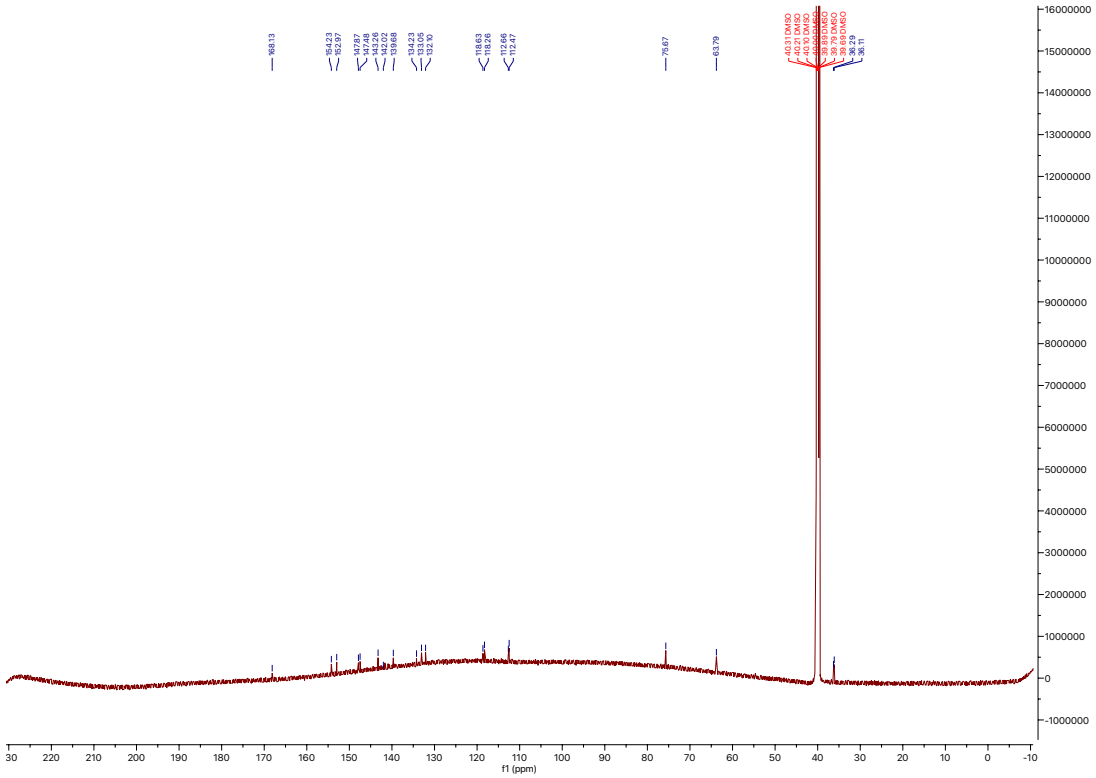

COSY spectrum of baraphenazine H (**3**)

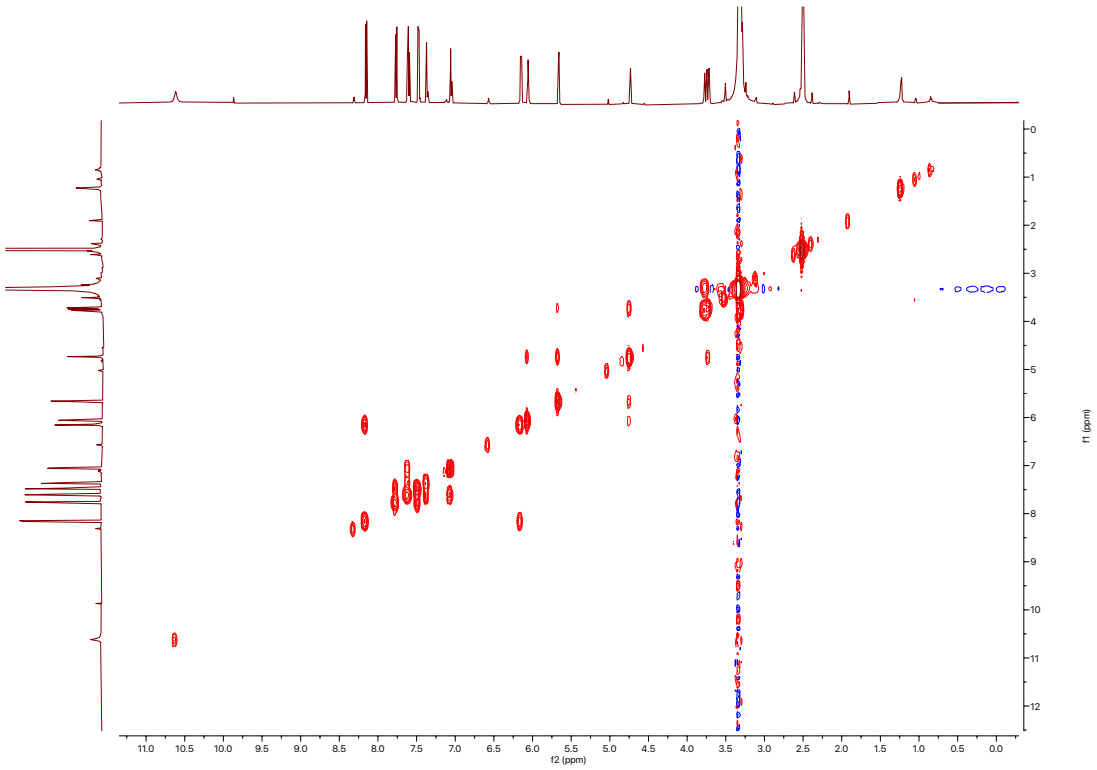

HSQC spectrum of baraphenazine H (**3**)

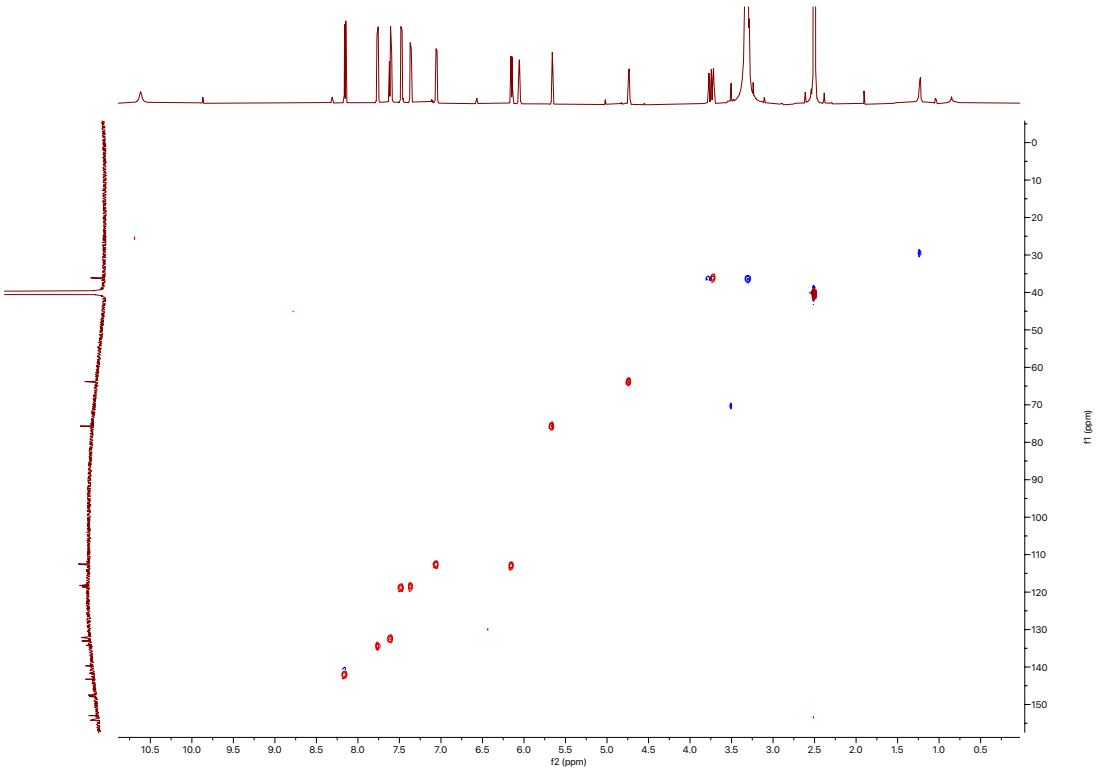

^{1}H-^{13}C HMBC spectrum of baraphenazine H (**3**)

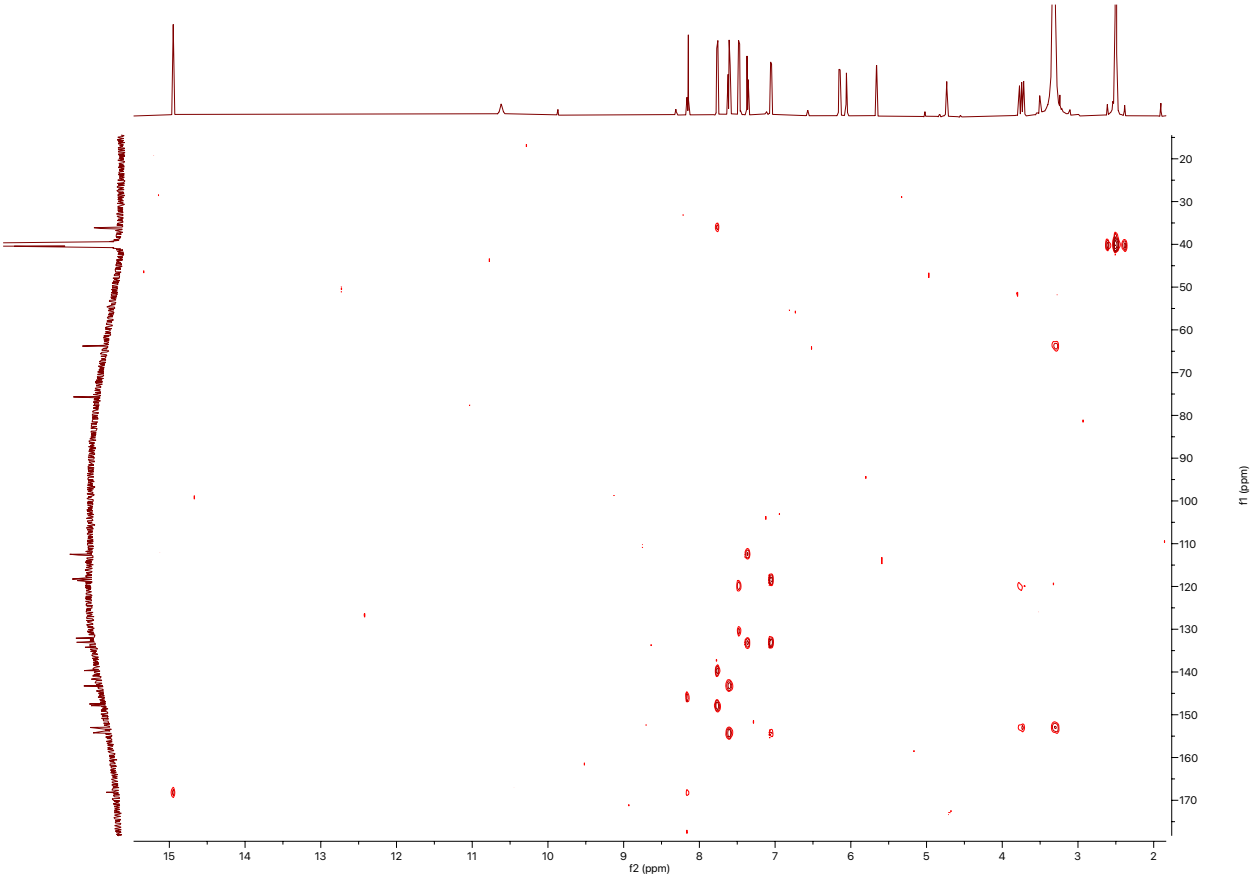

Close-up view of ^{1}H-^{13}C HMBC correlations in the aromatic region of baraphenazine H (**3**)

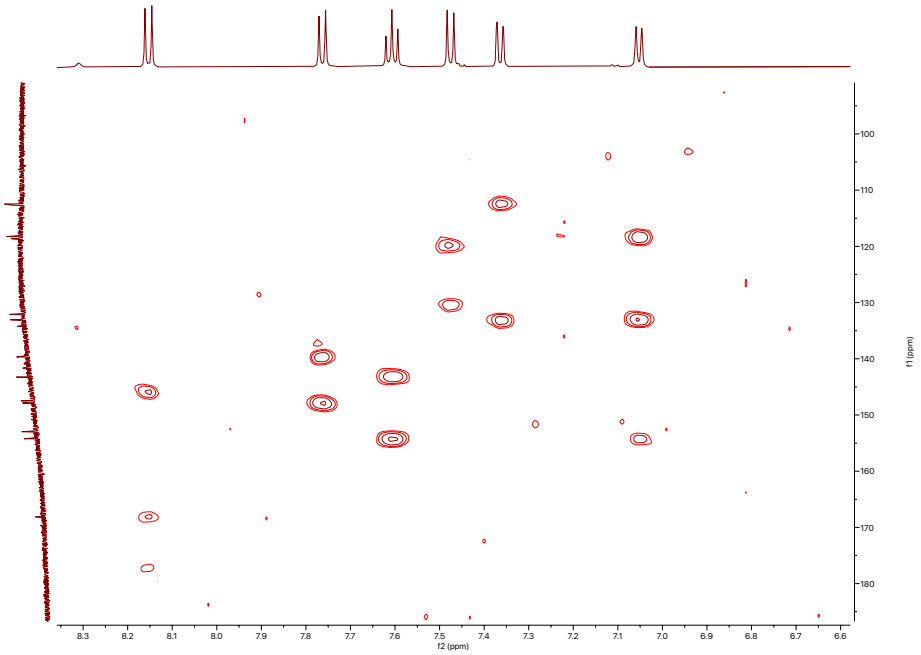

TOCSY spectrum of baraphenazine H (**3**)

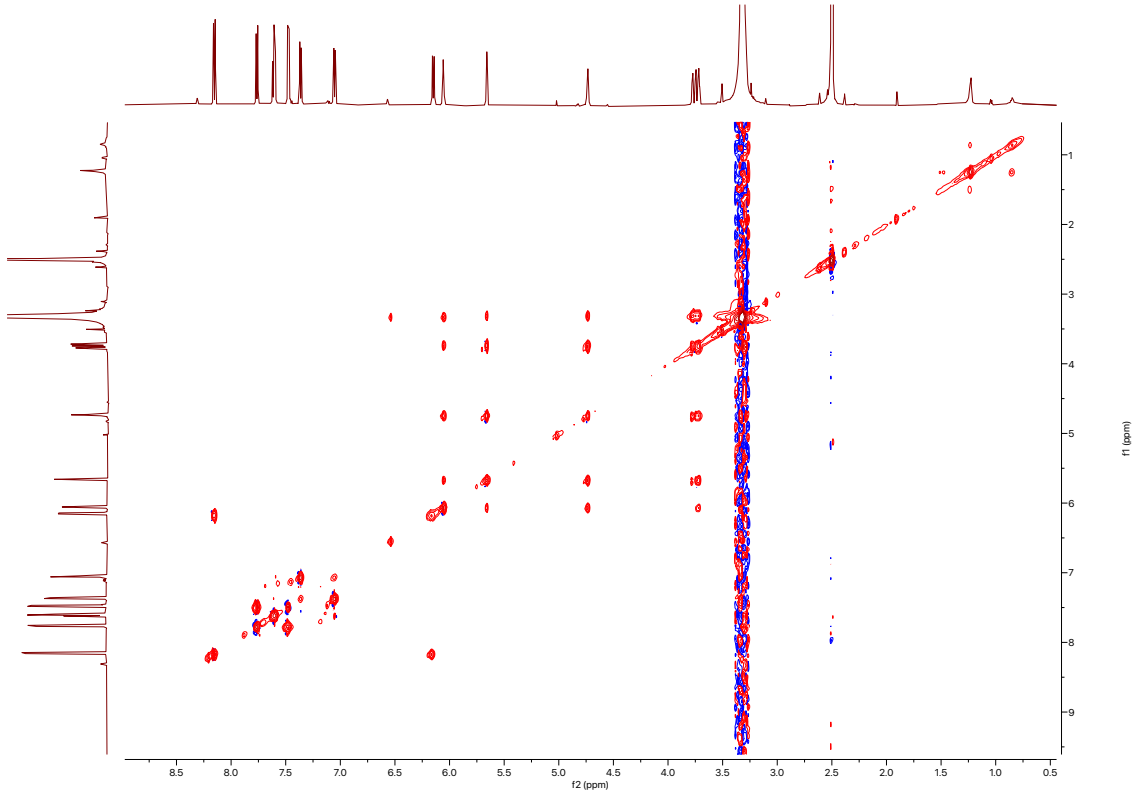

ROESY spectrum of baraphenazine H (**3**)

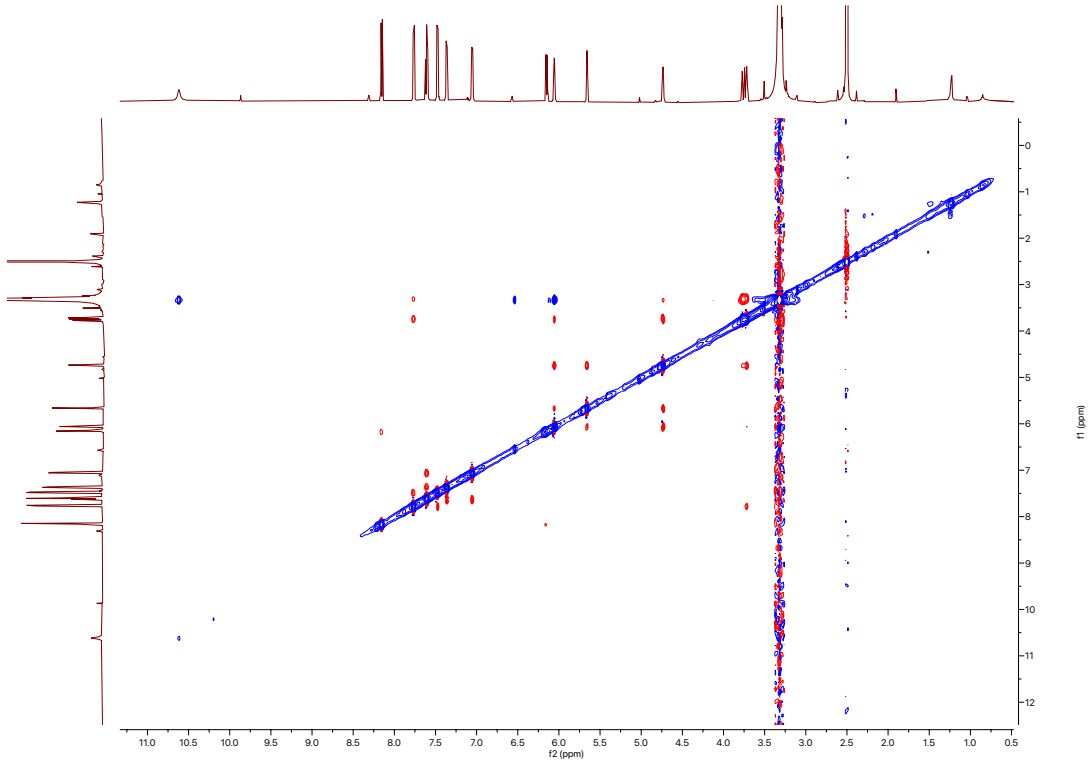

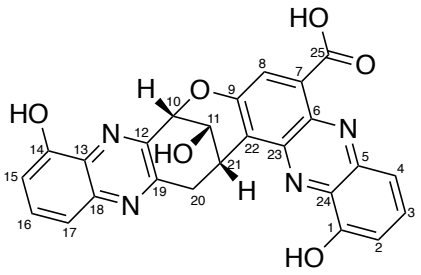

phenazinolin D (**4**)

Position	δ_C (type)	δ_H, multiplets (*J* in Hz)	COSY	HMBC	NOE
1	153.4 (C)				
1-OH		10.73, s			
2	111.7 (CH)	7.32, d (7.6)	3	1, 4, 24	
3	132.5 (CH)	7.83, t (8.2)	2, 4	1, 5	
4	118.0 (CH)	7.71, d (8.7)	3	2, 24, **N-5**	
5	139.5 (C)				
5-N		298.6 (δ_N)			
6	137.1 (C)				
7	128.0 (C)				
8	127.6 (CH)	7.95, s		6, 7, 9, 22, 25, **N-5**	
9	151.1 (C)				
10	76.1 (CH)	5.60, t (2.8)	11	9, 11, 12, 19, 21, **N-12**	11, 11-OH
11	62.7 (CH)	4.77, dd (5.7, 3.5)	10, 11-OH, 21	12	10, 11-OH
11-OH		6.20, s	11	21	10, 11
12	146.5 (C)				
12-N		325.9 (δ_N)			
13	132.7 (C)				
14	153.7 (C)				
14-OH		10.55, s		13, 14, 15	
15	111.7 (CH)	7.09, d (7.7)	16	13, 14, 17, **N-12**	
16	131.6 (CH)	7.59, t (8.1)	15, 17	14, 17	
17	117.8 (CH)	7.29, d (8.4)	16	13, 15, **N-18**	
18	142.8 (C)				
18-N		324.5 (δ_N)			
19	152.9 (C)				
20a	34.6 (CH_2)	3.87, dd (18.1, 5.3)	20b, 21	11, 12, 13, 18, 19, 21, 22, **N-18**	21
20b	34.6 (CH_2)	3.42, d (17.9)	20a	11, 12, 19, 21, 22, **N-18**	21
21	30.9 (CH)	4.85, t (5.2)	20a	9, 10, 11, 19, 20, 22, 23	20a, 20b
22	122.2 (C)				
23	140.1 (C)				
24	135.2 (C)				
25	165.5 (C)				
25-COOH		14.77, br s			

^{1}H spectrum of phenazinolin D (**4**)

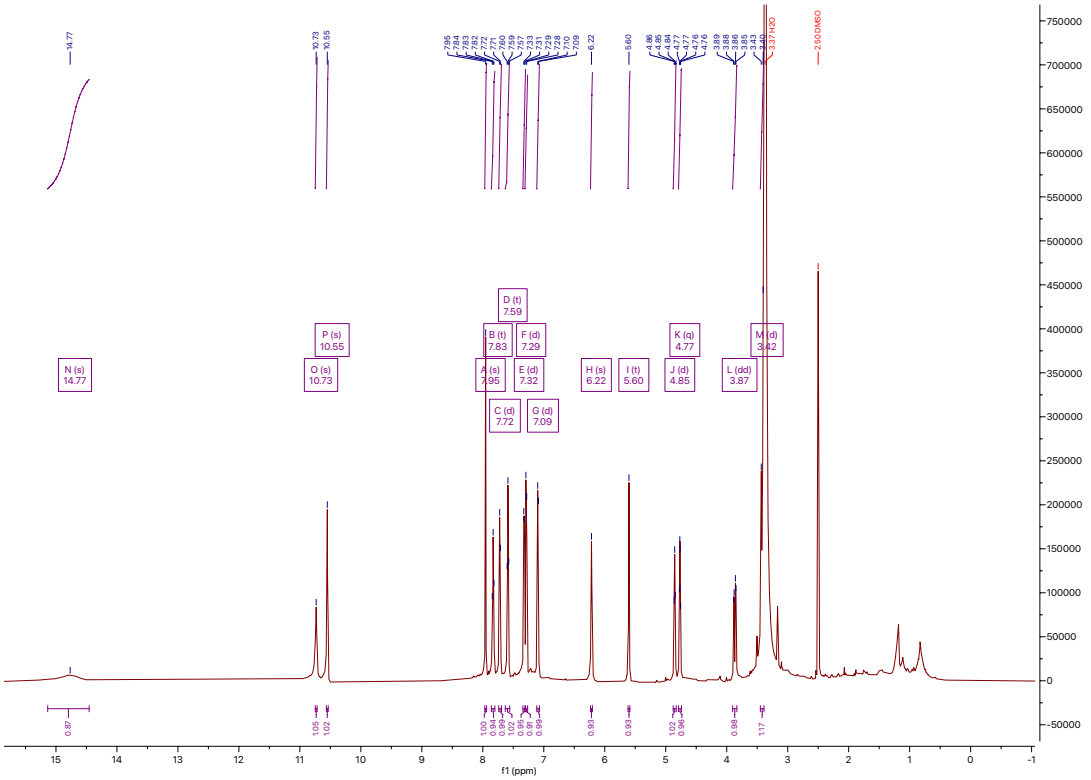

^{13}C spectrum of phenazinolin D (**4**)

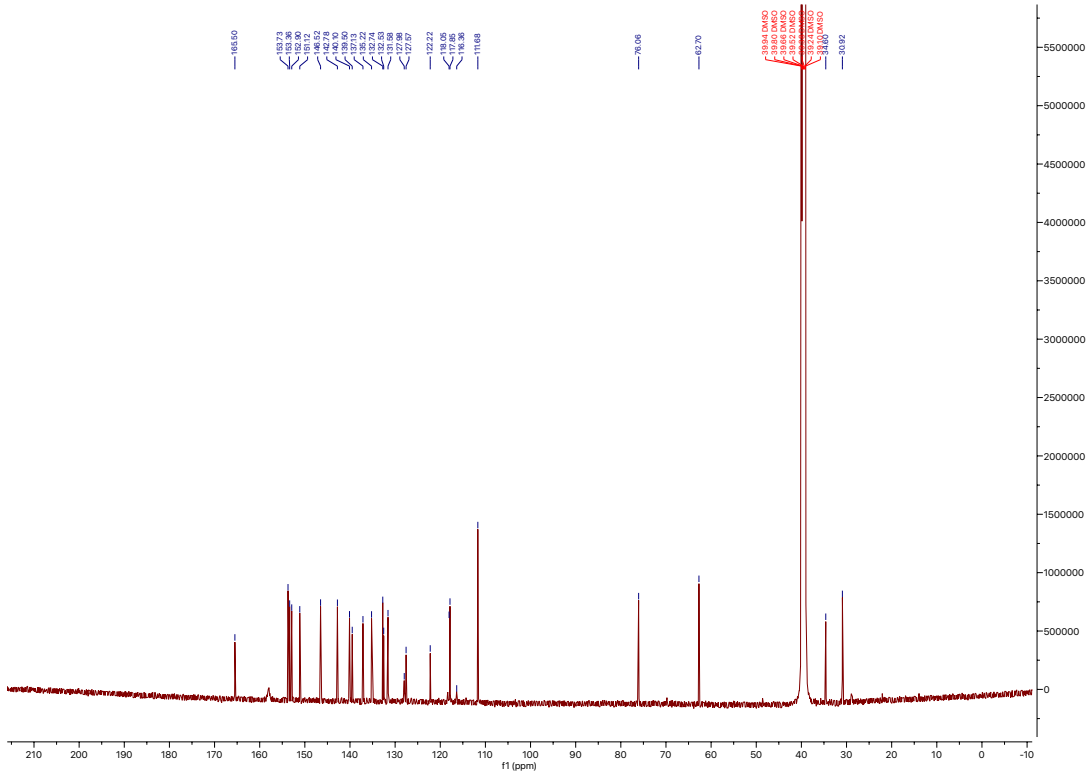

COSY spectrum of phenazinolin D (**4**)

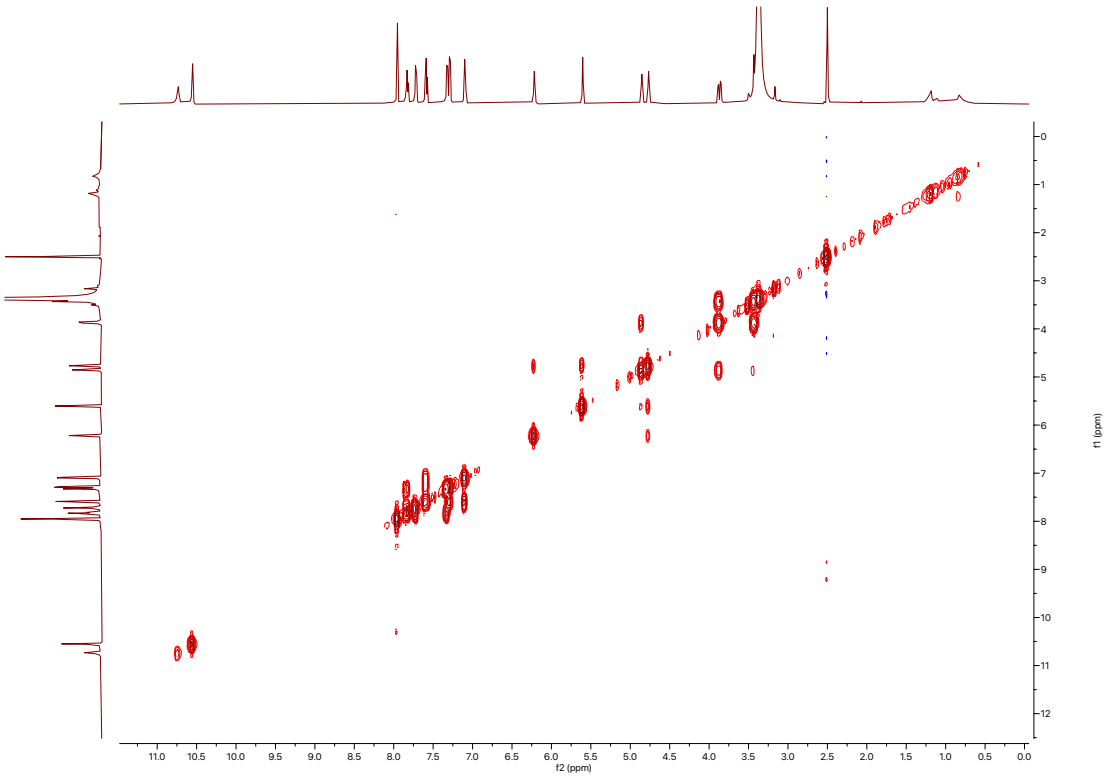

HSQC spectrum of phenazinolin D (**4**)

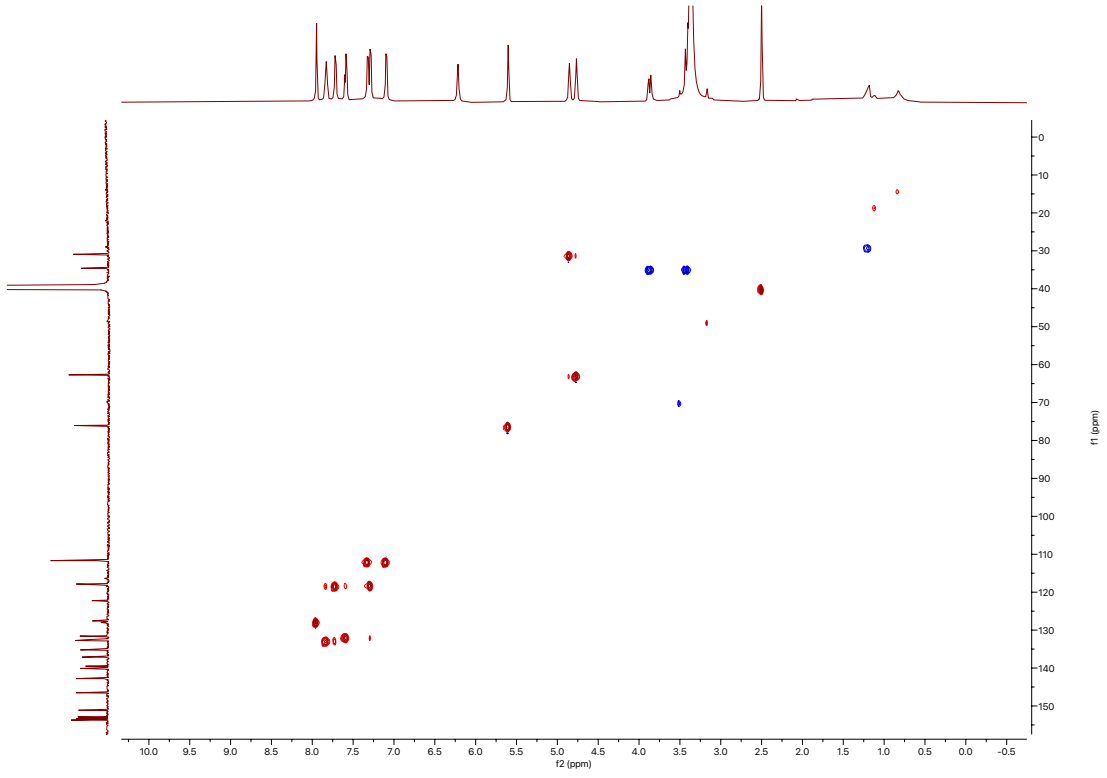

^{1}H-^{13}C HMBC spectrum of phenazinolin D (**4**)

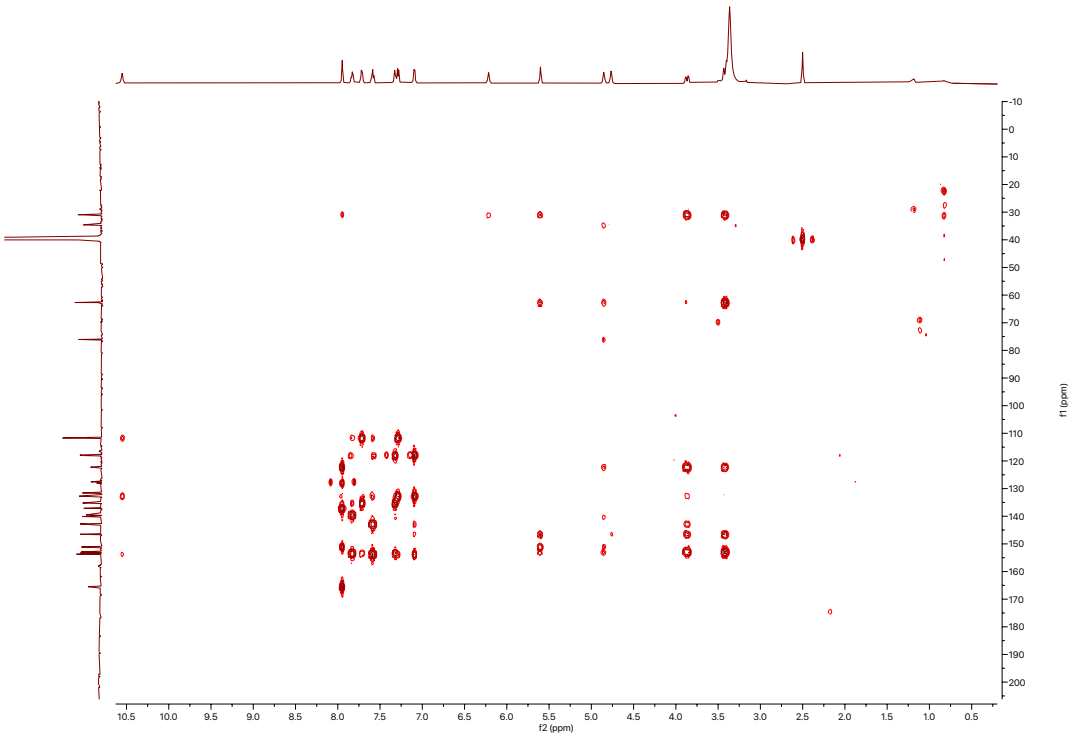

^{1}H-^{15}N HMBC spectrum of phenazinolin D (**4**)

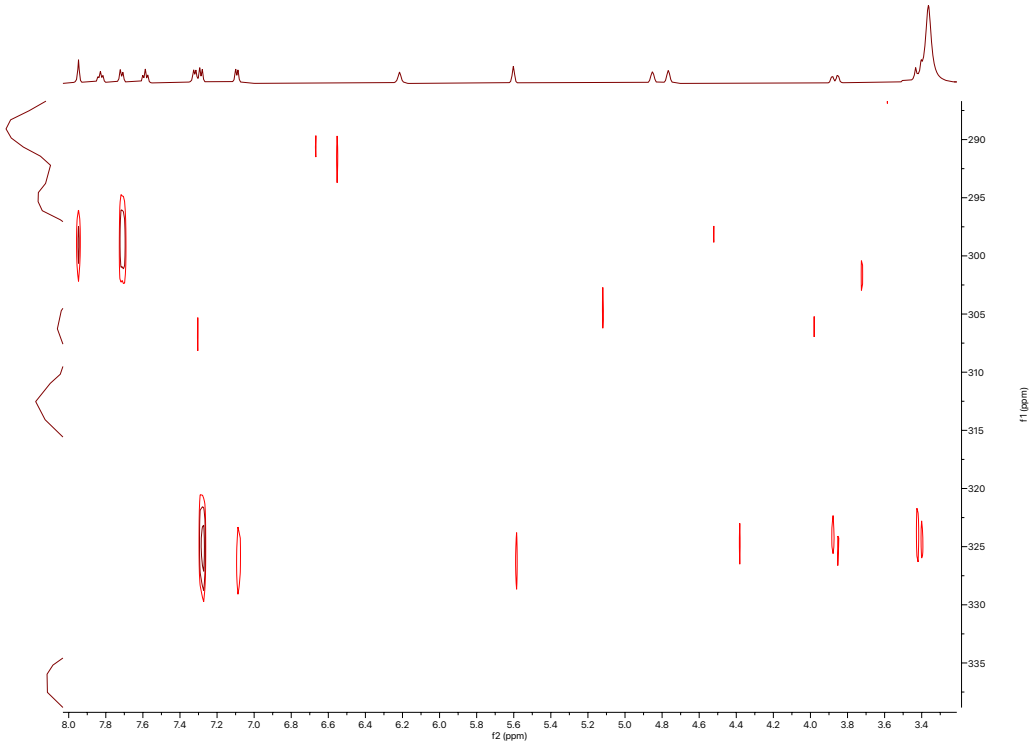

TOCSY spectrum of phenazinolin D (**4**)

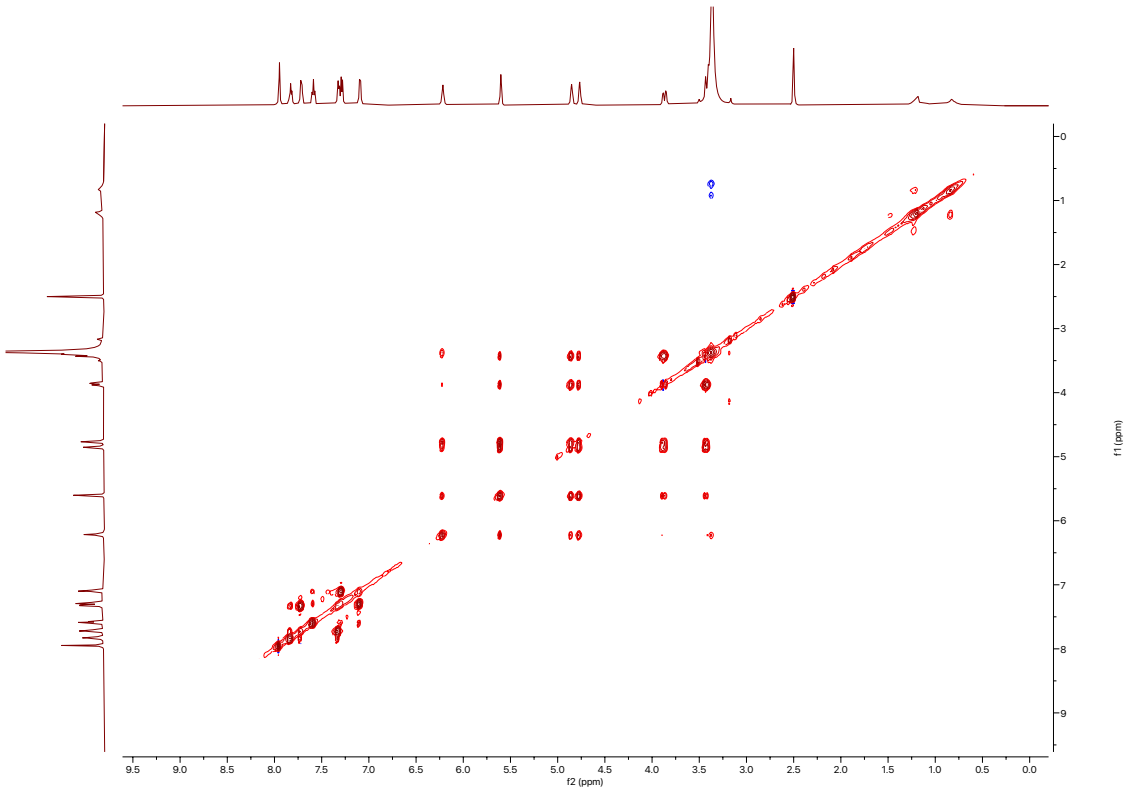

ROESY spectrum of phenazinolin D (**4**)

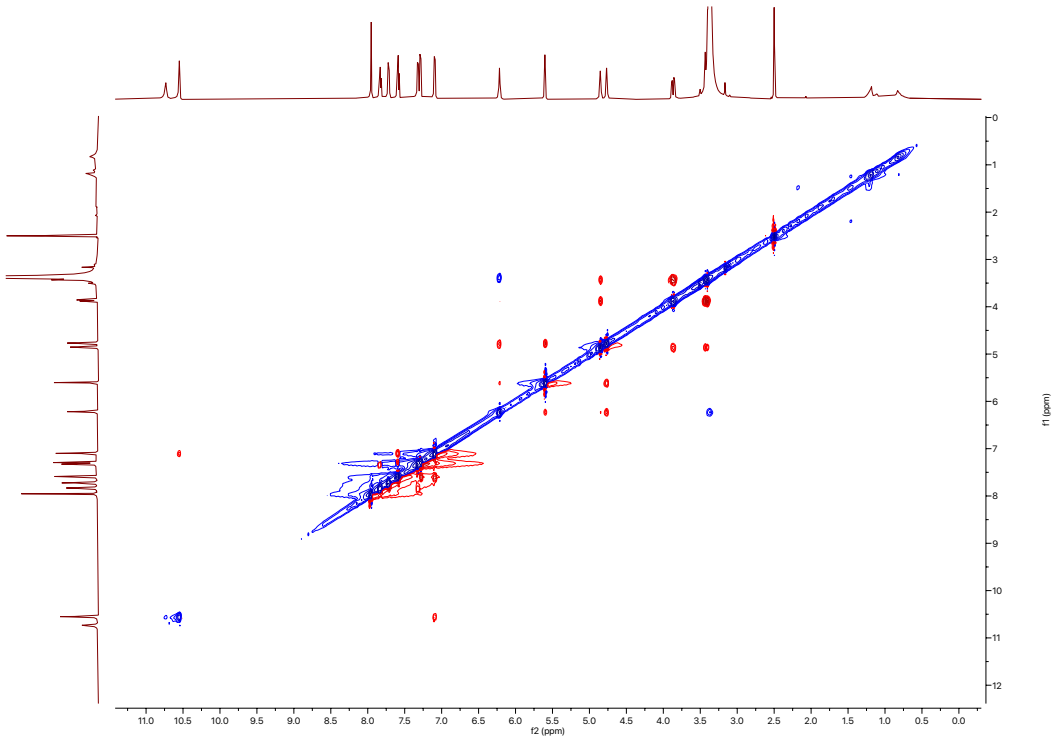

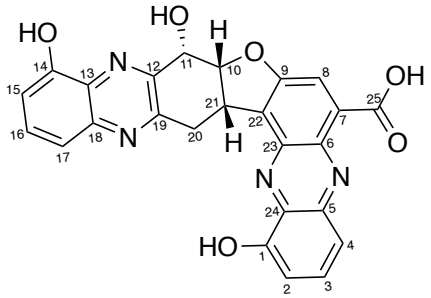

izumiphenazine A (**5**)

Position	δ_C (type)	δ_H, multiplets (*J* in Hz)	COSY	HMBC	NOE
1	153.2				
1-OH		10.78, s		1, 2, 24	
2	111.8 (CH)	7.33, d (7.5)	3	1, 4, 24, **N-23**	
3	132.3 (CH)	7.83, t (8.1)	2, 4	1, 4, 5	
4	118.5 (CH)	7.73, d (8.6)	3	2, 24, **N-5**	
5	139.6 (C)				
5-N		301.6 (δ_N)			
6	137.4 (C)				
7	130.7 (C)				
8	121.2 (CH)	8.15, s		6, 9, 22, 25	
9	158.8 (C)				
10	88.7 (CH)	5.59, dd (10.3, 5.6)	11, 21	9, 11, 12, 20, 22	11, 11-OH, 21
11	71.6 (CH)	5.35, dd (5.8, 3.3)	10, 11-OH	10, 12, 19, 21, **N-12**	10, 11-OH, 20a
11-OH		6.33, d (3.6)	11	10, 11, 12	10, 11
12	149.8 (C)				
12-N		305.4 (δ_N)			
13	131.4 (C)				
14	153.6 (C)				
14-OH		10.29, s		13, 14, 15	
15	111.7 (CH)	7.12, d (7.7)	16	13, 14, 17	
16	130.7 (CH)	7.60, t (8.0)	15, 17	14, 18	
17	118.1 (CH)	7.40, d (8.3)	16	13, 15, **N-18**	
18	142.3 (C)				
18-N		321.9 (δ_N)			
19	153.5 (C)				
20a	33.4 (CH_2)	4.19 dd (15.1, 6.7)	20b, 21	10, 12, 19, 21, 22, **N-18**	20b, 21
20b	33.4 (CH_2)	3.69, dd (15.1, 7.1)	20a, 21	10, 12, 19, 21, 22, **N-18**	10, 11, 20a
21	39.2 (CH)	4.84, dt (10.5, 6.9)	10, 20a, 20b	9, 10, 11, 19, 20, 23	10, 20a, 20b
22	124.9 (C)				
23	138.8 (C)				
23-N		306.3 (δ_N)			
24	135.9 (C)				
25	165.8 (C)				
25-COOH		14.95, br s			

^{1}H spectrum of izumiphenazine A (**5**)

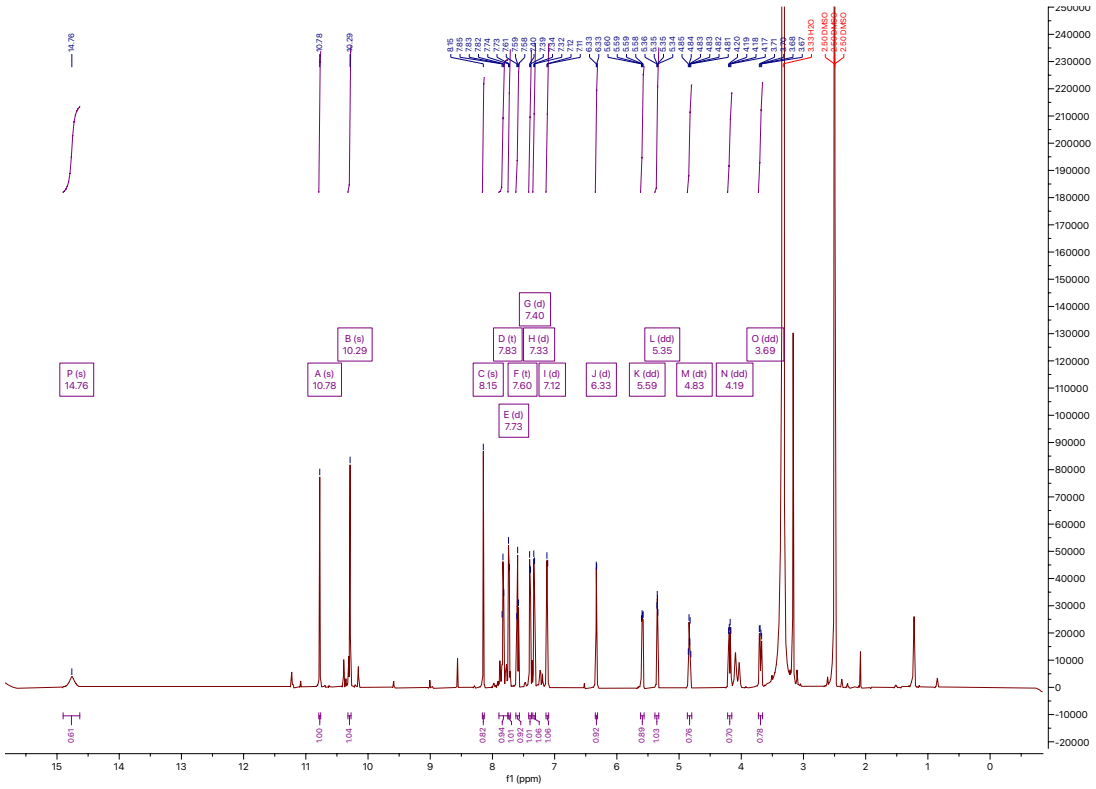

^{13}C spectrum of izumiphenazine A (**5**)

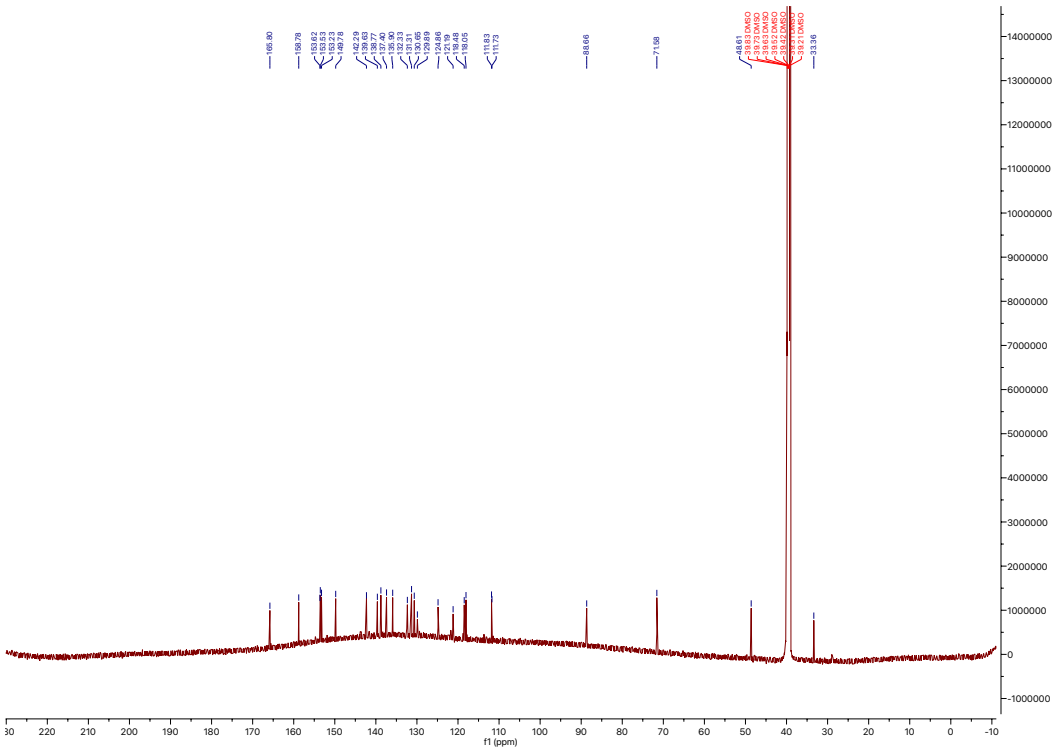

COSY spectrum of izumiphenazine A (**5**)

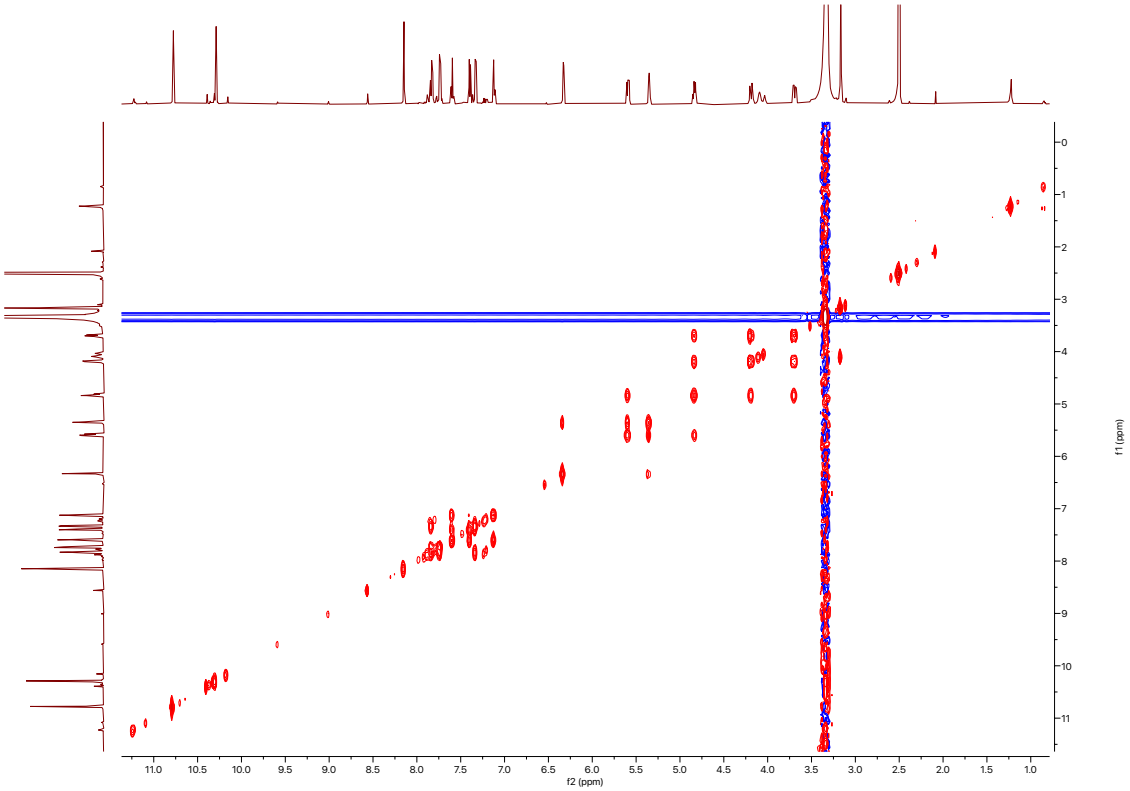

HSQC spectrum of izumiphenazine A (**5**)

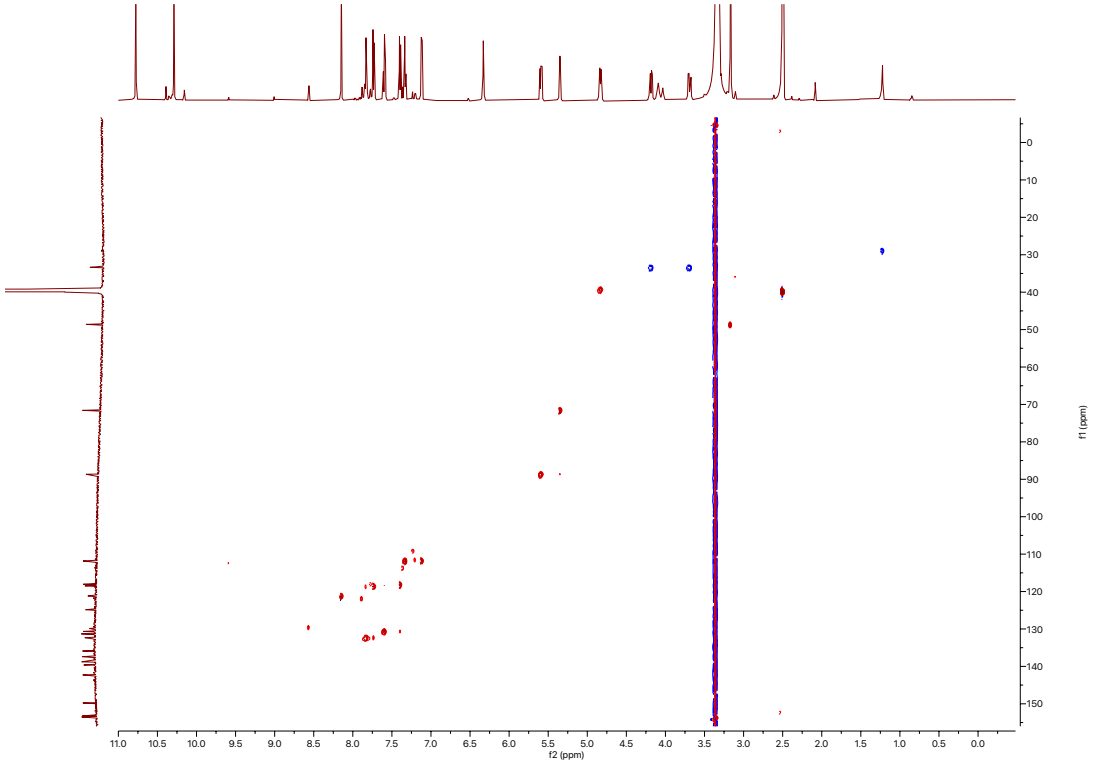

^{1}H-^{13}C HMBC spectrum of izumiphenazine A (**5**)

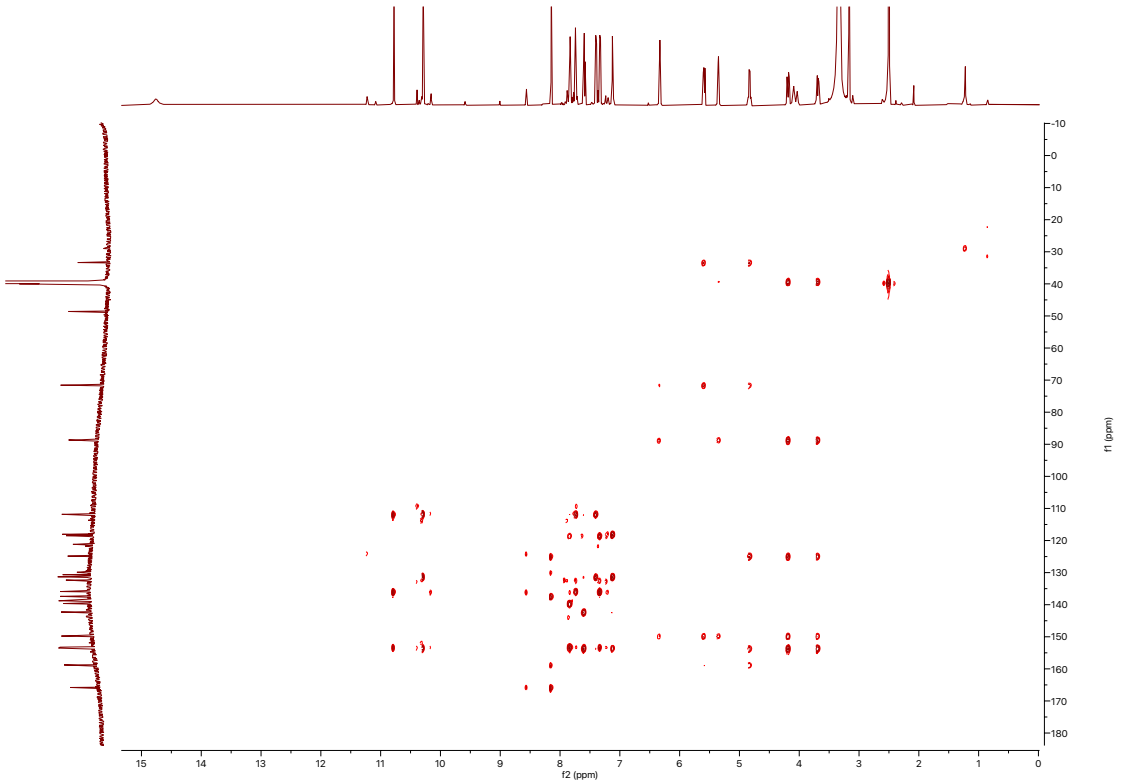

^{1}H-^{15}N HMBC spectrum of izumiphenazine A (**5**)

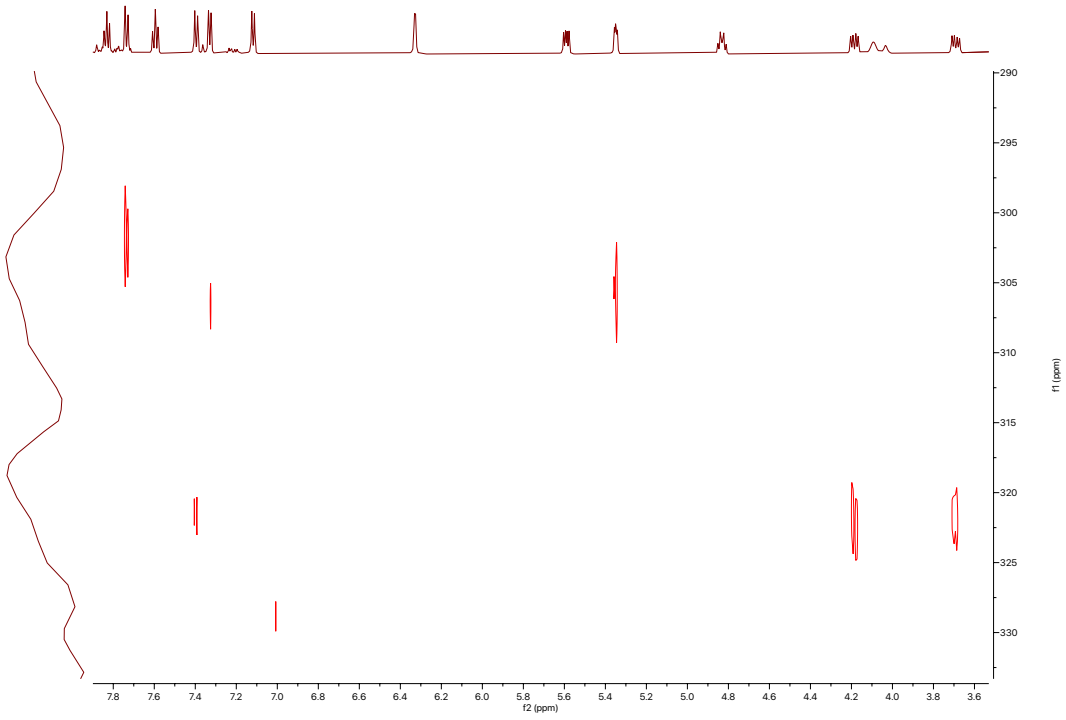

TOCSY spectrum of izumiphenazine A (**5**)

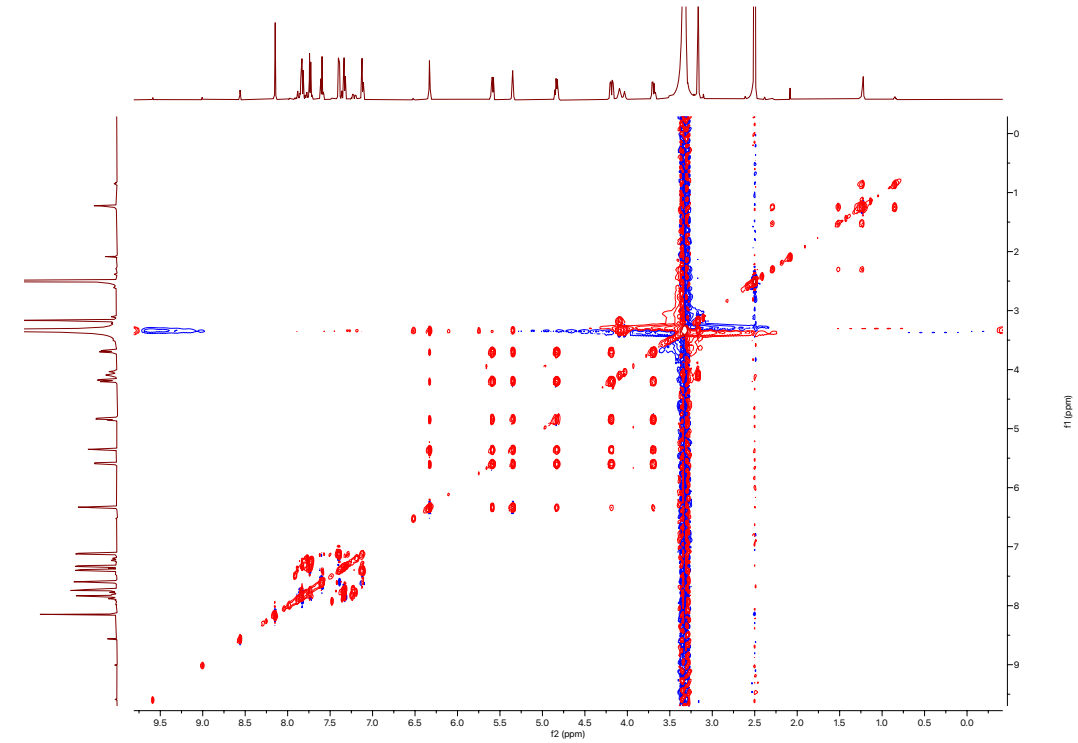

ROESY spectrum of izumiphenazine A (**5**)

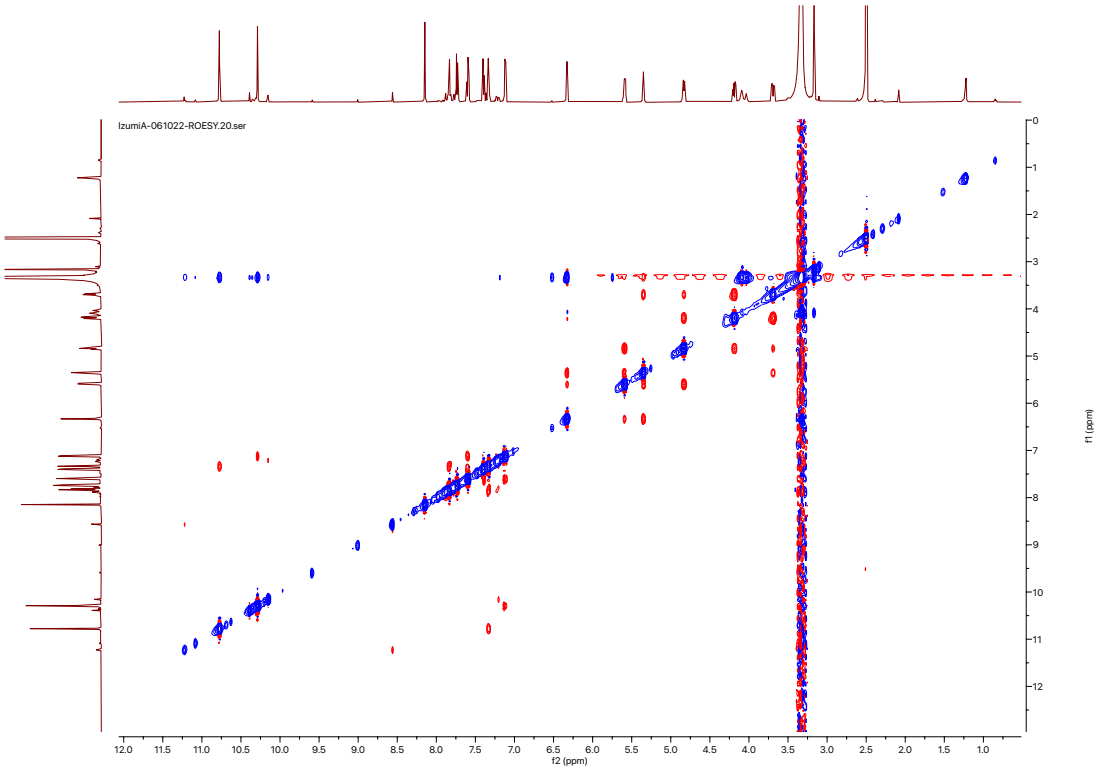

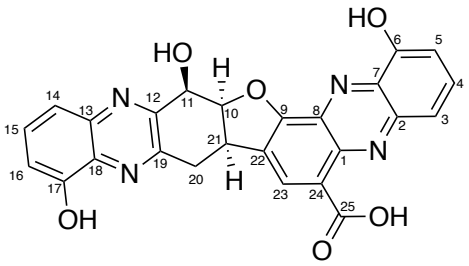

izumiphenazine E (**6**)

Position	δC (type)	δH, multiplets (J in Hz)	COSY	HMBC
1	139.0 (C)			
2	141.7 (C)			
3	120.3 (CH)	7.55, d	4	5
4	129.8 (CH)	7.63, t (8.0)	3, 5	2, 6
5	110.9 (CH)	7.18, d (7.3)	4	3, 6, 7
6	153.5 (C)			
6-OH		10.3, obscure		
7	135.0 (C)			
8				
9	160.2 (C)			
10	88.3 (CH)	5.50, dd (10.2, 5.4)	11, 21	11, 12, 20
11	72.3 (CH)	5.29, d (5.3)	10	10, 12, 19, 21
11-OH		6.30, s		
12	150.4 (C)			
13	135.0 (C)			
14	153.2 (C)			
14-OH		10.3, obscure		
15	118.5 (CH)	7.08, d (7.7)	16	13, 14, 17
16	131.1 (CH)	7.55, t	15, 17	14, 18
17	112.2 (CH)	7.33, d (8.4)	16	13, 15
18	141.6 (C)			
19	154.0 (C)			
20a	34.0 (CH_2)	4.09, dd (15.0, 6.6)	21	10, 12, 19, 21, 22
20b	34.0 (CH_2)	3.67, dd (15.0, 6.3)	21	10, 12, 19, 21, 22
21	39.5 (CH)	4.70, dd (10.8, 5.7)	10, 20a, 20b	9, 11, 19, 20, 22
22	116.6 (C)			
23	112.6 (CH)	7.05, s		8, 22, 25
24				
25	169.7 (C)			
25-COOH				

^{1}H spectrum of izumiphenazine E (**6**)

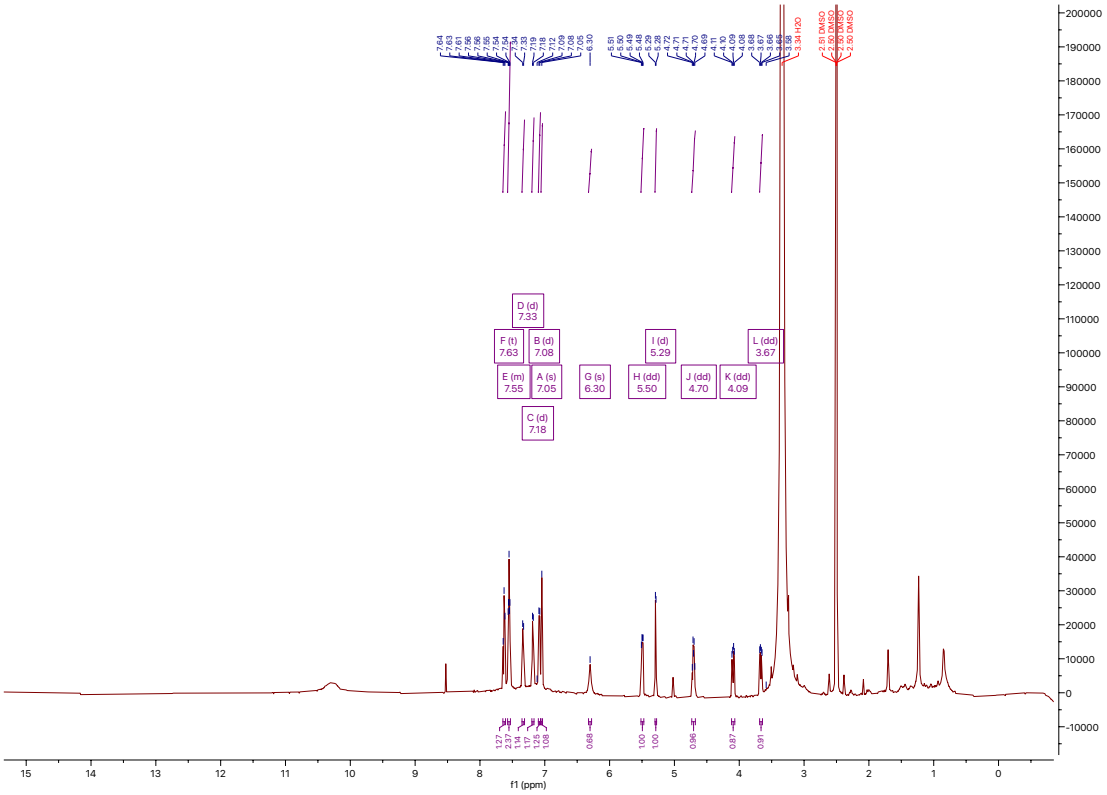

^{13}C spectrum of izumiphenazine E (**6**)

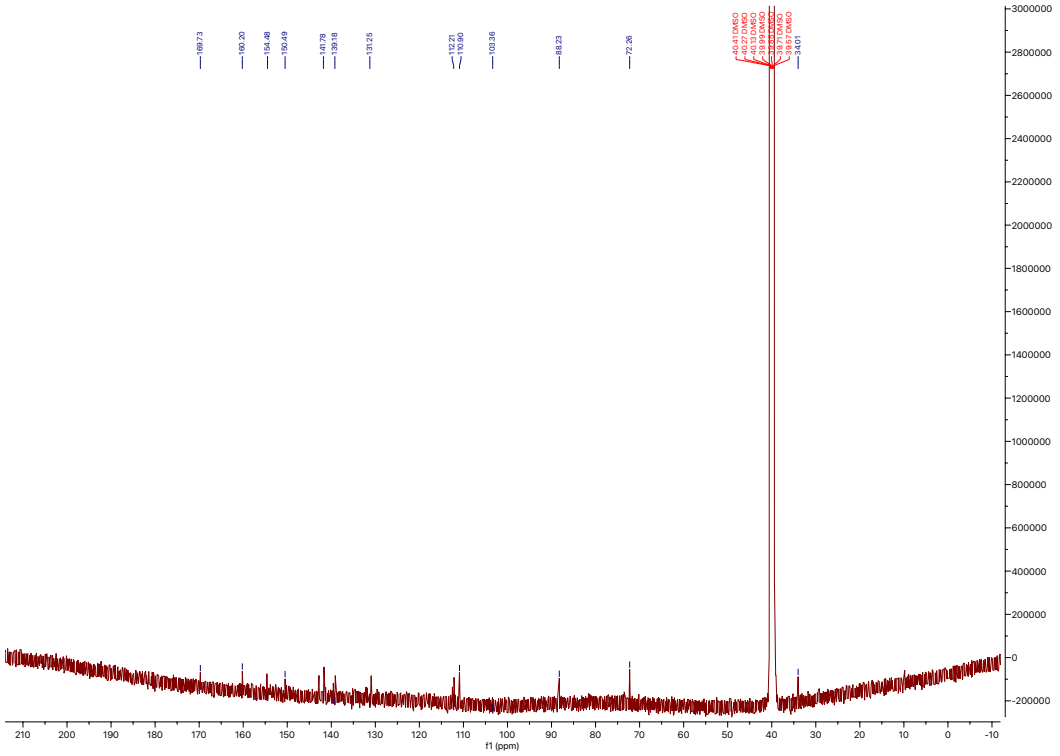

COSY spectrum of izumiphenazine E (**6**)

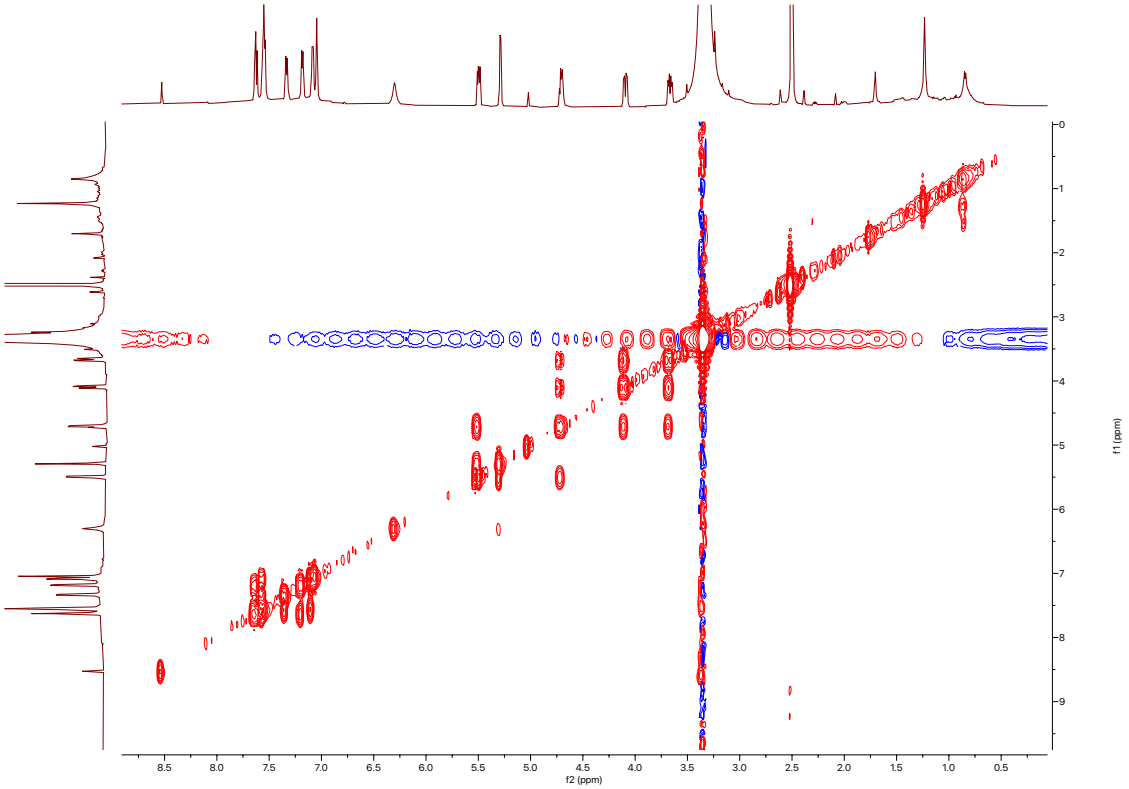

HSQC spectrum of izumiphenazine E (**6**)

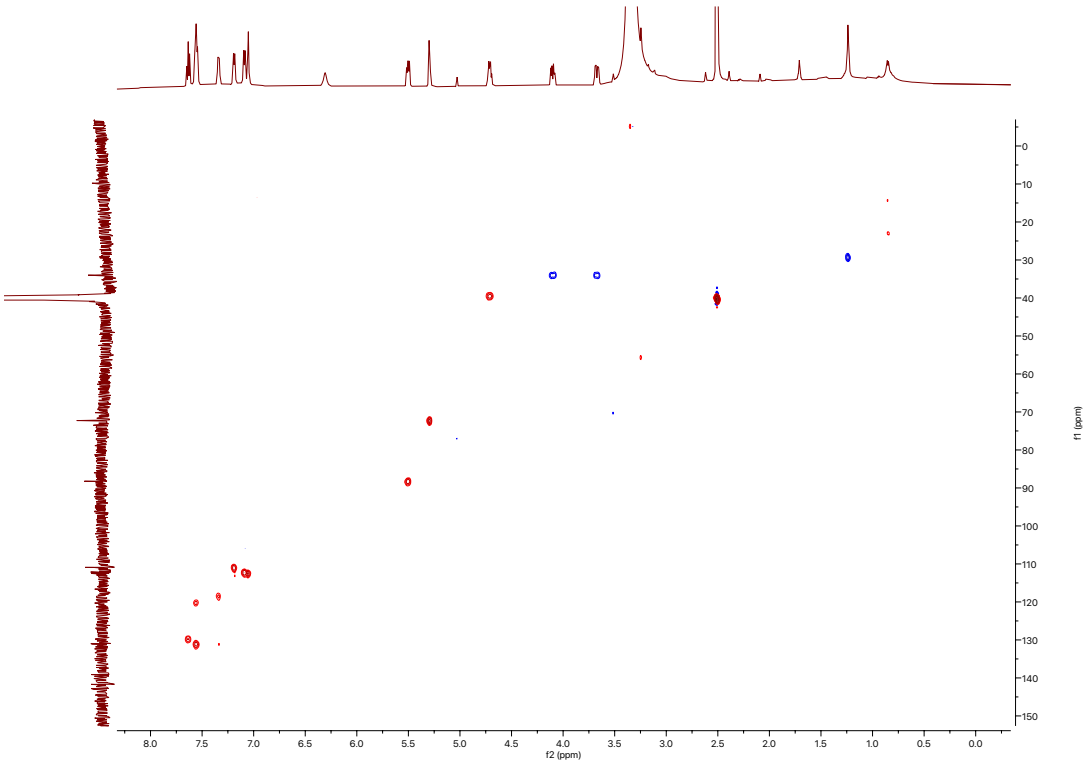

^{1}H-^{13}C HMBC spectrum of izumiphenazine E (**6**)

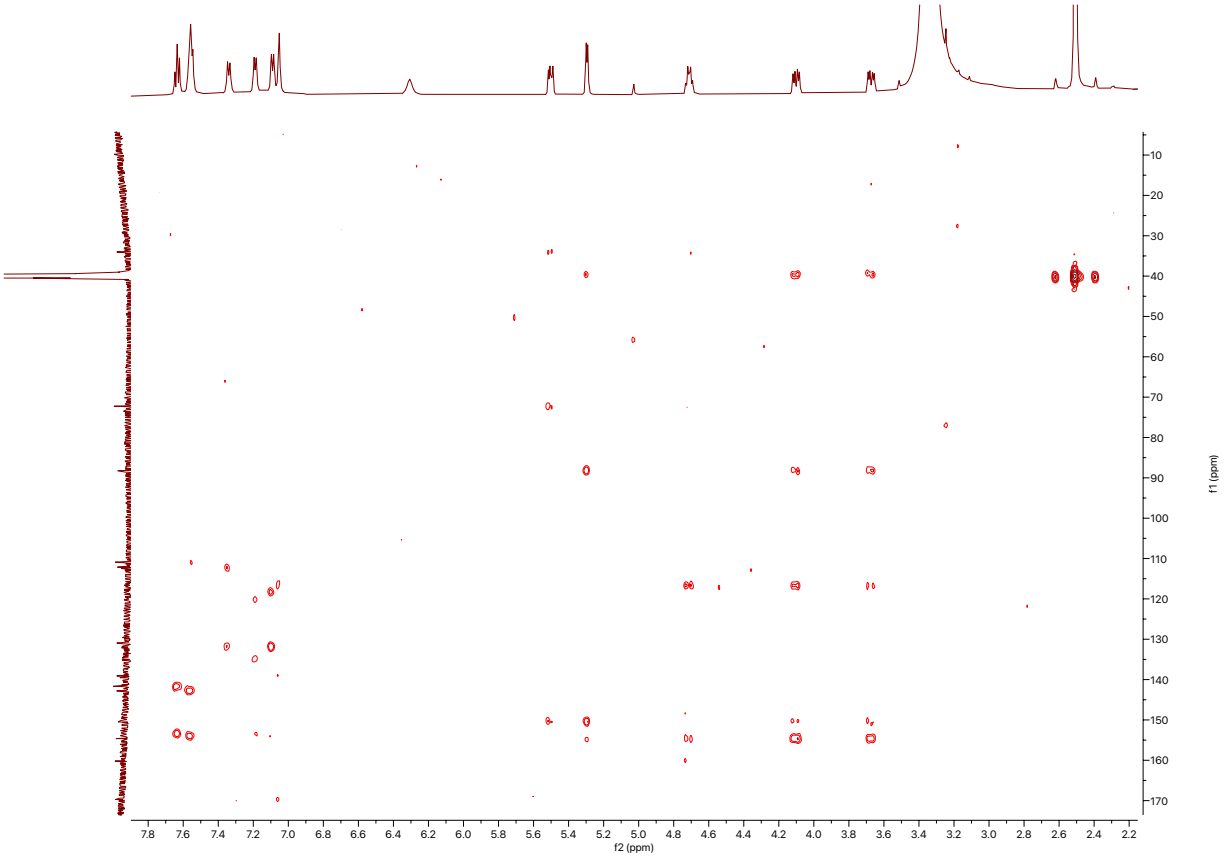

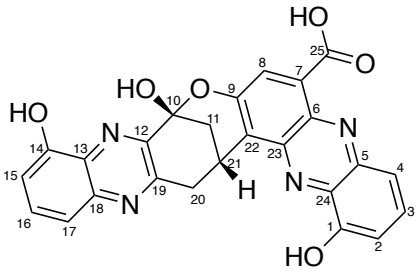

baraphenazine G (**7**)

Position	δ_C (type)	δ_H, multiplets (*J* in Hz)	COSY	HMBC	NOE
1	153.4 (C)				
1-OH		10.67, s		1, 2, 24	
2	111.6 (CH)	7.32, d (8.2)	3	4, 24	
3	132.5 (CH)	7.84, t (8.1)	2, 4	1, 5	
4	118.1 (CH)	7.73, d (8.6)	3	2, 24, **N-5**	
5	139.8 (C)				
5-N		298.1 (δ_N)			
6	137.0 (C)				
7	127.6 (C)				
8	128.0 (CH)	7.92, s		6, 22, 25, **N-5**	
9	152.7 (C)				
10	97.3 (C)				
10-OH		8.30, s		10, 11, 12, **N-12**	
11a	31.4 (CH_2)	2.83, dd (13.4, 2.3)	11b	10, 21, 22	20a, 21
11b	31.4 (CH_2)	2.64, dd (13.2, 2.0)	11a, 21	10, 12	21
12	147.4 (C)				
12-N		302.8 (δ_N)			
13	130.8 (C)				
14	153.4 (C)				
14-OH		10.23, s		13, 14, 15, **N-12**	
15	111.0 (CH)	7.12, d (7.6)	16	13, 17, **N-12**	
16	132.2 (CH)	7.65, t (8.1)	15, 17	14, 18	
17	117.7 (CH)	7.32, d (8.2)	16	13, 15, **N-18**	
18	142.6 (C)				
N-18		305.9 (δ_N)			
19	152.0 (C)				
20a	39.3 (CH_2)	3.77, dd (18.0, 5.2)	20b, 21	19, 21, 22, **N-18**	11a, 20b
20b	39.3 (CH_2)	3.61, dd (18.0, 2.5)	20a	11, 22	21
21	27.1 (C)	4.91, dp (4.9, 2.5)	11b, 20a		11a, 11b, 20a, 20b
22	122.3 (C)				
23	140.0 (C)				
24	135.2 (C)				
25	165.4 (C)				
25-COOH		14.73, br s			

^{1}H spectrum of baraphenazine G (**7**)

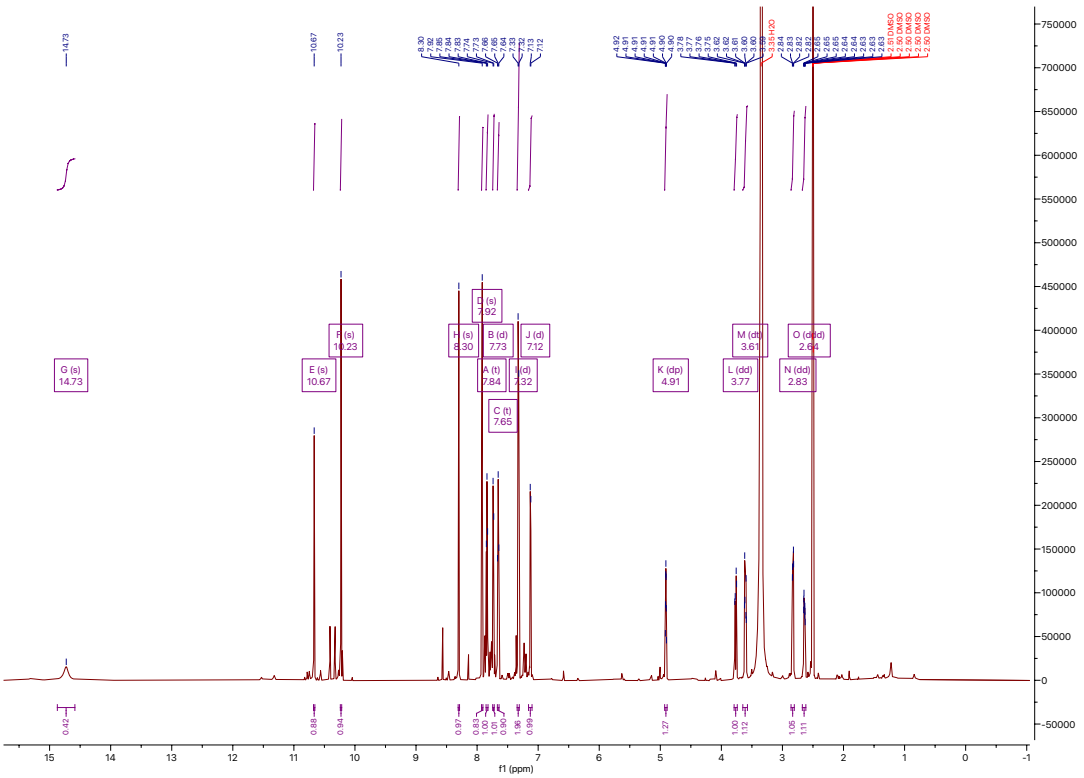

^{13}C spectrum of baraphenazine G (**7**)

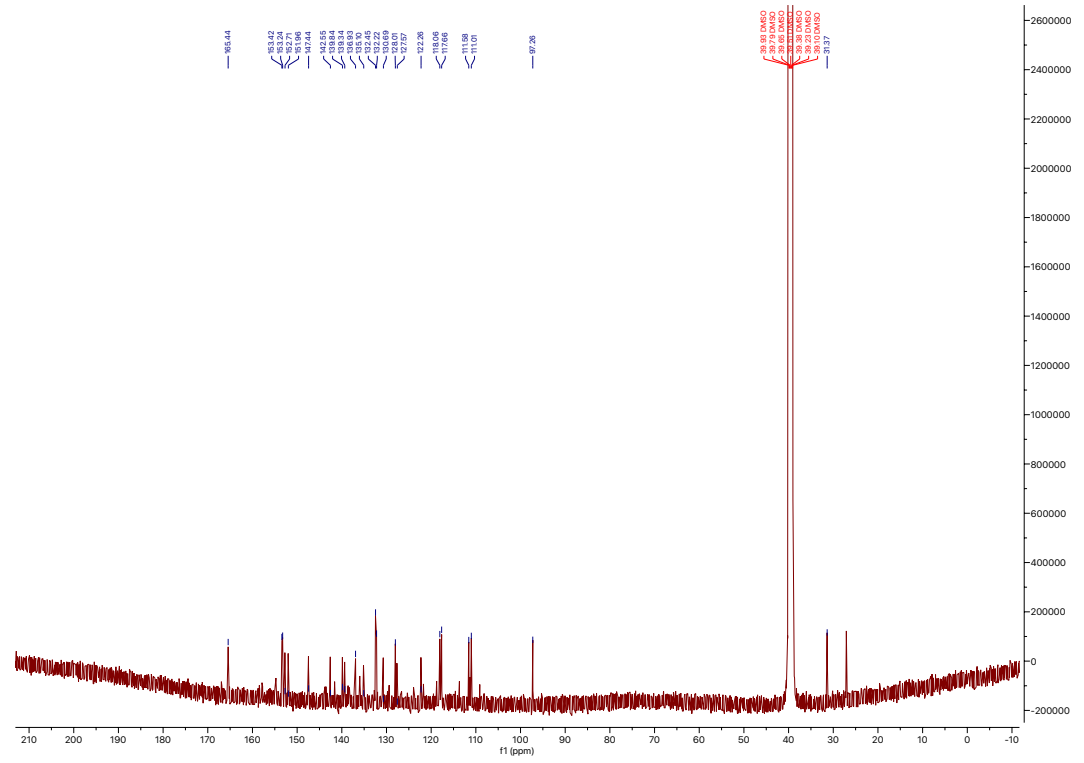

COSY spectrum of baraphenazine G (**7**)

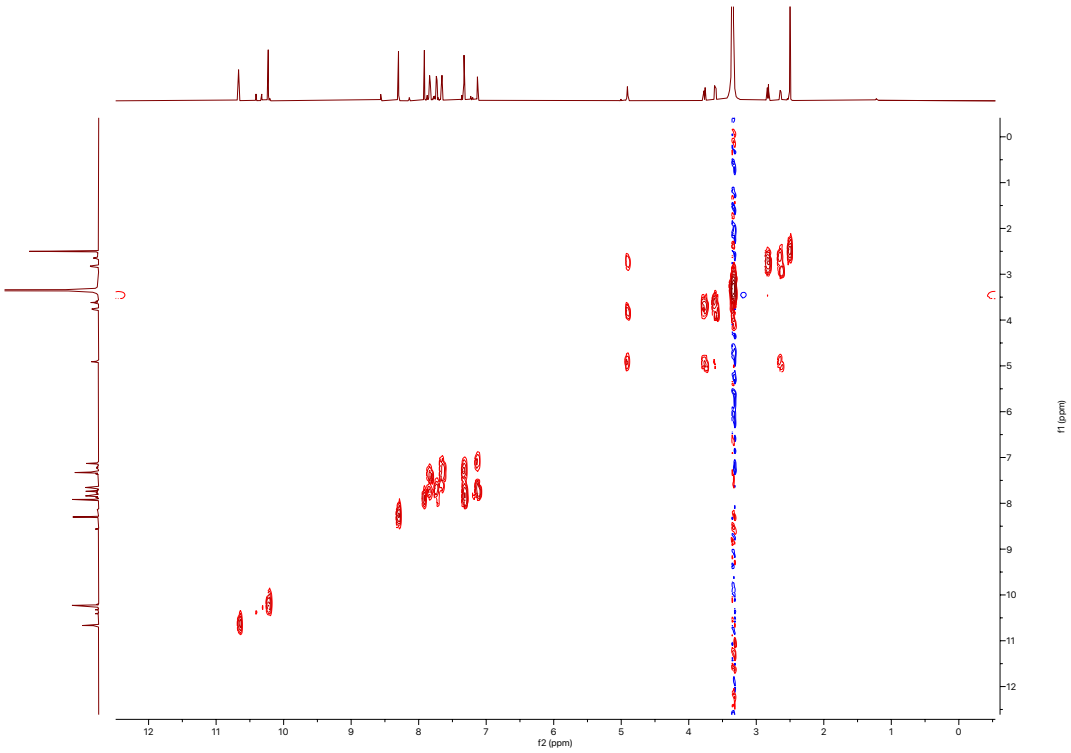

HSQC spectrum of baraphenazine G (**7**)

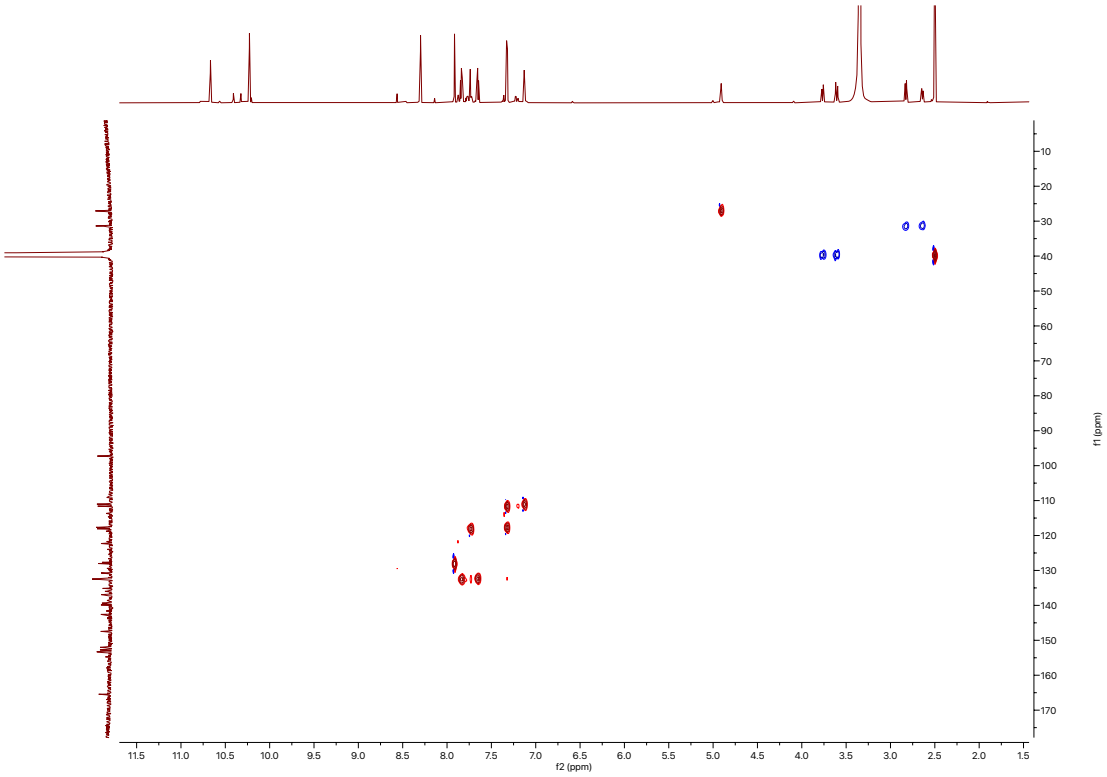

^{1}H-^{13}C HMBC spectrum of baraphenazine G (**7**)

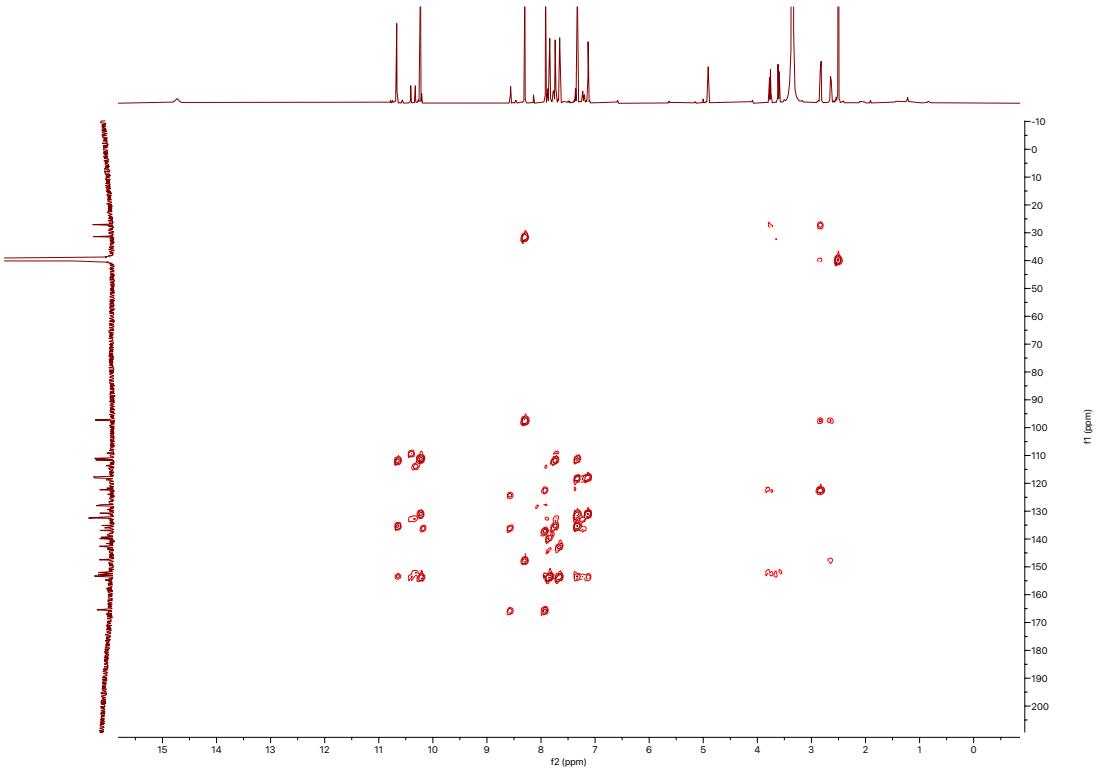

^{1}H-^{15}N HMBC spectrum of baraphenazine G (**7**)

TOCSY spectrum of baraphenazine G (**7**)

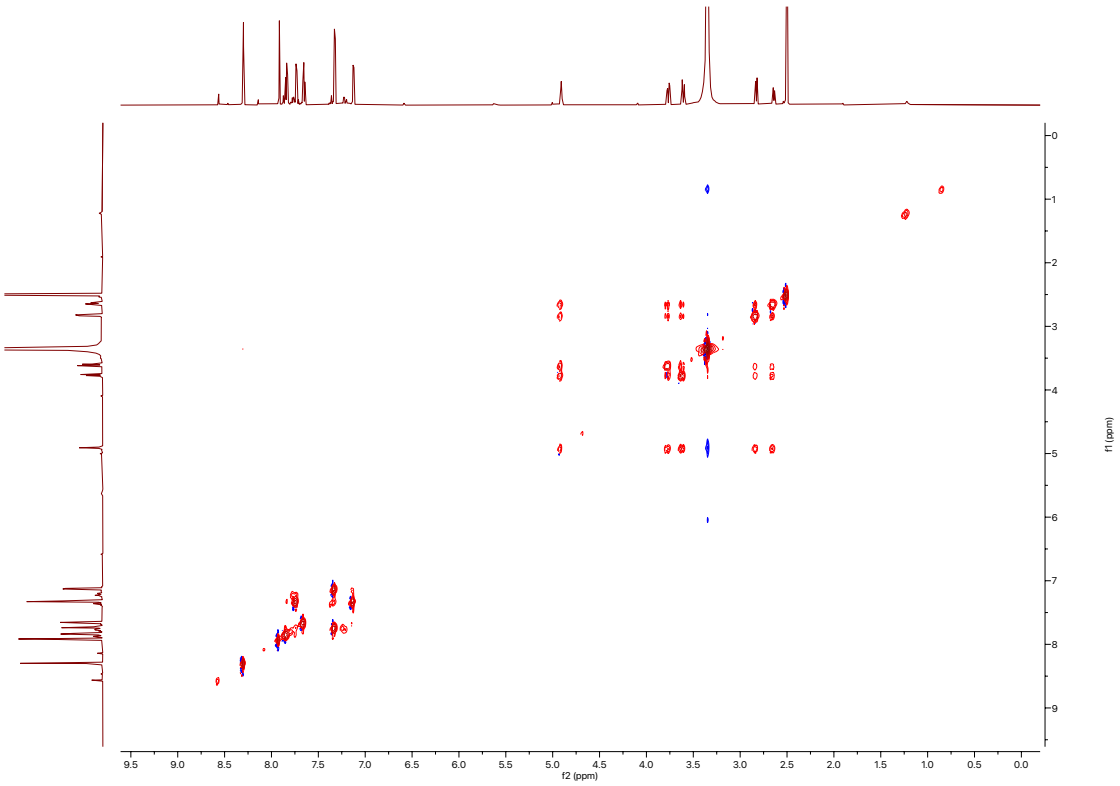

ROESY spectrum of baraphenazine G (**7**)

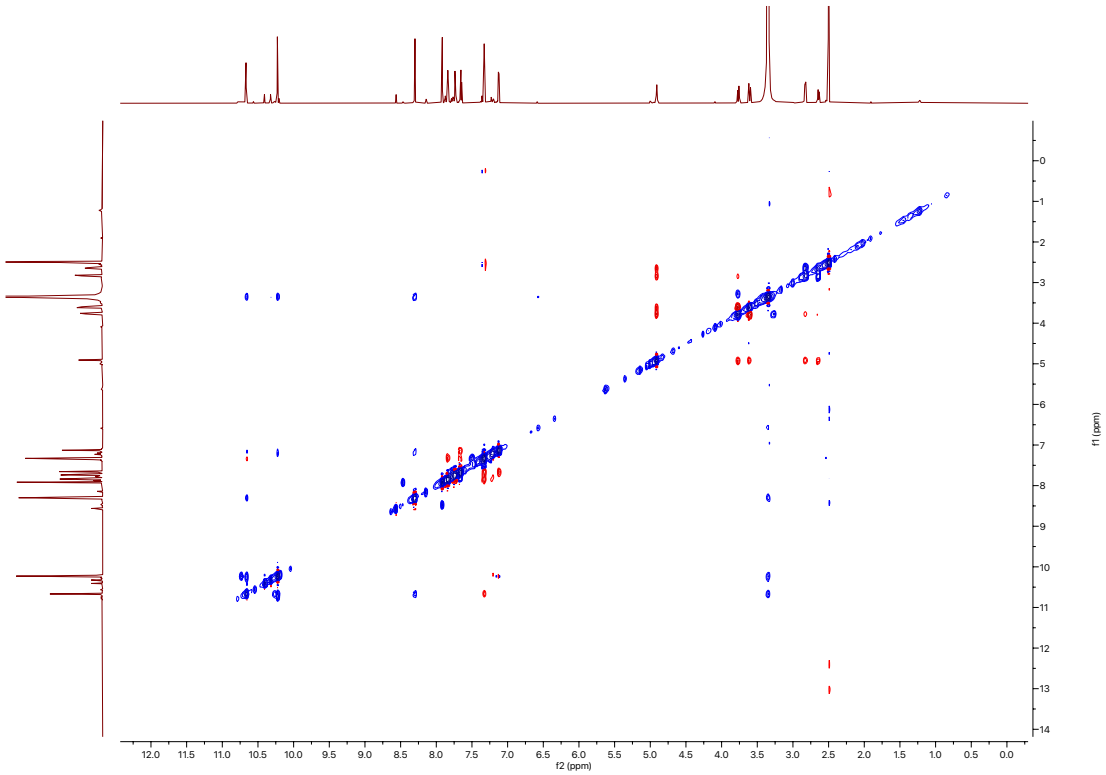

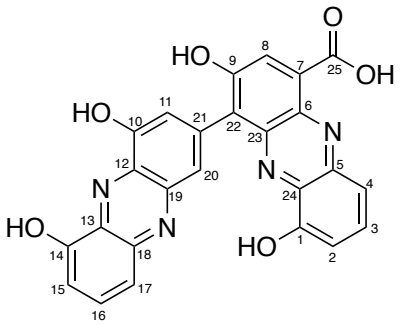

baraphenazine I (**8**)

Position	δ_C (type)	δ_H, multiplets (J in Hz)	COSY	HMBC
1	153.9 (C)			
1-OH		10.40 (s)		1, 2, 24
2	109.6 (CH)	7.23, d	3	1, 4, 24
3	133.0 (CH)	7.85, t	2, 4	1, 5
4	119.1 (CH)	7.72, d	3	2, 24
5	144.3 (C)			
6	136.4 (C)			
7	127.3 (C)			
8	129.8 (CH)	8.56, s		6, 7, 9, 22, 25
9	155.2 (C)			
9-OH		11.29 (s)		
10	152.3 (C)			
10-OH		10.31 (s)		10, 11, 12
11	114.1 (CH)	7.36 (s)		10, 12, 20
12	133.0 (C)			
13	136.6 (C)			
14	153.7 (C)			
14-OH		10.17 (s)		13, 14, 15
15	111.9 (CH)	7.20 (d)	16	13, 14, 17
16	132.8 (CH)	7.79 (t)	15, 17	14, 18
17	118.3 (CH)	7.77 (d)	16	13, 15
18	139.1 (C)			
19				
20	122.1 (CH)	7.88 (s)		11, 12, 22
21				
22	124.5 (C)			
23	139.0 (C)			
24	133.2 (C)			
25	166.1 (C)			
25-COOH		15.30 (s)		

^{1}H spectrum of baraphenazine I (**8**)

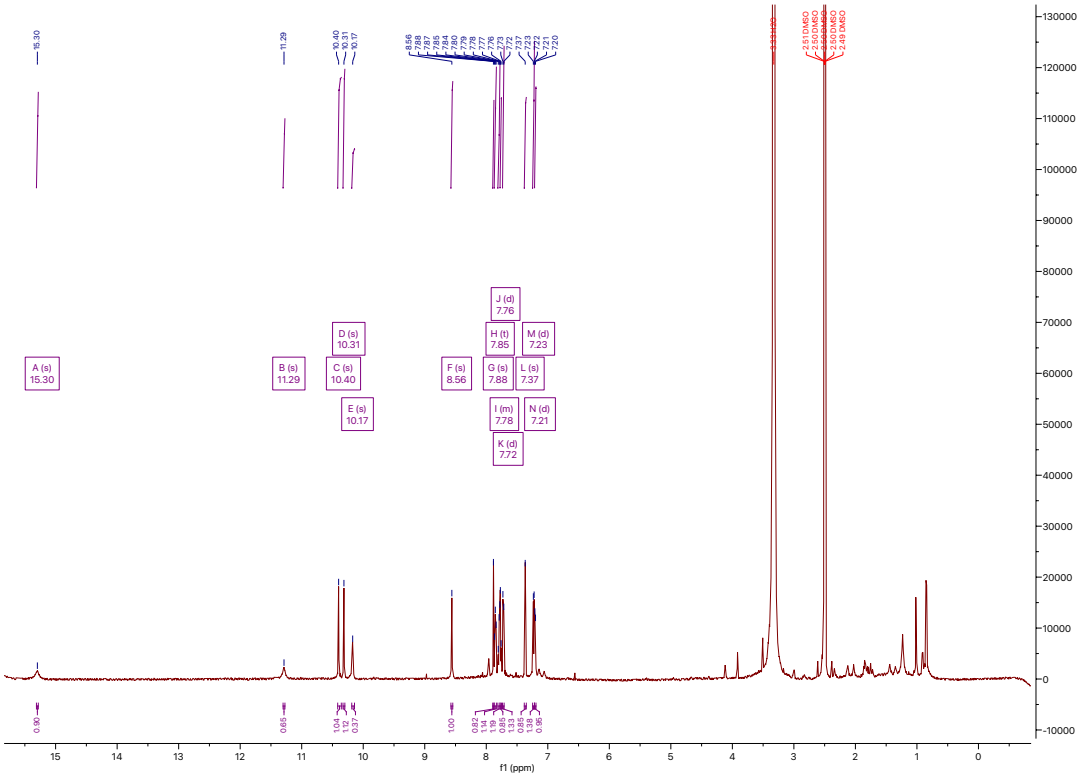

COSY spectrum of baraphenazine I (**8**)

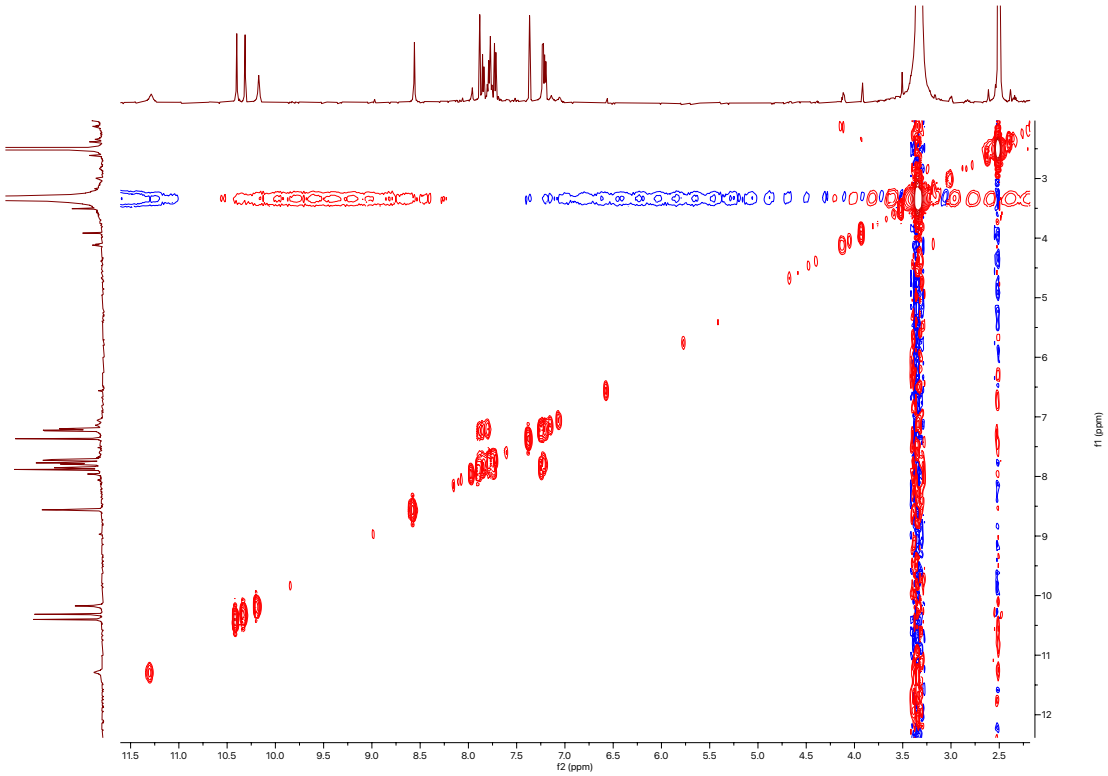

HSQC spectrum of baraphenazine I (**8**)

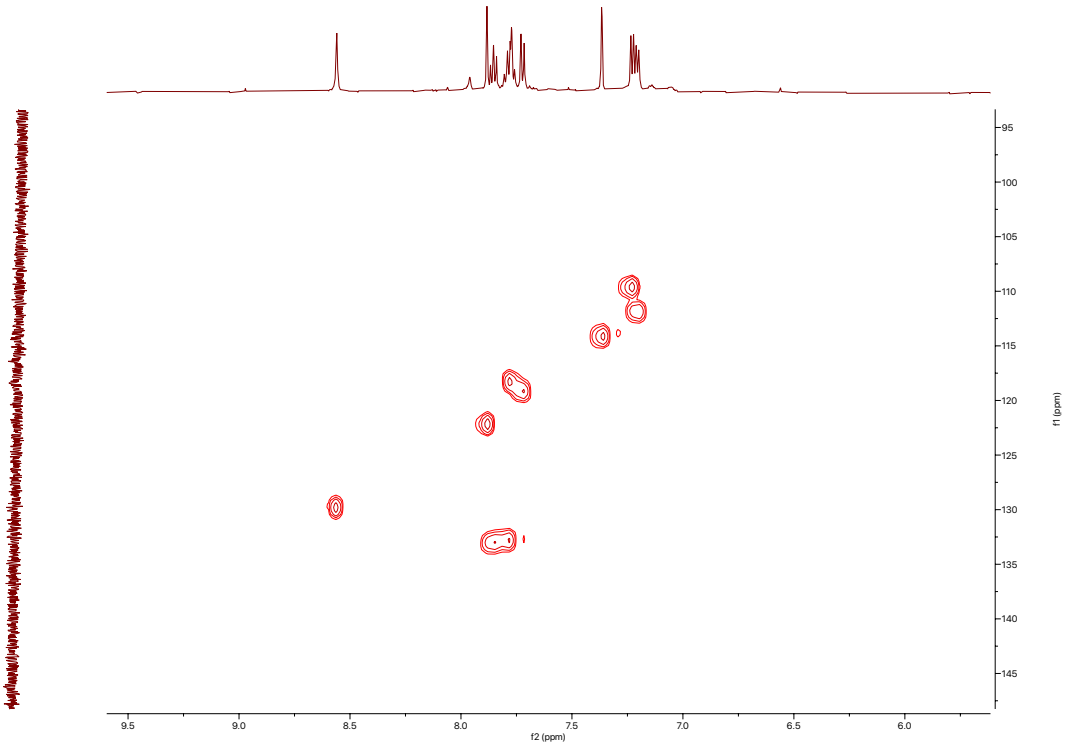

^{1}H-^{13}C HMBC spectrum of baraphenazine I (**8**)

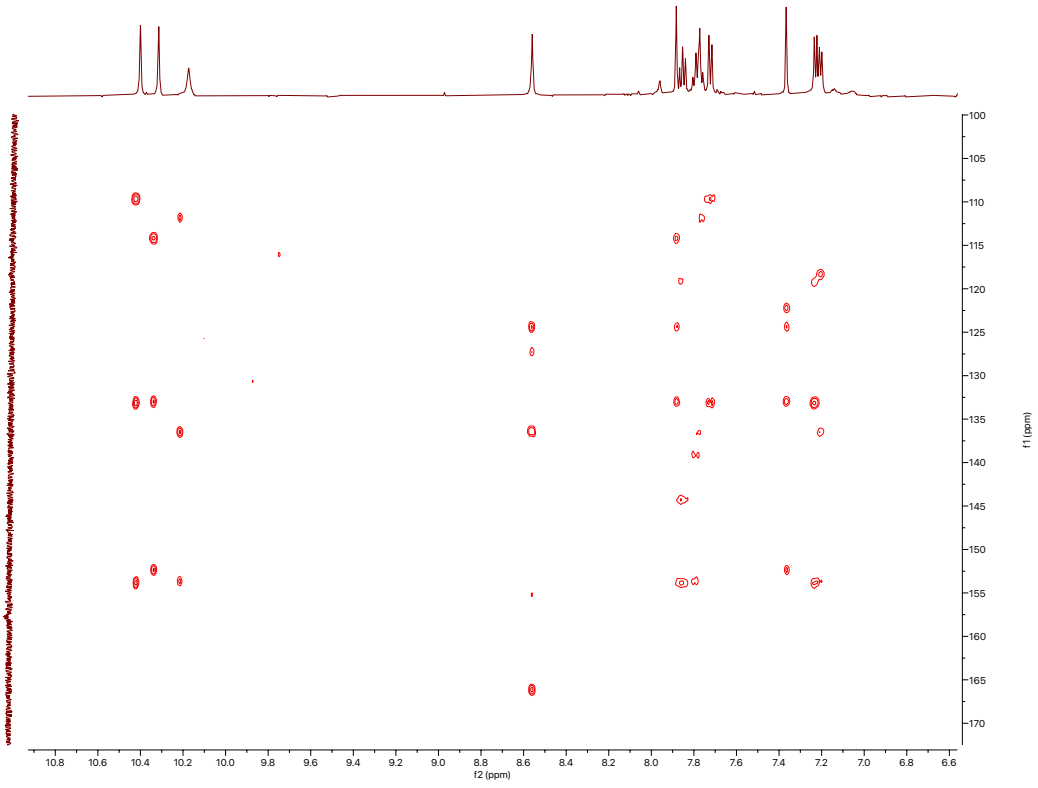

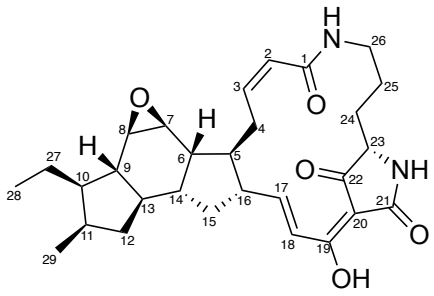

epoxyikarugamycin (**10**)

Position	δ_C (type)	δ_H, multiplets (*J* in Hz)	COSY	HMBC	ROESY
1	165.9 (C)				
2	125.6 (CH)	5.85, d (11.5)	3	1, 4	
3	138.0 (CH)	5.99, td (11.1, 2.8)	2, 4a, 4b	1	
4a	25.6 (CH_2)	2.21, m	3, 4b, 5		
4b	25.6 (CH_2)	3.48, m	3, 4a, 5		
5	45.7 (CH)	1.50, ddd (15.8, 12.2, 3.7)	4, 6, 16	7	7
6	40.6 (CH)	2.33, dd (12.8, 9.5)	5, 7, 14		
7	53.2 (CH)	2.92, d (4.0)	6, 8	5, 6	5
8	57.0 (CH)	3.12, dd (3.9, 2.1)	7, 9	9	10
9	50.1 (CH)	0.84, m	8, 10, 13		
10	46.2 (CH)	1.67, m	9, 11, 27	28	8
11	33.1 (CH)	2.20, m	10, 12, 29		
12a	38.7 (CH_2)	0.60, tq (11.9, 7.6)	11, 12b, 13	9, 29	
12b	38.7 (CH_2)	2.00, m	11, 2a, 13		
13	47.6 (CH)	1.06, m	9, 12a, 12b, 14		
14	40.7 (CH)	1.63, m	6, 13, 15		
15a	37.3 (CH_2)	1.03, m	14, 15b, 16		
15b	37.3 (CH_2)	1.98, m	14, 15a, 16		
16	47.3 (CH)	2.23, m	5, 15a, 15b, 17		
17	140.3 (CH)	6.06, dd (15.2, 9.8)	16, 18	16, 19	
18	132.7 (CH)	7.51, d (15.3)	17	16, 19	
19	181.6 (C)				
20	102.5 (C)				
21	177.2 (C)				
21-NH		6.47, d (6.1)		20, 22, 23	
22	195.9 (C)				
23	58.9 (CH)	3.32, m	24a, 24b	21, 22, 24, 25	
24a	27.7 (CH_2)	1.67, m	23, 24b, 25a, 25b		
24b	27.7 (CH_2)	1.74, dd (11.7, 8.2)	23, 24a, 25a, 25b		
25a	21.8 (CH_2)	1.18, m	24a, 24b, 25b, 26a, 26b		
25b	21.8 (CH_2)	1.27, m	24a, 24b, 25a, 26a, 26b		
26a	38.4 (CH_2)	2.41, m	25a, 25b, 26b, 26-NH		
26b	38.4 (CH_2)	3.31, m	25a, 25b, 26a, 26-NH		
26-NH		7.72, t (5.9)	26a, 26b	1, 26	
27	22.8 (CH_2)	1.45, m	10, 28	9, 10, 11, 28	
28	13.5 (CH_3)	0.98, t (7.3)	27	10, 27	
29	17.8 (CH_3)	0.86, d (7.1)	11	10, 11, 12	

^{1}H spectrum of epoxyikarugamycin (**10**)

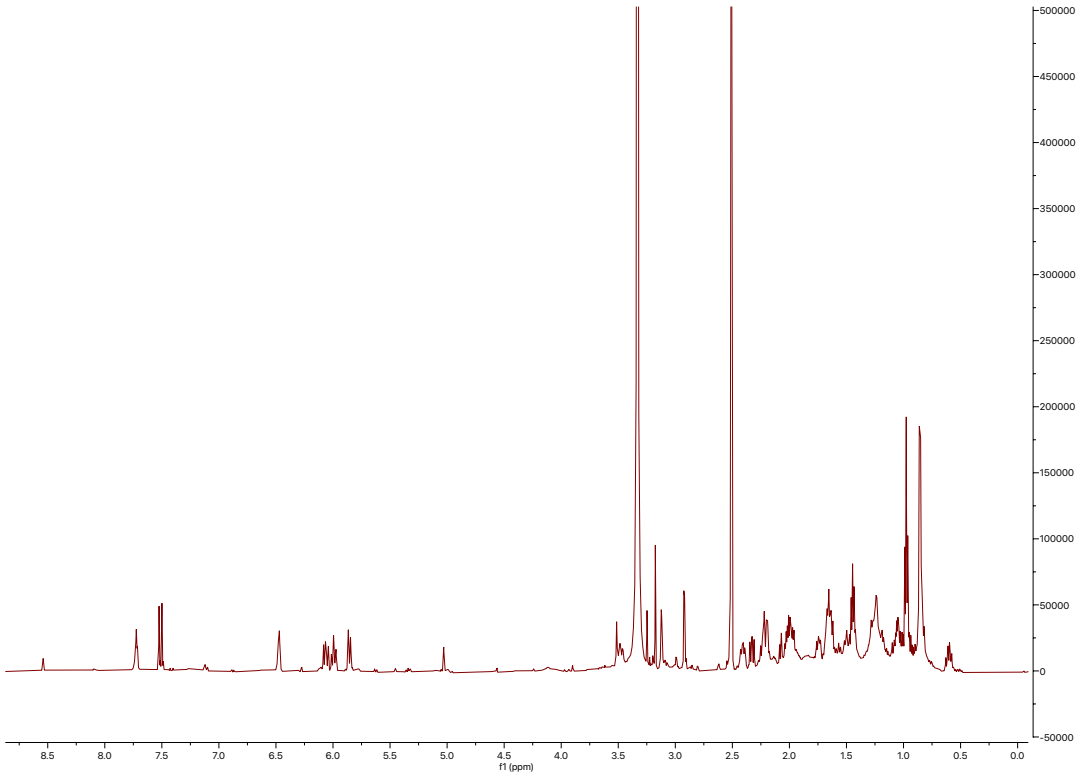

^{13}C spectrum of epoxyikarugamycin (**10**)

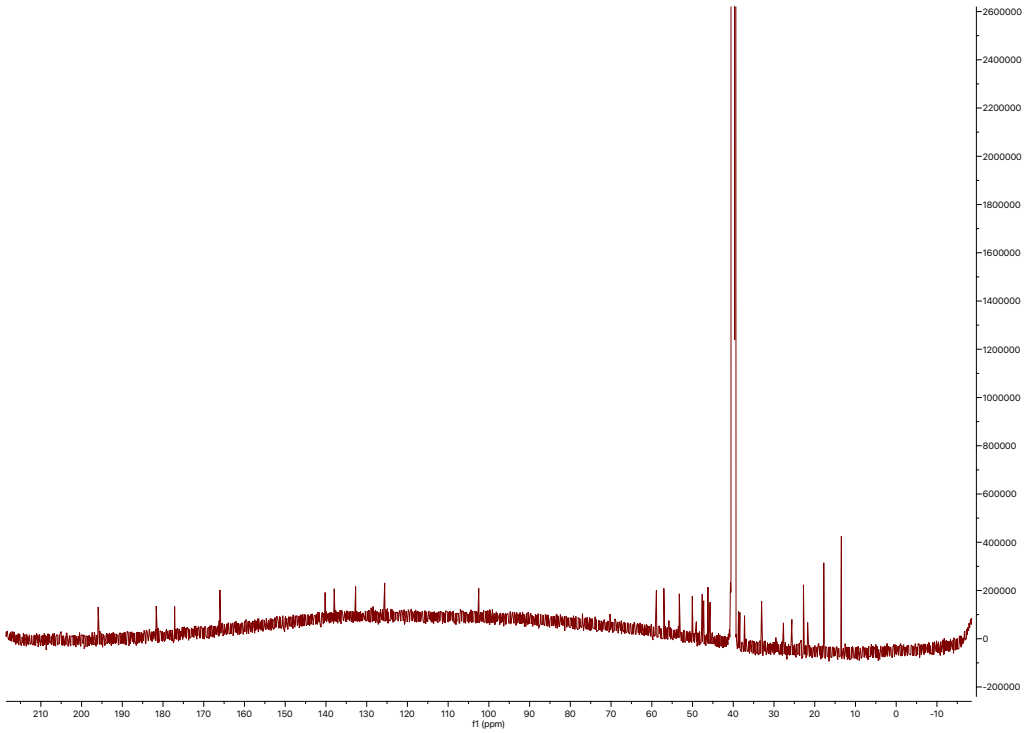

COSY spectrum of epoxyikarugamycin (**10**)

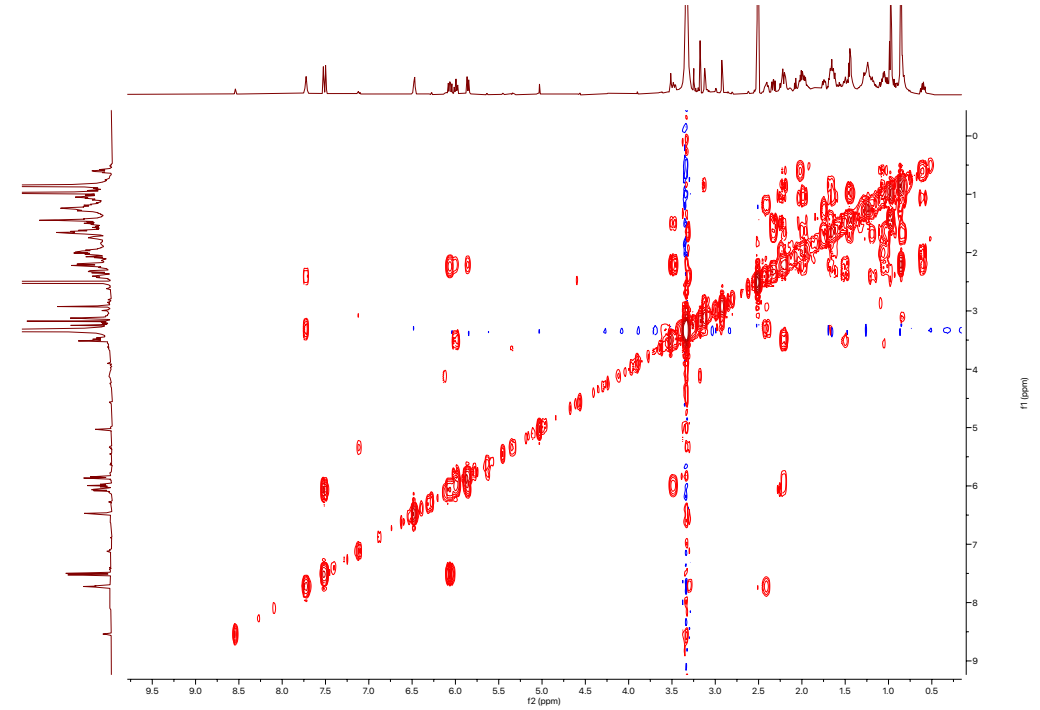

HSQC spectrum of epoxyikarugamycin (**10**)

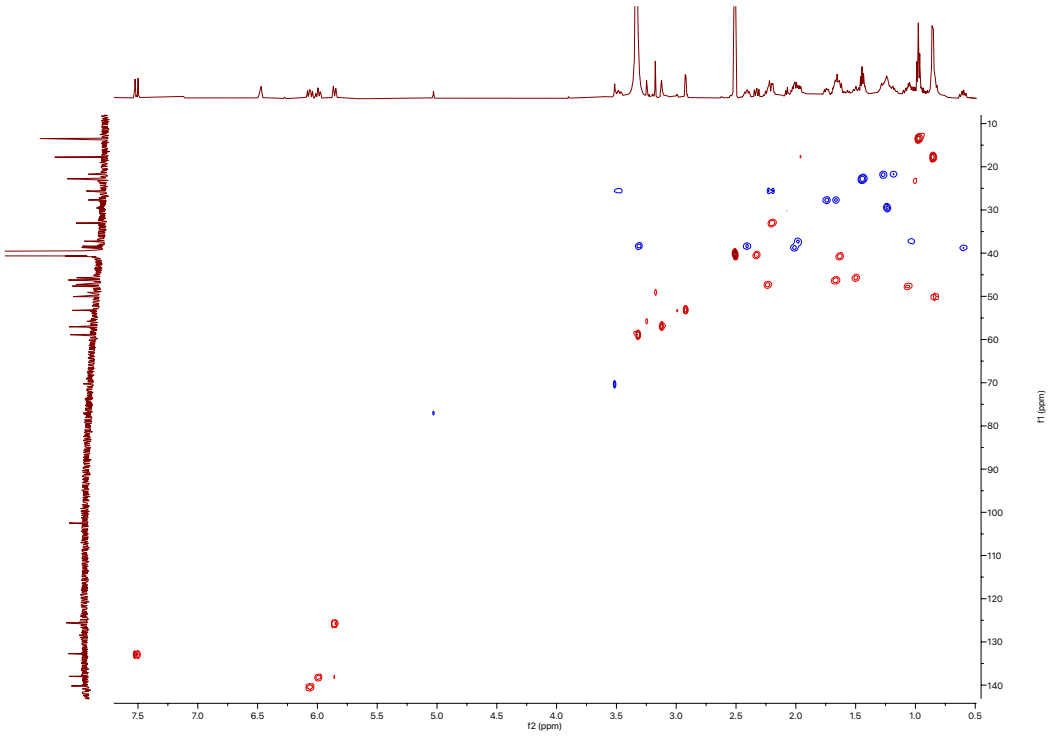

^{1}H-^{13}C HMBC spectrum of epoxyikarugamycin (**10**)

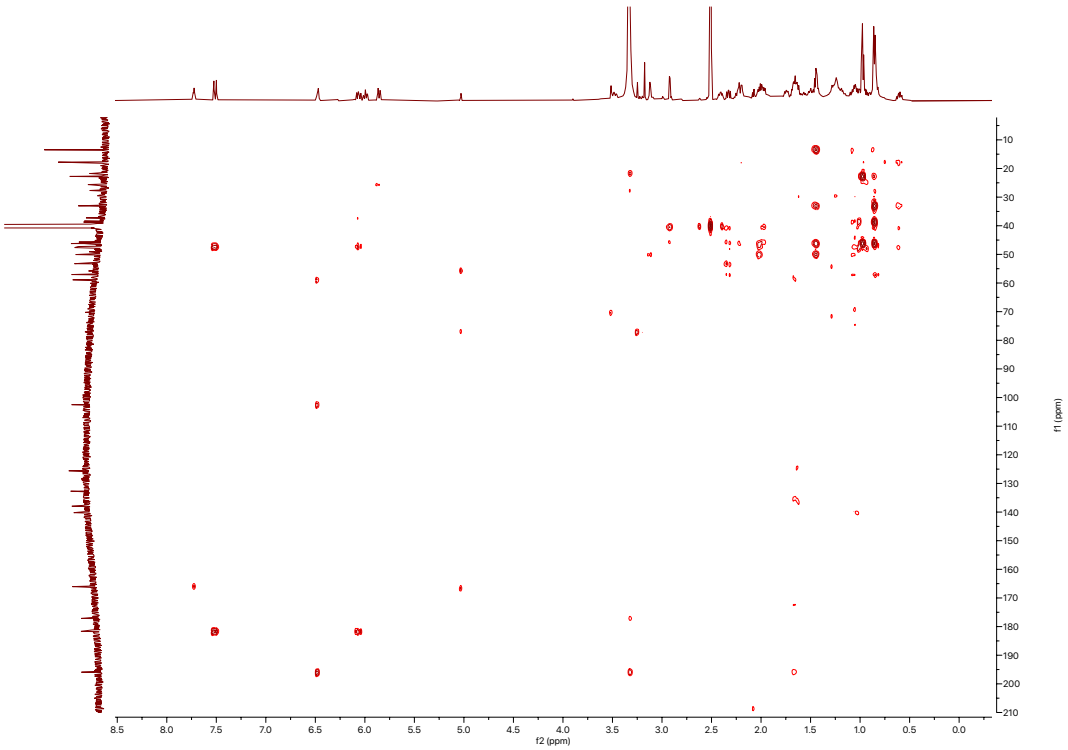

ROESY spectrum of epoxyikarugamycin (**10**)

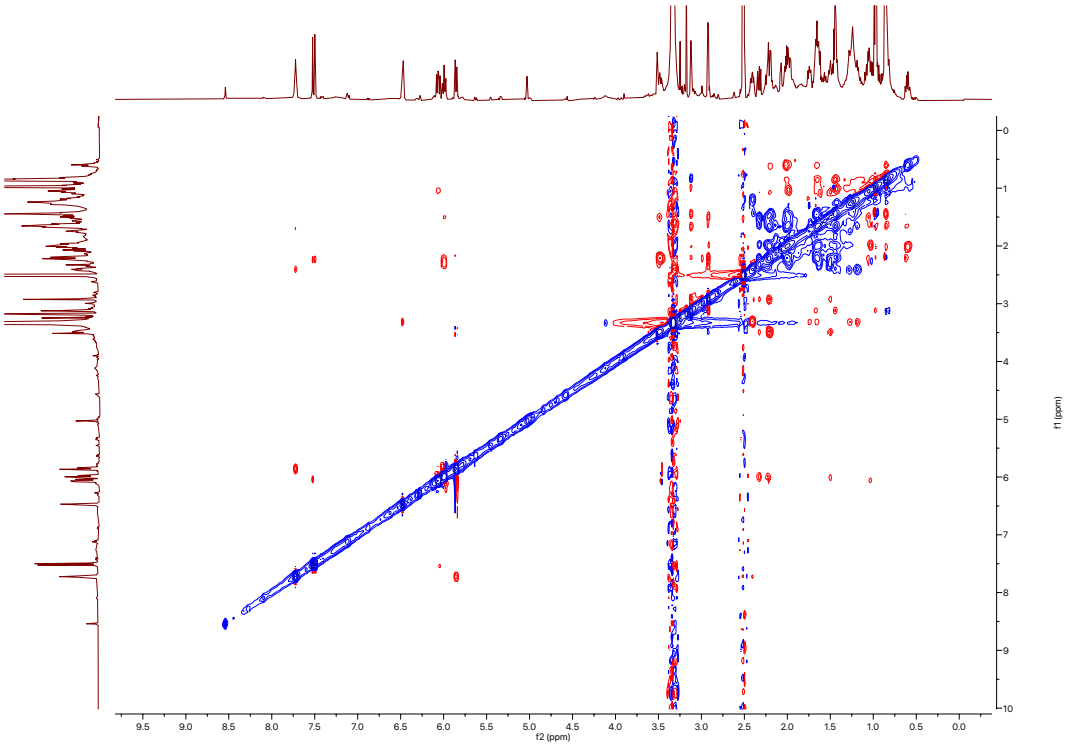

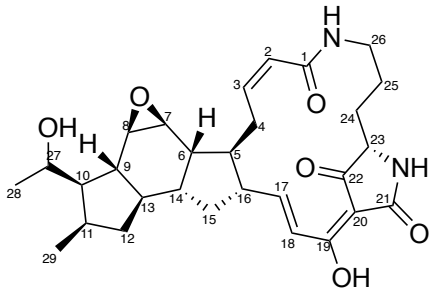

capsimycin G (**11**)

Position	δ_C (type)	δ_H, multiplets (*J* in Hz)	COSY	HMBC	ROESY
1	165.3 (C)				
2	125.1 (CH)	5.85, d (12.0)	3	1, 4	
3	137.4 (CH)	5.98, t (11.1)	2, 4a, 4b	1	
4a	25.2 (CH_2)	2.19, dd (19.1, 12.4)	3, 4b, 5		
4b	25.2 (CH_2)	3.47, m	3, 4a, 5		
5	45.6 (CH)	1.48, ddd (14.9, 11.6, 4.3)	4, 6, 16	7	7
6	40.6 (CH)	1.63, m	5, 7, 14		
7	53.1 (CH)	2.88, dd (4.1, 1.2)	6, 8	5, 6	5
8	57.4 (CH)	3.17, t (3.3)	7, 9	9	10
9	46.8 (CH)	0.87, t (12.1)	8, 10, 13		
10	51.4 (CH)	1.76, m	9, 11, 27	28	8
11	33.2 (CH)	2.26, m	10, 12, 29		
12a	38.8 (CH_2)	0.59, q (11.6)	11, 12b, 13	9, 29	
12b	38.8 (CH_2)	1.98, m	11, 2a, 13		
13	47.2 (CH)	1.09, dd (11.7, 6.8)	9, 12a, 12b, 14		
14	39.8 (CH)	2.29, m	6, 13, 15		
15a	37.1 (CH_2)	1.02, m	14, 15b, 16		
15b	37.1 (CH_2)	1.97, m	14, 15a, 16		
16	46.7 (CH)	2.22, m	5, 15a, 15b, 17		
17	139.6 (CH)	6.06, dd (15.5, 9.8)	16, 18	16, 19	
18	132.3 (CH)	7.51, d (15.2)	17	16, 19	
19	181.2 (C)				
20	102.0 (C)				
21	176.7 (C)				
21-NH		6.47, s		20, 22, 23	
22	195.4 (C)				
23	58.4 (CH)	3.31, m	24a, 24b	21, 22, 24, 25	
24a	27.2 (CH_2)	1.65, m	23, 24b, 25a, 25b		
24b	27.2 (CH_2)	1.74, m	23, 24a, 25a, 25b		
25a	21.2 (CH_2)	1.18, m	24a, 24b, 25b, 26a, 26b		
25b	21.2 (CH_2)	1.26, m	24a, 24b, 25a, 26a, 26b		
26a	37.9 (CH_2)	2.40, m	25a, 25b, 26b, 26-NH		
26b	37.9 (CH_2)	3.30, m	25a, 25b, 26a, 26-NH		
26-NH		7.72, t (6.0)	26a, 26b	1, 26	
27	66.5 (CH)	3.71, m	10, 27-OH, 28		
27-OH		4.34, d (4.8)		10, 27	
28	23.4 (CH_3)	1.22, d (6.2)	27	10, 27	
29	18.1 (CH_3)	1.01, d (7.2)	11	10, 11, 12	

^{1}H spectrum of capsimycin G (**11**)

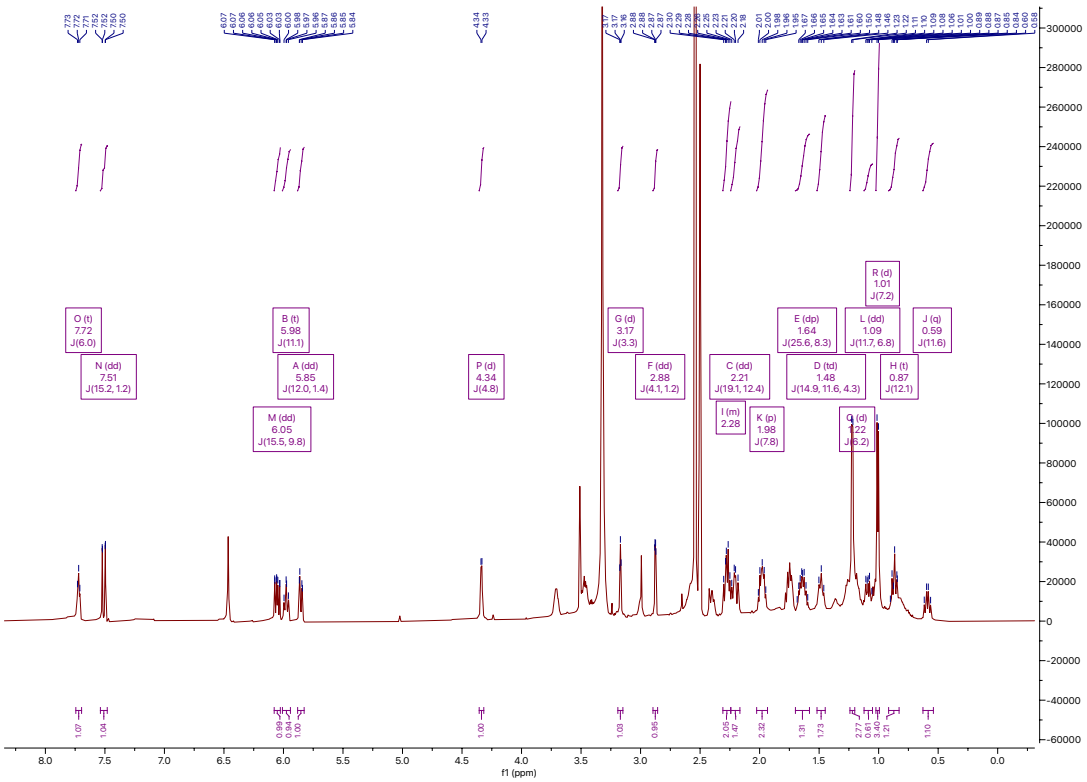

^{13}C spectrum of capsimycin G (**11**)

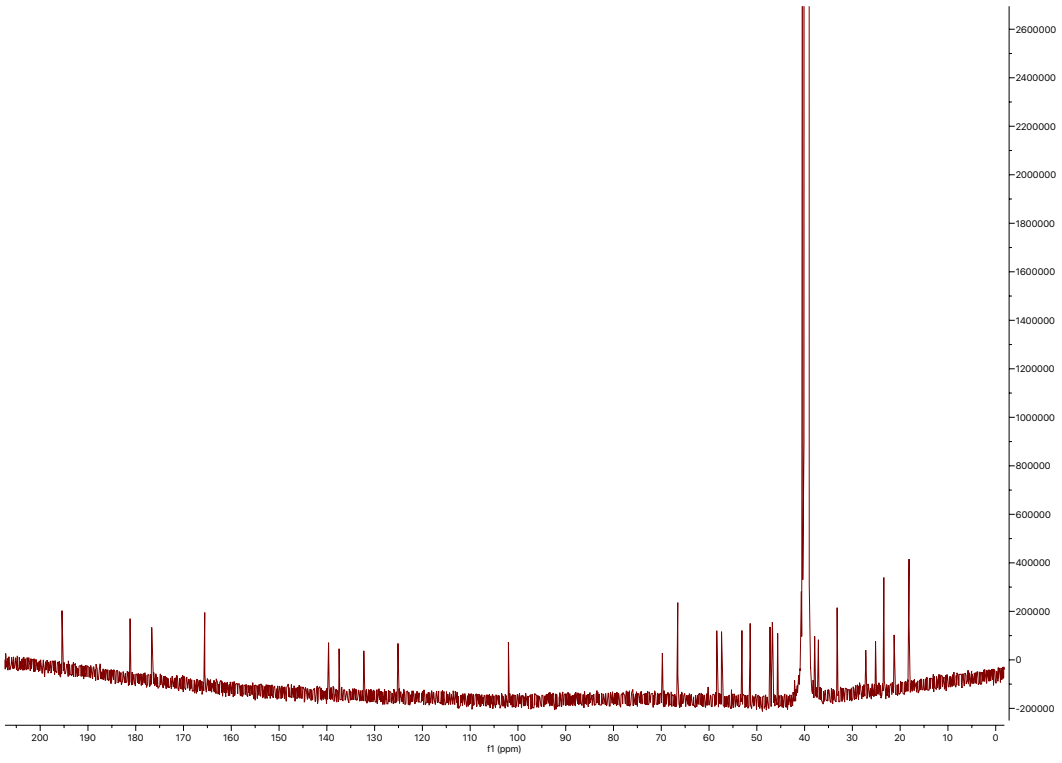

COSY spectrum of capsimycin G (**11**)

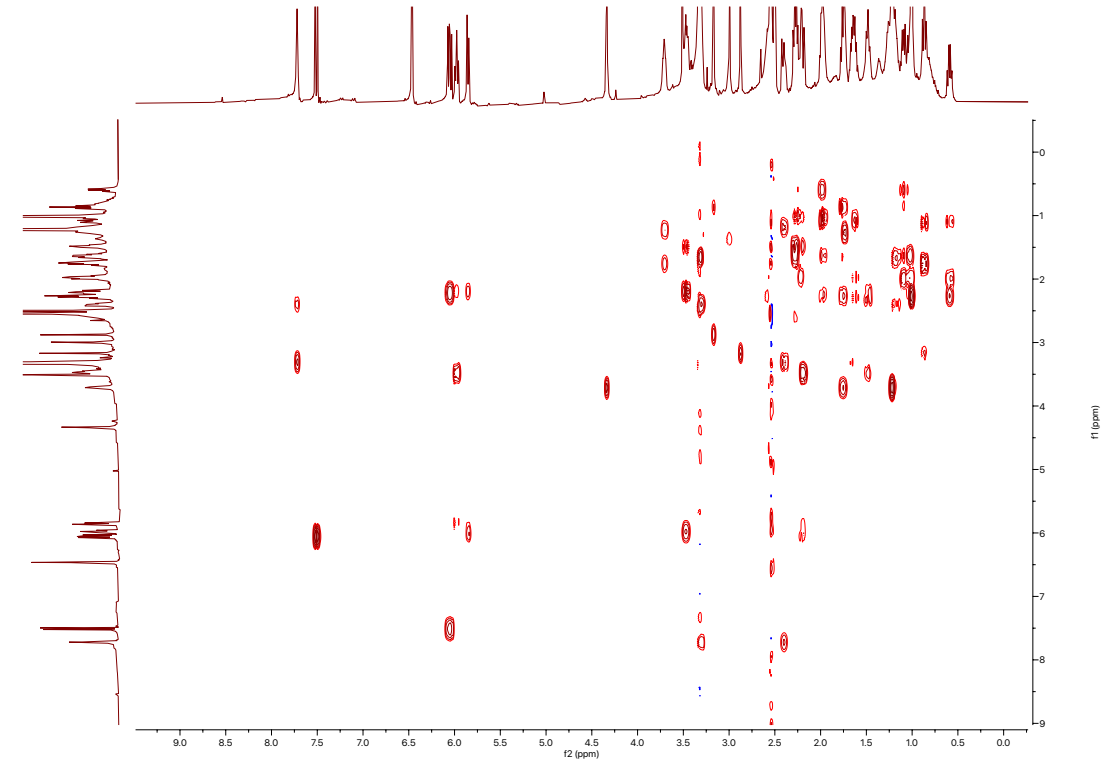

HSQC spectrum of capsimycin G (**11**)

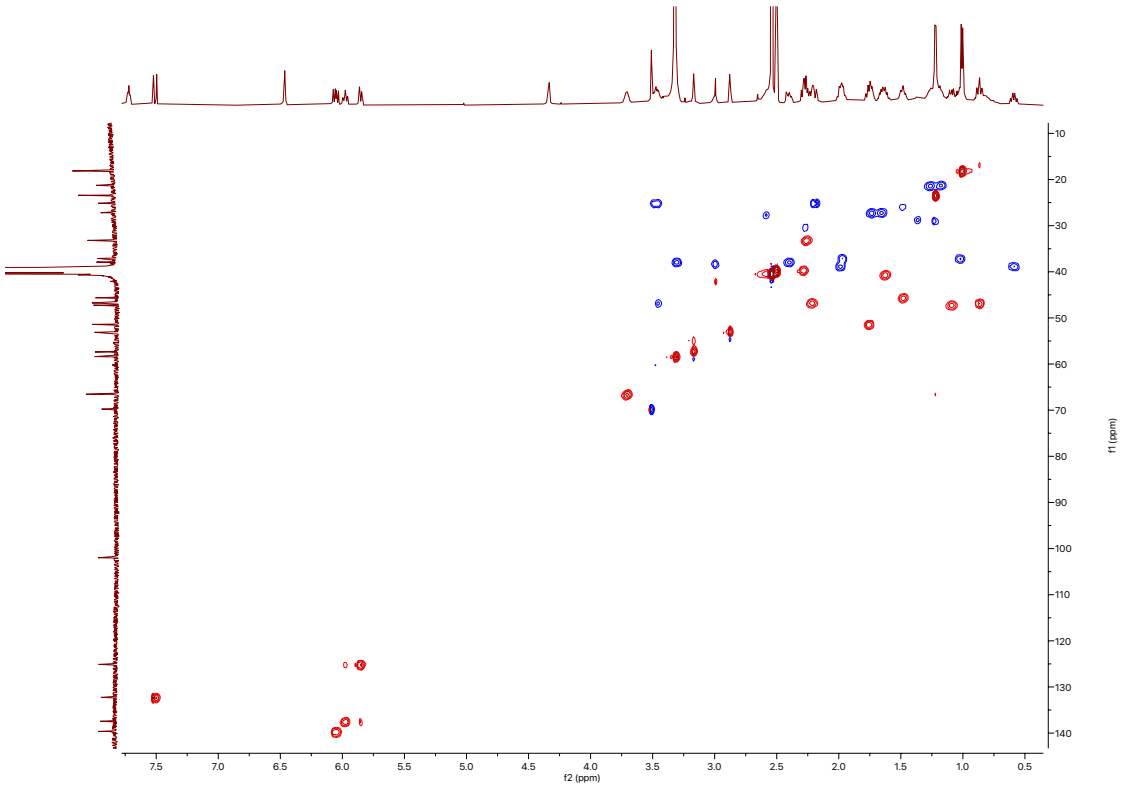

^{1}H-^{13}C HMBC spectrum of capsimycin G (**11**)

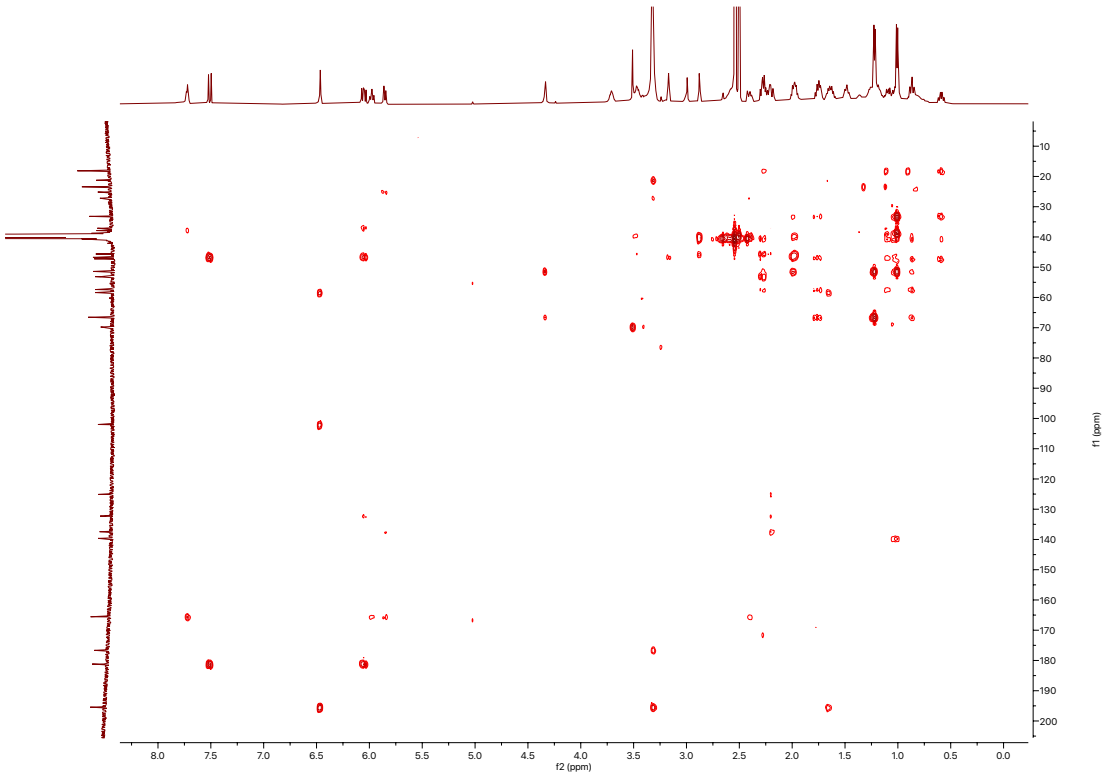

NOESY spectrum of capsimycin G (**11**)

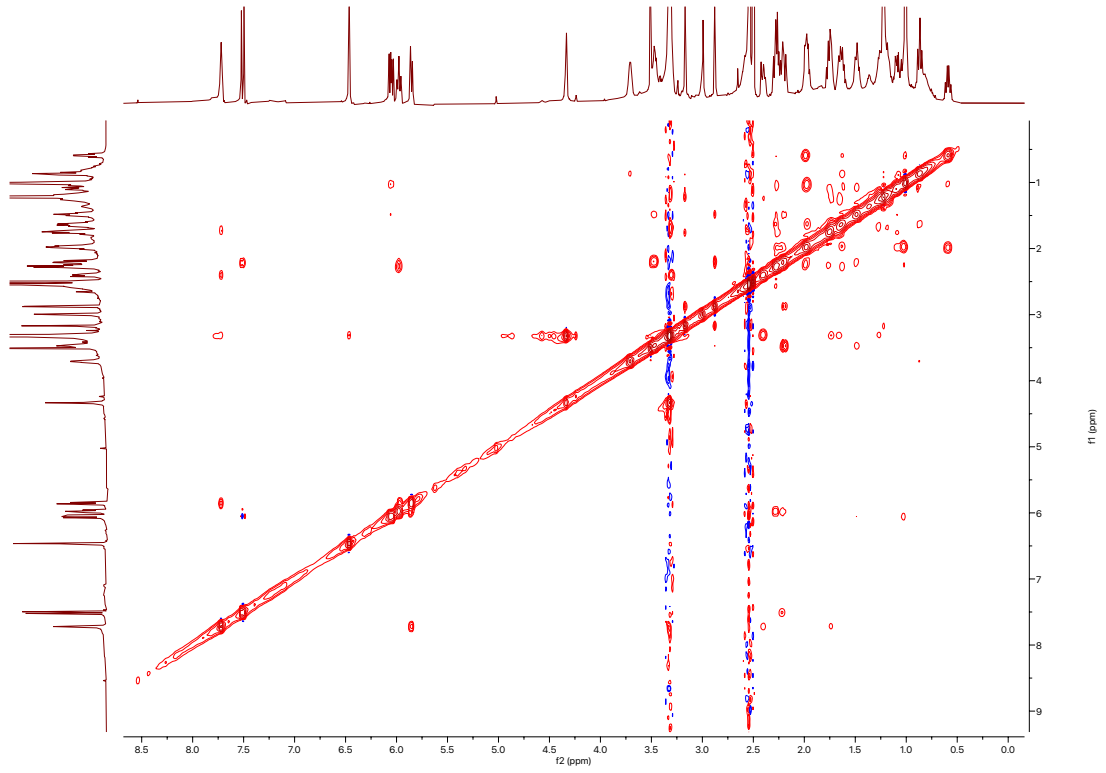

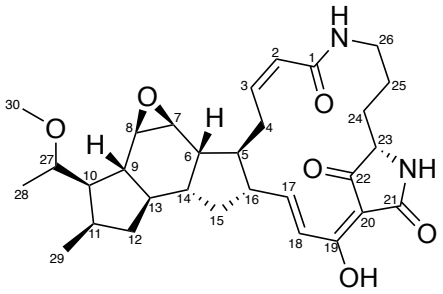

capsimycin (**12**)

Position	δ_C (type)	δ_H, multiplets (*J* in Hz)	COSY	HMBC	ROESY
1	165.5 (C)				
2	125.2 (CH)	5.88, d (11.7)	3	1, 4	
3	137.4 (CH)	5.97, t (11.5, 2.0)	2, 4a, 4b	1	
4a	25.1 (CH_2)	2.19, m	3, 4b, 5		
4b	25.1 (CH_2)	3.49, m	3, 4a, 5		
5	45.6 (CH)	1.49, tt (12.2, 3.8)	4, 6, 16	7	7
6	40.5 (CH)	1.63, m	5, 7, 14		
7	53.1 (CH)	2.88, d (4.0)	6, 8	5, 6	5
8	57.3 (CH)	3.18, t (3.3)	7, 9	9	10
9	46.9 (CH)	0.89, t (12.1)	8, 10, 13		
10	49.4 (CH)	1.88, m	9, 11, 27	28	8
11	33.3 (CH)	2.25, m	10, 12, 29		
12a	38.9 (CH_2)	0.60, td (11.9, 8.6)	11, 12b, 13	9, 29	
12b	38.9 (CH_2)	1.97, m	11, 2a, 13		
13	47.0 (CH)	1.09, dd (11.7, 6.4)	9, 12a, 12b, 14		
14	39.6 (CH)	2.29, m	6, 13, 15		
15a	37.1 (CH_2)	1.03, m	14, 15b, 16		
15b	37.1 (CH_2)	1.98, m	14, 15a, 16		
16	46.8 (CH)	2.22, m	5, 15a, 15b, 17		
17	139.8 (CH)	6.07, dd (15.2, 9.7)	16, 18	16, 19	
18	132.2 (CH)	7.52, d (15.3)	17	16, 19	
19	181.3 (C)				
20	102.0 (C)				
21	176.8 (C)				
21-NH		6.57, s		20, 22, 23	
22	195.5 (C)				
23	58.5 (CH)	3.32, m	24a, 24b	21, 22, 24, 25	
24a	27.2 (CH_2)	1.67, m	23, 24b, 25a, 25b		
24b	27.2 (CH_2)	1.75, td (13.3, 1.9)	23, 24a, 25a, 25b		
25a	21.2 (CH_2)	1.18, m	24a, 24b, 25b, 26a, 26b		
25b	21.2 (CH_2)	1.26, d (7.4)	24a, 24b, 25a, 26a, 26b		
26a	37.9 (CH_2)	2.39, m	25a, 25b, 26b, 26-NH		
26b	37.9 (CH_2)	3.31, m	25a, 25b, 26a, 26-NH		
26-NH		7.80, t (5.5)	26a, 26b	1, 26	
27	76.8 (CH)	3.32, m	10, 28	10, 11, 30	
28	17.2 (CH_3)	1.21, d (6.1)	27	10, 27	
29	17.7 (CH_3)	0.94, d (7.1)	11	10, 11, 12	
30	54.6 (CH_3)	3.21, s		27	

^{1}H spectrum of capsimycin (**12**)

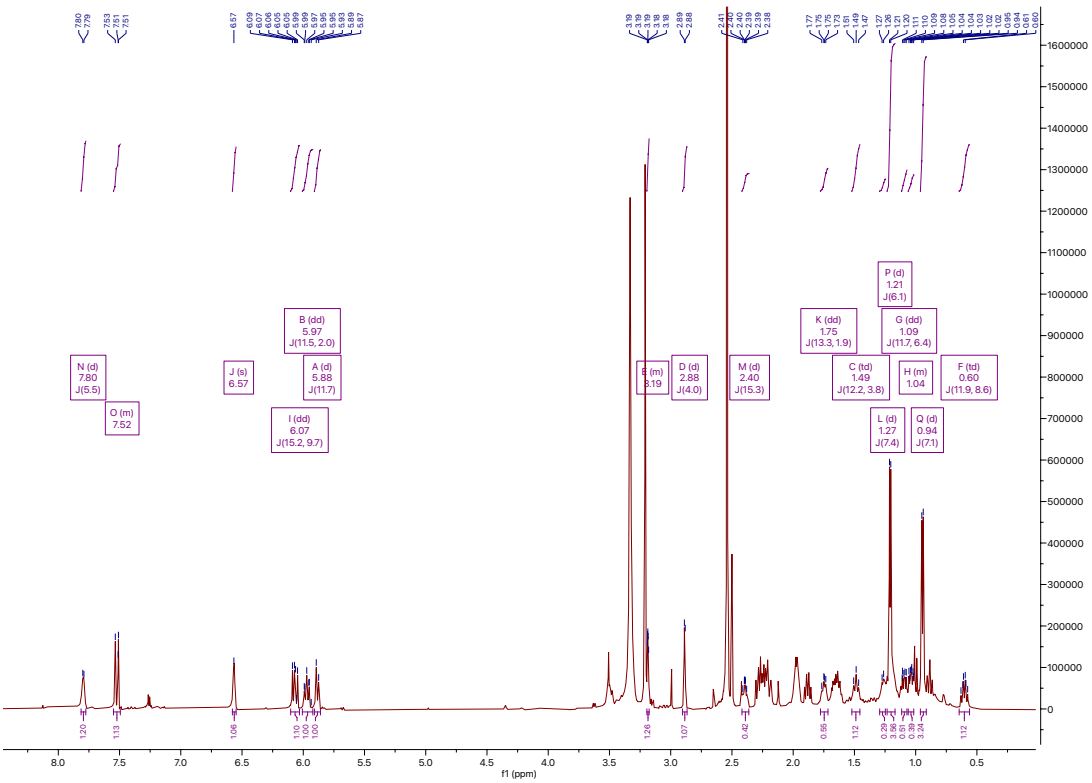

^{13}C spectrum of capsimycin (**12**)

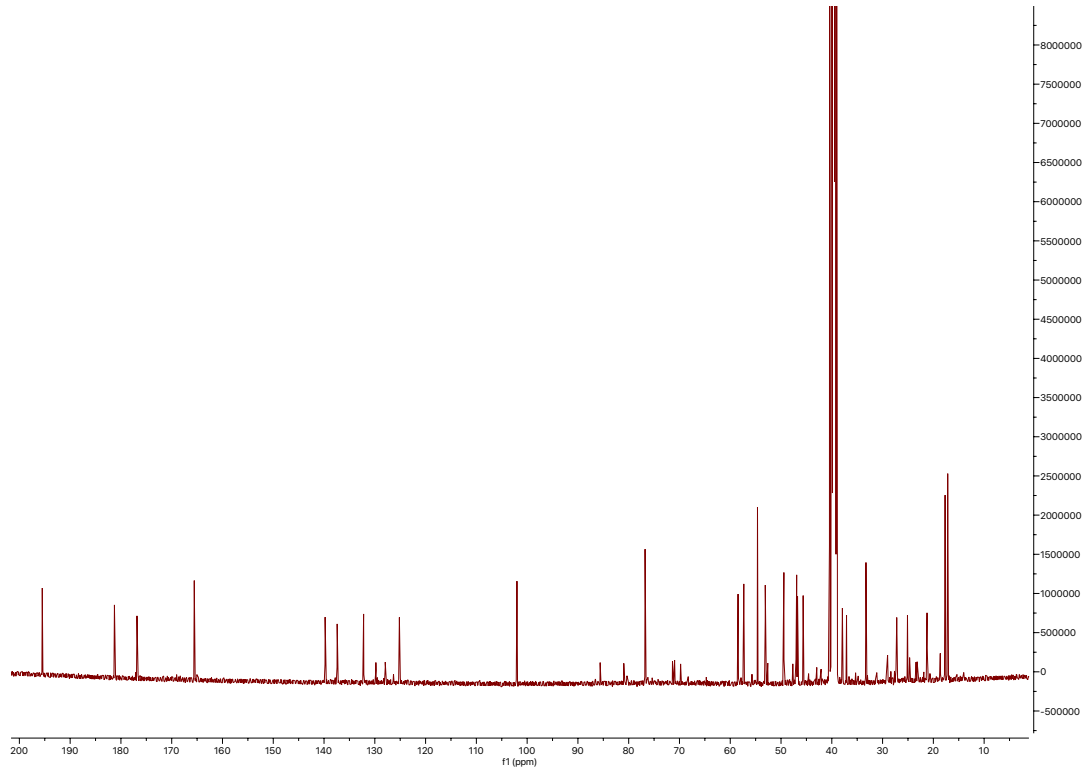

COSY spectrum of capsimycin (**12**)

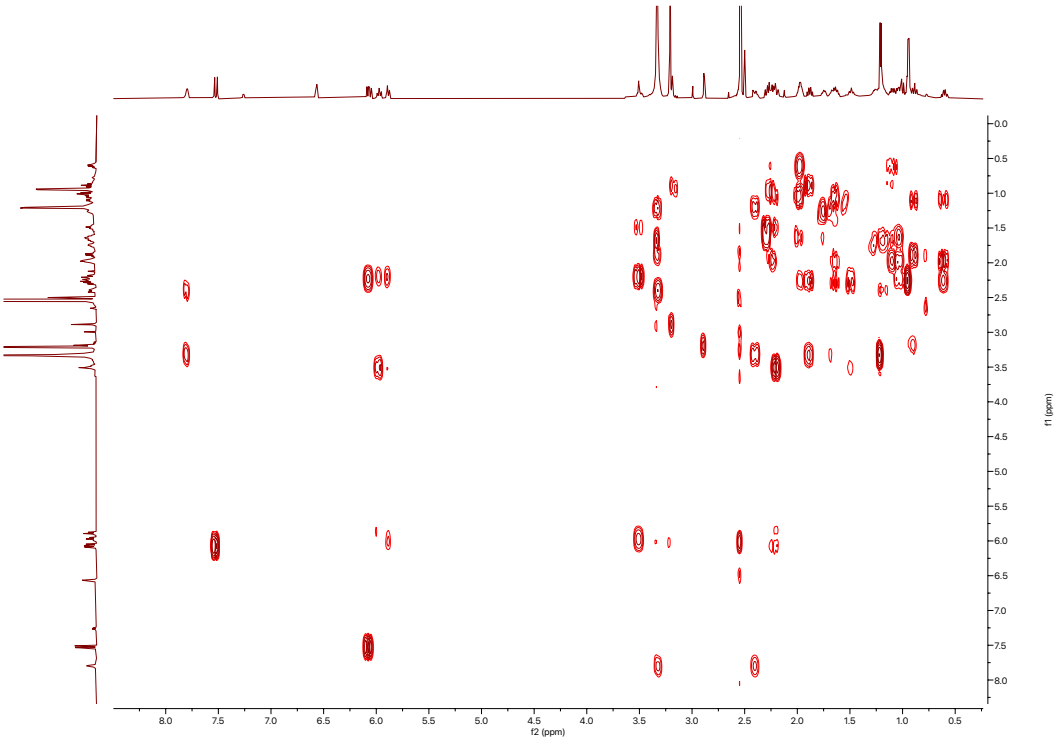

HSQC spectrum of capsimycin (**12**)

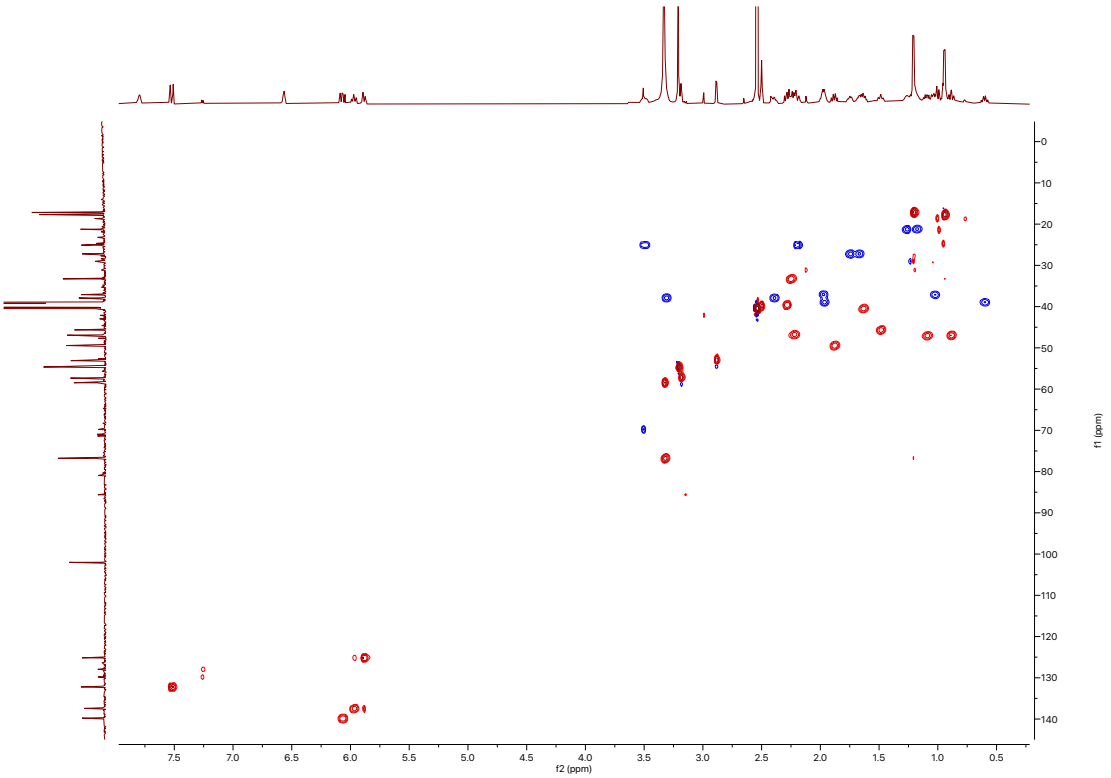

^{1}H-^{13}C HMBC spectrum of capsimycin (**12**)

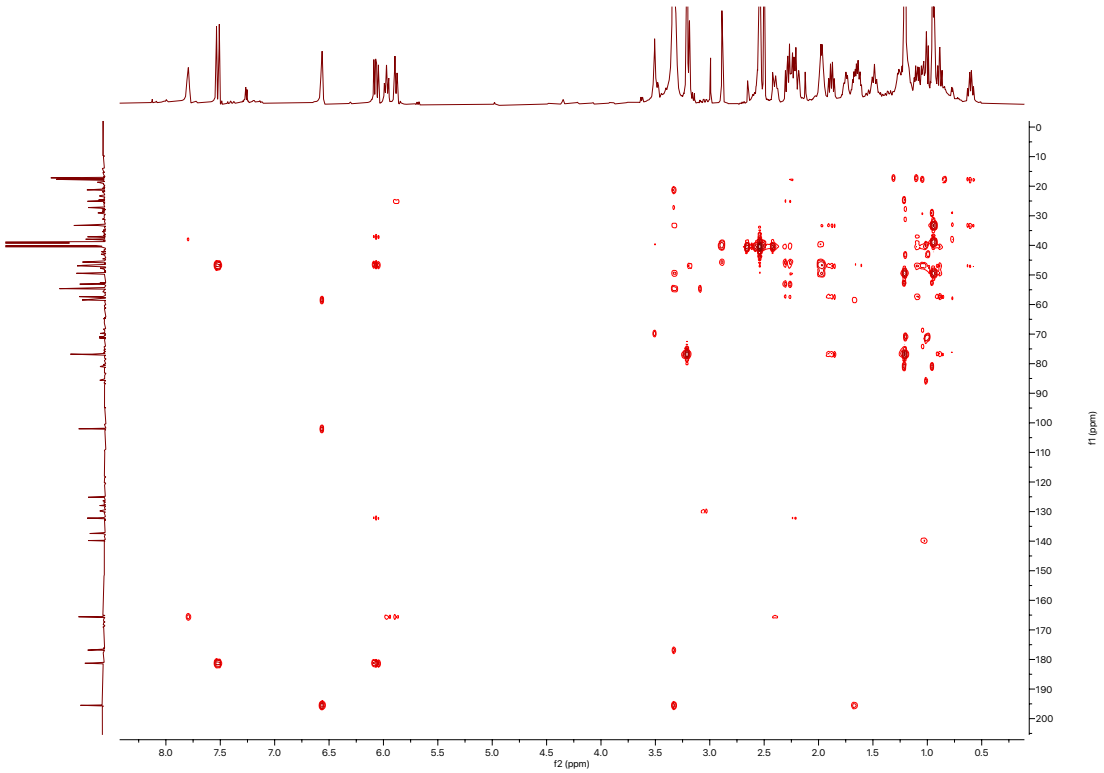

ROESY spectrum of capsimycin (**12**)

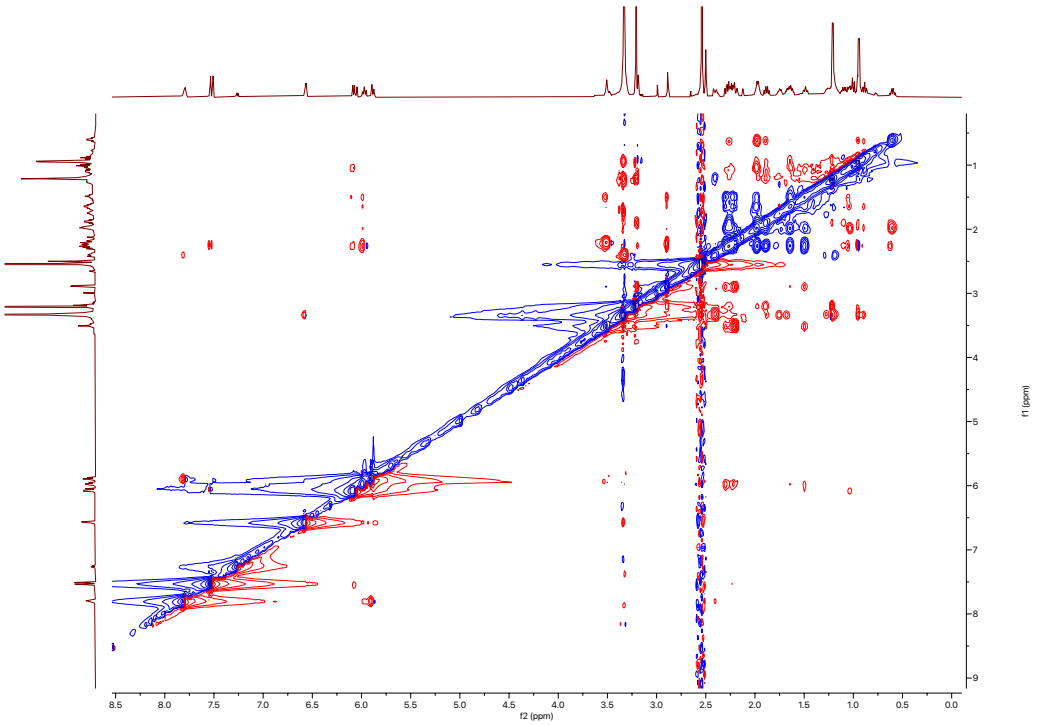

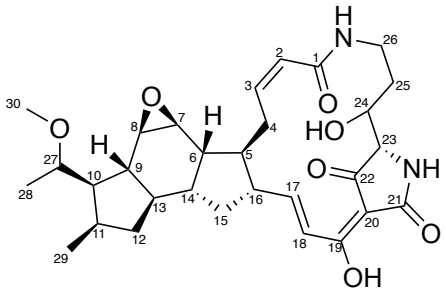

capsimycin H (**13**)

Position	δ_C (type)	δ_H, multiplets (*J* in Hz)	COSY	HMBC	ROESY
1	165.9 (C)				
2	124.8 (CH)	5.82, dd (11.4, 2.8)	3	1, 4	
3	138.0 (CH)	6.00, td (11.3, 2.6)	2, 4a, 4b	1	
4a	24.9 (CH_2)	2.15, m	3, 4b, 5		
4b	24.9 (CH_2)	3.63, ddd (16.2, 11.0, 4.0)	3, 4a, 5		
5	45.6 (CH)	1.55, td (12.4, 5.9)	4, 6, 16	7	7
6	40.5 (CH)	1.63, m	5, 7, 14		
7	53.1 (CH)	2.88, d (4.0)	6, 8	5, 6	5
8	57.3 (CH)	3.18, t (2.9)	7, 9	9	10
9	46.9 (CH)	0.88, td (11.9, 2.3)	8, 10, 13		
10	49.5 (CH)	1.88, dq (16.2, 7.7, 6.3)	9, 11, 27	28	8
11	33.3 (CH)	2.25, m	10, 12, 29		
12a	38.9 (CH_2)	0.60, td (11.9, 8.6)	11, 12b, 13	9, 29	
12b	38.9 (CH_2)	1.97, m	11, 2a, 13		
13	46.9 (CH)	1.10, m	9, 12a, 12b, 14		
14	39.4 (CH)	2.31, dd (12.7, 9.7)	6, 13, 15		
15a	36.8 (CH_2)	1.07, m	14, 15b, 16		
15b	36.8 (CH_2)	1.97, m	14, 15a, 16		
16	47.2 (CH)	2.22, m	5, 15a, 15b, 17		
17		6.10, br s			
18		7.25, d (11.2)			
19	176.6 (C)				
20	100.9 (C)				
21	177.6 (C)				
21-NH					
22	193.6 (C)				
23	66.8 (CH)	3.56, m	24	21, 22, 24, 25	
24	70.8 (CH_2)	3.78, d (6.7)	23, 25a, 25b	22, 25, 26	23, 25b, 26a
24-OH					
25a	31.3 (CH_2)	1.14, m	24, 25b, 26a, 26b		
25b	31.3 (CH_2)	1.41, q (13.6)	24, 25a, 26a, 26b		
26a	36.1 (CH_2)	2.60, tq (13.3, 8.3, 6.6)	25a, 25b, 26b, 26-NH		
26b	36.1 (CH_2)	3.32, m	25a, 25b, 26a, 26-NH		
26-NH		7.98, t (5.5)	26a, 26b	1, 26	
27	76.8 (CH)	3.32, m	10, 28	10, 11, 30	
28	17.2 (CH_3)	1.20, d (6.1)	27	10, 27	
29	17.7 (CH_3)	0.94, d (7.1)	11	10, 11, 12	
30	54.8 (CH_3)	3.20, s		27	

^{1}H spectrum of capsimycin H (**13**)

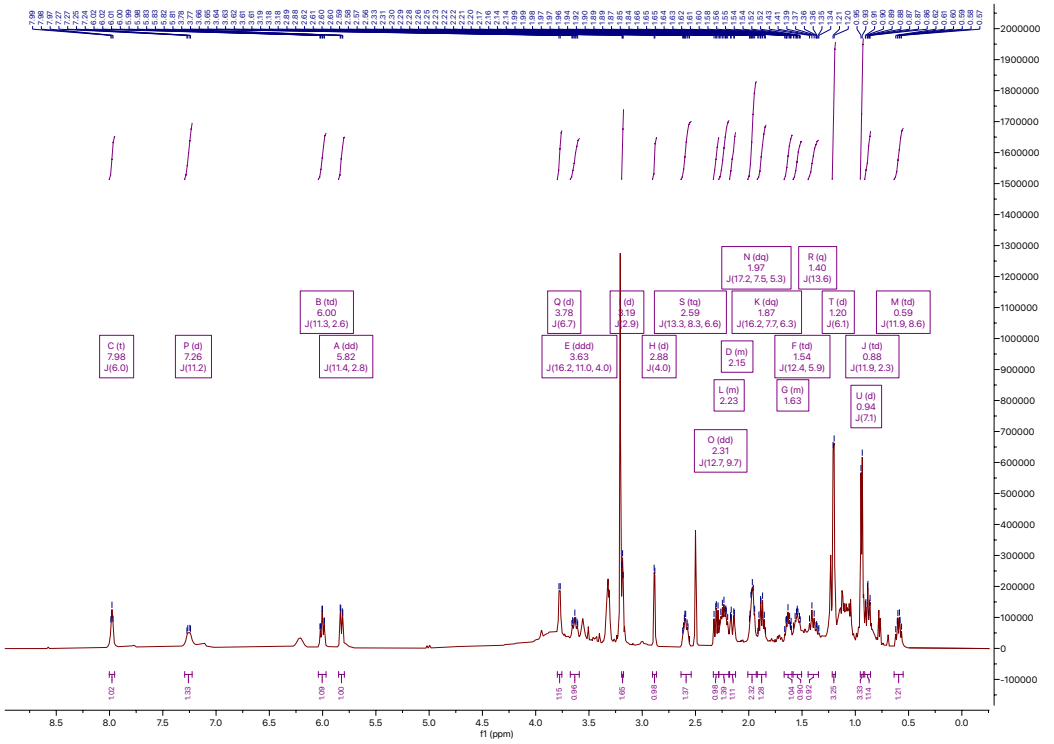

^{13}C spectrum of capsimycin H (**13**)

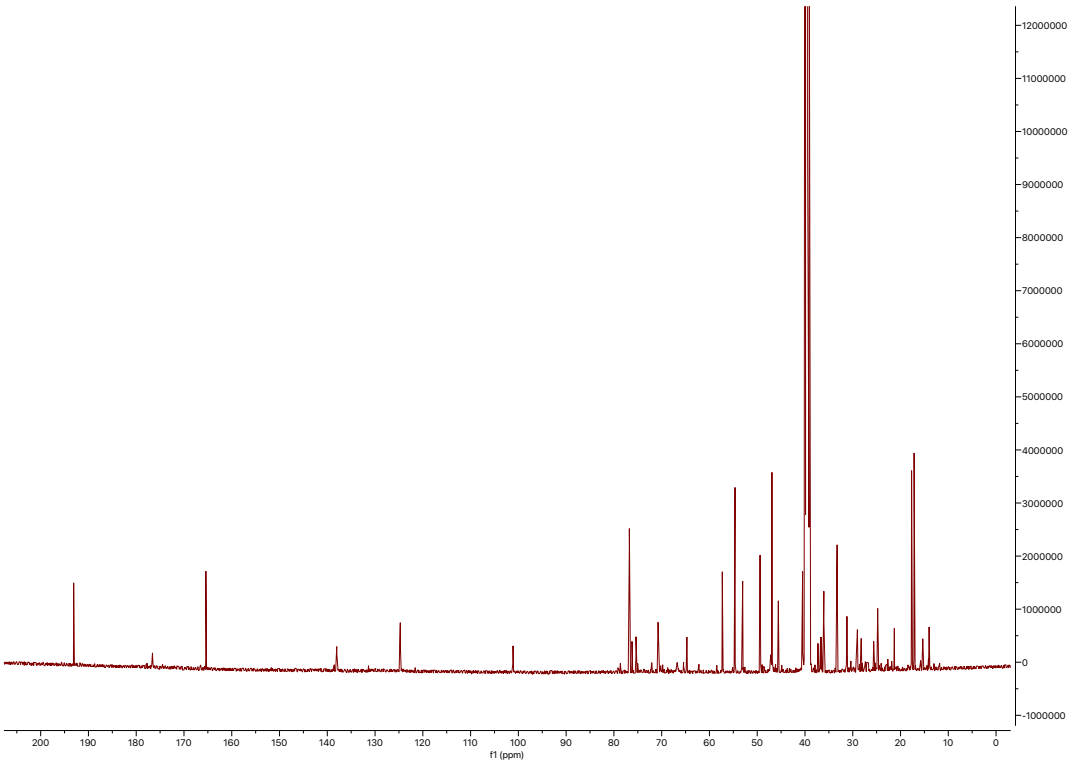

COSY spectrum of capsimycin H (**13**)

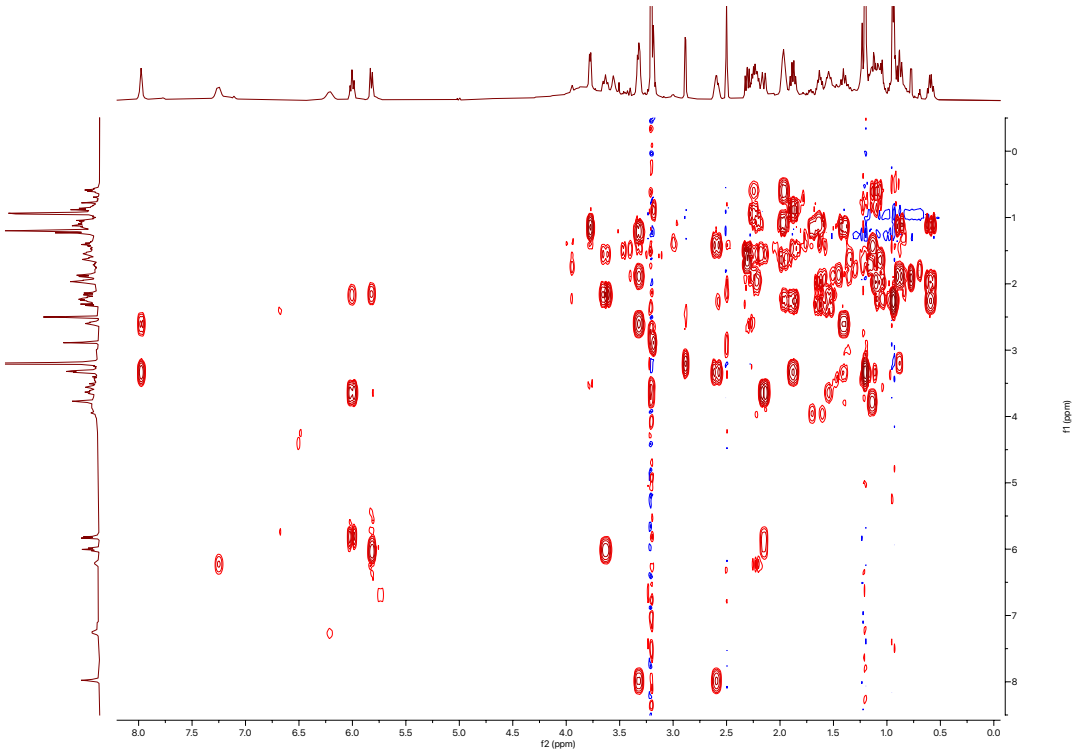

HSQC spectrum of capsimycin H (**13**)

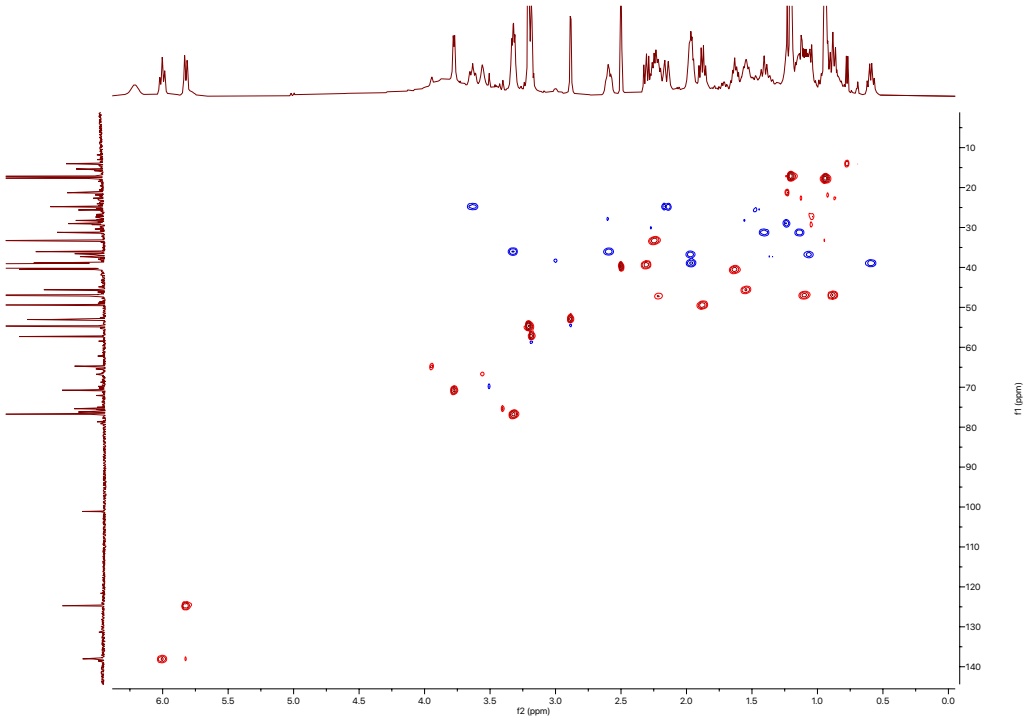

^{1}H-^{13}C HMBC spectrum of capsimycin H (**13**)

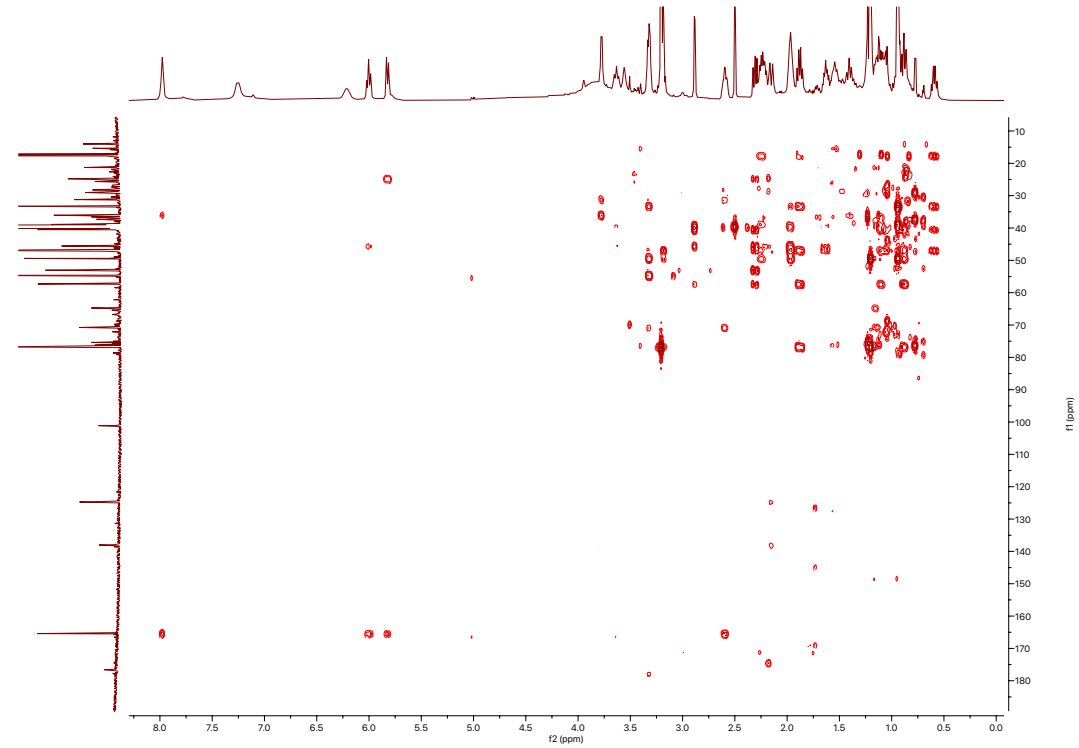

ROESY spectrum of capsimycin H (**13**)

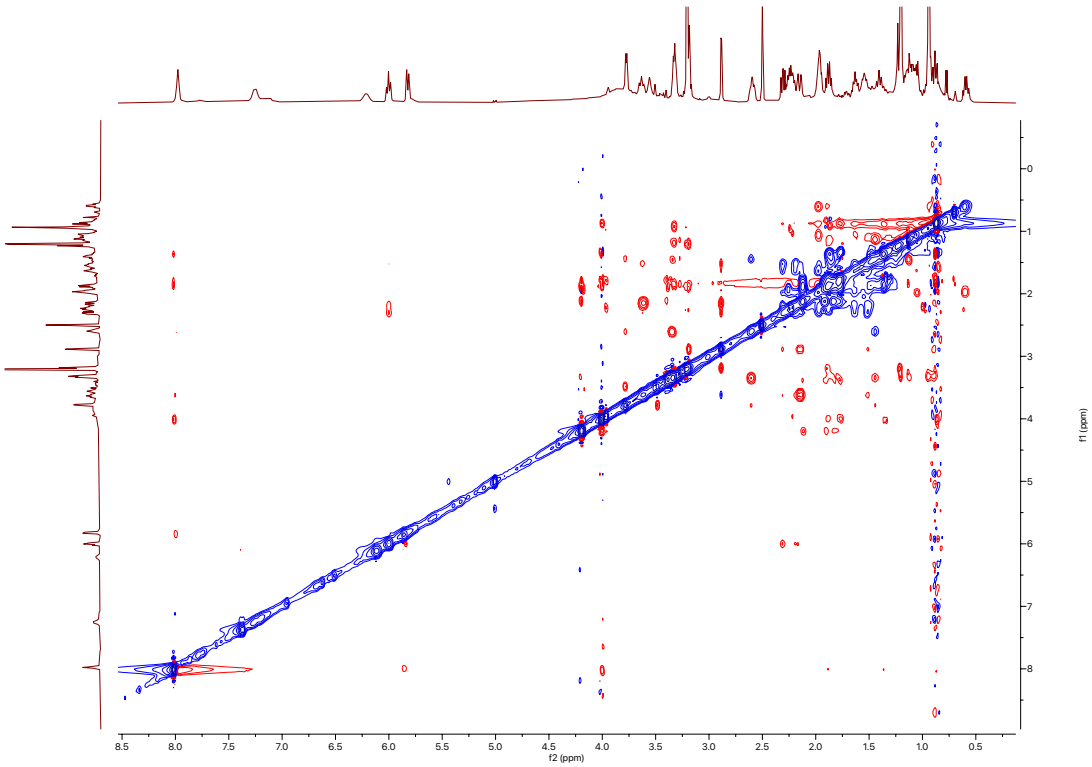

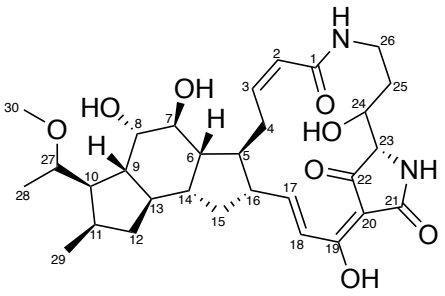

hydroxyikarugamycin A (**14**)

^{1}H spectrum of hydroxyikarugamycin A (**14**)

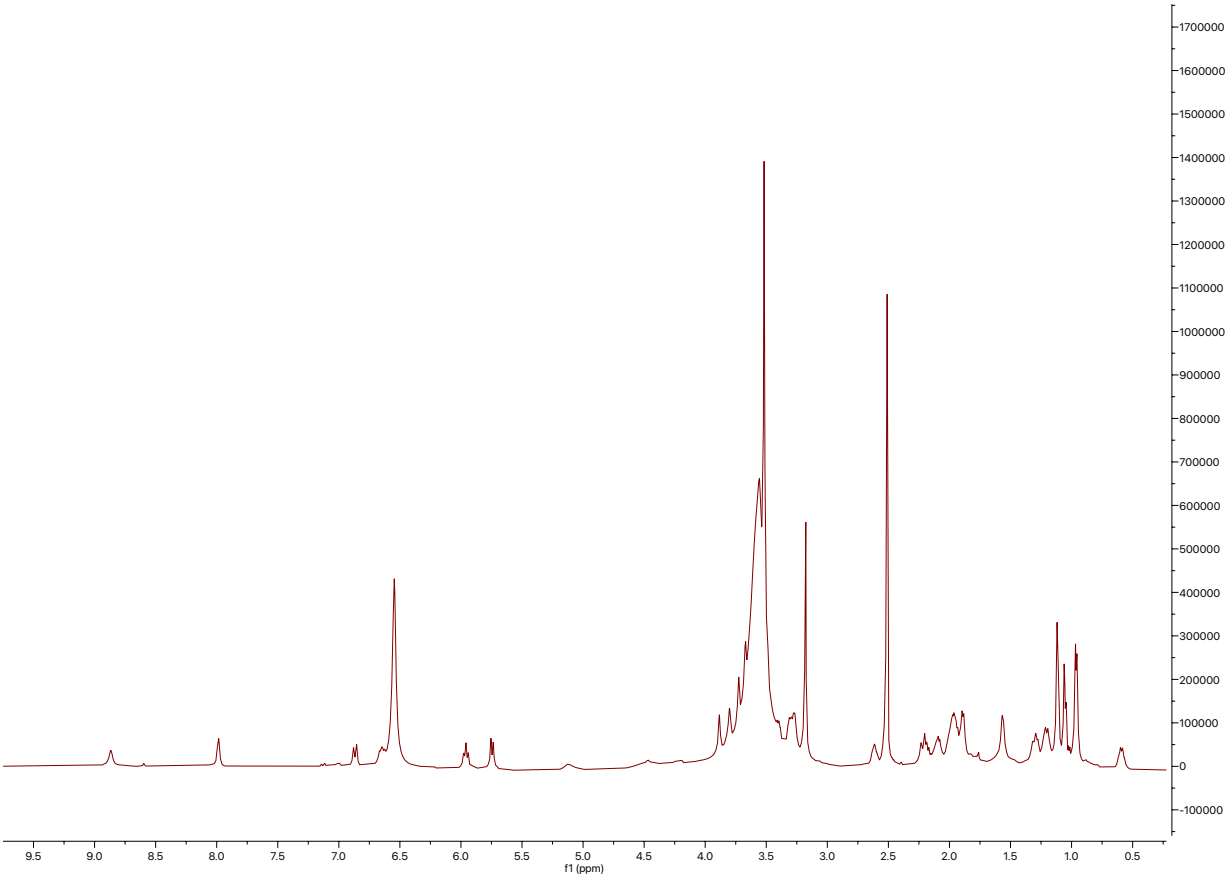

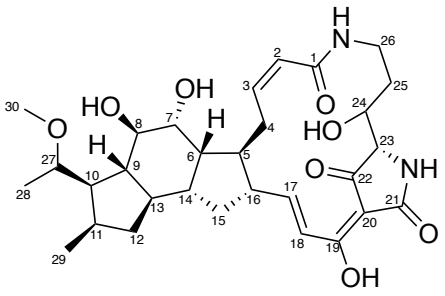

hydroxyikarugamycin A-2 (**15**)

^{1}H spectrum of hydroxyikarugamycin A-2 (**15**)

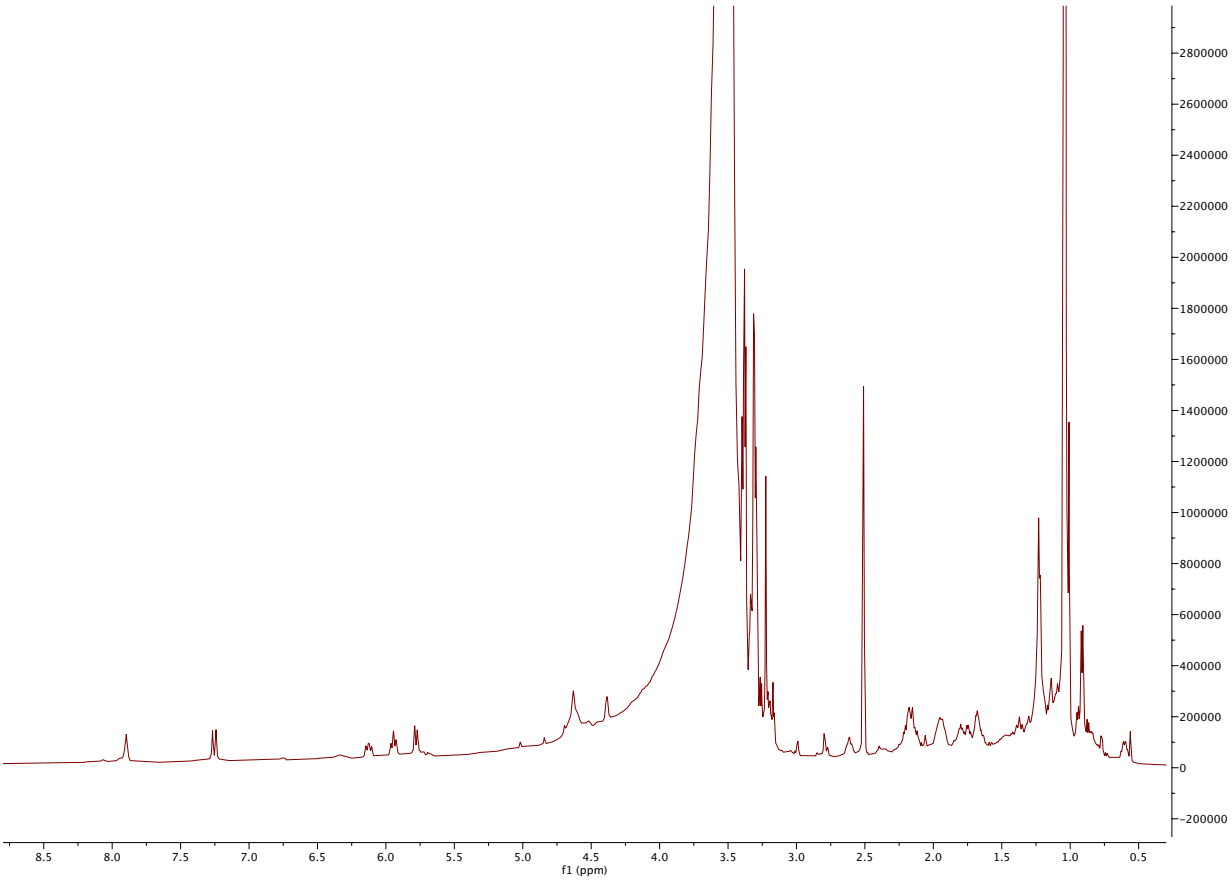

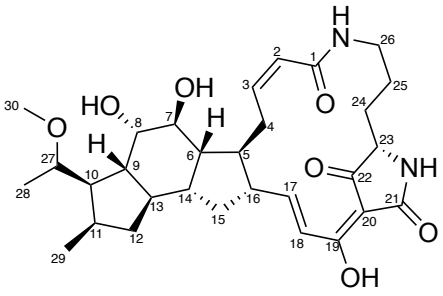

hydroxyikarugamycin B (**16**)

Position	δ_C (type)	δ_H, multiplets (*J* in Hz)	COSY	HMBC	ROESY
1	165.6 (C)				
2	123.9 (CH)	5.75, d (11.4)	3	1, 4	
3	140.2 (CH)	5.94, ddd (11.5, 10.0, 4.0)	2, 4a, 4b	1	
4a	26.0 (CH_2)	2.35, dt (16.8, 3.5)	3, 4b, 5		
4b	26.0 (CH_2)	3.39, tq (10.2, 4.9, 3.9)	3, 4a, 5		
5	44.7 (CH)	1.95, m	4, 6, 16	7	
6	41.5 (CH)	1.88, m	5, 7, 14		
7	70.8 (CH)	3.73, dd (3.6, 1.9)	6, 8	8, 9, 14	5, 13
7-OH					
8	71.5 (CH)	3.68, t (3.0)	7, 9	6, 7	6
8-OH					
9	40.2 (CH)	1.56, ddd (12.1, 8.8, 4.5)	8, 10, 13		
10	44.5 (CH)	1.96, m	9, 11, 27	28	
11	33.3 (CH)	2.09, ddd (15.8, 9.0, 7.0)	10, 12, 29		
12a	39.7 (CH_2)	0.59, tq (18.3, 10.3, 9.4)	11, 12b, 13	9, 29	
12b	39.7 (CH_2)	1.97, m	11, 2a, 13		
13	43.9 (CH)	1.56, ddd (12.1, 8.8, 4.5)	9, 12a, 12b, 14		
14	47.1 (CH)	1.87, m	6, 13, 15		
15a	34.8 (CH_2)	1.19, ddd (13.1, 9.5, 3.2)	14, 15b, 16		
15b	34.8 (CH_2)	1.98, m	14, 15a, 16		
16	49.4 (CH)	2.22, p (9.8)	5, 15a, 15b, 17		
17	151.1 (CH)	6.65, dd (15.4, 10.2)	16, 18	16, 19	
18	121.7 (CH)	6.94, d (15.5)	17	16, 19	
19	171.2 (C)				
20	100.7 (C)				
21	175.0 (C)				
21-NH		8.68, s		20, 22, 23	
22	195.8 (C)				
23	61.0 (CH)	3.84, dd (5.8, 2.2)	24a, 24b	21, 22, 24, 25	
24a	27.0 (CH_2)	1.72, m	23, 24b, 25a, 25b		
24b	27.0 (CH_2)	1.84, m	23, 24a, 25a, 25b		
25a	20.6 (CH_2)	1.05, m	24a, 24b, 25b, 26a, 26b		
25b	20.6 (CH_2)	1.39, m	24a, 24b, 25a, 26a, 26b		
26a	38.2 (CH_2)	1.49, m	25a, 25b, 26b, 26-NH		
26b	38.2 (CH_2)	3.23, m	25a, 25b, 26a, 26-NH		
26-NH		7.85, t (5.7)	26a, 26b	1, 26	
27	76.9 (CH)	3.26, m	10, 28	10, 11, 30	
28	16.9 (CH_3)	1.12, d (6.2)	27	10, 27	
29	18.1 (CH_3)	0.96, d (7.1)	11	10, 11, 12	
30	54.8 (CH_3)	3.18, s		27	

^{1}H spectrum of hydroxyikarugamycin B (**16**)

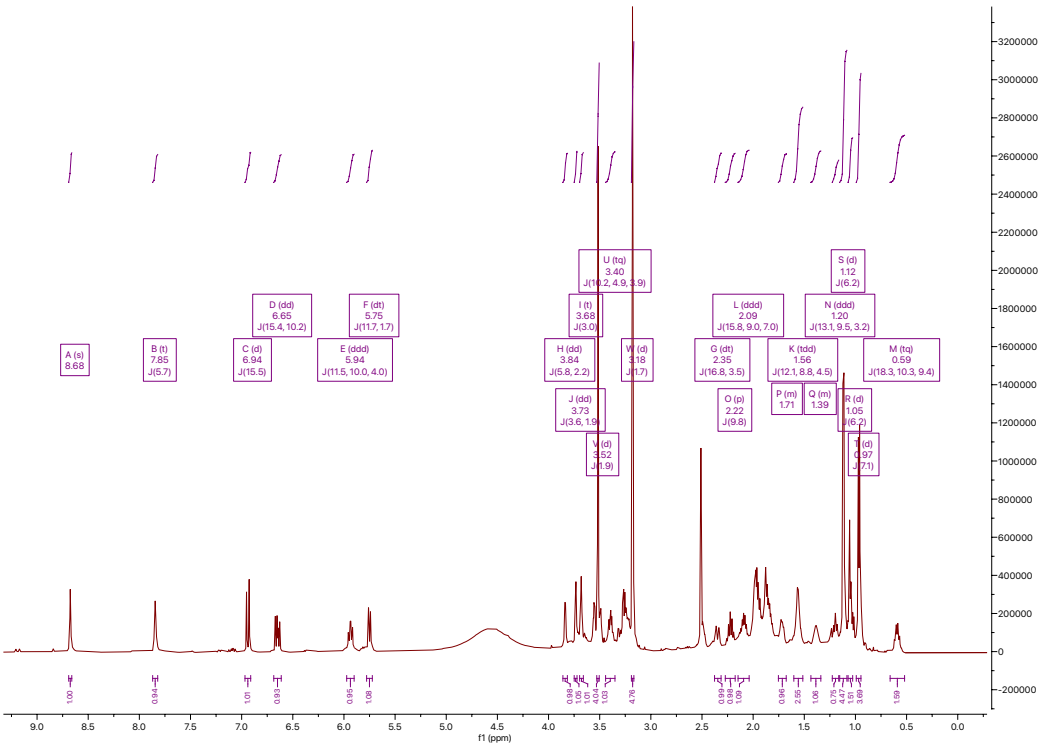

^{13}C spectrum of hydroxyikarugamycin B (**16**)

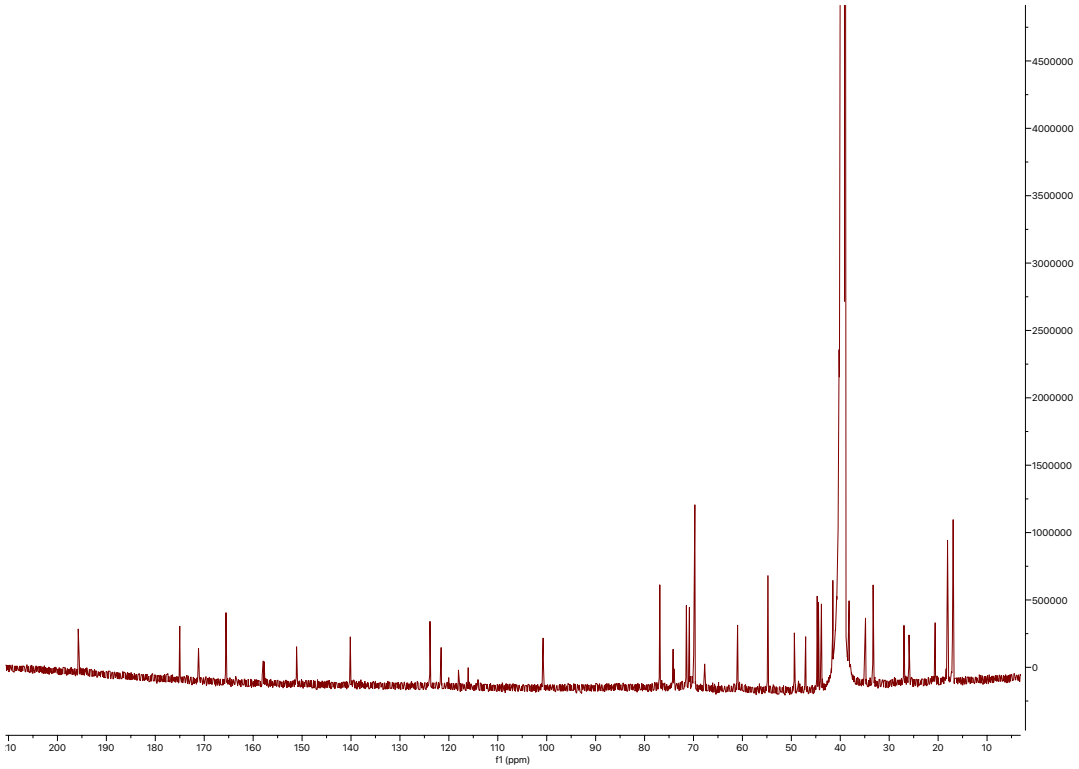

COSY spectrum of hydroxyikarugamycin B (**16**)

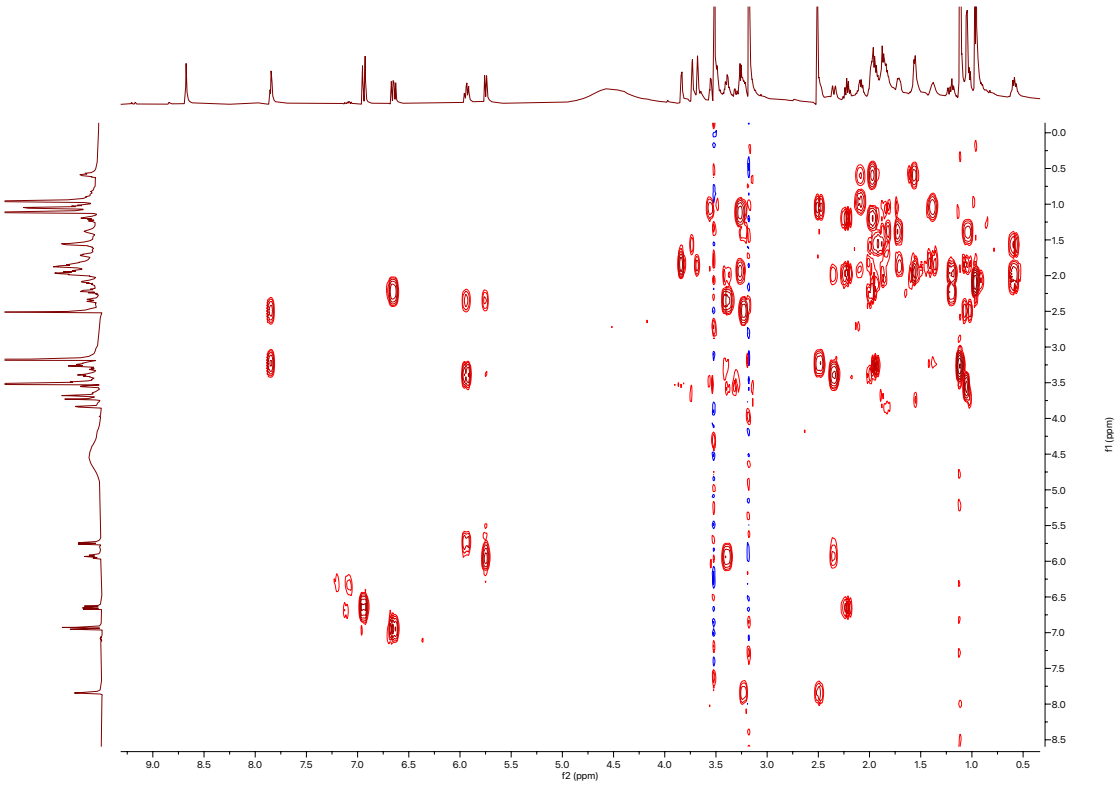

HSQC spectrum of hydroxyikarugamycin B (**16**)

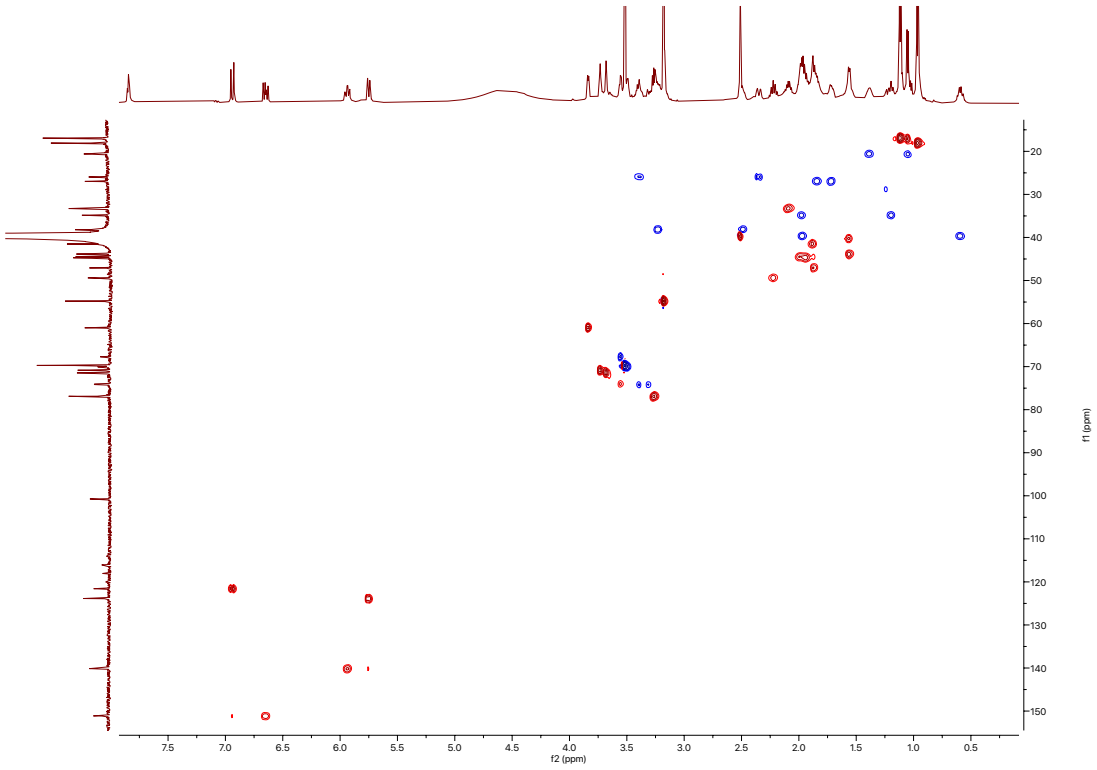

^{1}H-^{13}C HMBC spectrum of hydroxyikarugamycin B (**16**)

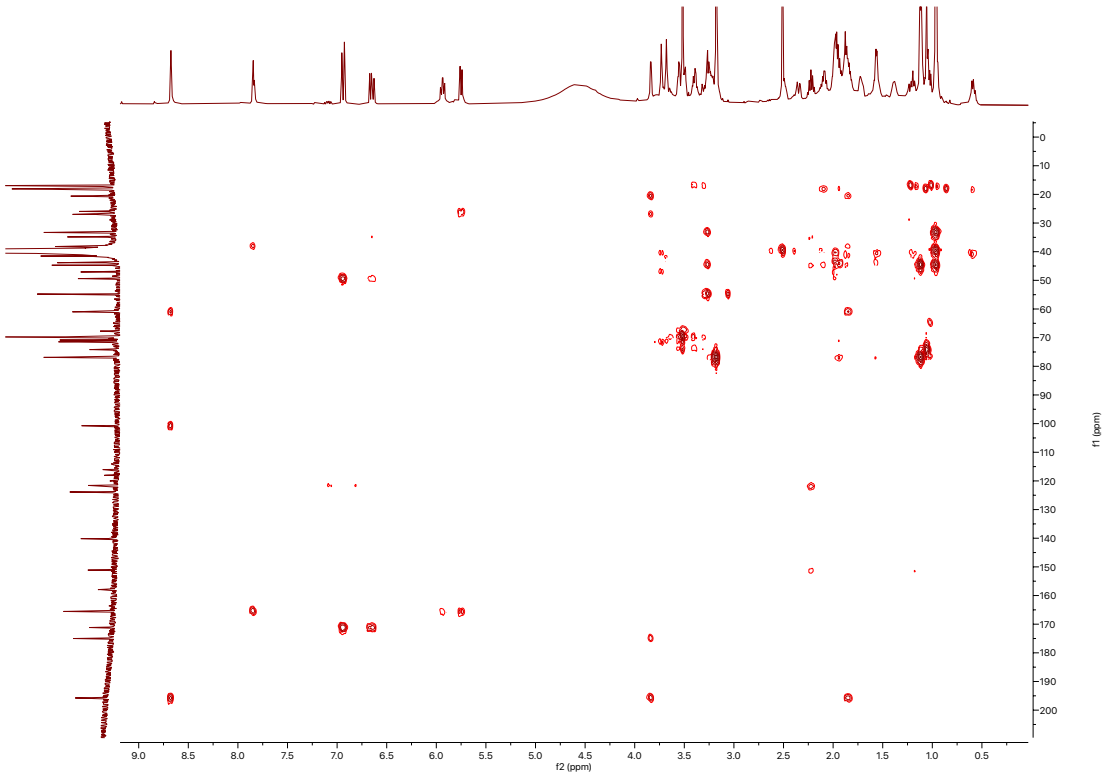

TOCSY spectrum of hydroxyikarugamycin B (**16**)

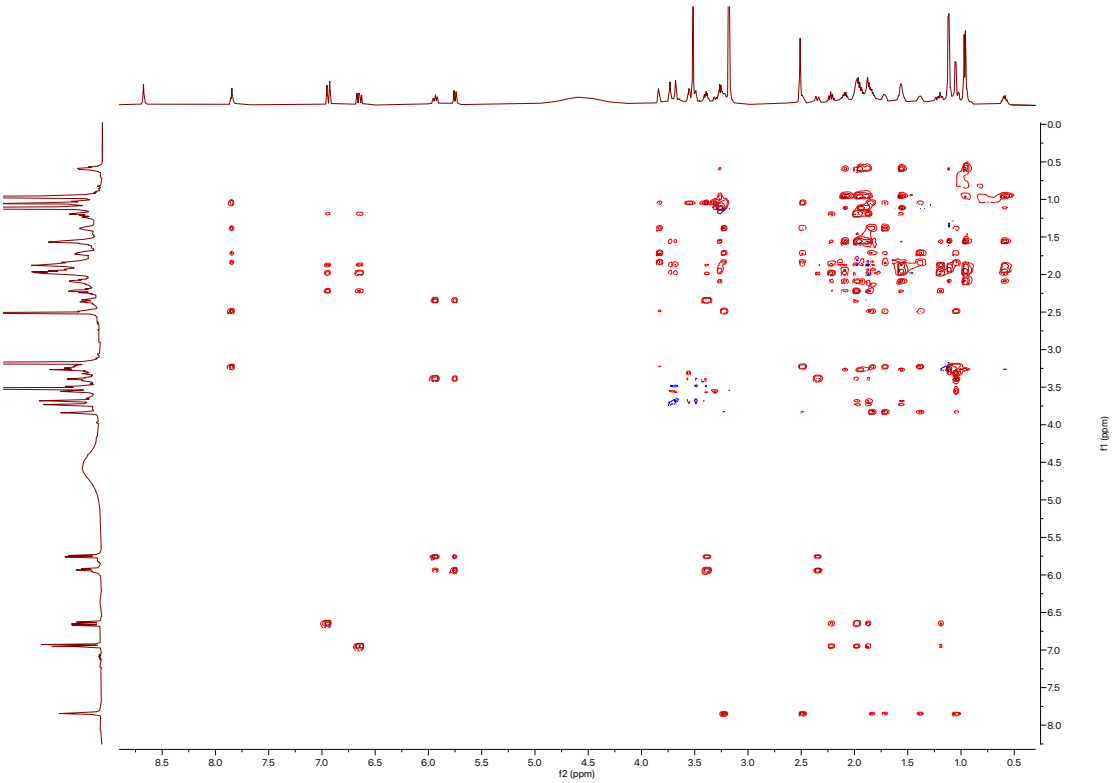

NOESY spectrum of hydroxyikarugamycin B (**16**)

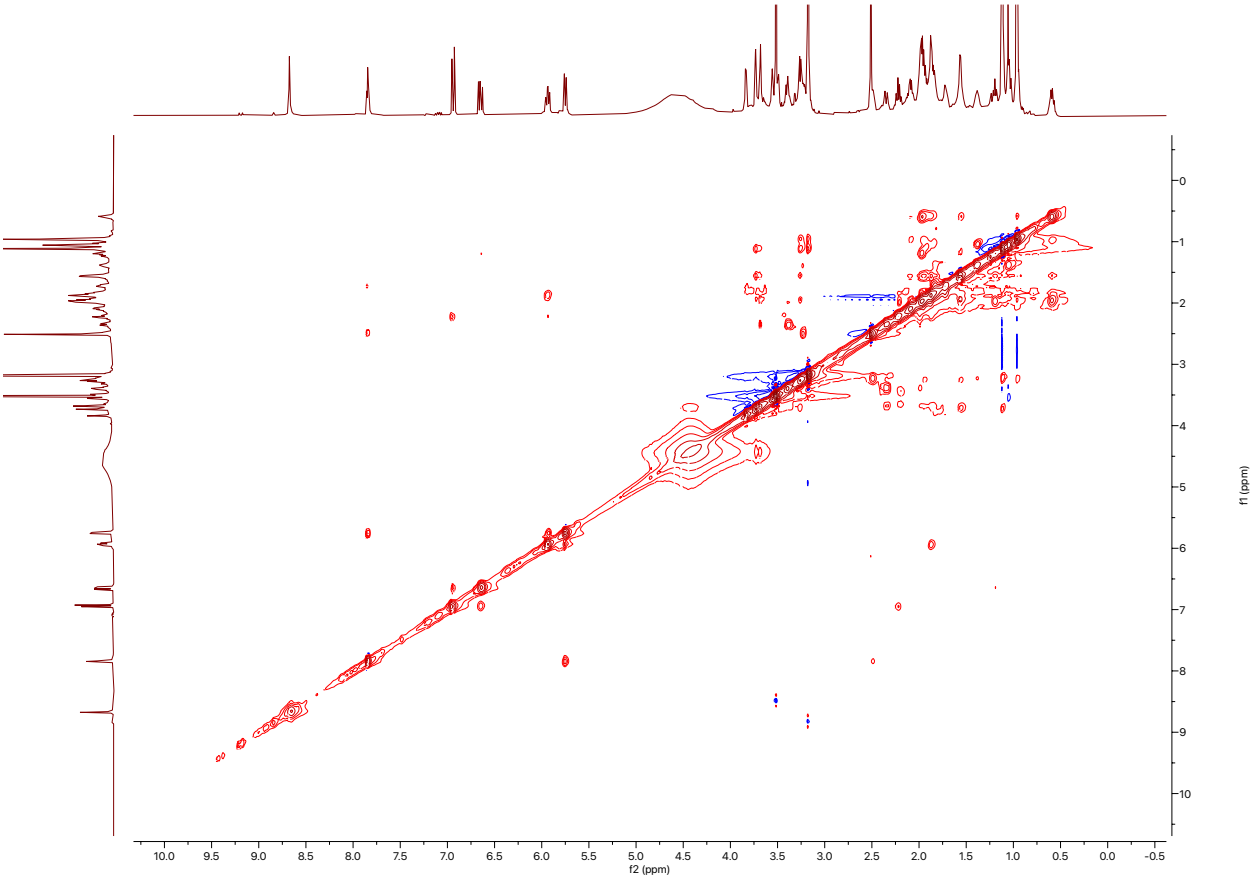

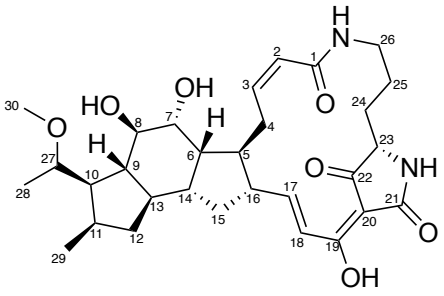

hydroxyikarugamycin B-2 (**17**)

Position	δ_C (type)	δ_H, multiplets (*J* in Hz)	COSY	HMBC	ROESY
1	166.2 (C)				
2	124.3 (CH)	5.76, d (11.4)	3	1, 4	
3	141.3 (CH)	5.98, dd (10.8, 3.8)	2, 4a, 4b	1	
4a	27.0 (CH_2)	2.32, m	3, 4b, 5		
4b	27.0 (CH_2)	3.39, m	3, 4a, 5		
5	43.9 (CH)	2.05, ddt (15.1, 10.5, 4.1)	4, 6, 16	7	
6	43.1 (CH)	2.18, m	5, 7, 14		
7	74.9 (CH)	3.58, m	6, 8	8, 9, 14	5, 13
7-OH					
8	75.8 (CH)	3.51, m	7, 9	6, 7	6
8-OH					
9	50.2 (CH)	1.23, m	8, 10, 13		
10	52.0 (CH)	1.75, m	9, 11, 27	28	
11	33.9 (CH)	2.20, m	10, 12, 29		
12a	39.9 (CH_2)	0.60, m	11, 12b, 13	9, 29	
12b	39.9 (CH_2)	1.96, dt (12.0, 7.2)	11, 2a, 13		
13	43.0 (CH)	1.71, m	9, 12a, 12b, 14		
14	45.2 (CH)	1.74, m	6, 13, 15		
15a	37.8 (CH_2)	1.14, m	14, 15b, 16		
15b	37.8 (CH_2)	1.85, tq (13.8, 6.9)	14, 15a, 16		
16	49.8 (CH)	2.29, m	5, 15a, 15b, 17		
17		6.59, s	16, 18	16, 19	
18		7.03, d (15.4)	17	16, 19	
19					
20					
21					
21-NH					
22	195.8 (C)				
23	61.2 (CH)	3.77, m	24a, 24b	21, 22, 24, 25	
24a	27.5 (CH_2)	1.71, m	23, 24b, 25a, 25b		
24b	27.5 (CH_2)	1.84, m	23, 24a, 25a, 25b		
25a	21.3 (CH_2)	1.05, m	24a, 24b, 25b, 26a, 26b		
25b	21.3 (CH_2)	1.36, m	24a, 24b, 25a, 26a, 26b		
26a	38.7 (CH_2)	2.47, m	25a, 25b, 26b, 26-NH		
26b	38.7 (CH_2)	3.25, m	25a, 25b, 26a, 26-NH		
26-NH		7.82, t (5.7)	26a, 26b	1, 26	
27	77.3 (CH)	3.44, m	10, 28	10, 11, 30	
28	17.5 (CH_3)	1.23, d (6.1)	27	10, 27	
29	18.8 (CH_3)	0.91, d (7.1)	11	10, 11, 12	
30	55.6 (CH_3)	3.23, s		27	

^{1}H spectrum of hydroxyikarugamycin B-2 (**17**)

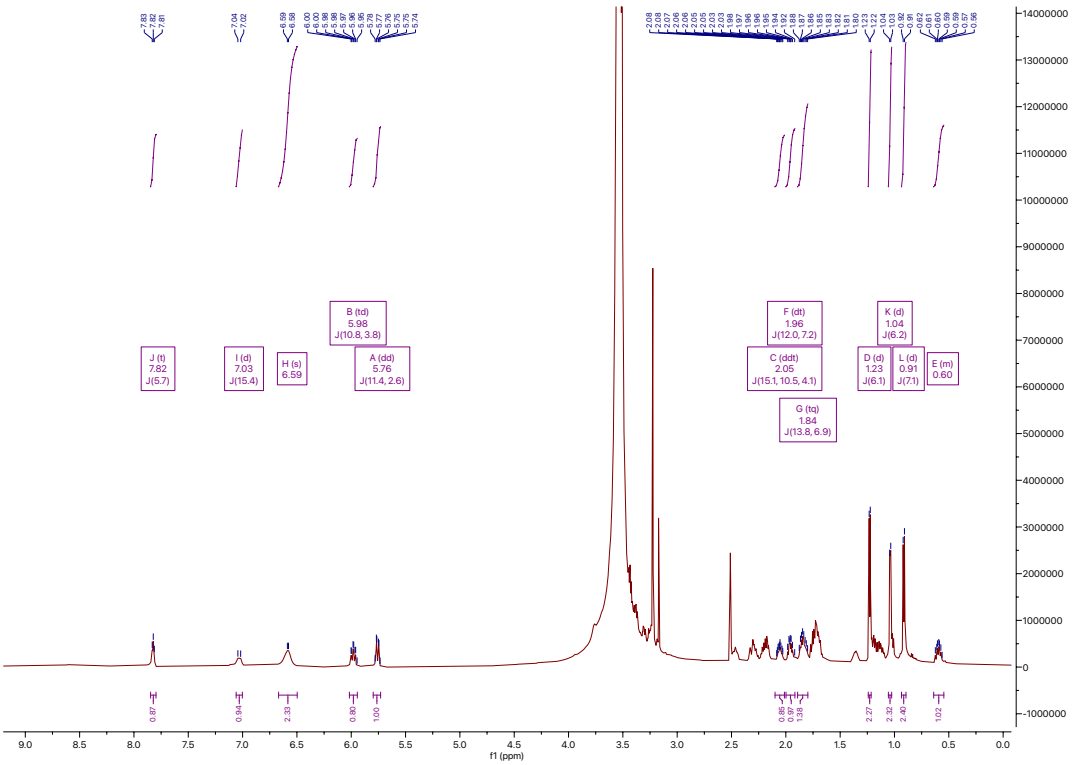

^{13}C spectrum of hydroxyikarugamycin B-2 (**17**)

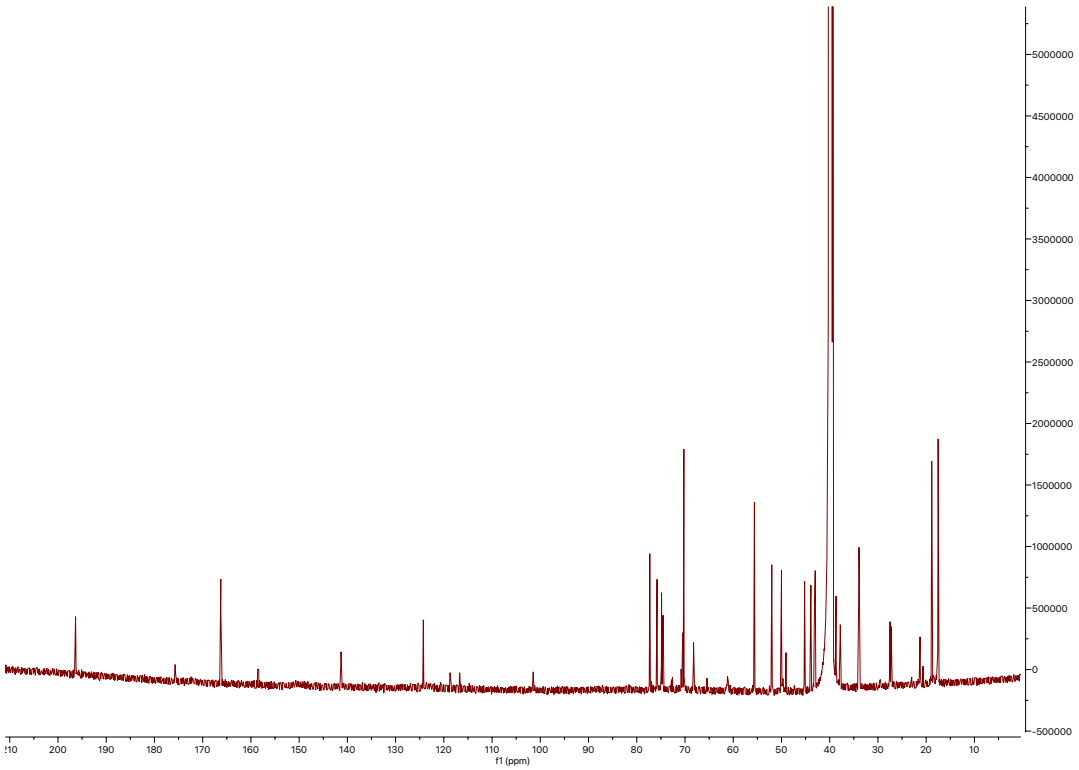

COSY spectrum of hydroxyikarugamycin B-2 (**17**)

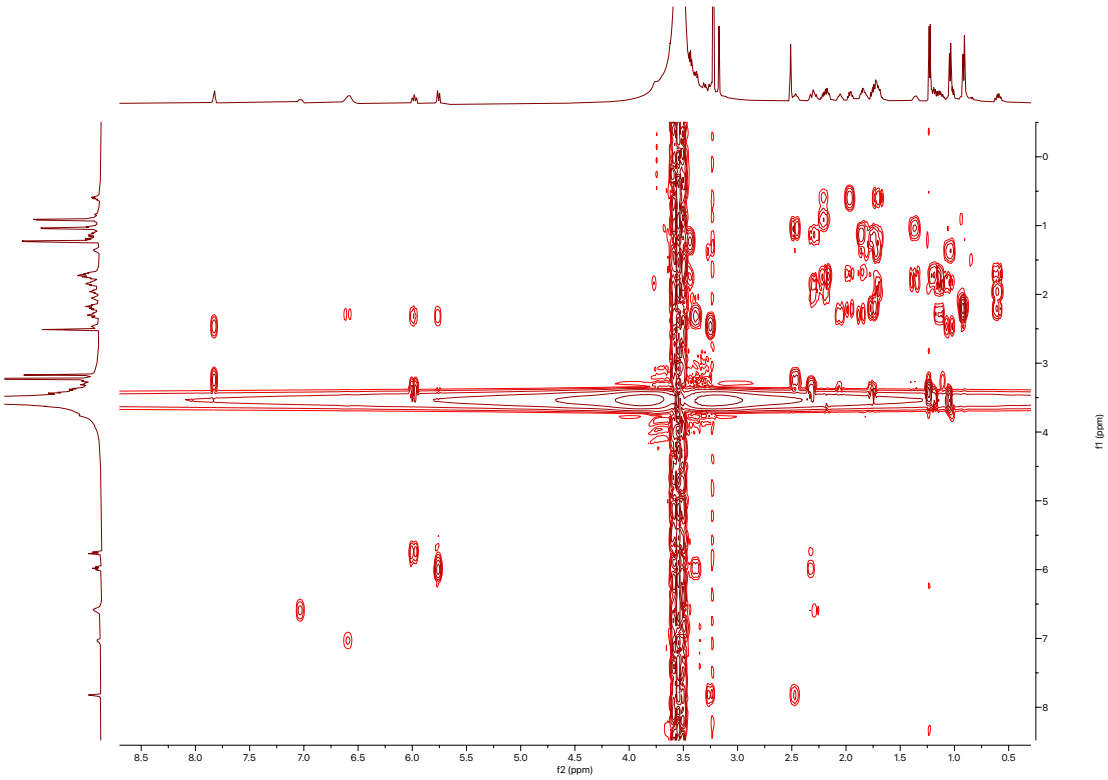

HSQC spectrum of hydroxyikarugamycin B-2 (**17**)

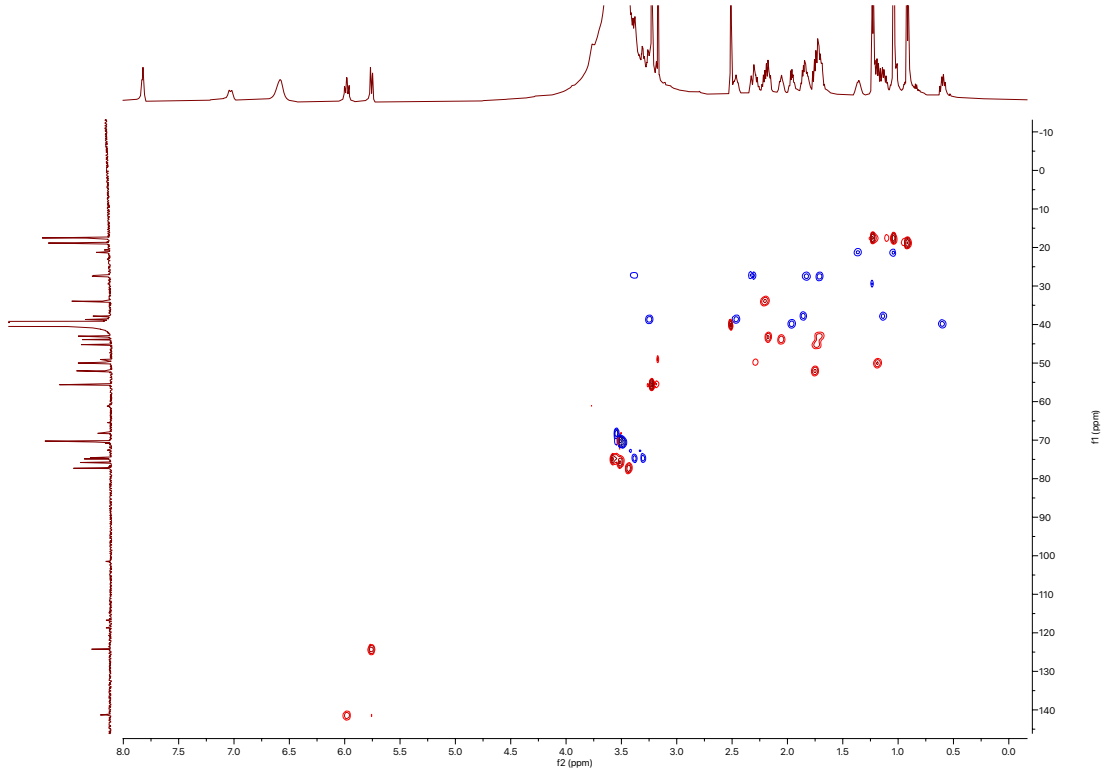

^{1}H-^{13}C HMBC spectrum of hydroxyikarugamycin B-2 (**17**)

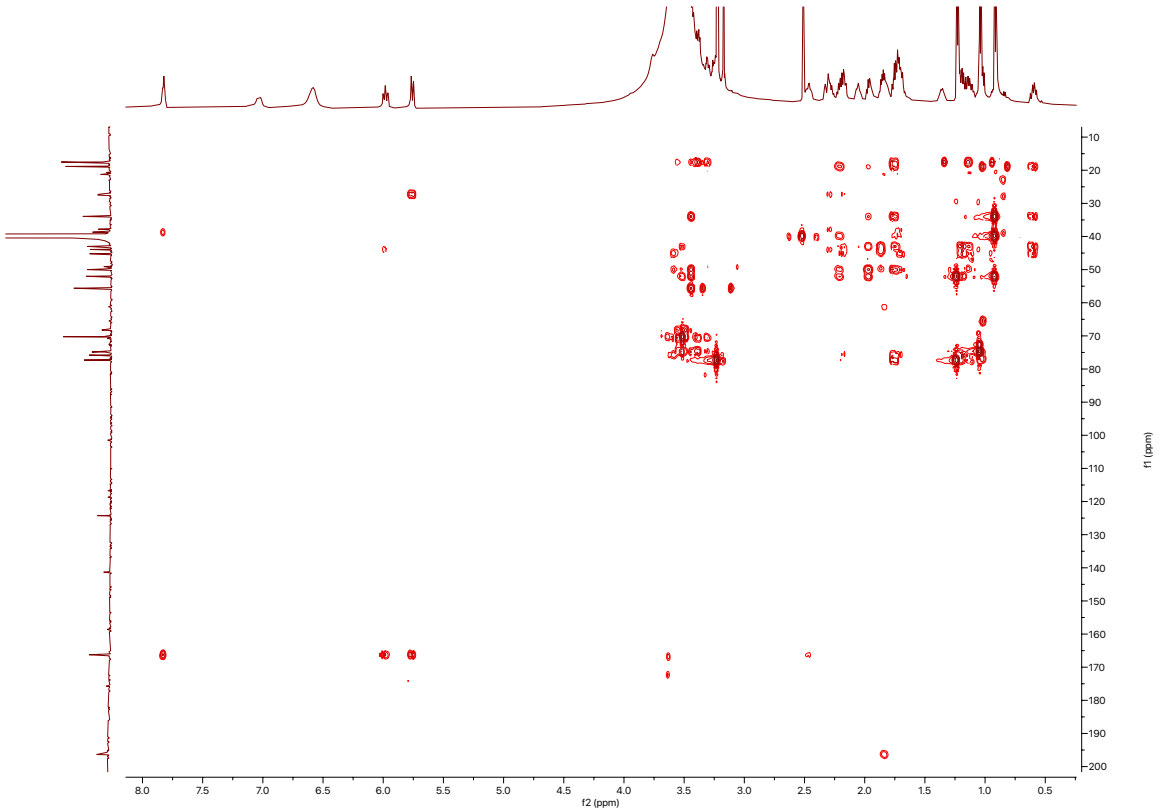

NOESY spectrum of hydroxyikarugamycin B-2 (**17**)

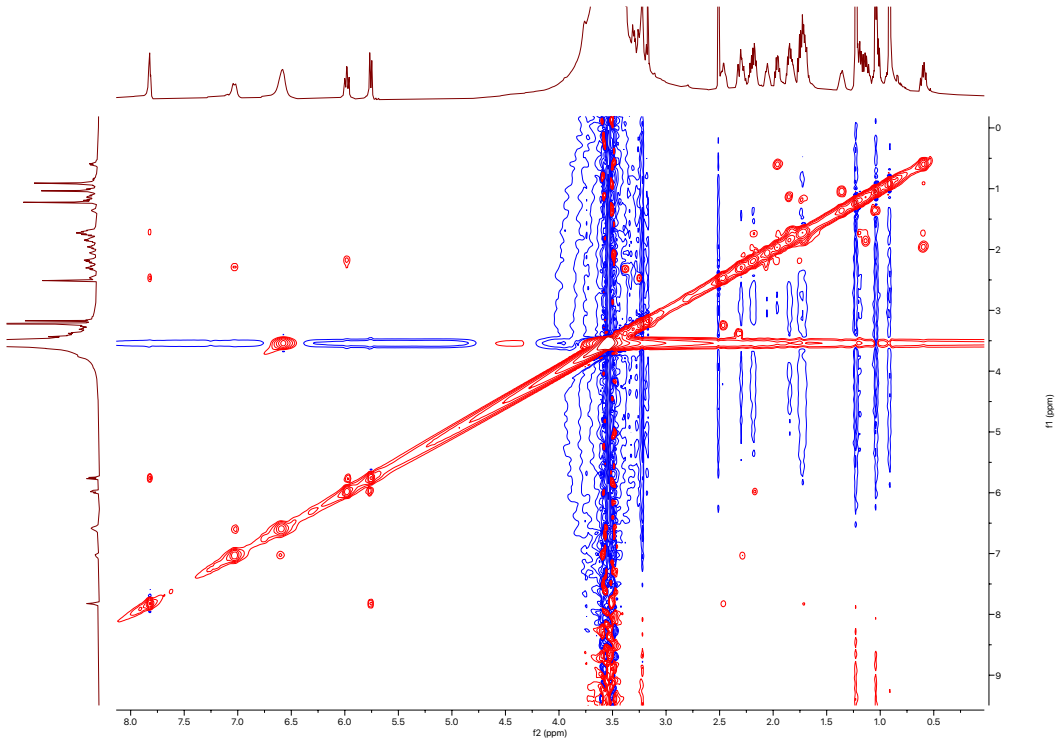

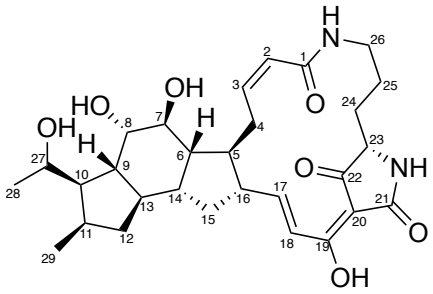

hydroxyikarugamycin C (**18**)

^{1}H spectrum of hydroxyikarugamycin C (**18**)

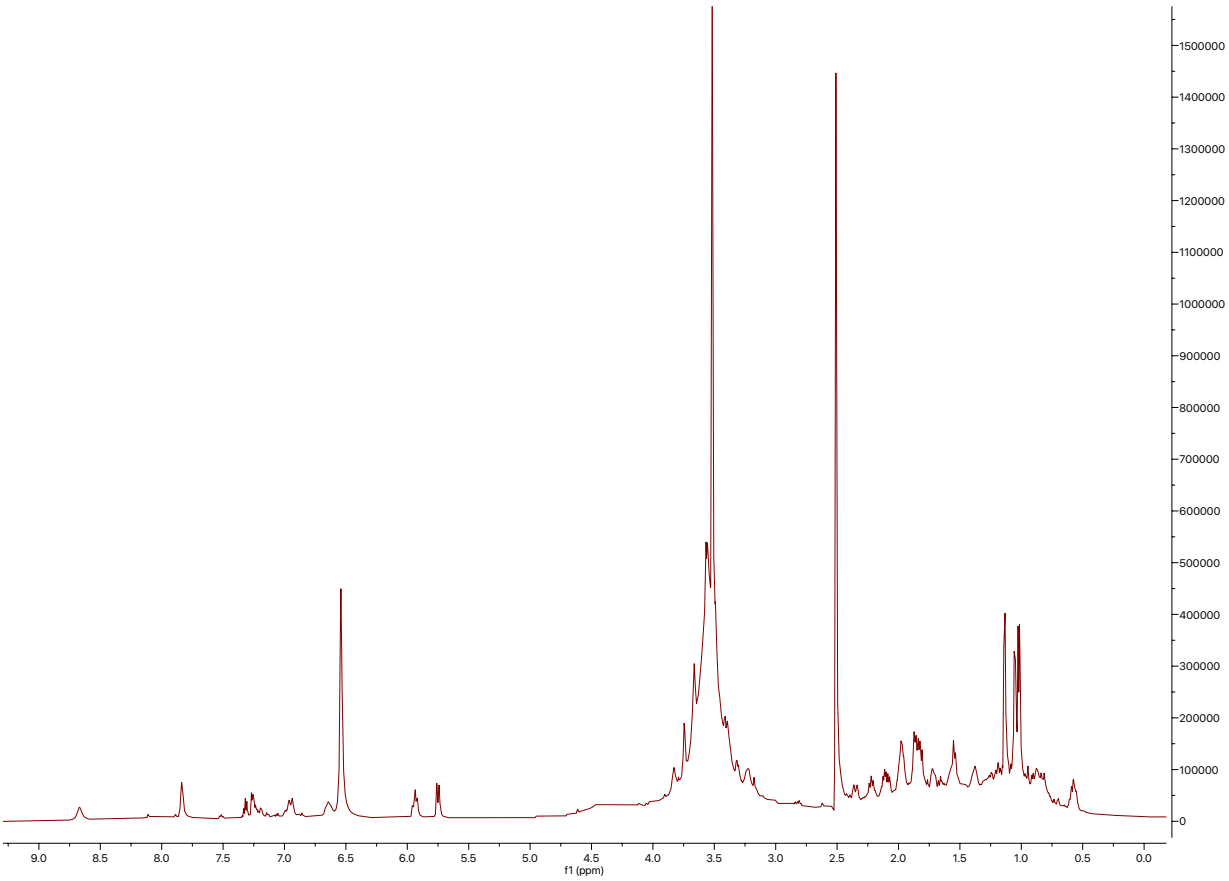

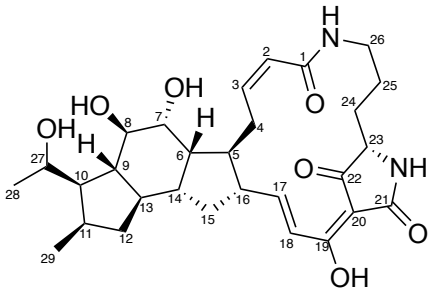

hydroxyikarugamycin C-2 (**19**)

^{1}H spectrum of hydroxyikarugamycin C (**19**)

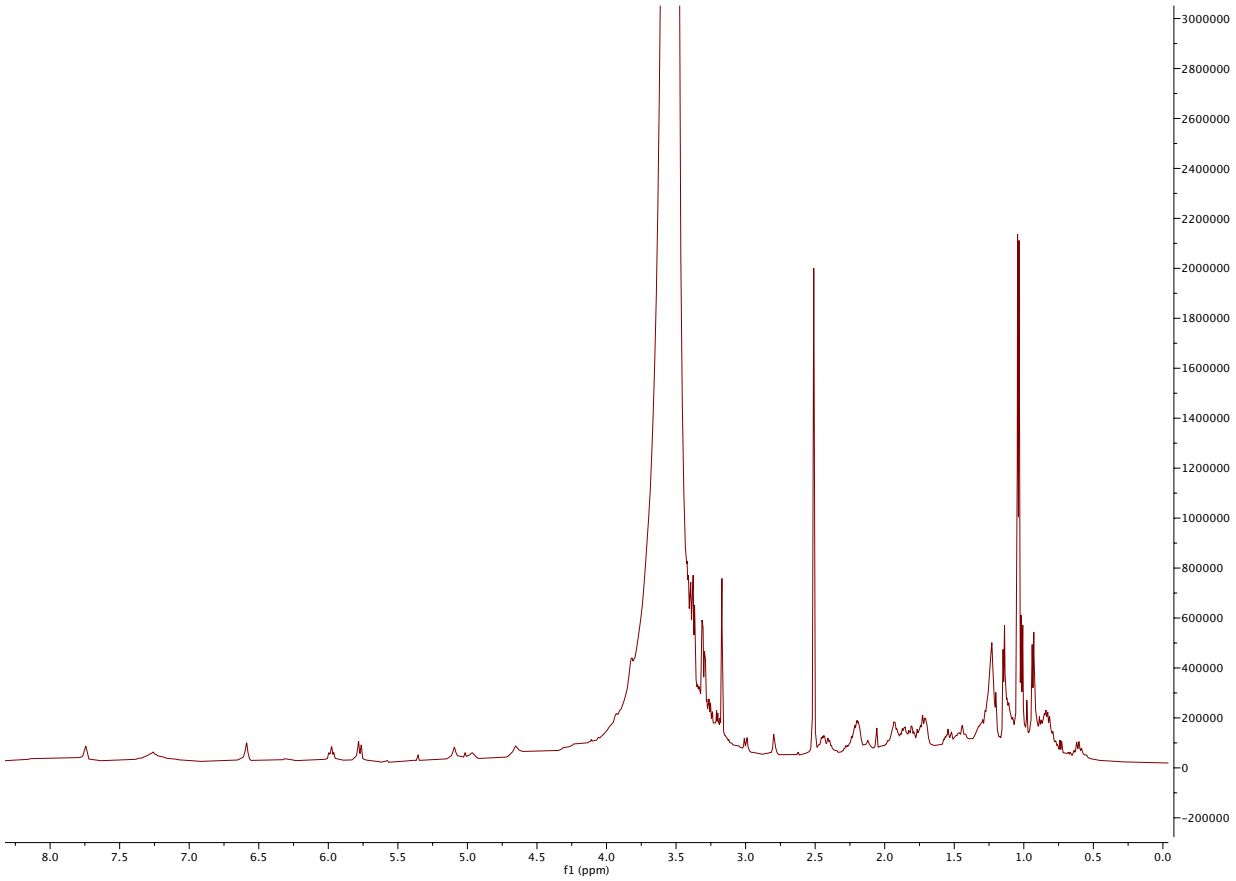

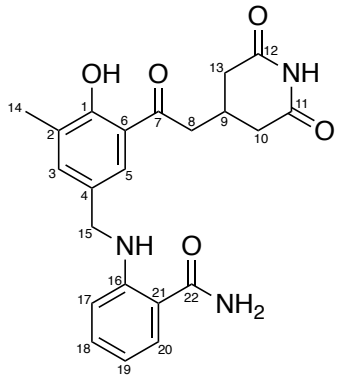

2-aminobenzamide-actiphenol
(**20**)

Position	δ_C (type)	δ_H, multiplets (*J* in Hz)	COSY	HMBC	ROESY
1	159.3 (C)				
1-OH		12.33, s		1, 2, 6	
2	127.0 (C)				
3	136.9 (CH)	7.45, s		1, 5, 14, 15	14, 15a, 15b
4	130.0 (C)				
5	127.6 (CH)	7.82, s		1, 3, 7, 15	8a, 8b, 15a, 15b
6	118.7 (C)				
7	205.6 (C)				
8a	42.9 (CH_2)	3.18, d (6.4)	9	7, 9, 10, 13	5, 10a, 10b, 13a, 13b
8b	42.9 (CH_2)	3.18, d (6.4)	9	7, 9, 10, 13	5, 10a, 10b, 13a, 13b
9	26.6 (CH)	2.62, m	8a, 8b		
10a	37.5 (CH_2)	2.39, dd (16.5, 10.7)	10b	11, 12	5
10b	37.5 (CH_2)	2.58, dd (16.5, 10.7)	10a	11, 12	5
11	173.4 (C)				
11-NH		10.76, s		10, 13	
12	173.4 (C)				
13a	37.5 (CH_2)	2.39, d (16.5, 10.7)	13b	11, 12	5
13b	37.5 (CH_2)	2.58, d (16.5, 10.7)	13a	11, 12	5
14	15.8 (CH_3)	2.17, s		1, 2, 3	3
15a	45.9 (CH_2)	4.30, s		3, 4, 5, 16	3, 5, 17
15b	45.9 (CH_2)	4.30, s		3, 4, 5, 16	3, 5, 17
15-NH		8.47, br s			
16	149.9 (C)				
17	112.1 (CH)	6.69, d (8.4)	18	19, 21	15a, 15b, 18
18	132.8 (CH)	7.23, t (7.9)	17, 19	16, 20	17, 19
19	114.9 (CH)	6.54, t (7.5)	18, 20	17, 21	18, 20
20	129.5 (CH)	7.61, d (7.8)	19	16, 18, 22	18, 19
21	114.9 (C)				
22	171.9 (C)				
22-NHa		7.17, br s			
22-NHb		7.86, br s			

^{1}H spectrum of 2-aminobenzamide-actiphenol (**20**)

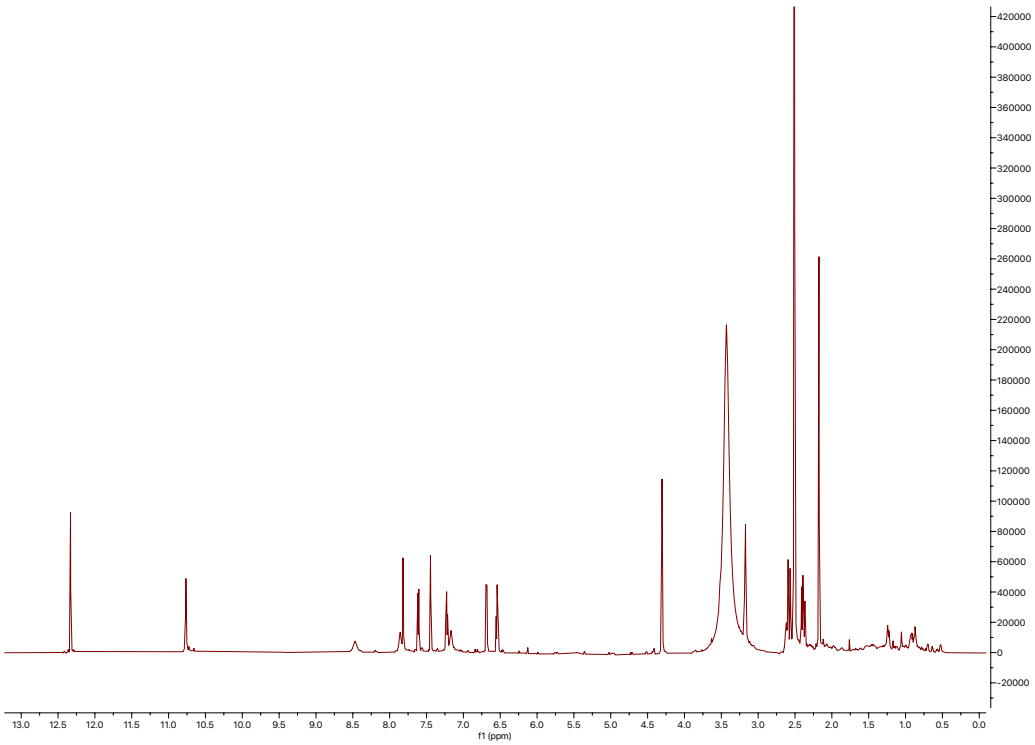

^{13}C spectrum of 2-aminobenzamide-actiphenol (**20**)

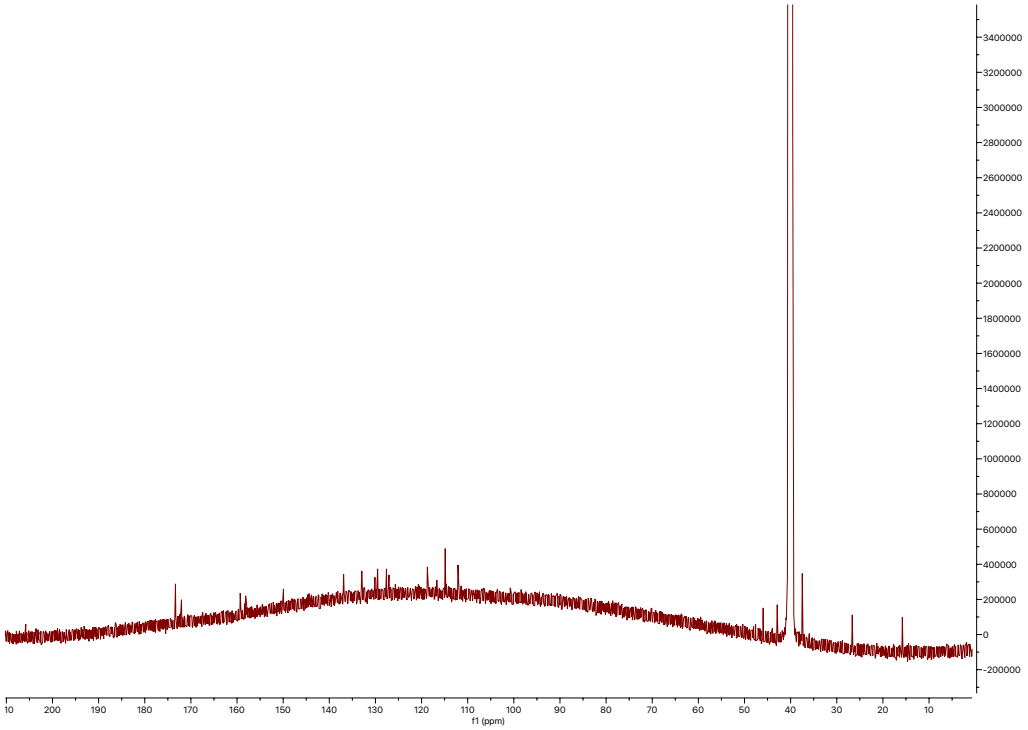

COSY spectrum of 2-aminobenzamide-actiphenol (**20**)

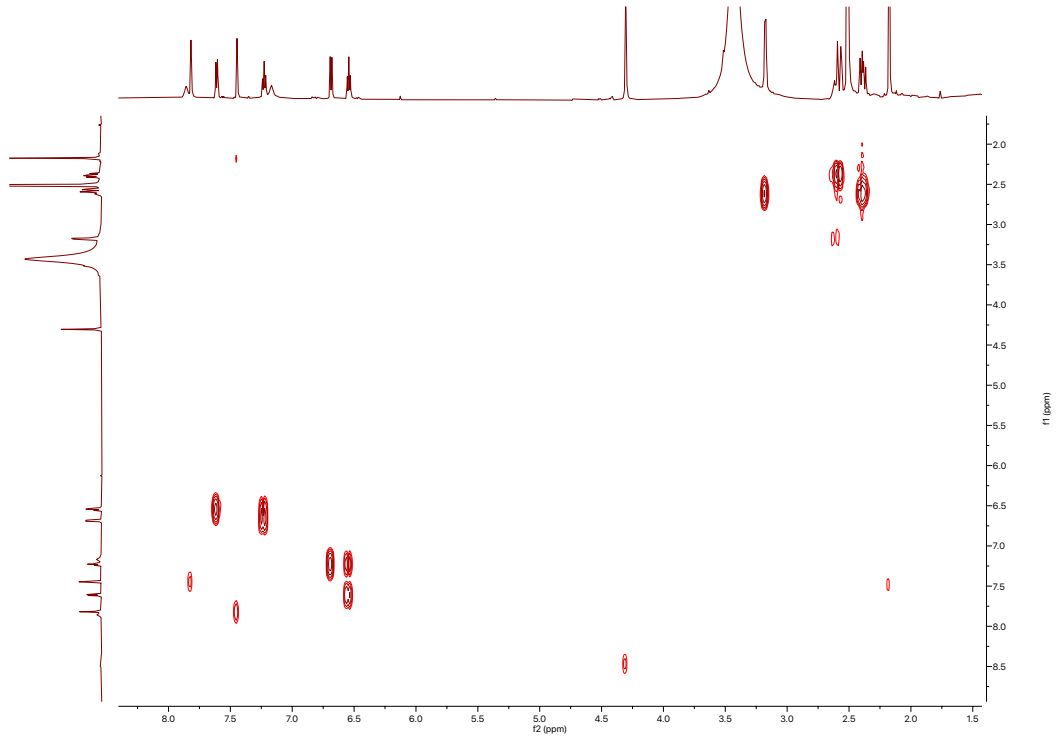

HSQC spectrum of 2-aminobenzamide-actiphenol (**20**)

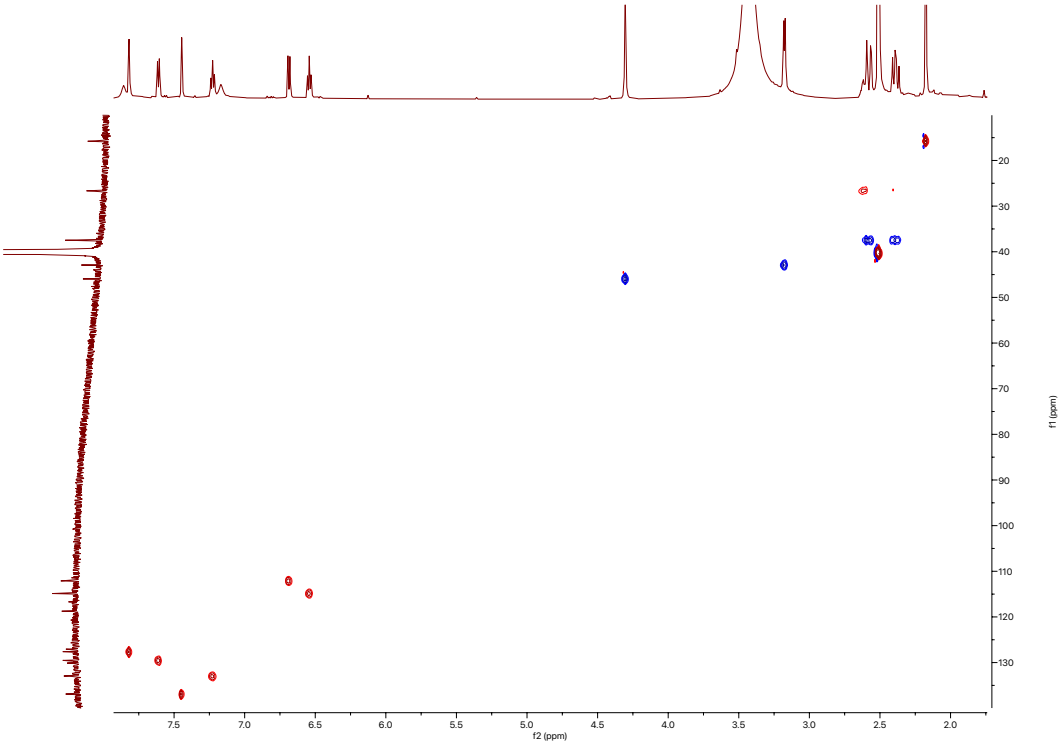

^{1}H-^{13}C HMBC spectrum of 2-aminobenzamide-actiphenol (**20**)

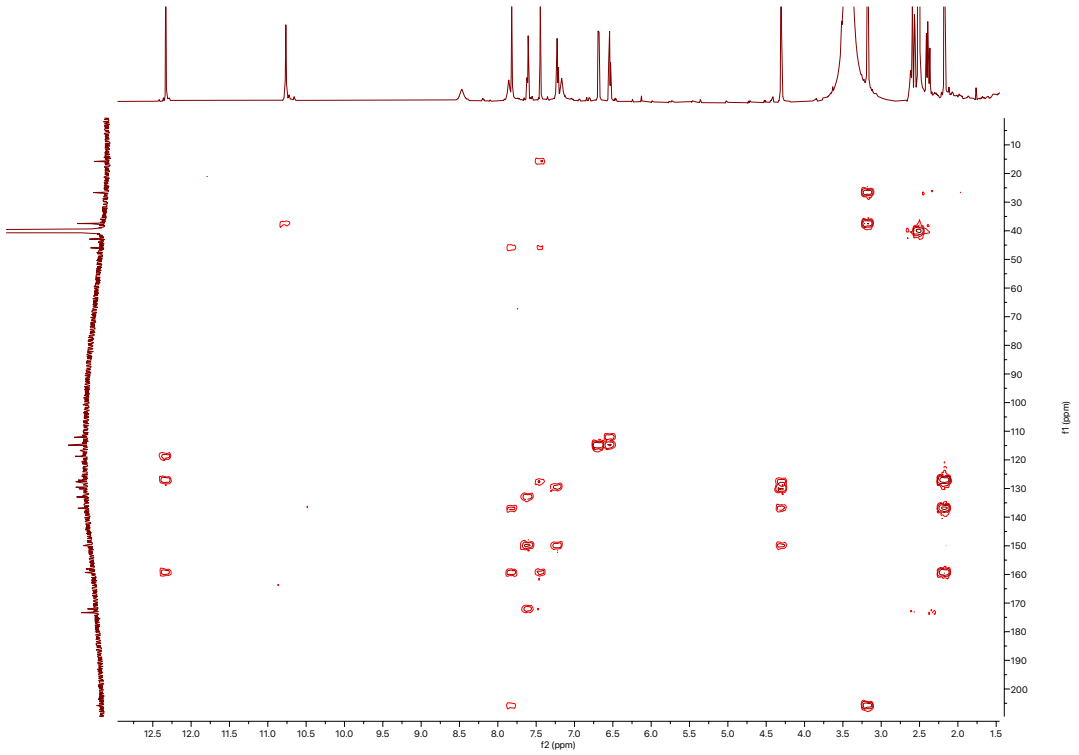

ROESY spectrum of 2-aminobenzamide-actiphenol (**20**)

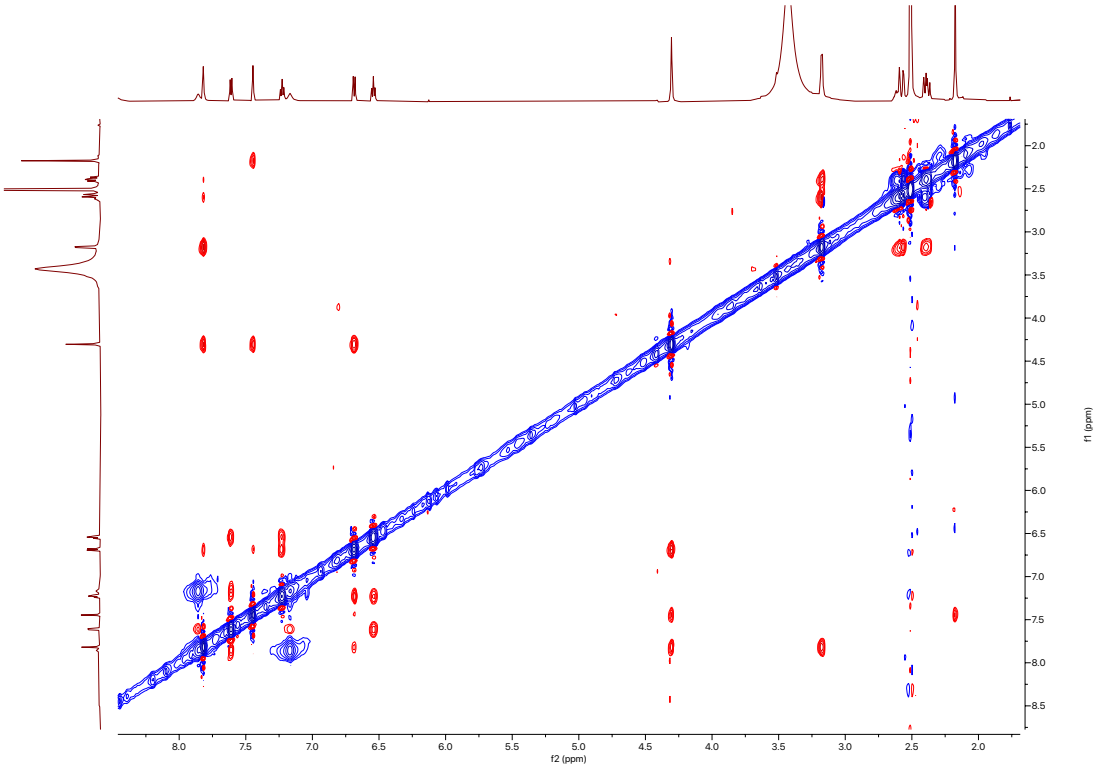

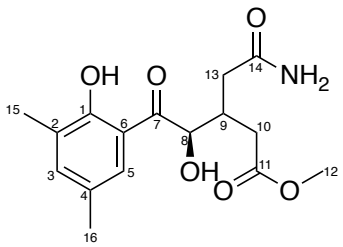

methyl phenatate C (**21**)

Position	δ_C (type)	δ_H, multiplets (*J* in Hz)	COSY	HMBC	ROESY
1	158.1 (C)				
1-OH		12.21, s			
2	126.5 (C)				
3	138.9 (CH)	7.31, s		1, 5, 15, 16	16
4	127.4 (C)				
5	128.2 (CH)	7.99, s		1, 3, 7, 16	8, 9
6	118.9 (C)				
7	207.7 (C)				
8	72.7 (CH)	5.14, dd (6.0, 2.7)	8-OH, 9		5
8-OH		5.38, d (5.9)	8	9	
9	36.1 (CH)	2.80, m	10a, 10b, 13a, 13b		
10a	32.4 (CH_2)	2.20, m	9, 10b	9, 11	
10b	32.4 (CH_2)	2.31, dd (16.4, 6.0)	9, 10a	9, 11	
11	172.8 (C)				
12	51.7 (CH_3)	3.46, s		11	
13a	37.0 (CH_2)	2.19, m	9, 13b	9, 14	
13b	37.0 (CH_2)	2.45, dd (15.7, 9.7)	9, 13a	9, 14	
14	173.6 (C)				
14-NHa		6.99, s			
14-NHb		7.47, s			
15	15.6 (CH_3)	2.17, s		1, 2, 3	
16	20.5 (CH_3)	2.26, s		3, 5	

^{1}H spectrum of methyl phenatate C (**21**)

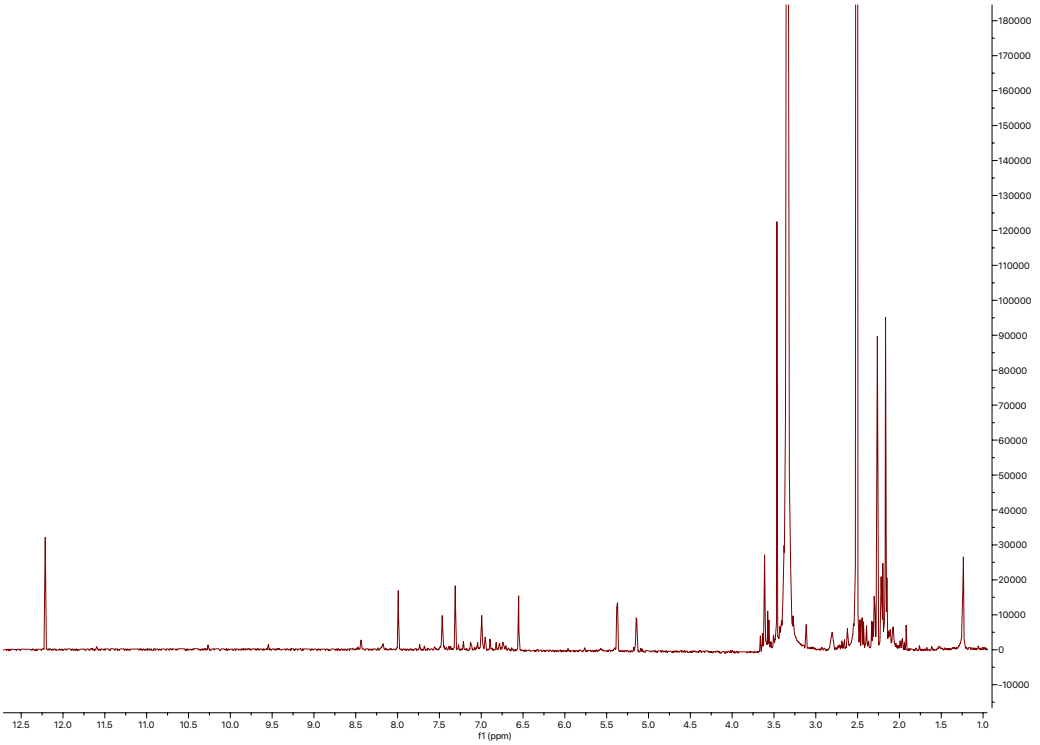

^{13}C spectrum of methyl phenatate C (**21**)

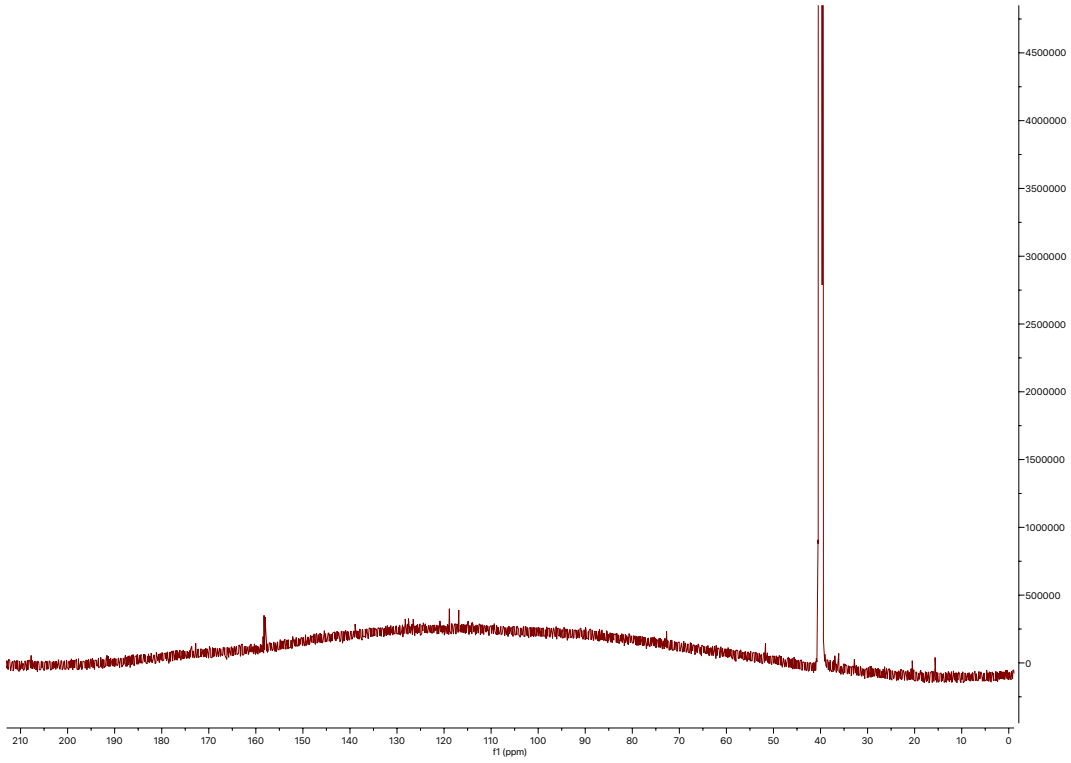

COSY spectrum of methyl phenatate C (**21**)

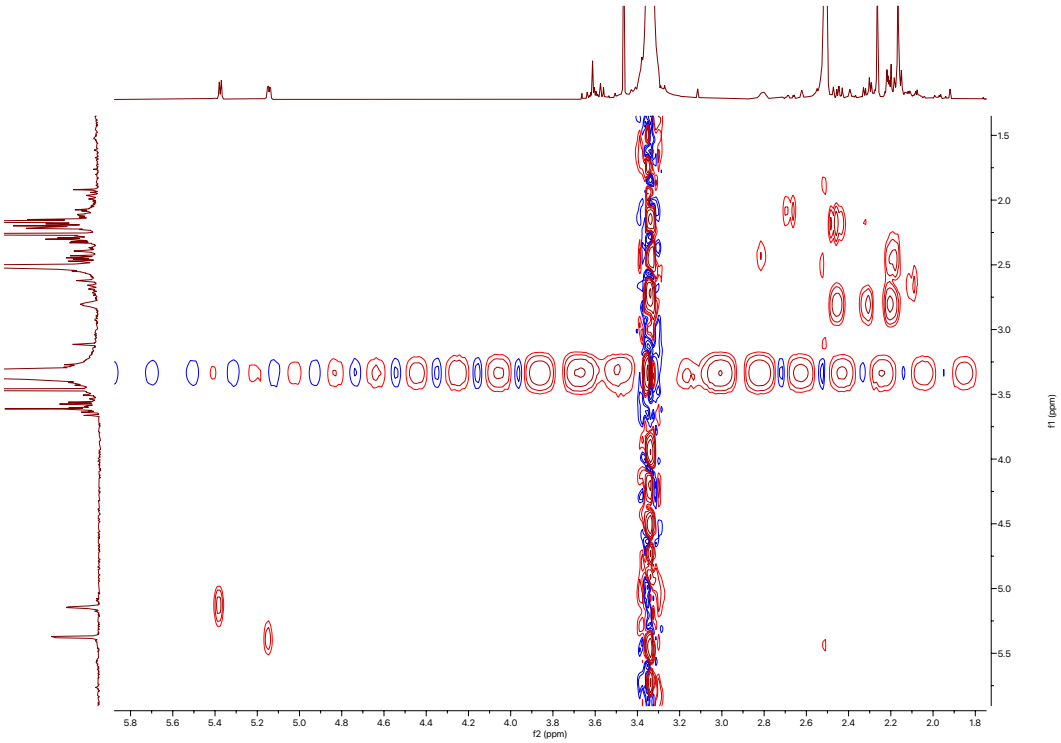

HSQC spectrum of methyl phenatate C (**21**)

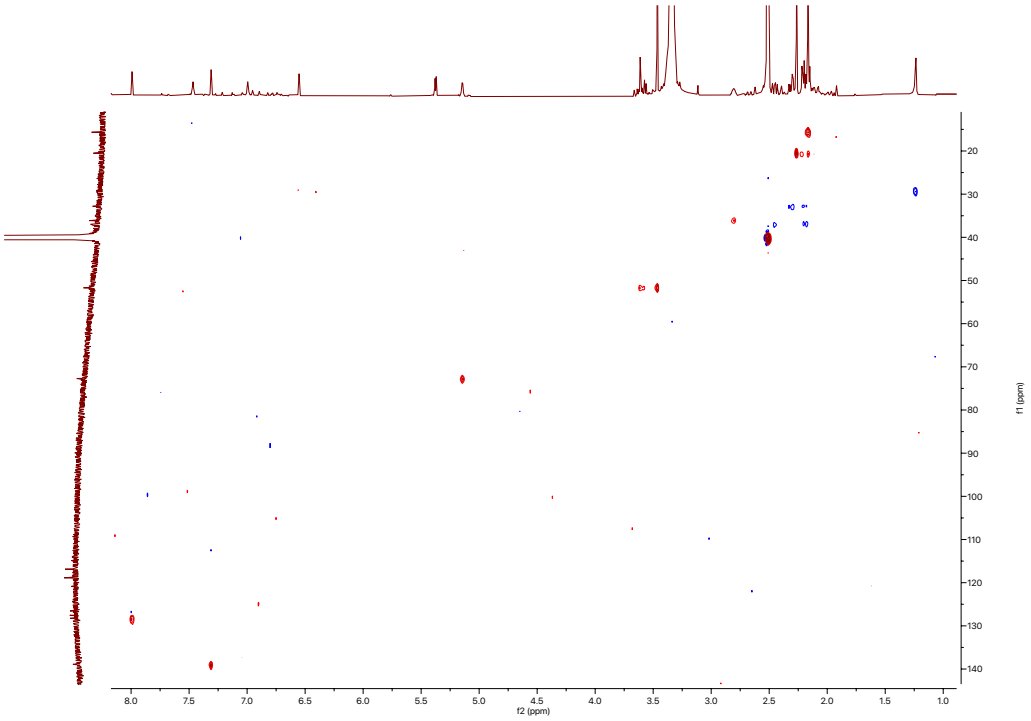

^{1}H-^{13}C HSQC spectrum of methyl phenatate C (**21**)

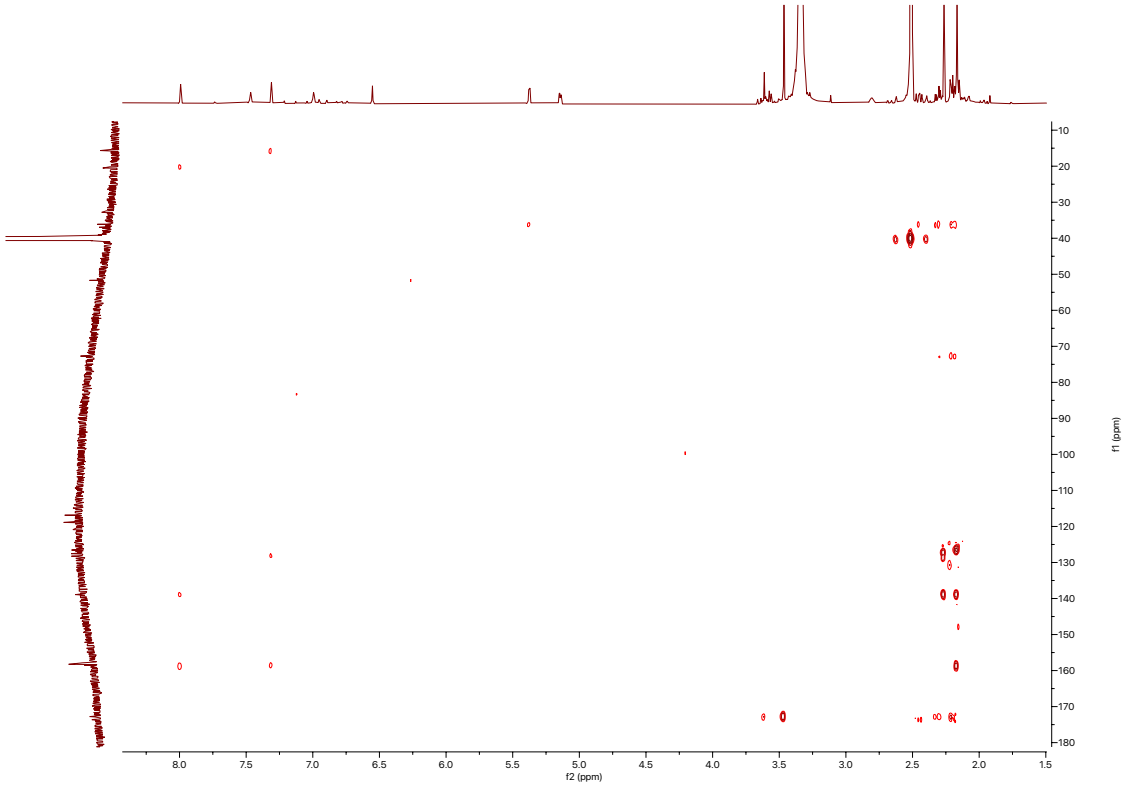

ROESY spectrum of methyl phenatate C (**21**)

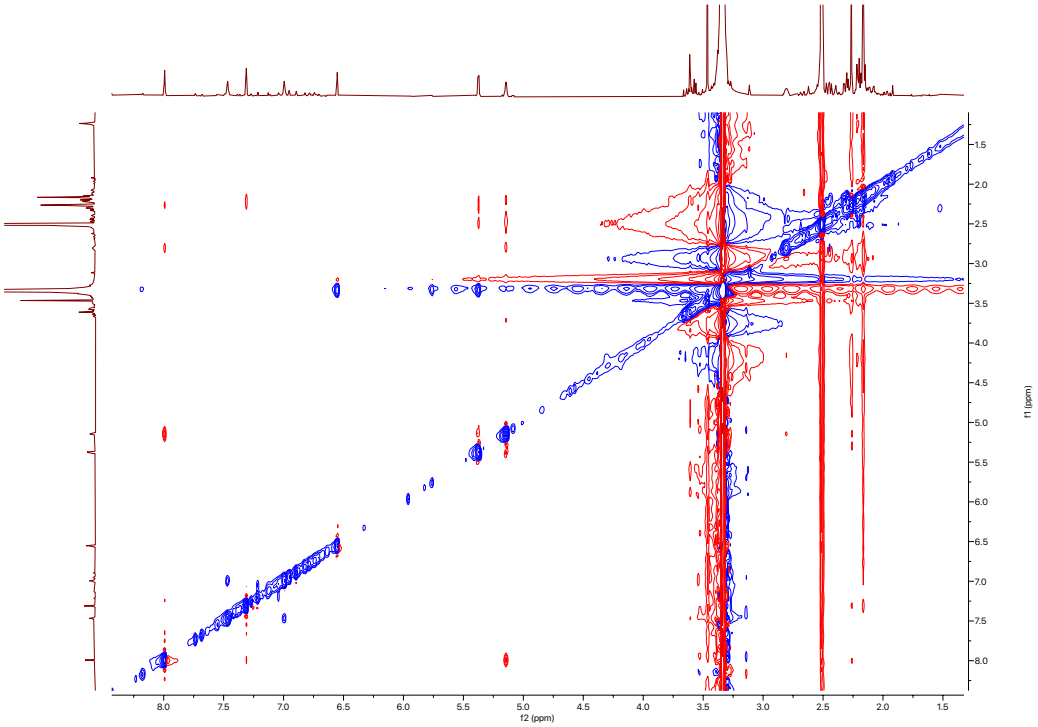

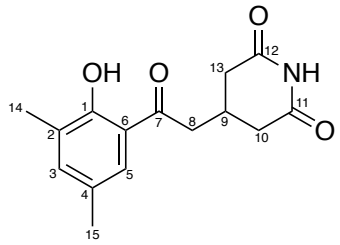

actiphenol (**22**)

Position	δ_C (type)	δ_H, multiplets (*J* in Hz)	COSY	HMBC
1	157.7 (C)			
1-OH		12.23, s		1, 2, 6
2	127.2 (C)			
3	138.4 (CH)	7.27, s		1, 5, 14, 15
4	126.1 (C)			
5	127.9 (CH)	7.59, s		1, 3, 7, 15
6	118.3 (C)			
7	205.3 (C)			
8	42.3 (CH_2)	3.17, d (6.4)	9	7, 9, 10, 13
9	26.0 (CH)	2.64, dt (10.7, 5.3)	8, 10a, 13a	8, 10, 11, 12, 13
10a	37.0 (CH_2)	2.38, dd (16.5, 10.7)	9, 10b	8, 9, 11
10b	37.0 (CH_2)	2.59, dd (16.2, 4.0)	9, 10a	8, 9, 11
11	172.9 (C)			
11-NH		10.76, s		10, 13
12	172.9 (C)			
13a	37.0 (CH_2)	2.38, dd (16.5, 10.7)	9, 13b	9, 12
13b	37.0 (CH_2)	2.59, dd (16.2, 4.0)	9, 13a	9, 12
14	15.1 (CH_3)	2.14, s		1, 2, 3
15	20.0 (CH_3)	2.24, s		3, 4, 5

^{1}H spectrum of actiphenol (**22**)

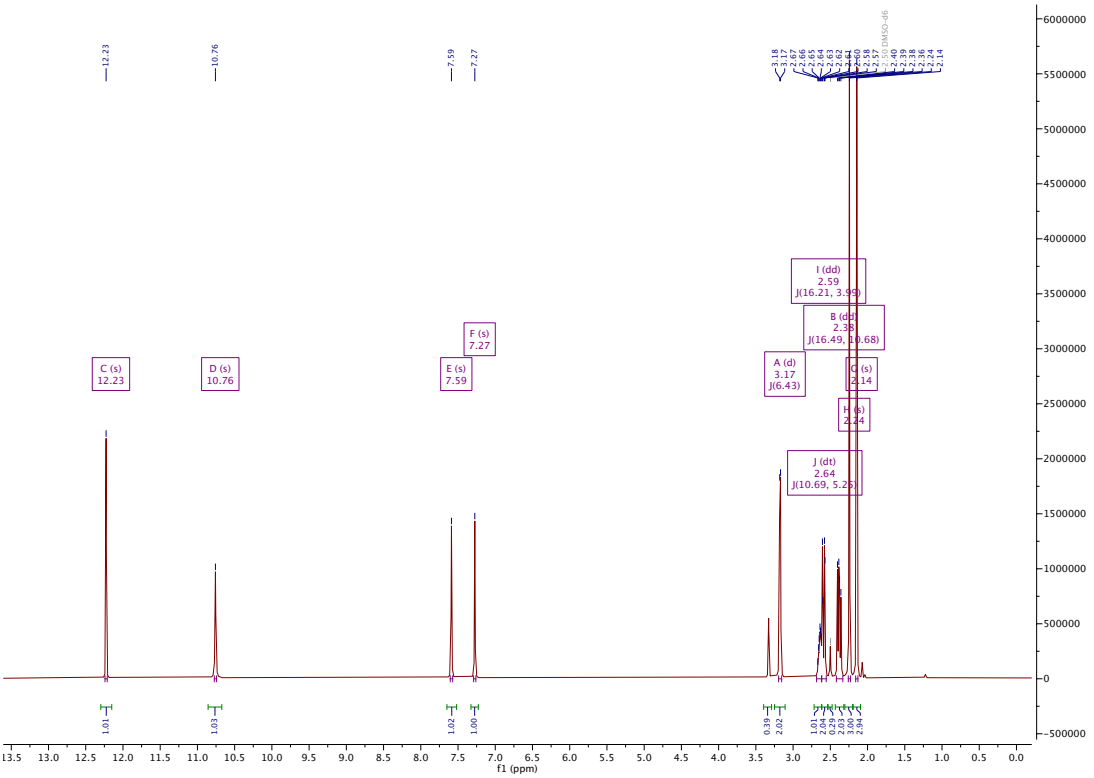

^{13}C spectrum of actiphenol (**22**)

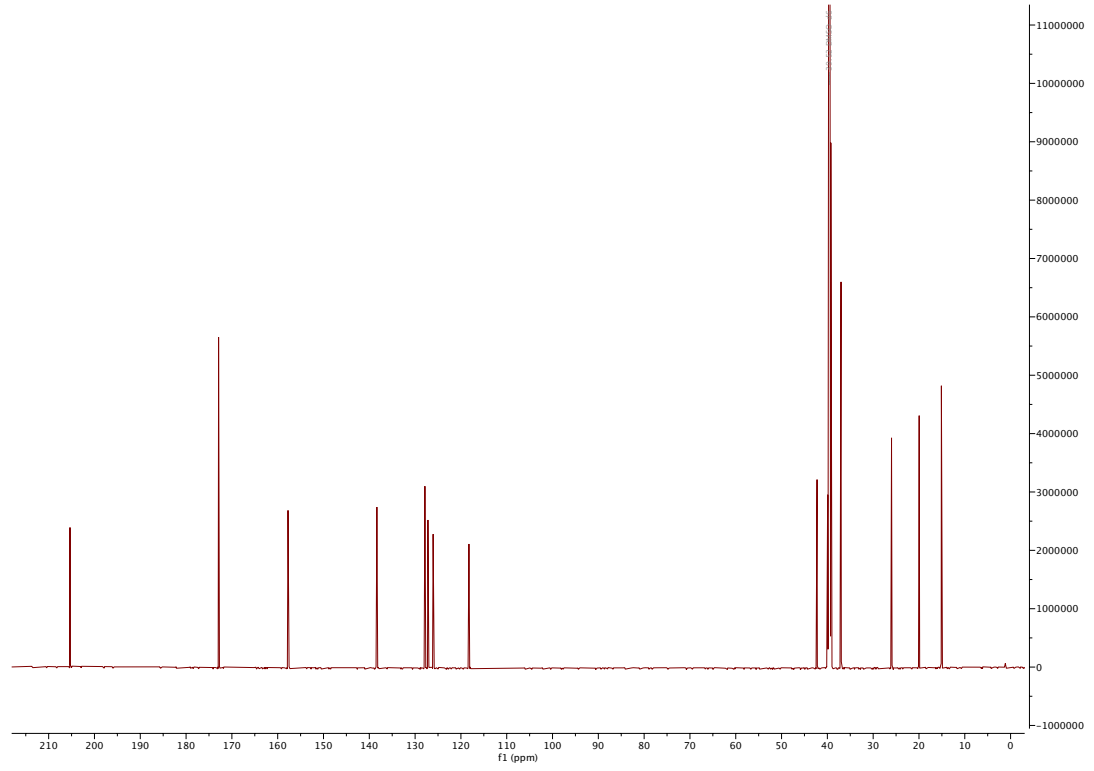

COSY spectrum of actiphenol (**22**)

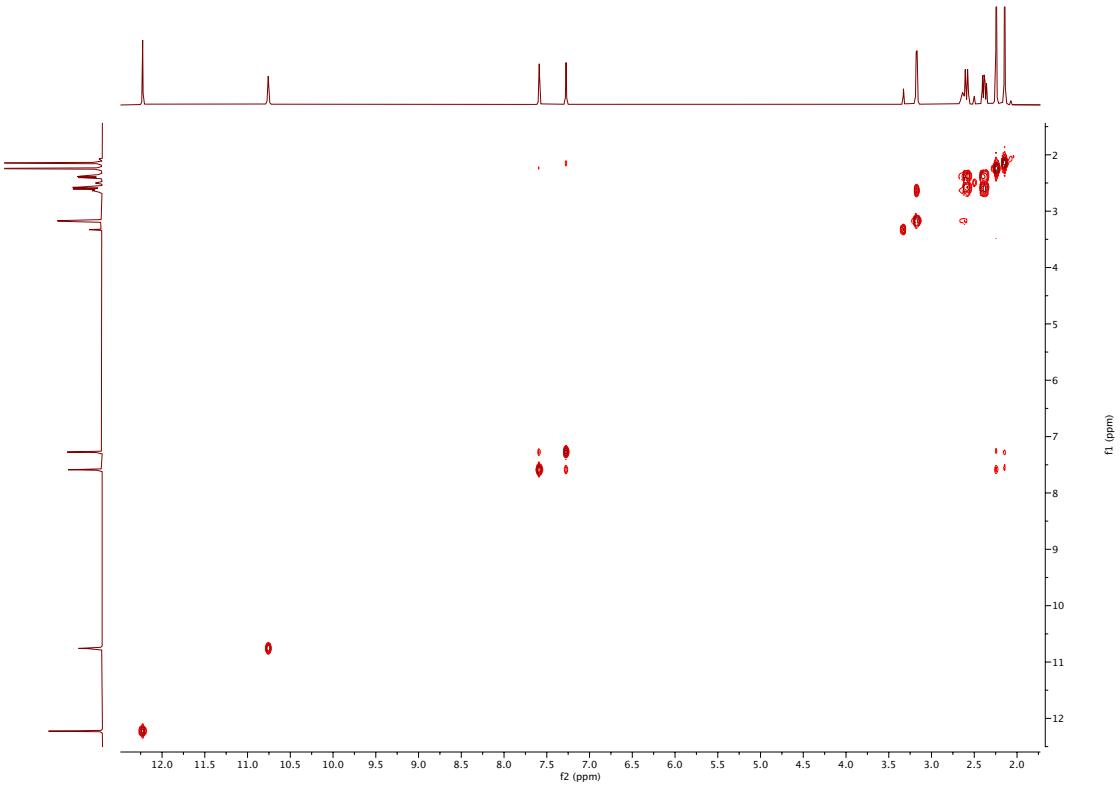

HSQC spectrum of actiphenol (**22**)

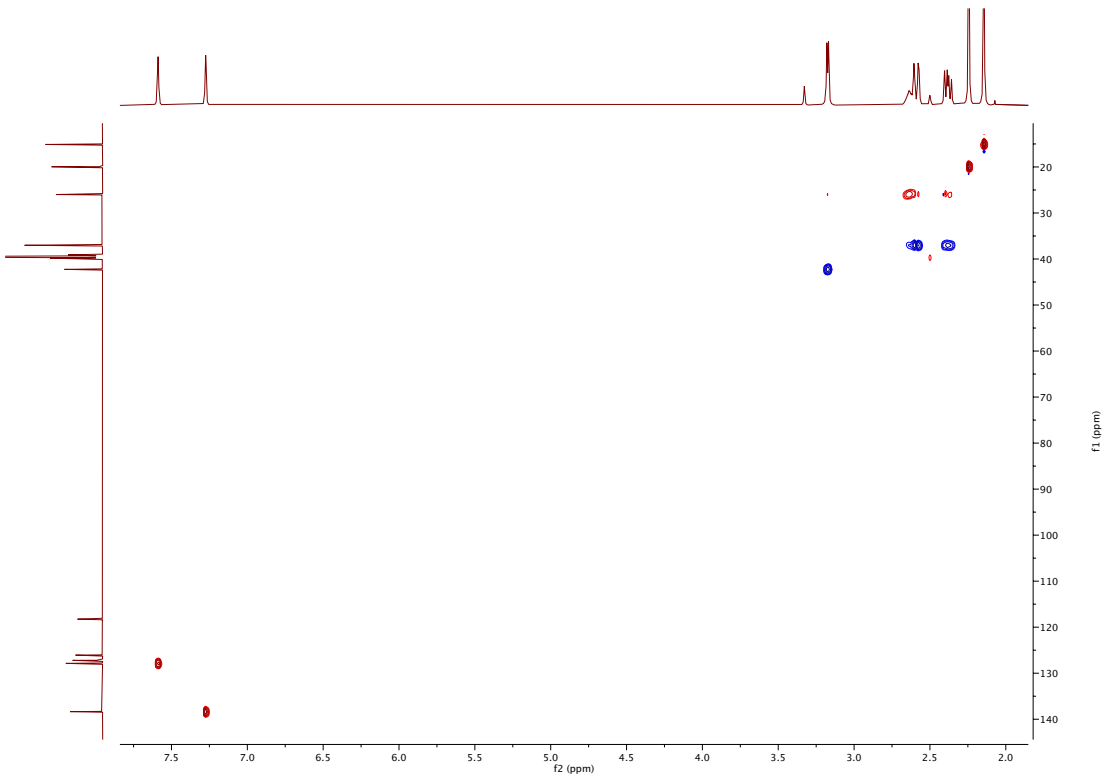

^{1}H-^{13}C HMBC spectrum of actiphenol (**22**)

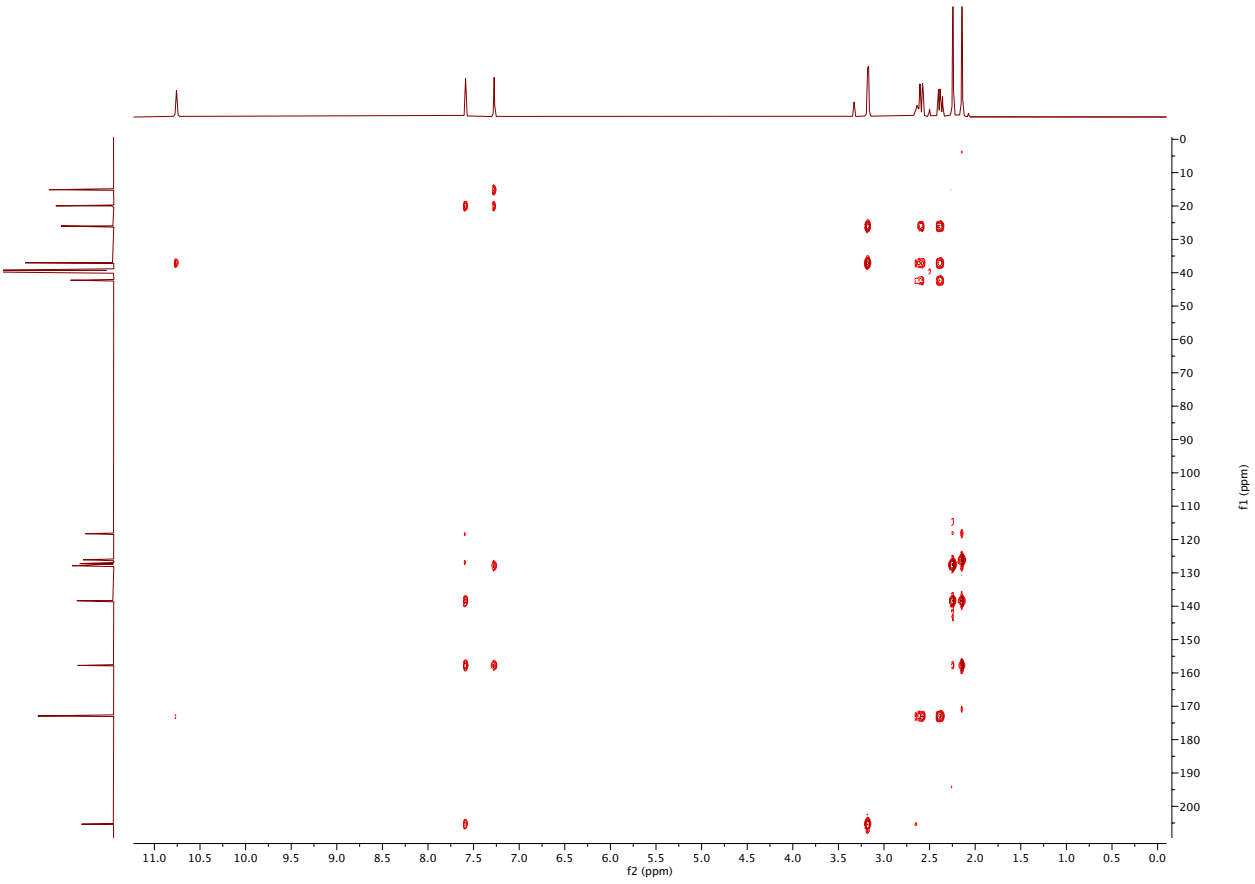

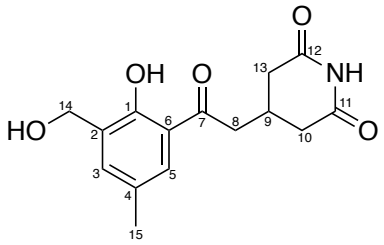

AH-135Y (**23**)

Position	δ_C (type)	δ_H, multiplets (*J* in Hz)	COSY	HMBC
1	156.8 (C)			
1-OH		12.19, s		1, 2, 6
2	156.8 (C)			
3	131.2 (CH)	7.48, s		1, 5, 14, 15
4	127.8 (C)			
5	128.9 (CH)	7.64, s		1, 3, 7, 15
6	118.7 (C)			
7	205.9 (C)			
8	42.8 (CH_2)	3.19, d (6.4)	9	9
9	26.5 (CH)	2.64, dt (10.7, 5.3)	8, 10a, 10b	8, 10, 11, 12, 13
10a	37.5 (CH_2)	2.38, dd (16.5, 10.7)	9, 10b	8, 9, 11
10b	37.5 (CH_2)	2.59, dd (16.2, 4.0)	9, 10a	8, 9, 11
11	173.4 (C)			
11-NH		10.76, s		10, 13
12	173.4 (C)			
13a	37.5 (CH_2)	2.38, dd (16.5, 10.7)	9, 13b	9, 12
13b	37.5 (CH_2)	2.59, dd (16.2, 4.0)	9, 13a	9, 12
14	57.7 (CH_2)	4.51, s		1, 2, 3
15	20.7 (CH_3)	2.29, s		3, 4, 5

^{1}H spectrum of AH-135Y (**23**)

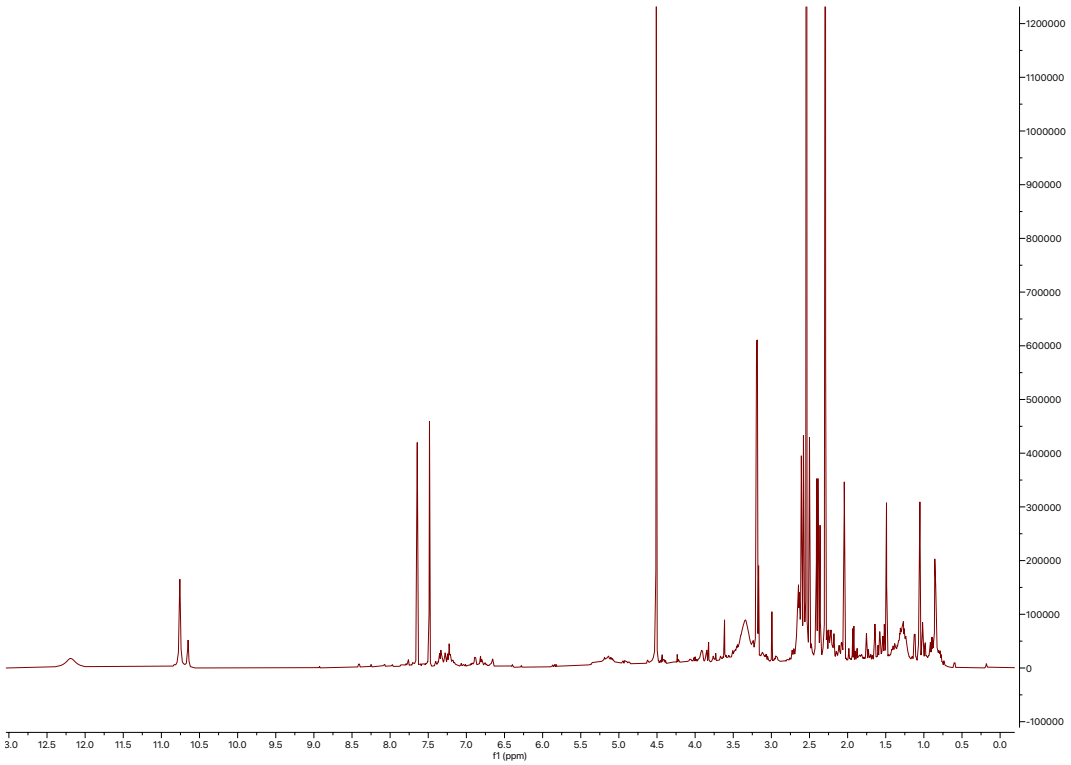

^{13}C spectrum of AH-135Y (**23**)

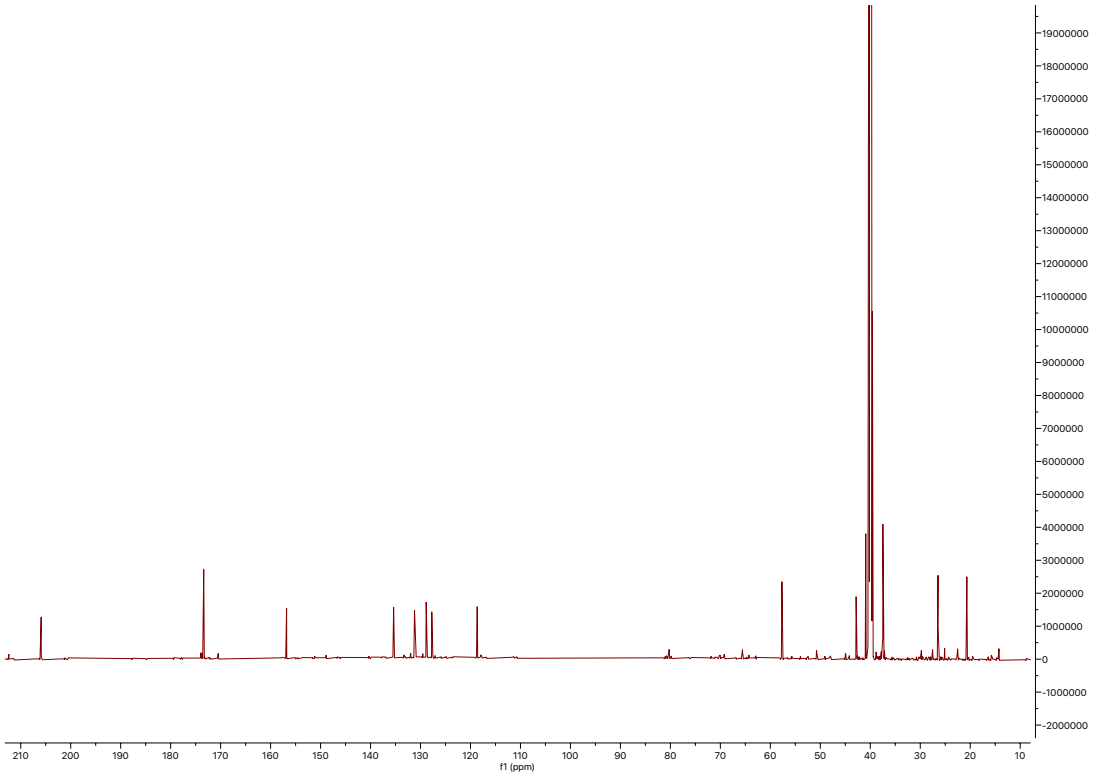

COSY spectrum of AH-135Y (**23**)

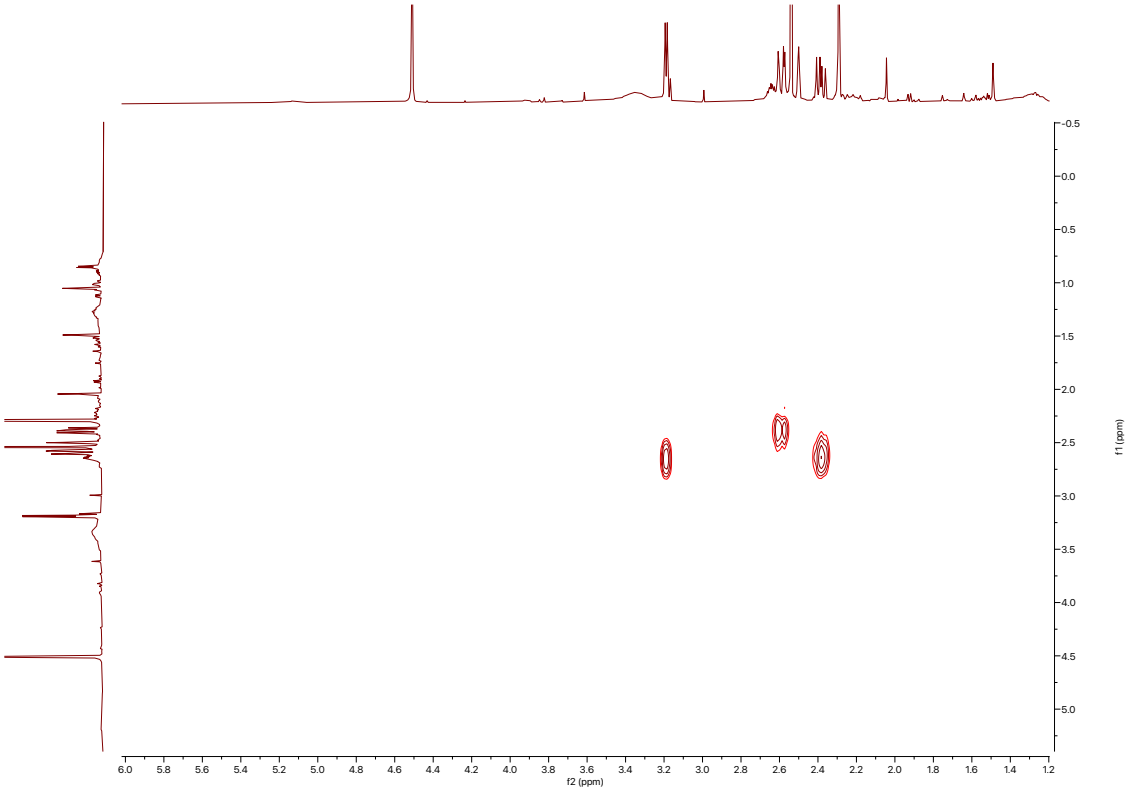

HSQC spectrum of AH-135Y (**23**)

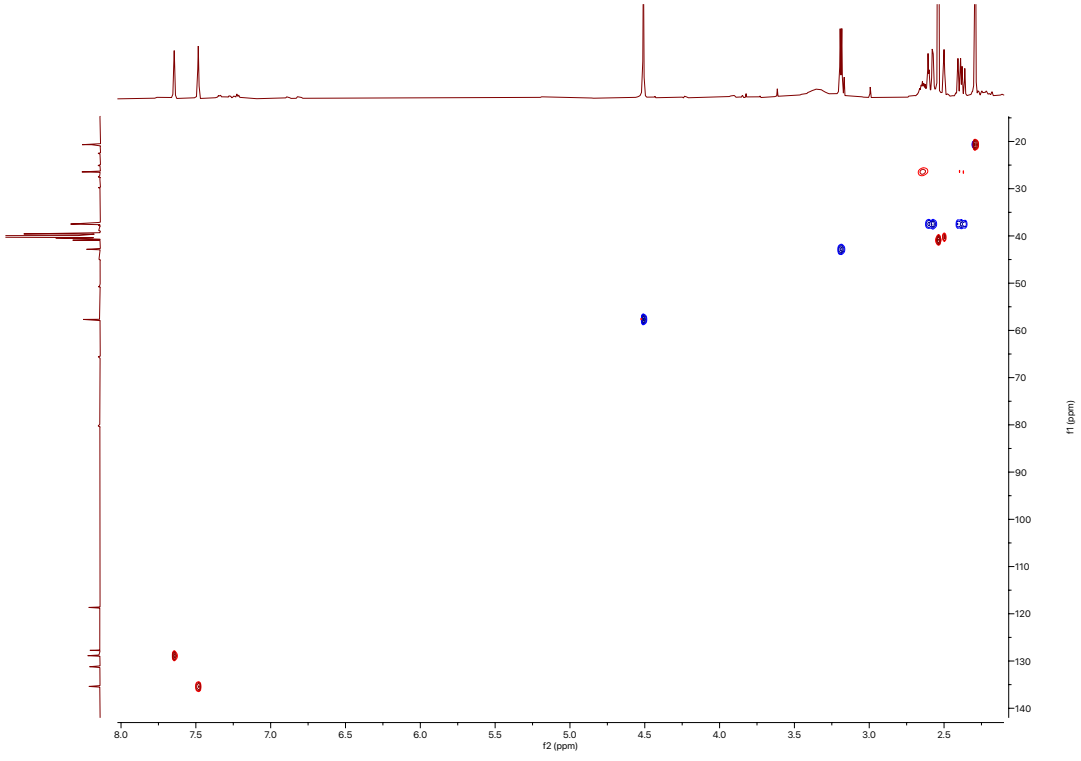

^{1}H-^{13}C HMBC spectrum of AH-135Y (**23**)

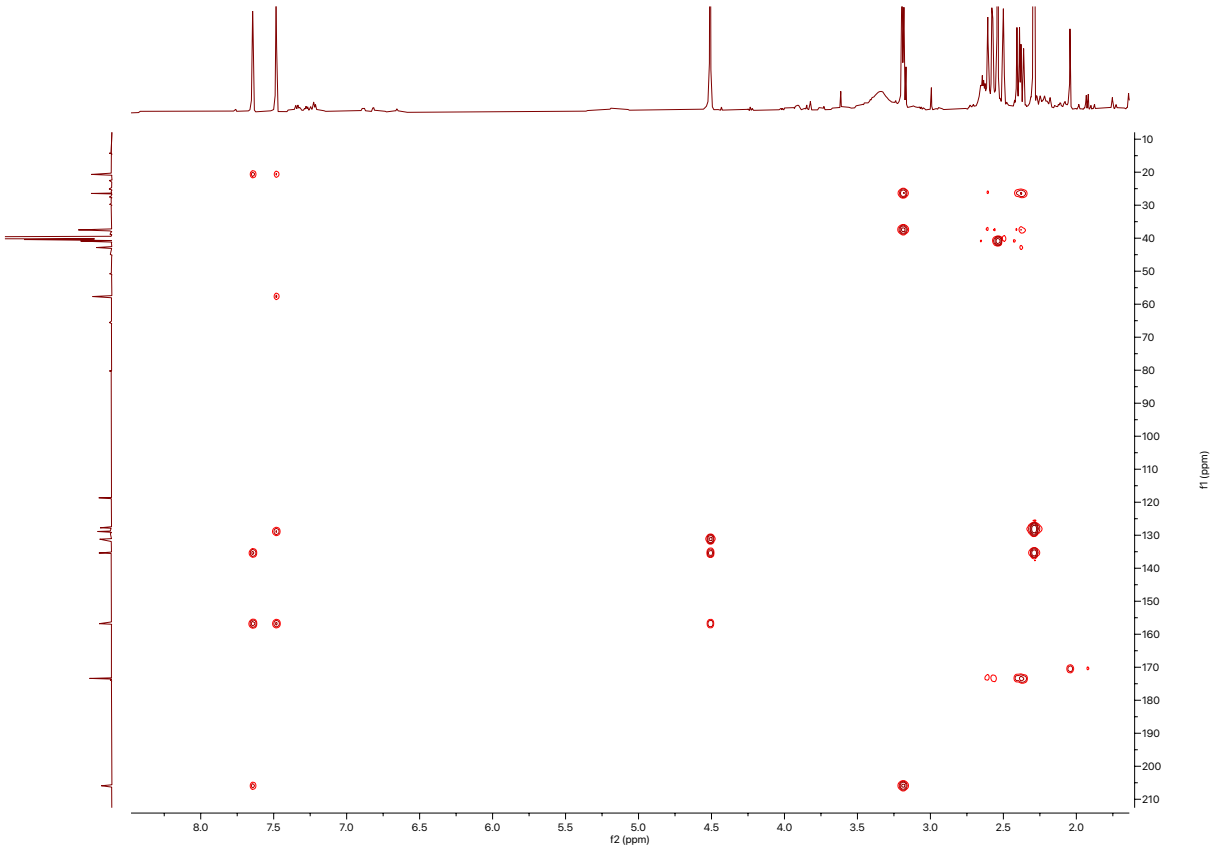

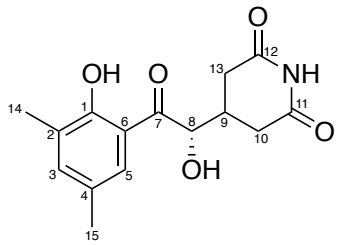

Nong-kang 101-G (**24**)

Position	δ_C (type)	δ_H, multiplets (*J* in Hz)	COSY	HMBC	ROESY
1	158.6 (C)				
1-OH		12.03, s		1, 2, 6	
2	127.8 (C)				
3	139.1 (CH)	7.31, s		1, 5, 14, 15	
4	126.7 (C)				
5	128.4 (CH)	7.69, s		1, 3, 7, 15	8
6	117.4 (C)				
7	206.3 (C)				
8	73.5 (CH)	5.03, d (4.4)	9	9	5, 8-OH, 10a
8-OH		5.78, br s			8
9	33.9 (CH)	2.58, m	8		
10a	35.0 (CH_2)	2.55, m	9	8, 11	
10b	35.0 (CH_2)	2.58, m	9	8, 11	
11	173.4 (C)				
11-NH		10.69, s		10, 13	
12	173.4 (C)				
13a	32.4 (CH_2)	2.28, dd (17.0, 10.3)	9, 13b	9, 12	
13b	32.4 (CH_2)	2.44, dd (17.0, 10.3)	9, 13a	8, 12	
14	15.7 (CH_3)	2.16, s		1, 2, 3	
15	20.6 (CH_3)	2.25, s		3, 4, 5	

^{1}H spectrum of Nong-kang 101-G (**24**)

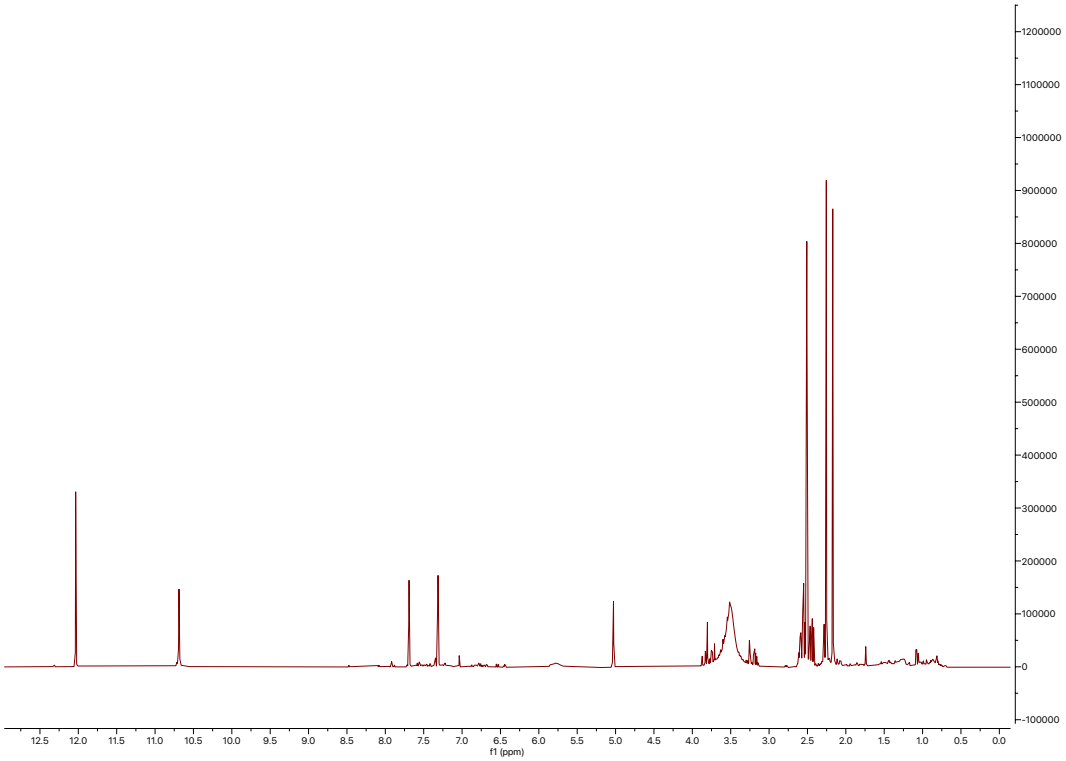

^{13}C spectrum of Nong-kang 101-G (**24**)

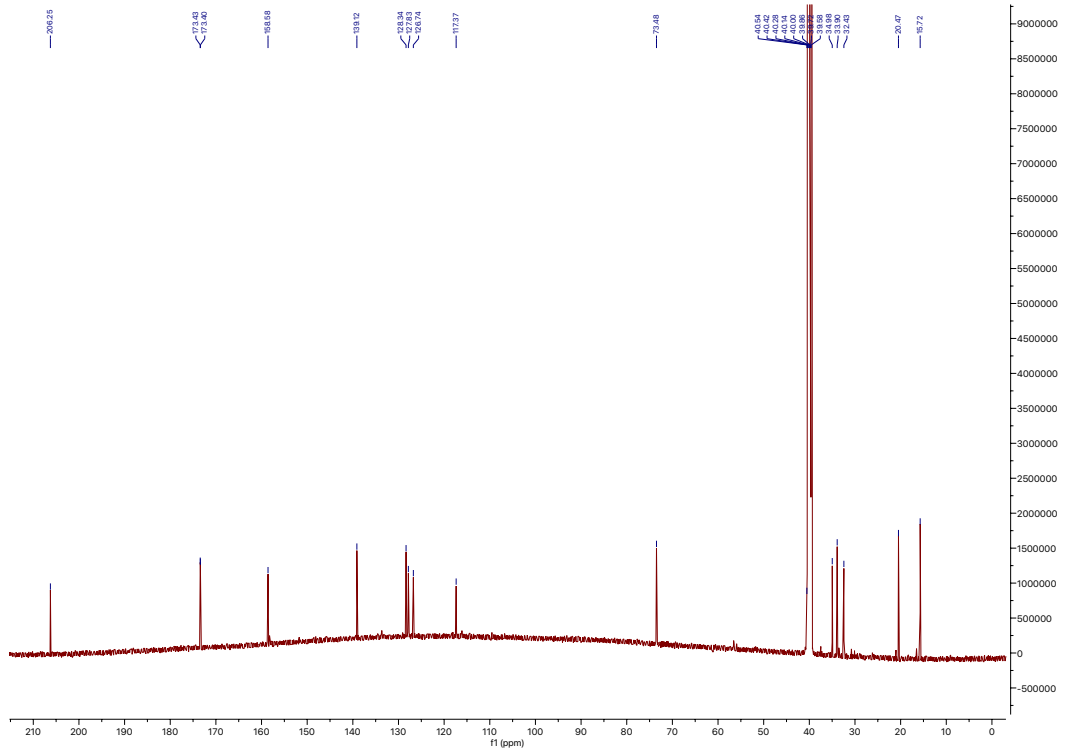

COSY spectrum of Nong-kang 101-G (**24**)

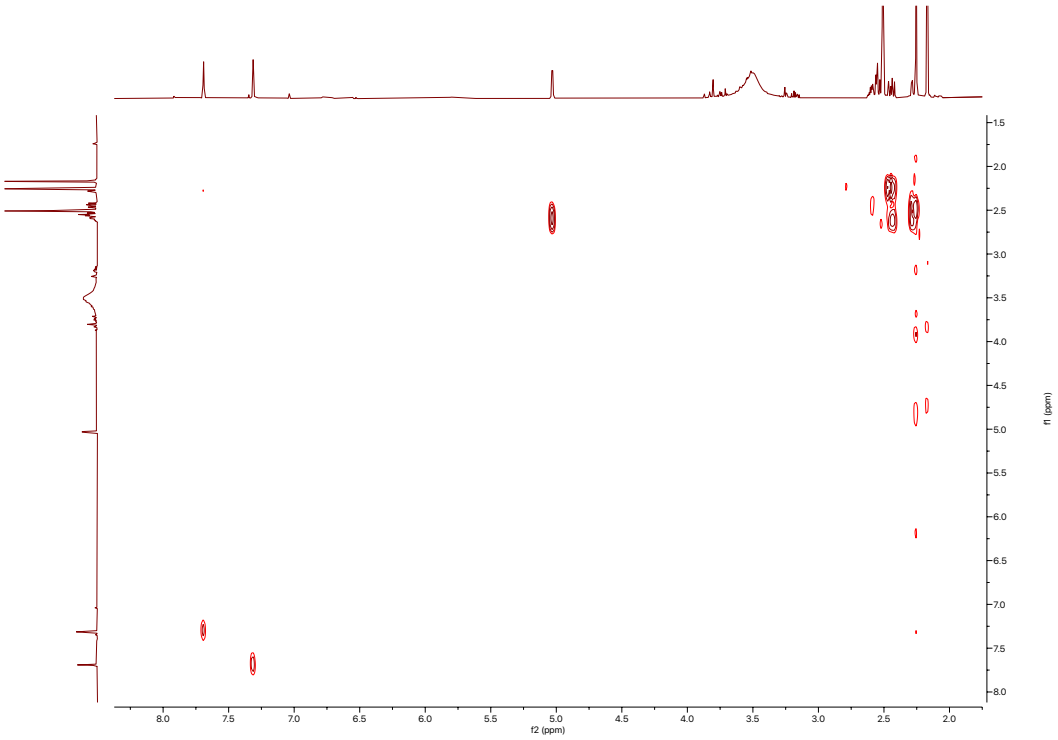

HSQC spectrum of Nong-kang 101-G (**24**)

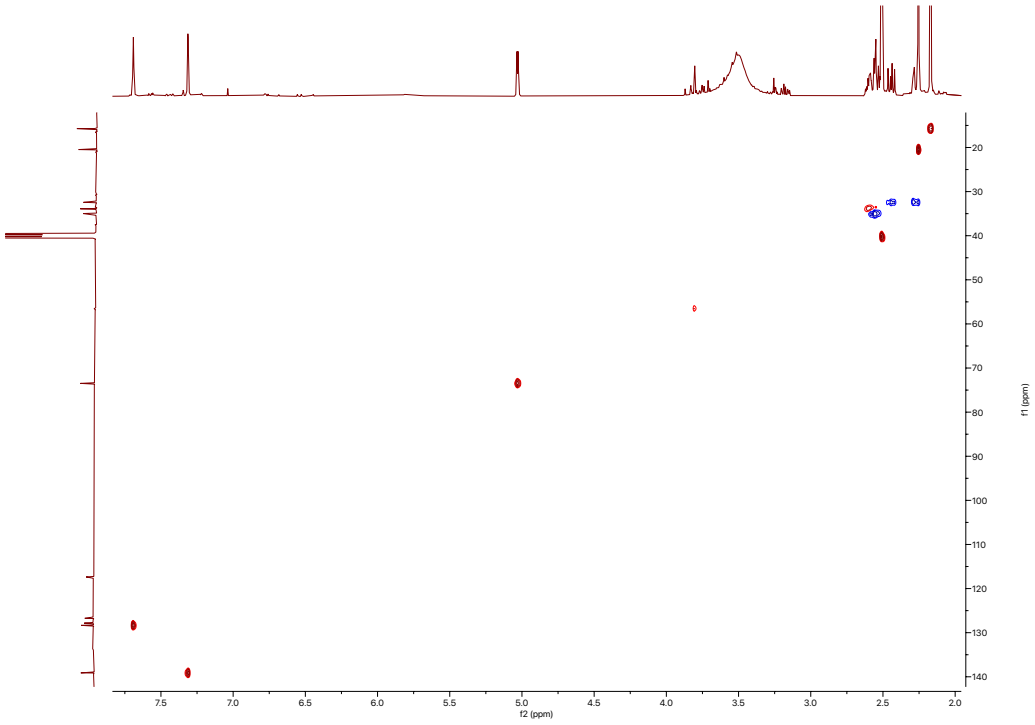

^{1}H-^{13}C HMBC spectrum of Nong-kang 101-G (**24**)

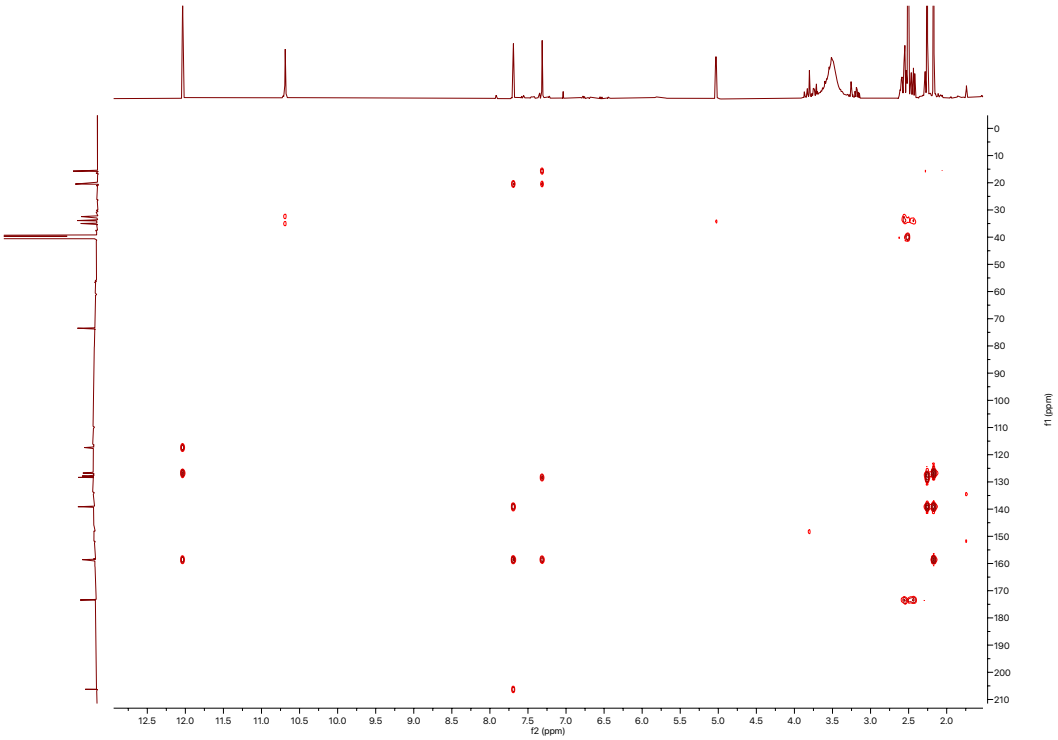

ROESY spectrum of Nong-kang 101-G (**24**)

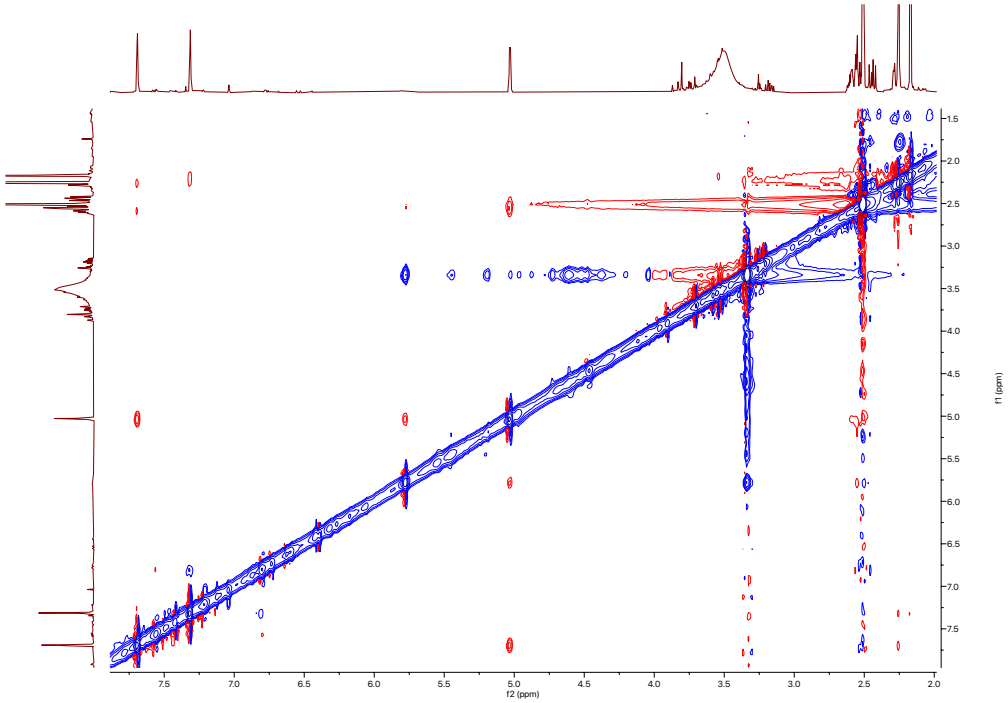

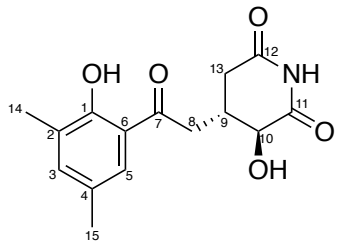

C-73X (**25**)

Position	δ_C (type)	δ_H, multiplets (*J* in Hz)	COSY	HMBC	ROESY
1	158.2 (C)				
1-OH		12.27, s		1, 2, 6	
2	127.6 (C)				
3	138.7 (CH)	7.29, s		1, 5, 14, 15	15
4	126.5 (C)				
5	128.3 (CH)	7.59, s		1, 3, 7, 15	8a, 8b, 9, 15
6	118.9 (C)				
7	206.2 (C)				
8a	40.4 (CH_2)	3.04, dd (17.1, 8.0)	9, 10b	7, 9, 10, 13	5, 9, 10
8b	40.4 (CH_2)	3.48, dd (17.1, 3.6)	9, 10a	7, 9, 10, 13	5, 9, 10
9	34.1 (CH)	2.57, m	8, 10a, 10b		
10	70.8 (CH)	4.06, dd (10.5, 4.2)	8-OH, 9	9, 11	8a, 8b, 10-OH, 9
10-OH		5.80, d (5.5)	8	9	10
11	175.2 (C)				
11-NH		10.84, s		10, 13	13b
12	172.3 (C)				
13a	36.6 (CH_2)	2.54, m	13b	9, 10, 12	
13b	36.6 (CH_2)	2.62, dd (15.6, 3.6)	13a	9, 10, 12	
14	15.6 (CH_3)	2.16, s		1, 2, 3	
15	20.5 (CH_3)	2.26, s		3, 4, 5	

^{1}H spectrum of C-73X (**25**)

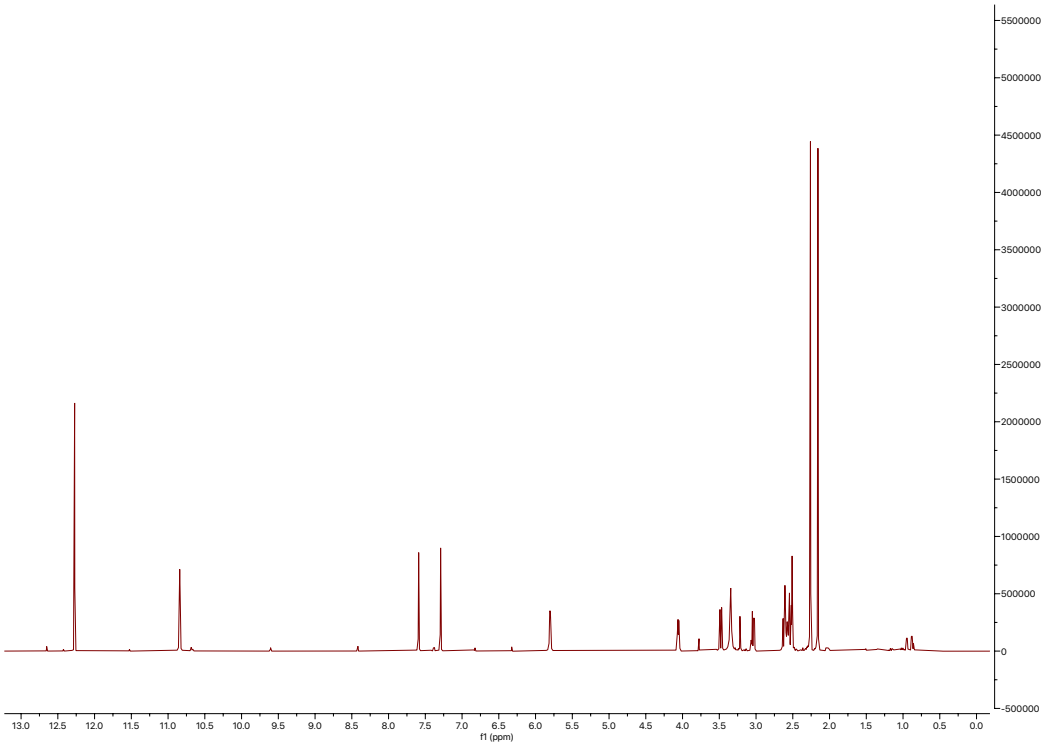

^{13}C spectrum of C-73X (**25**)

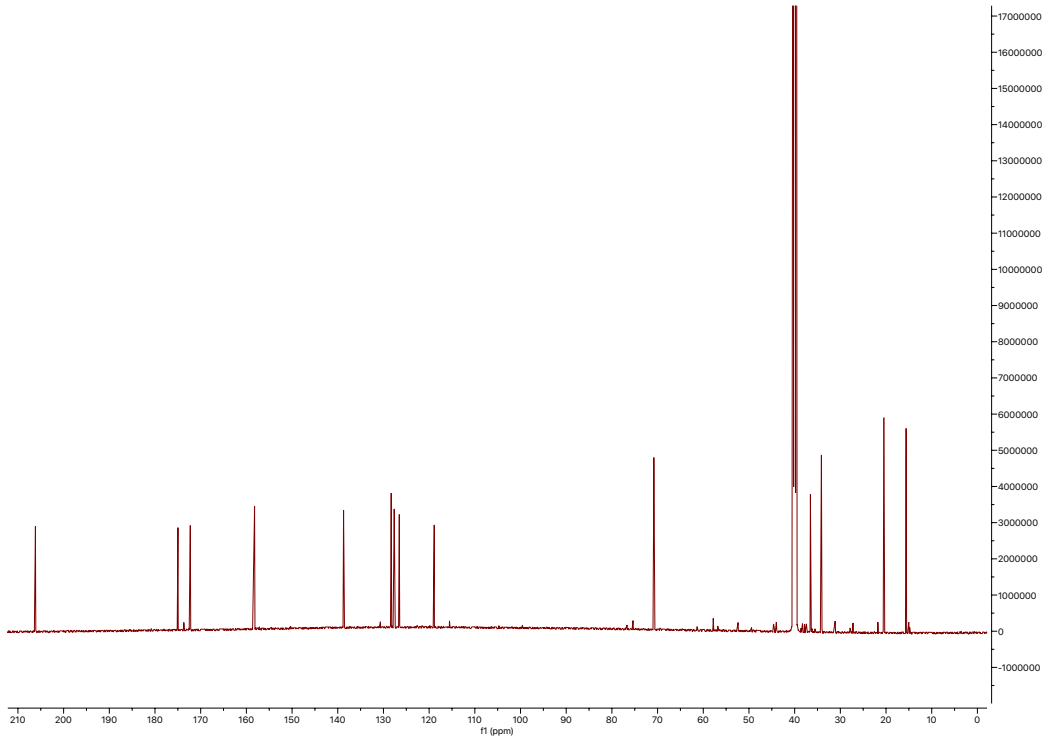

COSY spectrum of C-73X (**25**)

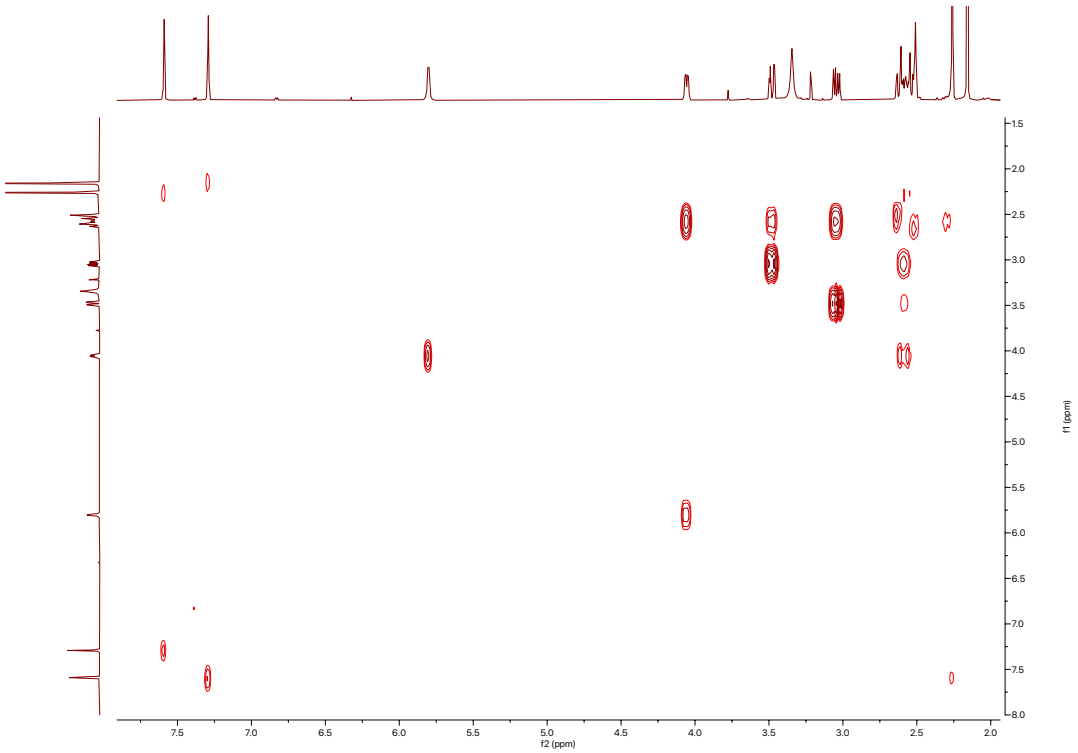

HSQC spectrum of C-73X (**25**)

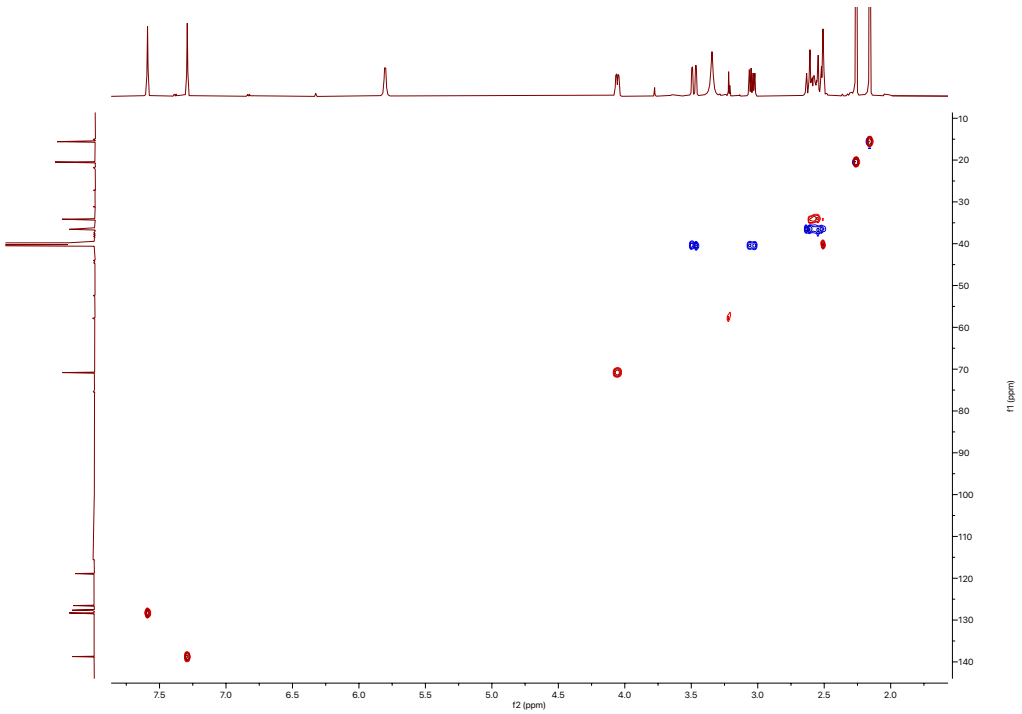

^{1}H-^{13}C HMBC spectrum of C-73X (**25**)

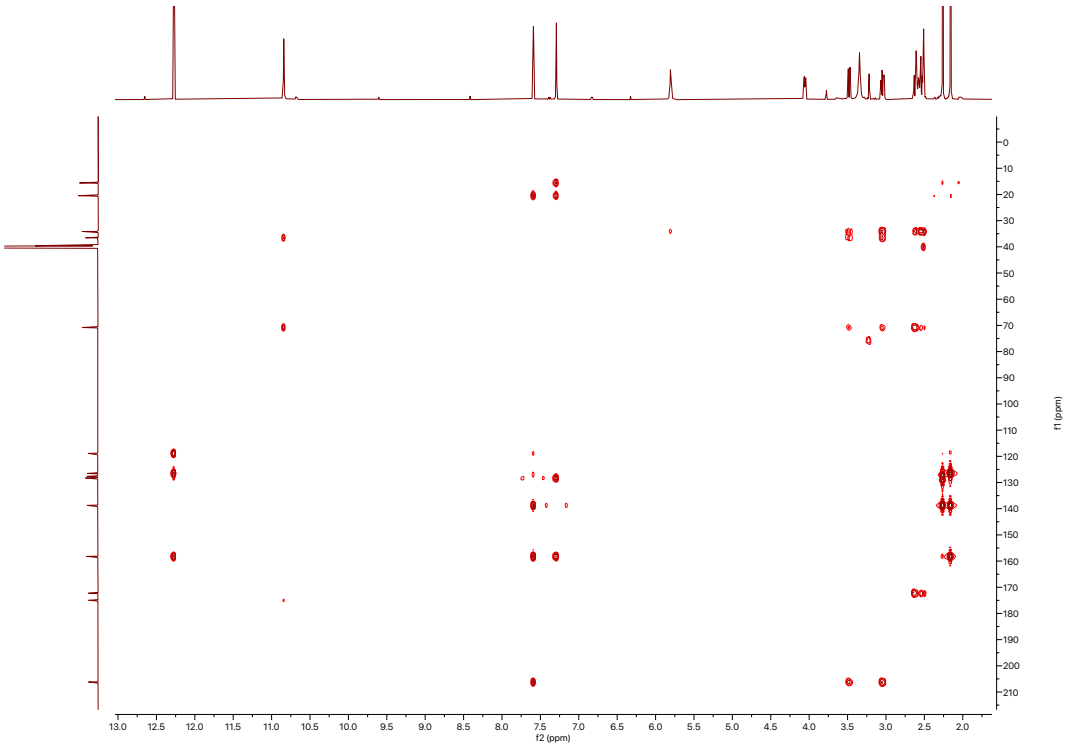

ROESY spectrum of C-73X (**25**)

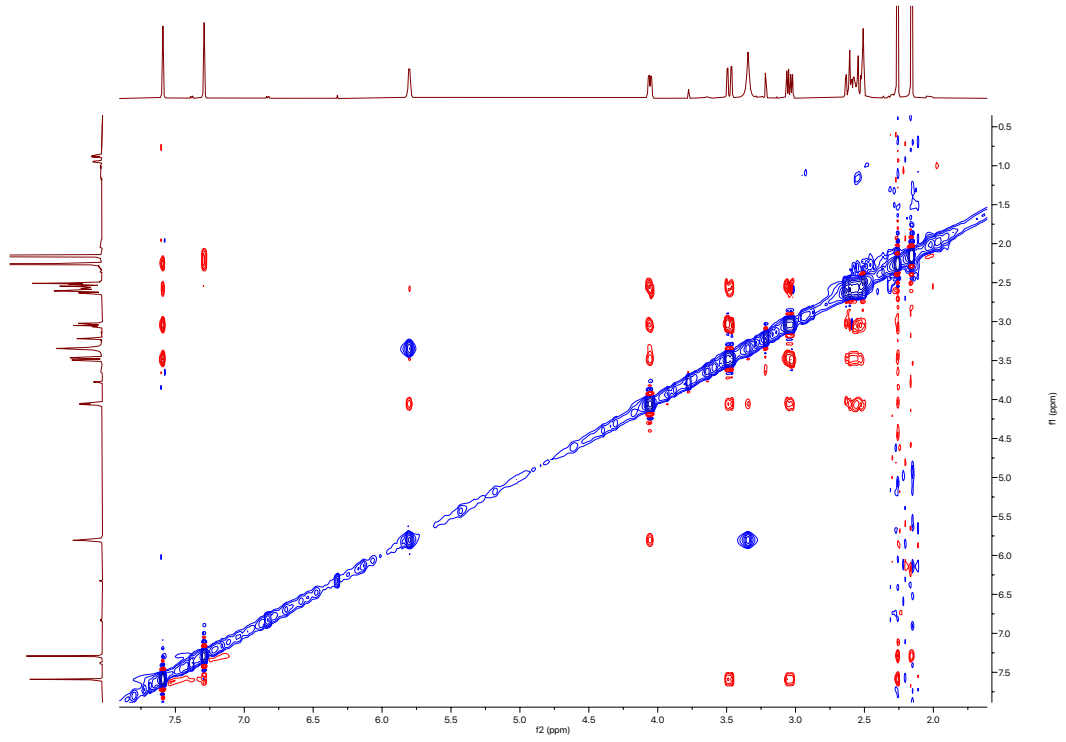

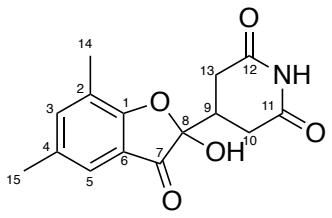

actiketal (**26**)

Position	δ_C (type)	δ_H, multiplets (*J* in Hz)	COSY	HMBC	ROESY
1	167.7 (C)				
2	123.2 (C)				
3	141.2 (CH)	7.43, s		1, 5, 14, 15	14, 15
4	132.2 (C)				
5	121.2 (CH)	7.25, s		1, 3, 15	
6	120.9 (C)				
7	199.4 (C)				
8	105.2 (C)				
8-OH		8.04, s		7, 8, 9	
9	35.5 (CH)	2.59, m	10a, 10b, 13	11, 13	
10a	31.9 (CH_2)	2.29, m	9, 10b	11	
10b	31.9 (CH_2)	2.45, dd (17.0, 5.1)	9, 10a	11	
11	172.6 (C)				
11-NH		10.73, s			
12	172.9 (C)				
13	31.0 (CH_2)	2.67, m	9	8, 9, 10, 12	
14	14.2 (CH_3)	2.20, s		3, 4, 5	
15	20.5 (CH_3)	2.29, s		1, 2, 3	

^{1}H spectrum of actiketal (**26**)

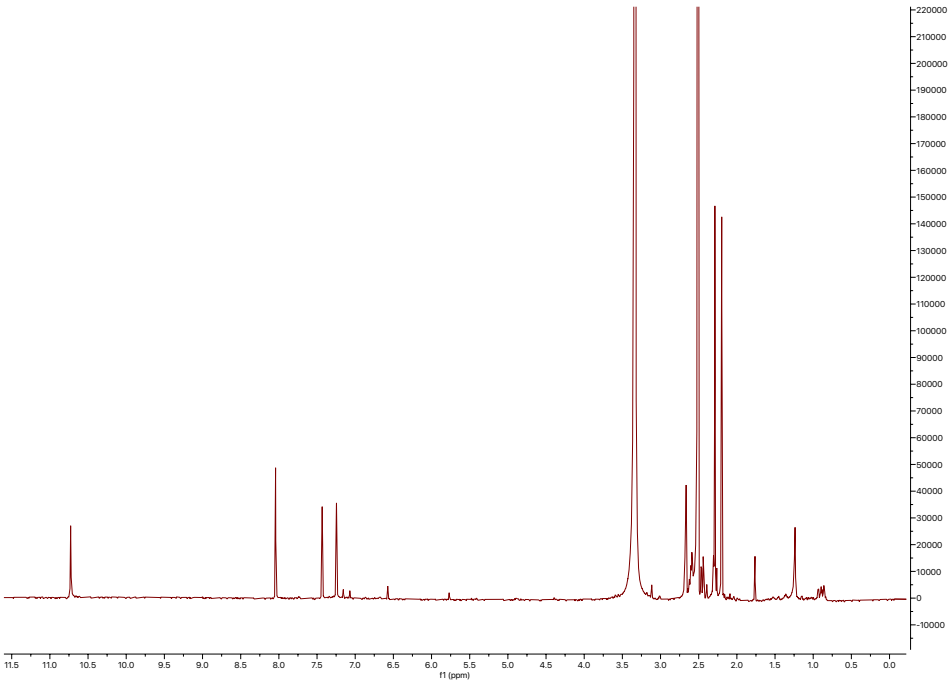

^{13}C spectrum of actiketal (**26**)

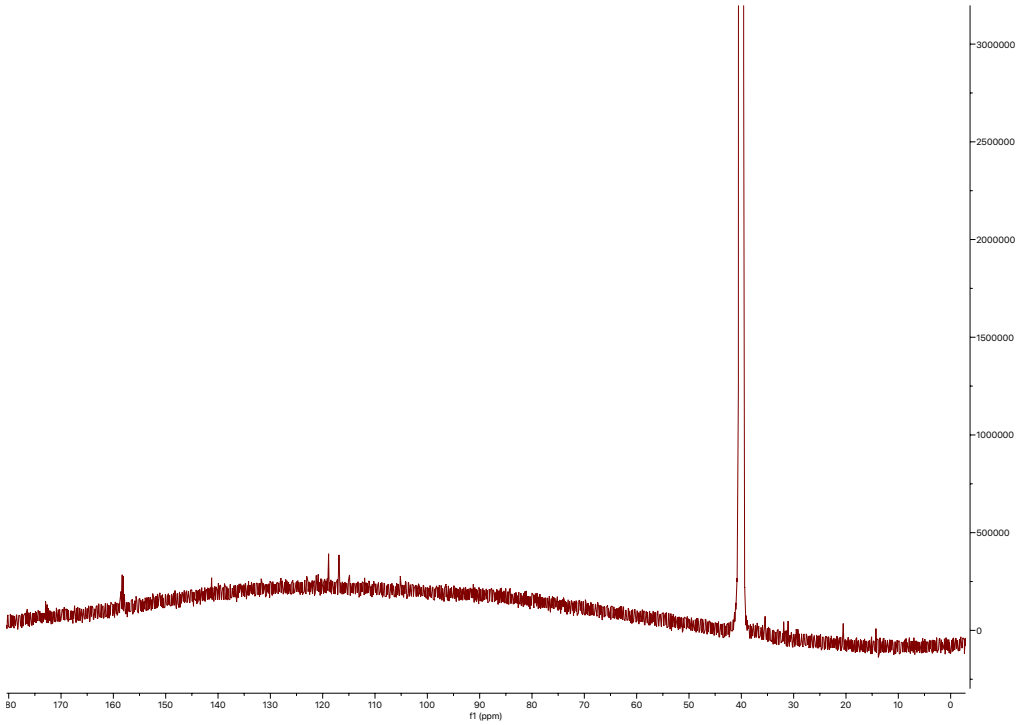

COSY spectrum of actiketal (**26**)

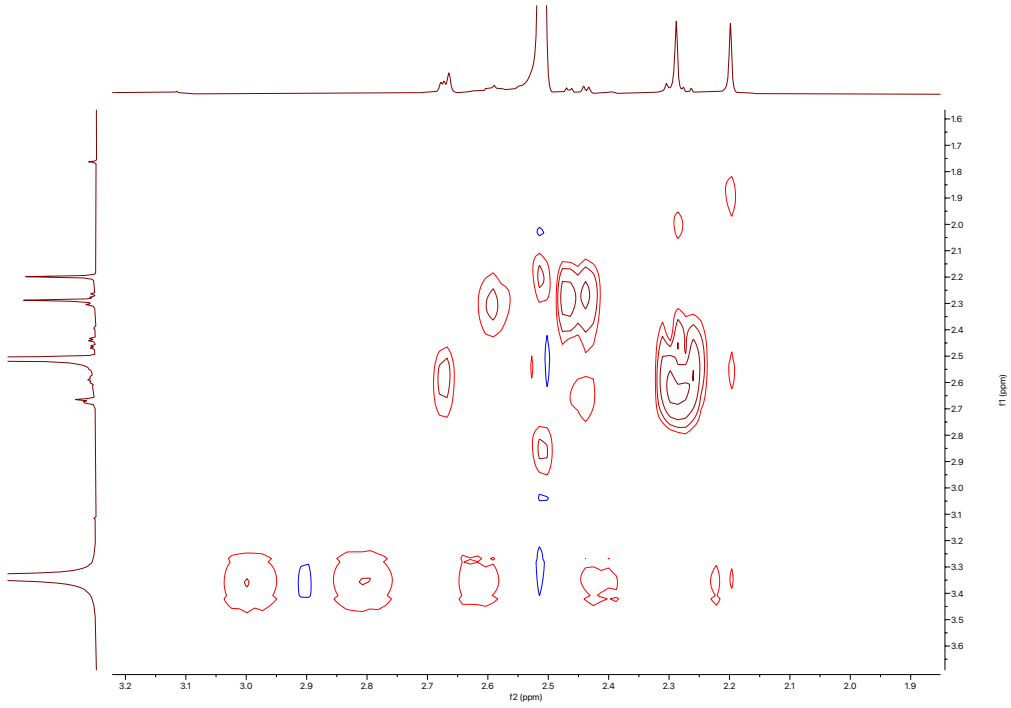

HSQC spectrum of actiketal (**26**)

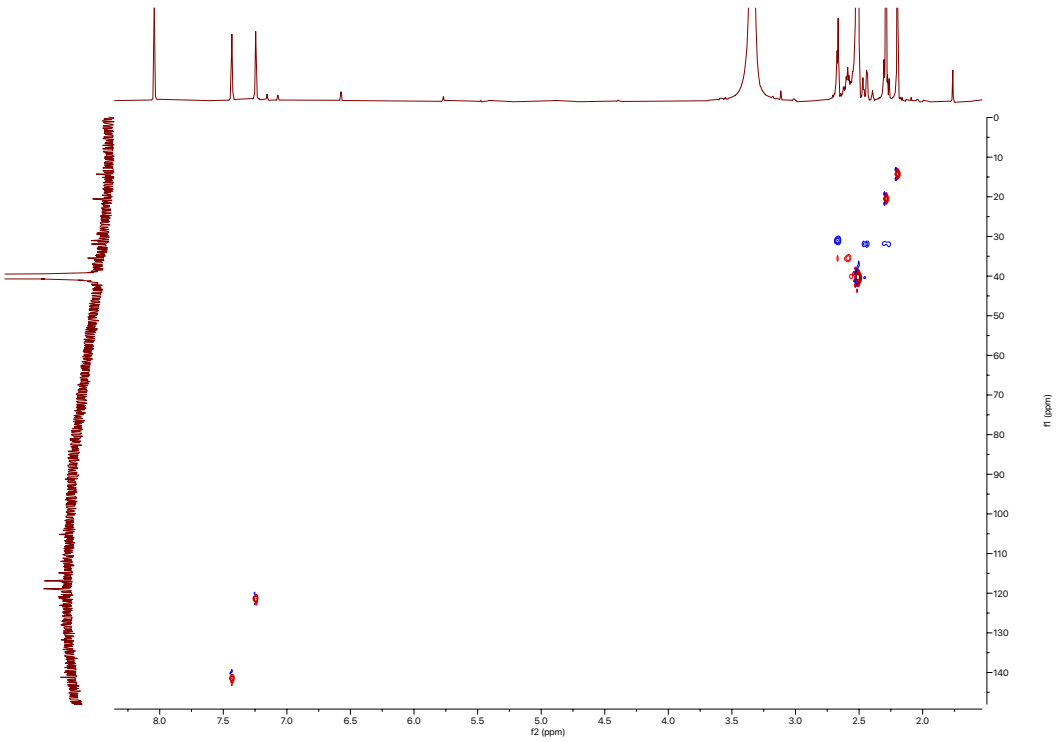

^{1}H-^{13}C HMBC spectrum of actiketal (**26**)

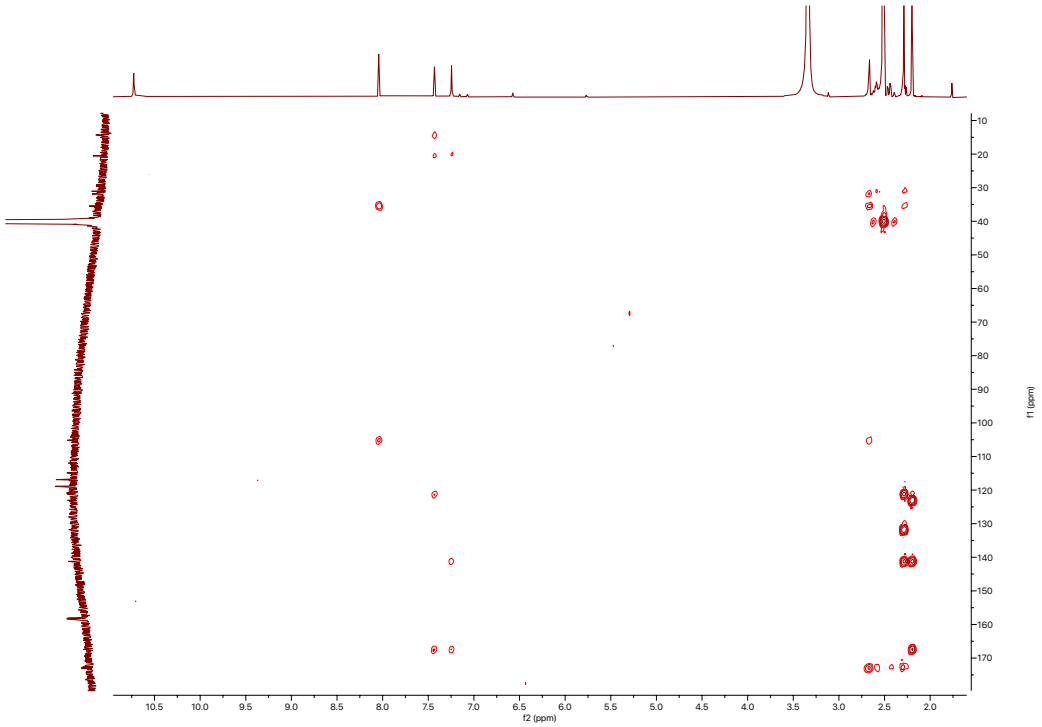

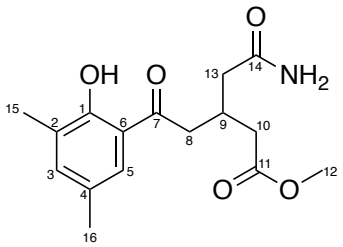

methyl phenatate A (**27**)

Position	δ_C (type)	δ_H, multiplets (*J* in Hz)	COSY	HMBC	ROESY
1	158.2 (C)				
1-OH		12.35, s		1, 2, 6	
2	126.4 (C)				
3	138.7 (CH)	7.29, s		1, 5, 15, 16	15, 16
4	126.7 (C)				
5	128.4 (CH)	7.65, s		1, 3, 7, 16	8a, 8b, 9, 16
6	118.8 (C)				
7	206.9 (C)				
8a	42.3 (CH_2)	3.07, dd (16.5, 7.1)	8b, 9	7, 9, 13	5, 9, 10a, 10b, 13
8b	42.3 (CH_2)	3.16, dd (16.5, 6.1)	8a, 9	7, 9, 13	5, 9, 10a, 10b, 13
9	28.9 (CH)	2.77, h (2.77)	8a, 8b, 10a, 10b, 13	8, 11, 13	8a, 8b, 10a, 10b, 13
10a	32.4 (CH_2)	2.36, dd (16.8, 6.5)	9	8, 9, 11, 13	8a, 8b, 9
10b	32.4 (CH_2)	2.46, dd (16.8, 6.5)	9	8, 9, 11, 13	8a, 8b, 9
11	172.8 (C)				
12	51.7 (CH_3)	3.57, s		11	
13	39.1 (CH_2)	2.19, d (7.0)	9	8, 9, 10, 14	8a, 8b, 9, 14-NHb
14	173.2 (C)				
14-NHa		6.84, s			
14-NHb		7.34, s			13
15	15.6 (CH_3)	2.15, s		1, 2, 3	3, 16
16	20.5 (CH_3)	2.26, s		3, 5	3, 5, 15

^{1}H spectrum of methyl phenatate A (**27**)

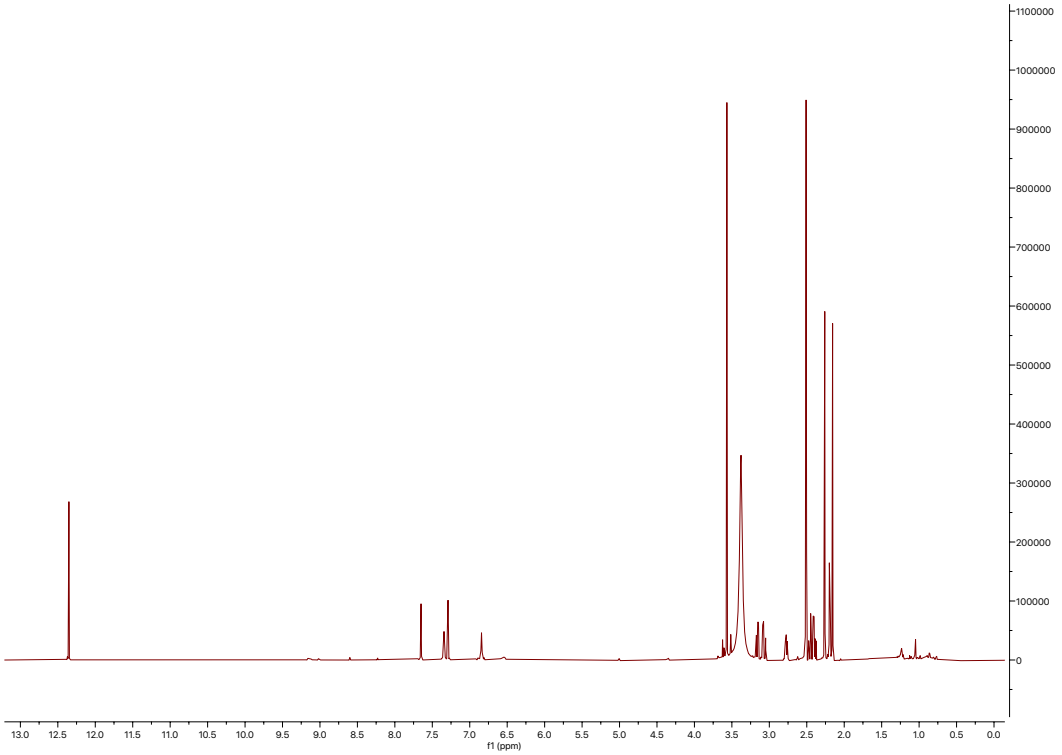

^{13}C spectrum of methyl phenatate A (**27**)

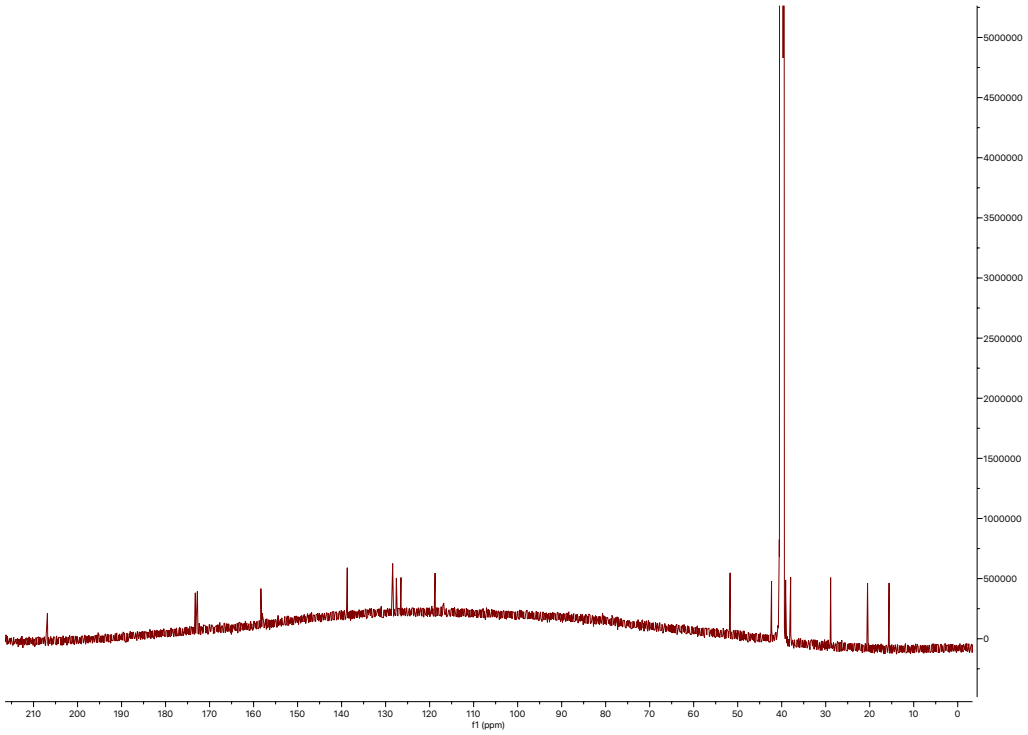

COSY spectrum of methyl phenatate A (**27**)

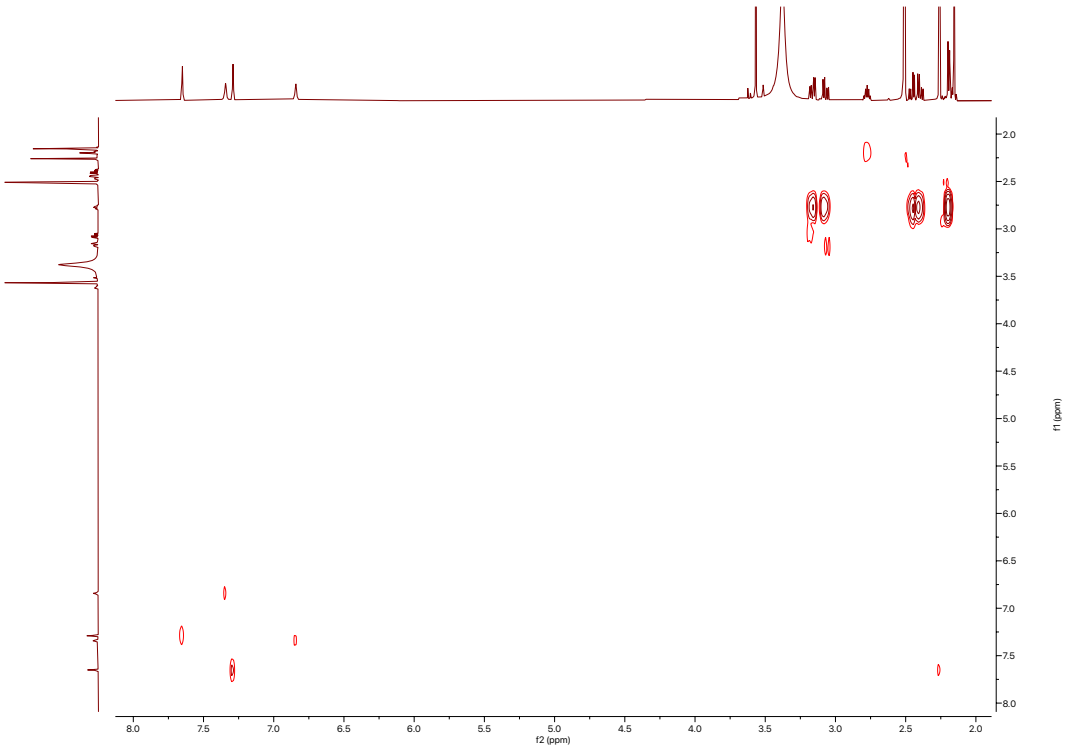

HSQC spectrum of methyl phenatate A (**27**)

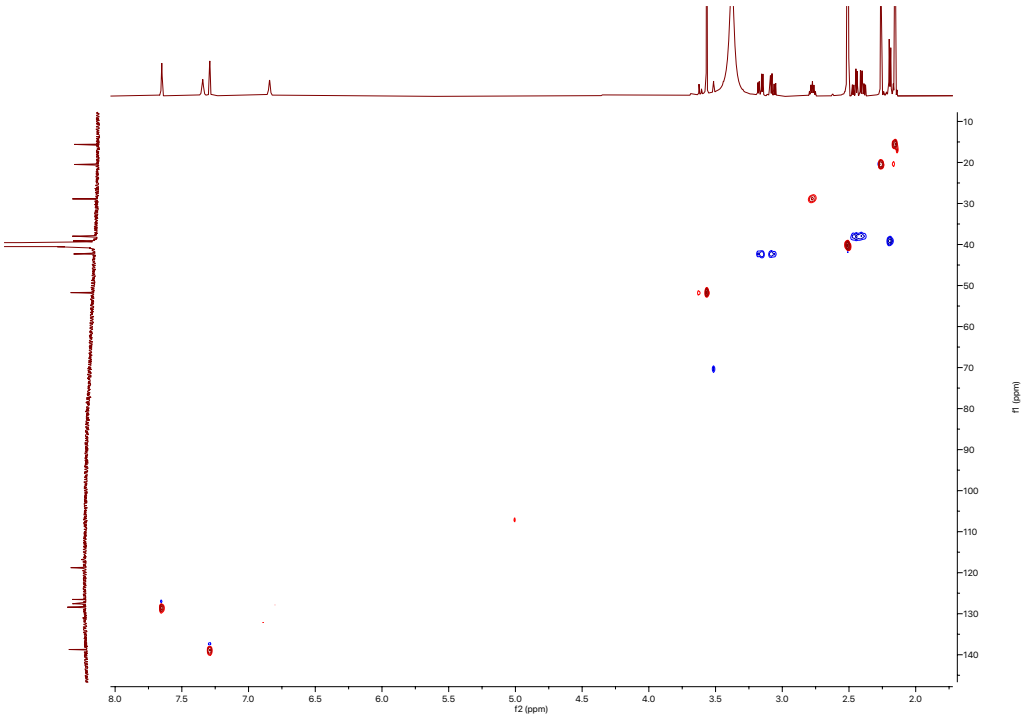

^{1}H-^{13}C spectrum of methyl phenatate A (**27**)

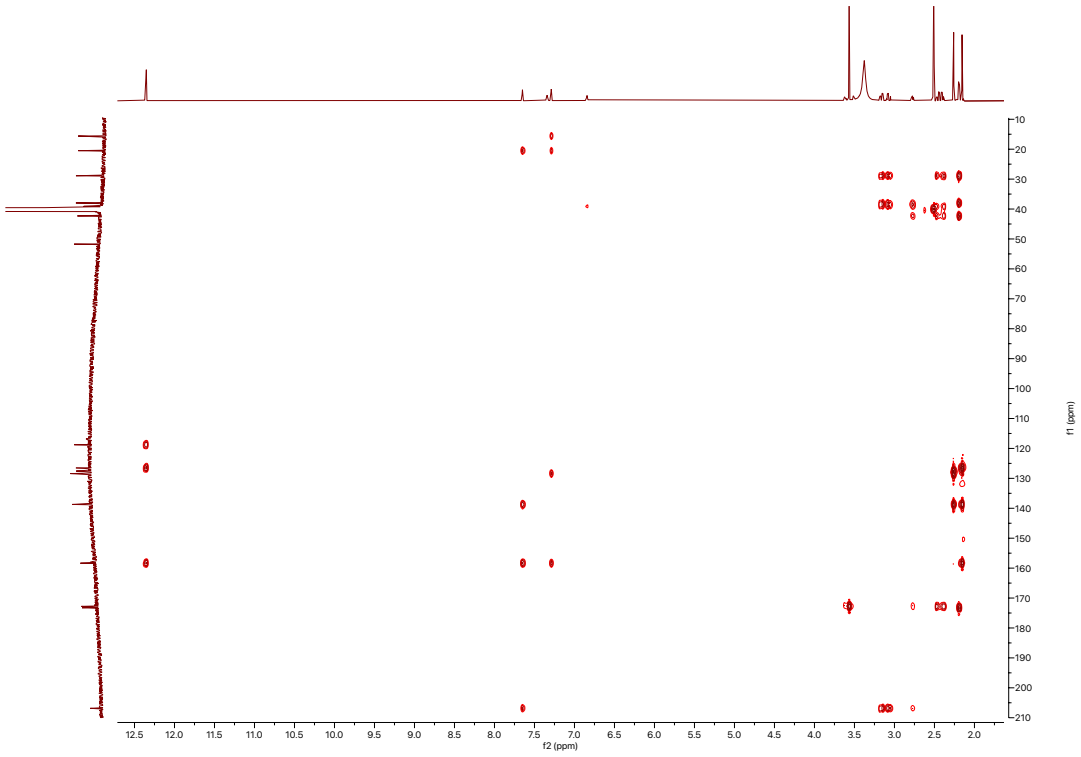

ROESY spectrum of methyl phenatate A (**27**)

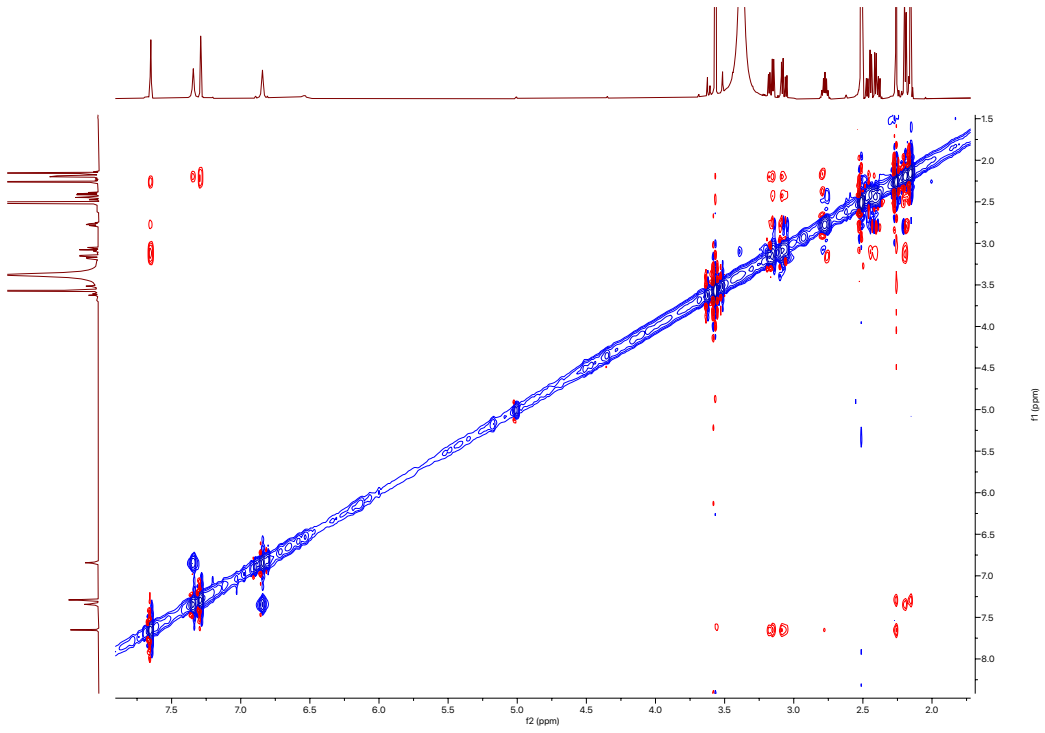

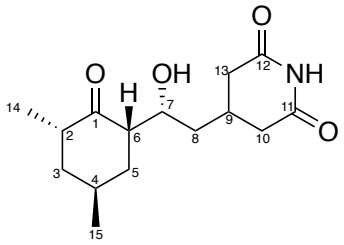

cycloheximide (**28**)

Position	δ_C (type)	δ_H, multiplets (*J* in Hz)	COSY	HMBC	ROESY
1	213.9 (C)				
2	40.3 (CH)	2.55, m	3a, 3b, 14	3, 14	15
3a	42.8 (CH_2)	1.42, td (12.9, 4.7)	2, 3b, 4	2, 4, 5, 14, 15	
3b	42.8 (CH_2)	1.73, ddt (13.0, 5.7, 2.8)	2, 3a, 4	2, 4, 5, 15	
4	26.9 (CH)	2.01, m	3a, 3b, 5a, 5b, 15		3a
5a	35.5 (CH_2)	1.56, td (13.1, 4.1)	4, 5b, 6	3, 4, 6, 7, 15	
5b	35.5 (CH_2)	1.89, ddt (13.2, 5.7, 2.9)	4, 5a, 6	3, 4, 6, 15	
6	51.0 (CH)	2.39, dd (12.1, 5.7)	5a, 5b, 7	4, 5, 7, 8	7, 15
7	65.4 (CH)	3.76, dd (6.3, 5.9)	6, 8	5, 6, 8, 9	6
7-OH		4.33, br s			
8	40.6 (CH_2)	1.24, m	7, 9	6, 7, 9, 10, 13	
9	27.4 (CH)	2.18, m	8, 10a, 10b, 13a, 13b	8, 10, 13	
10a	38.4 (CH_2)	2.21, m	9, 10b	8, 9, 11	
10b	38.4 (CH_2)	2.42, m	9, 10a	8, 9, 11	
11	173.8 (C)				
11-NH		10.58, br s		10, 11, 12, 13	
12	173.9 (C)				
13a	37.2 (CH_2)	2.19, m	9, 13b	8, 9, 12	
13b	37.2 (CH_2)	2.51, m	9, 13a	8, 9, 12	
14	15.0 (CH_3)	0.79, d (6.4)	2	2, 3	
15	18.7 (CH_3)	1.12, d (7.2)	4	3, 4, 5	2, 6

^{1}H spectrum of cycloheximide (**28**)

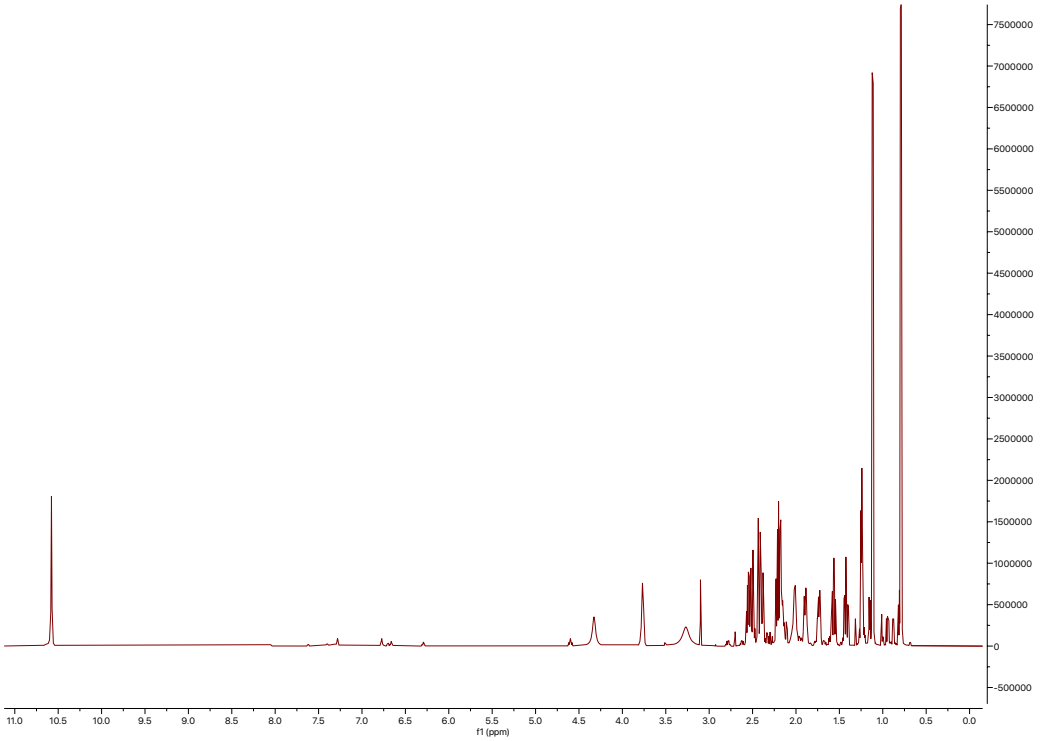

^{13}C spectrum of cycloheximide (**28**)

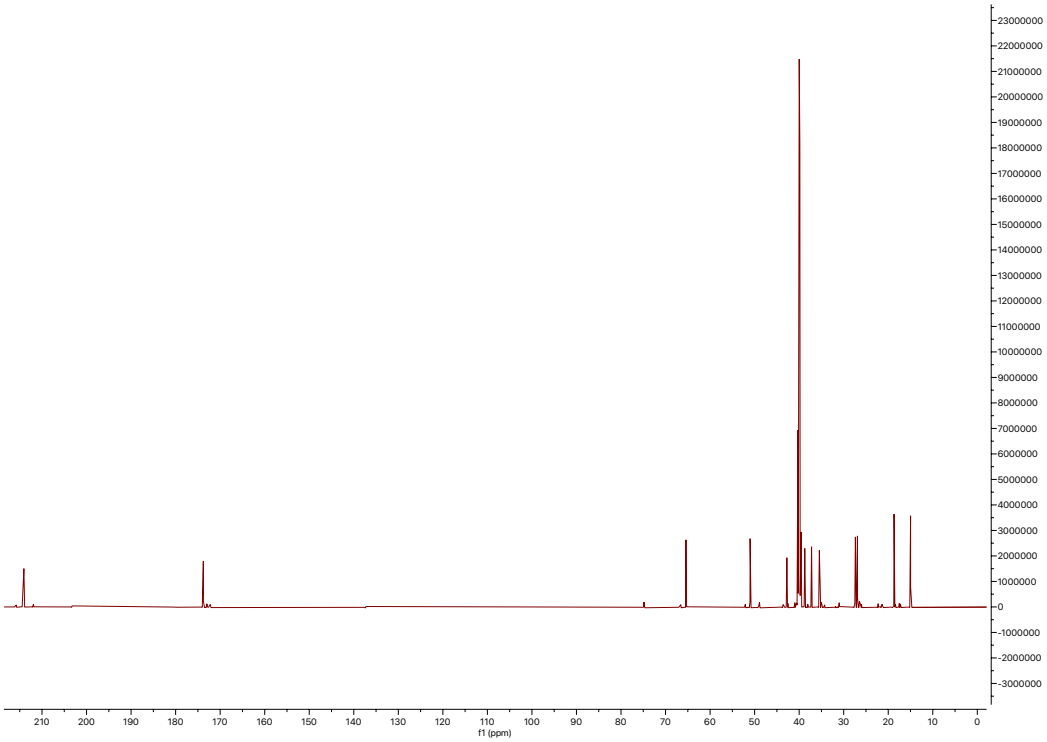

COSY spectrum of cycloheximide (**28**)

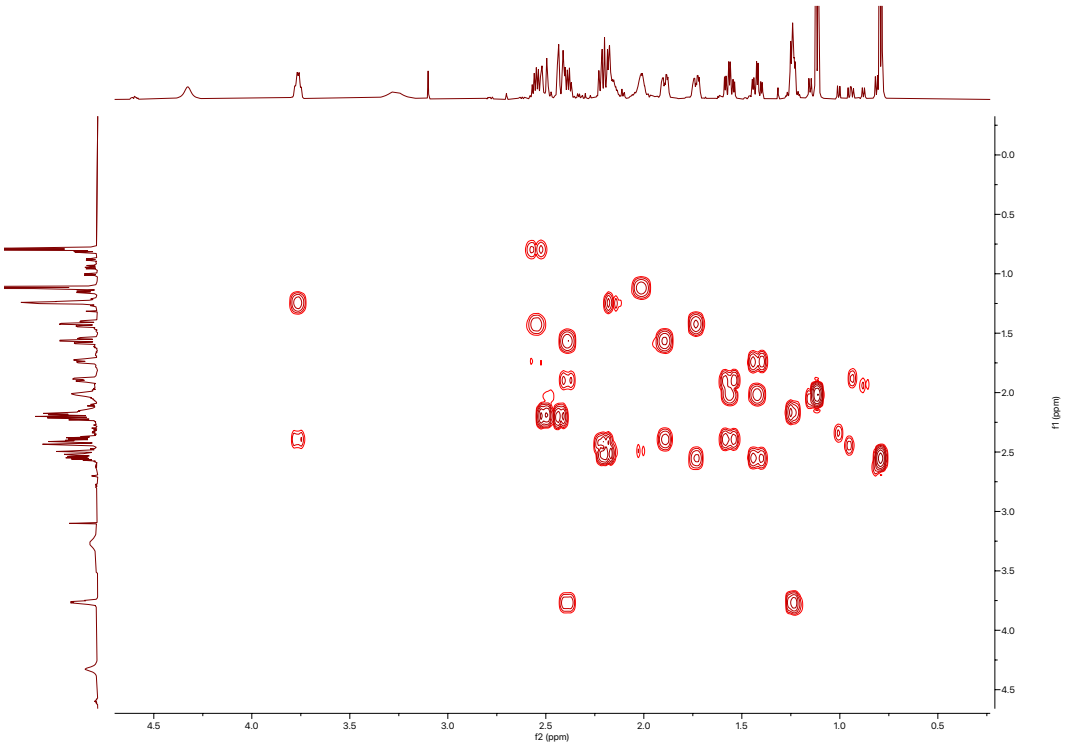

HSQC spectrum of cycloheximide (**28**)

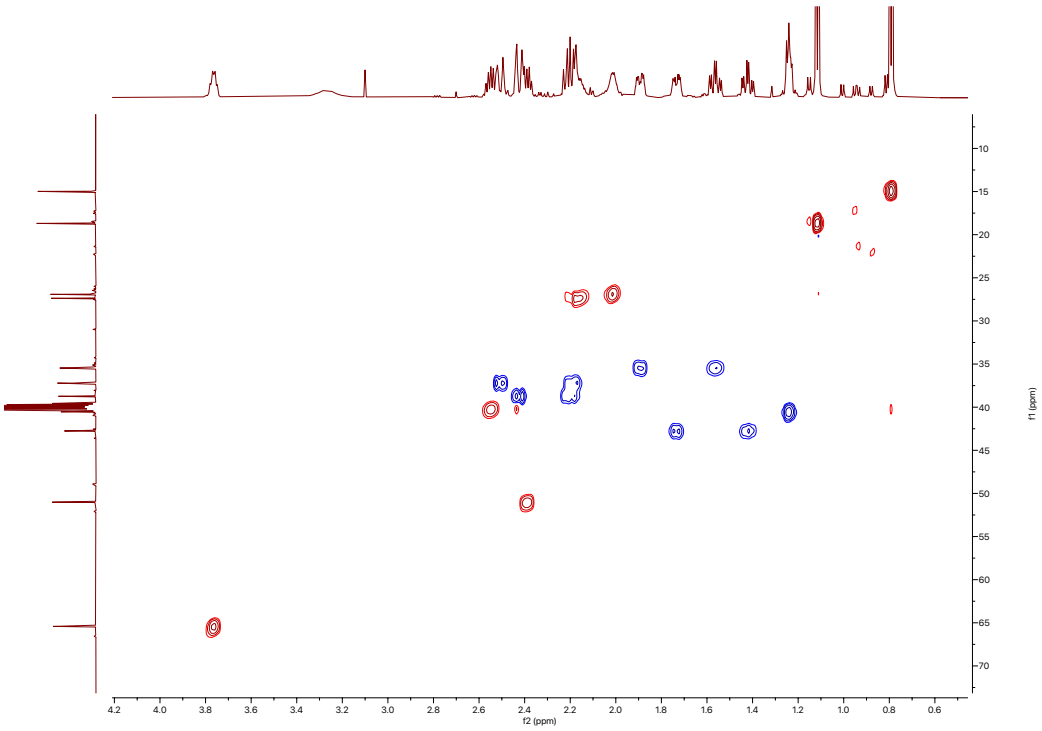

^{1}H-^{13}C HMBC spectrum of cycloheximide (**28**)

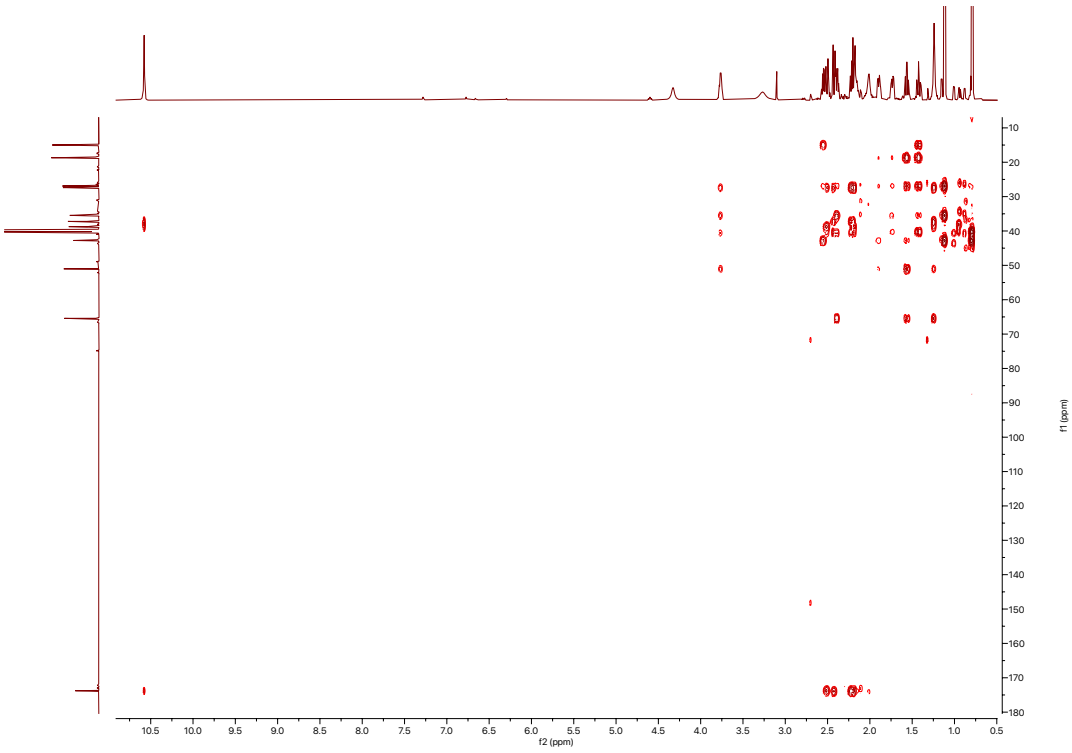

ROESY spectrum of cycloheximide (**28**)

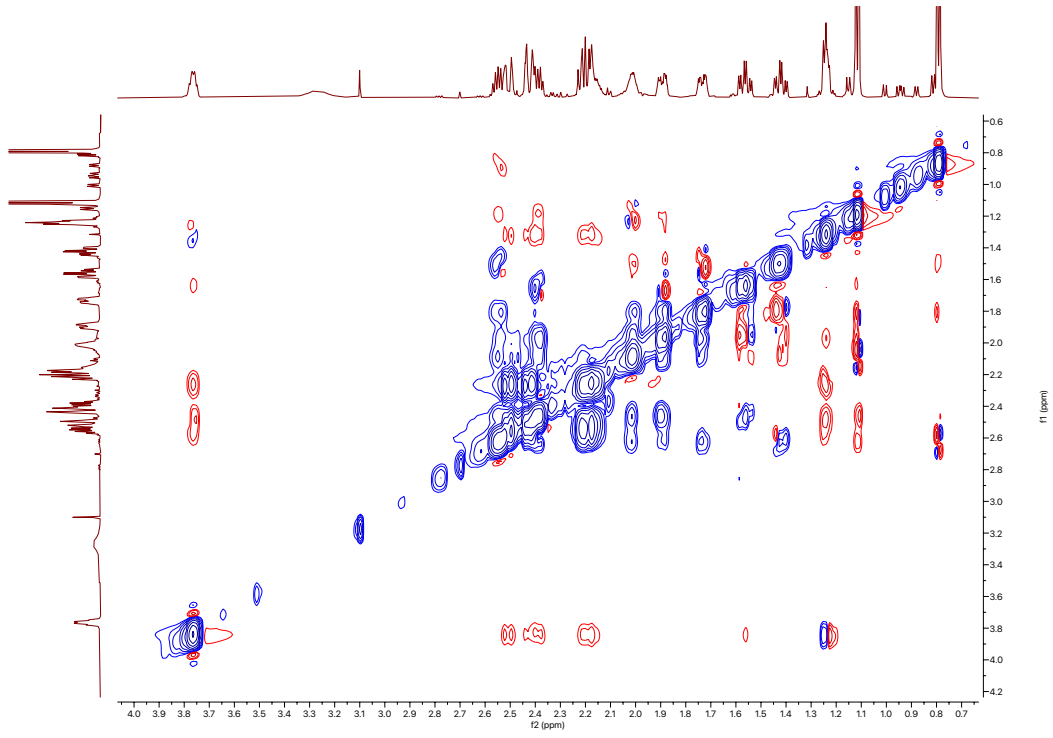

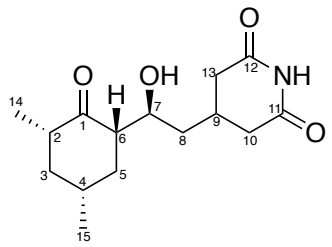

cycloheximide-2 (**29**)

Position	δ_C (type)	δ_H, multiplets (*J* in Hz)	COSY	HMBC	ROESY
1	214.7 (C)				
2	42.3 (CH)	2.46, m	3a, 3b, 14	3, 14	3a, 7, 14
3a	44.8 (CH_2)	1.00, m	2, 3b, 4	2, 4, 5, 14, 15	
3b	44.8 (CH_2)	1.96, ddt (12.7, 6.0, 3.5)	2, 3a, 4	2, 4, 5, 15	5a, 7, 14, 15
4	26.6 (CH)	2.21, m	3a, 3b, 5a, 5b, 15		
5a	36.7 (CH_2)	1.22, m	4, 5b, 6	3, 4, 6, 7, 15	3b, 15
5b	36.7 (CH_2)	2.24, m	4, 5a, 6	3, 4, 6, 15	6, 7
6	58.5 (CH)	2.09, ddd (9.3, 5.3, 1.9)	5a, 5b, 7	4, 5, 7, 8	5b, 7, 8a
7	66.0 (CH)	3.90, d (9.9)	6, 7-OH, 8		2, 3b, 5b, 6, 13b
7-OH		5.00, br s	7		
8a	40.5 (CH_2)	0.95, m	7, 9	6, 7, 9, 10, 13	
8b	40.5 (CH_2)	1.26, ddd (13.1, 10.1, 2.8)		8, 10, 13	6, 7, 8a
9	27.0 (CH)	2.25, m	8, 10a, 10b, 13a, 13b	8, 9, 11	
10a	38.7 (CH_2)	2.27, m	9, 10b	8, 9, 11	
10b	38.7 (CH_2)	2.47, m	9, 10a		
11	173.8 (C)			10, 11, 12, 13	
11-NH		10.65, br s			10a
12	173.9 (C)			8, 9, 12	
13a	37.0 (CH_2)	2.20, m	9, 13b	8, 9, 12	
13b	37.0 (CH_2)	2.60, m	9, 13a	2, 3	7, 8a, 8b
14	15.2 (CH_3)	0.85, d (6.4)	2	3, 4, 5	2, 3b, 4
15	21.0 (CH_3)	0.90, d (6.3)	4		3b, 4, 5a

^{1}H spectrum of cycloheximide-2 (**29**)

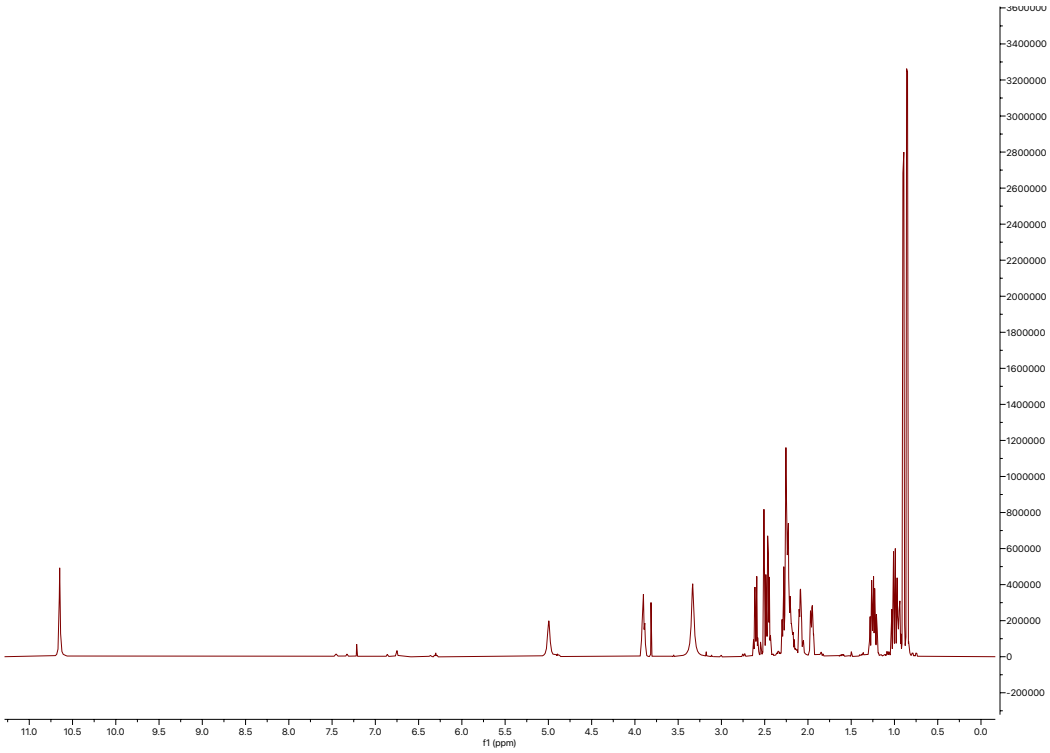

^{13}C spectrum of cycloheximide-2 (**29**)

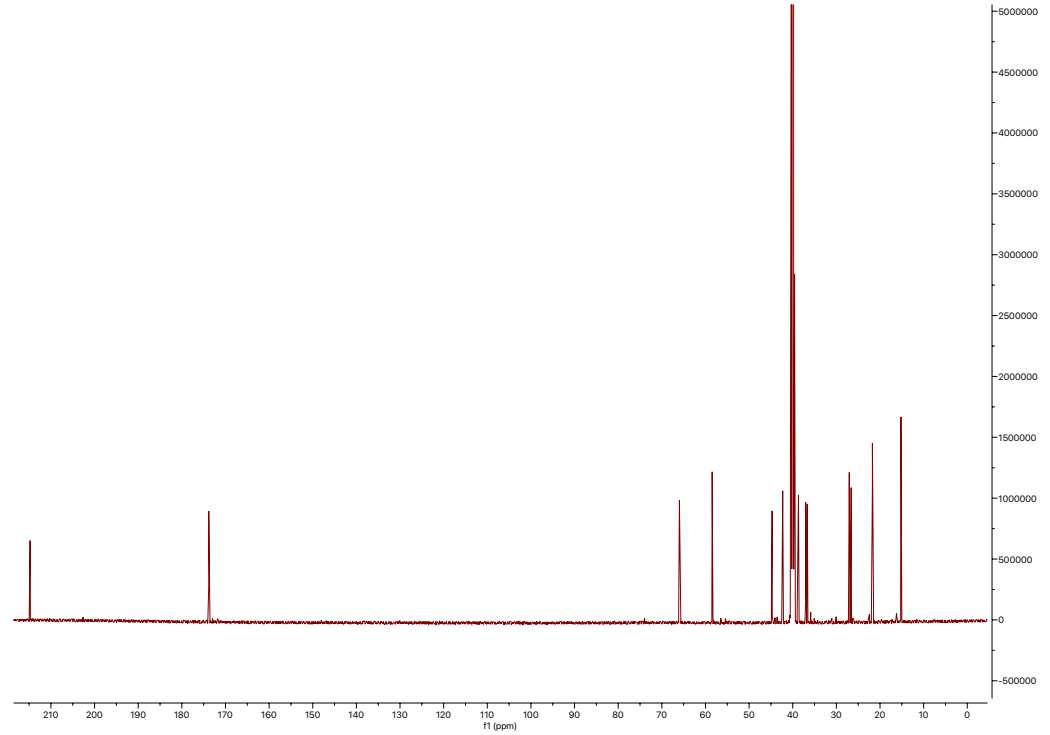

COSY spectrum of cycloheximide-2 (**29**)

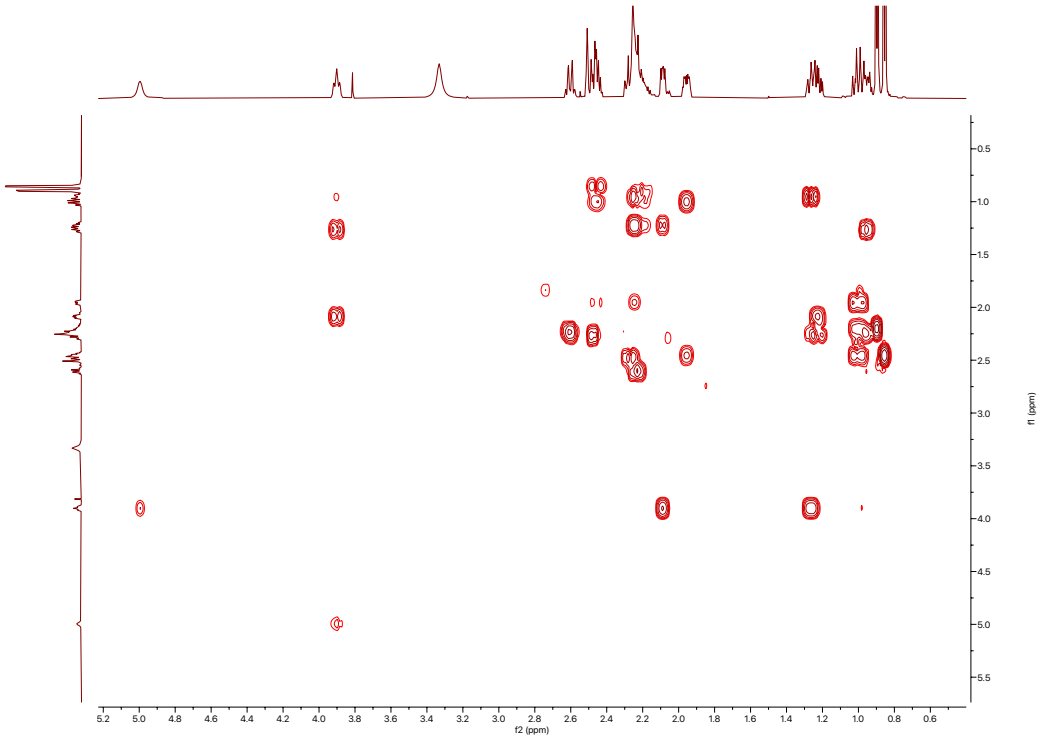

HSQC spectrum of cycloheximide-2 (**29**)

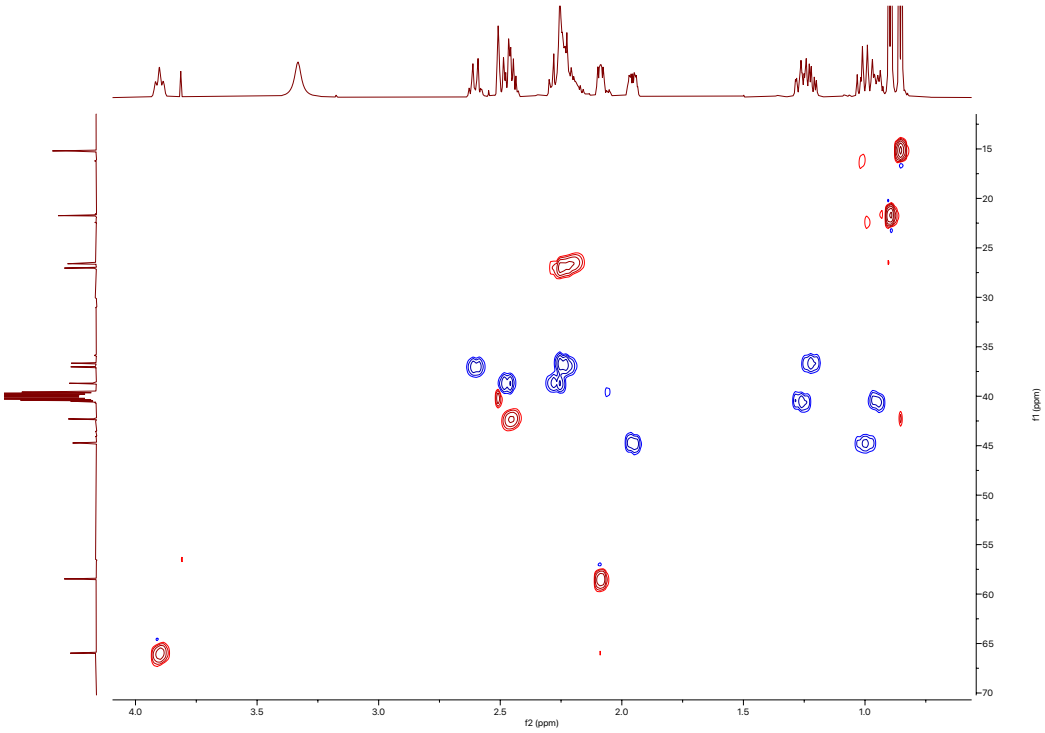

^{1}H-^{13}C HMBC spectrum of cycloheximide-2 (**29**)

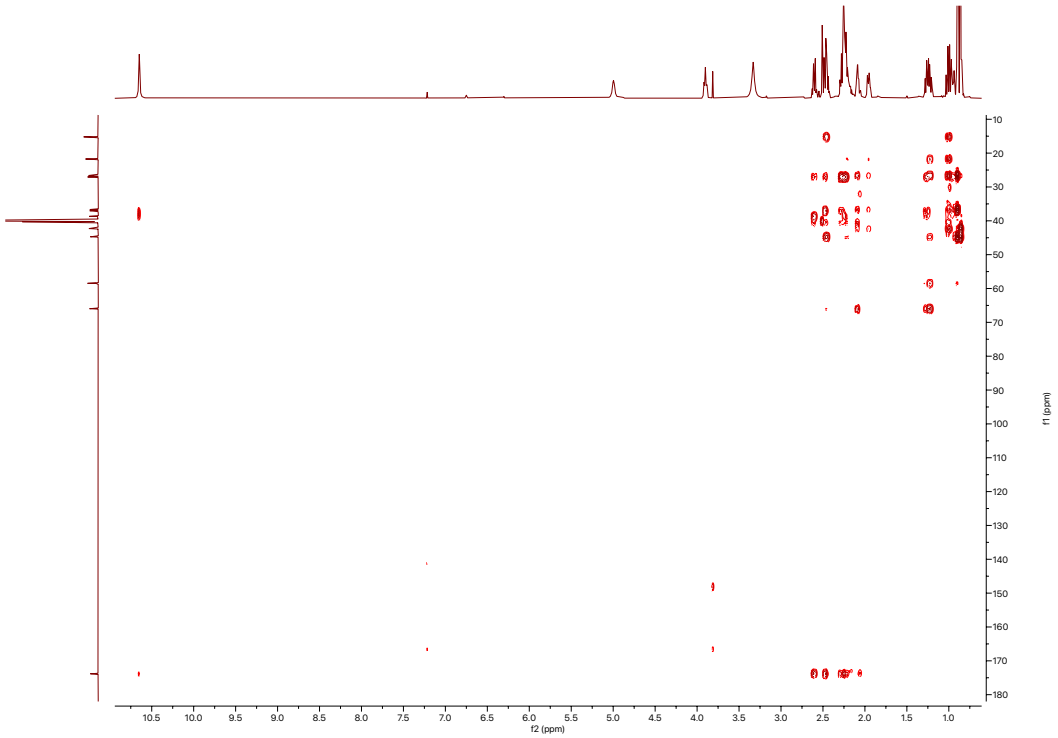

ROESY spectrum of cycloheximide-2 (**29**)

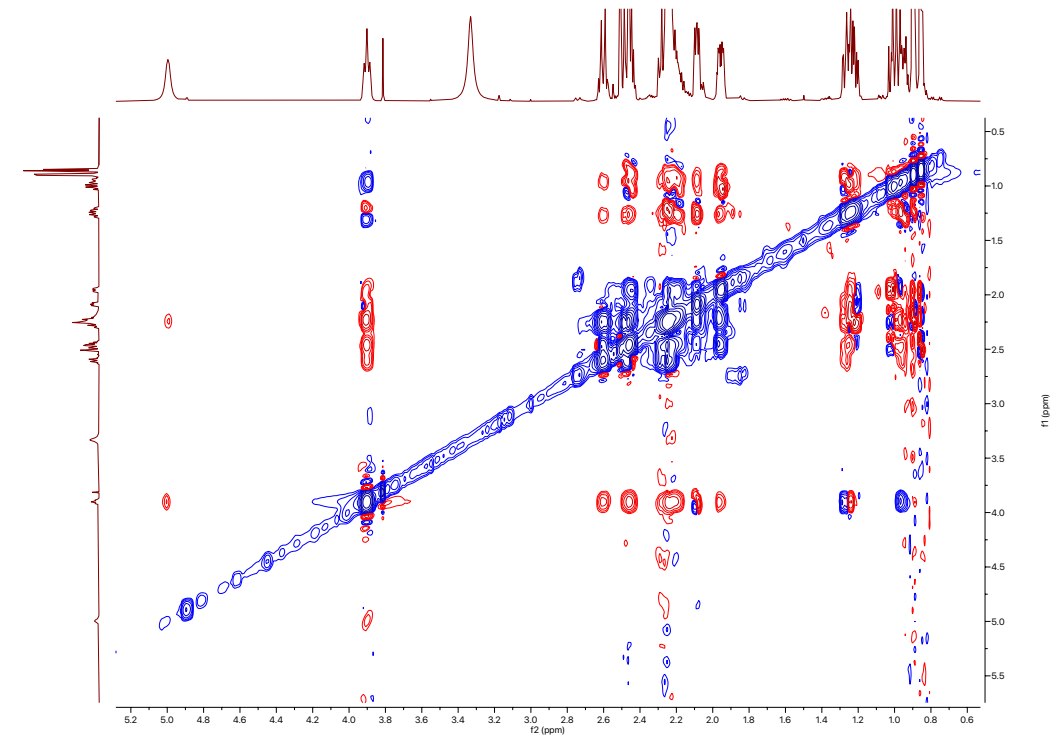

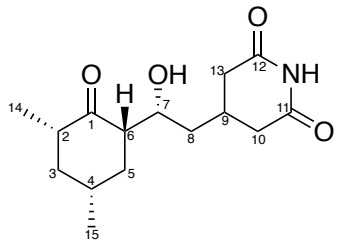

cycloheximide-3 (**30**)

Position	δ_C (type)	δ_H, multiplets (*J* in Hz)	COSY	HMBC	ROESY
1	213.4 (C)				
2	44.1 (CH)	2.51, m	3a, 3b, 14	3	3a, 14
3a	45.0 (CH_2)	1.01, m	2, 4	1, 2, 5	3b
3b	45.0 (CH_2)	1.96, m	2	2, 4, 5	3a
4	31.4 (CH)	2.00, m	5a, 15	2, 6	3a, 3b, 15
5a	36.7 (CH_2)	1.07, q (14.1)	4, 5b, 6	1, 3, 6, 7	5b
5b	36.7 (CH_2)	2.02, m	5a, 6	3, 4, 6	5a
6	55.4 (CH)	2.57, m	5a, 5b, 7	4, 5, 7	7, 8
7	65.9 (CH)	3.87, dt (8.7, 4.0)	6, 8	5, 6, 8	6, 8, 10a
7-OH		4.45, br s			
8	38.0 (CH_2)	1.29, m	7, 9	6, 7, 10	6, 7, 9
9	27.5 (CH)	2.25, m	8, 13b	8, 11, 12	7, 8
10a	38.9 (CH_2)	2.28, m	10b	9, 11	
10b	38.9 (CH_2)	2.52, m	10a	9, 11	8
11	173.8 (C)				
11-NH		10.65, br s		10, 11, 12, 13	
12	174.0 (C)				
13a	37.2 (CH_2)	2.26, m	9, 13b	9, 12	
13b	37.2 (CH_2)	2.58, m	9, 13b	9, 12	
14	14.8 (CH_3)	0.86, d (6.5)	2	2, 3	2, 3b
15	21.7 (CH_3)	0.94, d (6.2)	4	3, 4, 5	3b, 5b

^{1}H spectrum of cycloheximide-3 (**30**)

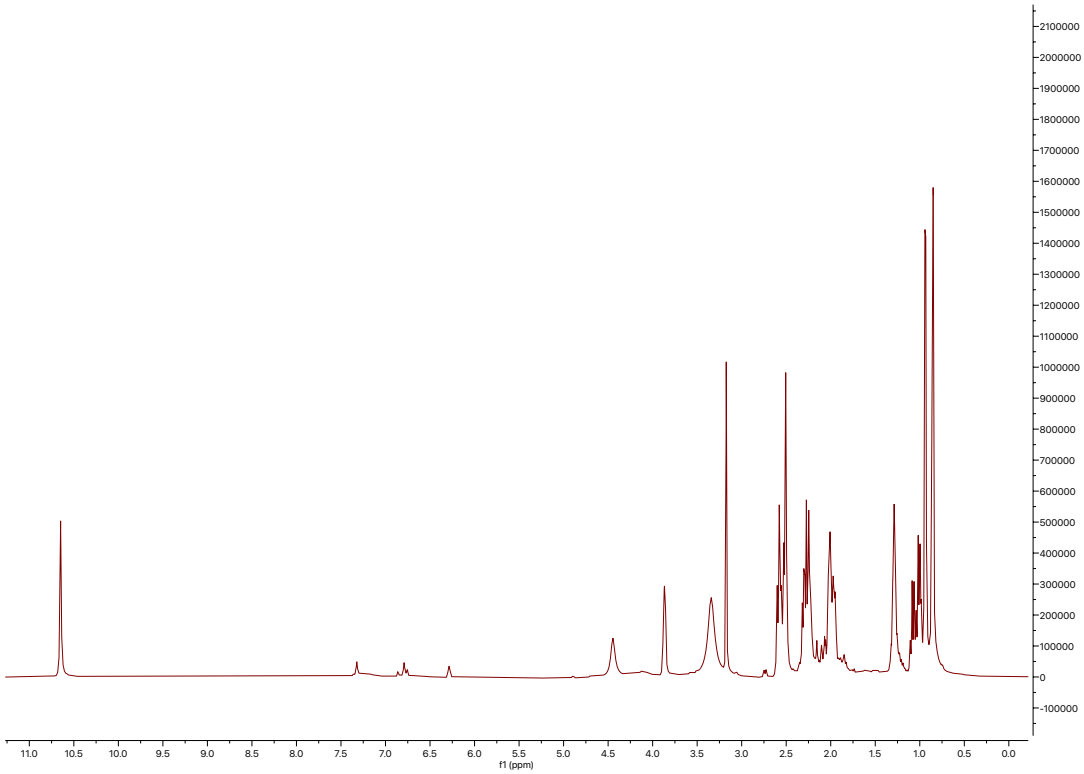

^{13}C spectrum of cycloheximide-3 (**30**)

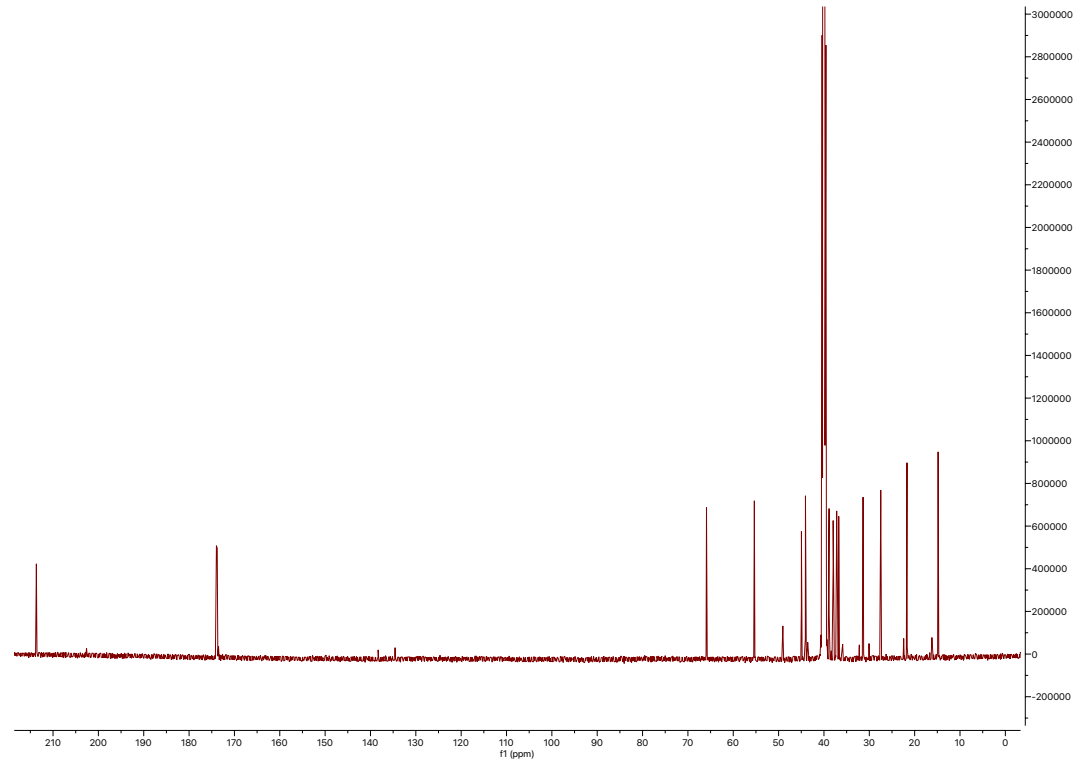

COSY spectrum of cycloheximide-3 (**30**)

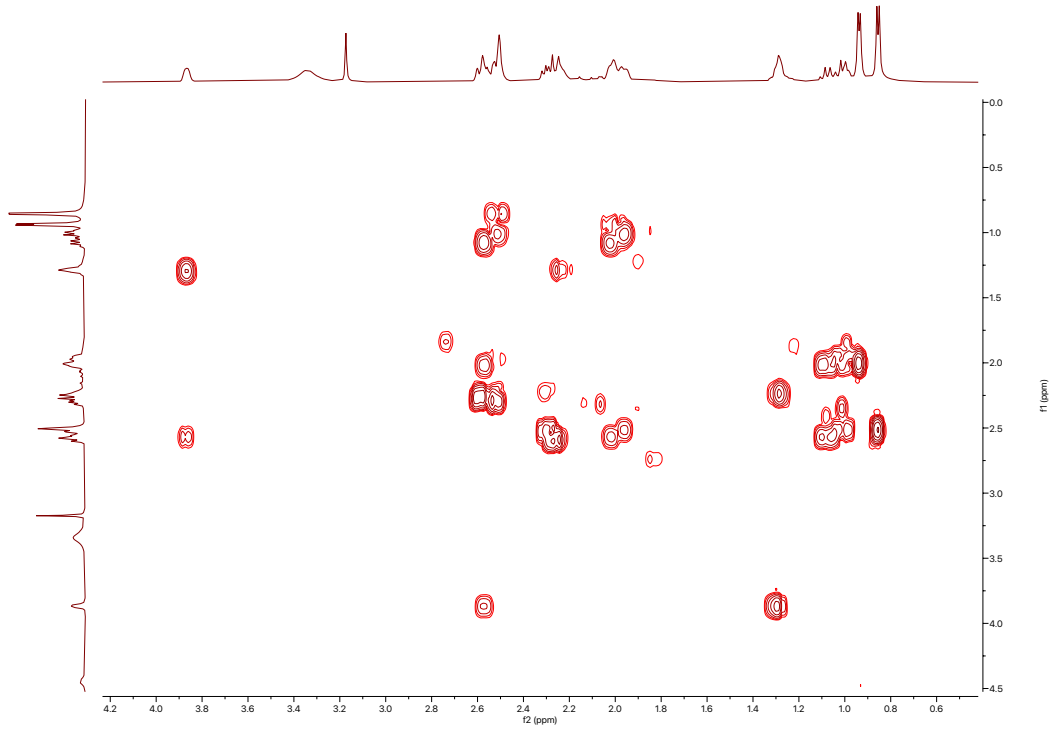

HSQC spectrum of cycloheximide-3 (**30**)

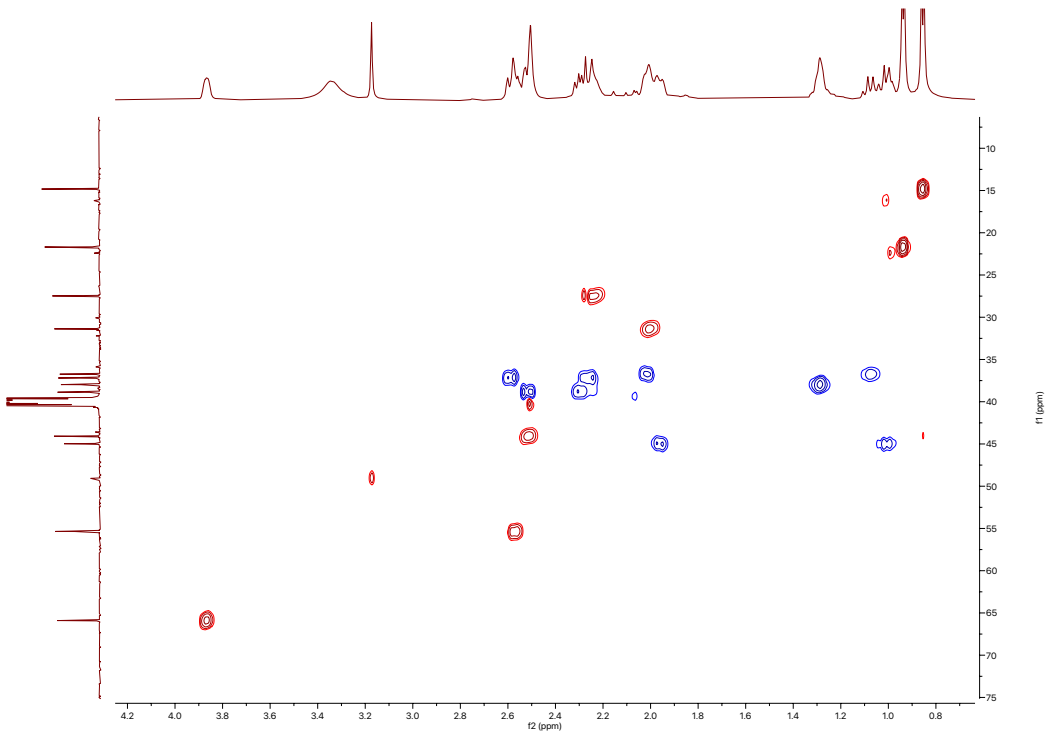

^{1}H-^{13}C HMBC spectrum of cycloheximide-3 (**30**)

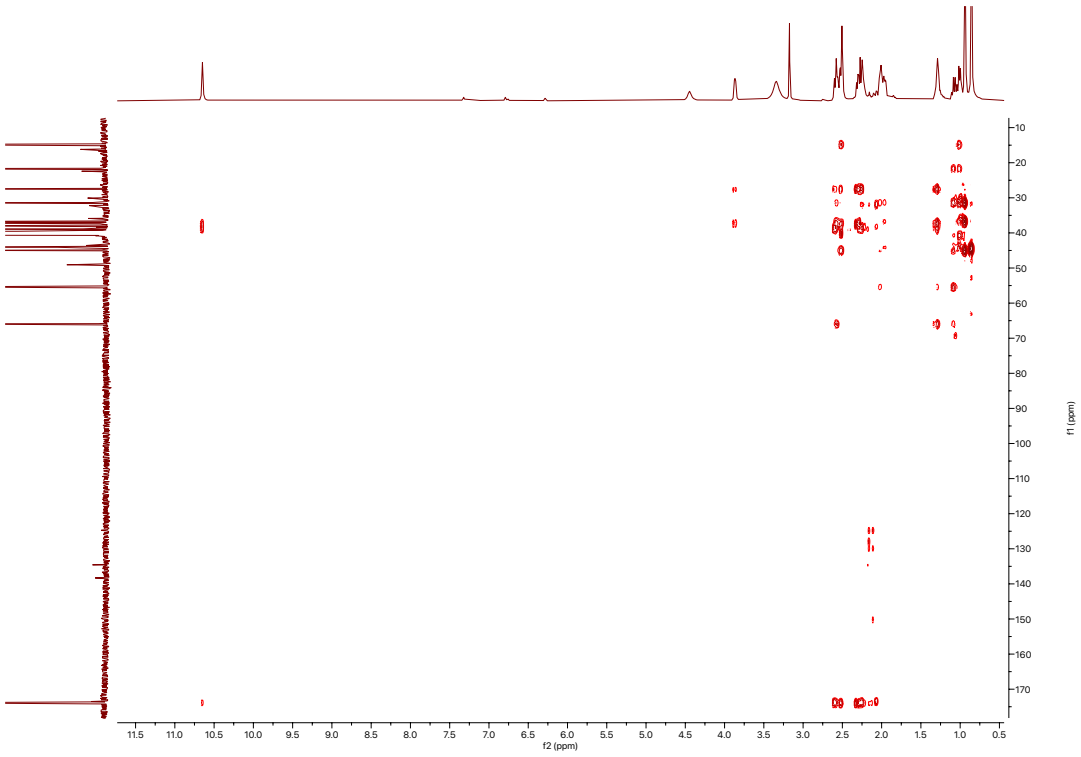

ROESY spectrum of cycloheximide-3 (**30**)

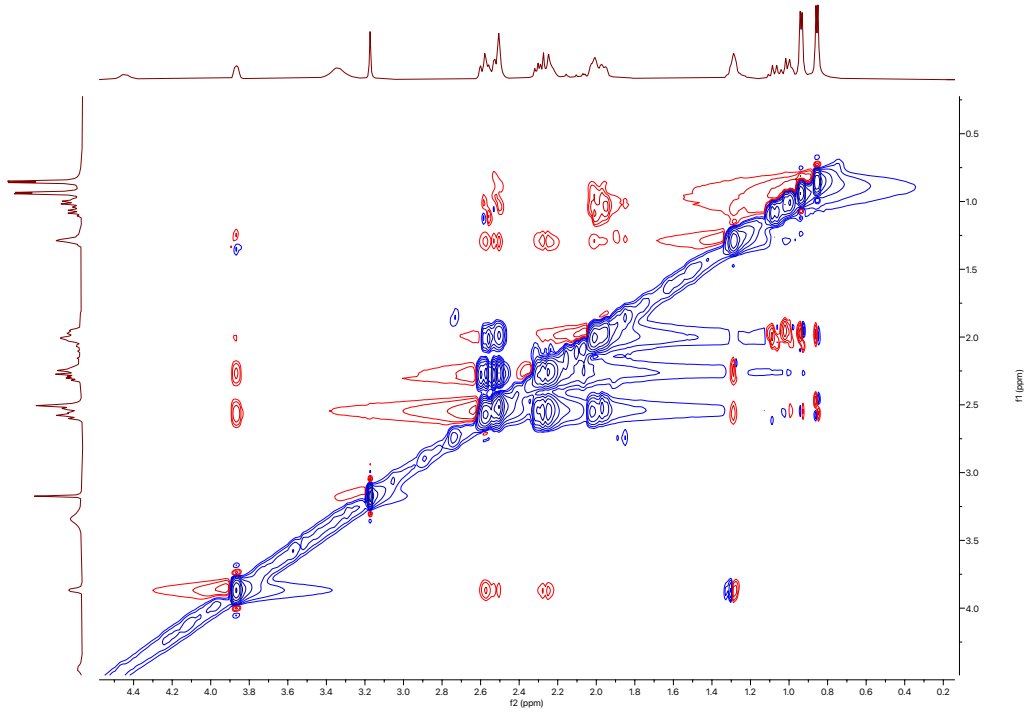

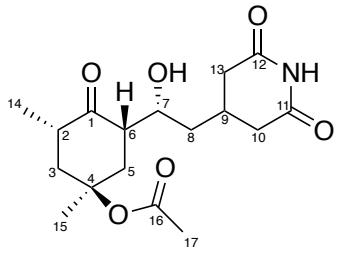

acetoxycycloheximide (**31**)

Position	δ_C (type)	δ_H, multiplets (*J* in Hz)	COSY	HMBC	ROESY
1	212.2 (C)				
2	39.8 (CH)	2.63, tq (12.9, 6.5)	3a, 3b, 14	3	
3a	45.0 (CH_2)	1.52, m	2, 3b, 4	2, 14	3b
3b	45.0 (CH_2)	2.52, m	2, 3a, 4	4, 5	3a
4	80.2 (C)				
5a	37.7 (CH_2)	1.59, m	4, 5b, 6	6, 7	5b, 7, 8
5b	37.7 (CH_2)	2.54, m	4, 5a, 6		5a, 7
6	50.8 (CH)	2.72, dt (14.0, 4.9)	5a, 5b, 7	5, 7	7, 17
7	65.6 (CH)	3.92, dt (9.8, 3.4)	6, 8	5, 8	5a, 5b, 6, 8, 13a
7-OH		4.51, br s			
8	37.8 (CH_2)	1.28, m	7, 9	7, 9, 10	5a, 6, 7, 10a, 13b,
9	27.5 (CH)	2.23, m	8, 10a, 10b, 13a, 13b	12, 13	
10a	38.8 (CH_2)	2.29, m	9, 10b	9, 10, 12, 13	8
10b	38.8 (CH_2)	2.52, m	9, 10a	9, 10, 12, 13	
11	173.8 (C)				
11-NH		10.65, br s		10, 12, 13	
12	173.9 (C)				
13a	37.2 (CH_2)	2.26, m	9, 13b	8, 9, 10, 12	7
13b	37.2 (CH_2)	2.58, m	9, 13a	8, 9, 10, 12	8
14	14.3 (CH_3)	0.86, d (6.6)	2	2, 3	2, 3a, 6
15	25.1 (CH_3)	1.50, s		3, 5	
16	170.4 (C)				
17	22.5 (CH_3)	2.05, s		16	6, 15

^{1}H spectrum of acetoxycycloheximide (**31**)

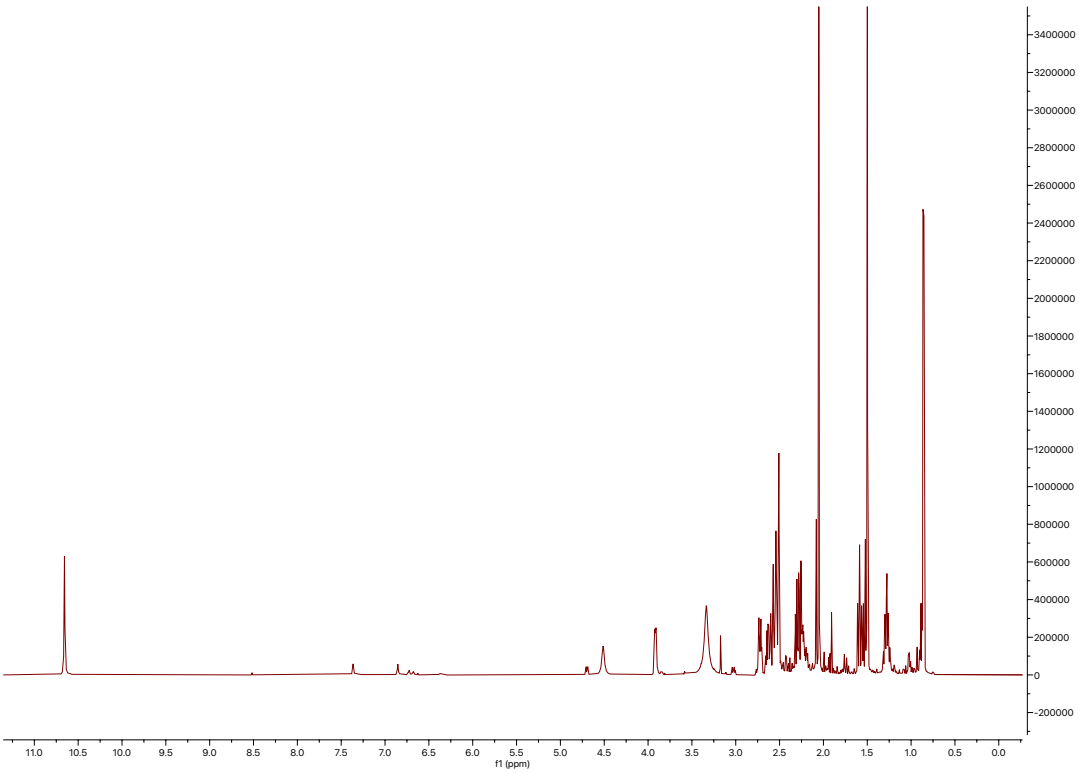

^{13}C spectrum of acetoxycycloheximide (**31**)

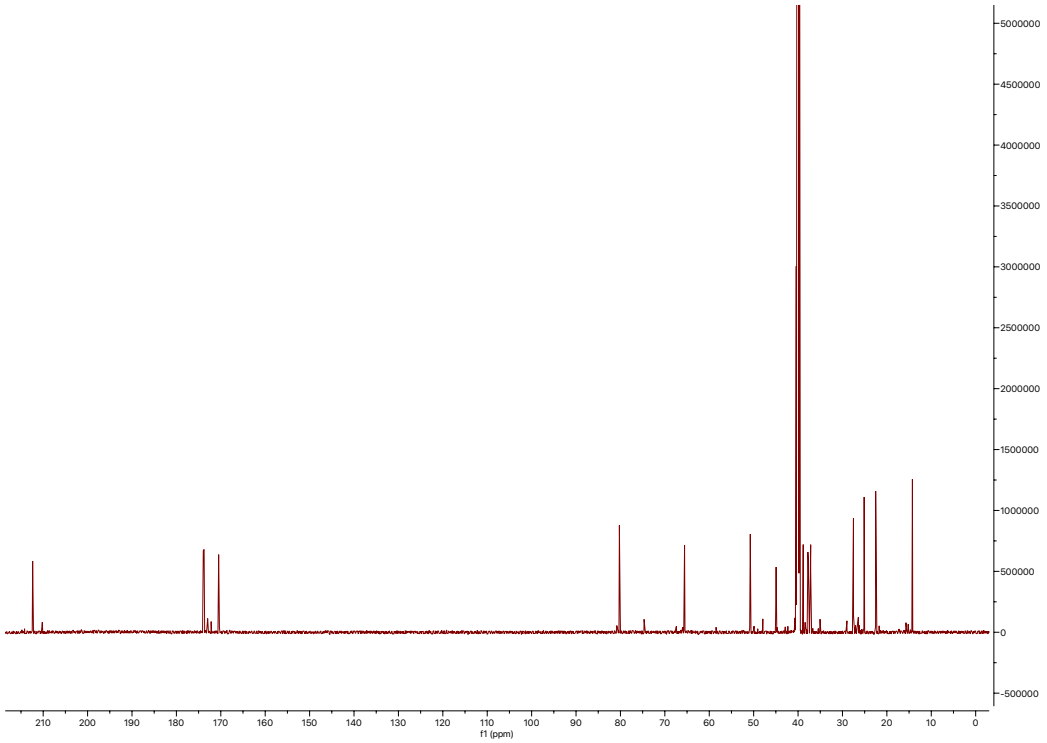

COSY spectrum of acetoxycycloheximide (**31**)

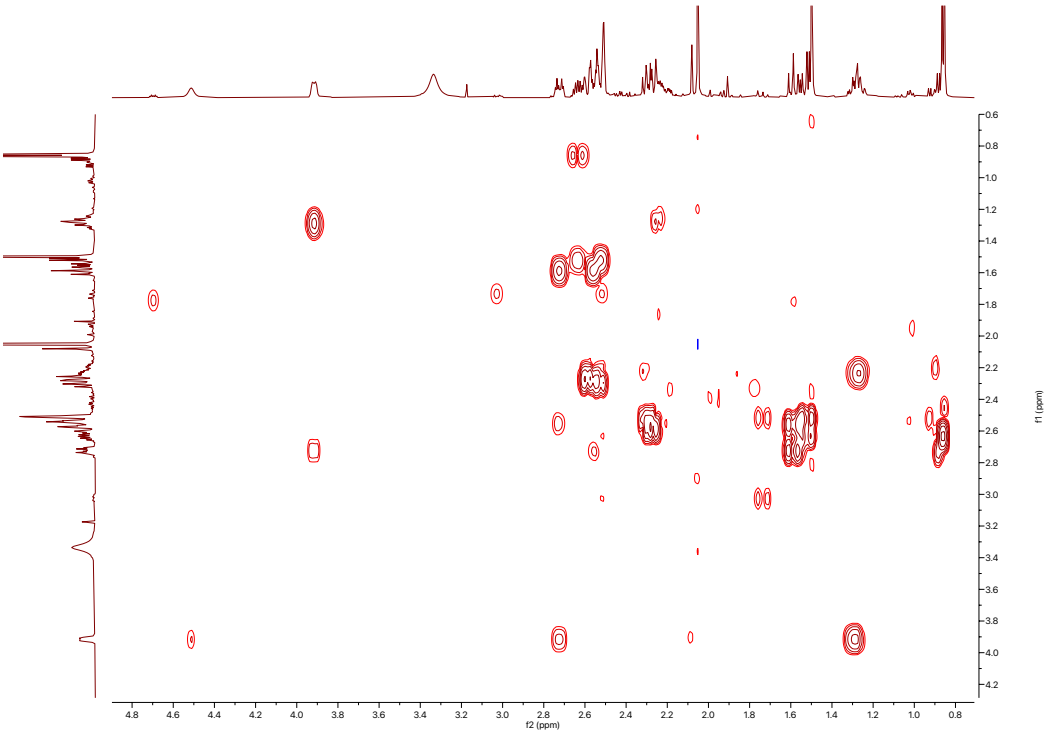

HSQC spectrum of acetoxycycloheximide (**31**)

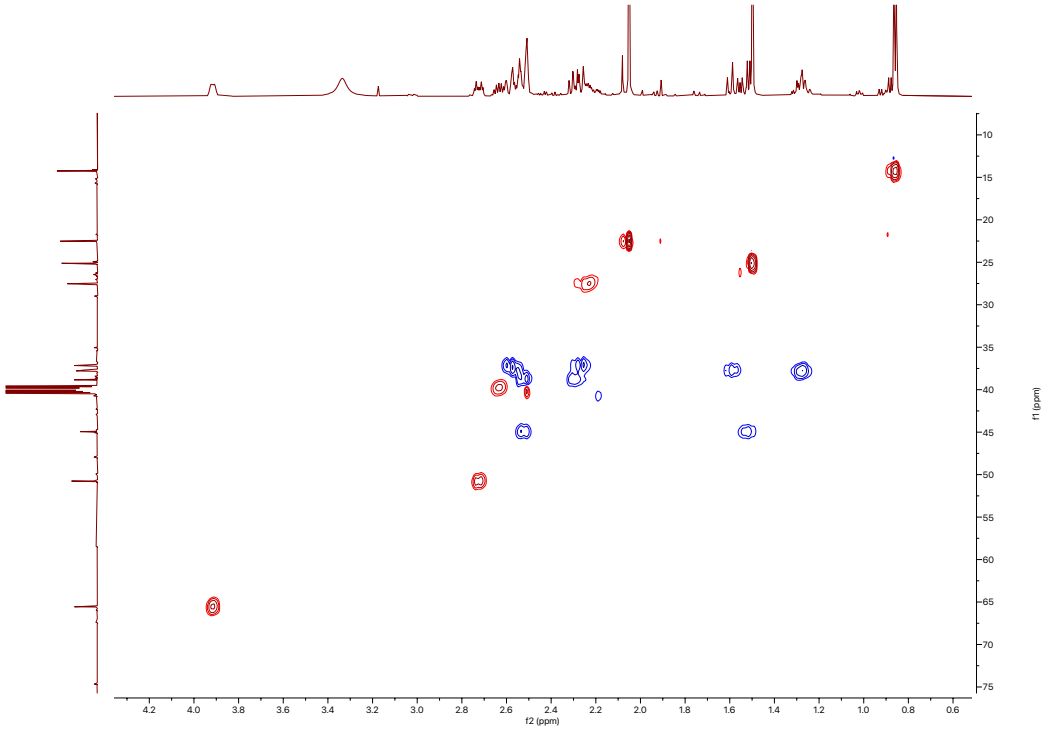

^{1}H-^{13}C HMBC spectrum of acetoxycycloheximide (**31**)

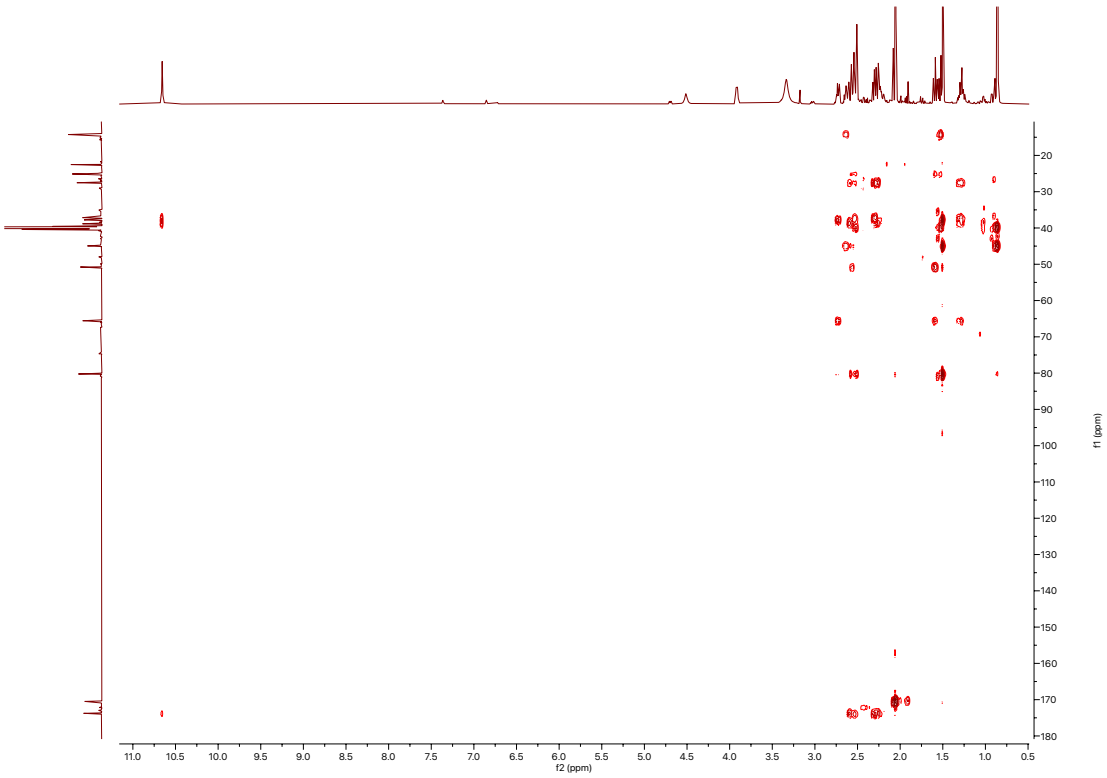

ROESY spectrum of acetoxycycloheximide (**31**)

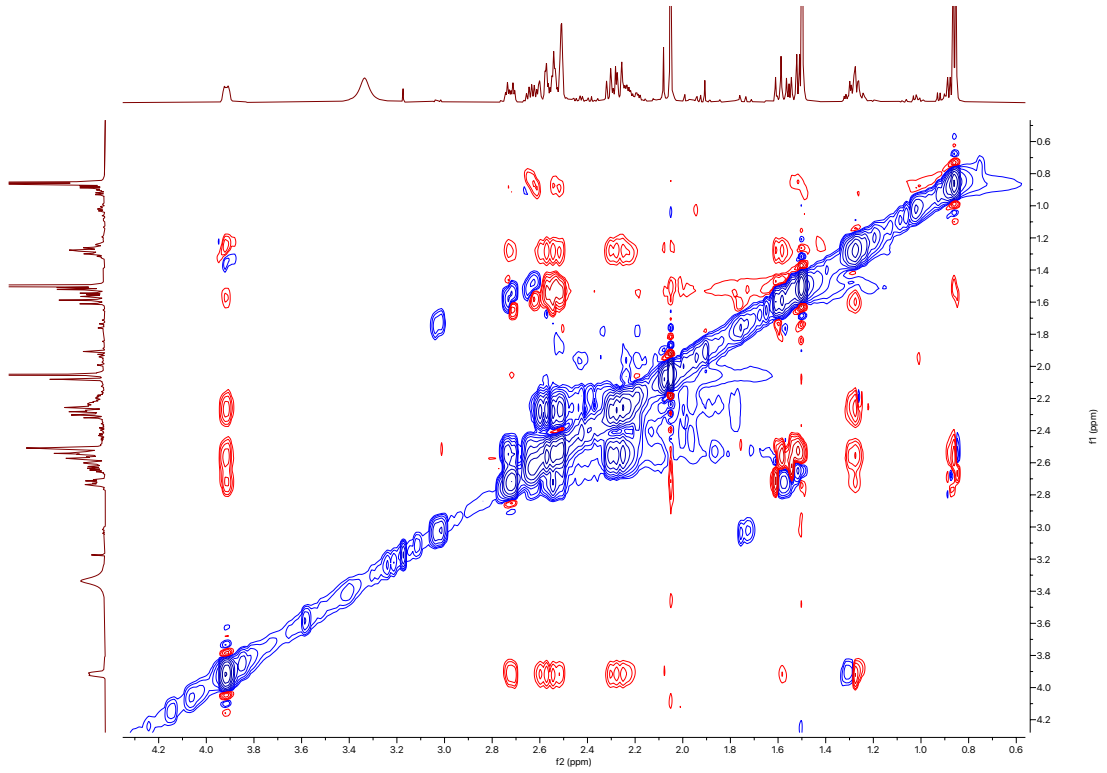

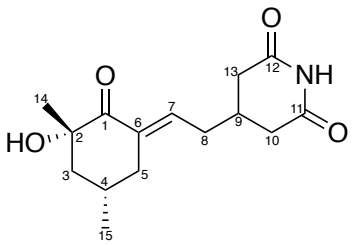

dipteronine D (**32**)

Position	δ_C (type)	δ_H, multiplets (*J* in Hz)	COSY	HMBC	ROESY
1	200.6 (C)				
2	72.4 (C)				
2-OH		5.24, br s		1, 2, 3	
3a	46.7 (CH_2)	1.45, t (13.0)	3b, 4	4, 5	14, 15
3b	46.7 (CH_2)	1.85, t (13.0)	3a, 4	4, 5	14, 15
4	25.1 (CH)	2.11, m	3a, 5a, 15		
5a	35.6 (CH_2)	1.81, dt (15.5, 3.6)	4, 5b	4	3a, 5b, 9
5b	35.6 (CH_2)	2.71, dt (15.5, 3.6)	4, 5a		3a, 5a, 9
6	138.0 (C)				
7	134.7 (CH)	6.25, dt (7.7, 2.6)	8a, 8b	1, 5, 8	8a, 8b, 10a, 10b
8a	32.5 (CH_2)	2.14, m	7, 9	6, 7, 9, 10	5b
8b	32.5 (CH_2)	2.18, m	7, 9	6, 7, 9, 10	5b
9	30.0 (CH)	2.24, m			5a, 5b
10a	37.6 (CH_2)	2.28, m	10b	9, 11, 13	
10b	37.6 (CH_2)	2.50, m	10a	9, 11, 13	
11	173.5 (C)				
11-NH		10.72, br s		10, 13	
12	173.5 (C)				
13a	37.4 (CH_2)	2.30, m		9, 12	
13b	37.4 (CH_2)	2.30, m		9, 12	
14	25.4 (CH_3)	1.17, s		1, 2, 3	3a, 3b, 4
15	22.2 (CH_3)	0.94, d (6.6)	4	3, 5	3a, 3b, 5a, 5b

^{1}H spectrum of dipteronine D (**32**)

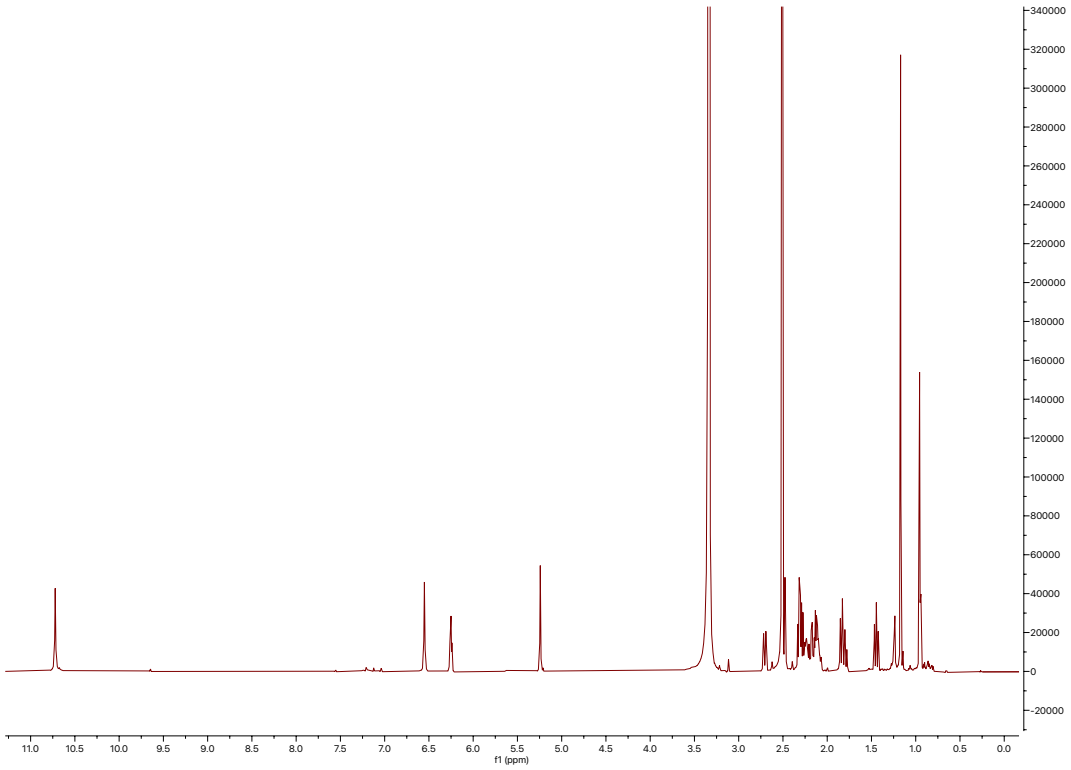

^{13}C spectrum of dipteronine D (**32**)

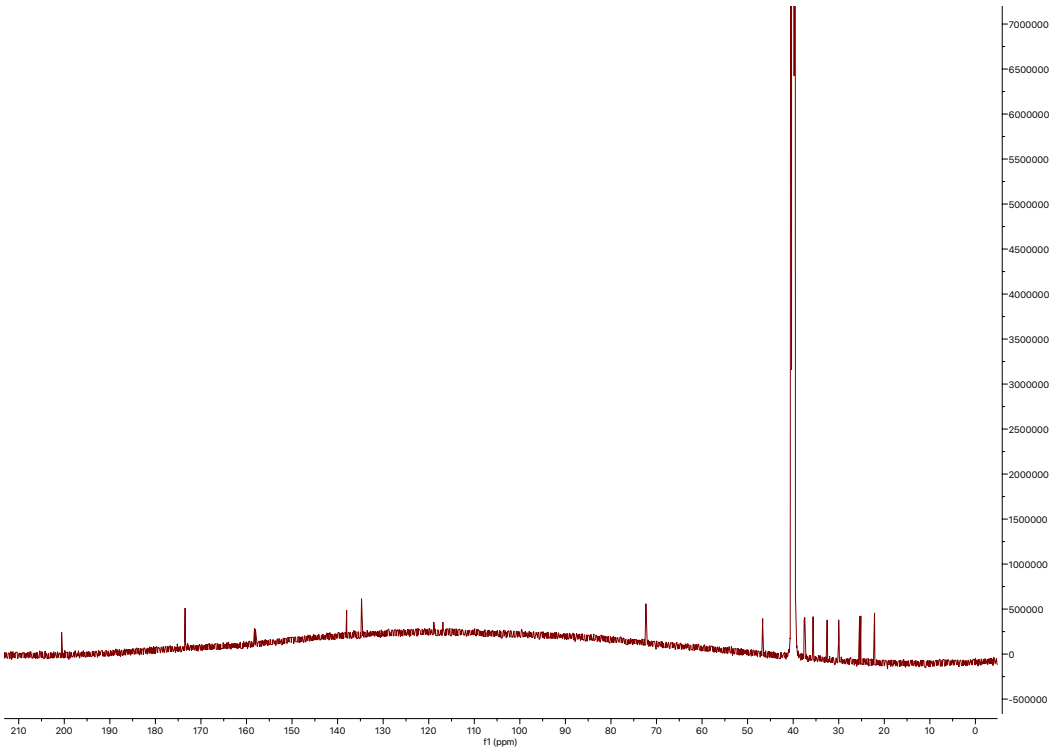

COSY spectrum of dipteronine D (**32**)

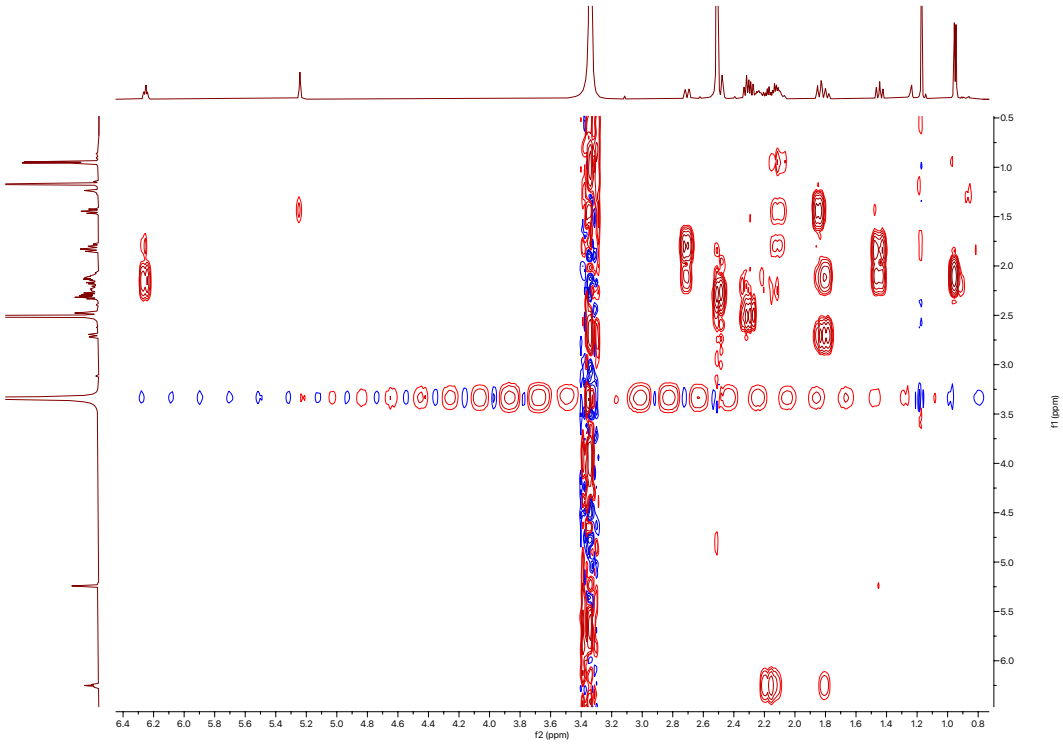

HSQC spectrum of dipteronine D (**32**)

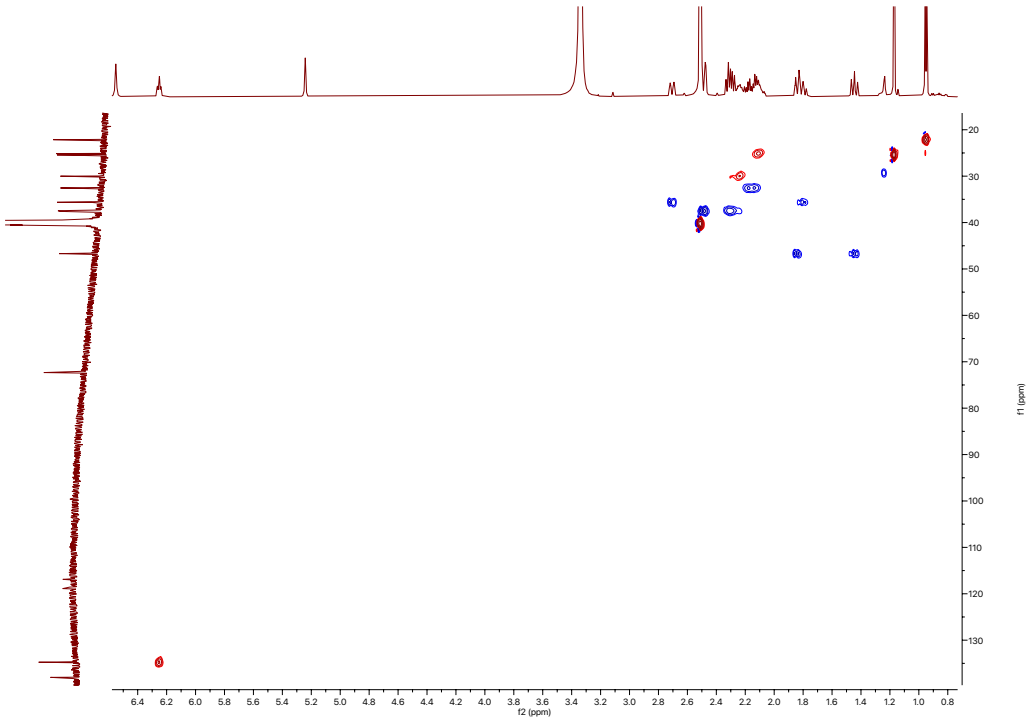

^{1}H-^{13}C HMBC spectrum of dipteronine D (**32**)

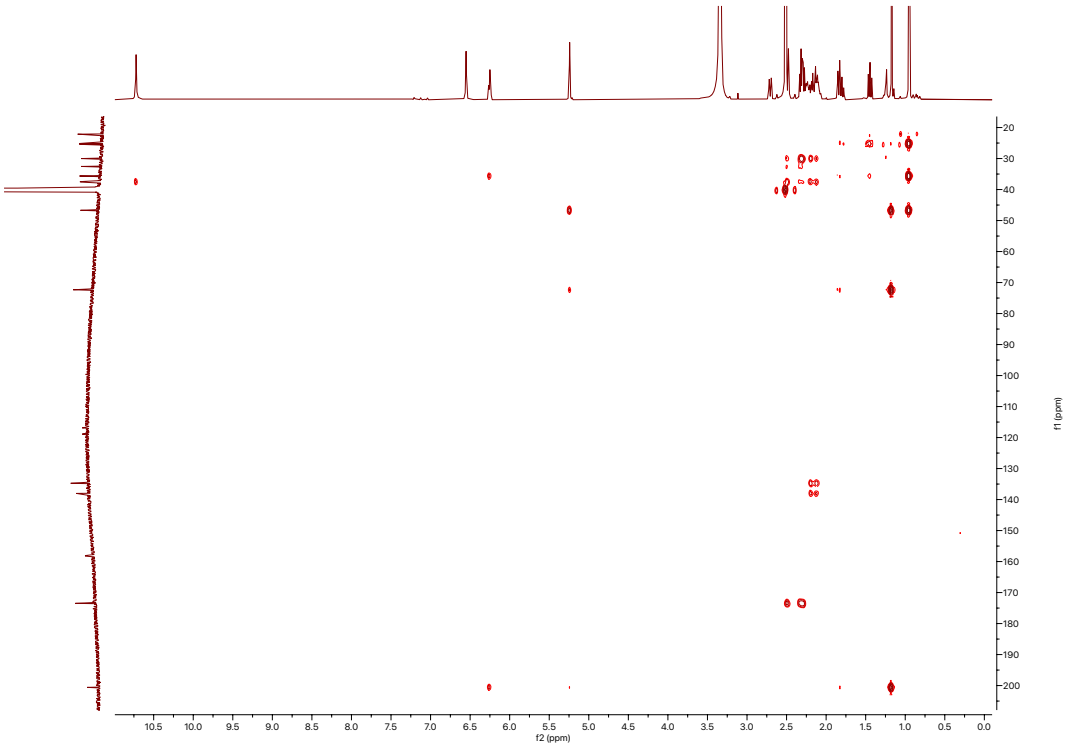

ROESY spectrum of dipteronine D (**32**)

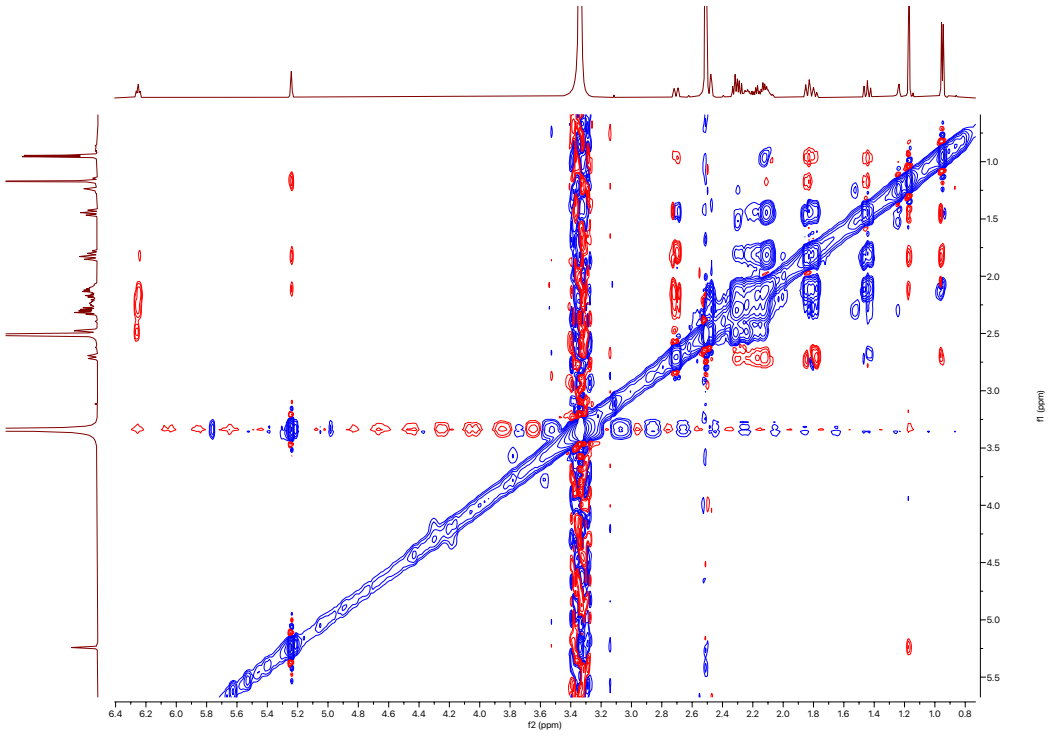

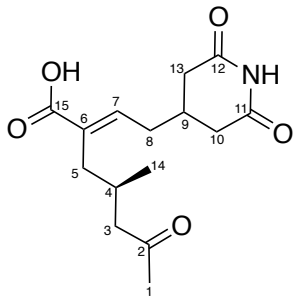

cycloheximide acid A (**33**)

Position	δ_C (type)	δ_H, multiplets (*J* in Hz)	COSY	HMBC	ROESY
1	30.6 (CH_3)	2.06, s		2, 3	
2	208.7 (C)				
3a	50.3 (CH_2)	2.26, m	3b, 4	1, 2	
3b	50.3 (CH_2)	2.33, m	3a, 4	1, 2	
4	29.3 (CH)	2.07, m	3a, 3b, 5a, 5b, 14		
5a	33.4 (CH_2)	2.13, m	4, 5b	15	
5b	33.4 (CH_2)	2.16, m	4, 5a		
6	133.3 (C)				
7	139.9 (CH)	6.68, t (7.0)	8a, 8b	8, 9, 15	
8	33.4 (CH_2)	2.24, m	7, 8b, 9	6, 7	14
9	30.1 (CH)	2.24, m	8a, 8b, 10a ,10b		
10a	37.6 (CH_2)	2.31, m	9, 10b	11	
10b	37.6 (CH_2)	2.49, m	9, 10a	11	
11	173.5 (C)				
11-NH		10.72, br s			
12	173.5 (C)				
13a	37.6 (CH_2)	2.31, m	9, 13b	12	
13b	37.6 (CH_2)	2.49, m	9, 13a	12	
14	19.9 (CH_3)	0.78, d (6.4)	4	3, 4, 5	8
15	169.0 (C)				
15-COOH		12.28, br s			

^{1}H spectrum of cycloheximide acid A (**33**)

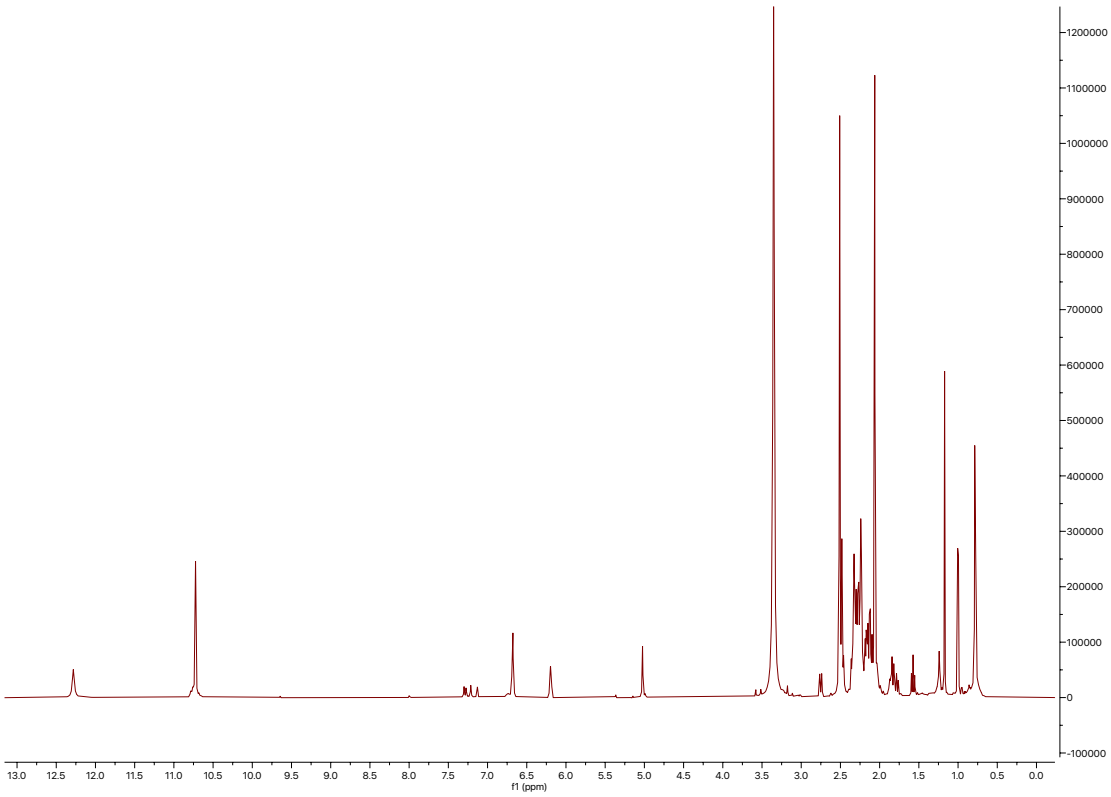

^{13}C spectrum of cycloheximide acid A (**33**)

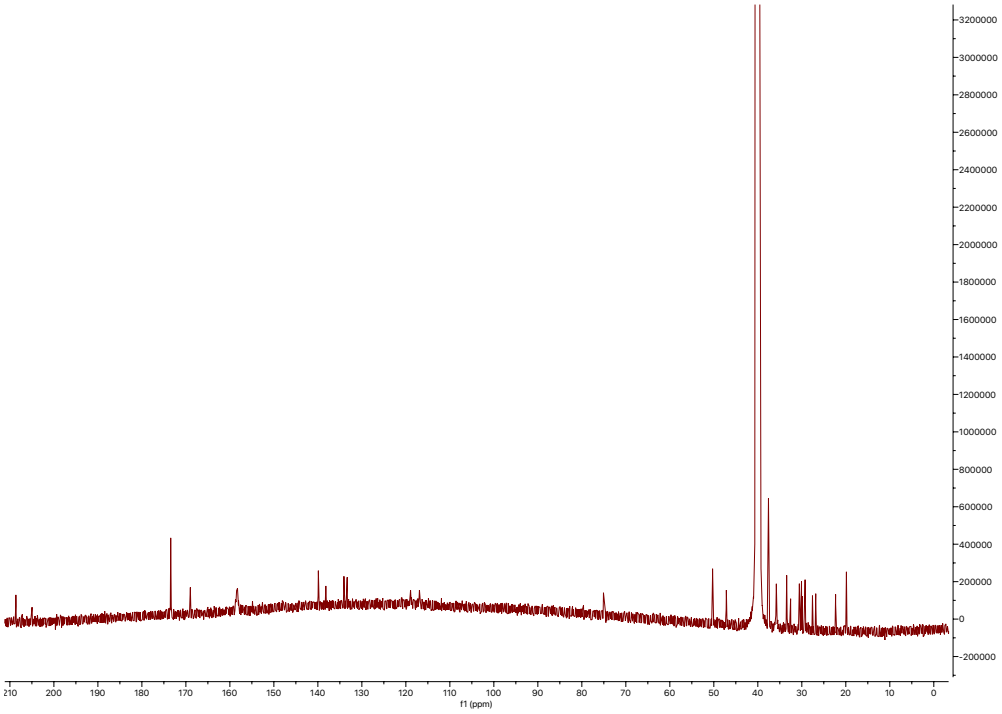

COSY spectrum of cycloheximide acid A (**33**)

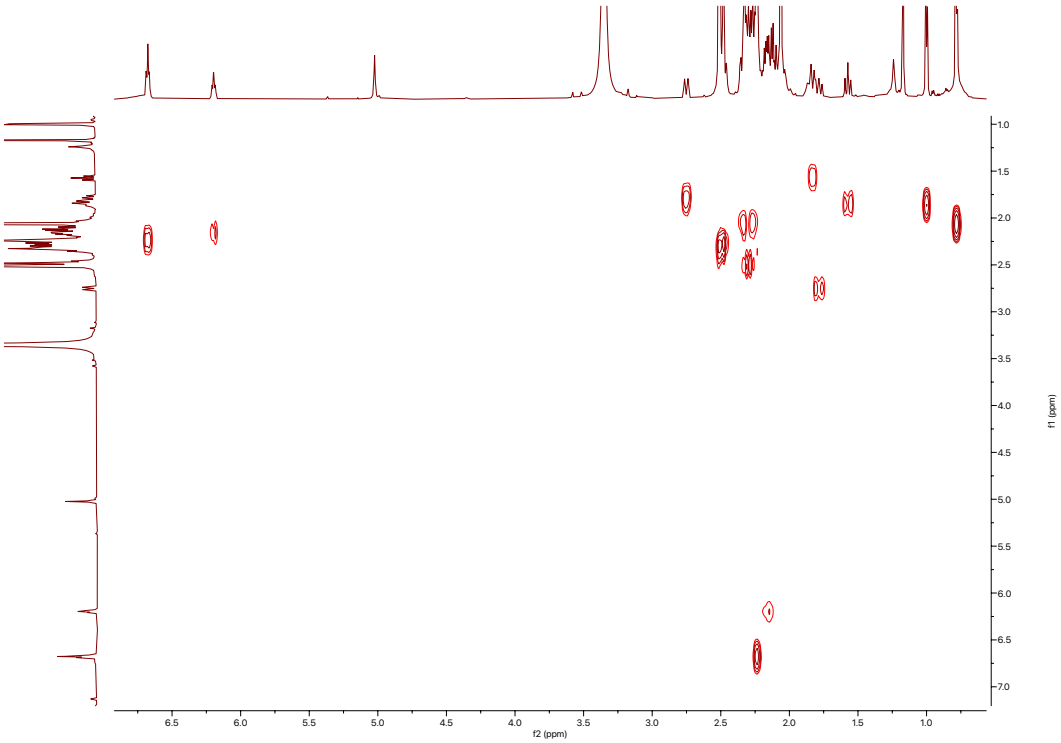

HSQC spectrum of cycloheximide acid A (**33**)

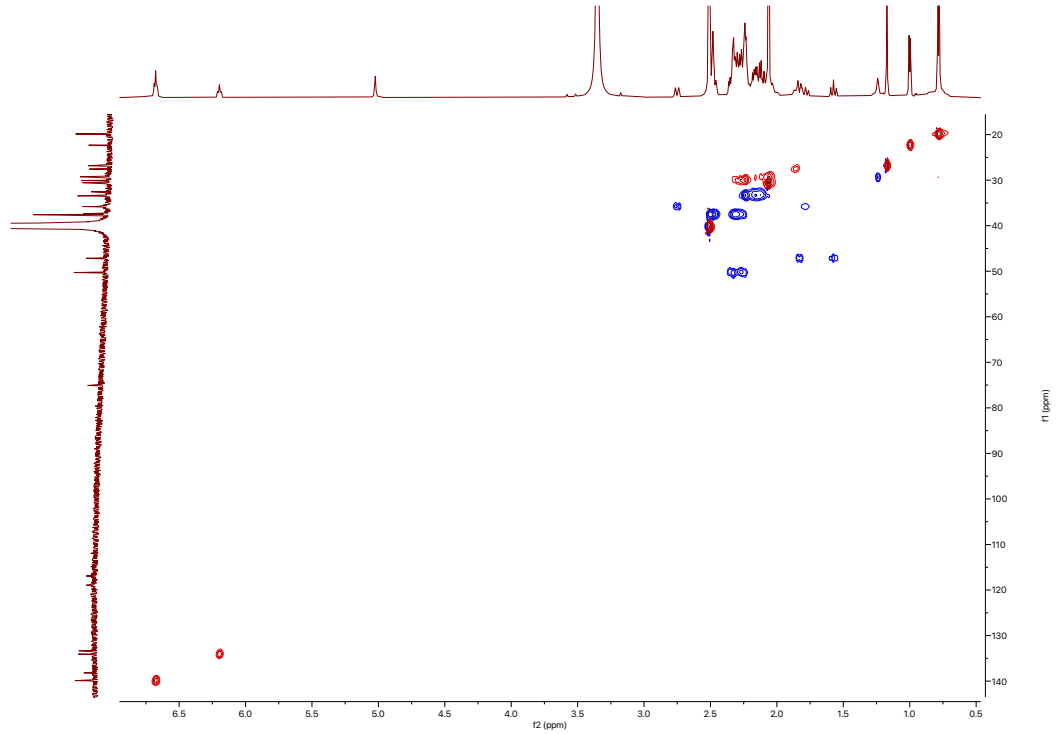

^{1}H-^{13}C HMBC spectrum of cycloheximide acid A (**33**)

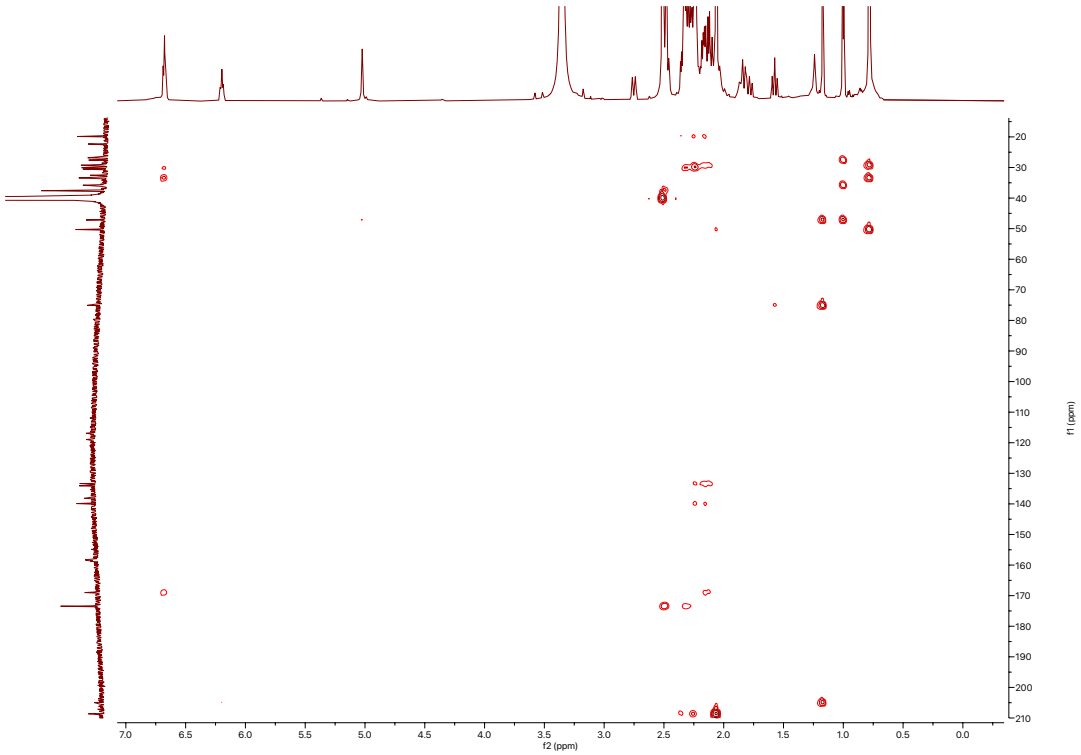

ROESY spectrum of cycloheximide acid A (**33**)

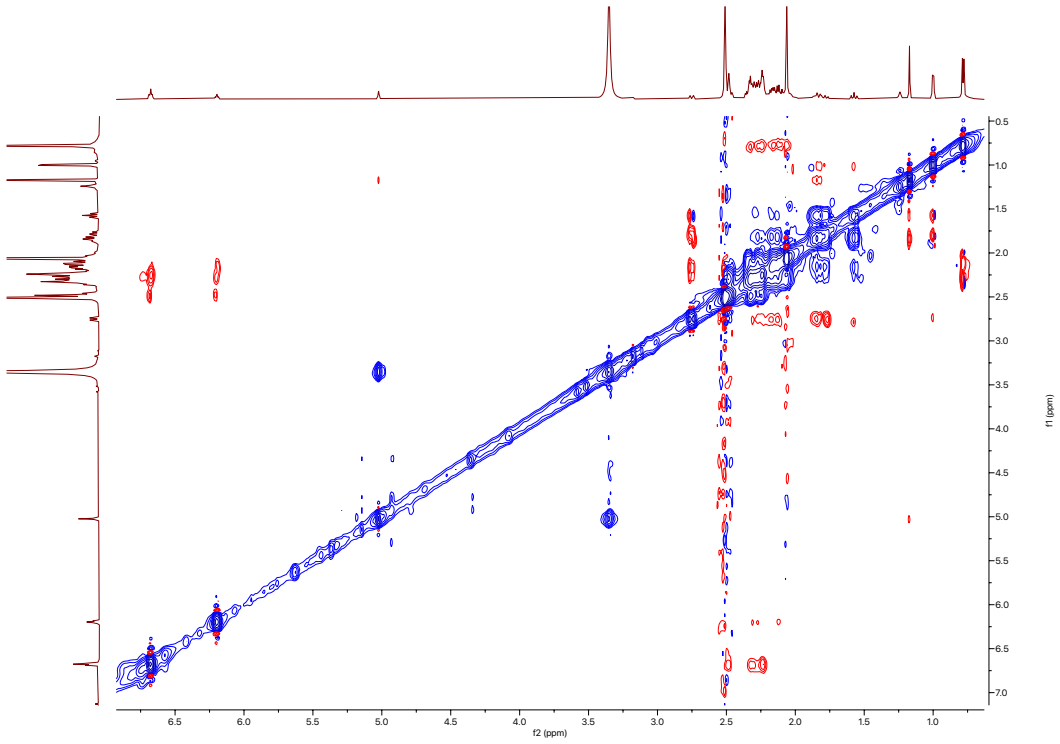

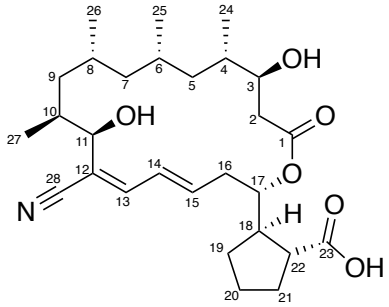

borrelidin (**34**)

Position	δ_C (type)	δ_H, multiplets (*J* in Hz)	COSY	HMBC	ROESY
1	171.5 (C)				
2a	37.4 (CH_2)	2.08, dd (15.5, 9.7)	2b, 3	1, 3, 4	
2b	37.4 (CH_2)	2.26, dd (15.6, 3.5)	2a, 3		
3	70.8 (CH)	3.76, dq (10.3, 3.5)	2a, 2b, 3-OH, 4	5	2a, 2b, 4, 6
3-OH		4.47, d (4.2)	3	2, 3, 4	2a, 3, 4
4	35.8 (CH)	1.74, m	3, 5a, 5b, 24		5a, 5b, 25
5a	43.4 (CH_2)	0.88, ddd (14.1, 10.7, 3.1)	4, 5b, 6		
5b	43.4 (CH_2)	1.12, ddd (14.0, 7.0, 4.4)	4, 5a, 6	6, 24, 25	
6	27.3 (CH)	1.83, m	5a, 5b, 7a, 7b, 25		2a, 3, 5b, 25
7a	48.2 (CH_2)	0.96, m	6, 7b, 8	8, 25, 26	
7b	48.2 (CH_2)	1.00, m	6, 7a, 8	8, 25, 26	
8	26.5 (CH)	1.56, m	7a, 7b, 9a, 9b, 26		7a, 9b, 25
9a	37.7 (CH_2)	0.61, ddd (13.8, 11.0, 3.2)	8, 9b, 10	8, 10, 27	
9b	37.7 (CH_2)	1.12, ddd (14.0, 7.0, 4.4)	8, 9a, 10	7, 8, 10, 27	
10	35.0 (CH)	1.63, m	9a, 9b, 11, 27	11	7a, 9a, 26
11	71.1 (CH)	4.07, dd (9.7, 3.8)	10, 11-OH	10, 13, 28	7a, 9b, 10, 11-OH, 14
11-OH		5.48, d (4.1)	11	10, 12	7a, 10, 11
12	117.0 (C)				
13	143.7 (CH)	6.97, d (11.2)	14	11, 12, 14, 15, 28	15
14	127.9 (CH)	6.47, dd (14.7, 11.3)	13, 15	12, 13, 15, 16	
15	139.3 (CH)	6.32, ddd (14.8, 10.5, 4.3)	14, 16a, 16b	13, 14, 16	13
16a	36.0 (CH_2)	2.38, ddd (14.9, 10.4, 4.2)	15, 16b, 17	14, 15, 17	
16b	36.0 (CH_2)	2.50, m	15, 16a, 17	14, 15, 17	
17	75.4 (CH)	4.89, dt (10.7, 3.6)	16a, 16b	15	16a, 18, 19a, 19b, 20, 22
18	46.0 (CH)	2.51, m	19a, 19b, 22	16, 19, 22, 23	15, 17, 19b
19a	29.3 (CH_2)	1.37, dq (12.2, 8.5)	18, 19b, 20	17, 18, 20, 21	
19b	29.3 (CH_2)	1.88, m	18, 19a, 20	17, 18, 20, 21, 22	
20	25.3 (CH_2)	1.66, m	19a, 19b, 21a, 21b	18, 19, 20, 21	
21a	31.3 (CH_2)	1.69, m	20, 21b, 22	18, 19, 20, 22, 23	
21b	31.3 (CH_2)	1.90, m	20, 21a, 22	18, 19, 20, 22, 23	
22	48.5 (CH)	2.31, q (7.9)	18, 21a, 21b	17, 18, 19, 20, 21, 23	17
23	177.8 (C)				
23-COOH		12.03, s			
24	18.7 (CH_3)	0.76, d (6.3)	4	3, 4	
25	18.8 (CH_3)	0.78, d (6.3)	6	5, 6, 7	
26	20.9 (CH_3)	0.78, d, (6.3)	8	7, 8, 9	
27	15.5 (CH_3)	0.94, d (6.3)	10	9, 10, 11	9, 11
28	119.7 (C)				

^{1}H spectrum of borrelidin (**34**)

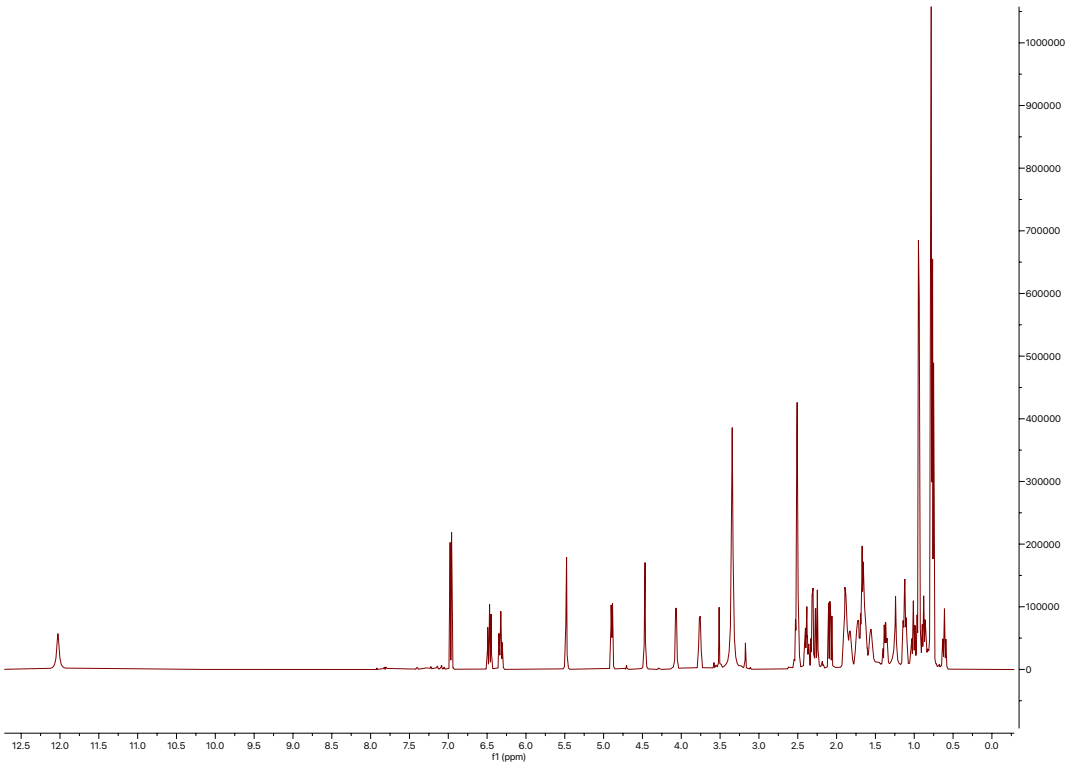

^{13}C spectrum of borrelidin (**34**)

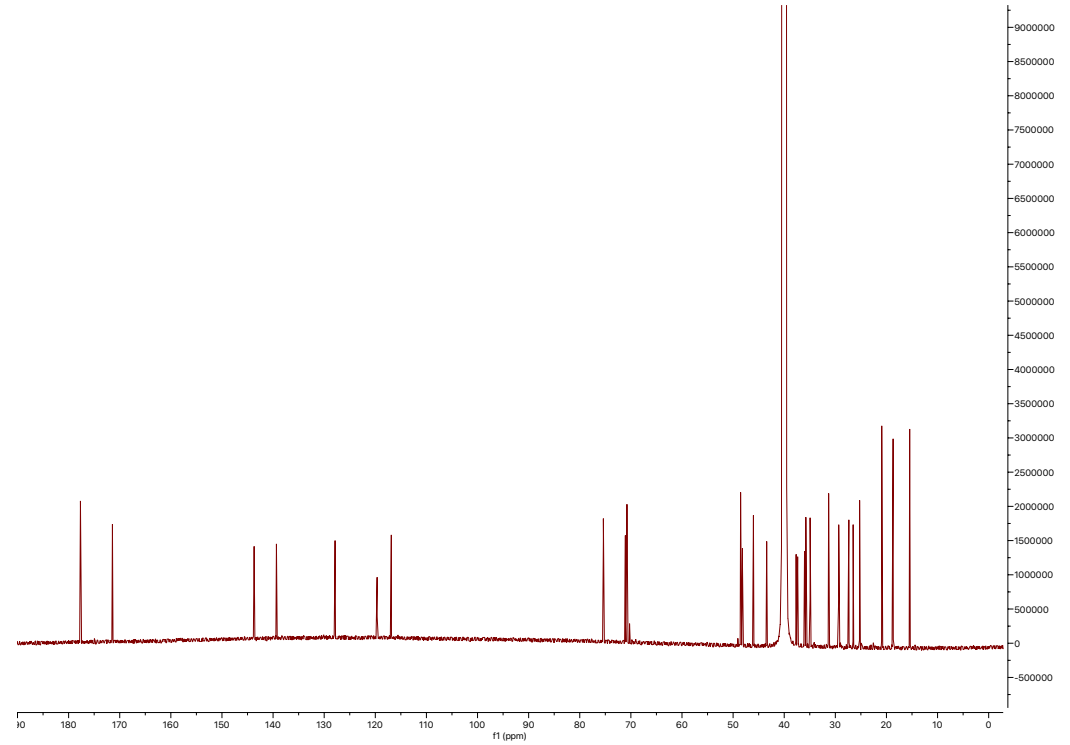

COSY spectrum of borrelidin (**34**)

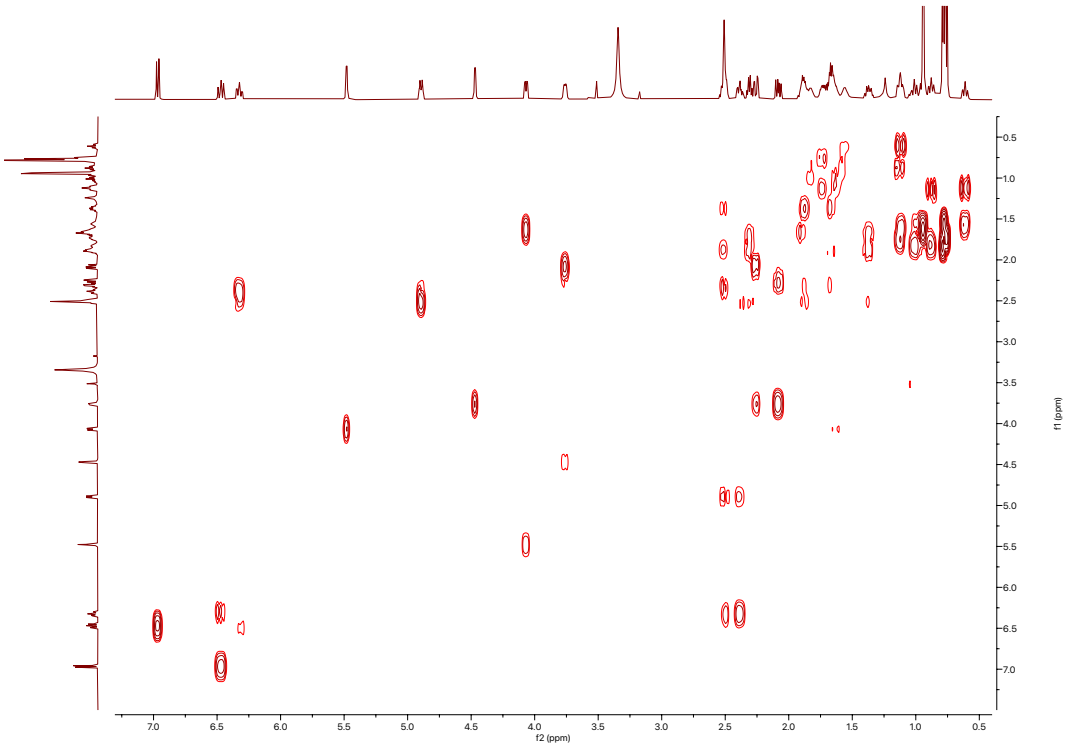

HSQC spectrum of borrelidin (**34**)

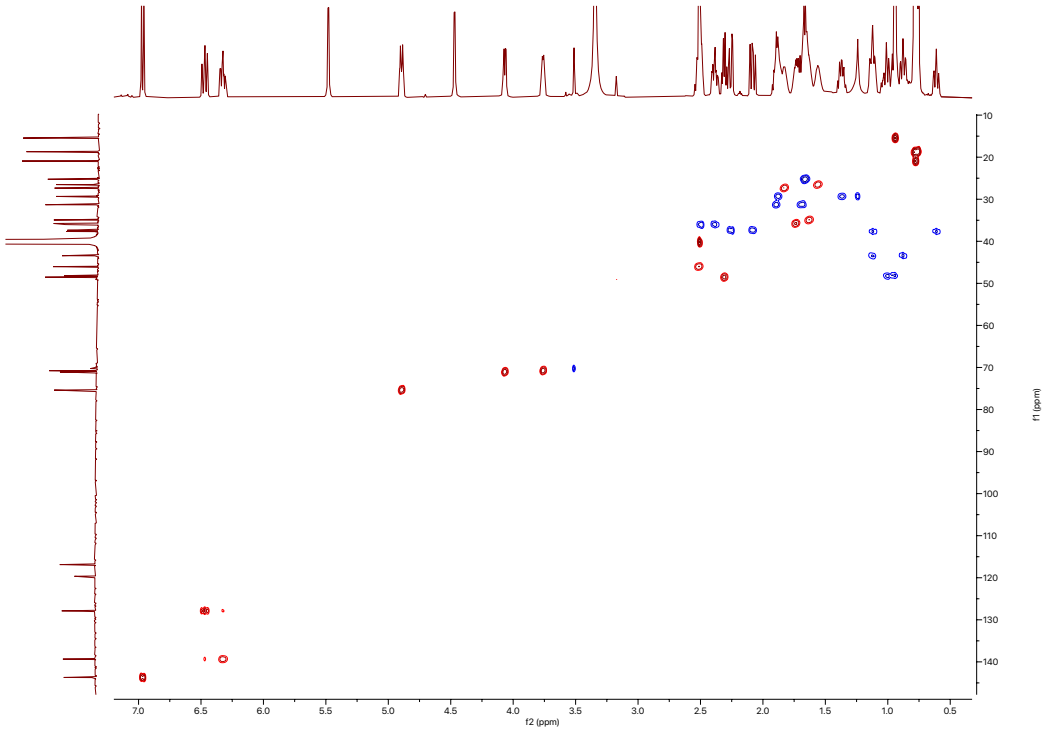

^{1}H-^{13}C HMBC spectrum of borrelidin (**34**)

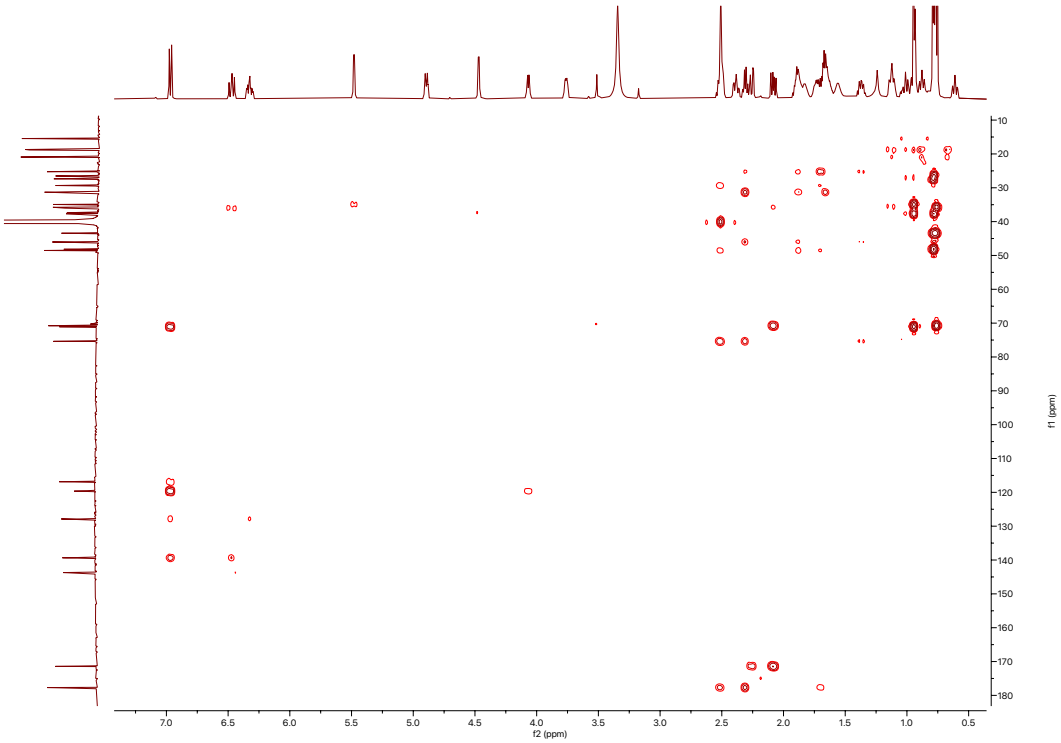

ROESY spectrum of borrelidin (**34**)

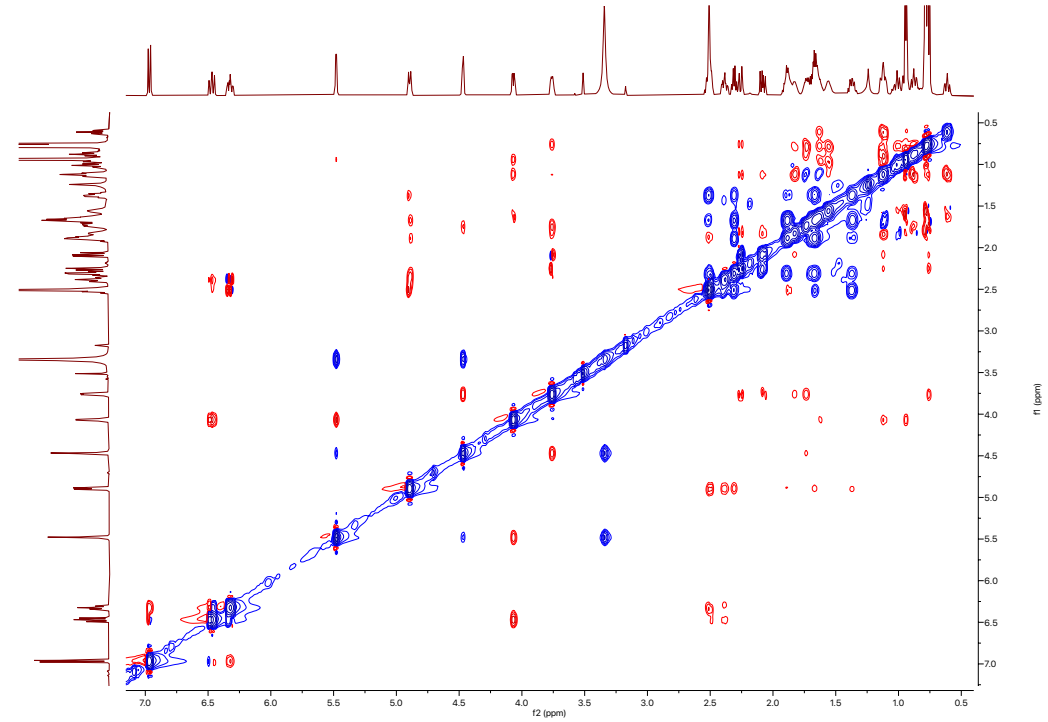

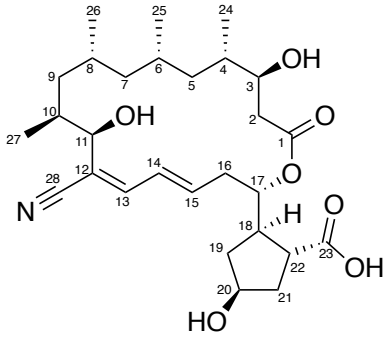

borrelidin C (**35**)

Position	δ_C (type)	δ_H, multiplets (*J* in Hz)	COSY	HMBC	ROESY
1	171.5 (C)				
2a	37.7 (CH_2)	2.09, dd (15.6, 9.6)	2b, 3	1, 3, 4	
2b	37.7 (CH_2)	2.25, dd (15.6, 3.6)	2a, 3		
3	70.6 (CH)	3.75, dt (9.7, 3.3)	2a, 2b, 3-OH, 4		2a, 2b, 4, 6
3-OH		4.68, br s			
4	35.8 (CH)	1.73, m	3, 5a, 5b, 24		3, 5a
5a	48.2 (CH_2)	0.96, m	4, 5b, 6		
5b	48.2 (CH_2)	1.01, ddd (13.9, 11.1, 3.1)	4, 5a, 6		
6	27.4 (CH)	1.82, m	5a, 5b, 7a, 7b, 25		
7a	43.4 (CH_2)	0.88, ddd (13.6, 10.4, 3.0)	6, 7b, 8		
7b	43.4 (CH_2)	1.13, m	6, 7a, 8		
8	26.5 (CH)	1.56, ddd (13.1, 9.8, 6.3)	7a, 7b, 9a, 9b, 26		7a, 9b
9a	37.7 (CH_2)	0.62, ddd (13.7, 11.1, 3.3)	8, 9b, 10		
9b	37.7 (CH_2)	1.12, m	8, 9a, 10		
10	35.0 (CH)	1.64, m	9a, 9b, 11, 27		9a, 26
11	71.1 (CH)	4.07, d (9.6)	10	10, 13, 28	7a, 9b, 10, 14
11-OH		5.47, s			
12	116.9 (C)				
13	143.7 (CH)	6.98, d (11.3)	14	11, 12, 15, 28	
14	127.8 (CH)	6.48, ddd (13.2, 11.4, 1.6)	13, 15	16	
15	139.2 (CH)	6.28, ddd (4.8, 10.4, 4.5)	14, 16a, 16b		
16a	36.0 (CH_2)	2.39, ddd (15.0, 10.4, 4.2)	15, 16b, 17		
16b	36.0 (CH_2)	2.48, m	15, 16a, 17		
17	75.5 (CH)	4.87, dt (10.5, 3.7)	16a, 16b		16a, 18, 19a, 19b, 22
18	47.2 (CH)	2.32, q (8.5)	19a, 19b, 22	17, 22, 23	
19a	40.5 (CH_2)	1.66, m	18, 19b, 20	20	
19b	40.5 (CH_2)	2.16, ddd (13.0, 9.0, 5.7)	18, 19a, 20		
20	70.9 (CH)	4.15, p (5.6)	19a, 19b, 21a, 21b		18, 19a, 19b, 21a, 21b
20-OH		4.44, br s			
21a	38.6 (CH_2)	1.57, m	20, 21b, 22		
21b	38.6 (CH_2)	1.74, m	20, 21a, 22		
22	43.3 (CH)	2.79, p (8.8)	18, 21a, 21b		
23	177.2 (C)				
23-COOH		12.05, s			
24	18.6 (CH_3)	0.76, d (6.3)	4	3, 4	
25	18.9 (CH_3)	0.78, d (6.3)	6	5, 6, 7	
26	20.9 (CH_3)	0.79, d, (6.3)	8	7, 8, 9	
27	15.5 (CH_3)	0.94, d (6.3)	10	9, 10, 11	9a, 11
28	119.6 (C)				

^{1}H spectrum of borrelidin C (**35**)

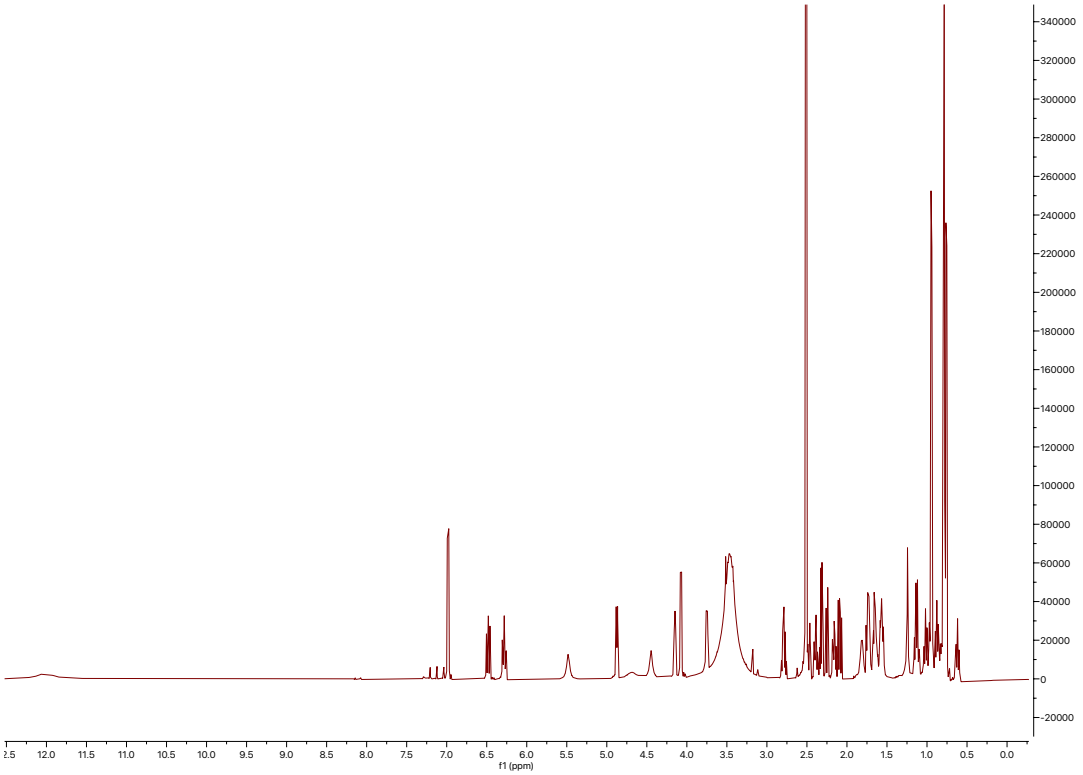

^{13}C spectrum of borrelidin C (**35**)

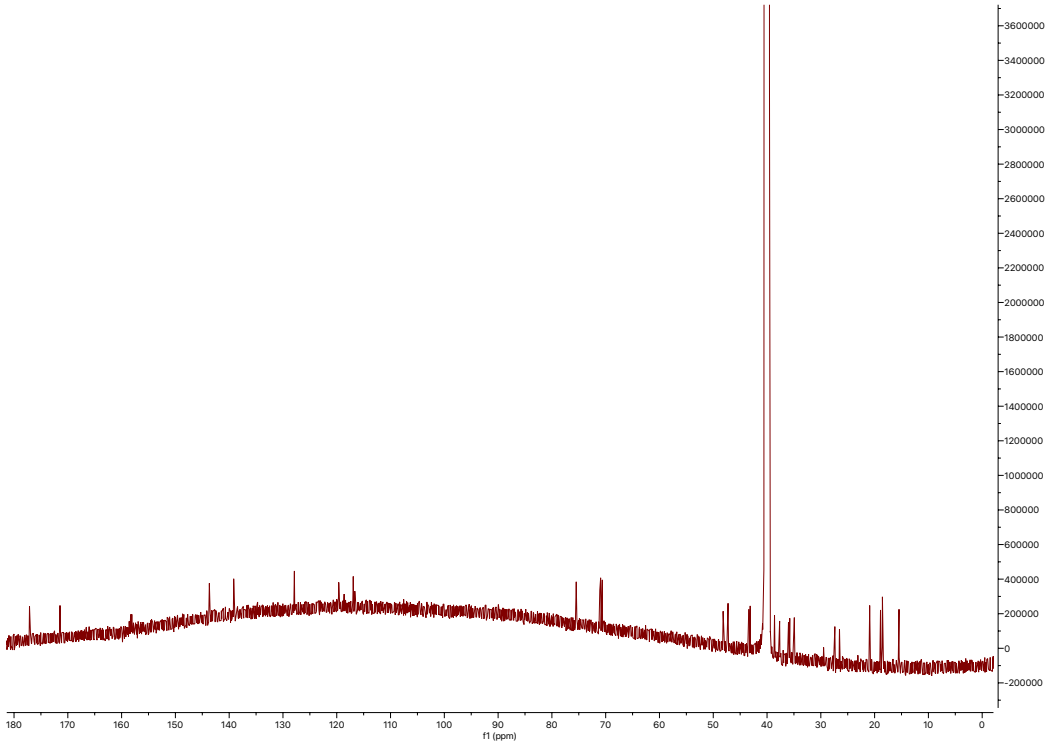

COSY spectrum of borrelidin C (**35**)

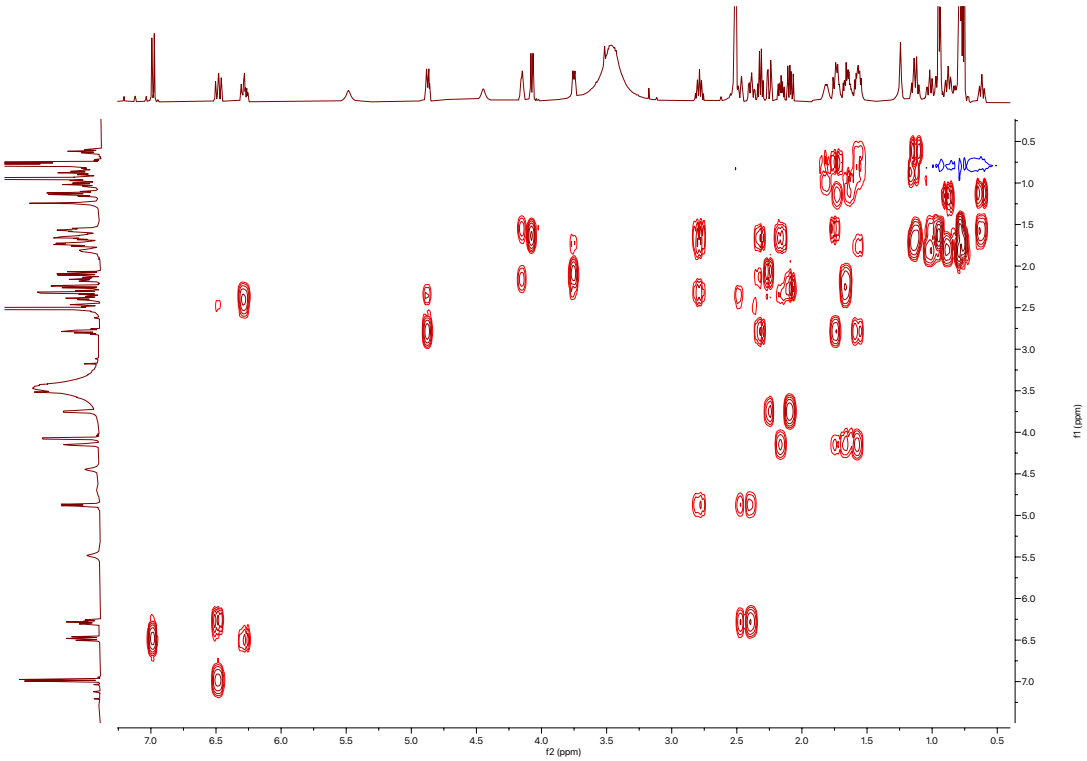

HSQC spectrum of borrelidin C (**35**)

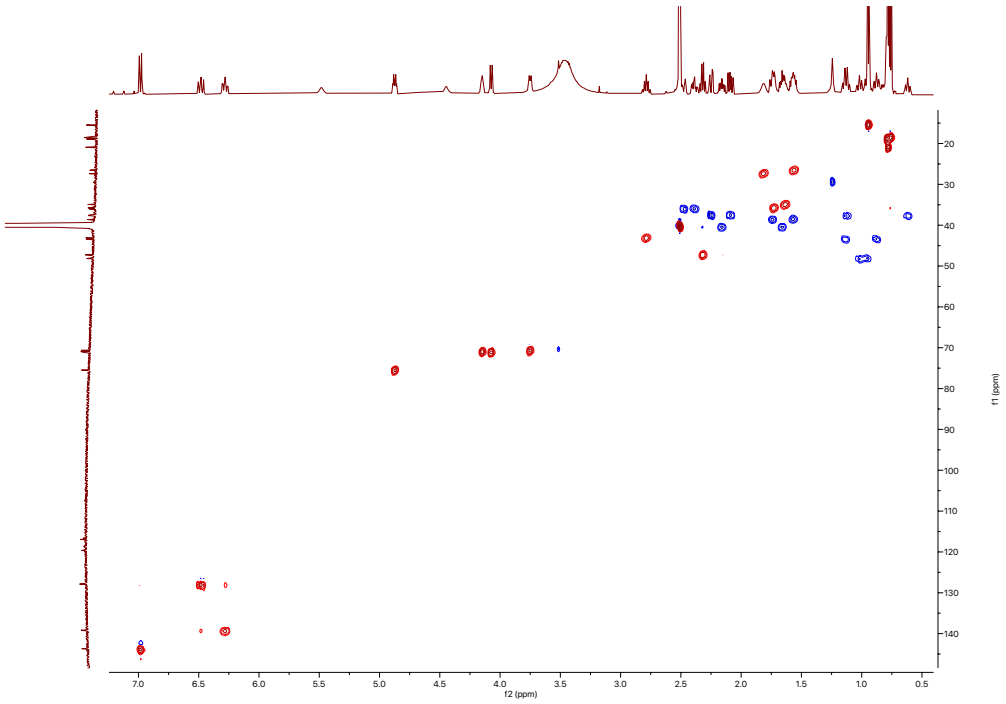

^{1}H-^{13}C HMBC spectrum of borrelidin C (**35**)

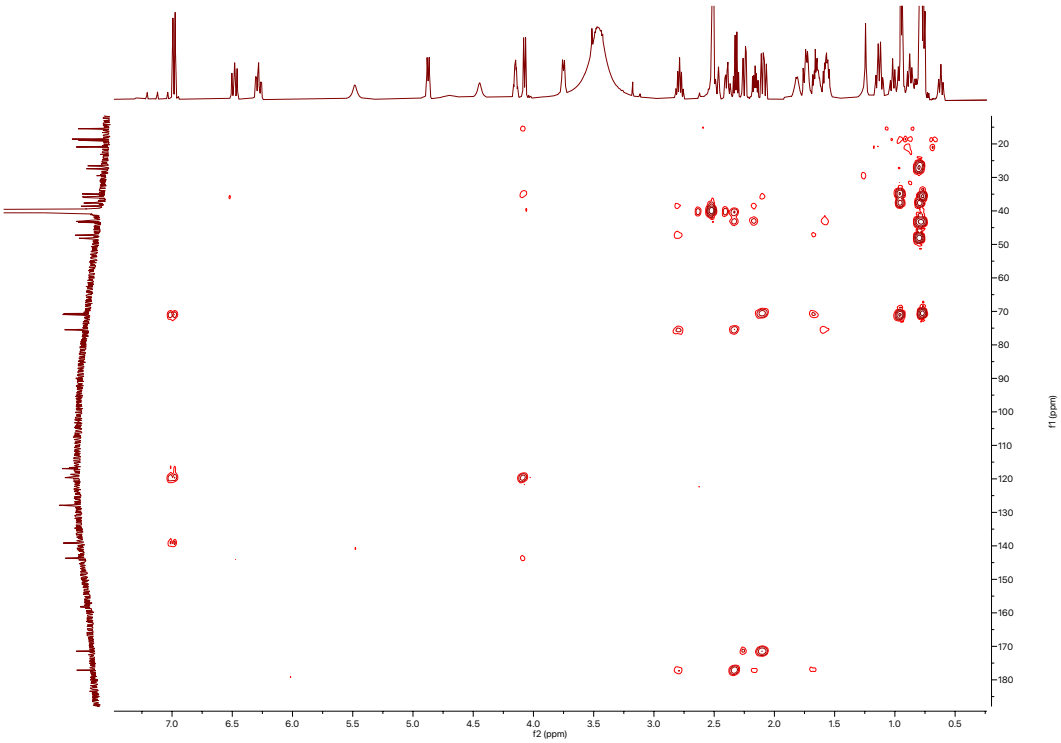

ROESY spectrum of borrelidin C (**35**)

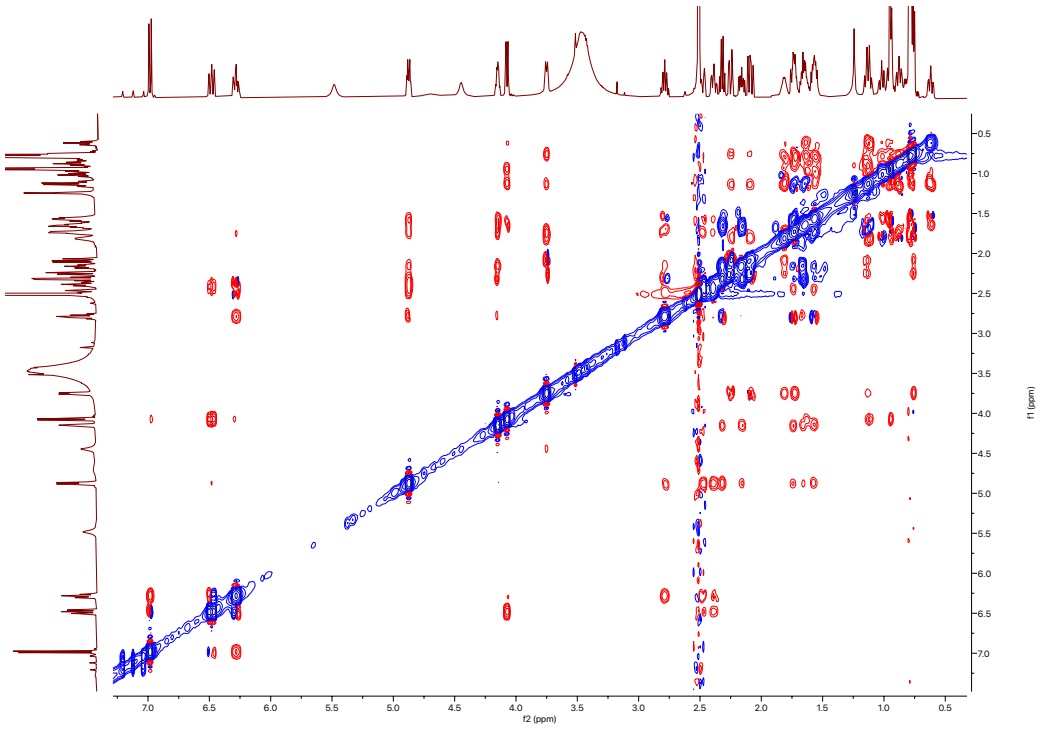

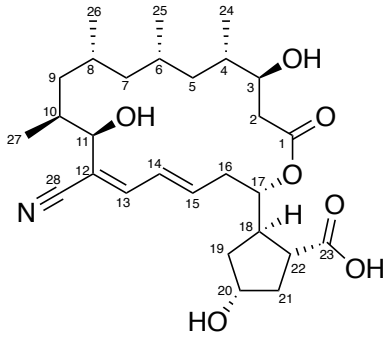

borrelidin D (**36**)

Position	δ_C (type)	δ_H, multiplets (*J* in Hz)	COSY	HMBC	ROESY
1	171.4 (C)				
2a	37.4 (CH_2)	2.09, m	2b, 3	1, 3, 4	
2b	37.4 (CH_2)	2.26, dd (15.6, 3.5)	2a, 3		
3	70.8 (CH)	3.76, dq (10.3, 3.5)	2a, 2b, 3-OH, 4		2a, 2b, 4, 6
3-OH		4.47, br s			
4	35.8 (CH)	1.74, m	3, 5a, 5b, 24		3, 5a
5a	48.1 (CH_2)	0.88, ddd (13.9, 10.6, 3.1)	4, 5b, 6		
5b	48.1 (CH_2)	1.12, dt (14.0, 7.7)	4, 5a, 6		
6	27.4 (CH)	1.83, m	5a, 5b, 7a, 7b, 25		
7a	43.5 (CH_2)	0.96, m	6, 7b, 8		
7b	43.5 (CH_2)	1.01, td (12.5, 11.2, 3.1)	6, 7a, 8		
8	26.6 (CH)	1.56, m	7a, 7b, 9a, 9b, 26		7a, 9b
9a	37.7 (CH_2)	0.61, ddd (13.8, 11.1, 3.3)	8, 9b, 10		
9b	37.7 (CH_2)	1.12, dt (14.4, 7.7)	8, 9a, 10		
10	35.0 (CH)	1.63, m	9a, 9b, 11, 27		9a, 26
11	71.1 (CH)	4.07, d (9.6)	10	10, 13, 28	7a, 9b, 10, 14
11-OH		5.48, s			
12	116.9 (C)				
13	143.7 (CH)	6.96, d (11.2)	14	11, 12, 14, 15, 28	
14	127.8 (CH)	6.47, dd (14.7, 11.3)	13, 15	16	
15	139.3 (CH)	6.30, ddd (14.8, 10.6, 4.3)	14, 16a, 16b		
16a	35.9 (CH_2)	2.38, ddd (14.9, 10.6, 4.3)	15, 16b, 17		
16b	35.9 (CH_2)	2.51, m	15, 16a, 17		
17	76.0 (CH)	4.98, dt (10.5, 3.7)	16a, 16b		16a, 18, 19a, 19b, 22
18	44.0 (CH)	2.52, m	19a, 19b, 22	17, 22, 23	
19a	38.3 (CH_2)	1.35, ddd (12.5, 7.5, 4.2)	18, 19b, 20	20	
19b	38.3 (CH_2)	1.88, m	18, 19a, 20		
20	71.4 (CH)	4.20, p (4.7)	19a, 19b, 21a, 21b		19a, 19b, 21a, 21b, 22
20-OH		4.47, br s			
21a	40.7 (CH_2)	1.78, m	20, 21b, 22		
21b	40.7 (CH_2)	1.82, m	20, 21a, 22		
22	46.7 (CH)	2.55, m	18, 21a, 21b		
23	177.6 (C)				
23-COOH		12.05, s			
24	18.7 (CH_3)	0.76, d (6.3)	4	3, 4	
25	18.9 (CH_3)	0.78, d (6.3)	6	5, 6, 7	
26	21.0 (CH_3)	0.79, d, (6.3)	8	7, 8, 9	
27	15.5 (CH_3)	0.94, d (6.3)	10	9, 10, 11	9a, 11
28	119.6 (C)				

^{1}H spectrum of borrelidin D (**36**)

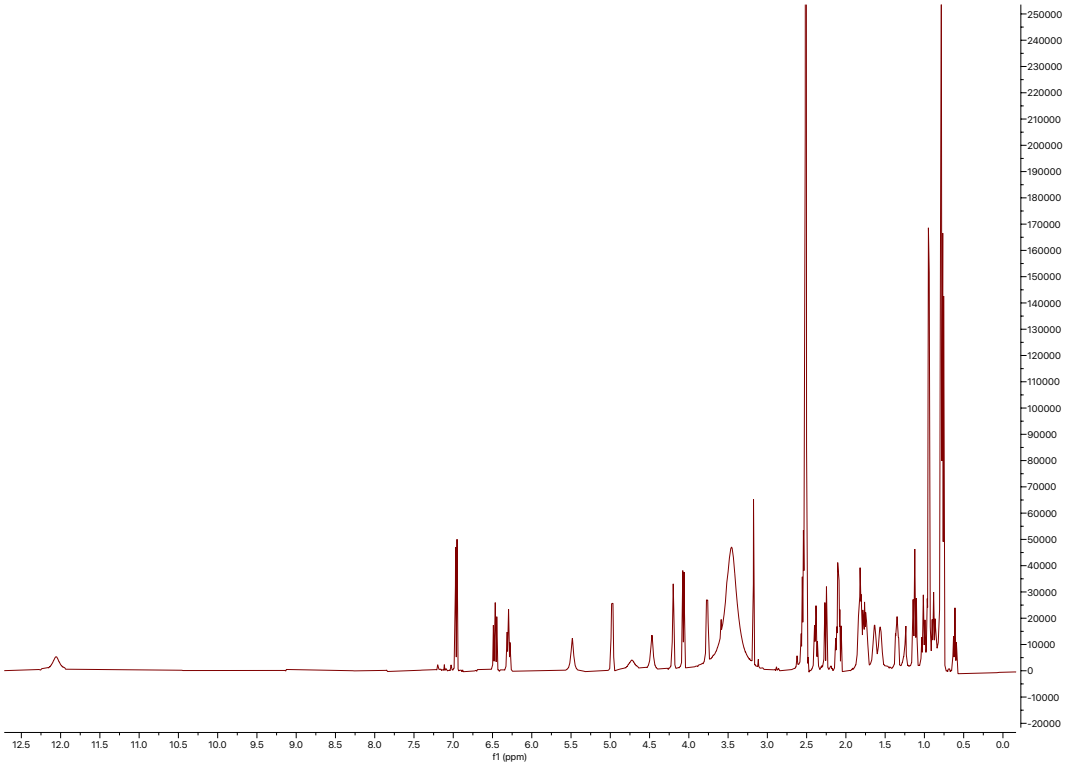

^{13}C spectrum of borrelidin D (**36**)

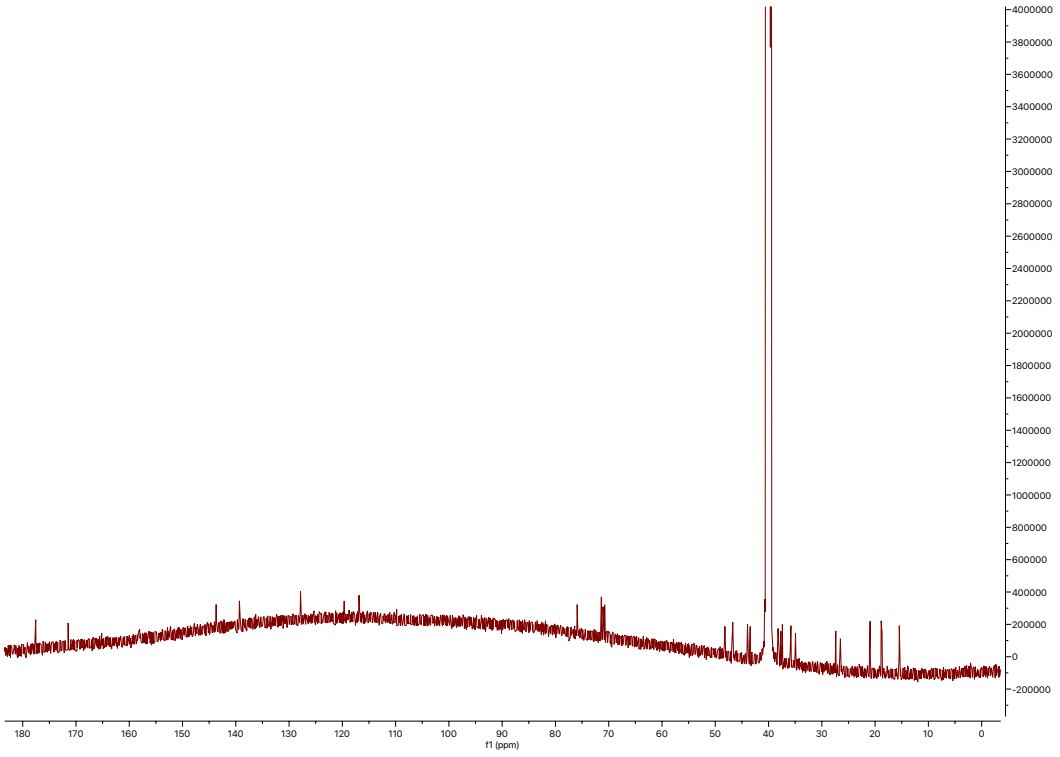

COSY spectrum of borrelidin D (**36**)

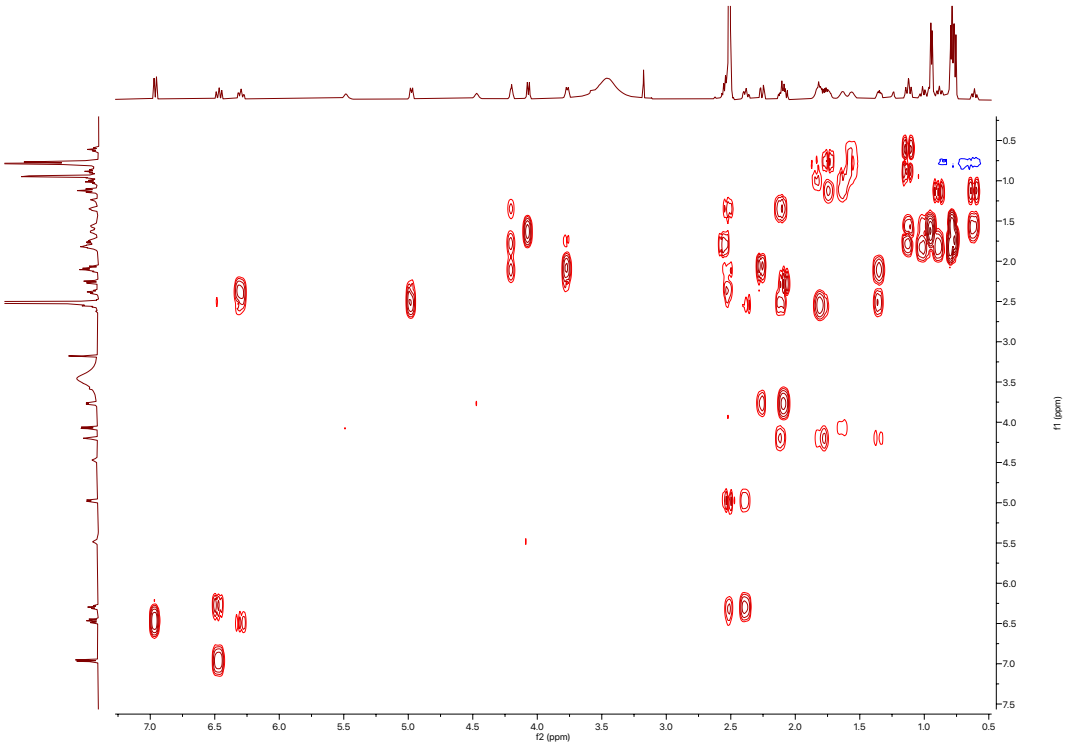

HSQC spectrum of borrelidin D (**36**)

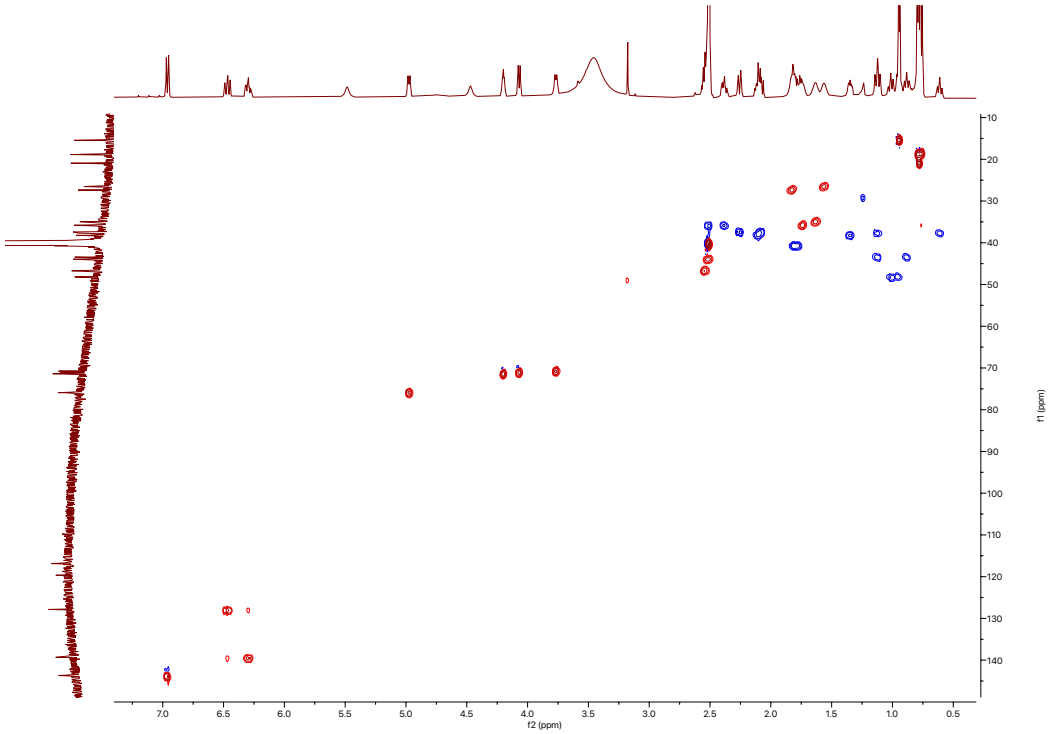

^{1}H-^{13}C HMBC spectrum of borrelidin D (**36**)

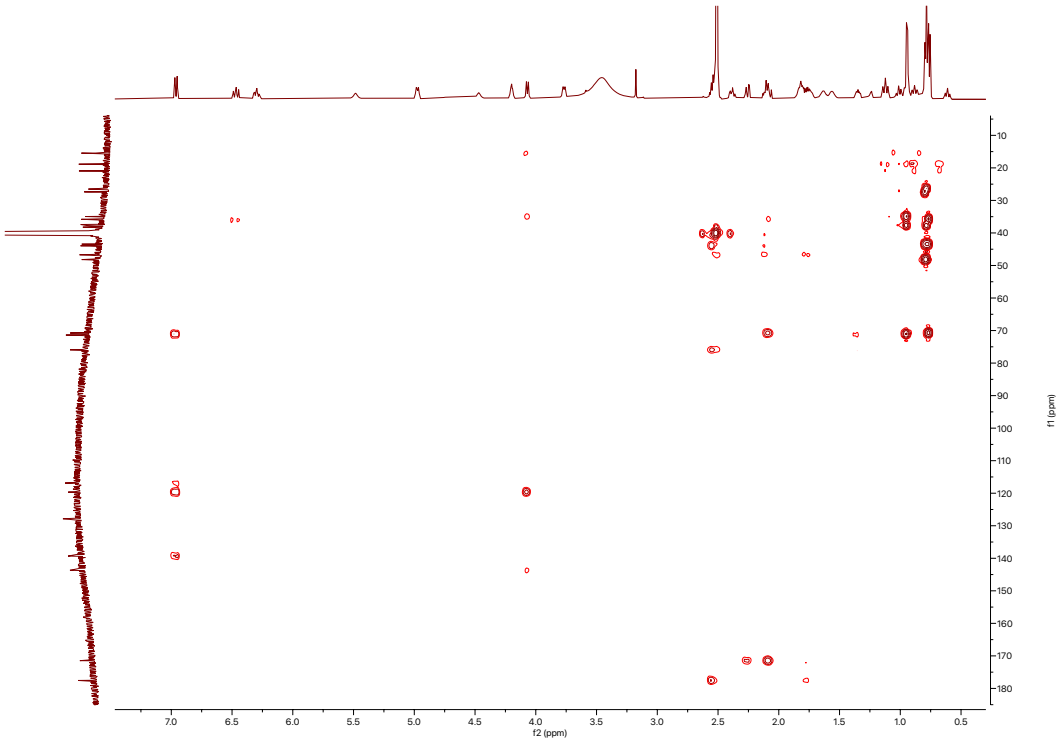

ROESY spectrum of borrelidin D (**36**)

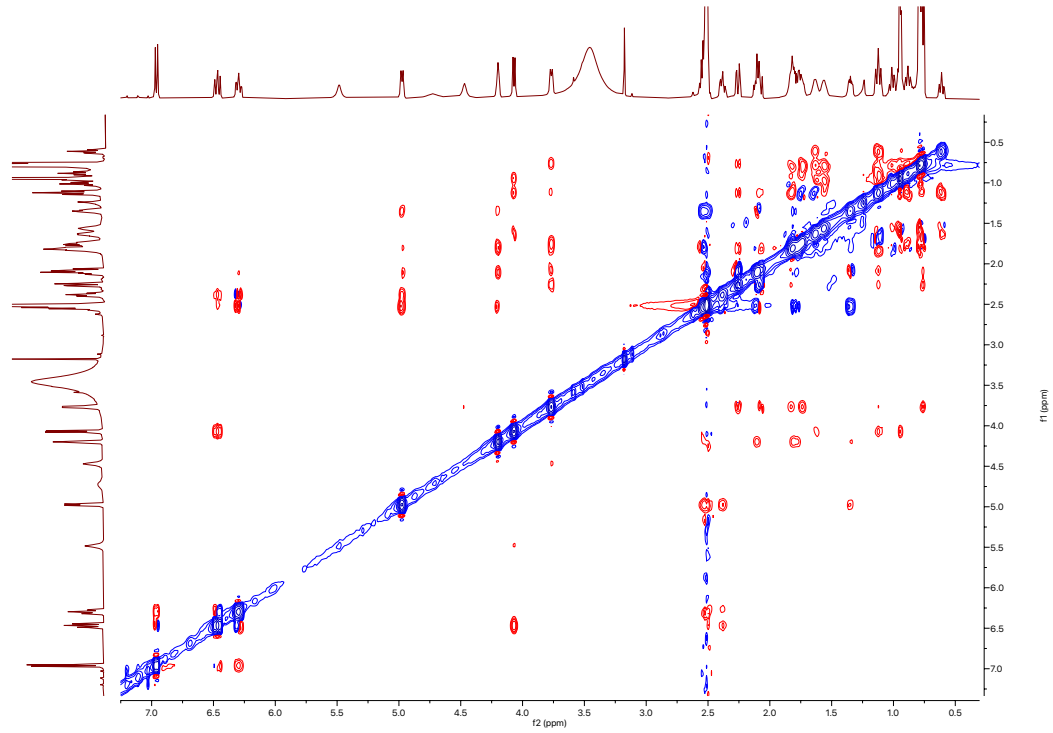

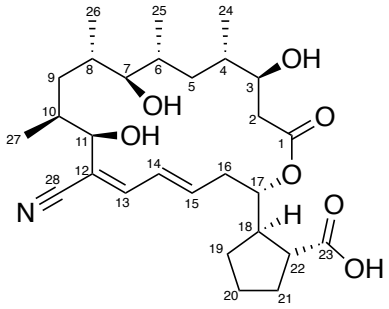

borrelidin E (**37**)

Position	δ_C (type)	δ_H, multiplets (*J* in Hz)	COSY	HMBC	ROESY
1	171.8 (C)				
2a	36.6 (CH_2)	2.20, dd (15.5, 3.7)	2b, 3	1, 3, 4	
2b	36.6 (CH_2)	2.32, m	2a, 3		
3	71.3 (CH)	3.78, dt (9.6, 2.9)	2a, 2b, 4	5	2a, 2b, 4, 6
3-OH		4.36, br s		2, 3, 4	2a, 3, 4
4	35.3 (CH)	1.80, m	3, 5a, 5b, 24		5a, 5b, 25
5a	37.7 (CH_2)	0.63, t (10.9)	4, 5b, 6		
5b	37.7 (CH_2)	1.81, m	4, 5a, 6	6, 24, 25	
6	33.0 (CH)	1.86, m	5a, 5b, 7, 25		2a, 3, 5b, 25
7	79.5 (CH)	2.82, dd (9.9, 1.9)	6, 7, 8	8, 25, 26	5b, 8, 25, 26
7-OH		4.27, br s			
8	30.9 (CH)	1.69, m	7, 9a, 9b, 26		7a, 9b, 25
9a	29.8 (CH_2)	0.81, m	8, 9b, 10	8, 10, 27	
9b	29.8 (CH_2)	1.07, ddd (14.7, 11.7, 3.1)	8, 9a, 10	7, 8, 10, 27	
10	34.6 (CH)	1.53, ddqd (12.6, 9.7, 6.3, 3.0)	9a, 9b, 11, 27	11	7a, 9a, 26
11	71.6 (CH)	4.03, d (9.8)	10	10, 13, 28	7a, 9b, 10, 14
11-OH		5.46, br s		10, 12	7a, 10, 11
12	117.0 (C)				
13	143.7 (CH)	6.95, d (11.2)	14	11, 12, 14, 15, 28	15
14	127.7 (CH)	6.43, dd (13.2, 11.3)	13, 15	12, 13, 15, 16	
15	139.2 (CH)	6.31, ddd (14.7, 10.5, 4.2)	14, 16a, 16b	13, 14, 16	13
16a	36.2 (CH_2)	2.36, m	15, 16b, 17	14, 15, 17	
16b	36.2 (CH_2)	2.51, m	15, 16a, 17	14, 15, 17	
17	75.2 (CH)	4.92, dt (10.5, 3.6)	16a, 16b	1, 15, 18, 22	16a, 18, 19a, 19b, 20, 22
18	46.1 (CH)	2.51, m	19a, 19b, 22	16, 19, 22, 23	15, 17, 19b
19a	29.4 (CH_2)	1.37, dq (12.4, 8.6)	18, 19b, 20	17, 18, 20, 21	
19b	29.4 (CH_2)	1.88, m	18, 19a, 20	17, 18, 20, 21, 22	
20	25.3 (CH_2)	1.66, m	19a, 19b, 21a, 21b	18, 19, 20, 21	
21a	31.2 (CH_2)	1.70, m	20, 21b, 22	18, 19, 20, 22, 23	
21b	31.3 (CH_2)	1.89, m	20, 21a, 22	18, 19, 20, 22, 23	
22	48.6 (CH)	2.32, m	18, 21a, 21b	17, 18, 19, 20, 21, 23	17
23	177.7 (C)				
23-COOH		12.04, s			
24	19.2 (CH_3)	0.79, d, (6.2)	4	3, 4, 5	
25	16.6 (CH_3)	0.72, d (6.3)	6	5, 6, 7	
26	17.5 (CH_3)	0.83, d (6.7)	8	7, 8, 9	
27	15.5 (CH_3)	0.92, d (6.4)	10	9, 10, 11	9, 11
28	119.7 (C)				

^{1}H spectrum of borrelidin E (**37**)

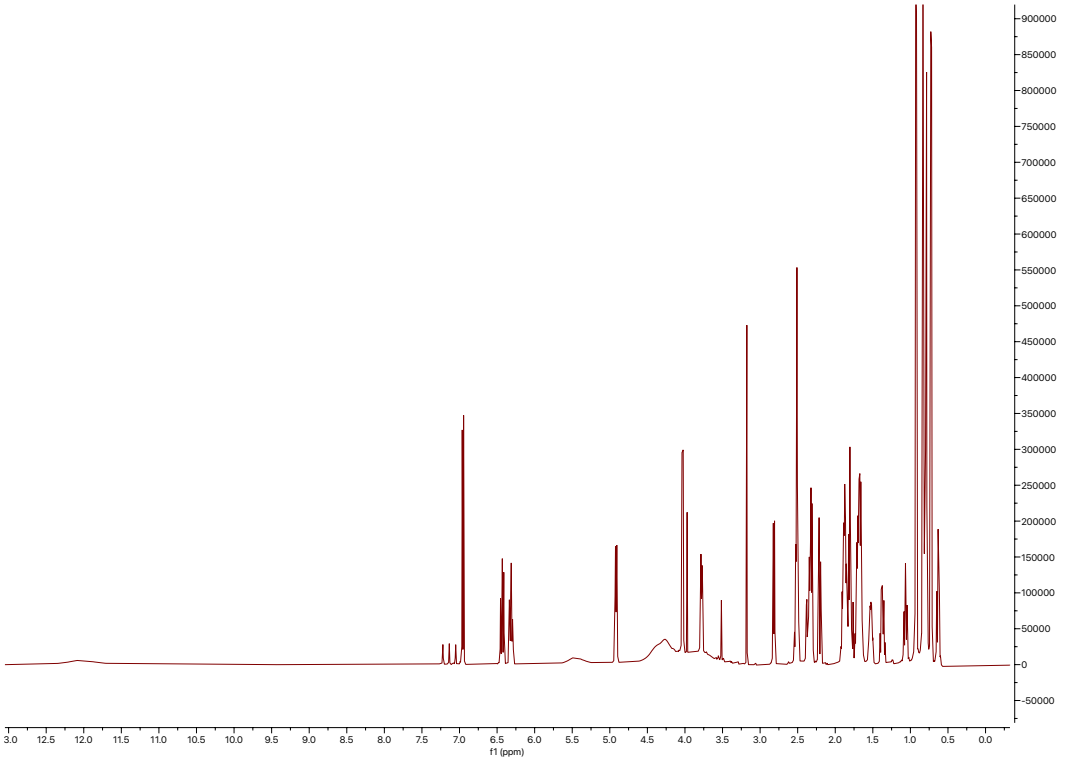

^{13}C spectrum of borrelidin E (**37**)

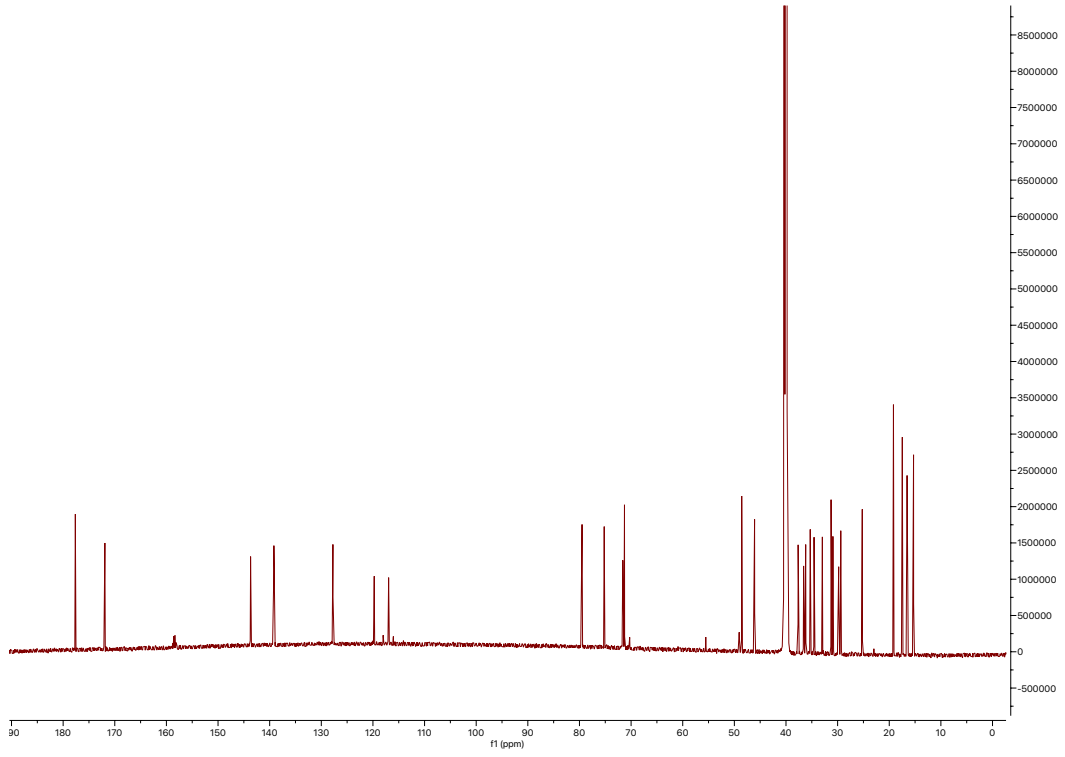

COSY spectrum of borrelidin E (**37**)

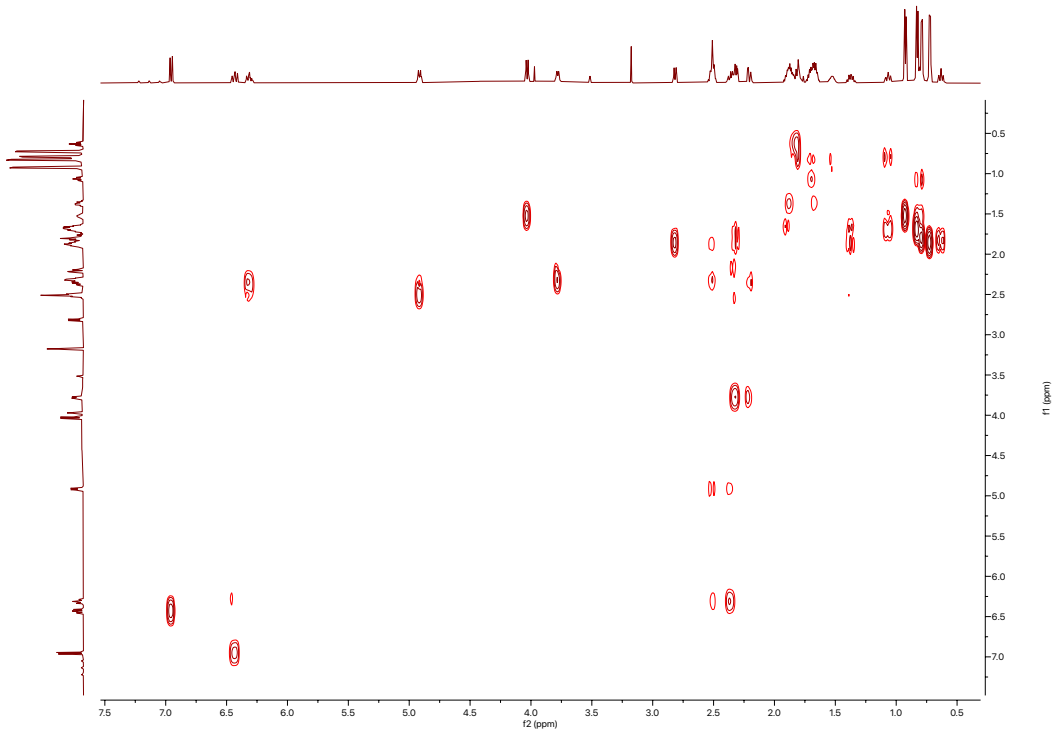

HSQC spectrum of borrelidin E (**37**)

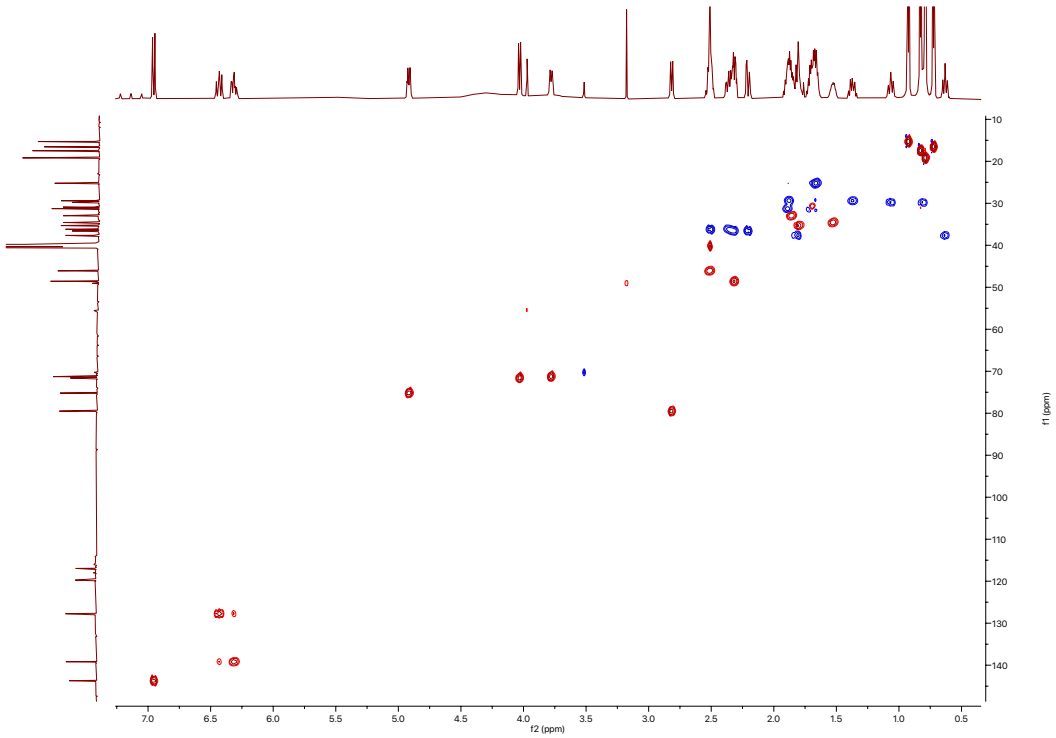

^{1}H-^{13}C HMBC spectrum of borrelidin E (**37**)

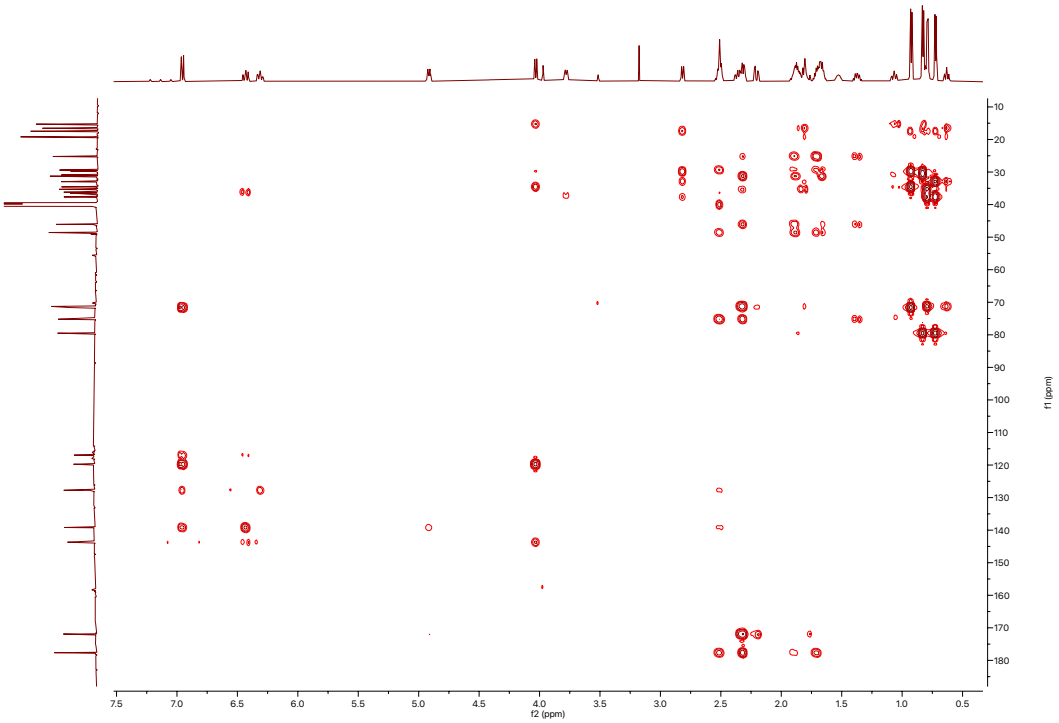

ROESY spectrum of borrelidin E (**37**)

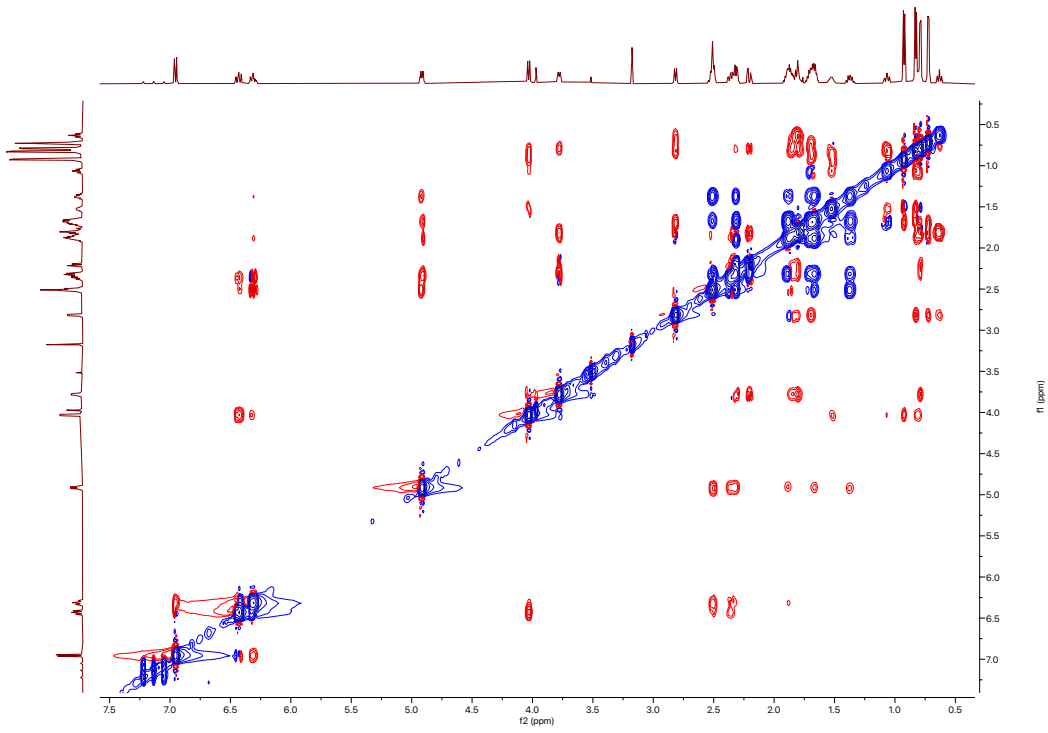

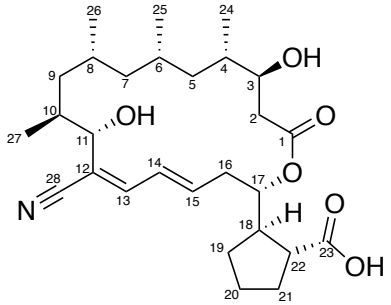

borrelidin F (**38**)

Position	δ_C (type)	δ_H, multiplets (*J* in Hz)	COSY	HMBC	ROESY
1	171.9 (C)				
2a	39.6 (CH_2)	2.11, dd (15.1, 8.5)	2b, 3	1, 3	
2b	39.6 (CH_2)	2.32, dd (15.0, 3.8)	2a, 3		
3	70.1 (CH)	3.63, dt (8.5, 4.2)	2a, 2b, 4		2a, 2b, 4, 5b, 24
3-OH					
4	35.8 (CH)	1.64, dq (12.3, 6.9)	3, 5a, 5b, 24		
5a	43.4 (CH_2)	0.79, m	4, 5b, 6		
5b	43.4 (CH_2)	1.22, m	4, 5a, 6		
6	27.7 (CH)	1.59, q (7.2, 6.3)	5a, 5b, 7a, 7b, 25		
7a	48.3 (CH_2)	0.98, m	6, 7b, 8		
7b	48.3 (CH_2)	1.04, m	6, 7a, 8		
8	26.4 (CH)	1.53, dq (12.7, 5.9)	7a, 7b, 9a, 9b, 26		
9a	37.4 (CH_2)	0.73, m	8, 9b, 10		
9b	37.4 (CH_2)	0.97, m	8, 9a, 10		
10	35.4 (CH)	1.67, m	9a, 9b, 11, 27		
11	77.6 (CH)	3.74, d (8.0)	10	10, 13, 27, 28	
11-OH		5.48, br s	11		
12	115.3 (C)				
13	144.5 (CH)	6.82, d (11.1)	14	11, 15	
14	128.4 (CH)	6.34, dd (15.0, 11.1)	13, 15		
15	141.2 (CH)	6.06, ddd (14.9, 9.8, 5.0)	14, 16a, 16b		
16a	37.5 (CH_2)	2.37, m	15, 16b, 17		
16b	37.5 (CH_2)	2.57, d (14.7)	15, 16a, 17		
17	75.4 (CH)	4.94, t (8.4)	16a, 16b		16a, 18, 19a, 19b, 20, 22
18	48.2 (CH)	2.39, dd (10.6, 3.4)	19a, 19b, 22	17	
19a	29.6 (CH_2)	1.30, m	18, 19b, 20		
19b	29.6 (CH_2)	1.74, dq (13.1, 6.8)	18, 19a, 20		
20	25.8 (CH_2)	1.59, m	19a, 19b, 21a, 21b		
21a	31.6 (CH_2)	1.67, m	20, 21b, 22	19	
21b	31.6 (CH_2)	1.73, m	20, 21a, 22		
22	49.0 (CH)	2.24, q (7.8)	21a, 21b		
23					
23-COOH					
24	18.3 (CH_3)	0.79, d (6.6)	4	3, 4	
25	19.1 (CH_3)	0.76, d, (6.6)	6	5, 7	
26	20.7 (CH_3)	0.78, d (6.6)	8	7, 9	
27	16.2 (CH_3)	0.92, d (6.6)	10	9, 10, 11	
28	117.3 (C)				

^{1}H spectrum of borrelidin F (**38**)

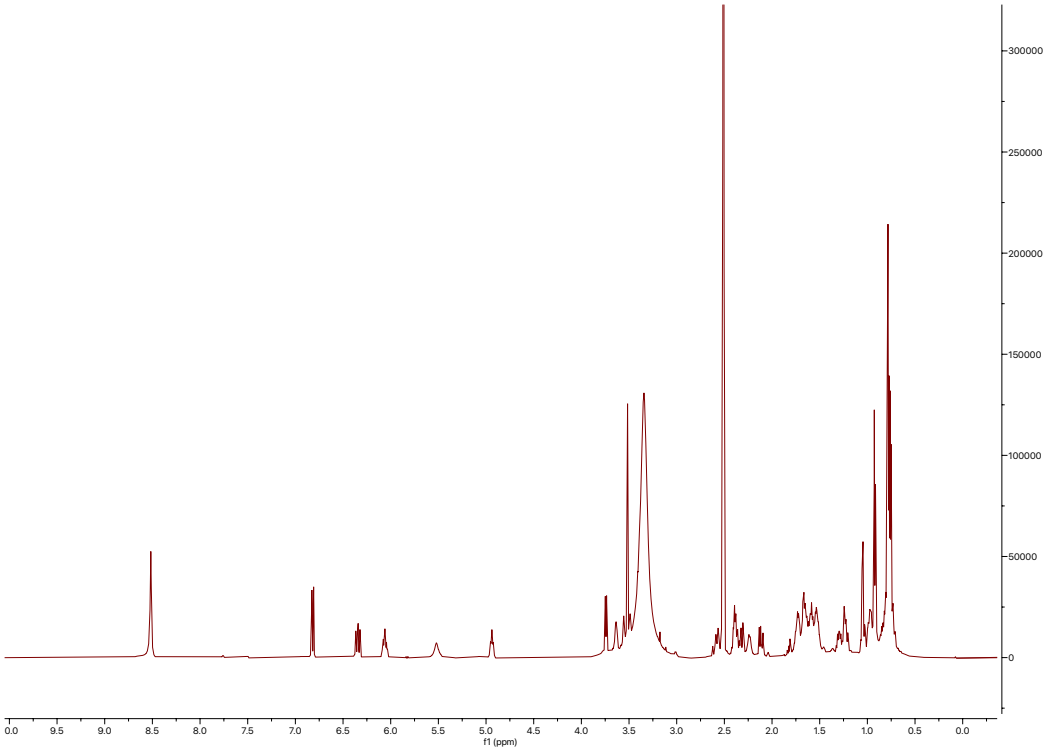

^{13}C spectrum of borrelidin F (**38**)

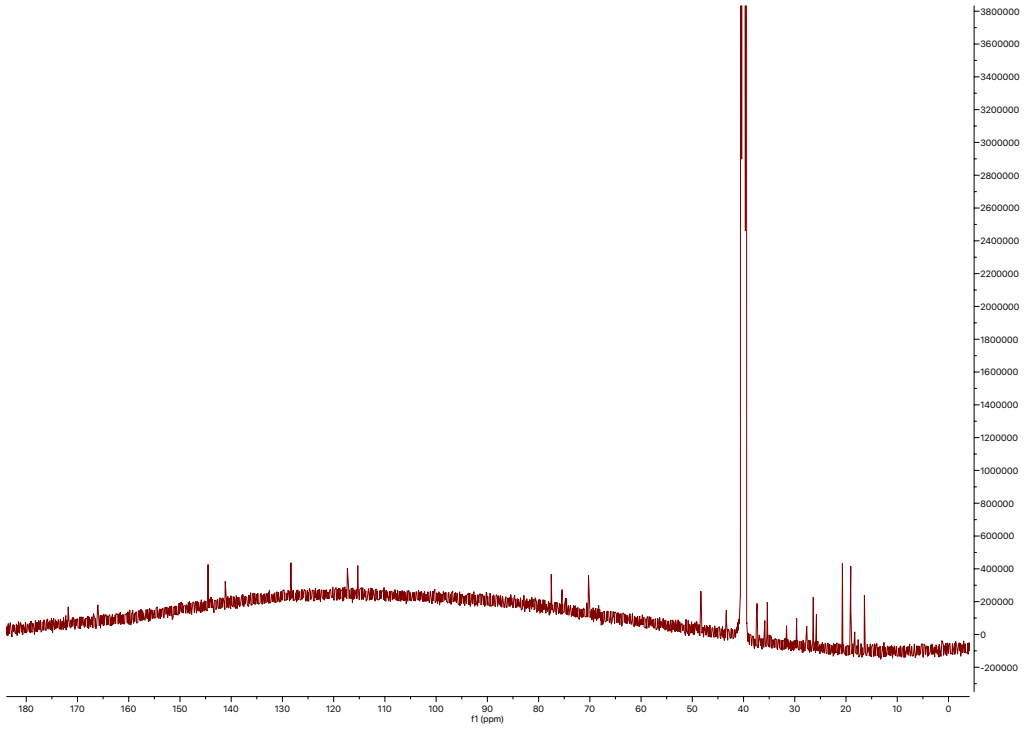

COSY spectrum of borrelidin F (**38**)

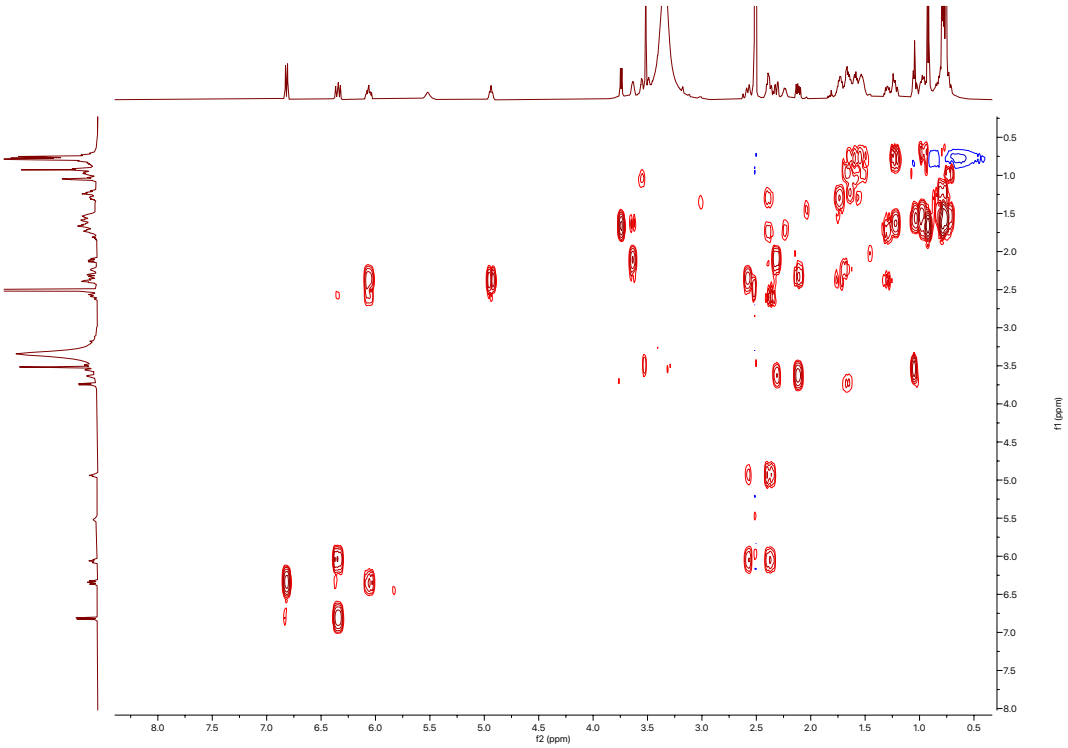

HSQC spectrum of borrelidin F (**38**)

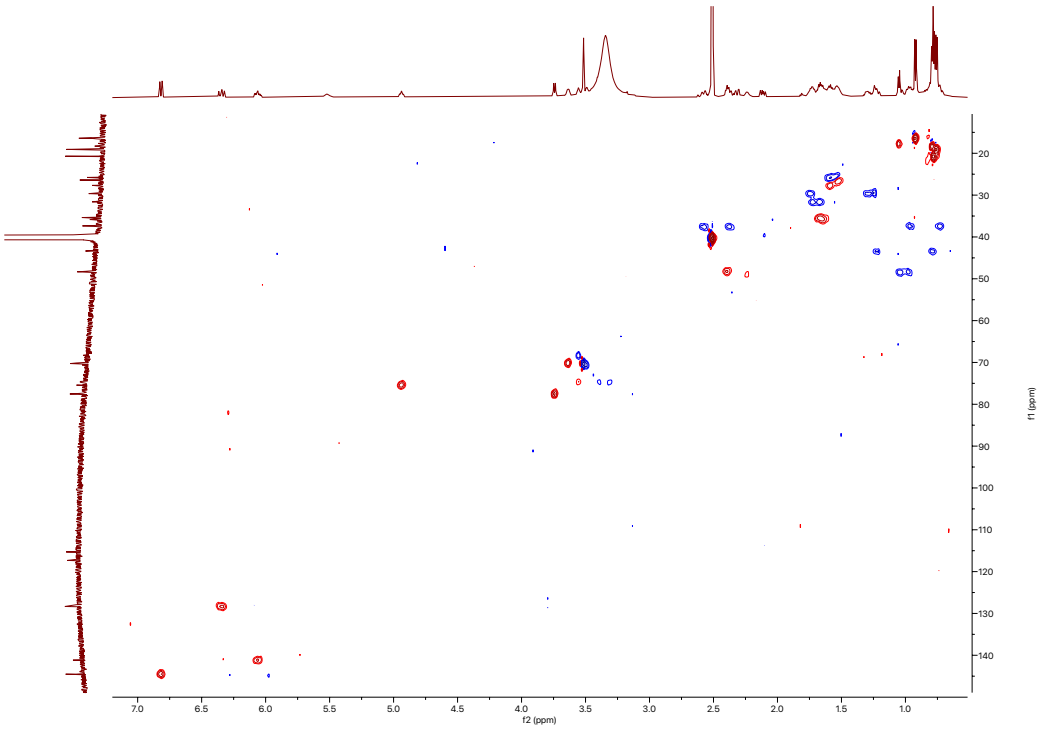

^{1}H-^{13}C HMBC spectrum of borrelidin F (**38**)

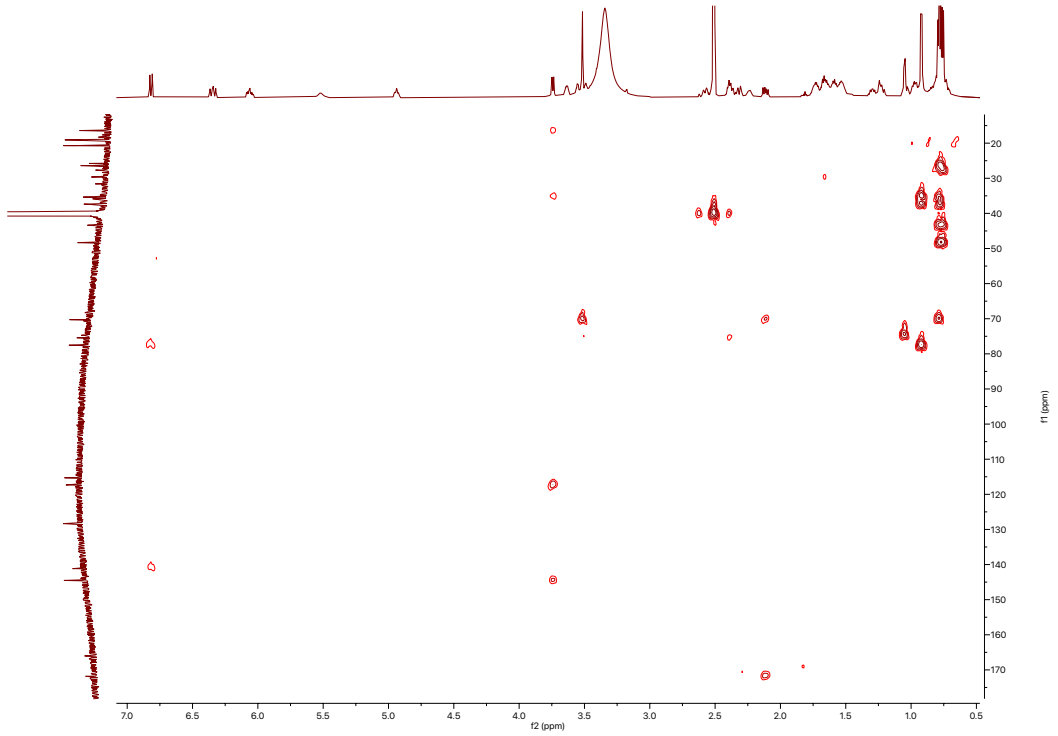

ROESY spectrum of borrelidin F (**38**)

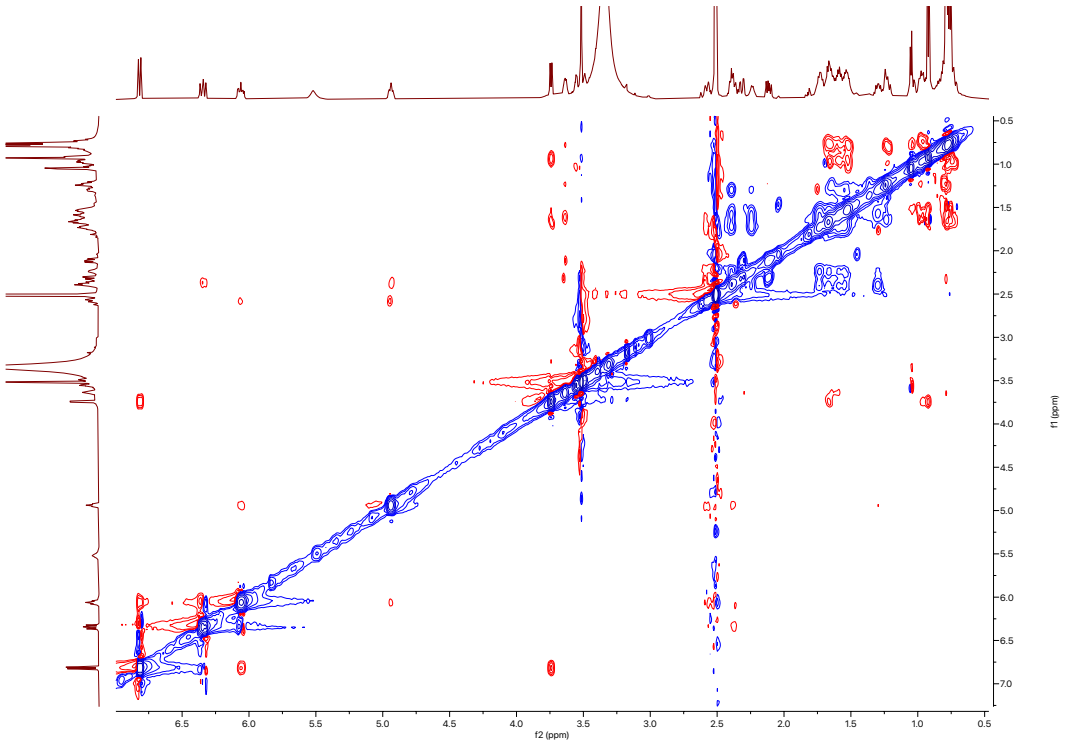

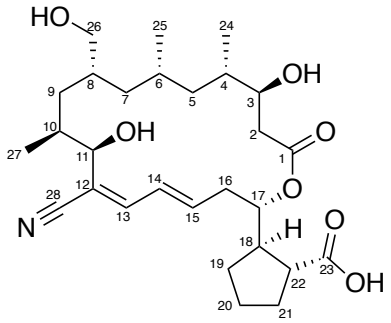

borrelidin J (**39**)

Position	δ_C (type)	δ_H, multiplets (*J* in Hz)	COSY	HMBC	ROESY
1	171.4 (C)				
2a	37.7 (CH_2)	2.10, ddd (15.5, 9.5, 2.7)	2b, 3	1, 3, 4	
2b	37.7 (CH_2)	2.27, m	2a, 3		
3	70.7 (CH)	3.77, dq (9.7, 3.4)	2a, 2b, 4		2a, 2b, 4, 6
3-OH		4.50, br s			2a, 3, 4
4	35.7 (CH)	1.74, m	3, 5a, 5b, 24		5a, 5b, 25
5a	43.7 (CH_2)	0.91, m	4, 5b, 6		
5b	43.7 (CH_2)	1.17, ddd (13.5, 10.9, 2.3)	4, 5a, 6	6, 24, 25	
6	27.3 (CH)	1.80, m	5a, 5b, 7a, 7b, 25		2a, 3, 5b, 25
7a	42.4 (CH_2)	0.88, m	6, 7b, 8	8, 25, 26	
7b	42.4 (CH_2)	1.28, m	6, 7a, 8	8, 25, 26	
8	34.6 (CH)	1.54, dtt (11.0, 7.3, 3.4)	7a, 7b, 9a, 9b, 26		7a, 9b, 25
9a	33.4 (CH_2)	0.87, m	8, 9b, 10	8, 10, 27	
9b	33.4 (CH_2)	0.95, m	8, 9a, 10	7, 8, 10, 27	
10	35.0 (CH)	1.66, m	9a, 9b, 11, 27	11	7a, 9a, 26
11	71.0 (CH)	4.06, d (9.0)	10		9b, 10, 14
11-OH		5.46, br s			7a, 10, 11
12	117.0 (C)				
13	143.6 (CH)	6.95, d (11.3)	14	11, 12, 14, 15, 28	
14	127.9 (CH)	6.45, dd (14.7, 11.0)	13, 15	13	11
15	139.3 (CH)	6.32, ddd (14.9, 10.9, 4.7)	14, 16a, 16b		13
16a	36.1 (CH_2)	2.38, ddd (14.9, 10.4, 4.1)	15, 16b, 17	14, 15, 17	
16b	36.1 (CH_2)	2.51, m	15, 16a, 17	14, 15, 17	
17	75.5 (CH)	4.89, dt (10.6, 3.6)	16a, 16b		18, 19a, 19b, 20, 22
18	46.0 (CH)	2.51, m	19a, 19b, 22	16, 19, 22, 23	
19a	29.3 (CH_2)	1.37, dq (12.1, 8.5)	18, 19b, 20	17, 18, 20, 21	
19b	29.3 (CH_2)	1.88, m	18, 19a, 20		
20	25.3 (CH_2)	1.67, m	19a, 19b, 21a, 21b	21	
21a	31.3 (CH_2)	1.69, m	20, 21b, 22	18, 19, 20, 22, 23	
21b	31.3 (CH_2)	1.89, m	20, 21a, 22	22	
22	48.6 (CH)	2.30, q (8.4)	18, 21a, 21b	17, 18, 21, 23	17
23	177.7 (C)				
23-COOH		12.04, s			
24	18.5 (CH_3)	0.77, d (6.3)	4	3, 4	
25	19.0 (CH_3)	0.79, d (6.3)	6	5, 6, 7	
26a	65.0 (CH_2)	3.02, dd, (10.3, 7.4)	8	7, 8, 9	
26b	65.0 (CH_2)	3.39, dd (10.2, 3.9)	8	7	
26-OH					
27	15.9 (CH_3)	0.97, d (6.5)	10	9, 10, 11	9, 11
28	119.7 (C)				

^{1}H spectrum of borrelidin J (**39**)

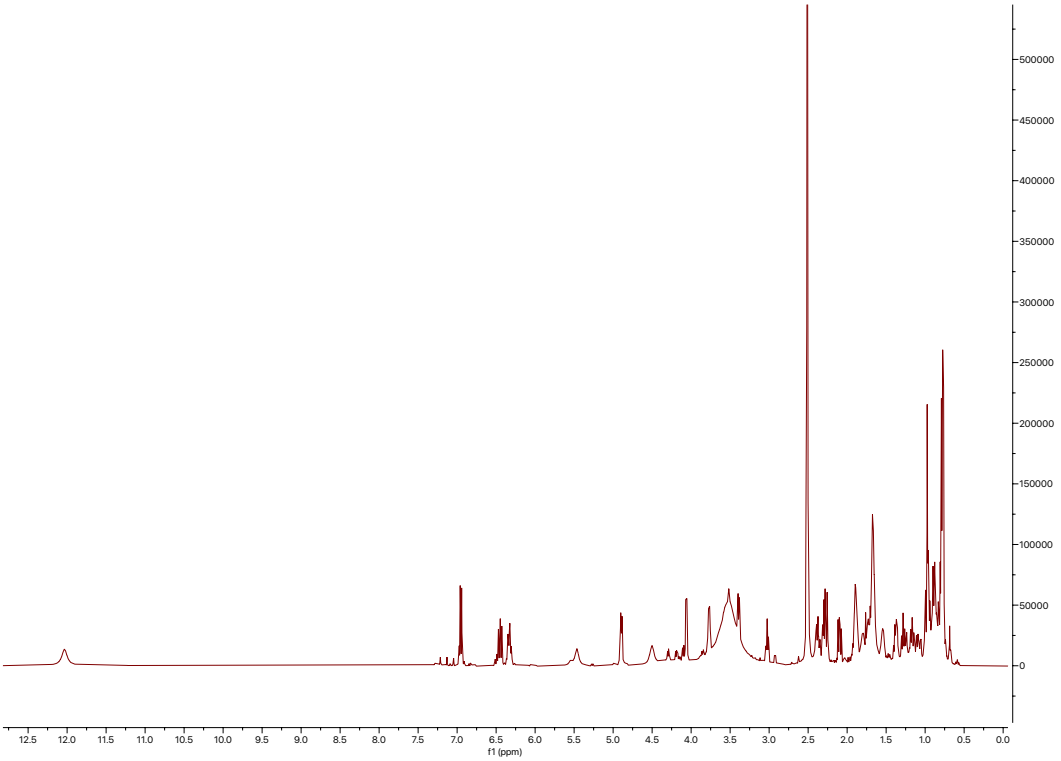

^{13}C spectrum of borrelidin J (**39**)

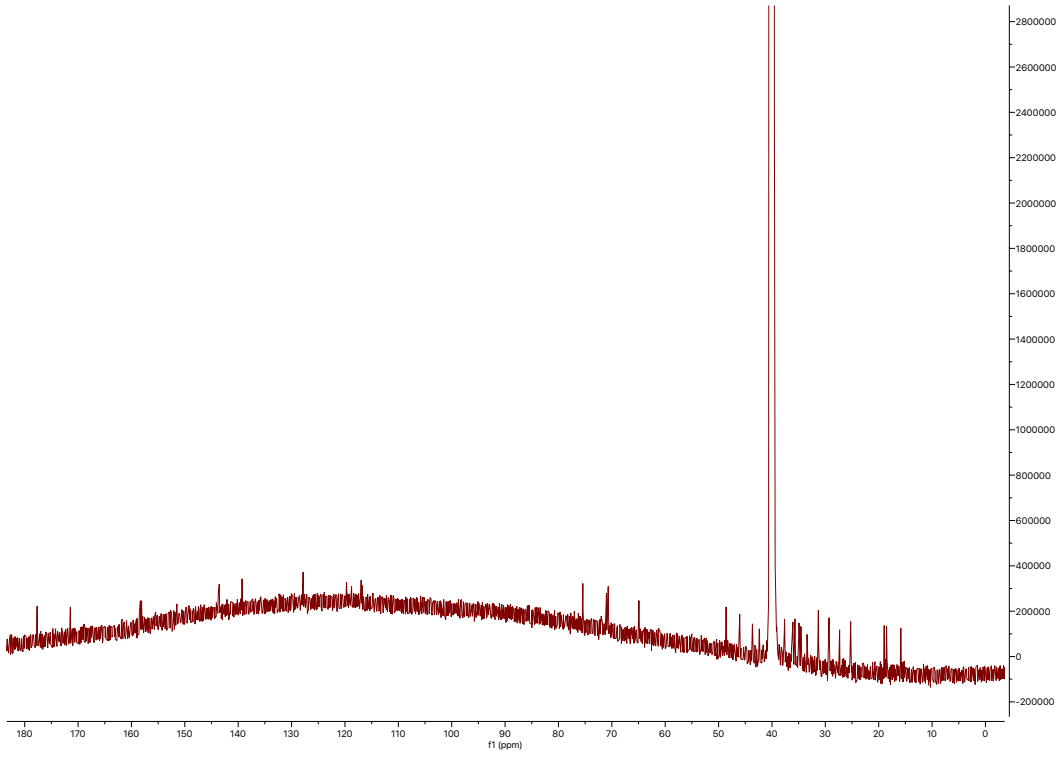

COSY spectrum of borrelidin J (**39**)

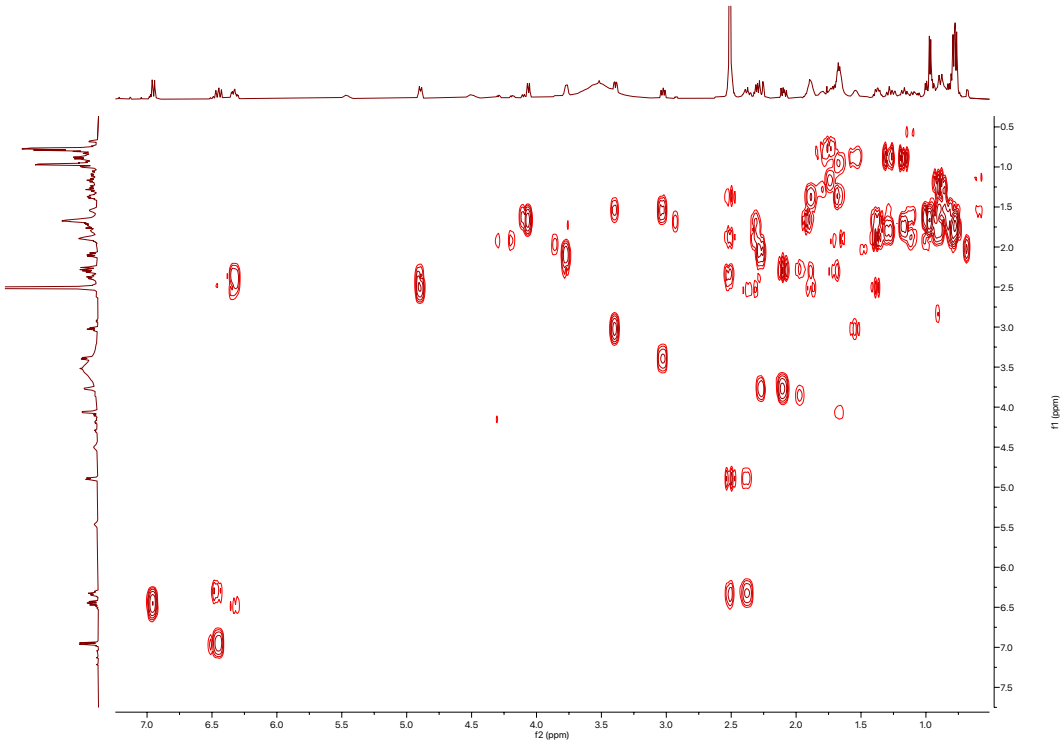

HSQC spectrum of borrelidin J (**39**)

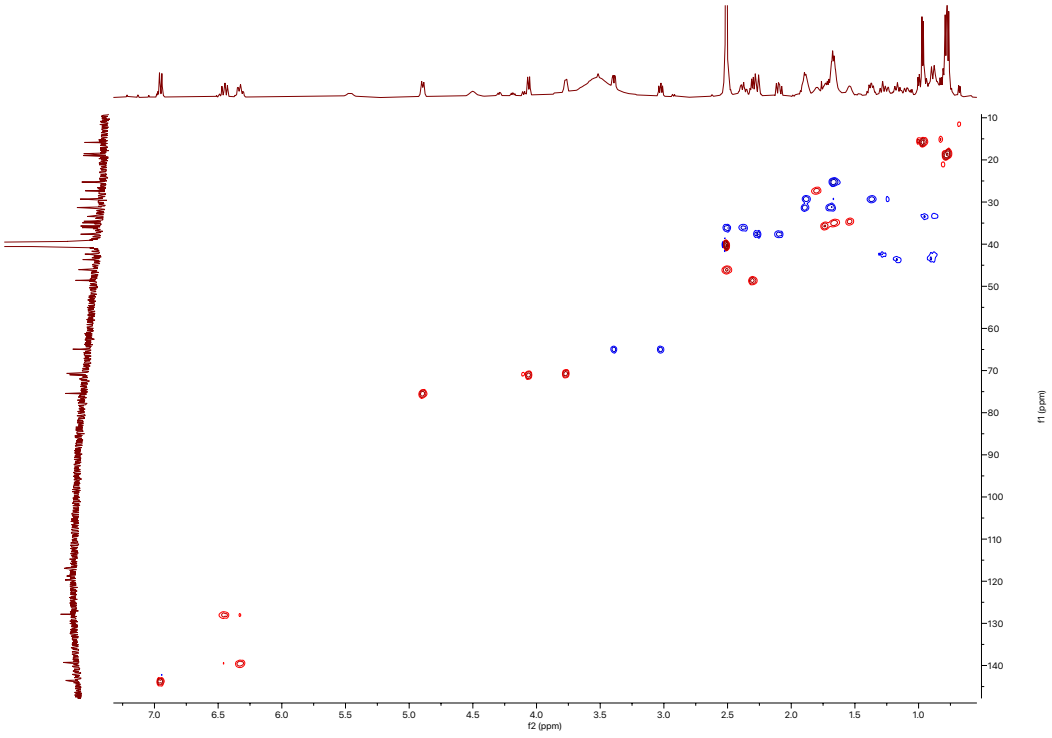

^{1}H-^{13}C HMBC spectrum of borrelidin J (**39**)

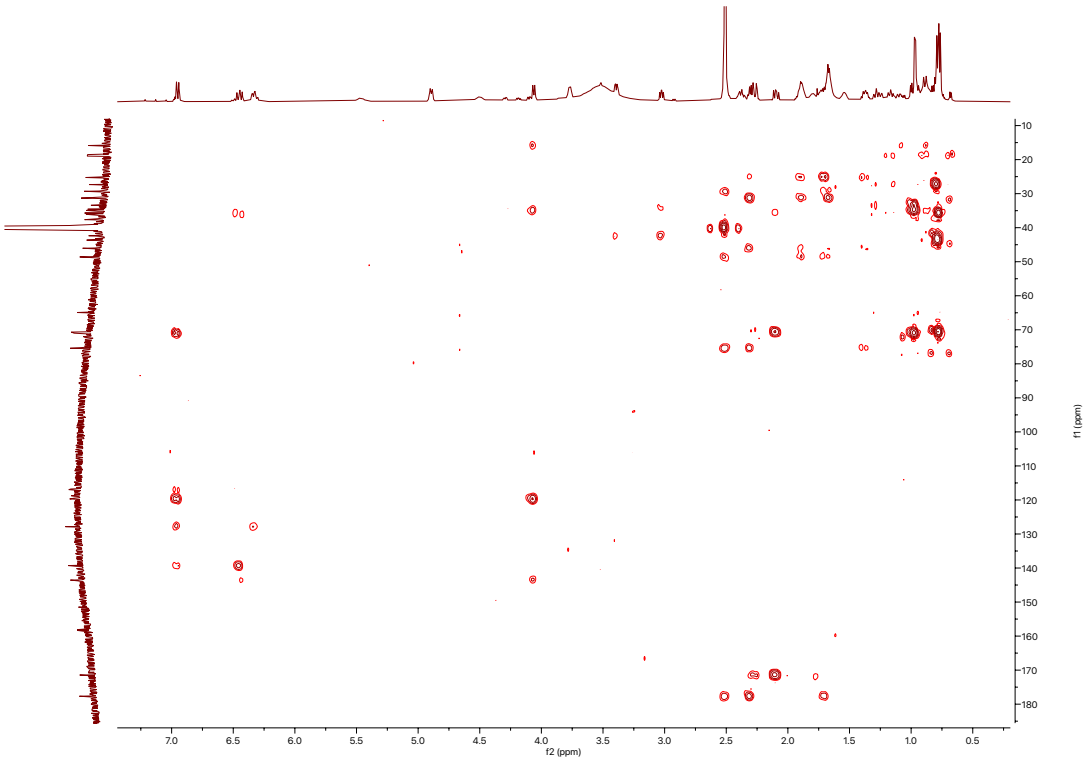

ROESY spectrum of borrelidin J (**39**)

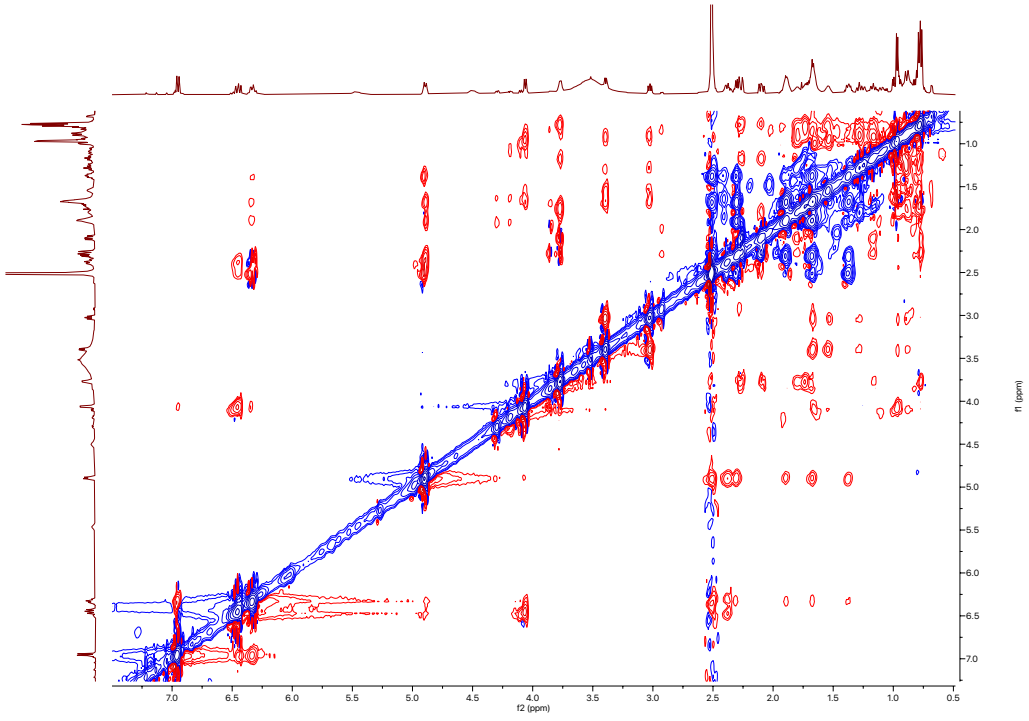

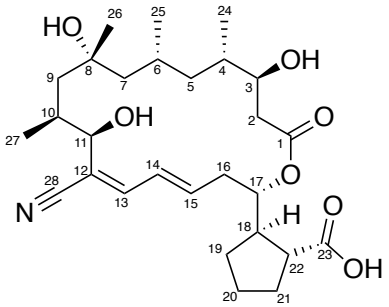

borrelidin K (**40**)

Position	δ_C (type)	δ_H, multiplets (*J* in Hz)	COSY	HMBC	ROESY
1	171.4 (C)				
2a	39.4 (CH_2)	2.15, dd (14.3, 8.4)	2b, 3	1, 3, 4	
2b	39.4 (CH_2)	2.30, dd (13.7, 4.7)	2a, 3		
3	70.7 (CH)	3.66, dt (8.5, 4.4)	2a, 2b, 4	5	
3-OH		4.46, br s			
4	36.4 (CH)	1.54, tt (7.4, 4.3)	3, 5a, 5b, 24		
5a	43.8 (CH_2)	0.76, m	4, 5b, 6		
5b	43.8 (CH_2)	1.28, m	4, 5a, 6	6, 24, 25	
6	27.8 (CH)	1.65, m	5a, 5b, 7a, 7b, 25		
7a	53.0 (CH_2)	1.20, td (13.5, 6.8)	6, 7b	8, 25, 26	
7b	53.0 (CH_2)	1.24, m	6, 7a	25, 26	
8	72.2 (C)				
8-OH		3.92, br s			
9a	42.8 (CH_2)	1.10, m	9b, 10	10, 27	
9b	42.8 (CH_2)	1.28, m	9a, 10	7, 8, 10, 27	
10	34.8 (CH)	1.78, td (7.3, 2.2)	9a, 9b, 11, 27	11	26
11	70.7 (CH)	4.15, d (8.4)	10	10, 13, 28	9a, 9b, 10, 27
11-OH		5.38, br s			
12	117.5 (C)				
13	143.6 (CH)	6.92, d (11.2)	14	11, 12, 14, 15, 28	
14	128.1 (CH)	6.48, dd (14.8, 11.3)	13, 15	12, 13, 15, 16	
15	139.1 (CH)	6.28, ddd (14.8, 9.1, 5.5)	14, 16a, 16b	13, 14, 16	
16	35.4 (CH_2)	2.47, m	15, 16b, 17	14, 15, 17	
17	75.6 (CH)	4.82, dt (10.2, 3.8)	16a, 16b	15	18, 19a, 19b, 20, 22
18	45.8 (CH)	2.52, m	19a, 19b, 22	16, 19, 22, 23	15, 17
19a	29.3 (CH_2)	1.36, dt (12.4, 8.5)	18, 19b, 20	17, 18, 20, 21	17
19b	29.3 (CH_2)	1.85, m	18, 19a, 20	17, 18, 20, 21, 22	17
20	25.3 (CH_2)	1.65, m	19a, 19b, 21a, 21b	18, 19, 20, 21	17
21a	31.3 (CH_2)	1.70, m	20, 21b, 22	18, 19, 20, 22, 23	
21b	31.3 (CH_2)	1.89, m	20, 21a, 22	18, 19, 20, 22, 23	
22	48.3 (CH)	2.33, q (7.8)	18, 21a, 21b	17, 18, 19, 20, 21, 23	17
23	177.7 (C)				
23-COOH		12.06, s			
24	17.3 (CH_3)	0.79, d (6.3)	4	3, 4	
25	22.5 (CH_3)	0.90, d (6.3)	6	5, 6, 7	
26	29.3 (CH_3)	1.06, s		7, 8, 9	10
27	18.1 (CH_3)	1.09, d (6.3)	10	9, 10, 11	
28	120.1 (C)				

^{1}H spectrum of borrelidin K (**40**)

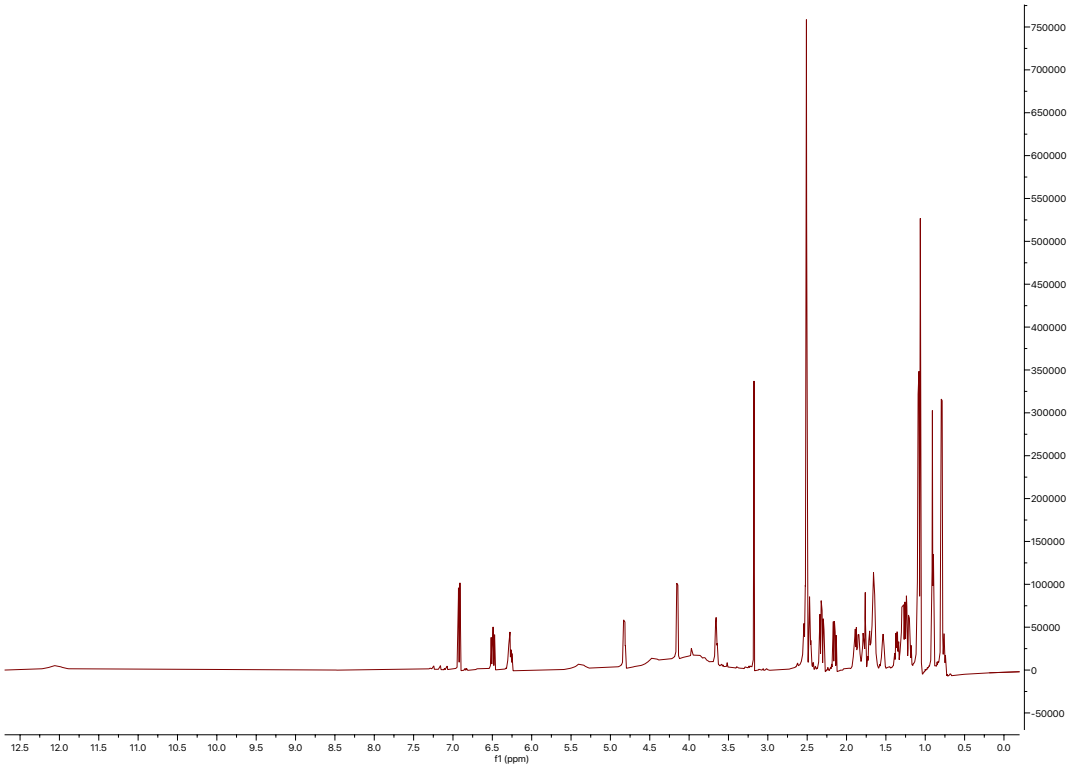

^{13}C spectrum of borrelidin K (**40**)

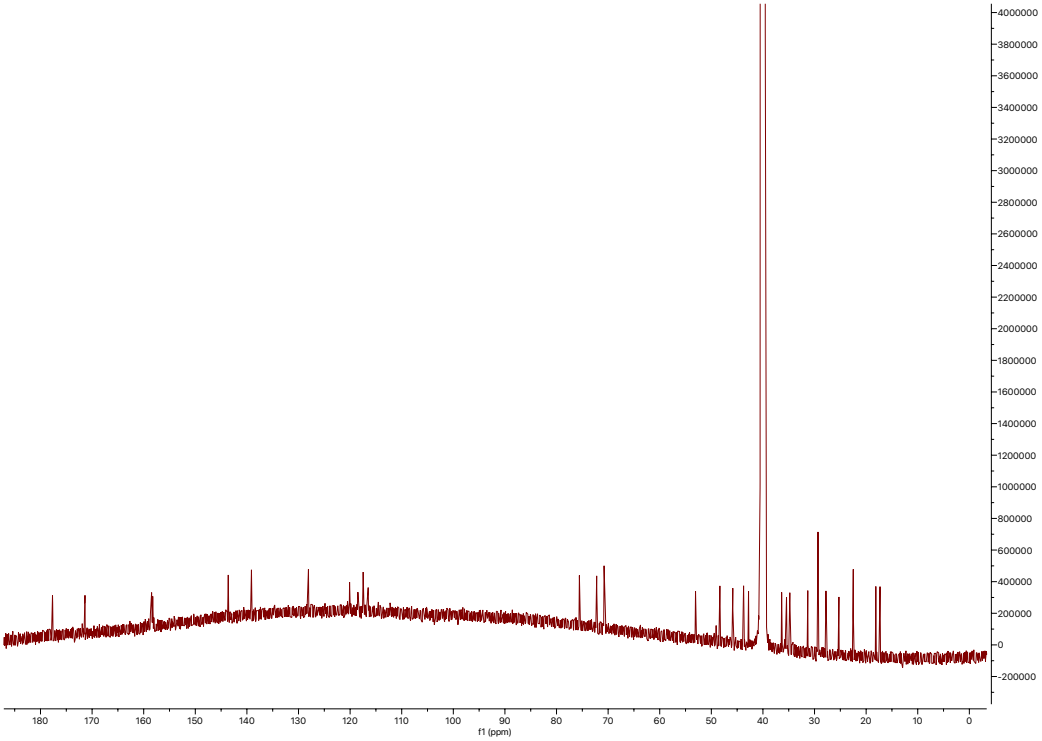

COSY spectrum of borrelidin K (**40**)

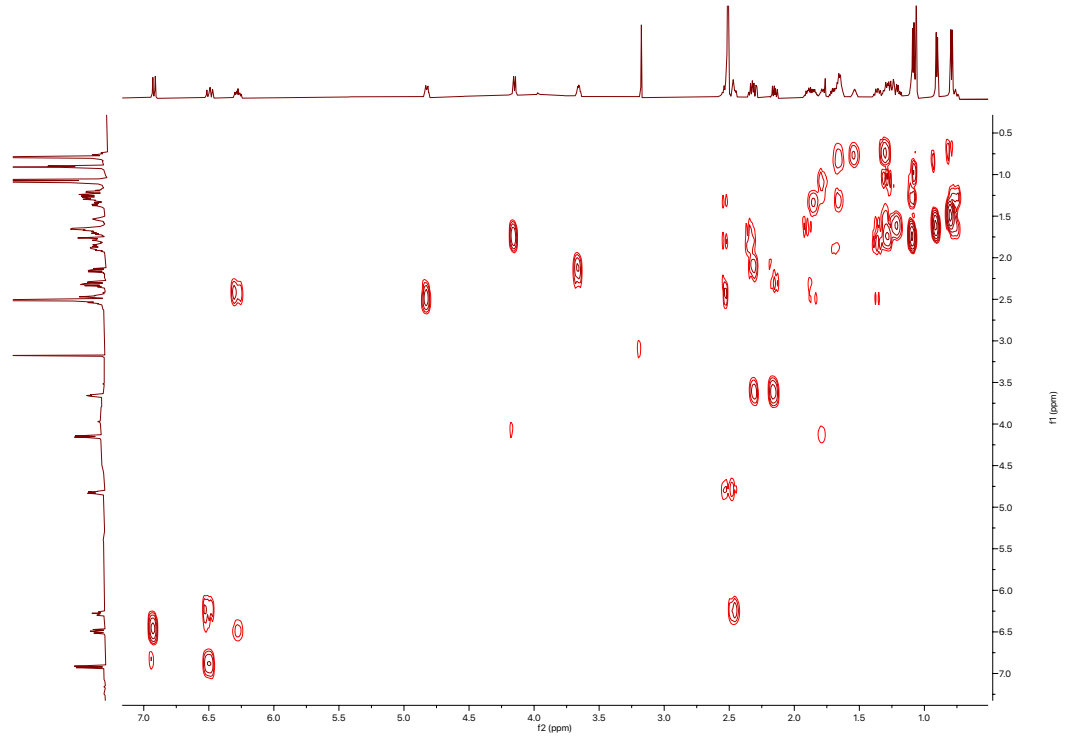

HSQC spectrum of borrelidin K (**40**)

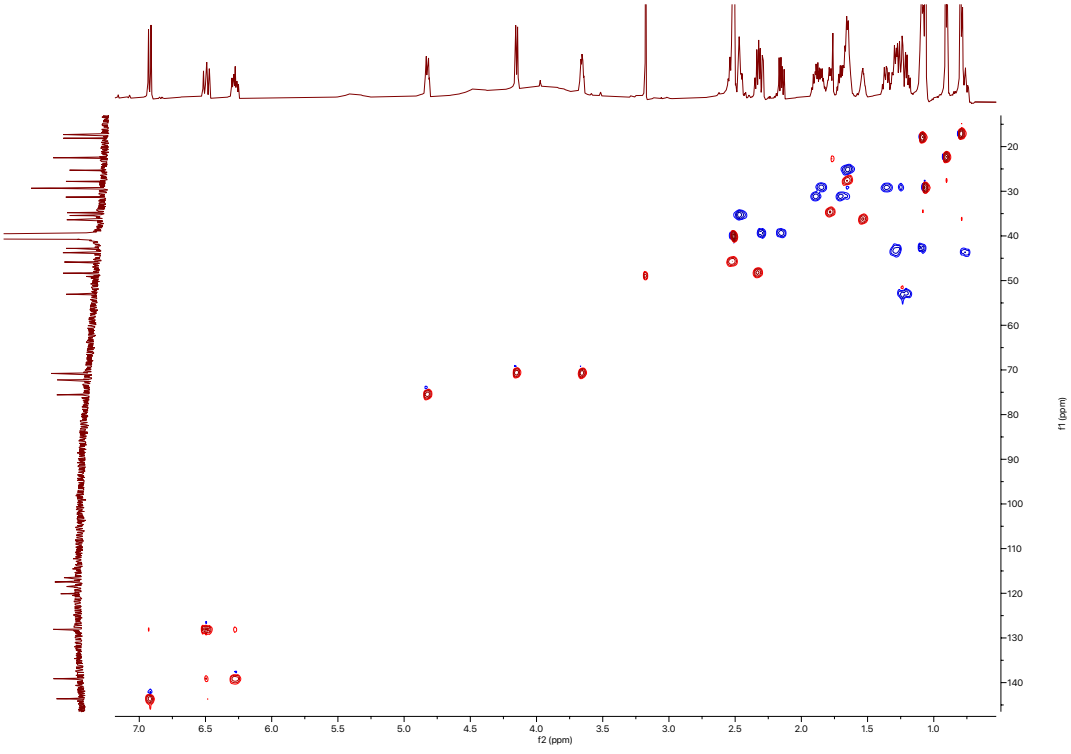

^{1}H-^{13}C HMBC spectrum of borrelidin K (**40**)

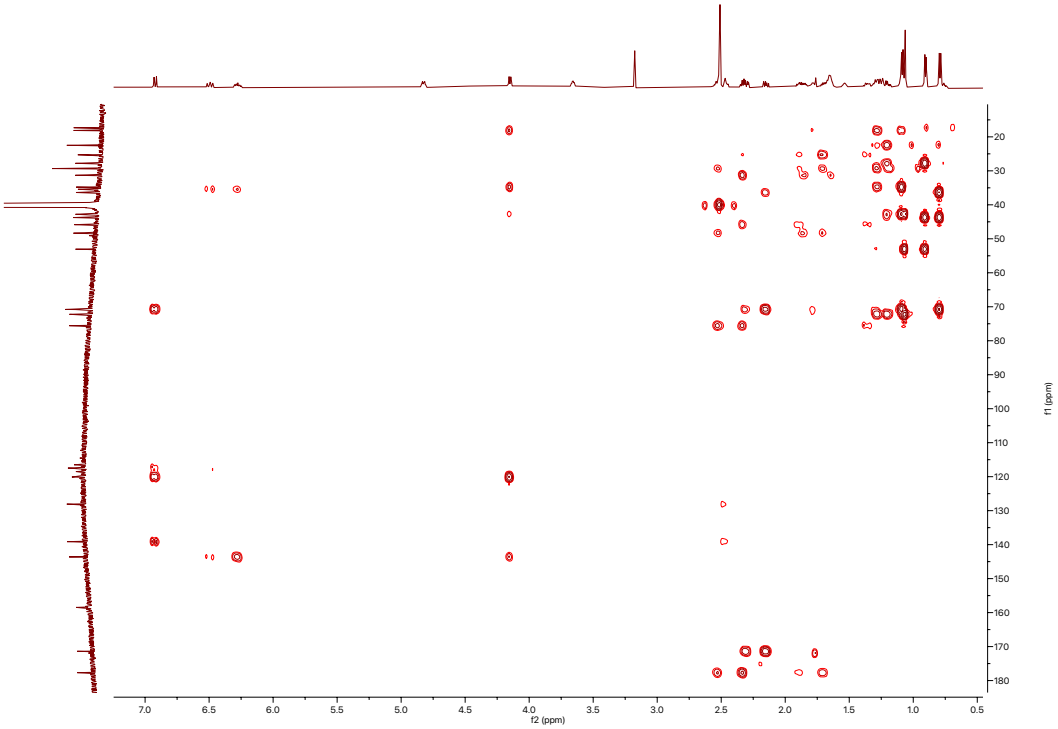

ROESY spectrum of borrelidin K (**40**)

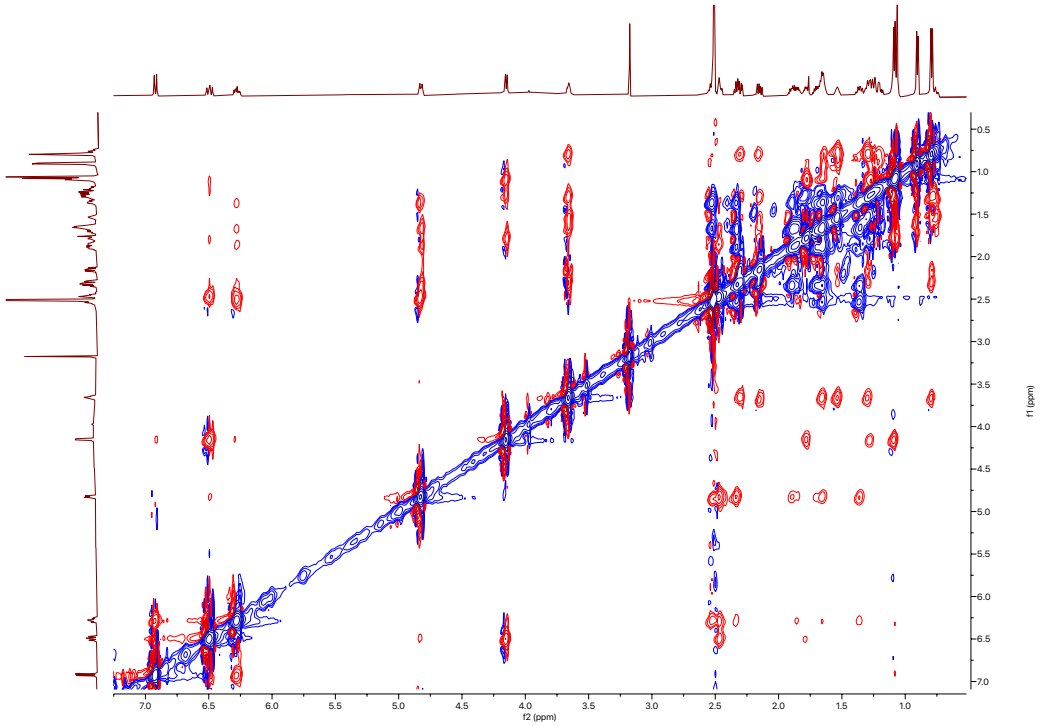

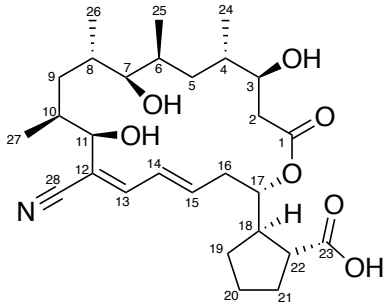

borrelidin P (**41**)

Position	δ_C (type)	δ_H, multiplets (*J* in Hz)	COSY	HMBC	ROESY
1	171.6 (C)				
2a	37.9 (CH_2)	2.11, dd (15.5, 9.2)	2b, 3	1, 3, 4	
2b	37.9 (CH_2)	2.27, dd (15.6, 3.9)			
3	70.2 (CH)	3.76, dt (9.2, 3.3)	2a, 2b, 4	24	2a, 2b, 4, 6
3-OH		4.37, s		2, 3, 4	2a, 3, 4
4	35.4 (CH)	1.70, m	3, 5a, 5b, 24		5a, 5b, 25
5a	40.4 (CH_2)	1.14, m	4, 5b, 6		
5b	40.4 (CH_2)	1.18, m	4, 5a, 6	6, 24, 25	
6	31.2 (CH)	1.98, p (7.0)	5a, 5b, 7, 25		2a, 3, 5b, 25
7	80.4 (CH)	2.75, dd (8.0, 3.0)	6, 8	8, 25, 26	5a, 5b, 6, 9a, 26
7-OH					
8	33.2 (CH)	1.45, dddd (12.2, 9.7, 6.3, 3.6)	7, 9a, 9b, 26		7a, 9b, 25
9a	35.5 (CH_2)	0.62, td (13.5, 2.3)	8, 9b, 10	8, 10, 27	
9b	35.5 (CH_2)	0.95, m	8, 9a, 10	7, 8, 10, 27	
10	34.9 (CH)	1.62, m	9a, 9b, 11, 27	11	7a, 9a, 26
11	71.1 (CH)	4.05, d (9.8)	10	10, 13, 28	7a, 9b, 10, 11-OH, 14
11-OH		5.48, br s		10, 12	7a, 10, 11
12	116.8 (C)				
13	143.9 (CH)	6.97, d (11.1)	14	11, 12, 14, 15, 28	15
14	127.8 (CH)	6.47, dd (14.4, 11.4)	13, 15	12, 13, 15, 16	
15	139.5 (CH)	6.32, ddd (14.8, 10.3, 4.4)	14, 16a, 16b	13, 14, 16	13
16a	35.9 (CH_2)	2.39, ddd (14.9, 10.4, 4.1)	15, 16b, 17	14, 15, 17	
16b	35.9 (CH_2)	2.51, m	15, 16a, 17	14, 15, 17	
17	75.5 (CH)	4.91, tt (10.6, 3.8)	16a, 16b	1, 15, 18, 22	16a, 18, 19a, 19b, 20, 22
18	46.1 (CH)	2.51, m	19a, 19b, 22	16, 19, 22, 23	15, 17, 19b
19a	29.3 (CH_2)	1.37, dq (12.4, 8.5)	18, 19b, 20	17, 18, 20, 21	
19b	29.3 (CH_2)	1.87, m	18, 19a, 20	17, 18, 20, 21, 22	
20	25.2 (CH_2)	1.67, m	19a, 19b, 21a, 21b	18, 19, 20, 21	
21a	31.2 (CH_2)	1.69, m	20, 21b, 22	18, 19, 20, 22, 23	
21b	31.2 (CH_2)	1.90, m	20, 21a, 22	22	
22	48.6 (CH)	2.31, q (8.0)	18, 21a, 21b	17, 18, 19, 20, 21, 23	17
23	177.7 (C)				
23-COOH		12.04, s			
24	18.3 (CH_3)	0.77, d, (6.9)	4	3, 4, 5	
25	11.2 (CH_3)	0.70, d (6.5)	6	5, 6, 7	
26	16.4 (CH_3)	0.84, d (6.3)	8	7, 8, 9	
27	15.4 (CH_3)	0.94, d (6.5)	10	9, 10, 11	9, 11
28	119.7 (C)				

^{1}H spectrum of borrelidin P (**41**)

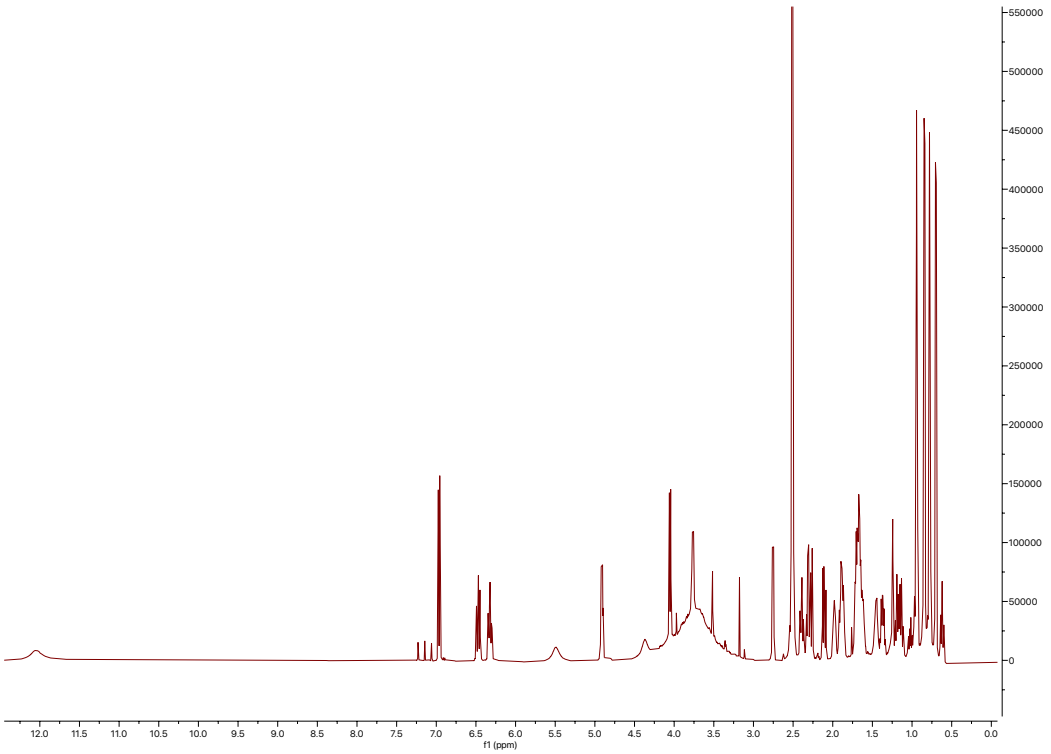

^{13}C spectrum of borrelidin P (**41**)

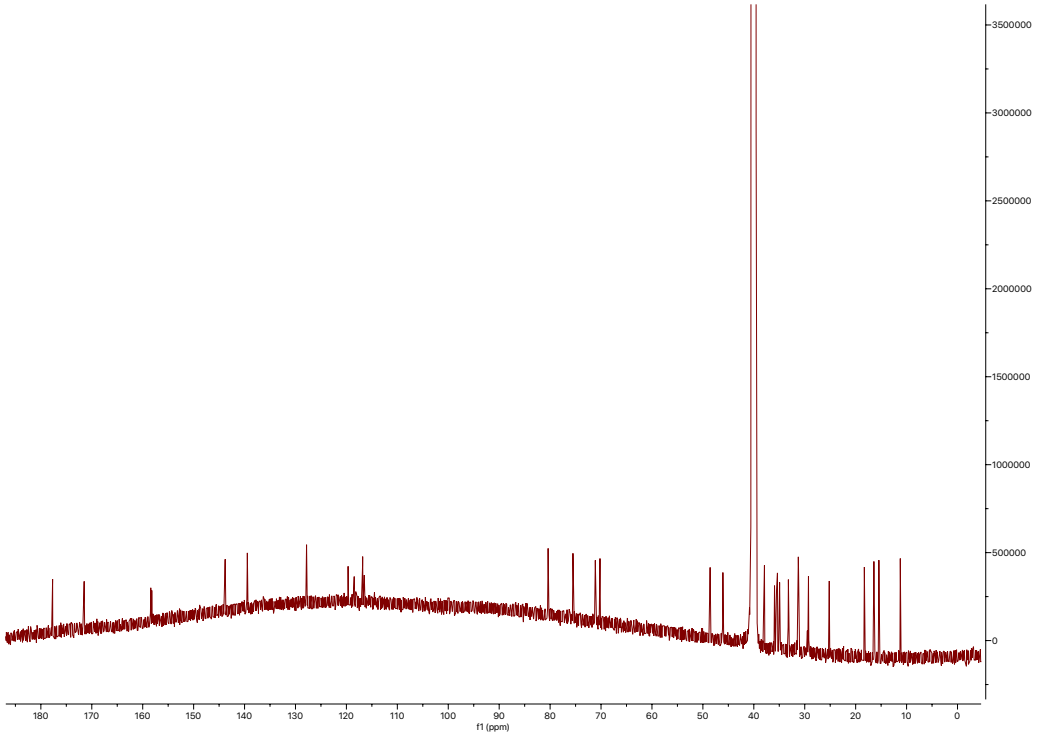

COSY spectrum of borrelidin P (**41**)

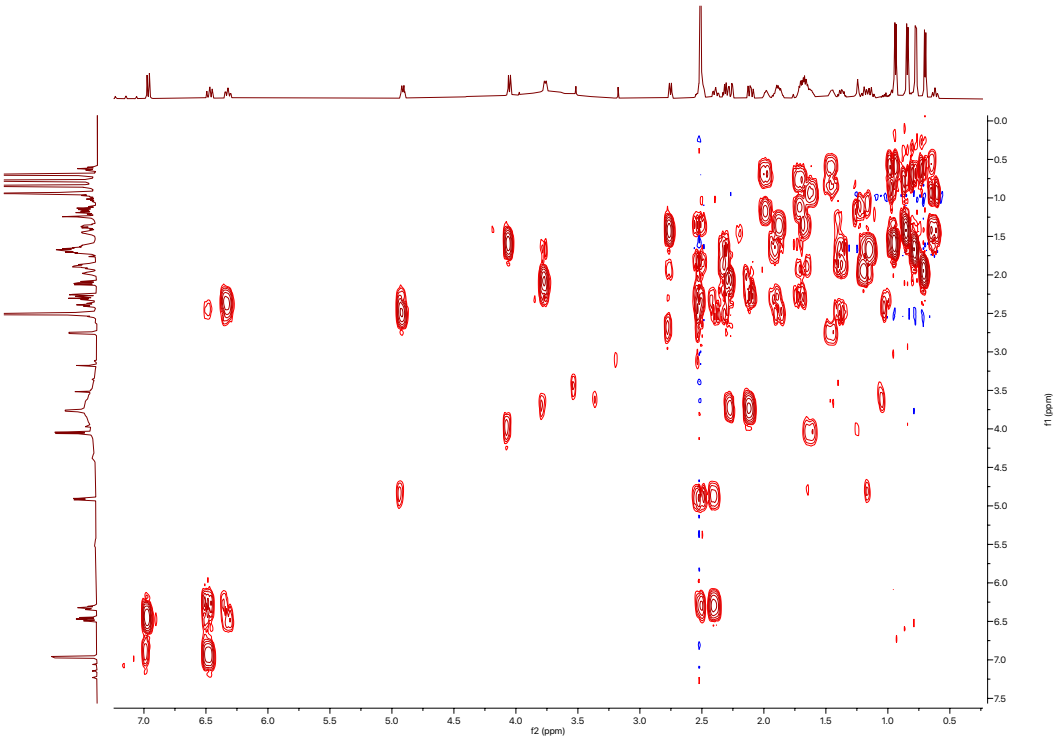

HSQC spectrum of borrelidin P (**41**)

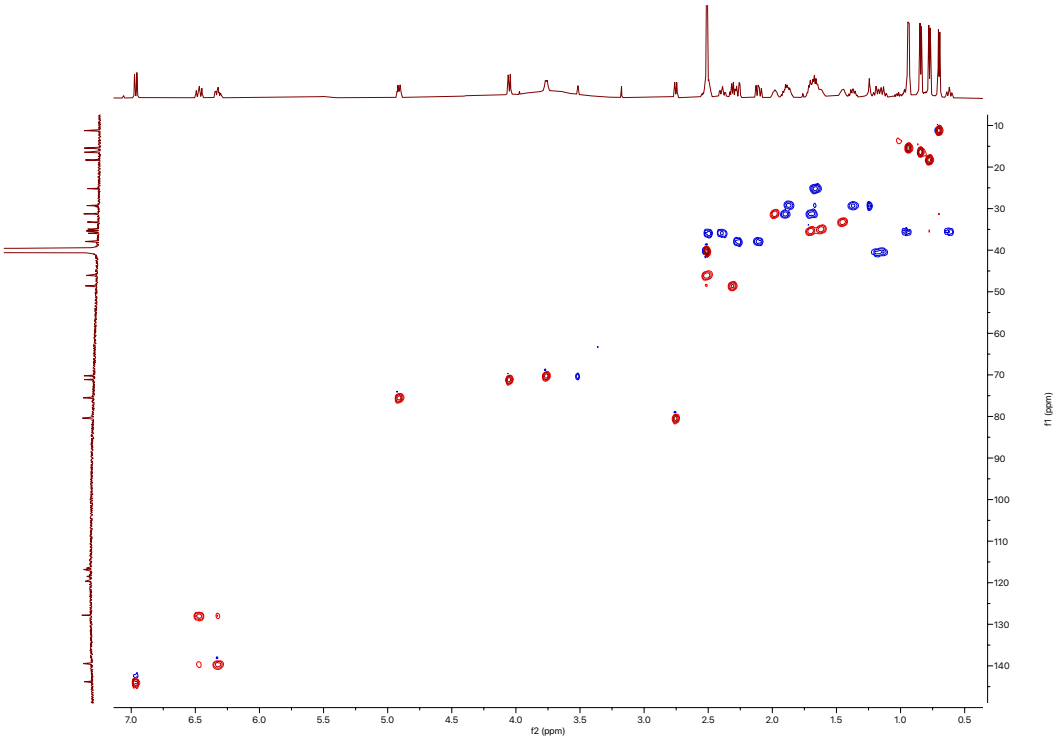

^{1}H-^{13}C HMBC spectrum of borrelidin P (**41**)

ROESY spectrum of borrelidin P (**41**)

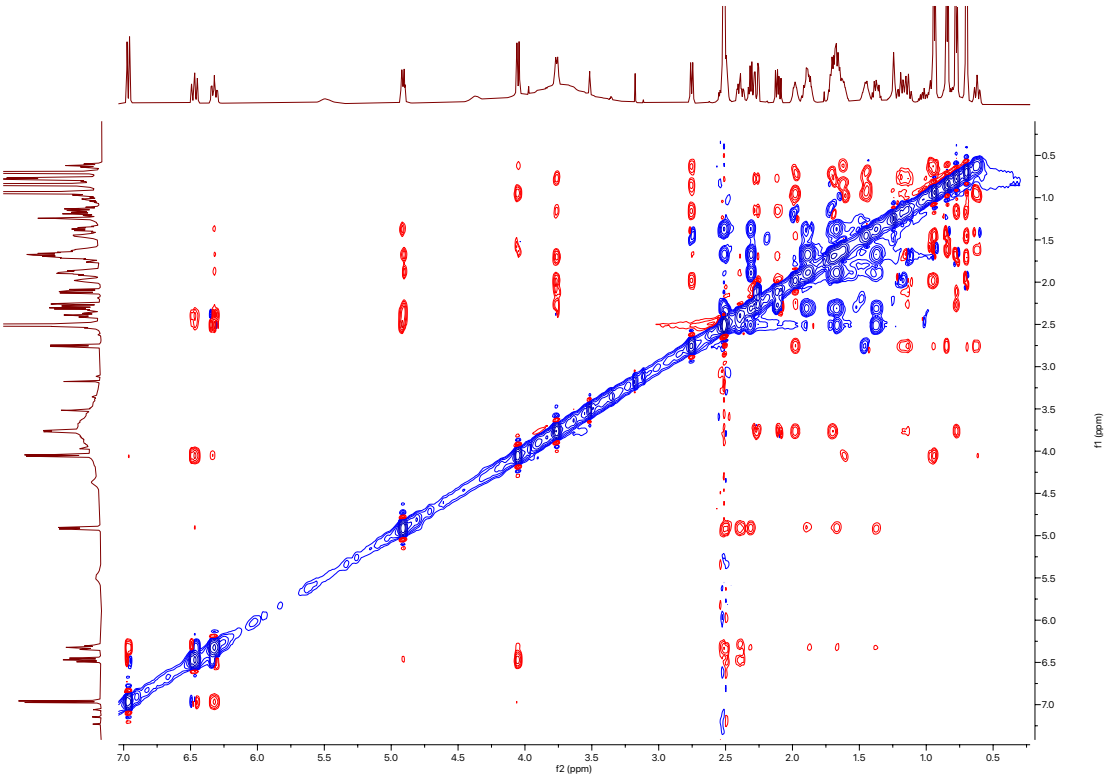

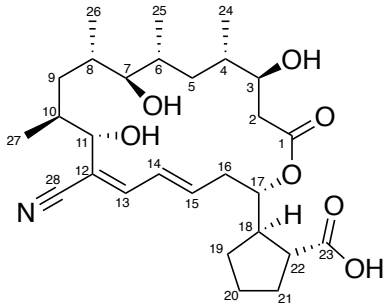

borrelidin Q (**42**)

Position	δ_C (type)	δ_H, multiplets (*J* in Hz)	COSY	HMBC	ROESY
1	172.6 (C)				
2	37.8 (CH_2)	2.25, m	2b, 3	1, 3, 4	
3	70.0 (CH)	3.74, t (6.5)	2a, 2b, 4	24	2a, 2b, 4, 6
3-OH		4.10, s		2, 3, 4	2a, 3, 4
4	34.9 (CH)	1.78, m	3, 5a, 5b, 24		5a, 5b, 25
5a	30.8 (CH_2)	0.64, m	4, 5b, 6		
5b	30.8 (CH_2)	1.13, dq (11.8, 7.7)	4, 5a, 6	6, 24, 25	
6	32.2 (CH)	1.73, m	5a, 5b, 7, 25		2a, 3, 5b, 25
7	79.2 (CH)	2.91, dd (8.0, 3.0)	6, 8	8, 25, 26	5a, 6, 8, 25, 26
7-OH		4.27, s			
8	31.2 (CH)	1.67, m	7, 9a, 9b, 26		7a, 9b, 25
9a	37.0 (CH_2)	0.67, m	8, 9b, 10	8, 10, 27	
9b	37.0 (CH_2)	1.78, m	8, 9a, 10	7, 8, 10, 27	
10	34.9 (CH)	1.57, m	9a, 9b, 11, 27	11	7a, 9a, 26
11	78.1 (CH)	3.67, d (8.6)	10	10, 13, 28	7a, 9b, 10, 14
11-OH		5.47, br s		10, 12	7a, 10, 11
12	115.8 (C)				
13	144.4 (CH)	6.75, d (11.0)	14	11, 12, 14, 15, 28	15
14	128.7 (CH)	6.37, dd (14.9, 11.1)	13, 15	12, 13, 15, 16	
15	134.0 (CH)	6.00, ddd (14.8, 10.1, 4.5)	14, 16a, 16b	13, 14, 16	13
16a	37.5 (CH_2)	2.36, m	15, 16b, 17	14, 15, 17	
16b	37.5 (CH_2)	2.60, dd (16.1, 3.8)	15, 16a, 17	14, 15, 17	
17	75.2 (CH)	5.01, tt (7.8, 3.1)	16a, 16b	1, 15, 18, 22	16a, 18, 19a, 19b, 20, 22
18	47.3 (CH)	2.39, m	19a, 19b, 22	16, 19, 22, 23	15, 17, 19b
19a	29.3 (CH_2)	1.37, dq (11.8, 7.7)	18, 19b, 20	17, 18, 20, 21	
19b	29.3 (CH_2)	1.80, m	18, 19a, 20	17, 18, 20, 21, 22	
20	25.2 (CH_2)	1.62, m	19a, 19b, 21a, 21b	18, 19, 20, 21	
21a	31.3 (CH_2)	1.68, m	20, 21b, 22	18, 19, 20, 22, 23	
21b	31.3 (CH_2)	1.87, dq (13.5, 6.8)	20, 21a, 22	22	
22	48.6 (CH)	2.39, m	18, 21a, 21b	17, 18, 19, 20, 21, 23	17
23	177.7 (C)				
23-COOH		12.04, s			
24	17.7 (CH_3)	0.76, d, (5.6)	4	3, 4, 5	
25	17.2 (CH_3)	0.73, d (6.5)	6	5, 6, 7	
26	16.3 (CH_3)	0.84, d (6.8)	8	7, 8, 9	
27	16.0 (CH_3)	0.90, d (6.4)	10	9, 10, 11	9, 11
28	117.2 (C)				

^{1}H spectrum of borrelidin Q (**42**)

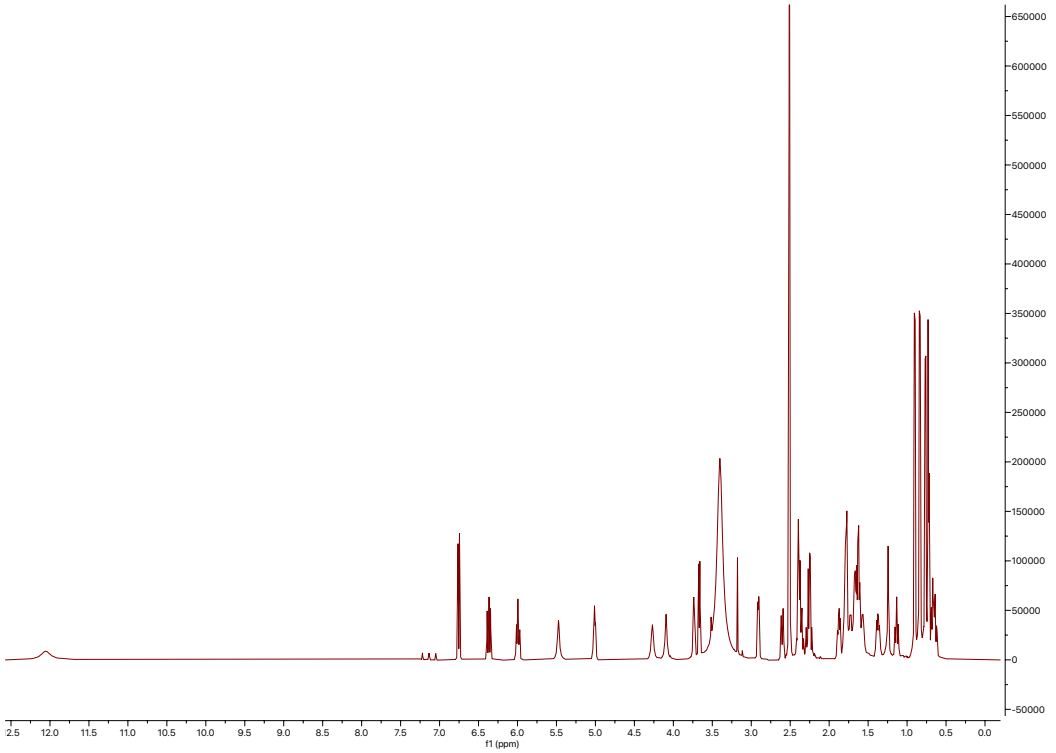

^{13}C spectrum of borrelidin Q (**42**)

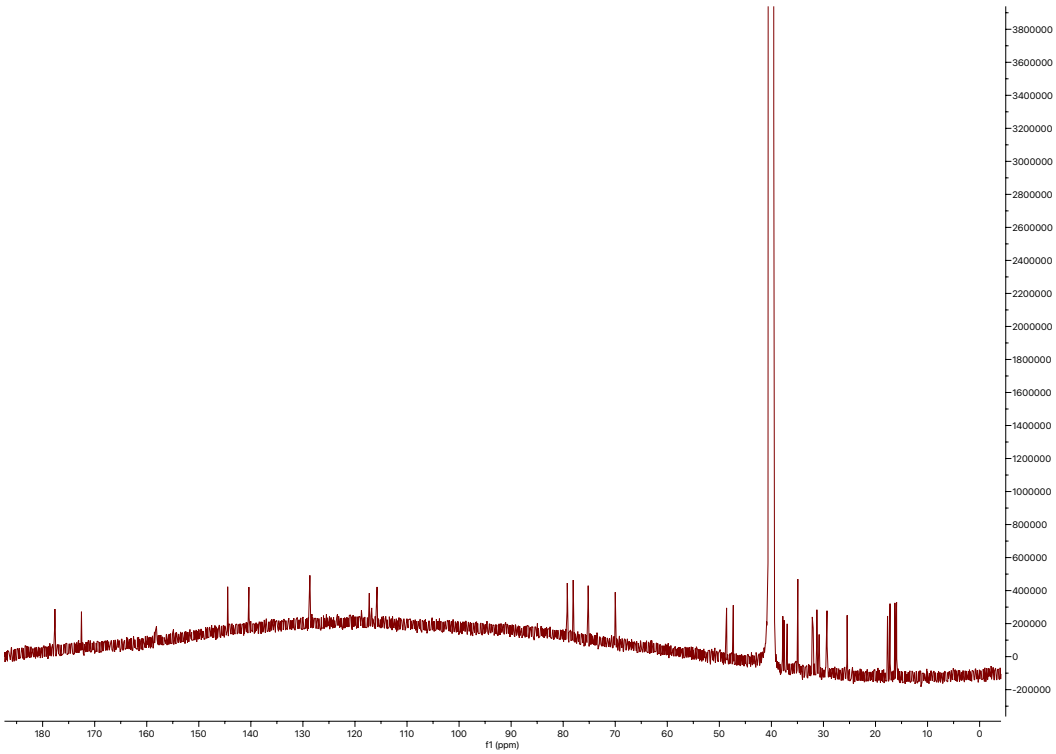

COSY spectrum of borrelidin Q (**42**)

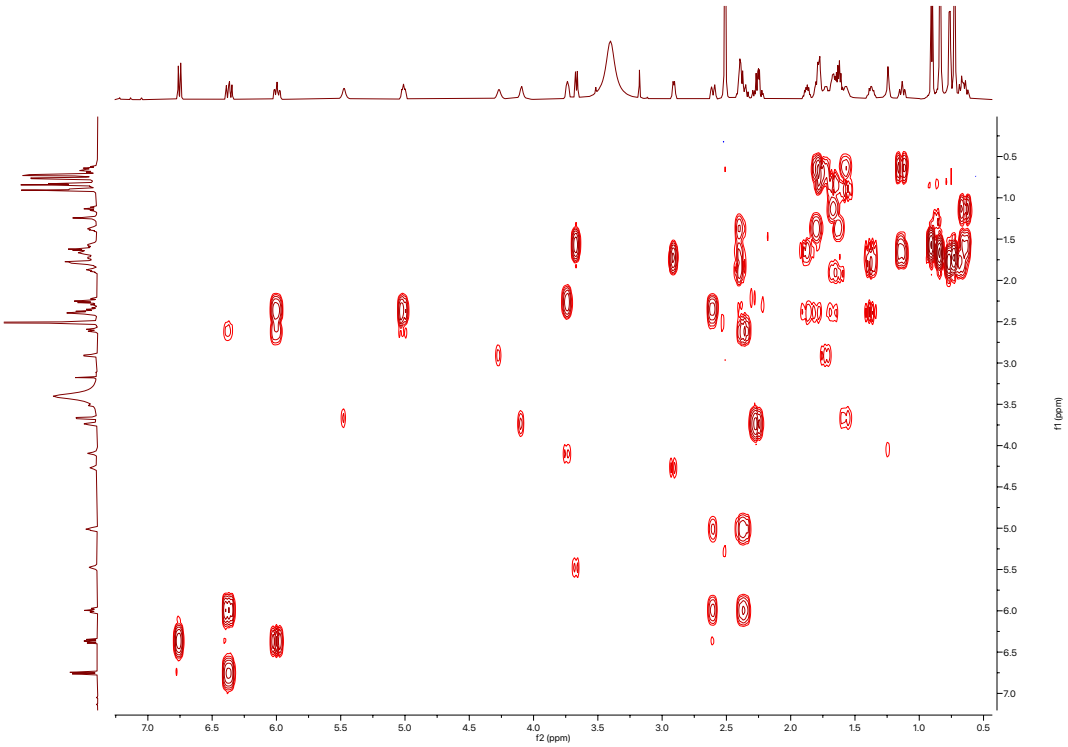

HSQC spectrum of borrelidin Q (**42**)

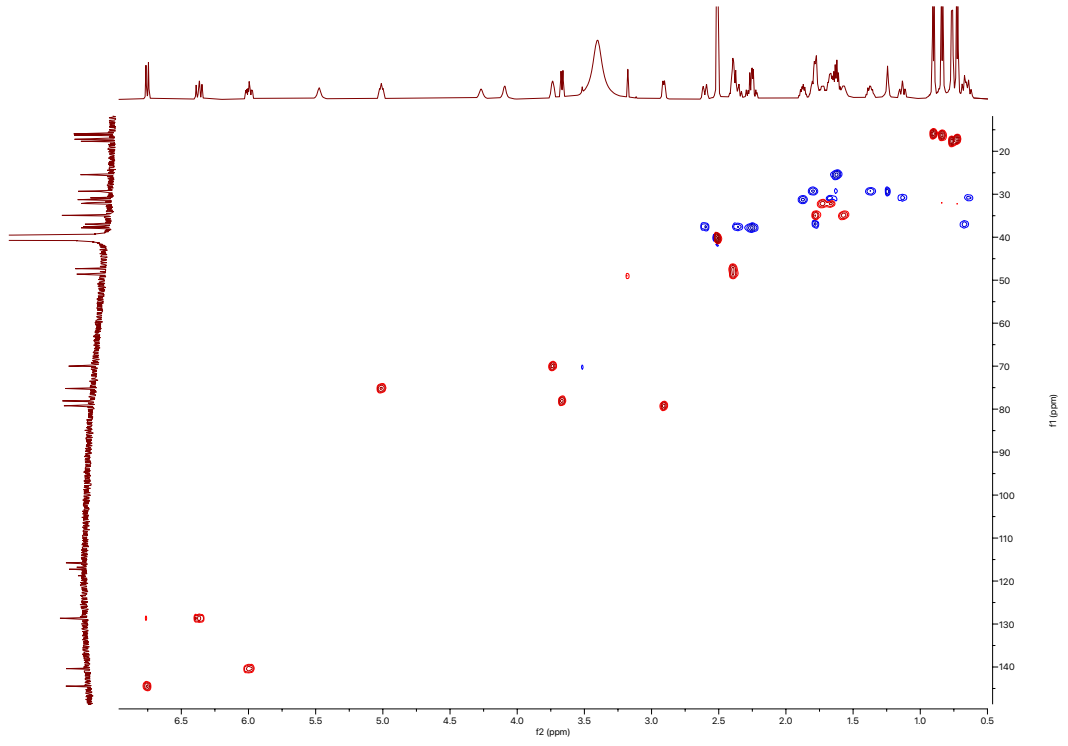

^{1}H-^{13}C HMBC spectrum of borrelidin Q (**42**)

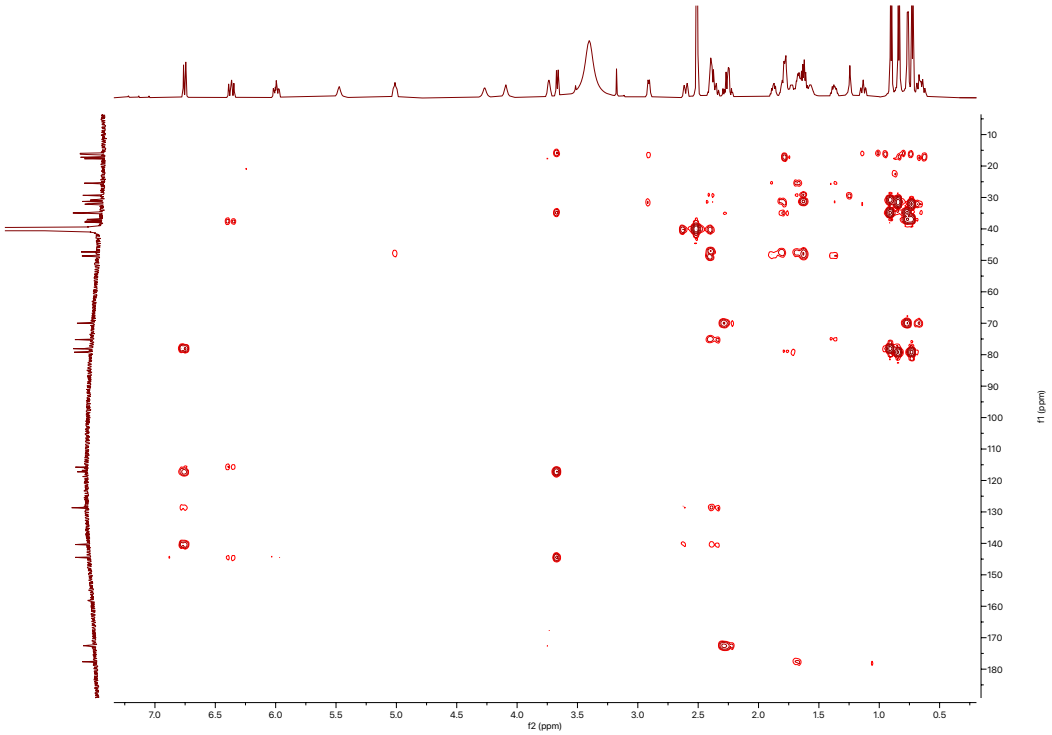

ROESY spectrum of borrelidin Q (**42**)

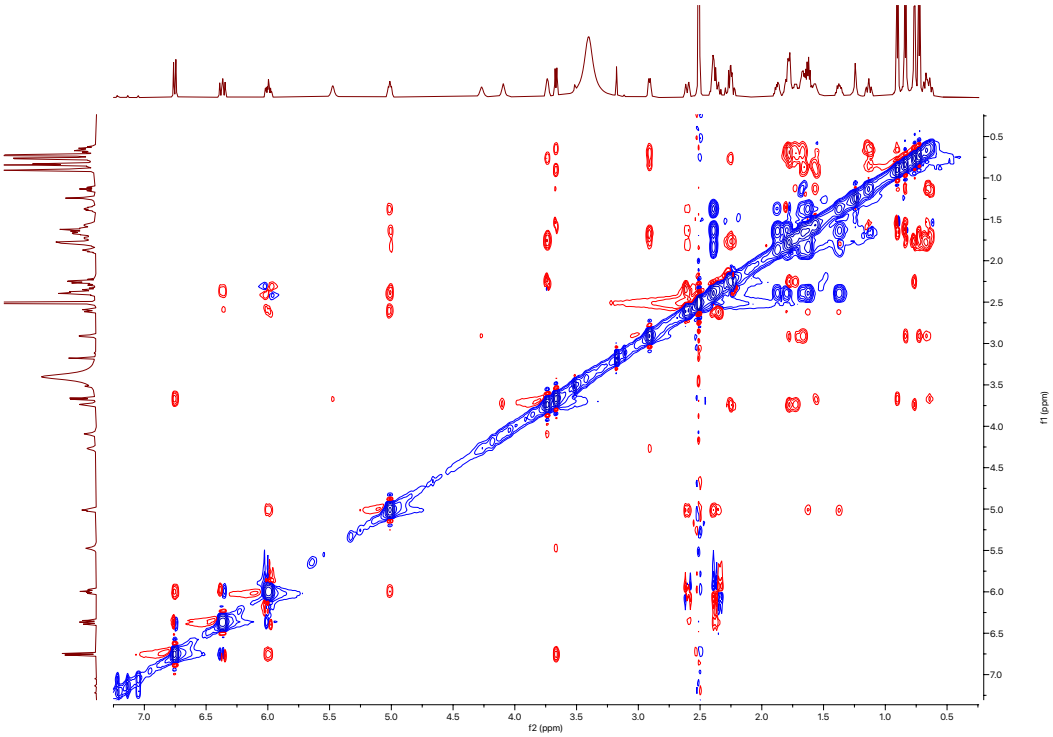

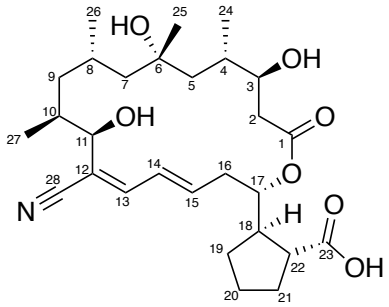

borrelidin R (**43**)

Position	δ_C (type)	δ_H, multiplets (*J* in Hz)	COSY	HMBC	ROESY
1	171.4 (C)				
2	38.9 (CH_2)	2.32, m	2a, 3	1, 3, 4	24
3	71.2 (CH)	3.73, td (6.4, 3.9)	2a, 2b, 4		
3-OH		4.74, br s			
4	33.1 (CH)	1.87, m	3, 5a, 5b, 24	6, 24, 25	5a, 5b, 25
5a	46.7 (CH_2)	1.07, m	4, 5b	4, 24	
5b	46.7 (CH_2)	1.58, dd (14.1, 6.1)	4, 5a	4, 24	
6	71.2 (C)				
6-OH		4.14, br s			
7a	50.5 (CH_2)	1.33, m	7b, 8		
7b	50.5 (CH_2)	1.45, dd (14.6, 5.1)	7a, 8	8, 9, 25, 26	
8	25.2 (C)	1.87, m	7a, 7b, 9a, 9b, 26		7a, 9b, 25
9a	41.8 (CH_2)	1.11, m	8, 9b, 10	8, 10, 27	
9b	41.8 (CH_2)	1.15, t (7.1)	8, 9a, 10	7, 8, 10, 27	
10	35.6 (CH)	1.66, dt (13.7, 7.4)	9a, 9b, 11, 27	9	
11	68.8 (CH)	4.28, d (6.5)	10	10, 13, 27, 28	
11-OH		5.39, br s			
12	117.5 (C)				
13	143.3 (CH)	6.89, d (11.3)	14	11, 12, 14, 15, 28	15
14	128.0 (CH)	6.50, dd (14.8, 11.4)	13, 15	12, 13, 15, 16	
15	139.5 (CH)	6.26, dt (14.9, 7.4)	14, 16a, 16b	13, 14, 16	13
16	36.1 (CH_2)	2.43, dd (7.6, 4.0)	15, 16b, 17	14, 15, 17	
17	75.5 (CH)	4.88, dq (9.9, 6.0, 5.0)	15, 17	15	18, 19a, 19b, 20, 22
18	46.1 (CH)	2.48, m	19a, 19b, 22	16, 19, 22, 23	15, 17
19a	29.2 (CH_2)	1.36, dt (12.3, 8.4)	18, 19b, 20	17, 18, 20, 21	17
19b	29.2 (CH_2)	1.88, m	18, 19a, 20	17, 18, 20, 21, 22	17
20	25.4 (CH_2)	1.65, m	19a, 19b, 21a, 21b	18, 19, 20, 21	17
21a	31.4 (CH_2)	1.68, m	20, 21b, 22	18, 19, 20, 22, 23	
21b	31.4 (CH_2)	1.89, m	20, 21a, 22	18, 19, 20, 22, 23	
22	48.2 (CH)	2.33, m	18, 21a, 21b	17, 18, 19, 20, 21, 23	17
23	177.6 (C)				
23-COOH		12.02, s			
24	17.9 (CH_3)	0.84, d (6.3)	4	3, 4	2
25	29.3 (CH_3)	1.10, s		5, 6, 7	
26	22.9 (CH_3)	0.86, d, (6.3)	8	7, 8, 9	
27	15.4 (CH_3)	0.92, d (6.3)	10	9, 10, 11	
28	120.3 (C)				

^{1}H spectrum of borrelidin R (**43**)

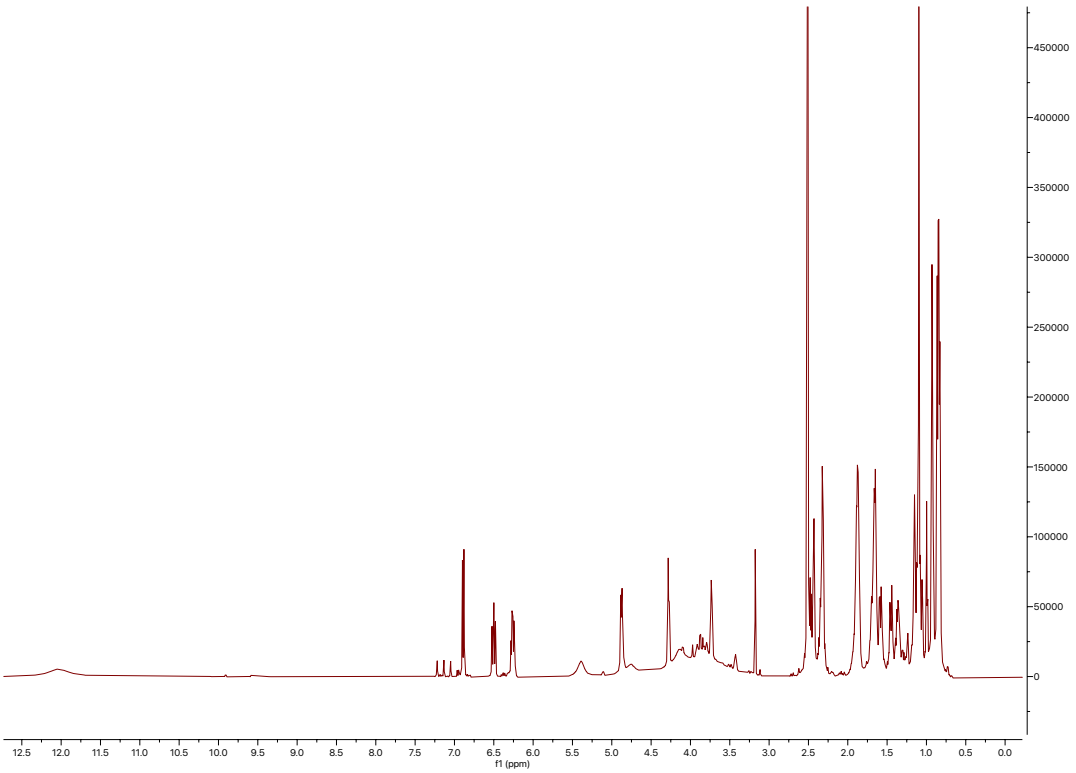

^{13}C spectrum of borrelidin R (**43**)

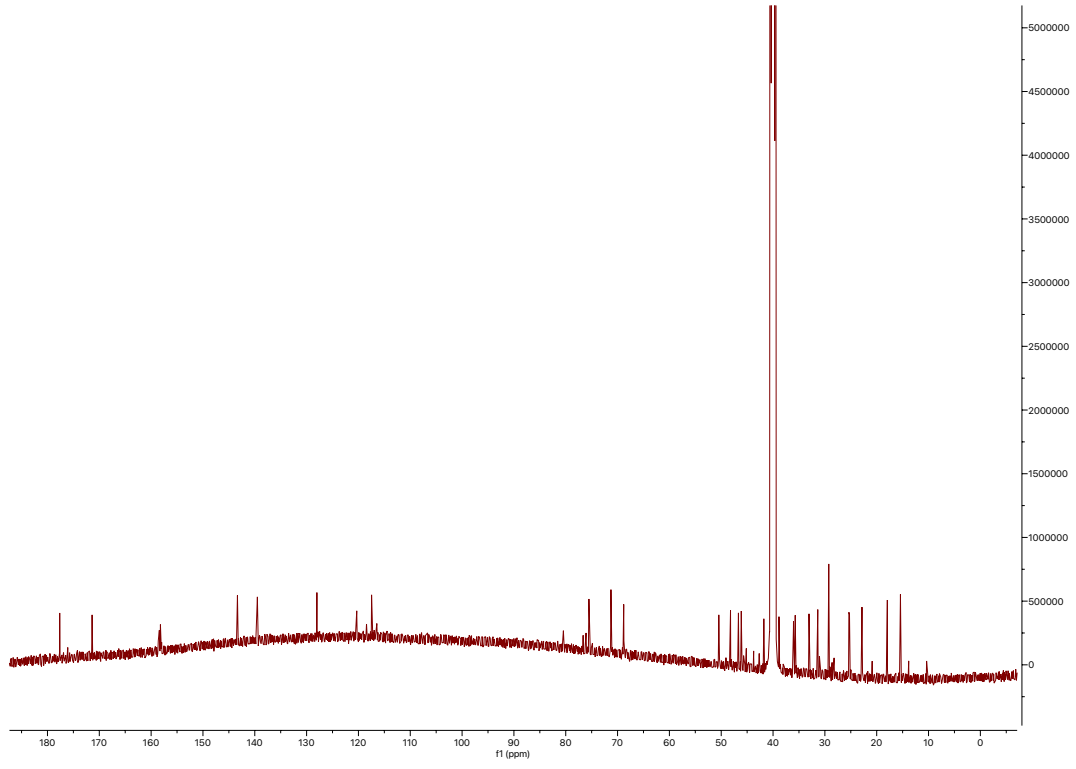

COSY spectrum of borrelidin R (**43**)

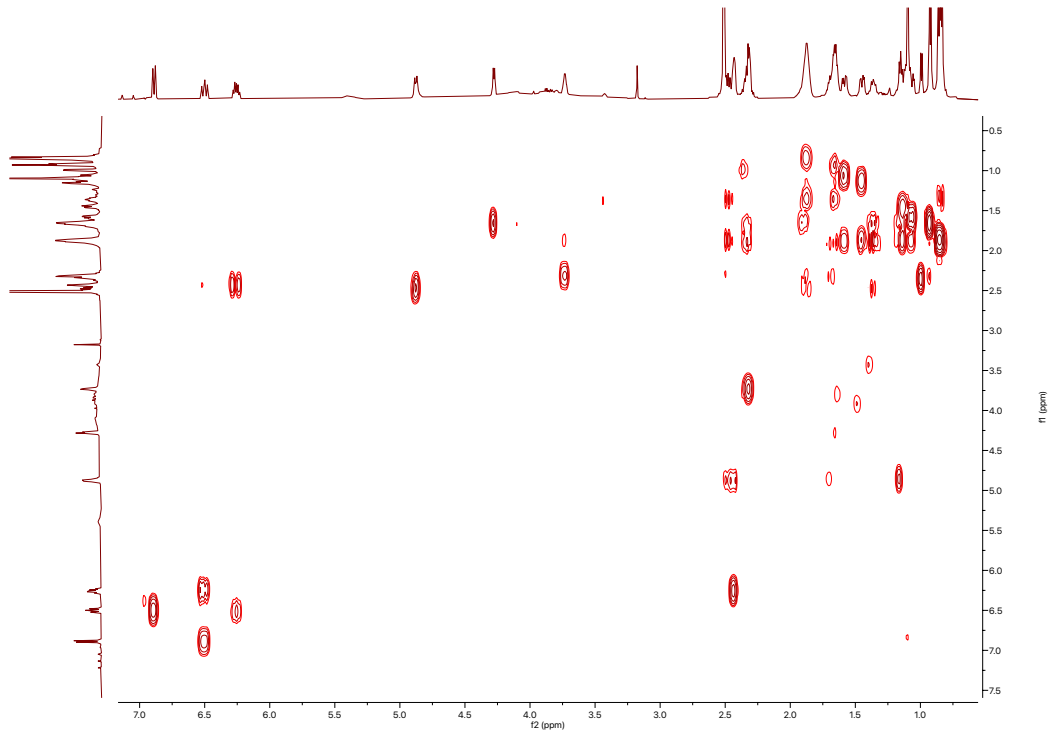

HSQC spectrum of borrelidin R (**43**)

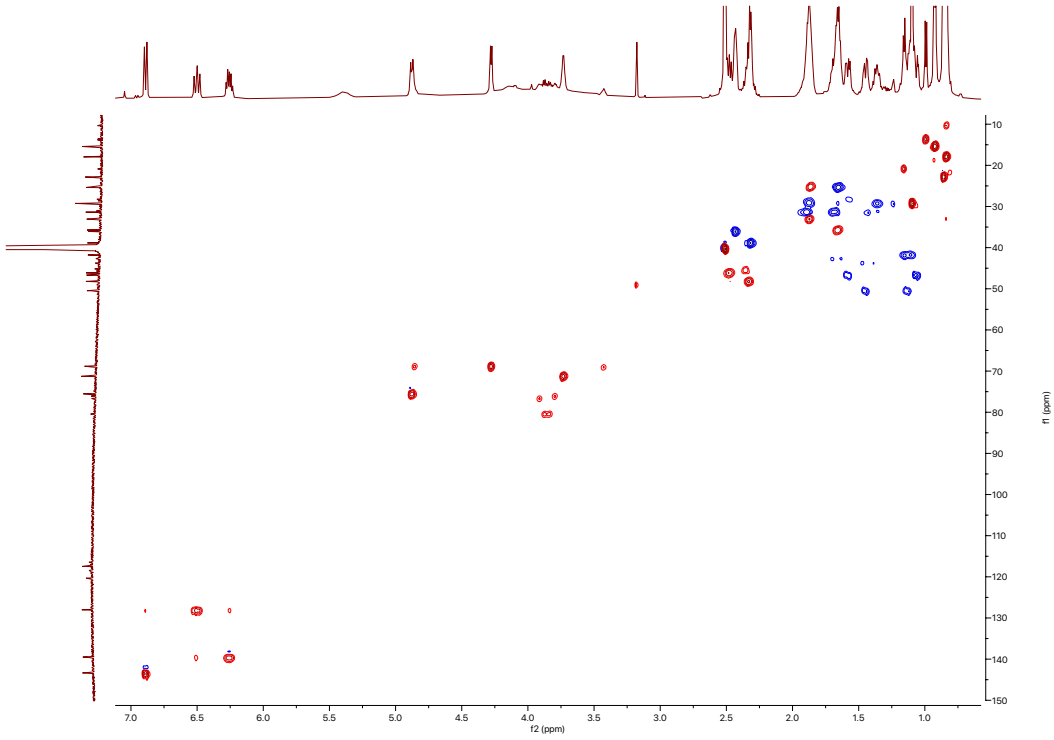

^{1}H-^{13}C HMBC spectrum of borrelidin R (**43**)

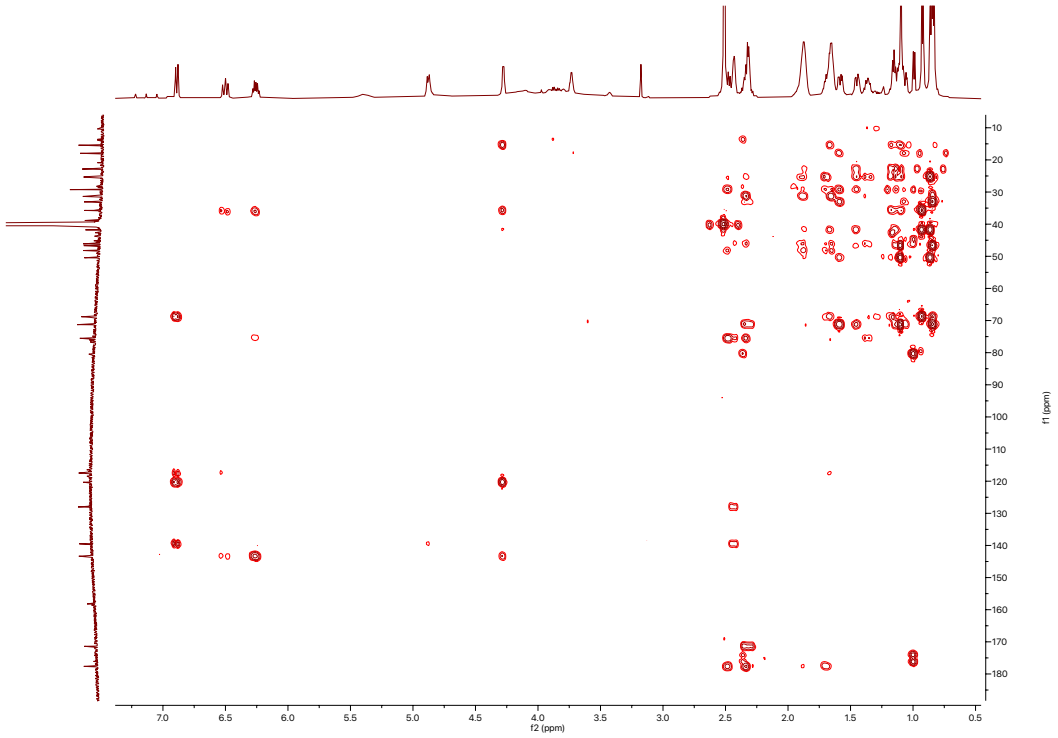

ROESY spectrum of borrelidin R (**43**)

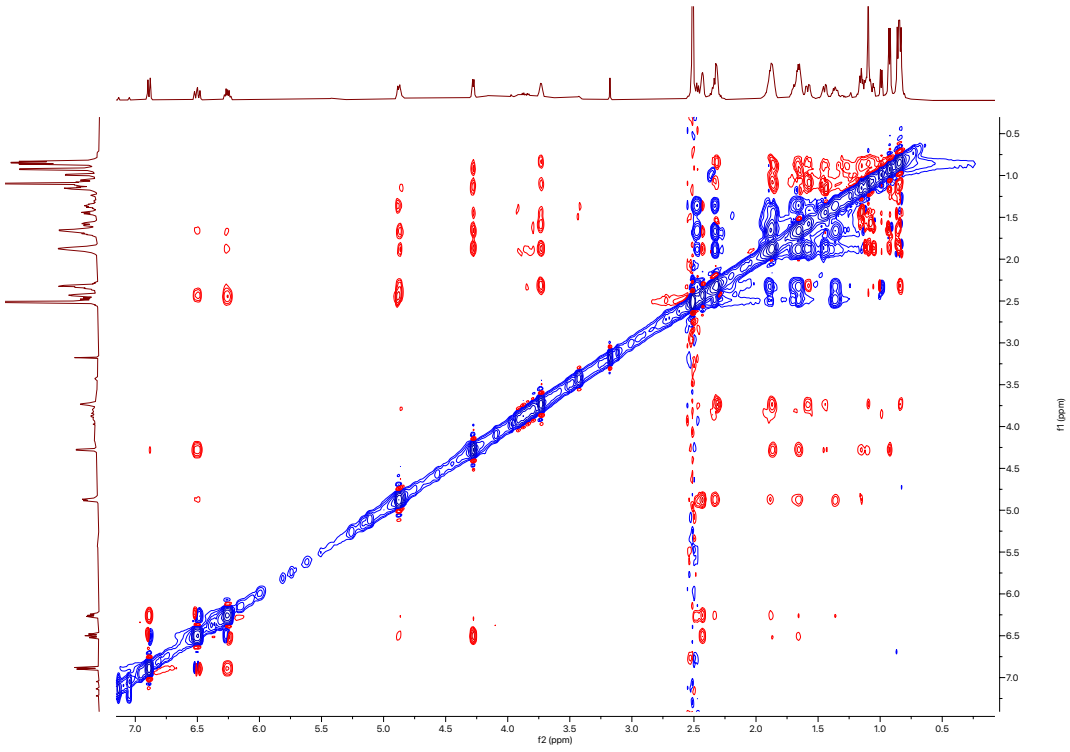

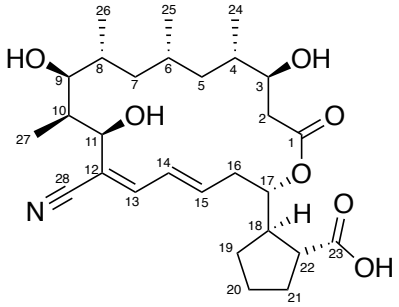

borrelidin S (**44**)

Position	δ_C (type)	δ_H, multiplets (*J* in Hz)	COSY	HMBC	ROESY
1	171.2 (C)				
2	39.7 (CH_2)	2.29, m	2b, 3	1, 3, 4	
3	69.5 (CH)	3.72, t (7.2)	2a, 2b, 4		2a, 2b, 4, 6
3-OH		4.48, s			2a, 3, 4
4	34.5 (CH)	1.60, m	3, 5a, 5b, 24		5a, 5b, 25
5a	42.8 (CH_2)	0.72, m	4, 5b, 6		
5b	42.8 (CH_2)	1.36, m	4, 5a, 6	6, 24, 25	
6	33.0 (CH)	1.68, m	5a, 5b, 7a, 7b, 25		2a, 3, 5b, 25
7a	42.5 (CH_2)	0.79, dd (8.0, 3.0)	6, 7b, 8		
7b	42.5 (CH_2)	1.37, s	6, 7a, 8		
8	28.1 (CH)	1.58, m	7a, 7b, 9, 26		
9	74.0 (CH)	3.16, m	8, 10		7a, 7b, 8, 9-OH, 11, 26, 27
9-OH		4.22, br s			
10	42.1 (CH)	1.69, m	9a, 9b, 11, 27	11	7a, 9a, 26
11	69.8 (CH)	4.40, d (6.8)	10		7a, 9b, 10, 14
11-OH		5.43, br s			7a, 10, 11
12	118.3 (C)				
13	141.7 (CH)	6.80, d (11.2)	14	11, 28	15
14	127.6 (CH)	6.48, dd (15.3, 11.4)	13, 15		
15	138.5 (CH)	6.25, ddd (14.7, 9.3, 5.1)	14, 16a, 16b	13	13
16a	35.9 (CH_2)	2.40, ddd (14.9, 11.2, 4.8)	15, 16b, 17	14, 15, 17	
16b	35.9 (CH_2)	2.49, m	15, 16a, 17	14, 15, 17	
17	75.4 (CH)	4.88, dt (10.1, 3.9)	16a, 16b		16a, 18, 19a, 19b, 20, 22
18	46.1 (CH)	2.52, m	19a, 19b, 22	16, 19, 22, 23	15, 17, 19b
19a	29.4 (CH_2)	1.36, m	18, 19b, 20	17, 18, 20, 21	
19b	29.4 (CH_2)	1.85, m	18, 19a, 20		
20	25.3 (CH_2)	1.65, m	19a, 19b, 21a, 21b	21	
21a	31.4 (CH_2)	1.69, m	20, 21b, 22	18, 19, 20, 22, 23	
21b	31.4 (CH_2)	1.90, m	20, 21a, 22	22	
22	48.3 (CH)	2.34, m	18, 21a, 21b	17, 18, 21, 23	17
23	177.7 (C)				
23-COOH		12.04, s			
24	16.5 (CH_3)	0.77, d, (5.4)	4	3, 4, 5	
25	16.4 (CH_3)	0.80, d (6.4)	6	5, 6, 7	
26	19.5 (CH_3)	0.81, d (6.4)	8	7, 8, 9	
27	13.7 (CH_3)	0.97, d (6.9)	10	9, 10, 11	9, 11
28	120.6 (C)				

^{1}H spectrum of borrelidin S (**44**)

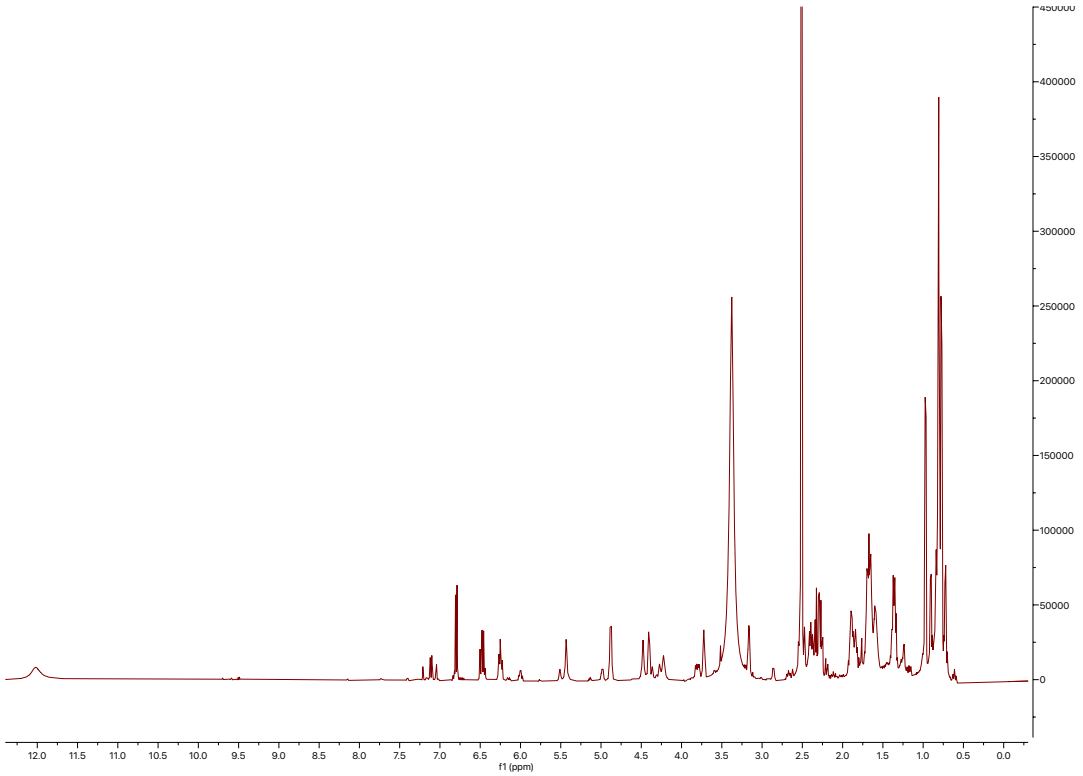

^{13}C spectrum of borrelidin S (**44**)

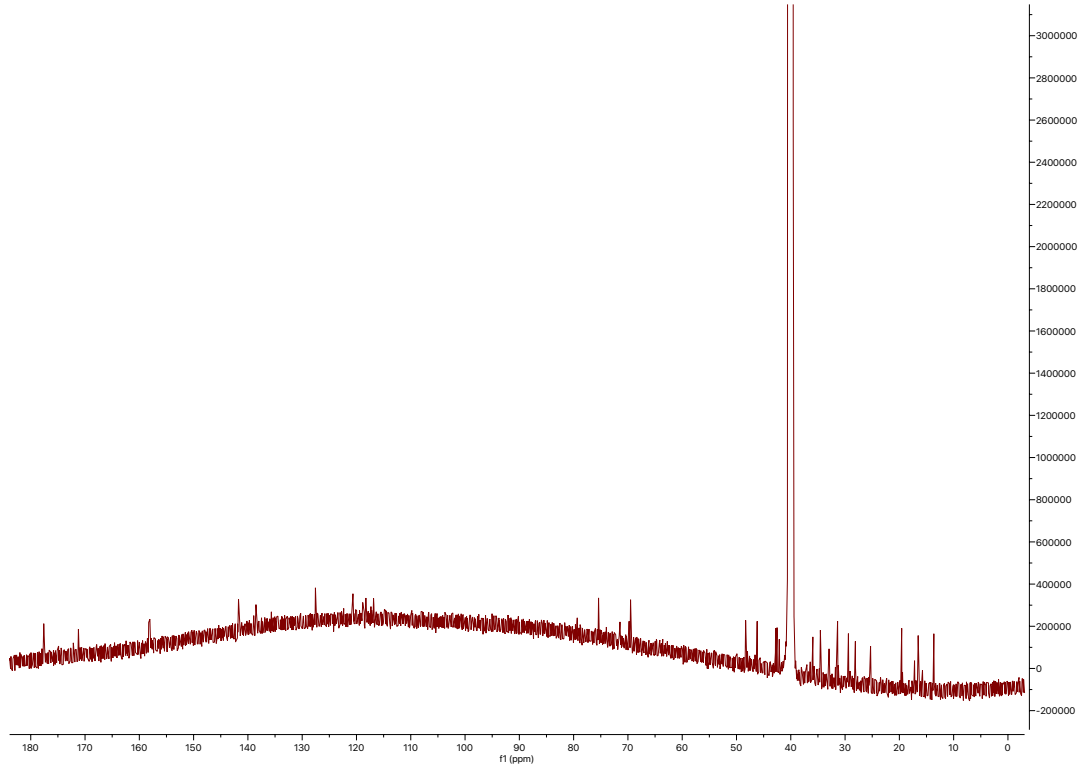

COSY spectrum of borrelidin S (**44**)

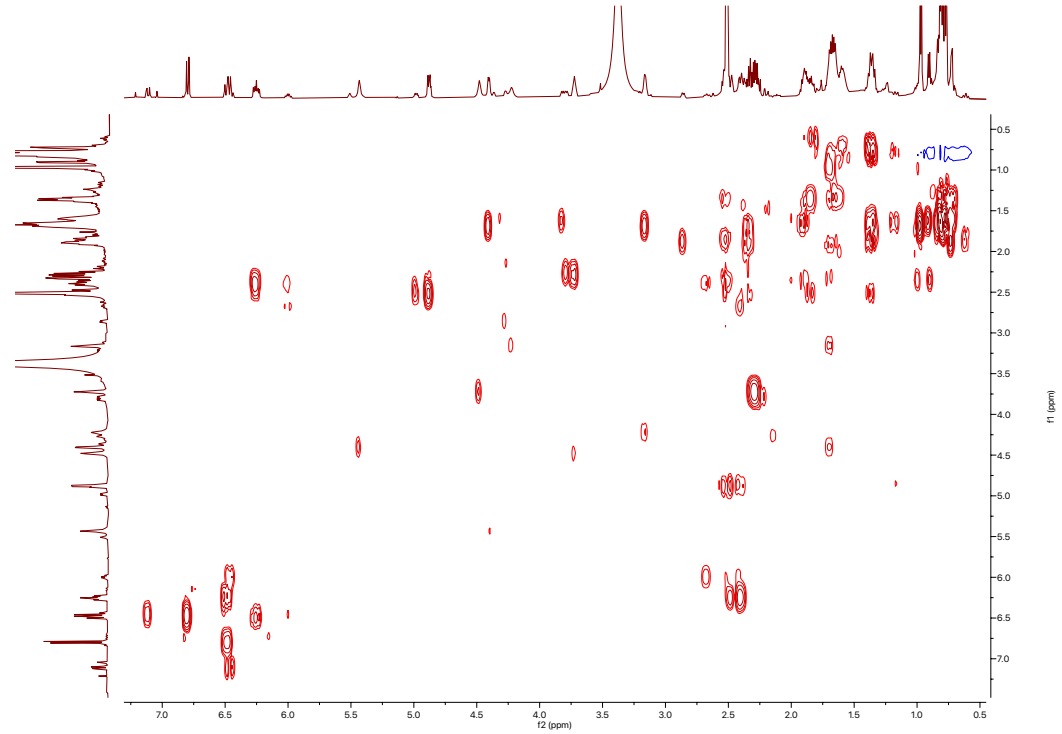

HSQC spectrum of borrelidin S (**44**)

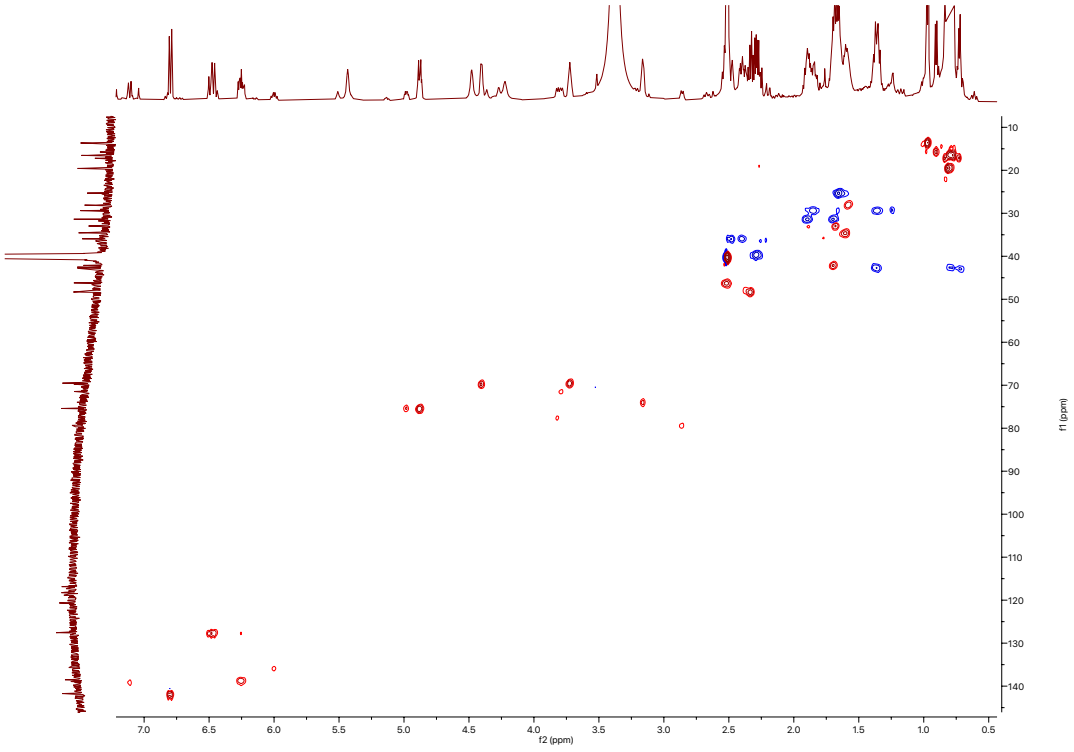

^{1}H-^{13}C HMBC spectrum of borrelidin S (**44**)

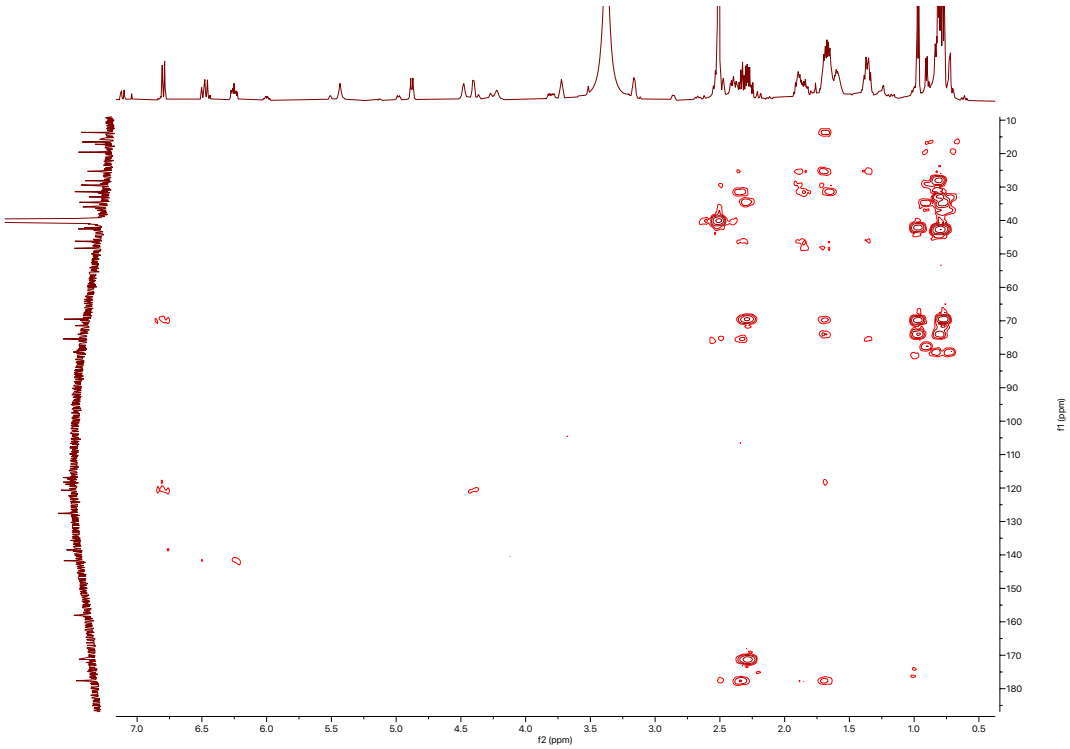

ROESY spectrum of borrelidin S (**44**)

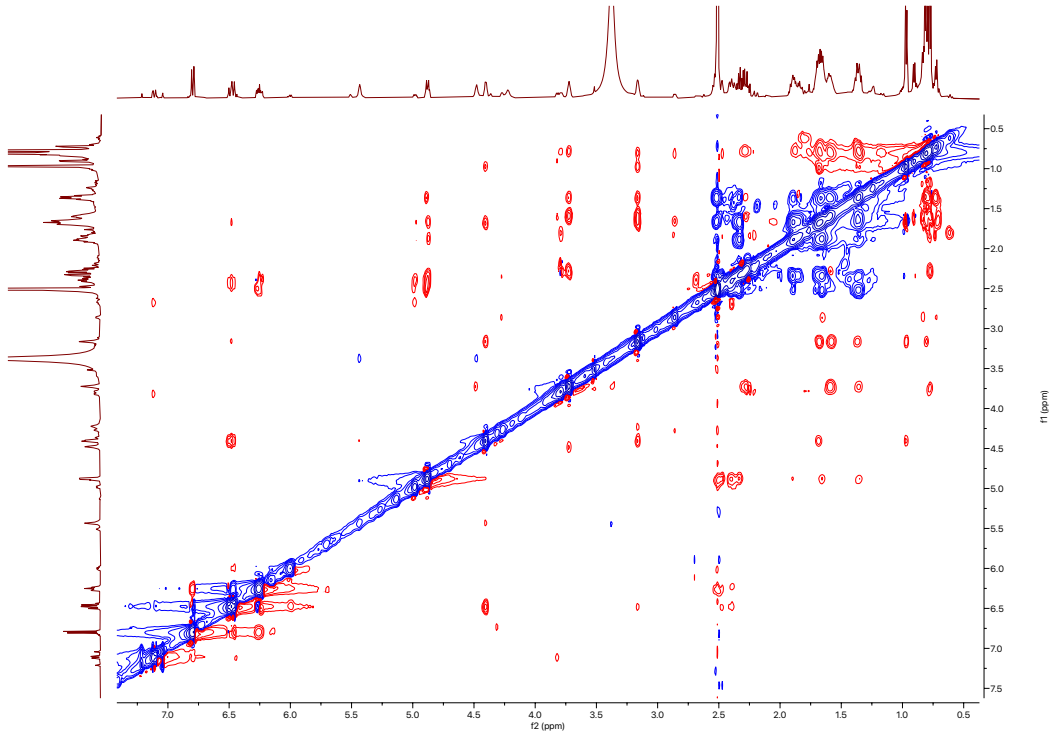

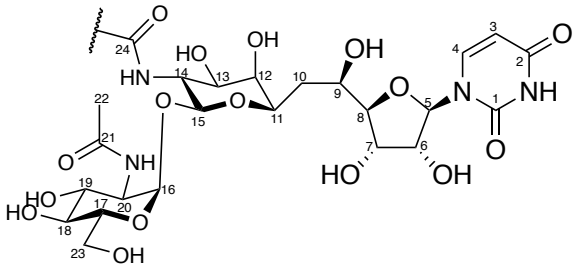

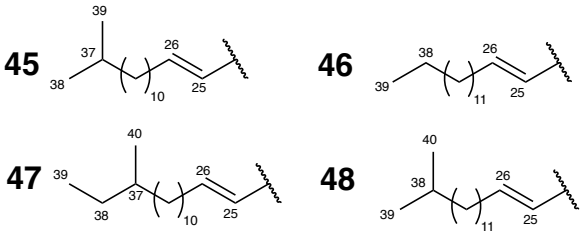

NMR data of tunicamycin VII (**45**)

Position	δ_C (type)	δ_H, multiplets (*J* in Hz)	COSY	HMBC
1	163.5 (C)			
1-NH		11.32, s		1, 2, 3
2	151.4 (CH)			
3	102.6 (CH)	5.70, dd	4	1, 2, 3
4	140.8 (CH)	7.79, d	3	2, 3, 5
5	86.8 (CH)	5.83, d	6	4, 6, 7
6	73.9 (CH)	3.99, dd	5, 6-OH, 7	
6-OH		5.34, dd	6	
7	69.7 (CH)	4.03, d	6, 7-OH, 8	5
7-OH		5.08, d	7	
8	89.0 (CH)	3.63, dd	7, 9	7, 9
9	71.6 (CH)	3.42, m	8, 9-OH, 10a, 10b	11
9-OH		4.74, d	9	
10a	61.0 (CH_2)	3.53, d	9, 10b, 11	
10b	61.0 (CH_2)	3.58, d	9, 10a, 11	
11	73.6 (CH)	3.70, m	10a, 10b, 12	
12	70.4 (CH)	3.22, ddd	11, 12-OH, 13	10, 11
12-OH		5.04, d	12	
13	70.8 (CH)	3.44, m	12, 13-OH, 14	14
13-OH		4.68, d	13	
14	53.4 (CH)	3.74, m	13, 14-NH, 15	15
14-NH		7.78, d	14	24, 25
15	101.4 (CH)	4.42, d	14	
16	99.3 (CH)	4.74, d	20	
17	71.1 (CH)	3.59, m	18, 23	
18	67.3 (CH)	3.72, m	17, 18-OH, 19	
18-OH		4.42, d	18	
19	71.4 (CH)	3.60, m	18, 19-OH, 20	
19-OH		5.06, d	19	
20	53.5 (CH)	3.63, m	16, 19, 20-NH	21
20-NH		6.65, d	20	21
21	169.6 (C)			
22	23.4 (CH_3)	1.77, s		21
23	70.4 (CH_2)	3.52, d	17, 23-OH	17
23-OH		4.61, t	23	
24	166.5 (C)			
25	125.3 (CH)	5.88, d	26	24, 27
26	143.1 (CH)	6.60, dt	25, 27	24, 27, 28
27	31.7 (CH_2)	2.12, dt	26, 28	
28	28.3 (CH_2)	1.38, tt	27	
29-35	29.4 (CH_2)	1.25, m		
36	38.9 (CH_2)	1.14, dt	37	
37	27.9 (CH)	1.50, qq	38, 39	36, 38, 39
38	23.0 (CH_3)	0.85, d	37	36, 37
39	23.0 (CH_3)	0.85, d	37	36, 37

^{1}H spectrum of tunicamycin VII (**45**)

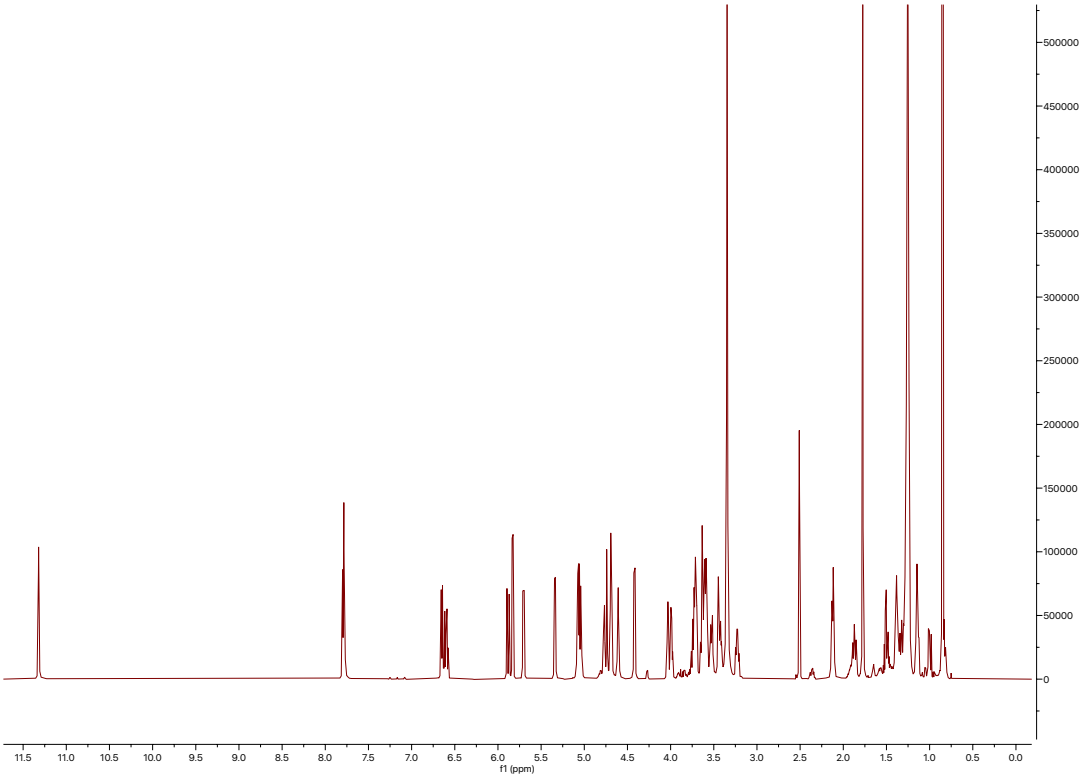

^{13}C spectrum of tunicamycin VII (**45**)

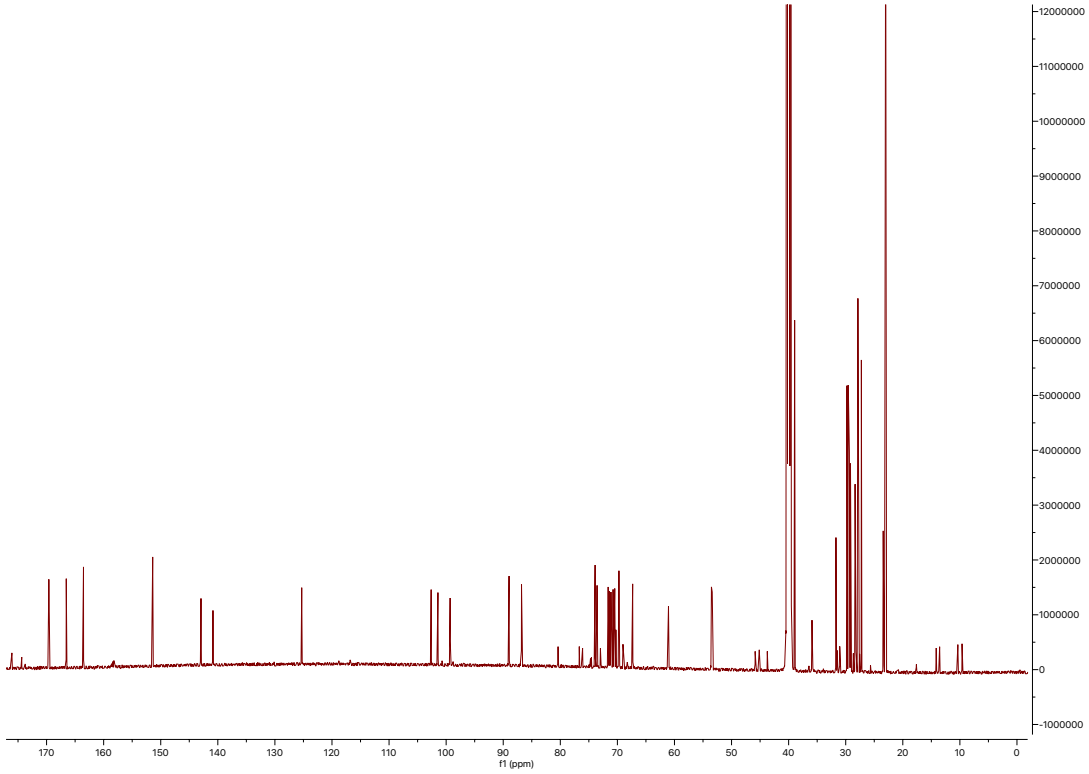

COSY spectrum of tunicamycin VII (**45**)

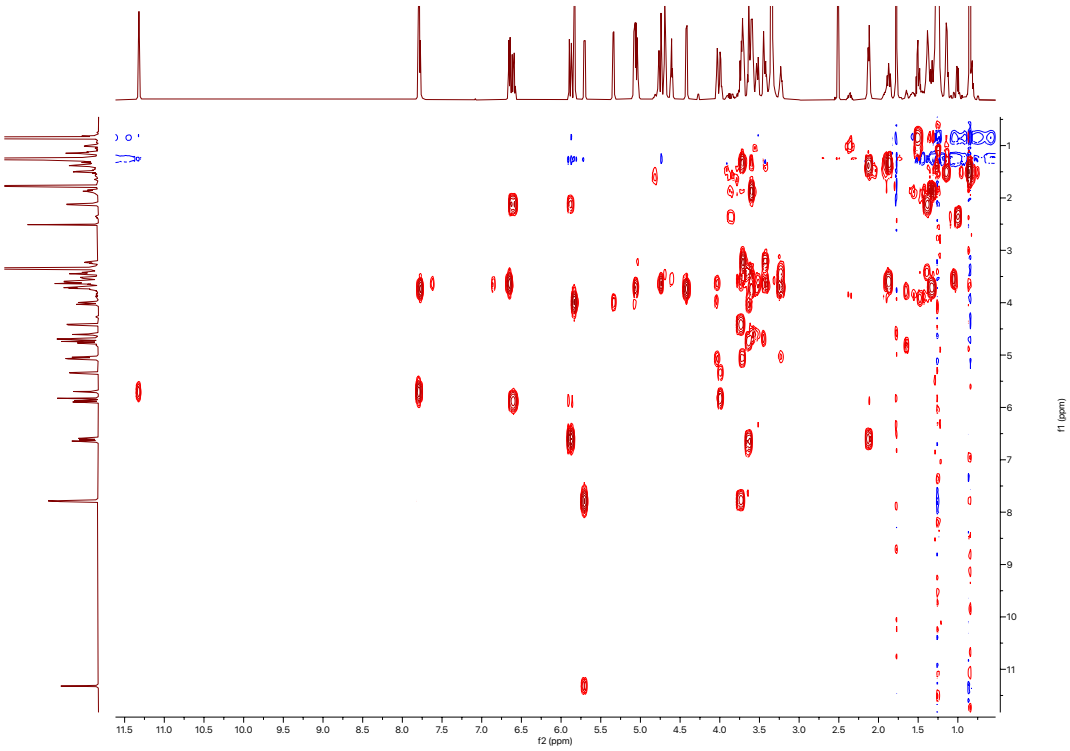

HSQC spectrum of tunicamycin VII (**45**)

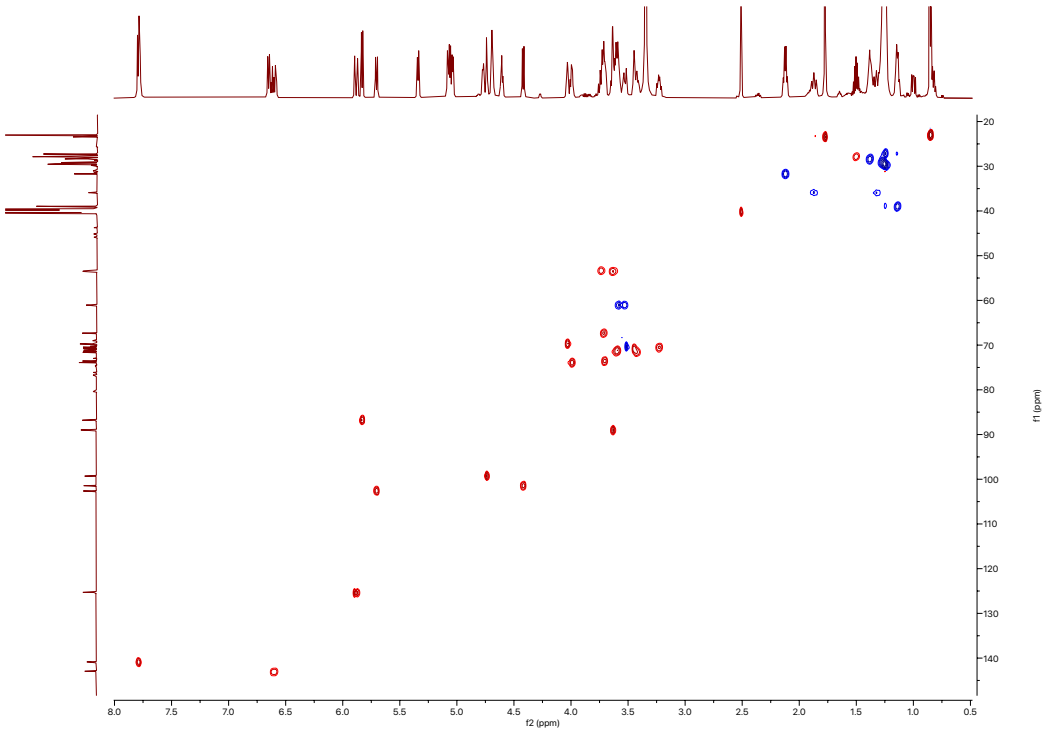

^{1}H-^{13}C HMBC spectrum of tunicamycin VII (**45**)

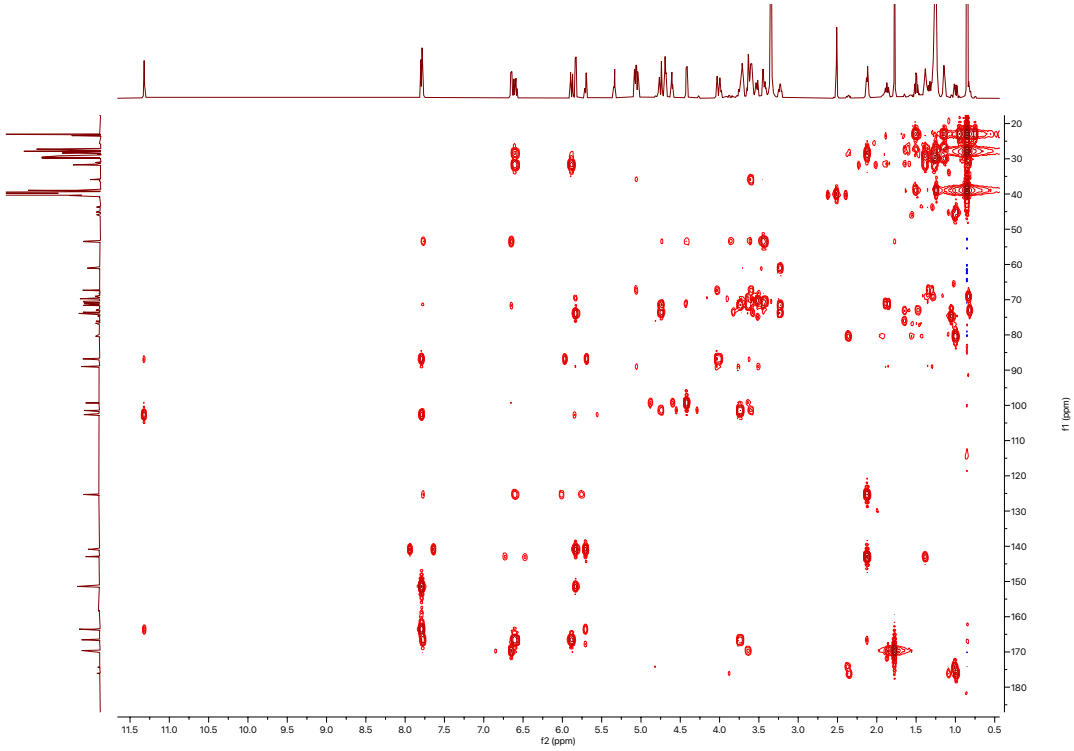

TOCSY spectrum of tunicamycin VII (**45**)

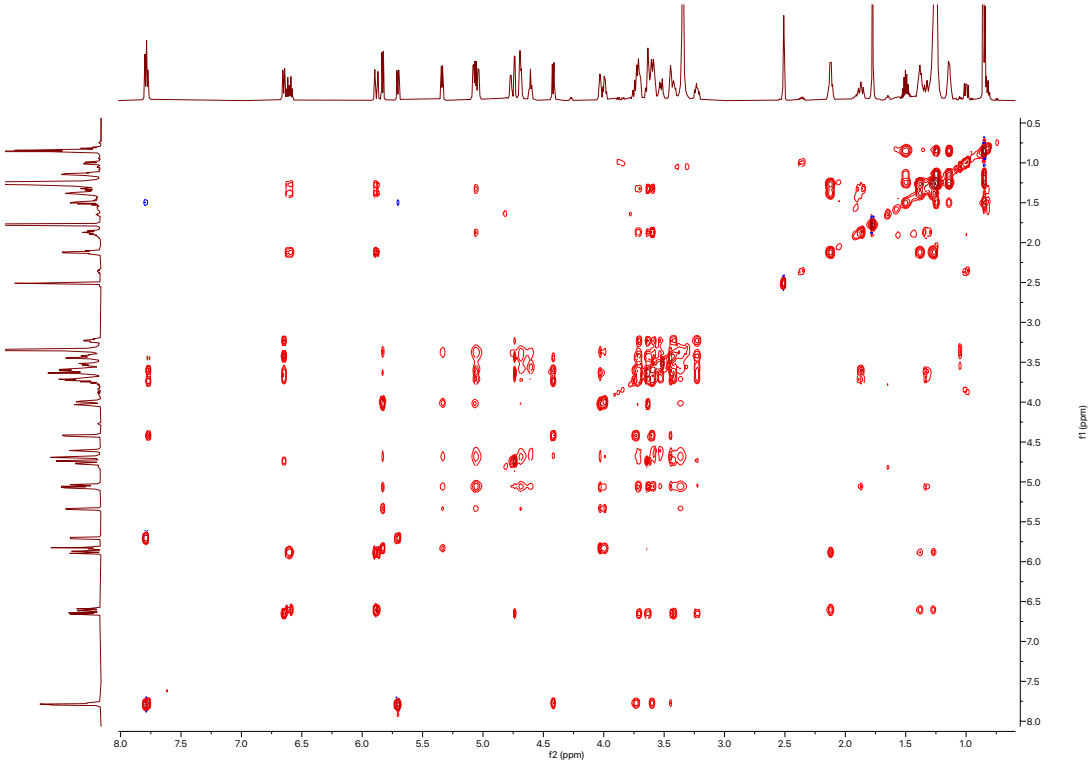

^{1}H spectrum of tunicamycin VIII (**46**)

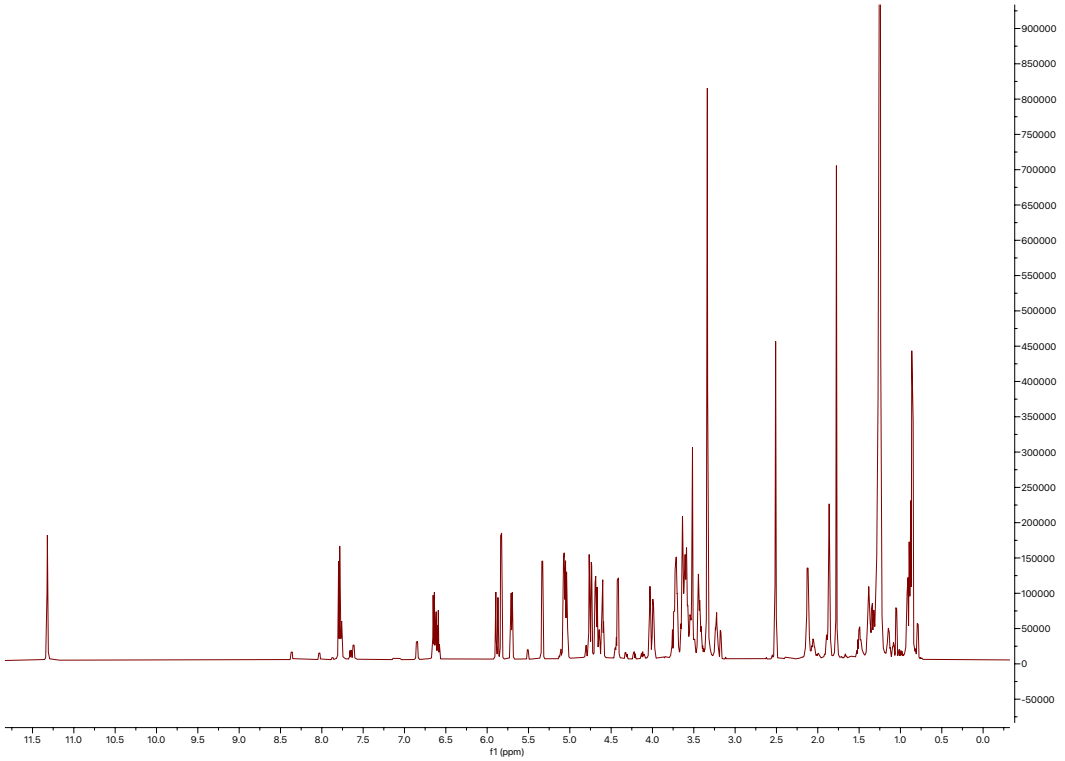

^{13}C spectrum of tunicamycin VIII (**46**)

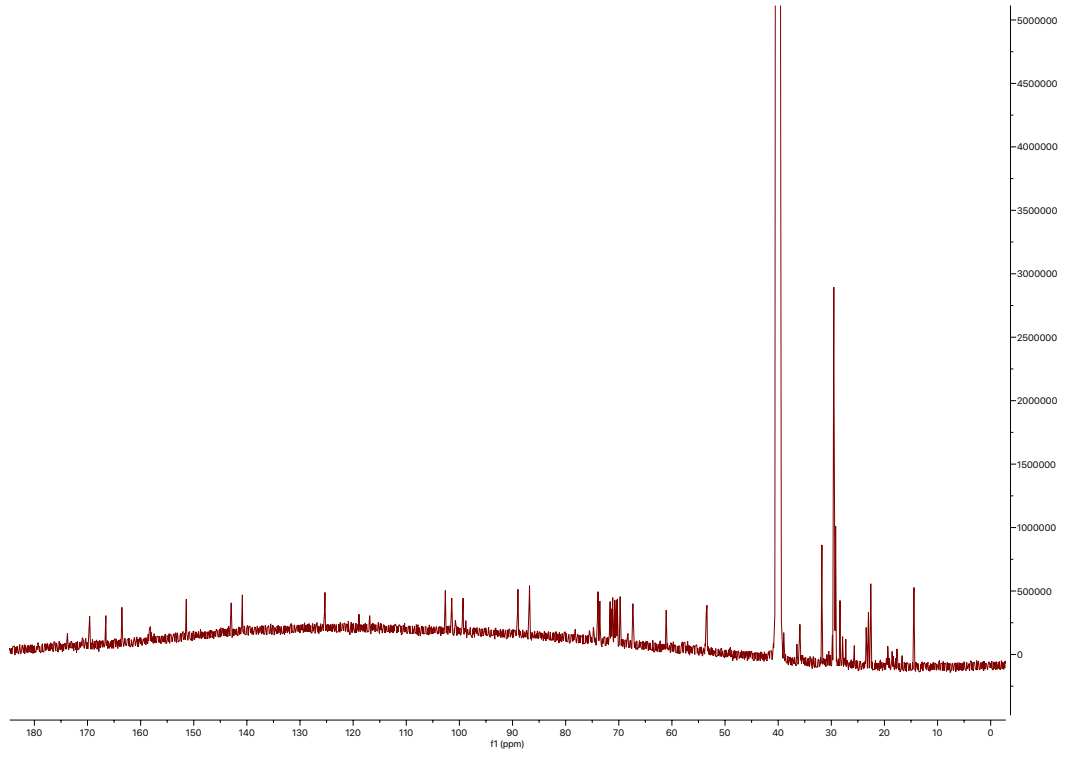

COSY spectrum of tunicamycin VIII (**46**)

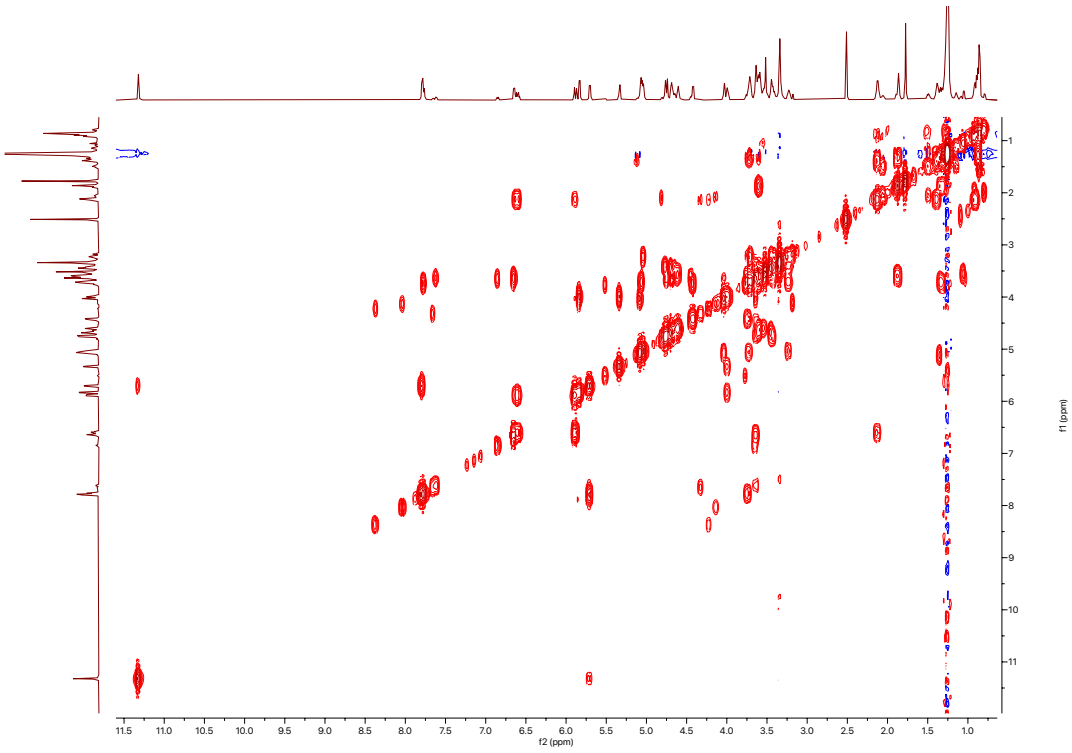

HSQC spectrum of tunicamycin VIII (**46**)

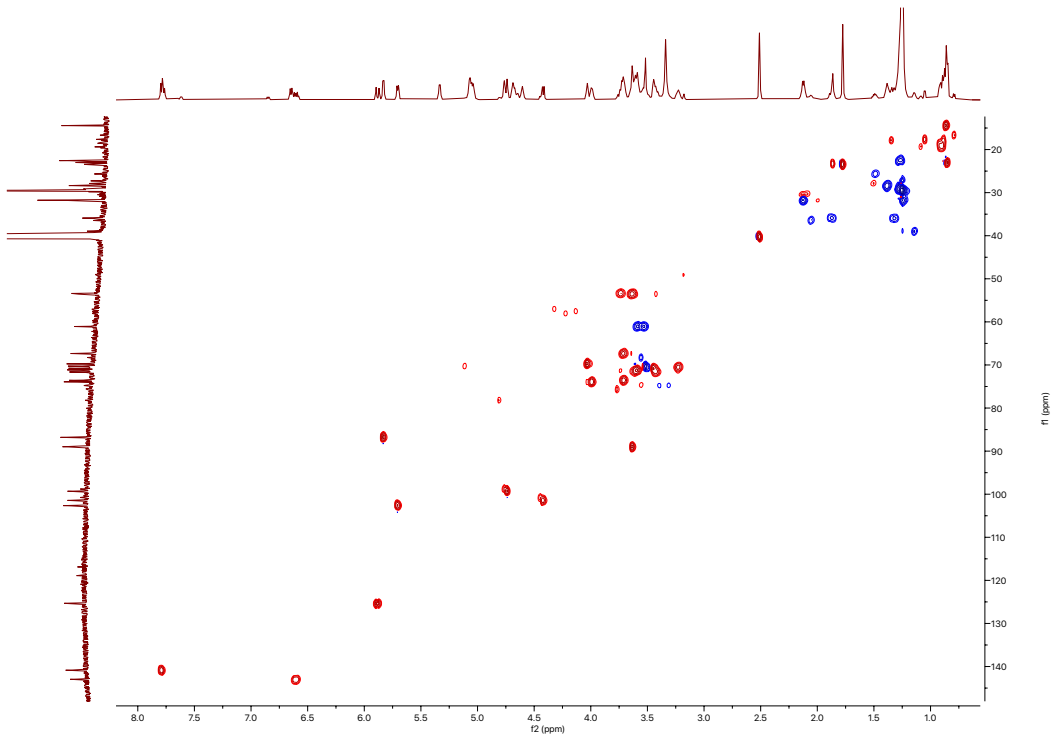

^{1}H-^{13}C HMBC spectrum of tunicamycin VIII (**46**)

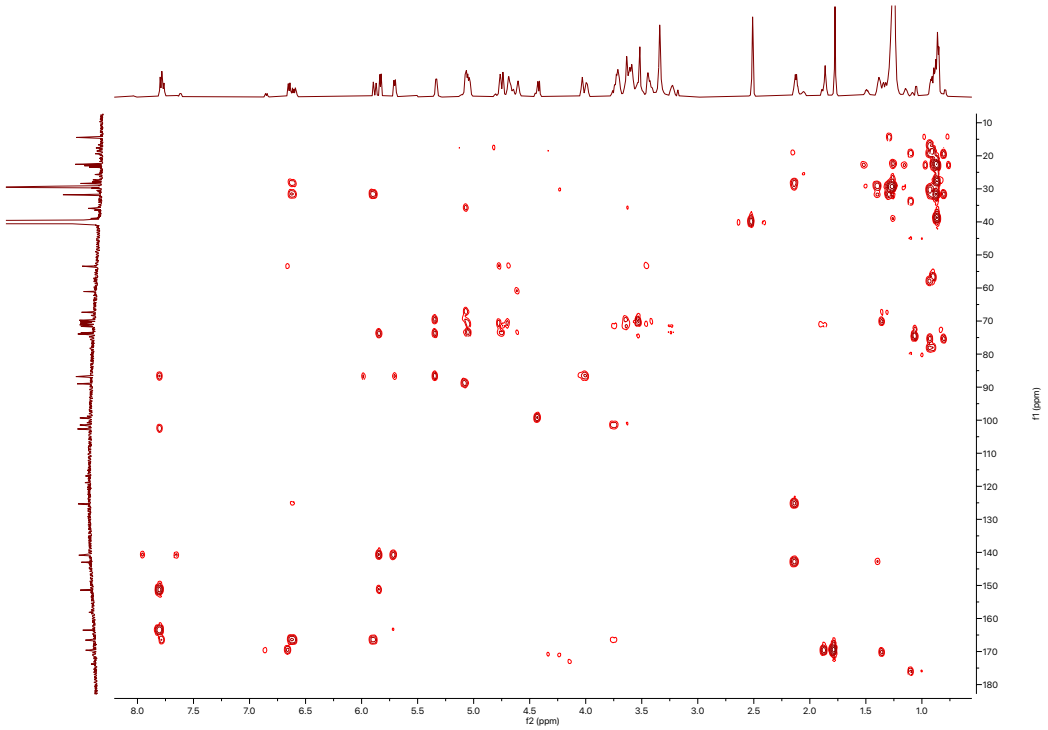

TOCSY spectrum of tunicamycin VIII (**46**)

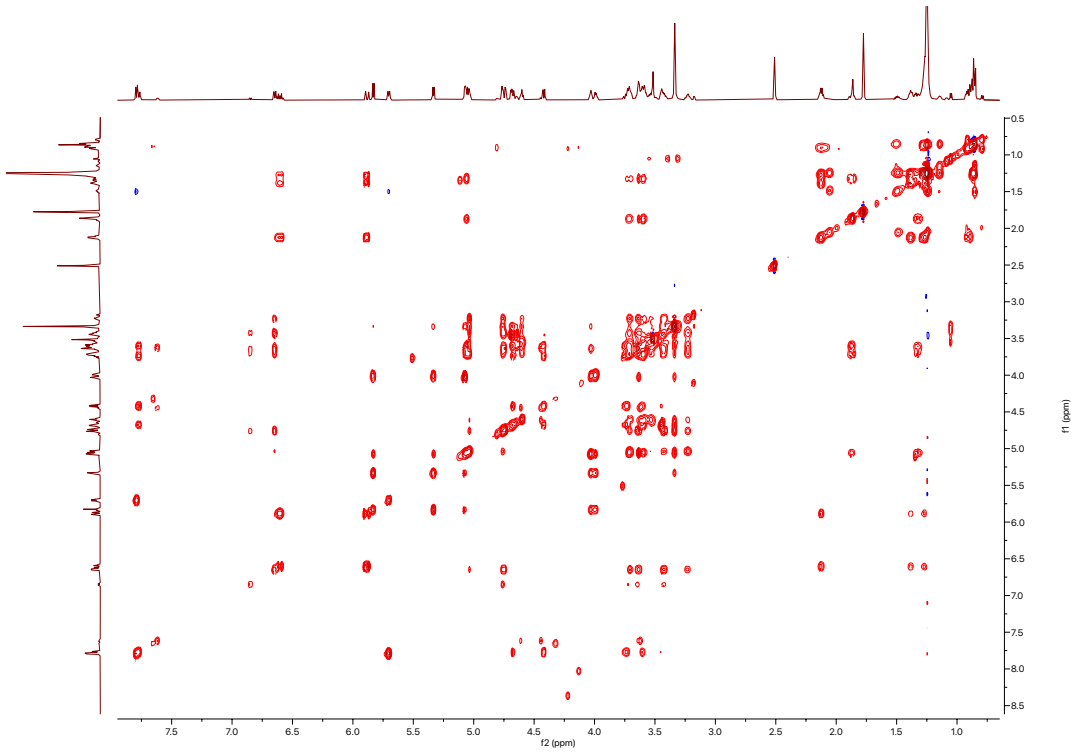

^{1}H spectrum of corynetoxin H17a (**47**)

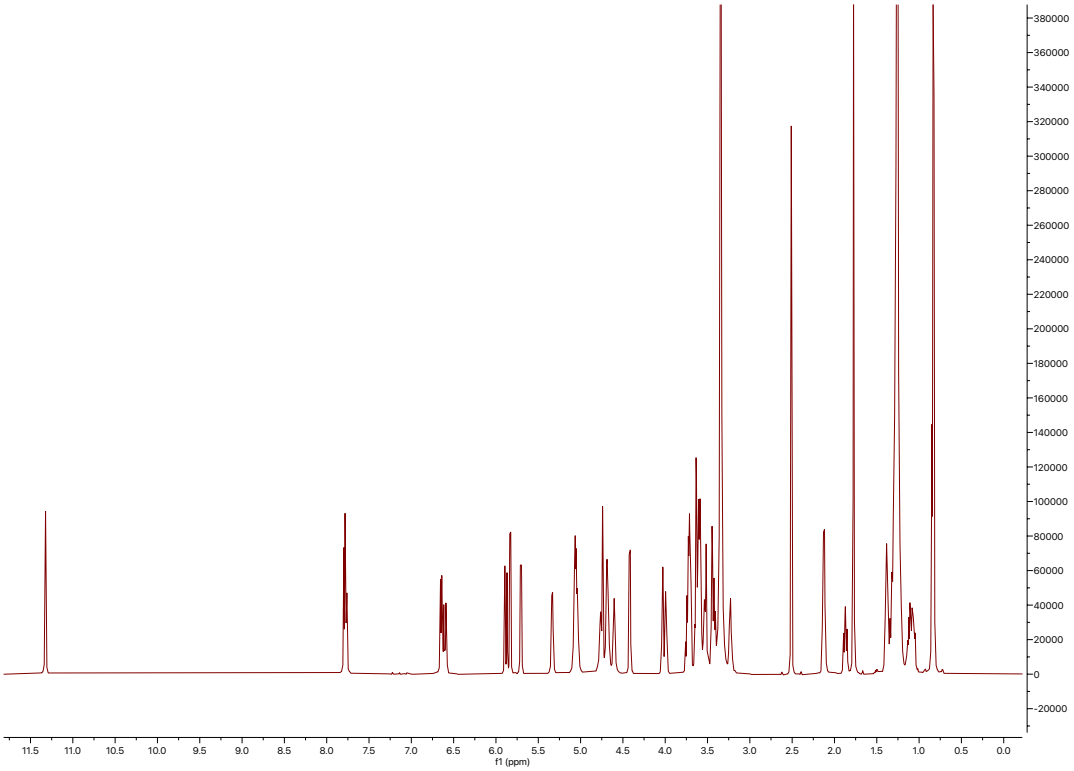

^{13}C spectrum of corynetoxin H17a (**47**)

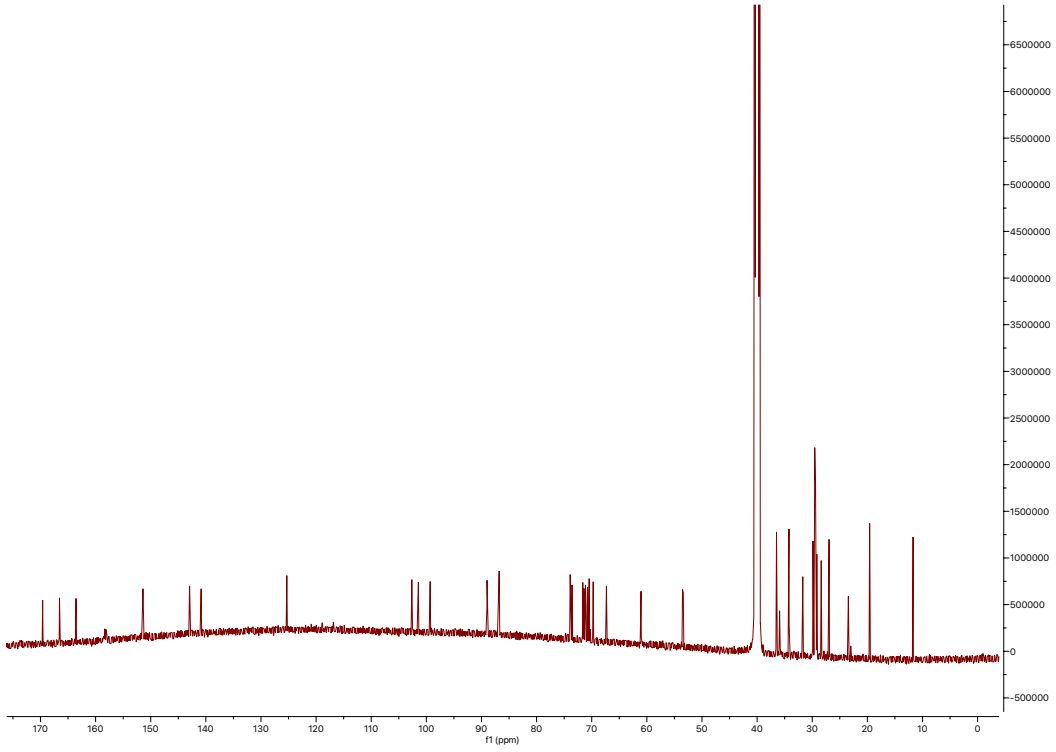

COSY spectrum of corynetoxin H17a (**47**)

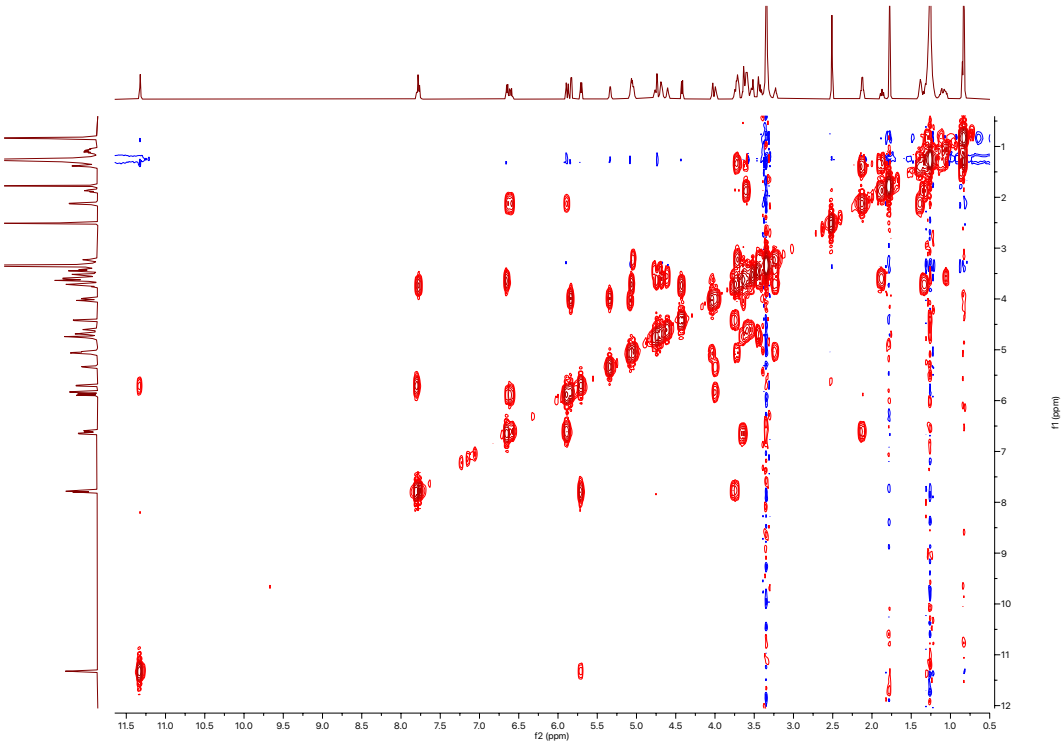

HSQC spectrum of corynetoxin H17a (**47**)

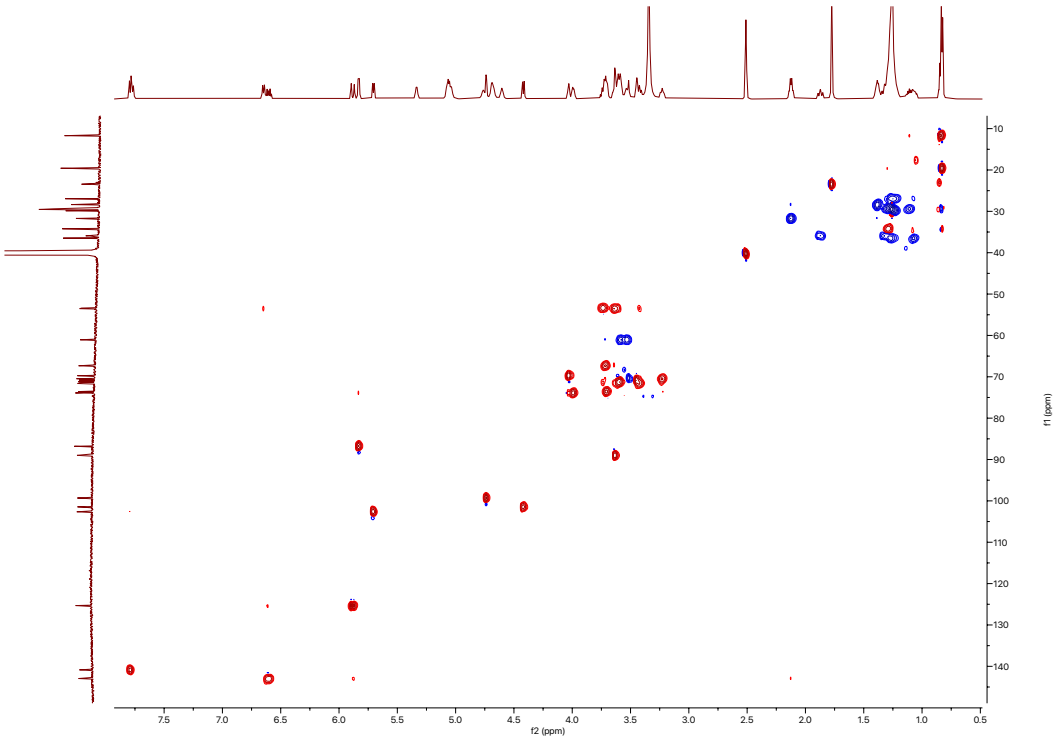

^{1}H-^{13}C HMBC spectrum of corynetoxin H17a (**47**)

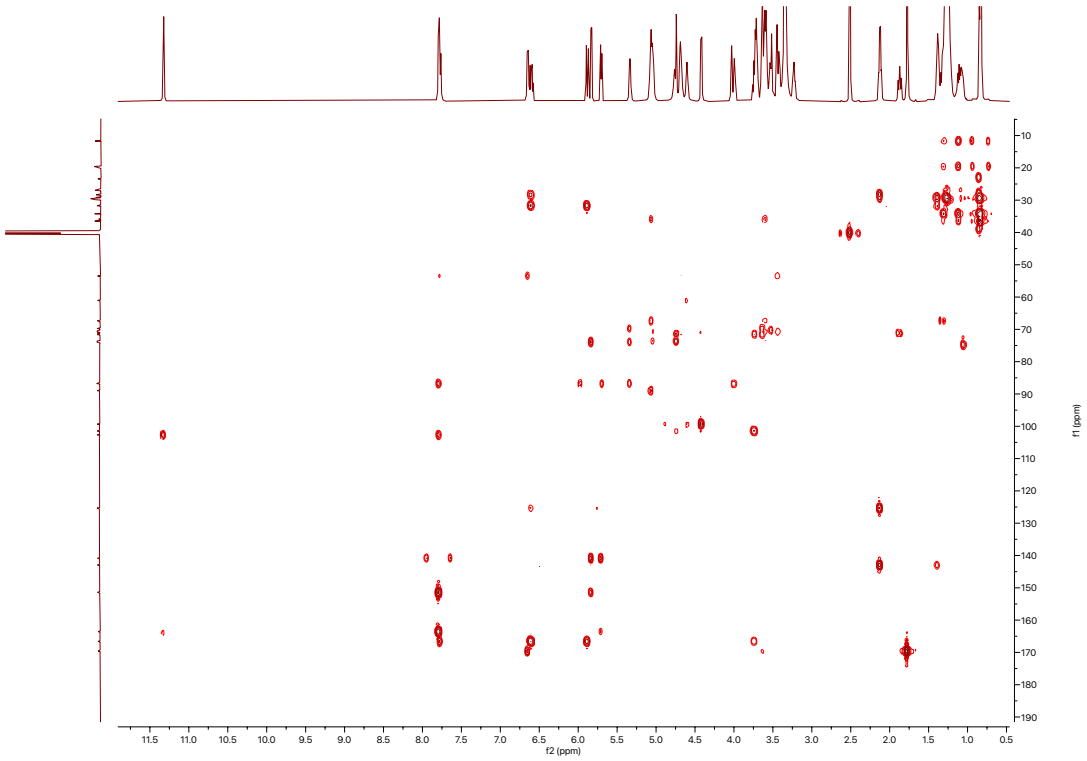

NOESY spectrum of corynetoxin H17a (**47**)

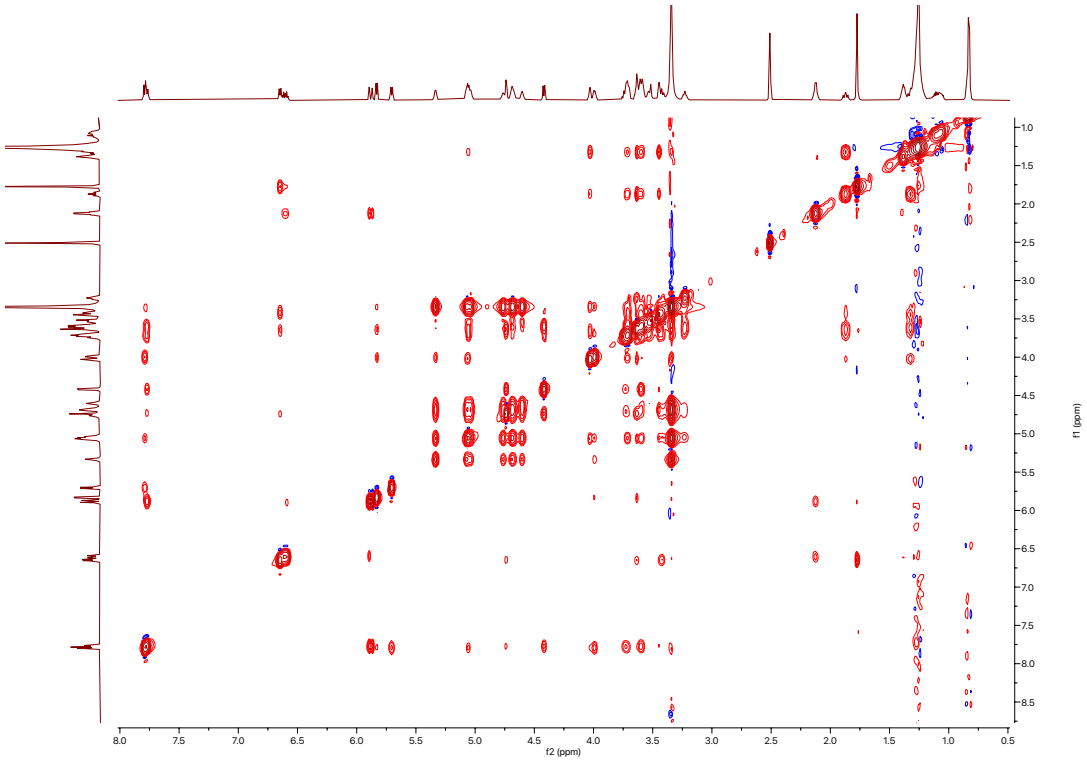

^{1}H spectrum of tunicamycin X (**48**)

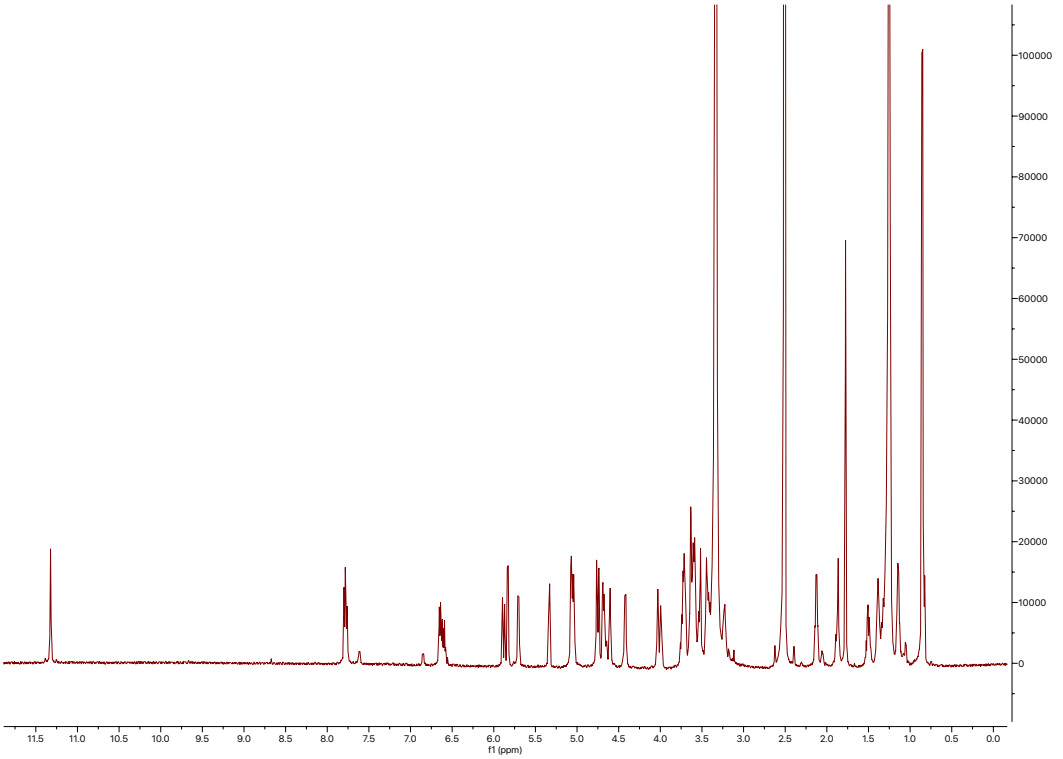

^{13}C spectrum of tunicamycin X (**48**)

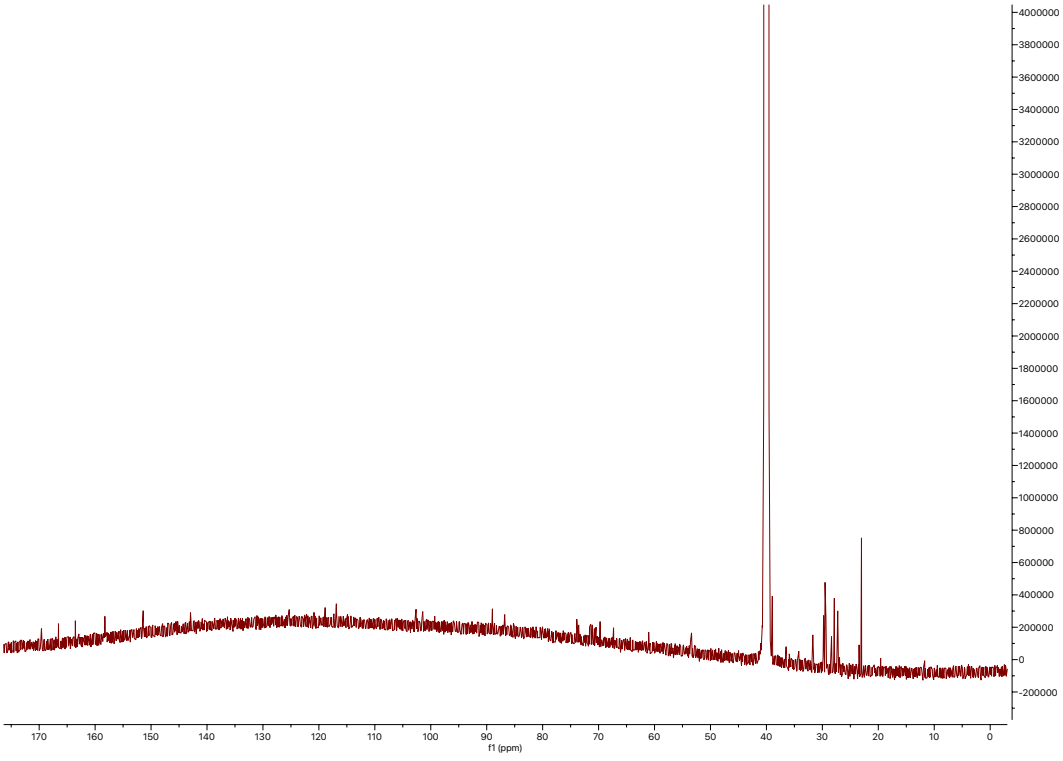

COSY spectrum of tunicamycin X (**48**)

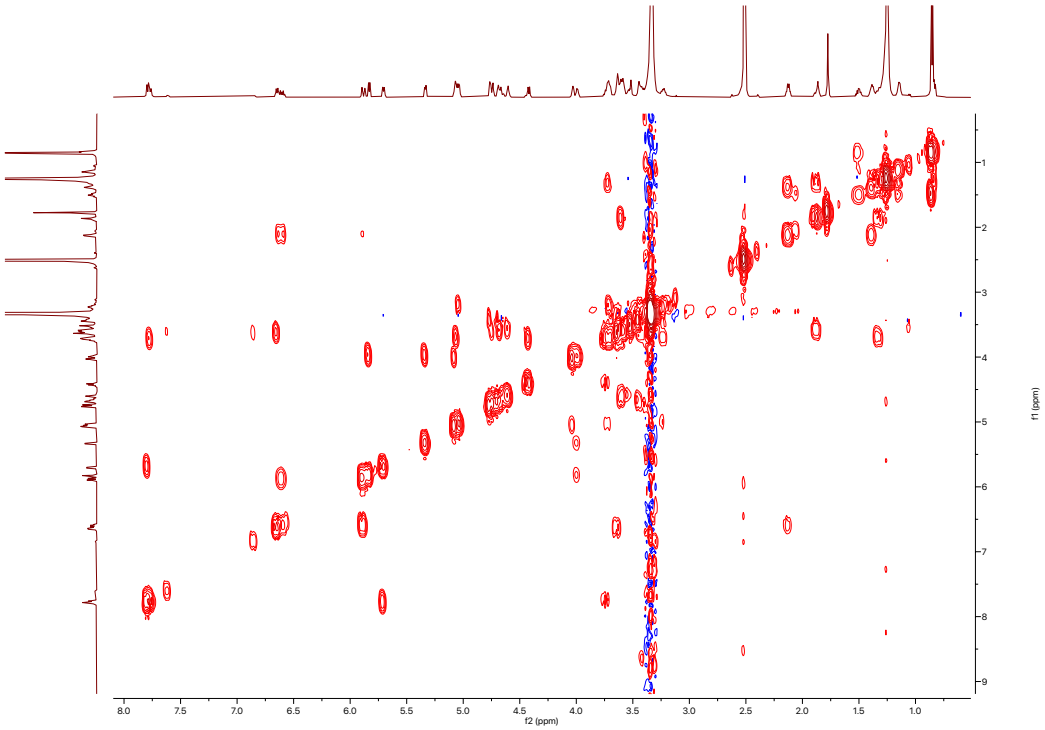

HSQC spectrum of tunicamycin X (**48**)

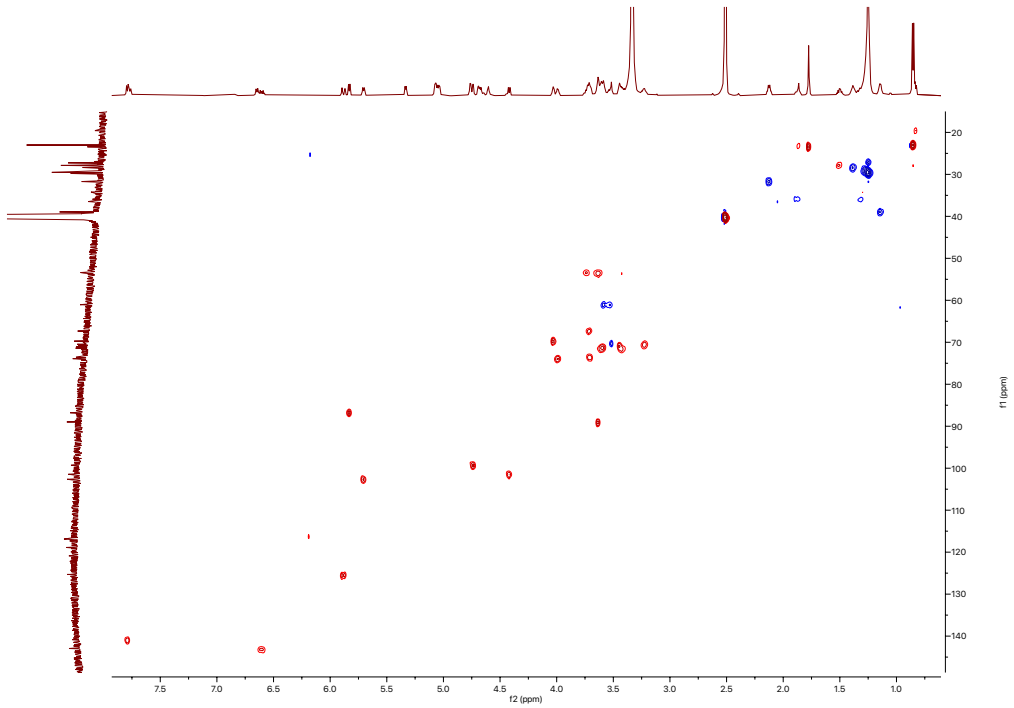

^{1}H-^{13}C HMBC spectrum of tunicamycin X (**48**)

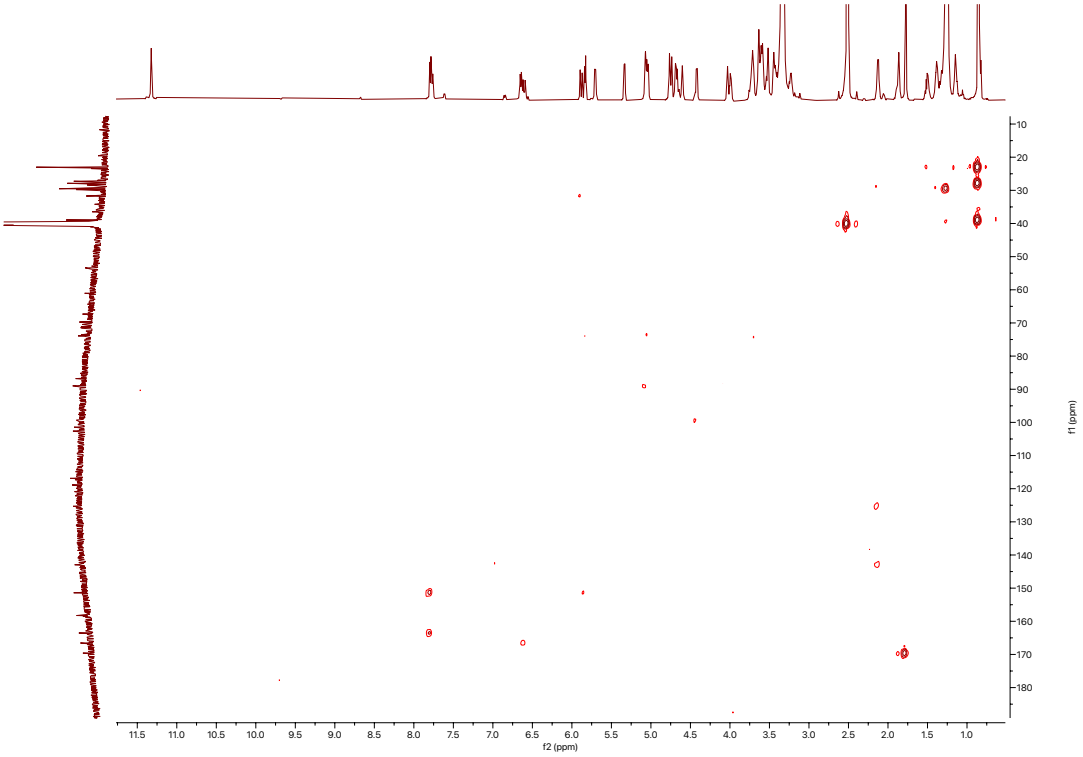

NOESY spectrum of tunicamycin X (**48**)

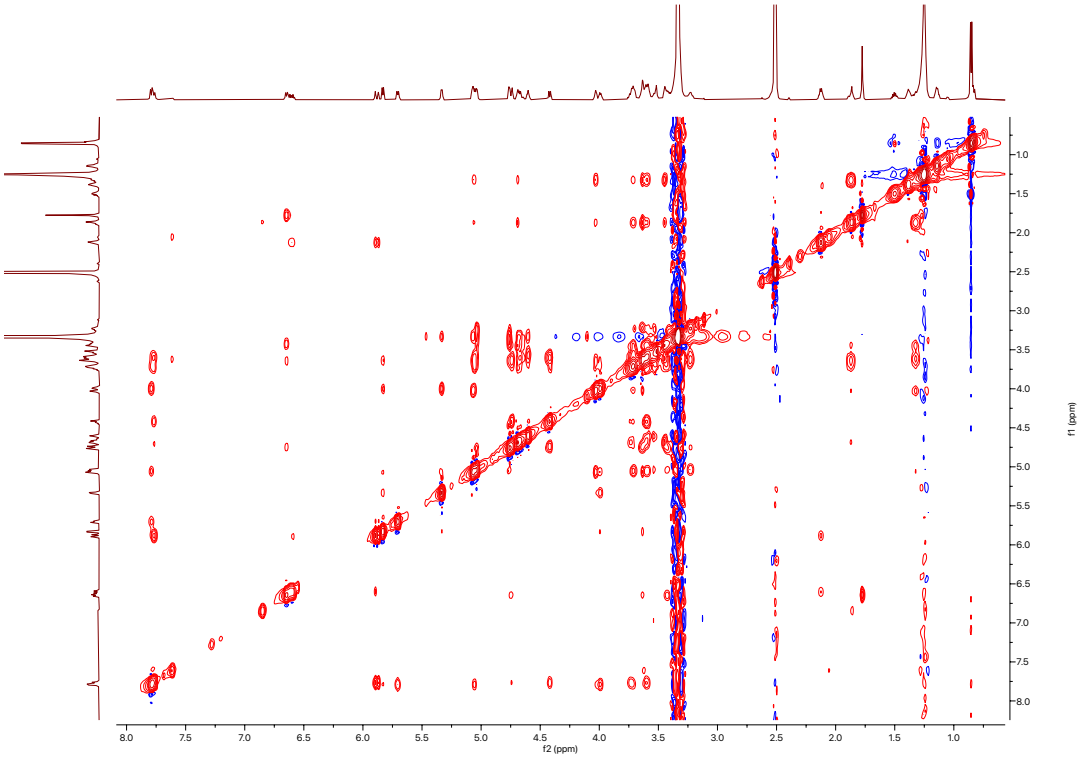

Appendix C: DFT Calculations and DP4+ Results

(All theoretical chemical shifts were calculated using B3LYP/6-311+G(d,p) with solvent effect of DMSO included using PCM model)

baraphenazine F (**2**)

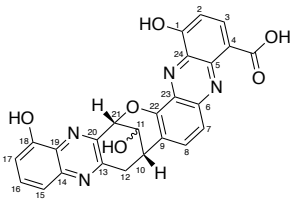

2a: 11*S*
2b: 11*R*

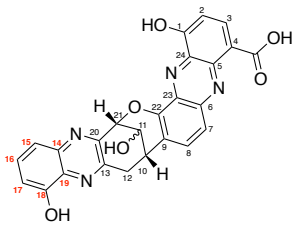

2c: 11*S*
2d: 11*R*

#C	experimental	2a	2b	2c	2d
1	159.9	167.5127409	167.5641996	167.5275592	167.5254733
2	110.5	114.6366376	114.6594338	114.6887915	114.7807036
3	139.1	149.2268916	149.1979132	149.2467868	149.2708583
4	114.5	120.2451375	120.3447366	120.3881685	120.4094847
5	140.7	147.6551074	147.5898165	147.591318	147.5804447
6	139.8	148.5998637	148.6044685	148.6458126	148.5312576
7	119.8	126.4935881	126.4136243	126.421438	126.4425797
8	135.8	144.5577026	145.3267109	144.5673382	145.2496896
9	123.0	133.3732436	132.101252	133.4042371	131.8806943
10	35.9	43.89430663	45.6216464	43.72962144	45.43173289
11	63.0	71.53218448	70.96793277	71.6565378	71.02048703
12	35.5	42.38098475	46.75073955	41.70541811	46.01884262
13	152.2	163.2284275	162.3054484	159.0198616	157.8409557
14	142.8	151.069466	151.1557128	150.2949734	149.8910152
15	117.8	125.1645955	125.0939122	125.8864349	126.1469219
16	131.6	140.4803852	140.8268806	138.7131063	139.3409511
17	111.8	116.4433285	116.7026284	117.734795	118.1695477
18	153.7	161.8896428	162.1115197	161.0036882	160.8175773
19	132.6	138.1235278	137.6675007	139.0401726	139.0528849
20	146.7	153.5007374	153.1238316	158.4691881	158.3256469
21	75.6	82.96731829	83.79841519	83.56126607	84.3378827
22	146.7	156.837247	156.4954886	157.0109921	156.6817975
23	134.2	140.0599916	139.994156	140.0887905	140.0412697
24	134.2	137.8568529	137.915285	137.9481054	137.8837945
25	165.7	175.9585153	175.8941993	175.8485996	175.9020095

#H	experimental	2a	2b	2c	2d
1-OH	12.03	9.18099719	9.237939872	9.182010068	9.208882422
2	7.28	7.565292624	7.570872075	7.554116498	7.551862581
3	8.59	9.1741858	9.163752016	9.14702223	9.161600712
7	7.89	8.120923834	8.126236246	8.117196748	8.124901257
8	8.06	8.314785701	8.330063828	8.32133432	8.334619673
10	3.82	3.880322381	3.669600503	3.884375311	3.680534549
11	4.79	5.135640391	4.870934626	5.131314789	4.879761678
11-OH	6.20	1.871566433	1.895202062	1.880029359	1.90412638
12a	3.80	4.181144807	3.873776155	4.225185211	3.932431699
12b	3.39	3.547660261	3.735416003	3.603529046	3.774309177
15	7.36	7.659798294	7.648019948	7.897031214	7.924384014
16	7.60	8.00250853	8.023711984	7.969532996	7.982087639
17	7.07	7.447518766	7.467535939	7.470275987	7.467311649
18-OH	10.61	8.46398866	8.451655728	8.173490318	8.147830274
21	5.74	5.924172501	6.070011419	5.848313225	5.988873035
25-COOH	14.91	14.47160452	14.49321164	14.46846019	14.50571666

DP4+	2a	2b	2c	2d
sDP4+ (^{1}H data)	40.93%	32.46%	18.50%	8.10%
sDP4+ (^{13}C data)	28.96%	1.97%	50.49%	18.58%
sDP4+ (all data)	50.79%	2.74%	40.02%	6.45%
uDP4+ (^{1}H data)	50.82%	40.64%	2.66%	5.89%
uDP4+ (^{13}C data)	49.02%	1.01%	48.83%	1.14%
uDP4+ (all data)	93.35%	1.54%	4.86%	0.25%
DP4+ (^{1}H data)	59.50%	37.73%	1.41%	1.36%
DP4+ (^{13}C data)	36.32%	0.05%	63.08%	0.05%
DP4+ (all data)	95.95%	0.09%	3.94%	0.09%

baraphenazine H (**3**)

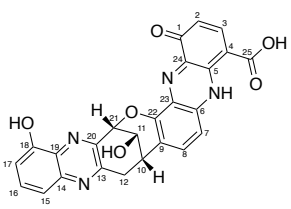

3a

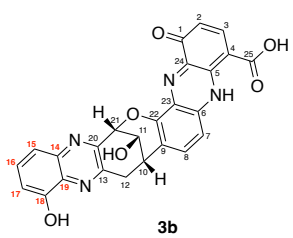

3b

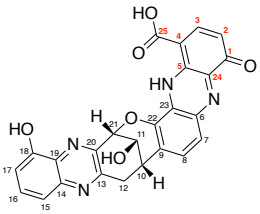

3c

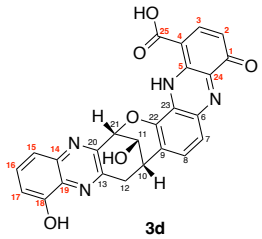

3d

#C	experimental	3a	3b	3c	3d
1	177.5	186.3191612	186.3151648	186.2791594	186.196461
2	112.7	122.9058614	123.0054751	122.7005001	122.685084
3	141.7	148.6349611	148.6309453	149.0347973	148.974656
4		95.69773364	95.99962047	96.11139608	96.03611208
5	145.8	144.1093667	144.149302	142.8541811	142.9474003
6	139.7	136.401506	136.4488048	145.6218934	145.7359069
7	118.6	114.9872504	114.9315029	131.8834472	131.7812212
8	134.2	147.2575679	147.25656	136.1623373	136.1856846
9	119.6	131.4629176	131.558757	141.2783477	141.2729833
10	36.1	43.46971264	43.29241555	44.33196933	44.04878586
11	63.8	71.45794377	71.56064238	71.23359253	71.34251387
12	36.3	42.62511687	41.9416316	42.42533033	41.78381058
13	153.0	163.171447	158.9475585	162.9208978	158.5925722
14	143.3	151.1301781	150.2383982	151.0696286	143.3044372
15	118.3	125.1375945	125.9829244	125.1988149	147.4480002
16	132.1	140.5298167	138.7743398	140.7566621	125.9813062
17	112.5	116.4942616	117.7807299	116.6179475	130.6265019
18	154.2	161.9672228	160.9848475	161.8030599	139.567315
19	133.1	138.1132109	139.0778285	138.2225971	145.8547012
20	147.5	153.1136538	158.144637	153.2273185	158.1442725
21	75.7	83.10310932	83.62732824	82.86960597	83.52308332
22	147.9	160.0044956	160.2009282	147.538456	147.6379964
23	130.5	136.8811227	136.9747636	125.5157641	125.5700443
24		150.2758947	150.288109	152.3871556	152.5058416
25	168.1	177.1081889	177.0630835	176.9615594	176.9935335

#H	experimental	3a	3b	3c	3d
2	6.15	6.523322254	6.518696885	6.576152708	6.570133368
3	8.15	8.395066661	8.389490718	8.449414883	8.439783522
5-NH		6.334038873	6.308389701	6.423494628	6.401311569
7	7.48	7.512277712	7.505062936	8.182641832	8.198610332
8	8.06	8.18021083	8.18138474	8.004643066	8.013054238
10	3.72	3.799704378	3.797931712	3.913105996	3.903698724
11	4.74	5.063227907	6.823142025	5.090374459	5.109508001
11-OH	6.06	1.840038482	1.846622883	1.915782169	1.88521555
12a	3.76	4.127210847	4.172520849	4.206363366	4.229487194
12b	3.30	3.460011221	3.516188621	3.525335139	3.567523139
15	7.36	7.674994432	7.907795805	7.681579701	7.871972881
16	7.61	8.021733356	7.986975207	8.018656759	7.999094782
17	7.05	7.462005602	7.491290718	7.458667591	7.496461105
18-OH	10.62	8.455694483	8.189297965	8.37140546	8.213616272
21	5.66	5.889195503	6.140862644	5.839002106	5.803863207
25-COOH	14.95	14.2071111	14.20481755	14.37783122	14.4105518

DP4+	3a	3b	3c	3d
sDP4+ (^{1}H data)	**50.85%**	0.30%	33.03%	15.82%
sDP4+ (^{13}C data)	11.96%	**88.03%**	0.01%	0.00%
sDP4+ (all data)	**95.76%**	4.17%	0.07%	0.00%
uDP4+ (^{1}H data)	96.87%	0.01%	2.92%	0.02%
uDP4+ (^{13}C data)	46.71%	**53.28%**	0.00%	0.00%
uDP4+ (all data)	99.99%	0.01%	0.00%	0.00%
DP4+ (^{1}H data)	**98.02%**	0.00%	1.92%	0.06%
DP4+ (^{13}C data)	10.64%	**89.36%**	0.00%	0.00%
DP4+ (all data)	**100.00%**	0.00%	0.00%	0.00%

phenazinolin D (**4**)

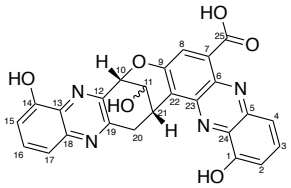

4a: 11*S*
4b: 11*R*

#C	Experimental	4a	4b
1	153.4	161.8935889	161.8393986
2	111.7	117.0236965	117.021487
3	132.5	142.1210829	141.9640165
4	118.0	123.6994264	123.735568
5	139.5	145.2965873	145.5213996
6	137.1	145.9864869	145.9172511
7	128.0	131.5984649	131.2028146
8	127.6	139.5811763	139.6646397
9	151.1	161.5459833	161.4564482
10	76.1	83.30976983	84.10817334
11	62.7	70.97178472	70.41110286
12	146.5	153.6183499	153.585184
13	132.7	138.2525138	137.9223237
14	153.7	162.0862278	161.7594091
15	111.7	116.4137588	116.9693256
16	131.6	140.3312028	141.1879124
17	117.8	124.7816951	125.2529935
18	142.8	150.9910249	150.9684574
19	152.9	163.1339232	162.6909693
20	34.6	40.94216329	45.09935739
21	30.9	38.85437919	39.42901424
22	122.2	133.4216427	132.6286834
23	140.1	146.2977233	147.0729679
24	135.2	140.122786	140.2084766
25	165.5	175.4581723	175.566342

#H	Experimental	4a	4b
1-OH	10.73	8.720506965	8.731076214
2	7.32	7.725364539	7.725846949
3	7.83	8.273720168	8.249074417
4	7.71	7.990623506	7.982198947
8	7.95	8.74303018	8.782121784
10	5.60	5.738032903	5.775616548
11	4.77	5.044941439	4.938066647
11-OH	6.20	1.920671619	1.811346685
14-OH	10.55	8.356546866	8.316322219
15	7.09	7.505636158	7.475349425
16	7.59	8.029018079	8.02852611
17	7.29	7.592122809	7.686879209
20a	3.87	4.257191527	4.402349631
20b	3.42	3.721799854	3.934796005
21	4.85	4.86646167	4.381053076
25-COOH	14.77	15.29143088	15.30880345

DP4+	4a	4b
sDP4+ (^{1}H data)	**98.41%**	1.59%
sDP4+ (^{13}C data)	**65.51%**	34.49%
sDP4+ (all data)	**99.16%**	0.84%
uDP4+ (^{1}H data)	**99.92%**	0.08%
uDP4+ (^{13}C data)	**91.81%**	8.19%
uDP4+ (all data)	**99.99%**	0.01%
DP4+ (^{1}H data)	**100.00%**	0.00%
DP4+ (^{13}C data)	**95.51%**	4.49%
DP4+ (all data)	**100.00%**	0.00%

izumiphenazine A (**5**)

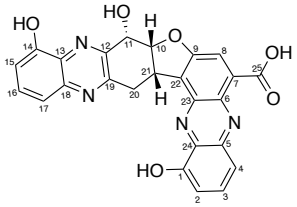

5d: R_1=OH, R_2=H

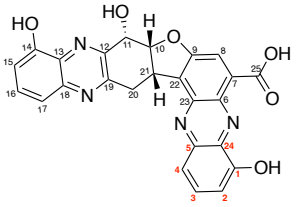

5h: R_1=H, R_2=OH

#C	Experimental	5d	5h
1	153.2	161.56241007	160.26089996
2	111.8	117.26101691	118.87895003
3	132.3	141.95389391	141.59245000
4	118.5	124.06499432	126.95820000
5	139.6	145.38669321	151.15444999
6	137.4	146.34638201	142.87125001
7	130.7	133.24970261	132.89529999
8	121.2	131.86040723	132.22340001
9	158.8	168.86790728	168.98210001
10	88.7	95.17733164	95.20064996
11	71.6	76.24682106	75.91785000
12	149.8	156.01523334	155.86029996
13	131.4	136.92416152	136.82790004
14	153.6	161.37821070	161.15985000
15	111.7	117.69618062	117.70039996
16	130.7	138.98093910	138.62510000
17	118.1	125.56510576	125.60594998
18	142.3	150.73202507	150.86315000
19	153.5	161.97614721	161.72354997
20	33.4	39.25821553	39.39104999
21	39.2	46.92666537	47.01955003
22	124.9	136.13608330	136.68789997
23	138.8	144.73563356	147.92725000
24	135.9	140.55227605	134.93965000
25	165.8	175.29986936	174.87435000
#H	**Experimental**	**5d**	**5h**
1-OH	10.78	8.67536440	6.98404999
2	7.33	7.71320615	7.75645000
3	7.83	8.22474281	8.33045000
4	7.73	7.95374946	8.18750000
8	8.15	8.50439166	8.49915000
10	5.59	6.10105140	6.15045000
11	5.35	5.56766912	5.56925000
11-OH	6.33	4.68310568	4.59149999
14-OH	10.29	7.95192821	7.92355001
15	7.12	7.52720463	7.48965000
16	7.60	7.90039014	7.87960000
17	7.40	7.38244247	7.49375000
20a	4.19	4.19988350	4.34075000
20b	3.69	3.66089112	3.71140000
21	4.84	5.11595998	5.15275000
25-COOH	14.95	15.29522569	14.11585001
DP4+		**5d**	**5h**
sDP4+ (^{1}H data)		**100.00%**	0.00%
sDP4+ (^{13}C data)		**99.81%**	0.19%
sDP4+ (all data)		**100.00%**	0.00%
uDP4+ (^{1}H data)		**98.44%**	1.56%
uDP4+ (^{13}C data)		**98.49%**	1.51%
uDP4+ (all data)		**99.98%**	0.02%
DP4+ (^{1}H data)		**100.00%**	0.00%
DP4+ (^{13}C data)		**100.00%**	0.00%
DP4+ (all data)		**100.00%**	0.00%

izumiphenazine E (**6**)

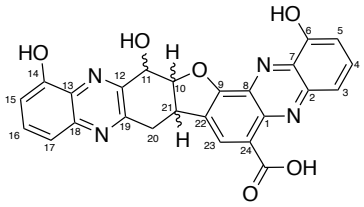

6e: 10*S*,11*R*,21*R*
6g: 10*S*,11*S*,21*R*

#C	Experimental	6e	6g
1	139.0	149.71640000	149.60740000
2	141.7	147.15220000	147.07980000
3	120.3	123.27770000	123.36070000
4	129.8	144.71960000	144.65160000
5	110.9	116.23930000	116.29530000
6	153.5	162.50380000	162.41010000
7	135.0	139.32230000	139.28130000
8			
9	160.2	169.06250000	168.50210000
10	88.3	96.15880000	95.13570000
11	72.3	75.80300000	79.93970000
12	150.4	155.66810000	155.79990000
13	135.0	136.77050000	137.71400000
14	153.2	161.10260000	161.96880000
15	118.5	117.83230000	116.73240000
16	131.1	138.91740000	139.82300000
17	112.2	125.86130000	125.15380000
18	141.6	150.95580000	151.17850000
19	154.0	161.68200000	164.20250000
20	34.0	41.78560000	41.56510000
21	39.5	47.16390000	47.84750000
22	116.6	135.43400000	135.54710000
23	112.6	143.74820000	143.60130000
24			
25	169.7	175.98040000	175.97300000
#H	**Experimental**	**6e**	**6g**
3	7.18	7.84540000	7.85900000
4	7.63	8.24210000	8.25580000
5	7.55	7.53460000	7.55970000
6-OH	10.30	8.42530000	8.47680000
10	5.50	6.28970000	6.28130000
11	5.29	5.60990000	5.80470000
11-OH	6.30	4.71900000	1.96280000
14-OH	10.30	7.89170000	8.24660000
15	7.08	7.43890000	7.37300000
16	7.55	7.88140000	7.90300000
17	7.33	7.61030000	7.58230000
20a	4.09	3.76240000	4.25130000
20b	3.67	3.56380000	3.67910000
21	4.70	4.73900000	4.88680000
23	7.05	9.32440000	9.33810000
25-COOH			

DP4+	6e	6g
sDP4+ (^{1}H data)	**80.41%**	19.59%
sDP4+ (^{13}C data)	30.31%	**69.69%**
sDP4+ (all data)	**64.10%**	35.90%
uDP4+ (^{1}H data)	**89.98%**	10.02%
uDP4+ (^{13}C data)	41.24%	**58.76%**
uDP4+ (all data)	**86.30%**	13.70%
DP4+ (^{1}H data)	**97.36%**	2.64%
DP4+ (^{13}C data)	23.39%	**76.61%**
DP4+ (all data)	**91.83%**	8.17%

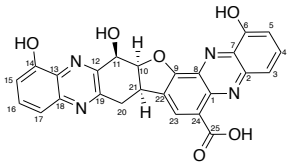

6e

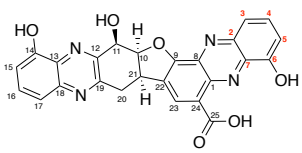

6i

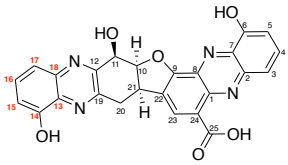

6j

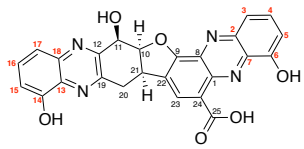

6k

#C	Experimental	6e	6i	6j	6k
1	139.0	149.71640000	146.37596925	149.84670000	146.52285004
2	141.7	147.15220000	149.89226399	147.19240000	149.90150000
3	120.3	123.27770000	127.92955637	123.31210000	128.09454996
4	129.8	144.71960000	140.24013283	144.64200000	140.31074994
5	110.9	116.23930000	120.71727535	116.17880000	120.88549991
6	153.5	162.50380000	159.93776268	162.36650000	159.72170011
7	135.0	139.32230000	136.59853336	139.35930000	136.64850016
8					
9	160.2	169.06250000	170.07810466	168.86120000	170.00555005
10	88.3	96.15880000	96.13680777	95.72410000	95.68014996
11	72.3	75.80300000	75.77791508	75.46740000	75.33409999
12	150.4	155.66810000	156.03798756	159.34900000	159.85519980
13	135.0	136.77050000	136.52612104	138.63700000	138.74950019
14	153.2	161.10260000	160.94796322	161.42150000	161.31195005
15	118.5	117.83230000	117.72091012	117.24310000	117.22955001
16	131.1	138.91740000	138.72742732	139.21900000	139.16020003
17	112.2	125.86130000	125.81952896	124.40550000	124.45065001
18	141.6	150.95580000	150.78884459	148.42920000	148.55155009
19	154.0	161.68200000	162.16062577	157.23730000	157.64034991
20	34.0	41.78560000	41.67654580	40.97440000	40.96770014
21	39.5	47.16390000	47.36912494	47.41970000	47.21899979
22	116.6	135.43400000	135.54620457	135.42890000	135.25925015
23	112.6	143.74820000	143.86555462	143.58420000	144.14194996
24					
25	169.7	175.98040000	175.36253387	175.90740000	175.44144999
#H	Experimental	6e	6i	6j	6k
3	7.18	7.84540000	7.99294990	7.84560000	8.01570000
4	7.63	8.24210000	8.18347749	8.23880000	8.17004999
5	7.55	7.53460000	7.75889773	7.52410000	7.74350000
6-OH	10.30	8.42530000	6.99378627	8.40860000	6.97680001
10	5.50	6.28970000	6.23519318	6.29050000	6.28200000
11	5.29	5.60990000	5.58289252	5.57220000	5.56140003
11-OH	6.30	4.71900000	4.65162558	5.29840000	5.25765005
14-OH	10.30	7.89170000	7.89639847	8.02640000	8.05195001
15	7.08	7.43890000	7.43459773	7.38010000	7.38975001
16	7.55	7.88140000	7.87040134	7.93020000	7.92550001
17	7.33	7.61030000	7.63230730	7.82250000	7.81425002
20a	4.09	3.76240000	3.71960663	3.74700000	3.74715001
20b	3.67	3.56380000	3.53860622	3.60480000	3.60509999
21	4.70	4.73900000	4.72293983	4.73630000	4.70224998
23	7.05	9.32440000	9.32181985	9.33810000	9.35280000
25-COOH					
DP4+		6e	6i	6j	6k
sDP4+ (^{1}H data)		31.46%	0.00%	**68.53%**	0.00%
sDP4+ (^{13}C data)		0.04%	19.56%	0.19%	**80.21%**
sDP4+ (all data)		9.21%	0.19%	**89.59%**	1.01%
uDP4+ (^{1}H data)		26.05%	22.47%	23.98%	**27.50%**
uDP4+ (^{13}C data)		0.65%	22.43%	2.07%	**74.85%**
uDP4+ (all data)		0.64%	19.17%	1.89%	**78.30%**
DP4+ (^{1}H data)		33.27%	0.00%	**66.72%**	0.00%
DP4+ (^{13}C data)		0.00%	6.81%	0.01%	**93.18%**
DP4+ (all data)		2.30%	1.41%	**65.64%**	30.66%